Transactions of the ASME

Journal of Engineering for Power (ISSN 0022-0825) is edited and published quarterly at the offices of The American Society of Mechanical Engineers, United Engineering Center, 345 E. 47th St., New York, N. Y. 10017. ASME-TWX No. 710-581-5267, New York. Second Class postage paid at New York, N.Y., and at additional mailing offices.

CHANGES OF ADDRESS must be received at Society headquarters seven weeks before they are to be effective. Please send old label and new address.

PRICES: To members, $25.00, annually; to nonmembers, $50.00. Single copies, $15.00 each. Add $1.50 for postage to countries outside the United States and Canada.

INDEXED by the Engineering Index, Inc.

Journal of Engineering for Power

Published Quarterly by The American Society of Mechanical Engineers
VOLUME 102 • NUMBER 1 • JANUARY 1980

(*contents continued on page 13*)

C. D. Clower
Supervisor.
Proposal Department.
Mem. ASME

F. E. Snider
Senior Consulting Mechanical Engineer.

J. F. Strickland
Process Section Leader.

McDermott Hudson Engineering
P.O. Box 36100
Houston, TX 77036

A System Approach to the Evaluation of a Gas Turbine Driven Compressor

A systematic, objective method for comparing bids on gas turbine driven compressor systems has been developed. In the process industries, gas turbines are evaluated in the context of the driven machinery. Due to the inherent fluctuations in the flow of process streams, a vendor's complete package must be studied over a wide range of capacities and operating conditions. In view of the multiple possibilities of equipment suited for a process, it is necessary to systematize the evaluation of vendor information. By comparing the available packages according to this method, the purchaser can more confidently select the equipment appropriate to a particular process and its project constraints.

Contractors are continually evaluating bids on a wide range of equipment. Obviously, most of the equipment is mechanically sound and strongly backed by vendor service, so the contractor must select the equipment best suited to the industrial application being considered.

Two major technical considerations dominate the contractor's evaluation: the equipment's mechanical qualities, and its range of operating possibilities. However, the less technical questions of cost-effective analysis, delivery schedule integrity, and vendor servicing also must weigh heavily in making a defensible choice. For the sake of consistency, most engineering firms develop a systematic method to organize and evaluate the pertinent information.

Before the evaluation can begin, the contractor's engineers must calculate the necessary design parameters and forward them to qualified vendors. Cognizant of these values and the peculiarities of the client's application, each vendor offers his most efficient, reliable system, and sends the equipment's specifications to the contractor.

Next, in collaboration with the client, the contractor develops an evaluation philosophy. It encompasses such information as the compatibility and operating flexibility of the components, a history of system reliability and vendor service, unit responsibility, and the desired delivery schedules. With these criteria settled, the contractor is ready to implement this philosophy within a workable format.

Decision Tree

Similarities and dissimilarities, critical to the client, are brought into perspective by constructing a decision tree (see Fig. 1). The branches of the tree further articulate the concerns of the client, progressing from a general difference to the specific offerings of the vendors. For example, if the client insists on a single shaft heavy in-

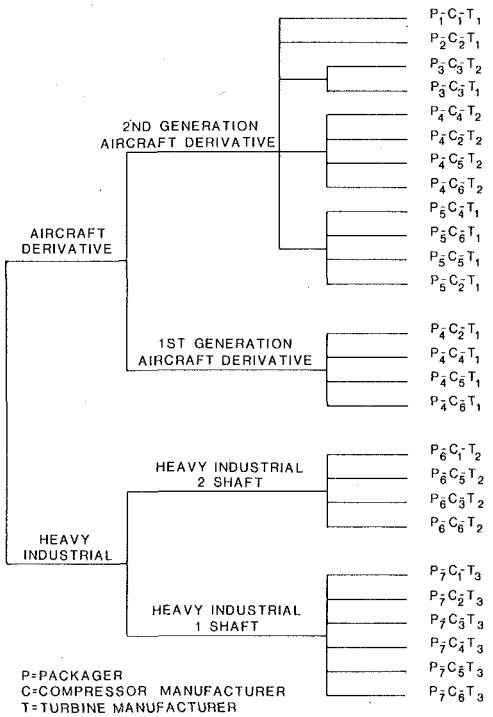

Fig. 1

Contributed by the Gas Turbine Division and presented at the Gas Turbine Conference, San Diego, California, March 12–15, 1979 of THE AMERICAN SOCIETY OF MECHANICAL ENGINEERS. Manuscript received at ASME Headquarters November 6, 1978. Paper No. 79-GT-3.

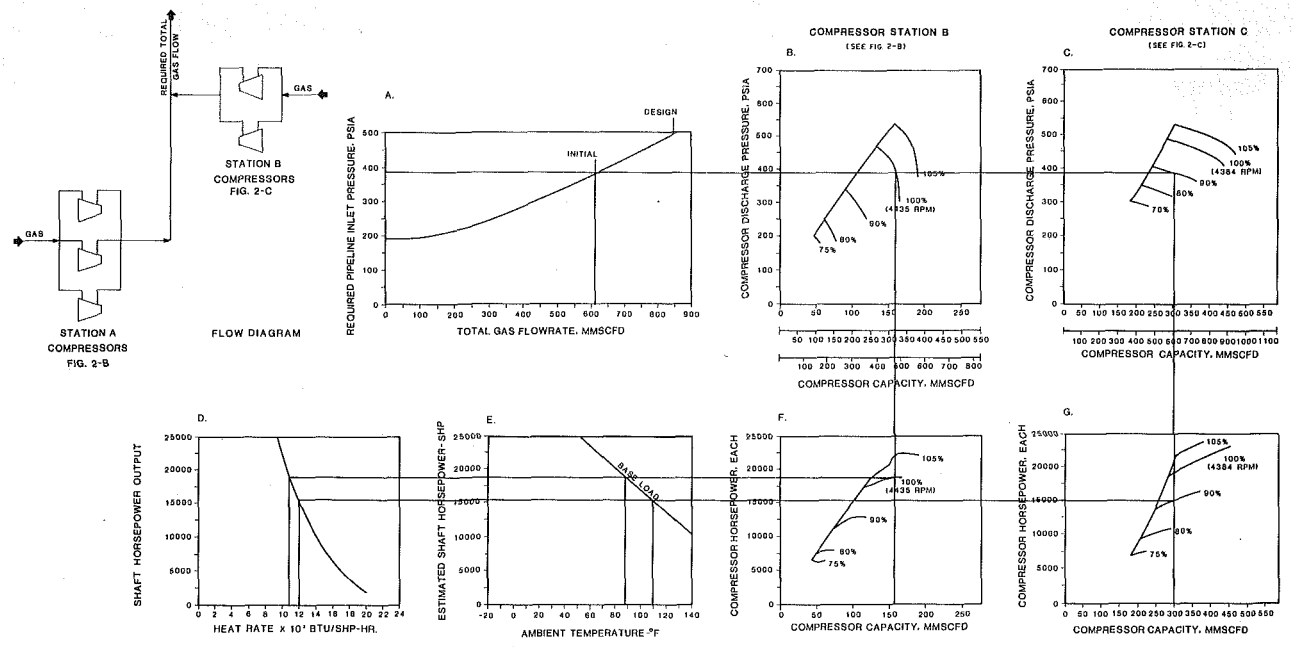

Fig. 2 (*a–g*)

dustrial turbine, or only a second generation aircraft derivative turbine, the contractor can quickly point out the consequences of implementing such a decision.

Obviously, the decision tree can only offer a highly condensed, superficial comparison of dominant factors concerning the equipment itself. Vendors submit detailed, technical descriptions, and this voluminous data can be aptly separated into three distinct categories: process data, gas turbine data, and compressor data. The last two concern the equipment's mechanical qualities, while the first concerns its performance variables. The overlap between these two almost artificial distinctions can be bridged by the use of a simple graphic technique that also recognizes economic and ambient variables.

Graphic Method

The system must simulate the desired process on paper before any equipment can be considered for purchase. All the vendors supply several characteristic curves for their systems, and by simultaneously using these curves, one can relate process variables to physical and economic constraints [1].

Fig. 2 relates the mechanical abilities of the machinery to the process demands for a compression facility and the pipeline hydraulics of an oil-associated gas-gathering system. After leaving the gas-oil separators, the associated gas flows to the centralized gas-compression facility, where gas turbine-driven compressors deliver gas at a constant pressure by varying the compressor speed in response to the gas flow oscillations.

Fig. 2(*a*) shows the calculations of the pressure requirements for a range of gas volumes. The required discharge pressure and total flowrate from the two compressor trains serving the pipeline are represented by the straight lines meeting on the curve. The conventional capacity versus pressure curves, Fig. 2(*b*) and 2(*c*), depict the operating envelopes for the compressors. By multiplying the capacity scale by the desired number, an engineer can easily represent more units.

It is important to recognize that once a system is purchased, it becomes a constraint on the process, which makes a wide operating envelope highly advantageous. Obviously, a turbine working well below its capacity possesses a highly desirable flexibility.

Directly below these curves, the horsepower requirements for the compressors are shown in terms of compressor speed and capacity (Figs. 2(*f*) and 2(*g*)). The horsepower supplied by the gas turbine is often limited by metallurgical, atmospheric, and financial constraints. Transposing the horsepower demands onto Fig. 2(*d*) and 2(*e*) helps to address these concerns. With higher ambient temperatures, the resulting lower density of air can hinder horsepower production. In the case illustrated, however, the ambient temperature provides no threat to the system. Temperatures must reach at least 60° F before the gas turbine will experience difficulties in delivering the needed horsepower.

Costs ($1,000'S)	No. 1	No. 2	No. 3	No. 4
Initial Purchase	1,565	1,600	1,930	2,000
Installation	1,000	750	1,000	750
Total Capital Costs	2,565	2,350	2,930	2,750
Turbine	2HWI	2LWI	3LWI	1LWI
Heat Rate Btu/hphr	10,800	9,800	9,042	9,050
*Horsepower	8,800	9,042	9,430	8,900
First year fuel	1,521	1,417	1,364	1,288
Maintenance	360	360	540	360
Net present value of project after 5 years	10,530	9,795	10,290	9,500
	No. 4	No. 2	No. 3	No. 1

HWI—Heavy weight industrial turbine
LWI—Light weight industrial turbine
*Horsepower is required, not what is available, because of compressor efficiency

Fig. 3

The heat rate curve, Fig. 2(*d*) is a measurement of the ever-increasing fuel costs. Often, lower maintenance and fuel costs can help discount the seemingly large price difference that discourages the more expensive purchase.

A five year cost-effective analysis can dispel any misconceptions about costs. Fig. 3 shows how a system study for one client produced startling results. In this somewhat extreme case, the initially most expensive purchase becomes the most economical system after five years, due to its relative fuel economy. Initial costs represent only a single element of a client's investment, and so both contractors and clients should be wary of describing the least expensive purchase as the most economical system; an easy way for contractors to cut construction costs at the expense of the owner.

Tabulations for Easy Comparison

The contractor can simplify his evaluation by sending the same formatted sheets to all vendors. The information is then tabulated into the three previously mentioned categories.

In the gas turbine section, details about the machine's parts and ratings, and the history of both the machine and manufacture, are provided for the client within discrete divisions. Table 1 shows the general layout of this section, which includes almost 200 elements of information; an excerpt from the gas turbine section is shown in Fig. 4.

Compressor Data

The layout of the compressor data section is similar. Technical data on the equipment and the equipment's performance by stage and by system are tabulated for quick location and comparison, as seen in Fig. 5. Of course, interpreting these data requires a technical understanding of the machinery; however, the interested engineer should have no difficulty locating descriptive information on the equipment [2].

Process Data

Each vendor calculates the package's process variables for the compressor, vessels, coolers, and piping. These data are recorded either summarily, or by stage, in the process data section, in a format similar to the one used in the other two sections. For the compressors, the contractor's calculations are presented alongside the vendor's calculations, to reveal and highlight any critical disagreement. The equipment data may be part of the vendor supplied information or contractor's estimate. At any rate it is an important item (oil cooler size, scrubber size, gas cooling heat load, fuel gas treatment, etc.) in total installed cost of the system.

Table 1

I Design performance requirements site conditions and requirements
II Operating experience (a history of the proposed gas turbine)
III Site available ratings (iso horsepower)
IV Maintenance—A technical summary of the units equipment, service (location)
V Manufacturing—Important locations and the manufacturer's history

VI Instrumentation Evaluation—Control systems instruments for the whole package

Timing

The contractor always receives a proposed schedule of a vendor's work. It is convenient to put all of these schedules in one section, appropriately called the delivery data section, to compare and evaluate the quoted delivery dates. A discussion of the integrity of each of the delivery dates should be included to identify the exceedingly optimistic ones.

Usually, the contractor presents a construction and delivery guideline called a "Preliminary Schedule of Critical Items" (Fig. 6). It works as a reference frame, its delivery data being used as the standard for comparing the vendors.

Conclusion

With all this information assembled and in view, the superior system in terms of the chosen evaluation philosophy should be clearly

4.2 REPAIR	BID 1	BID 2	BID 3	BID 4
4.2.1 FIRE HOURS TO FIRST HOT SECTION INSPECTION	4000	9000	15.000	INSPECTION REQUIRED EVERY 1 - 2 YEARS
4.2.2 FIRE HOURS TO SECOND HOT SECTION INSPECTION	8000	18.000	40.000	INSPECTION REQUIRED EVERY 1 - 2 YEARS
4.2.3 FIRE HOURS TO THIRD HOT SECTION INSPECTION	12.000	27.000	75.000	INSPECTION REQUIRED EVERY 1 - 2 YEARS
4.2.4 NO. OF MANHOURS FOR HOT SECTION INSPECTION	3	80	4	80
4.3 FIRING HOUSING				
4.3.1 NORMAL TEMPERATURE TO POWER TURBINE °F	1100	1247	924	1240
4.3.2 FIRING TEMPERATURE °F	1600	1800	1634	1750
4.3.3 TRIP FIRING TEMPERATURE °F	1795	1830	INFORMATION NOT SUPPLIED BY VENDOR	1830
4.3.4 NORMAL STARTING TEMPERATURE °F	350 IN 10 SEC	600	INFORMATION NOT SUPPLIED BY VENDOR	INFORMATION NOT SUPPLIED BY VENDOR

Fig. 4

1.2 PERFORMANCE, STAGE II	BID 1	BID 2	BID 3	BID 4
1.2.1 P1, PSIA	240.8	216	143	340
1.2.2 P2, PSIA	1030	597	372	1061
1.2.3 T1 °F	120	130	120	122
1.2.4 T2 °F	340	282	273	333
1.2.5 K, CP/CV	1.212	1.931	1.20	1.16
1.2.6 Q, CAPACITY IN MMSCFD AT 14.7 PSIA, 60 °F	11.67	12.4	18.75	17.5
1.2.7 ICFM	526	643	1444.6	600
1.2.8 W, WEIGHT FLOW LB./MIN.	500.01	529	800	781
1.2.9 POLYTROPIC HEAD, FT. LB./LB.	59.235	42.560	40.200	49.375
1.2.10 POLYTROPIC EFFICIENCY %	70.3	70.4	74	70.1

Fig. 5

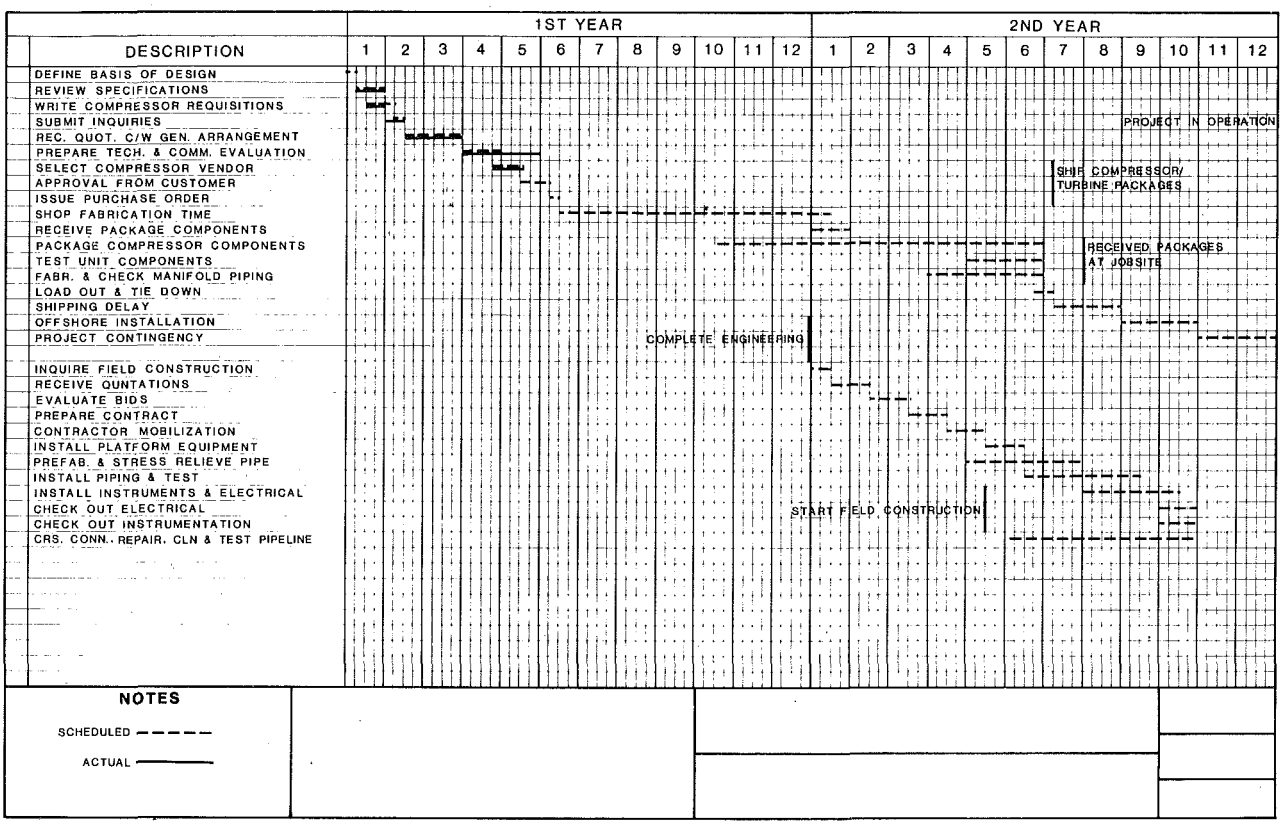

Fig. 6

discernable. The complete evaluation is presented to the client with a recommendation for the purchase of equipment. Using this method, the contractor can feel confident that all of the information has been objectively organized, and that the equipment has been scrutinized in detail and as a total, performing system.

Acknowledgment

The authors wish to acknowledge the services of Mr. Peter Mims for his aid in organizing and writing the paper.

References

1 Massey, J. R., "Installation of Large Rotating Equipment Systems, A Contractor's Comments," Fifth Turbomachinery Symposium, Texas A&M University, College Station, Texas, *Oil and Gas Journal,* Vol. 75, No. 8, Feb. 21, 1977, pp. 73–82.

2 Boyce, M. P., "How to Achieve Online Availability of Centrifugal Compressors," *Chemical Engineering,* Vol. 85, No. 13, June 5, 1978, pp. 115–127.

A. Schäffler
Motoren- und Turbinen-Union,
München GmbH,
Dachauer Str. 665,
8000 München 50,
Germany

Experimental and Analytical Investigation of the Effects of Reynolds Number and Blade Surface Roughness on Multistage Axial Flow Compressors

The general effect of Reynolds Number on axial flow compressors operating over a sufficiently wide range is described and illustrated by experimental data for four multistage axial compressors. The wide operating range of military aircraft engines leads in the back stages of high pressure ratio compression systems to three distinctly different regimes of operation, characterized by the boundary layer conditions of the cascade flow:

- *laminar separation,*
- *turbulent attached flow with hydraulically smooth blade surface,*
- *turbulent attached flow with hydraulically rough blade surface.*

Two "critical" Reynolds Numbers are defined, the "lower critical Reynolds Number" below which laminar separation occurs with a definite steepening of the efficiency/Reynolds Number relation and an "upper critical Reynolds Number" above which the blade surface behaves hydraulically rough, resulting in an efficiency independant of Reynolds Number. The permissible blade surface roughness for hydraulically smooth boundary layer conditions in modern high pressure ratio compression systems is derived from experimental data achieved with blades produced by grinding, electrochemical machining and forging. A correlation between the effect of technical roughness and sand type roughness is given. The potential loss of efficiency in the back end of compression systems due to excessive blade roughness is derived from experimental results. The repeatedly experienced different sensitivity of front and back stages towards laminar separation in the low Reynolds Number regime is explained by boundary layer calculations as a Mach Number effect on blade pressure distribution, i.e. transonic versus subsonic flow.

1 Introduction

During the development of a 70 kN (15000 lb) thrust class three-shaft military bypass engine the MTU designed core engine compressors underwent a considerable amount of high altitude testing. A large portion of the Reynolds Number range encountered within the flight envelope was covered with typical core engine compressors which do not only encounter the usual low Reynolds Number problem but also the roughness problem at high Reynolds Numbers. Testing was done with a three-stage intermediate pressure compressor, a five-stage high pressure research compressor and two modules of the six-stage high pressure compressor. The five-stage research compressor was tested at two different blade surface roughness levels and the six-stage units with standard production blades as well as reworked rotor blades after foreign object damage. All compressors have a typical Mach Number level around 1.1–1.05 at rotor 1 tip section.

The high pressure ratio of the engine above 22 in combination with a very high turbine entry temperature and a bypass ratio around 1.25 result in small blade dimensions in the core engine compressors which are typical for turboshaft engines in the 2500 kW power class as the T 64 engine. The blades of the last stage of the high pressure compressor are of the size of a dime.

Reynolds Numbers of the rotors are around 1.1×10^6 at sea level take off conditions, based on chord length and relative inlet velocity in the mid span section.

As usual, development testing was done at atmospheric inlet conditions at a considerably lower than design Reynolds Number level, about 35 percent and 50 percent for HPC and IPC respectively. To assure performance at low and high Reynolds Number levels variable inlet pressure testing was accomplished at the altitude test facility of Stuttgart University, which consists of a closed circuit test chamber where inlet pressure can be varied from 5–270 kPa. The results ob-

Contributed by the Gas Turbine Division and presented at the Gas Turbine Conference, San Diego, California, March 12–15, 1979, of THE AMERICAN SOCIETY OF MECHANICAL ENGINEERS. Manuscript received at ASME Headquarters November 6, 1978. Paper No. 79-GT-2.

tained there yielded an improved insight into the Reynolds Number behavior of axial flow compressors when tested over a sufficiently large range. This applies specifically to high pressure stages of modern high pressure ratio engines.

Fig. 1 shows the Reynolds Number index for a high pressure compressor of a two or three-shaft engine in the flight envelope of a typical modern Mach 2 fighter aircraft. The Reynolds Number varies about 14 to 1. In Fig. 1, three important regimes are denoted:

- the high altitude, i.e., low Reynolds Number regime, where laminar separation occurs at least in the front stages resulting in reduced flow and efficiency levels as well as stall margin,
- the intermediate range with turbulent attached boundary layer flow and hydrodynamically smooth blade surfaces,
- the low altitude, i.e., high Reynolds Number regime where the middle and back stages of high pressure ratio compression systems experience turbulent attached boundary layer flow with hydrodynamically rough blade surfaces.

General experience with multistage axial compressors shows the following behavior when tested over a wide Reynolds Number range:

- mass flow increases steadily with Reynolds Number up to the choking condition in the blade passage.
- surge line is essentially unaffected by Reynolds Number until severe laminar separation occurs at low Reynolds Number $<10^5$.
- polytropic efficiency varies in distinct slope changes depending on the specific boundary layer flow conditions.

Fig. 2 shows schematically the effect of the boundary layer conditions on the efficiency/Reynolds Number relationship of axial flow compressors at design point operation. There are three distinctly different regimes, divided or marked by a lower and an upper critical Reynolds Number, namely the laminar separation boundary and the surface roughness boundary. The expression critical is used for the

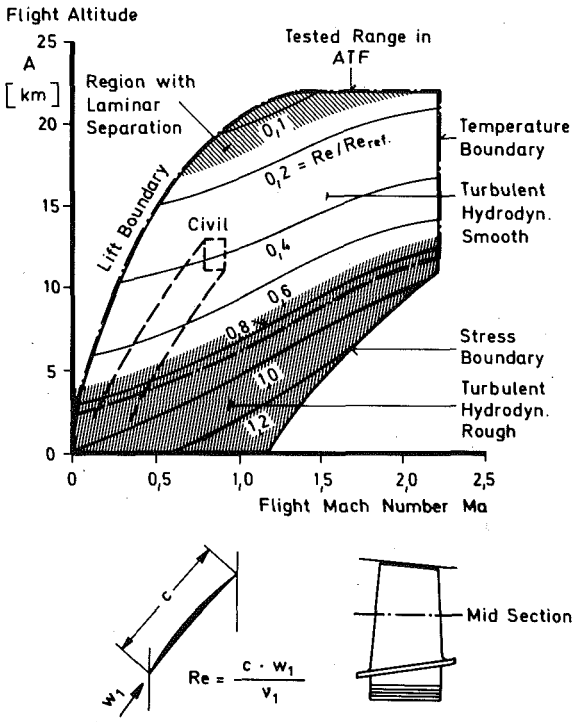

Fig. 1 Relative Reynolds Number of a high pressure compressor within the flight envelope

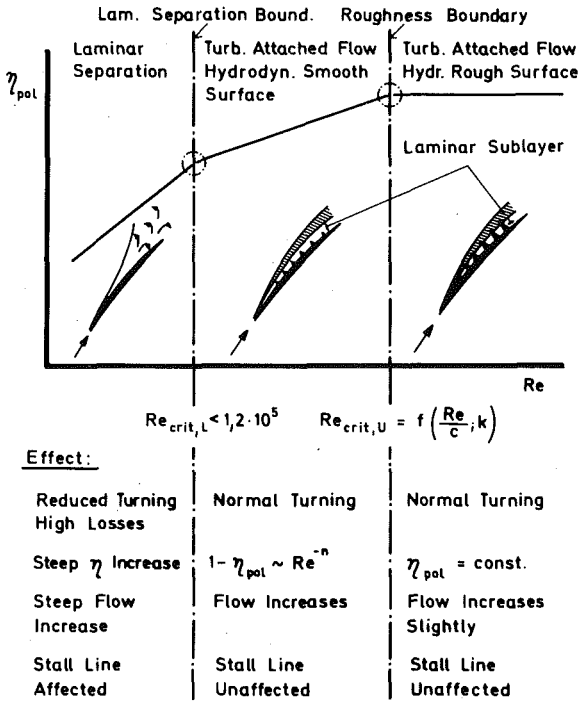

Fig. 2 Effect of boundary layer condition on compressor behavior

Nomenclature

a = average distance between roughness peaks, m
A = flight altitude, km
c = mid span chord length, m
H = specific work, $\frac{\text{J}}{\text{kg}}$
i = incidence angle, deg
k = roughness height, definition Fig. 11, μm
ks = sand type roughness height, μm
lm = roughness measuring length, mm
m = mass flow, kg/s
Ma = Mach Number
n = exponent of efficiency/Reynolds Number relation
N = rotational speed, 1/s
p = pressure, kPa
Ra = arithmetic average roughness; identical to AA or CLA, μm
Re = Reynolds Number
T = temperature, K
Tu = turbulence level
v = air velocity, m/s
w = air velocity relative to cascade, m/s
x = length coordinate, m
y = roughness height coordinate, m
z = number of stages
Δ = change of parameter
η = efficiency
π = total pressure ratio
ν = kinematic viscosity, m^2/s

Subscripts

a = axial component
is = isentropic
f = individual stage
k = technical roughness
ks = sand type roughness
crit, 1 = lower critical Reynolds Number
p = maximum permissible roughness for hydrodynamically smooth boundary layer flow
pol = polytropic
ref = reference condition
t = total or stagnation condition
crit, u = "upper" critical Reynolds Number
1 = entry to cascade

Superscripts

$-$ = arithmetic average

notation of a clear change in behavior. The schematic sketches in Fig. 2 describe the basic boundary layer flow conditions. Entering the picture from the left the laminar separated flow regime can be seen which means the boundary layer stalls in laminar state, thereby degrading the turning and drag characteristics of the cascades fundamentally. This regime is always characterized by a very steep efficiency versus Reynolds Number slope and can hardly be treated analytically with present methods. Sufficient experimental knowledge is available where the lower critical Reynolds Number must be expected.

The intermediate regime is characterized by turbulent attached boundary layer flow with hydrodynamically smooth blade surfaces. This is the generally experienced normal field of operation with clear conditions. Efficiency follows similar to flat plate flow a power law relation with exponents in the range of $n = 0.05$–0.2 depending on the Mach number level as well as the mean stage aspect ratio. In this range good performance predictability was encountered using the correlation presented by Wassel [1]. If the Reynolds Number is increased sufficiently, every compressor will meet a second critical condition manifesting itself in a curl over of the efficiency/Reynolds Number relation towards constant efficiency within a narrow Reynolds Number band namely the roughness boundary or upper critical Reynolds Number. This condition is met when the blade surface roughness elements protrude the laminar sublayer of the turbulent boundary layer. Efficiency becomes independent of Reynolds Number as does the friction coefficient in flow over rough flat plates. This behavior is first encountered in the high pressure stages of modern engines, which work in low kinematic viscosity air. The roughness boundary presents a serious performance limitation to all low level flight cases.

The potential efficiency gains in the high pressure turbomachinery components due to the high Reynolds Numbers cannot be verified due to insufficient blade surface quality available by present production methods.

2. Presentation of Experimental Results

Testing of intermediate and high pressure compressors followed a two way approach.

- normal performance characteristics at various inlet pressure levels,
- inlet pressure variation at fixed throttle setting and constant nondimensional speed at the design point.

Fig. 3 shows the overall characteristic of the intermediate pressure compressor at three levels of Reynolds Number ranging from 1.4×10^5 to 7.6×10^5. The compressor behaves normally over the tested range, the boundary layer flow is of the turbulent attached type with hydrodynamically smooth blade surface roughness. Testing was not extended to pressures low enough to experience laminar separation nor high enough to reach the roughness boundary; the latter was prevented by power limitations of the test plant.

A more interesting result was obtained with a six-stage high pressure compressor unit—nominated HPC "B"—equipped with a high percentage of reworked rotor blades after foreign object damage was experienced in a flight engine.

Fig. 4 shows the performance map together with the main type of blade rework which was primarily concentrated on the leading edge of the three front rotors, covering about 30 percent of the blade height of about 25 percent of the blades. The reprofiling resulted in rather blunt leading edges deviating considerably from an aerodynamicist's impression of a proper leading edge shape. The compressor experienced all three flow regimes described on Fig. 3 within the tested Reynolds Number range of 10^5–8.4×10^5. The shaded area on Fig. 4, i.e., Re = $(2$–$5) \times 10^5$ marks the turbulent attached flow with smooth blade surfaces. Above that Reynolds Number efficiency is virtually constant and below 2×10^5 a steep decrease in all performance parameters due to premature laminar separation can be seen. The various ranges of operation of that unit become more clearly evident in Fig. 5 where change of polytropic efficiency is plotted against Reynolds Number (triangular symbols). The compressor is operated at its design point which for all practical purposes coincides with the peak

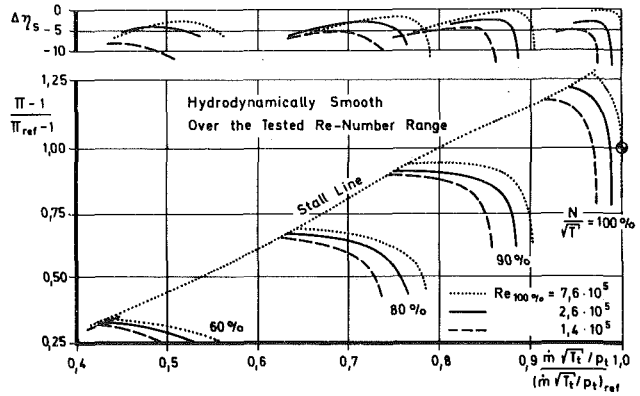

Fig. 3 Effect of Reynolds Number on performance of a three-stage intermediate pressure compressor

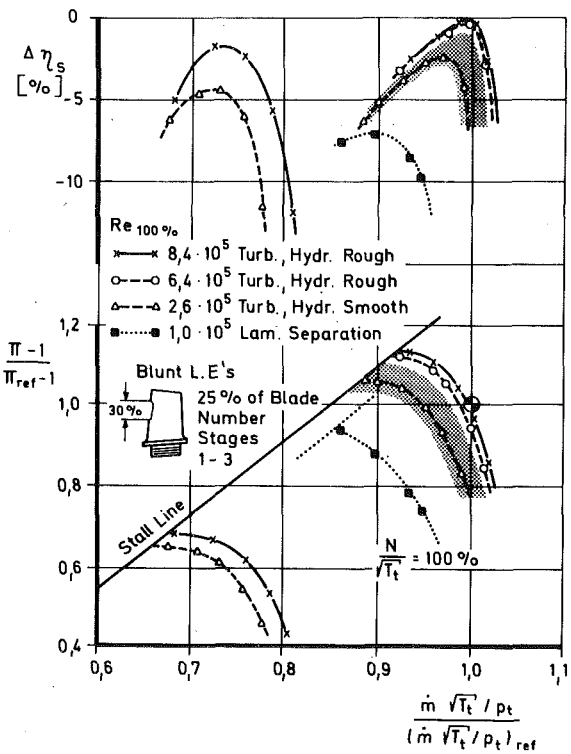

Fig. 4 Effect of Reynolds Number on performance of a six-stage high pressure compressor

efficiency contour. As already seen on the performance map a steep deterioration of efficiency is experienced below Re = 2.2×10^5 and constant efficiency above 5×10^5 Reynolds Number. Between these two boundaries a steady power law $1\text{-}\eta_{pol} \sim \mathrm{Re}^{-n}$ increase can be seen with an exponent of 0.10 which coincides with the prediction given in [1].

In the same picture a second test result is drawn from the same six-stage unit equipped with normal production type blades nominated HPC "A" (circular symbols).[1] General efficiency level was about 0.5 percent higher, otherwise a very similar behavior can be seen in the intermediate and high Reynolds Number regimes. No kink was met at low Reynolds Numbers within the range tested, which means that the lower critical Reynolds Number for standard production blades is at $\mathrm{Re}_{crit,1} \leqslant 10^5$. The curl over bands in the roughness boundary regions are quite narrow and have an almost kink type

[1] Note that curves "A" and "B" have different ordinate origins to avoid interference.

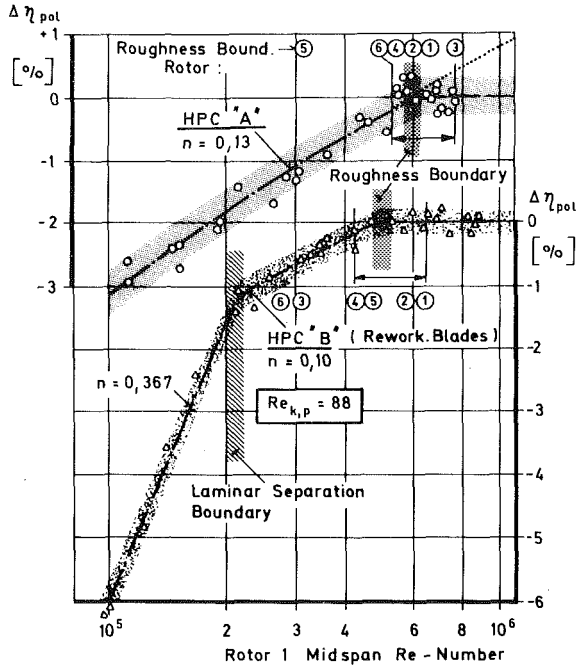

Fig. 5 Effect of Reynolds Number and surface roughness on polytropic efficiency of two six-stage high pressure compressors

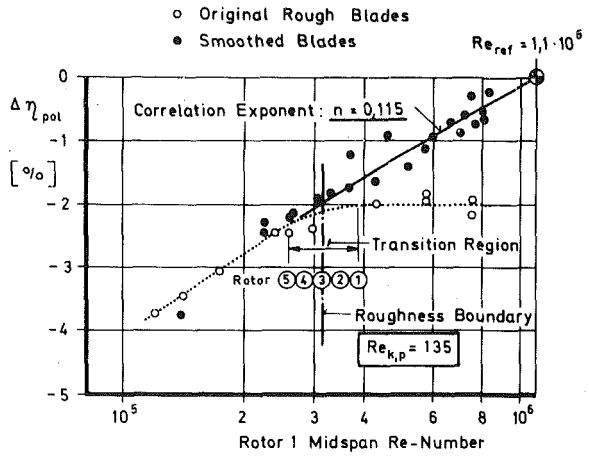

Fig. 6 Effect of Reynolds Number and surface roughness on polytropic efficiency of a five-stage high pressure compressor

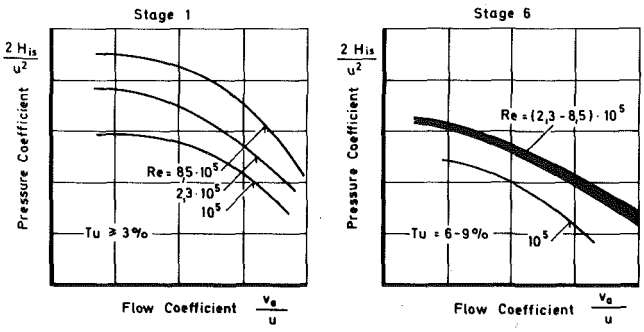

Fig. 7 Effect or Reynolds Number on stage characteristics of a six-stage high pressure compressor

character. The most remarkable result of this test is the strong effect of the unsatisfactory blade leading edge rework on the lower critical Reynolds Number. There was only a surprisingly small deterioration of peak efficiency noticed at atmospheric inlet conditions and the danger existed to draw conclusions on the general behavior of heavily reworked blades also in the low Reynolds Number regime if no altitude tests would have been done. A third test result obtained with a five-stage research high pressure compressor at two different levels of blade surface roughness is shown in Fig. 6. The compressor was built up of rotor blades produced by grinding and stator vanes manufactured by forging and etching. In the original state the rotors had a rather consistent medium roughness and the stators were of an excessive 15–20 μm roughness due to an erroneously applied treatment.

The open circles in Fig. 6 denote the first test result obtained with the rough blades where a clear curl over at a very low Reynolds Number of about 3.1×10^5 can be seen. In this test the stators became hydrodynamically rough at very low Reynolds Number. The distinct bend over towards constant efficiency is exclusively determined by the rotors. This is quite understandable for the high reaction design which concentrates about ¾ of the total losses on the rotors. After smoothing the blades by a mechanical polishing process a steady increase of polytropic efficiency with Reynolds Number was experienced up to the highest level tested, as denoted by the full circle symbols. This test is the direct proof that roughness is the genuine reason for the curl over towards constant efficiency at high Reynolds Number levels. As in case of the six-stage unit "A" no signs of laminar separation are noticed down to 1.2×10^5 Reynolds Number.

3 Analysis and Interpretation of Test Results

3.1 Low Reynolds Number Regime with Laminar Separated Flow. It is generally accepted that compressor behavior is hardly predictable in the very low Reynolds Number regime due to the significant changes of cascade turning characteristics and the resulting mismatching of multistage machines. Nevertheless an attempt is made to give an explanation for the interesting fact that in all the tests the front stages of the high pressure compressors showed a markedly stronger sensitivity to Reynolds Number changes than the back stages, in spite of almost constant Reynolds Number through the compressor. The intermediate pressure compressor on the contrary appeared to be more or less equally affected in all stages.

Fig. 7 shows the nondimensional characteristics of stages one and six of HPC "B" equipped with reworked rotor blades as an especially drastic but otherwise typical example. While stage one exhibits a steady decrease of the isentropic work coefficient with decreasing Reynolds Number, stage six does not show any reaction until most probably the preceding stator drops below its critical Reynolds Number resulting in reduced flow turning. The break down of the front stages is of course more detrimental to overall performance due to the resulting mismatching effects.

Initially the higher Reynolds Number sensitivity of the front stages was attributed to the lower turbulence level at compressor inlet (Tu = 3–4 percent) in the closed test chamber compared with 7–9 percent typical for compressor exit stages, as measured by Kiock [2].

Boundary layer calculations with the method of Rotta [3] revealed a very small effect of turbulence level on cascade flow between Tu = 3–8 percent, whereas a strong effect was indicated between 0.5–3 percent, as is confirmed by numerous cascade measurements.

Attention was then paid to the specific blade pressure distribution over the double circular arc profiles for transonic and subsonic flow as happens from front to back end of the high pressure compressor.

As shown schematically in Fig. 8, the subsonic and transonic flow over a DCA profile produces totally different pressure distributions around the suction surface. Whereas in subsonic flow a significant velocity peak can be observed at higher incidences stimulating favourable conditions for laminar/turbulent transition, transonic flow is characterized by a flat short supersonic expansion which keeps the boundary layer laminar. This is followed by a normal shock, the pressure rise of which cannot be sustained by the laminar boundary layer without separation at low Reynolds Numbers. Pressure distribution calculations were done using the extended singularity method of Fottner [4] and showed for increased incidences the typical suction peaks for subsonic flow while in the low transonic flow regime hardly

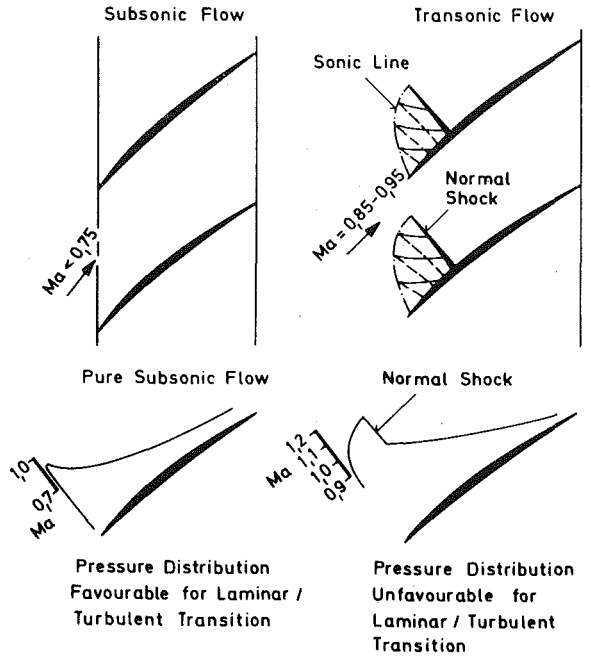

Fig. 8 Effect of Mach Number on blade velocity distribution

any difference in the pressure distribution could be found on the forward portion of the blade suction surface.

Fig. 9 shows the results of appropriate boundary layer calculations for subsonic flow. The position of the points of instability as well as the laminar separation points. i.e., the beginning of laminar/turbulent transition, is plotted as a function of relative chord length and Reynolds Number for two incidence angles. For high Reynolds Numbers the transition occurs within a very short distance. At lower Reynolds Numbers below about 3×10^5 laminar separation bubbles of increasing length are formed which can cover up to 25 percent of chord length at $Re = 5 \times 10^4$ even at very high turbulence levels as proven by newer cascade measurements of Kiock [2]. The length of these laminar separation bubbles cannot be determined by presently available boundary layer calculation methods, so that only those trends which correspond to the aforementioned cascade measurements are drawn in.

When the boundary layer calculations for the two incidence angles are compared it can be seen, that at high incidence angle the points of instability and laminar separation merge almost to a single line and move to a much forward position as a consequence of the steep adverse pressure gradient following the velocity peak at the leading edge. In the transonic flow as given in Fig. 10 two essential differences can be observed against the subsonic case:

- The points of instability and laminar separation are practically independent of incidence due to the very similar flow over the front part of the suction surface.
- The point of laminar separation is followed in a very short distance by the normal shock with a steep pressure rise.

It is easy to imagine that such an unstable flow region as a laminar separation bubble seen in noticeable size at $Re < 1.5 \times 10^5$ can hardly withstand a normal shock without changing the cascade turning characteristics.

The favorable performance demonstrated by innumerable successful transonic compressors is quite understandable at Reynolds Numbers above $(1.5–2) \times 10^5$ because, in that range, a quick enough transition into a turbulent boundary layer can be expected after the laminar separation point. This enables the boundary layer to cope with the pressure rise of the normal shock. The obvious ability to operate satisfactorily down to $Re = 10^5$ is rather a positive surprise.

3.2 Intermediate Reynolds Number Range: Turbulent Attached Flow with Hydrodynamically Smooth Blade Surfaces. Within the normal operating range, i.e., the Reynolds Number regime

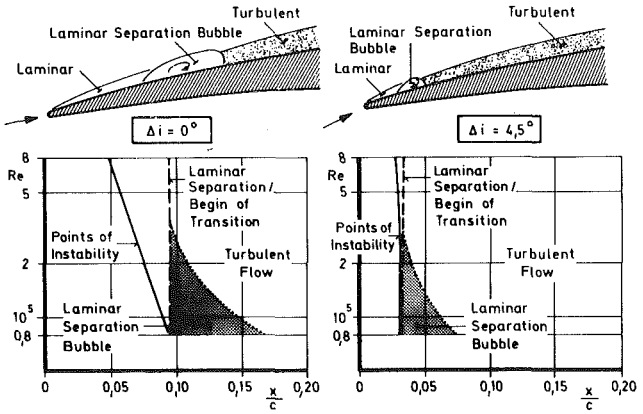

Fig. 9 Effect of Reynolds Number and incidence angle on boundary layer condition at subsonic flow $Ma_1 = 0, 7$, $Tu = 4$ percent

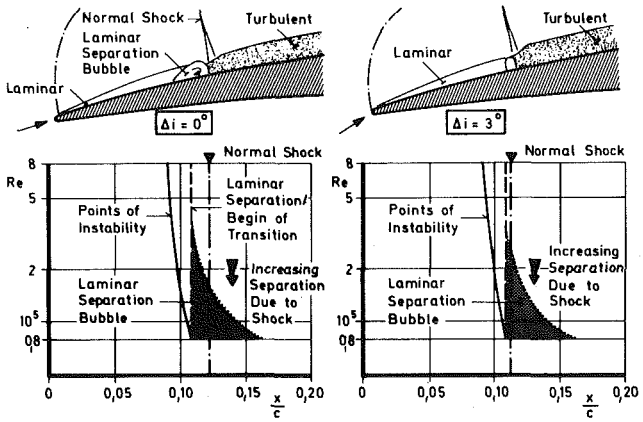

Fig. 10 Effect of Reynolds Number and incidence angle on boundary layer condition at transonic flow $Ma_1 = 0, 9$, $Tu = 4$ percent

Table 1 Comparison of experimental and predicted exponent *n*

Compressor	IPC (three-stg)	Research HPC (five-stg)	HPC "A" (six-stg)	HPC "B" (six-stg)
$n_{exper.}$	0.15	0.115	0.13	0.10
$n_{pred.Wassel}$	0.12	0.11	0.10	0.10

between the laminar separation boundary or lower critical Reynolds Number and the roughness boundary or upper critical Reynolds Number polytropic efficiency follows a power function:

$$\frac{1-\eta_{pol}}{1-\eta_{pol,ref}} = \left(\frac{Re}{Re_{ref}}\right)^{-n}$$

This regime covers a wide portion of the operating regime of the low and intermediate pressure stages. Quite good agreement was found between the experimentally obtained exponent n and the Wassel prediction [1] for all compressors tested. The exponent appeared to be valid also at part speed down to 80 percent $N/\sqrt{T}$. In Table 1, a comparison between the predicted and the experimentally obtained exponent is given.

3.3 High Reynolds Number Regime: Turbulent Attached Flow with Hydrodynamically Rough Blade Surfaces. At Reynolds Numbers higher than the upper critical Reynolds Number boundary layer flow is of the turbulent attached type with surface roughness elements protruding the laminar sublayer. As shown in Figs. 5 and 6 polytropic efficiency is independent of Reynolds Number in this regime and exclusively a function of the roughness itself, i.e., the characteristic roughness element shape, distance and height.

The analysis of test results confronts one with the fact that very little information is available in open literature on the behavior of

typical blade surfaces as produced by the usual manufacturing processes as grinding, forging and electrochemical machining.

3.4 Criterion for Hydrodynamically Rough Boundary Layer Flow. The classic Nikuradse [5] experiments on sand type roughness show that the minimum permissible roughness up to which hydrodynamically smooth boundary layer flow can be expected is given by a simple relation, called critical roughness Reynolds Number:

$$\mathrm{Re}_{ks,p} = \frac{ks \cdot w}{\nu} = 100$$

For other roughness types large differences can be found in the literature for the critical roughness Reynolds Number reaching from 50–260 [6,7].

The above mentioned equation does mean that the maximum permissible characteristic surface roughness height k_p for a certain roughness type depends exclusively on the velocity to kinematic viscosity ratio or in other words the Reynolds Number per unit length $w/\nu = \mathrm{Re}/c$ and the average geometry of the roughness elements and not on a characteristic length as blade chord or compressor size.

3.5 Roughness Types and Drag Characteristics. Investigations on rows of regularly spaced spheres, hemispheres, cones, sharp edged metal strips, etc. show a large variation of their effect on drag relative to sand type roughness. The distance to height ratio is of decisive importance, generally giving the impression that drag reduces linearly with distance between peaks above a ratio of $a/k \geq 8$, which means every peak acts as a single body. The technical surfaces produced by the typical blade manufacturing processes look like very flat hills and wide valleys with a slope hardly exceeding 10 deg and typical distance to height ratios of $a/k = 50$–200 for the largest peaks.

Table 2 summarizes a survey of the ratio between regularly spaced roughness elements and the equivalent sand roughness which produces the same drag on a flat plate flow according to measurements given in [6].

The data in Table 2 mean that generally very much less drag is produced by single regularly spaced roughness elements than by sand type roughness of the same roughness height. Only rows of spheres at $2 < a/k < 9$ produce significantly more drag than sand type rough surfaces.

3.6 Roughness Description and Measurement. The characterization of a technical roughness is very difficult due to various aspects as:

- individual shape of peaks
- density of essential roughness peaks per unit length
- spectrum of roughness height

Whereas sand type roughness described in text books is made up of sand grain of essentially constant diameter and distance a technical roughness contains a whole spectrum of peak heights and possibly also large scale waviness. Roughness is usually described in industry by an arithmetic average value (*RA, AA, CLA*) measured by a stylus which travels along a rough surface picking off roughness heights at constant distances. This arithmetic mean value alone is not too helpful in defining the hydrodynamic characteristic of the surface because a large portion of the smaller roughness elements is fully submerged in the laminar sublayer and therefore not at all felt by the turbulent flow, but are counted in the arithmetic mean value. It can be imagined that a constant arithmetic mean roughness could as well describe a roughness type of constant low height elements which are all submerged, as also a large spectrum of roughness types with certain numbers of peaks of different height which protrude the laminar sublayer and hence produce different drag characteristics.

We therefore looked for a roughness parameter k which describes the peaks rather than the average in a reasonably simple way.

Roughness k is defined as the difference between the arithmetic averages of the ten highest peaks and the ten deepest grooves which exist per millimetre length, i.e., in an average distance of 100 μm. Measuring length is 5 mm in chord and spanwise direction on the 20 percent chord position of the suction surface, the forward 50 percent of which are regarded as decisive for friction drag produced by surface roughness. In case that chordwise and spanwise measurement reveal different roughness levels, the higher value is chosen on the experimental evidence obtained in wind tunnel tests with a milled flat plate having considerable differences of roughness height in direction of milling and normal to it. The tests described in [8], show that only a ten degrees incidence relative to the low roughness direction makes the high roughness fully effective.

Fig. 11 shows the definitions of the roughness parameters. The author is fully aware of the limitations and arbitrariness of the definition used for k, which yields essentially similar data as the definition used by Hürlimann [9].

A considerable number of blade surface roughness measurements done on forged and electrochemically machined blades with a roughness measurement device called Perthometer were analysed. These revealed a sensible correlation between k and the readily obtainable arithmetic average *Ra* (*AA, CLA*):

$$k = 8{,}9 \cdot \mathrm{Ra}$$

The factor scattered from 7–12 with 80 percent of the samples placed between 8 and 10. The measurements are done with a stylus of 5 μm tip radius, a cut off length (wave length) of 0.075 mm and a stylus contact force of 4.9 *N*.

3.7 Correlation of Existing Data. Critical roughness Reynolds Numbers for blade surfaces produced by typical manufacturing methods can be obtained from the test results of the three high pressure compressors, which all met the roughness boundary.

From Figs. 5 and 6 a mean Reynolds Number was picked off at the crossing point of the elongations of the increasing efficiency slopes in the hydrodynamically smooth or intermediate regime with the constant η_{pol} line from the hydrodynamically rough regime. This kink point was used to calculate individual stage roughness Reynolds

Table 2 Comparison of drag equivalent roughness heights

roughness type	a/k	k/ks
spheres	19.5	4.4
	9.75	1.2
	4.87	0.33
	2.93	0.26
	1.41	1.6
hemispheres	10	8.4
	7.5	5.3
	5	1.7
	1.4	0.71
Cones	10	6.4
	7.5	2.3
	5	1.0

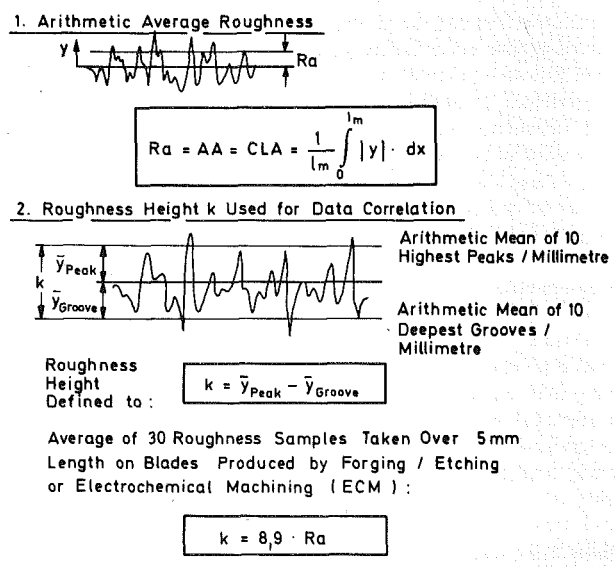

Fig. 11 Definition of roughness parameters

Numbers from the measured blade roughnesses of the various stages. Roughness Reynolds Number is based on relative cascade inlet velocity, roughness height k as defined on Fig. 11 and kinematic viscosity calculated from static pressure and temperature ahead of the respective cascade. A mean roughness Reynolds Number was calculated by arithmetically averaging the individual stage data omitting untypically high values which were due to distinctly higher than average roughness levels. This applies to rotor 5 of HPC "A" and rotors 3 and 6 of HPC "B". On this basis the analysis gave critical roughness Reynolds-Numbers of $Re_{k,p} = 88$ for forged and electrochemically machined blades and $Re_{k,p} = 137$ for ground blades.

In both six-stage compressors all stator blades were hydrodynamically smooth up to the highest Reynolds level tested, but in case of the five-stage research compressor the stators were all hydrodynamically rough far below the observed roughness boundary without really affecting the behavior noticeably. This is due to the small portion of the Reynolds Number dependent stator profile losses of the total losses in this high reaction compressor which is very much dominated by the rotors. The smoothed stator blades should increase efficiency level at $Re = 3.1 \times 10^5$ by 0.15 percent which is within the experimental accuracy achieved in the tests. In Table 3 stage and average roughness Reynolds Numbers are listed together with the manufacturing process.

A significant difference appears between the ground blades and the forged or electrochemically machined blades in their roughness behaviour. This may partly be connected with the definition of maximum roughness in case of the ground blades (see Section 3.6) which showed a 2:1 ratio of spanwise to chordwise roughness as opposed to forged and electrochemically machined blades which do have similar roughness in both directions. If an average value of spanwise and chordwise roughness is used the roughness Reynolds Number would drop to $Re_{k,p} = 103$ which is close to the other blades. Additional information will be needed for further clarification.

The average critical roughness Reynolds Numbers given in Table 3 can be used to locate the Reynolds Number where the individual stages enter the hydrodynamically rough boundary layer flow regime. These points are marked in Figs. 6 and 7 with encircled stage numbers. In case of the five-stage HPC this occurs in a band between 2.6×10^5 and 3.8×10^5 in a well ordered manner. In HPC "A" rotor 5 is distinctly rougher than the average stages and enters the rough regime at a Reynolds Number well below the experimentally observed roughness boundary which occurs where rotors 6, 4, 2 and 1 follow each other simultanously.

HPC "B" is the most complicated case due to the fact that two rotors (6, 3) enter the rough regime at around 3×10^5 Reynolds Number while stages 4 and 5 and 2 and 1 follow groupwise. The rough stages 6 and 3 are not immediately felt by the compressor in form of a bend over but the average exponent n of this compressor is noticeably lower than the one of HPC "A", which might be the effect of the two stages already operating with hydrodynamically rough surfaces.

The distinct curl over, however, is seen in these tests only when at least $^2/_3$ of the decisive cascades enter the rough boundary layer flow regime. The observed effect of the technical roughness on the compressor behavior is considerably more pronounced than would have been expected from an extrapolation of the data given in Table 2 using hemispheres or cones as a simulation of technical roughness elements.

The permissible blade roughness for hydrodynamically smooth flow is given in Table 4 for forged and electrochemically machined blades over a range of Reynolds Numbers per unit length using the critical roughness Reynolds Number of $Re_{k,p} = 88$.

3.8 Simple Method for Estimation of Roughness Effect on Efficiency. With the use of the obtained critical roughness Reynolds Number the upper critical Reynolds Number can be obtained for each stage and hence for the compressor by averaging:

$$\overline{Re}_{crit,u} = \frac{1}{z} \cdot \sum_{1}^{z} \left(Re_{k,p} \cdot \frac{c}{k} \right)_f$$

If the exponent n is known for the hydrodynamically smooth regime from easily obtainable subatmospheric test or a well working correlation, the potential efficiency versus Reynolds Number relation can be drawn for hydrodynamically smooth flow. By making use of the experience that the curl over occurs in a small Reynolds Number band the average upper critical Reynolds Number $\overline{Re}_{crit,u}$ can be marked on the $\eta_{pol} - Re$ curve as the bend over point towards constant efficiency for a certain roughness chosen. The potential efficiency losses can be picked off for various Reynolds Numbers between the constant and the increasing efficiency line for hydrodynamically rough or smooth flow, respectively.

If the picture is handled parametrically for various roughness heights it provides an easy and good insight into the potential efficiency losses involved in high Reynolds Number operating points. These can then be converted in thrust, specific fuel consumption and equivalent turbine inlet temperature changes.

3.9 Consequences of Blade Surface Roughness for High Pressure Ratio Engines. The analysis of the available test data for technical roughness types allows to draw conclusions on the consequences to high pressure ratio engines.

In Fig. 12, the ratio of blade inlet velocity/kinematic viscosity or Reynolds Number per unit length is plotted against pressure ratio and approximate stage number for three flight cases, i.e., take off, low level transonic flight and high altitude cruise, showing an increase of almost 17:1 between the extreme cases of first and last stage.

A constant mid span inlet flow velocity of $w_1 = 385$ m/s was assumed as a representative average value for the circumferential speeds presently achievable with the existing disk and blade materials.

Fig. 13 shows the permissible blade surface roughness height k_p against w_1/ν ratio for the roughness Reynolds Numbers seen in MTU-tests, showing the rapid reduction of surface roughness necessary in the back stages to keep the flow hydrodynamically smooth. An indication which stages are running into problems at the various flight cases can be seen from the columns drawn at a surface roughness of $k = 2\ \mu$m, which is about the best quality presently achievable with the mentioned manufacturing techniques.

As can be seen, all core engine compressor stages of a military engine operate in the hydrodynamically rough boundary layer flow regime at low level transonic flight conditions, which means that no performance improvement can be expected in the core engine compressor from the high Reynolds Number level.

On the contrary a civil engine at typical cruise conditions has a good chance to operate a large portion of the compressor stages in hydrodynamically smooth flow conditions. Even with todays good surface

Table 3 Stage roughness Reynolds Number at roughness boundary

Compressor		Res. HPC (five-stage)	HPC "A" (six-stage)	HPC "B" (six-stage)
Reynolds Number at roughness boundary		3.1×10^5	6.0×10^5	5.0×10^5
$Re_{k,p} = \frac{k \cdot w}{\nu}$ 1 stage	1	111	83	69
	2	119	91	74
	3	137	70	147^+
	4	153	97	105
	5	165	173^+	101
	6	—	101	166^+
$\overline{Re_{k,p}} = \frac{k \cdot w_1}{\nu}$		137	88	87
production method		grinding	ECM	ECM

$^+$ omitted in averaging process

Table 4 Permissible roughness height $Re_{k,p} = 88$

$\frac{Re}{c} \cdot 10^{-8} = \frac{w_1}{\nu} \cdot 10^{-8}$	m^{-1}	0.10	0.25	0.50	0.75	1.00	1.25	1.50
k_p	μm	8.8	3.5	1.75	1.2	0.9	0.7	0.6

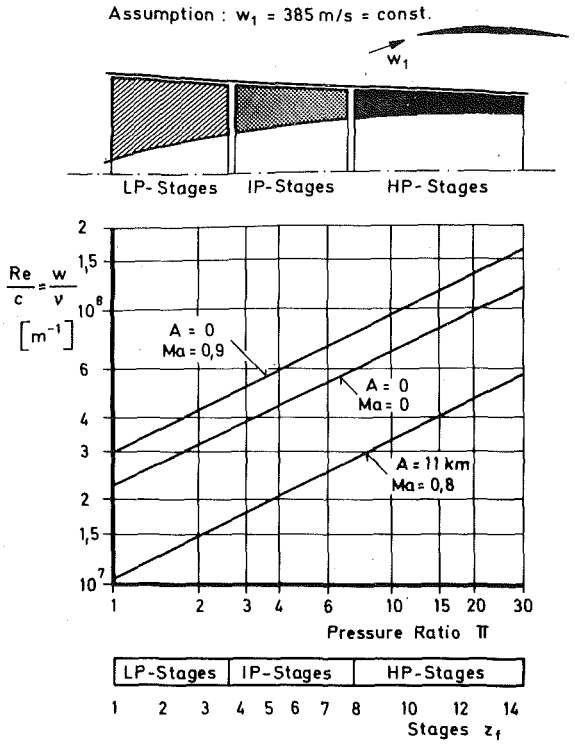

Fig. 12 Reynolds Number per unit length as a function of compressor pressure ratio and flight condition

quality blades potential efficiency gains of 1–3 percent cannot be utilized in the high pressure compressor stages of modern engines at low level flight due to excessive roughness.

4 Conclusions

Test results obtained at varying Reynolds Number with four different multistage transonic compressors yielded the following essential results:

- laminar separation of double circular arc profiles is below Re = 10^5
- laminar separation boundary can be drastically moved towards higher Reynolds Numbers by blade repair at the leading edges especially in the front stages.
- the Wassel efficiency correlation works well in the hydrodynamically smooth regime.
- critical roughness Reynolds Number has been determined to about 90 for electrochemically machined and forged blades.
- the type of manufacturing technique can alter the critical roughness Reynolds Number considerably.
- to keep boundary layer flow hydrodynamically smooth in the high pressure stages of modern engines requires a surface quality, which

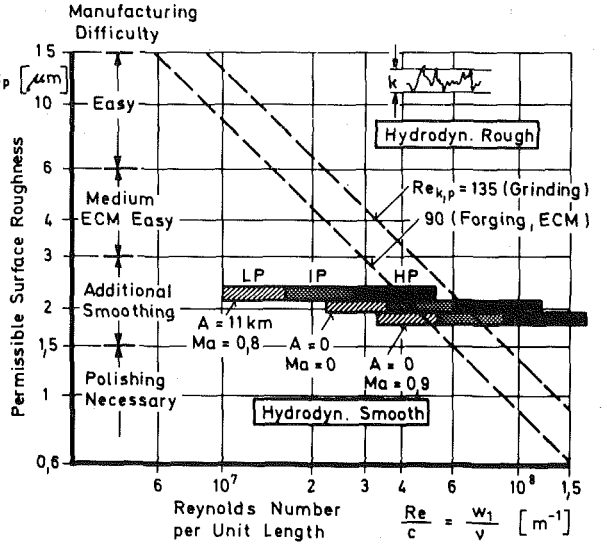

Fig. 13 Permissible surface roughness for hydrodynamically smooth boundary layer flow.

cannot be fullfilled with presently available production methods. Efficiency losses of 1–3 percent must be expected relative to the potentially achievable value at low level flight conditions.

Acknowledgment

The author wishes to thank Motoren- und Turbinen-Union, München GmbH for permission to publish this paper.

References

1 Wassel, A. B., "Reynolds-Number effects in Axial Compressors," ASME JOURNAL OF ENGINEERING FOR POWER, April 1968.

2 Kiock, R., "Einfluß des Turbulenzgrades auf die aerodynamischen Eigenschaften von ebenen Verzögerungsgittern," *DGLR-Vortrag* Nr. 71-096 4. Jahrestagung der DGLR, 11. Oct. 13, 1971.

3 Rotta, J.C., "Fortran IV—Rechenprogramm für Grenzschichten bei kompressiblen ebener und achsensymmetrischen Strömungen," *DLR* FB 71–51, 1971.

4 Fottner, L., "Ein halbempirisches Verfahren zur Bestimmung der reibungsbehafteten transsonischen Schaufelgitterströmung mit Einschluß von Überschallfeldern und Verdichtungsstößen," Dissertation TU München, 1970.

5 Nikuradse, J. "Gesetzmäßigkeit der turbulenten Strömung in glatten Rohren," *Forsch. Arb. Ing.* Wesen Heft 356, 1932.

6 Schlichting, H., *Grenzschicht-Theorie,* Verlag Braun Karlsruhe, 5. Auflage, Kapital XX,XXI.

7 Speidel, L., "Einfluß der Oberflächenrauhigkeit auf die Strömungsverluste in ebenen Schaufelgittern," *Forsch ung im Ingenieurwesen* 20 1954, pp. 124–140.

8 Scholz, N., *Aerodynamik der Schaufelgitter,* Vol. I, Verlag Braun, Karl ruhe, 1965 Chapter 7.3.4.

9 Hürlimann, R., "Zum Einfluß der Oberflächenrauheit, insbesondere der Fertigungsgüte auf die Strömungsverluste von Dampfturbinenschaufeln," VDI-Berichte Nr. 193, 1973.

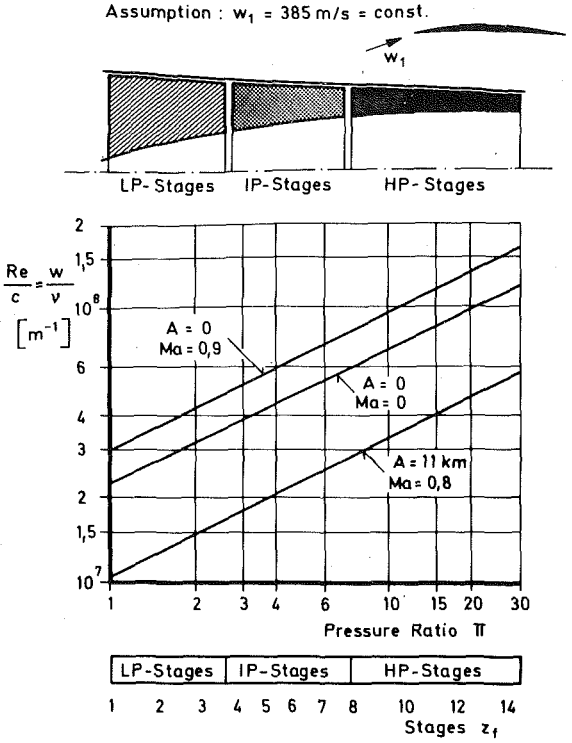

Fig. 12 Reynolds Number per unit length as a function of compressor pressure ratio and flight condition

quality blades potential efficiency gains of 1–3 percent cannot be utilized in the high pressure compressor stages of modern engines at low level flight due to excessive roughness.

4 Conclusions

Test results obtained at varying Reynolds Number with four different multistage transonic compressors yielded the following essential results:

- laminar separation of double circular arc profiles is below Re = 10^5
- laminar separation boundary can be drastically moved towards higher Reynolds Numbers by blade repair at the leading edges especially in the front stages.
- the Wassel efficiency correlation works well in the hydrodynamically smooth regime.
- critical roughness Reynolds Number has been determined to about 90 for electrochemically machined and forged blades.
- the type of manufacturing technique can alter the critical roughness Reynolds Number considerably.
- to keep boundary layer flow hydrodynamically smooth in the high pressure stages of modern engines requires a surface quality, which cannot be fullfilled with presently available production methods. Efficiency losses of 1–3 percent must be expected relative to the potentially achievable value at low level flight conditions.

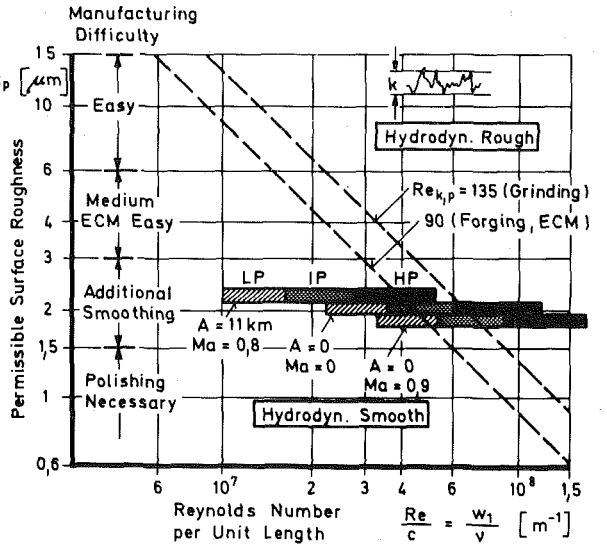

Fig. 13 Permissible surface roughness for hydrodynamically smooth boundary layer flow.

Acknowledgment

The author wishes to thank Motoren- und Turbinen-Union, München GmbH for permission to publish this paper.

References

1 Wassel, A. B., "Reynolds-Number effects in Axial Compressors," ASME JOURNAL OF ENGINEERING FOR POWER, April 1968.

2 Kiock, R., "Einfluß des Turbulenzgrades auf die aerodynamischen Eigenschaften von ebenen Verzögerungsgittern," *DGLR-Vortrag* Nr. 71-096 4. Jahrestagung der DGLR, 11. Oct. 13, 1971.

3 Rotta, J.C., "Fortran IV—Rechenprogramm für Grenzschichten bei kompressiblen ebener und achsensymmetrischen Strömungen," *DLR* FB 71–51, 1971.

4 Fottner, L., "Ein halbempirisches Verfahren zur Bestimmung der reibungsbehafteten transsonischen Schaufelgitterströmung mit Einschluß von Überschallfeldern und Verdichtungsstößen," Dissertation TU München, 1970.

5 Nikuradse, J. "Gesetzmäßigkeit der turbulenten Strömung in glatten Rohren," *Forsch. Arb. Ing.* Wesen Heft 356, 1932.

6 Schlichting, H., *Grenzschicht-Theorie,* Verlag Braun Karlsruhe, 5. Auflage, Kapital XX,XXI.

7 Speidel, L., "Einfluß der Oberflächenrauhigkeit auf die Strömungsverluste in ebenen Schaufelgittern," *Forsch ung im Ingenieurwesen* 20 1954, pp. 124–140.

8 Scholz, N., *Aerodynamik der Schaufelgitter,* Vol. I, Verlag Braun, Karl ruhe, 1965 Chapter 7.3.4.

9 Hürlimann, R., "Zum Einfluß der Oberflächenrauheit, insbesondere der Fertigungsgüte auf die Strömungsverluste von Dampfturbinenschaufeln," VDI-Berichte Nr. 193, 1973.

DISCUSSION

C. C. Koch[1] and L. H. Smith, Jr.[1]

We would like to thank Mr. Schaffler for presenting the test data in this paper that so clearly show the strong interaction of surface roughness with Reynolds Number in affecting compressor efficiency. It was of particular interest that Mr. Schaffler concluded that the critical roughness Reynolds number, above which efficiency depends upon roughness but not upon chord Reynolds number, has a value of approximately 90. This is the same value that we arrived at in ASME Paper 75-WA/GT-6 (published in the July 1976 issue of the *Journal of Engineering for Power*) after studying what limited data were available to us at that time; and we were thus pleased to find a confirmation of this value in Mr. Schaffler's new and highly relevant data.

Mr. Schaffler's analysis differs from ours somewhat in using an effective roughness height of 8.9 times the usual CLA roughness measurement given by a profilometer. After studying what data we could find, we related effective roughness to the CLA measurement with a proportionality constant of 6.3. This difference means that, for a given CLA roughness measurement, we would predict that roughness effects would become predominant at a somewhat higher chord Reynolds Number than would Mr. Schaffler. There is great difficulty, however, in defining a simple measure of surface roughness, since different manufacturing processes can create quite significant differences in the shape, directionality and uniformity of roughness patterns in addition to differences in average roughness height. We therefore feel that values of the proportionality constant of 6.3 and 8.9, as determined independently by ourselves and Mr. Schaffler, constitute quite good agreement.

[1] General Electric Aircraft Engine Group, Cincinnati, Ohio 45215. Members, ASME.

Author's Closure

I should like to thank Dr. Smith and Dr. Koch for their contribution which points out the very good agreement on the critical roughness Reynolds Number between their assessment in ASME Paper No. 75-WA/GT-6 and our experimental results. I fully agree with the discussers that the most difficult point for a more general relation of effective roughness to the easily obtainable CLA measurements is presented by the large variety of roughness types, especially if coatings are used. The relatively simple roughness definition used in my paper is a small step forward, as it at least defines the average height of the important large peaks, which cause the flow to change towards hydrodynamically rough behavior. It may be refined by adding a parameter which counts the number of large peaks per unit length. Systematic measurements on flat plates proposed to be persued by a research institute or an university with various roughness types typical for blade manufacturing processes or corrosion protective measures would be of great help to the industry.

C. C. Matthews

Power Systems Department
General Motors Research Laboratories
Warren, MI 48090

Measured Effects of Flow Leakage on the Performance of the GT-225 Automotive Gas Turbine Engine

A GT-225 regenerative gas turbine engine was used to obtain engine performance data with varied rates of simulated internal leakage. Regenerator hot surface rim and crossarm seal leaks as well as regenerator cold surface seal leaks were simulated. Instrumentation was included in external ducting to measure the leakage rates. Data were taken at three gasifier turbine speeds with turbine inlet temperature held constant by means of the variable power turbine nozzle and also with varied turbine inlet temperatures resulting from operation with the nozzle fixed at the design area. Component performance data were calculated from the engine measurements to determine the loss mechanisms associated with the leakage. The GT-225 was most sensitive to hot surface rim seal leakage, followed closely by the hot surface crossarm seal leakage, and then the cold surface leakage. Performance was degraded much more when turbine inlet temperature was fixed (by about a factor of three for specific fuel consumption) than for the fixed geometry mode. The effects of leakage became less severe as gasifier turbine speed was increased. The engine performance deterioration due simply to the flow bypass is compounded by induced losses in regenerator and compressor performance leading to very large changes in engine performance, e.g., specific fuel consumption increased up to 80 percent and power decreased as much as 40 percent with 8 percent additional leakage.

Introduction

The use of rotating heat exchangers, or regenerators, to recover exhaust heat on vehicular gas turbines has become almost universal. There is general agreement that some form of heat recovery is necessary, at least for light-duty vehicular gas turbines which spend much of their time producing only a fraction of the rated power. The usual disagreement among designers involves the merits of the rotating regenerator versus the stationary recuperator. The regenerator seems to offer an advantage in either size or pressure drop for a given value of heat transfer effectiveness, but is subject to flow leakage past the rubbing seals. Other heat exchanger performance parameters, such as effectiveness and pressure drop, are well defined and understood, but little quantitative data are available to show the effect of flow leakage on small gas turbine engine performance.

The drive for improved gas turbine engine efficiency demands better overall heat exchanger performance. This usually leads to regenerators of larger size which, with other factors remaining unchanged, probably will have more flow leakage. At some point, the performance degradation due to leakage will probably cancel the improvement due to the increased effectiveness.

Understanding how the flow leakage degrades engine performance may also lead to an engine design which is less sensitive to leakage.

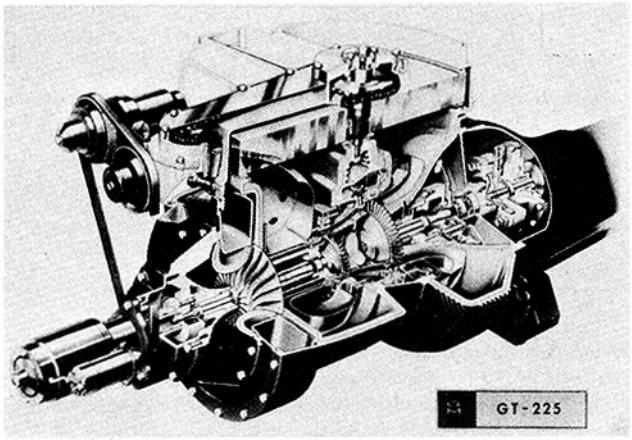

Fig. 1 Phantom view of the GT-225 engine

This requires some insight as to how the leakage affects component performance and how the component interactions affect the overall engine performance. This information could, for example, influence the compressor design or the engine control system.

The leakage data may also provide a basis for diagnosis of engine malfunctions. The diagnosis of substandard engine performance is usually difficult and time consuming. Hopefully, the data reported here may provide a basis to determine if the problem is leakage related, and the general area of the leakage.

Contributed by the Gas Turbine Division and presented at the Gas Turbine Conference, San Diego, California, March 12–15, 1979 of THE AMERICAN SOCIETY OF MECHANICAL ENGINEERS. Manuscript received at ASME Headquarters November 3, 1978. Paper No. 79-GT-1.

Engine Description

The GT-225 engine used for these tests has been described previously [1] and is shown in Fig. 1. It was designed specifically for passenger-car gas-turbine research, with emphasis on wide-range operating conditions. This engine, rated at 168 kW at sea-level standard conditions, uses a single rotating regenerator mounted horizontally at the top. It is a two-shaft engine which features variable power turbine nozzle vanes to control the turbine inlet temperature.

Test Description

Leakage Paths. The regenerator seals are normally subject to three different types of flow leakages. These will be described and defined using flow station numbers as shown on the engine flow schematic in Fig. 2. High pressure, low temperature air enters the air side of the regenerator from the compressor at station 2. The air exits the regenerator at high temperature and pressure at station 3. After being heated in the combustor and expanded in the turbines, the hot gas enters the gas side of the regenerator with low pressure at station 6. The gas exits from the regenerator at low temperature and pressure at station 7 to be exhausted from the engine.

In addition to the air side and gas side of the regenerator, the two regenerator surfaces are called the cold (stations 2 and 7) surface and the hot (stations 3 and 6) surface. The cold surface and hot surface seals are similarly noted.

The first leakage path to be encountered involves the cold surface seal. High pressure air from the compressor can leak across the cold surface seal directly into the exhaust stream at station 7. This flow is also similar to a leak of compressor discharge air out of the engine directly to the atmosphere, as with a faulty regenerator cover gasket. In either case, the flow returns almost directly to the atmosphere (station 0). Thus, this type of leakage will be referred to as 2–0 leakage.

The second leakage path involves the gas side portion of the rim seal on the hot surface of the regenerator. Low temperature, high pressure air from the compressor can leak directly across the hot surface rim seal into the turbine exhaust plenum at station 6. This type of flow leakage will be called 2–6 leakage.

Finally, the third leakage path involves the crossarm portion of the hot surface seal. Air at high temperature and pressure at station 3 may leak across the crossarm seal directly into the exhaust plenum at station 6. This will be called 3–6 leakage.

The performance of the GT-225 engine was measured while systematically changing the rate of each of these three types of flow leakage.

Test Method. Leakage flow was introduced during testing by installing an external duct on the engine. For the 3–6 leakage, the hot air was tapped from a single port in the combustor plenum and reinjected into the turbine exhaust plenum at a point approximately 50 mm below the hot surface of the regenerator and 170 mm to the left of the engine axial centerline.

For the 2–6 and 2–0 leakage tests the compressor discharge flow was taken from six small holes in the regenerator cover. These six ports were connected to a collection manifold and then to the external flow duct. For the 2–6 tests the air was injected into the turbine exhaust plenum at the same location as the 3–6 tests. For the 2–0 leakage, the bypass air was simply discharged into the test cell.

The central portion of the external flow duct (51 mm diameter) included a sharp-edged orifice plate along with an upstream thermocouple and static pressure taps. The bypass flow rate was both throttled and measured using orifice plates of various sizes. For the 3–6 leakage tests, the external flow duct was heavily covered with thermal insulation. For the 2–6 and 2–0 leakage tests, no thermal insulation was used in order to facilitate changing the orifice plates.

It is important to note that the engine contained the normal regenerator disk and associated seals. Since these elements were not modified in any way, the engine operated with the usual amount of internal leakage. Both the quantity and type of this inherent internal leakage are unknown. Thus, the leakage introduced in the external ducting was *in addition* to the normal internal leakage. In this paper, reference to zero leakage or baseline means that no external leakage was introduced; this does *not* mean that no internal leakage was present.

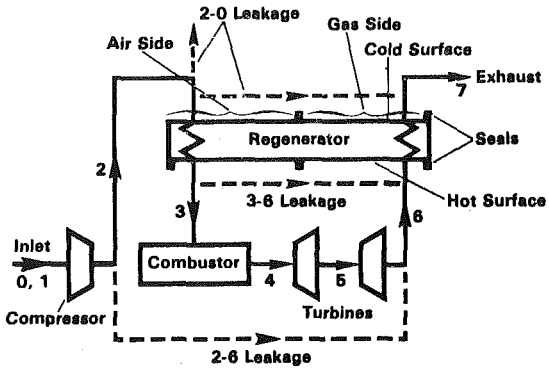

Fig. 2 GT-225 engine cycle schematic showing internal leakage paths

Engine Operating Modes. Two different engine operating modes were tested with leakage. For the first, fixed geometry mode, the power turbine (PT) nozzles were set at the design position. Then, as the engine speed or leakage changes, the turbine inlet temperature (T_4) is a dependent variable.

The second mode involved control of the turbine inlet temperature at each engine speed as the leakage changed. For each change in leakage, the PT nozzles were adjusted to hold T_4 at the baseline level. These two conditions are referred to as fixed nozzle area (Fixed A_n) or fixed turbine inlet temperature (Fixed T_4) modes of operation.

Engine Speed Range. In order to reduce the quantity of test data, the operation was restricted to three gasifier turbine speeds, 50 percent, 60 percent, and 70 percent of the design speed. The normal idle for this engine is 50 percent gasifier turbine speed (N_1). In either mode, the power turbine speed (N_2) and engine output speed (N_0) were constant at each gasifier speed for most of the testing. That is, for a given gasifier speed and operating mode a baseline was established with zero external leakage. During this baseline test, the power turbine speed was set for peak power. For all subsequent tests at the same N_1 and operating mode, the power turbine was set at the same speed.

As an exception to the above, one series of tests was run (3–6 leakage at fixed T_4) in which the PT speed was also adjusted to the peak power condition for each increment of the leakage. During this test sequence, the effect of leakage on the peak power speed was also determined.

Results

Results will be presented initially to show the overall effect of leakage on the engine performance, specifically output power and brake specific fuel consumption (BSFC). All data are shown relative to the appropriate baseline (zero external leakage) condition as a percent change from the baseline. The effect of leakage type, operating mode, gasifier turbine speed, and power turbine speed on relative engine performance will be shown individually.

Effect of Leakage Type and Operating Mode. The effects of the three types of leakage on engine performance are shown in Fig. 3 for the fixed A_n mode of operation at 50 percent N_1. It is interesting that, for the fixed A_n mode of operation, the increased leakage causes an increase in the output power, due to an associated rise in T_4. Even so, the BSFC increases rather sharply as the leakage increases, indicating that the fuel flow is increasing much faster than the output power.

One exception to this is that the 2–0 leakage actually reduces BSFC at leakage rates below 3.5 percent. The 2–6 and 3–6 types of leakage both show substantial increases in the BSFC with any added leakage.

The effect of the three types of leakage on engine performance in the fixed T_4 mode of operation at 50 percent N_1 is shown in Fig. 4. For this mode of operation, the output power decreases substantially with increased leakage of any type. Due in part to the loss of output power,

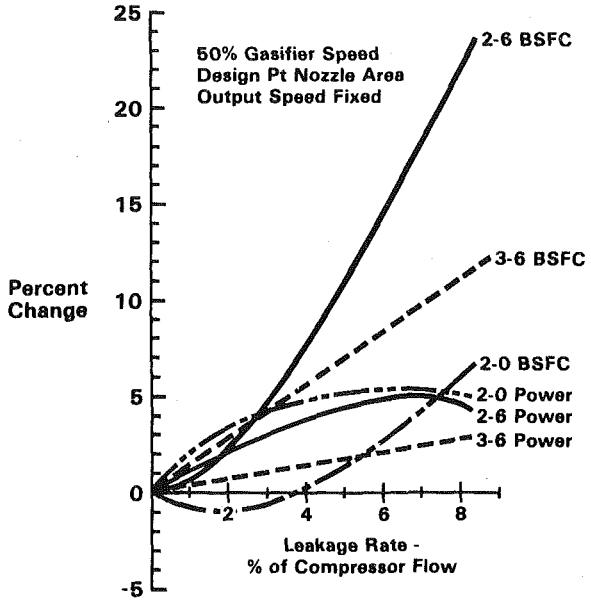

Fig. 3 Effects of internal leakage on GT-225 BSFC and output power—fixed A_n

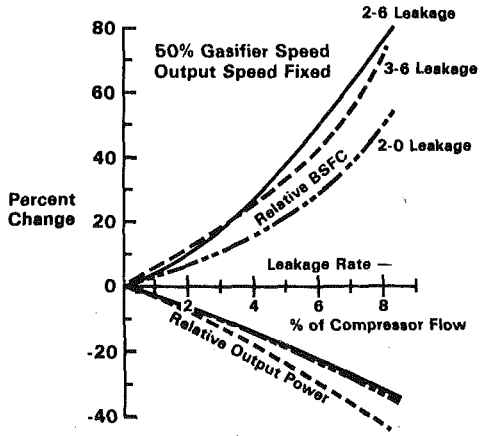

Fig. 4 Effects of internal leakage on GT-225 BSFC and output power—fixed T_4

the increases in BSFC are very large for this mode. In both cases, the 2–6 leakage causes the greatest increase in BSFC, followed closely by the 3–6 leakage and then the 2–0 leakage.

Figs. 3 and 4 may be compared to see the effect of operating mode for each type of leakage. Notice, however, the significant *ordinate scale change* from Fig. 3 to Fig. 4.

Effect of Gasifier Turbine Speed. The effect of leakage on engine performance at various gasifier turbine speeds for the fixed A_n mode is shown in Fig. 5 for 3–6 leakage, Fig. 6 for 2–6 leakage, and Fig. 7 for 2–0 leakage. In general, it appears that the effect of leakage on engine BSFC is reduced as the gasifier speed increases, at least over the range of speed investigated. While this general trend is independent of the leakage type the engine is always most sensitive to 2–6 leakage and least sensitive to 2–0 leakage.

Similarly, the effect of leakage on engine performance at various gasifier speeds for the fixed T_4 mode of operation is shown in Figs. 8, 9, and 10 for the 3–6, 2–6, and 2–0 types of leakage respectively. Again, note the ordinate scale change for this series of graphs. The sensitivity of engine performance to leakage decreases even faster with increasing gasifier speed for the fixed T_4 mode, but the magnitude of performance changes at 70 percent N_1 remains very high. The shape of the curves for the fixed T_4 mode is quite different than for the fixed A_n mode, suggesting that the engine may be less sensitive to leakage at design speed in the fixed T_4 mode. An extrapolation of these data, however, is highly speculative.

Effects of Peak Power Speed. It was found that, for the fixed

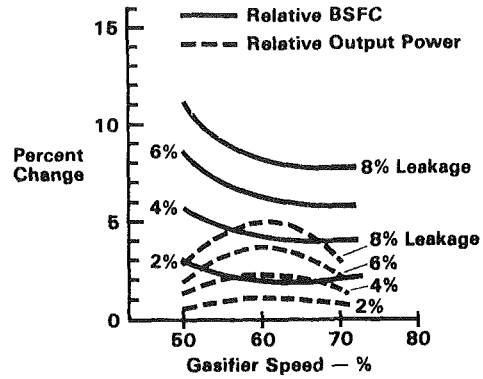

Fig. 5 GT-225 relative performance with 3–6 leakage versus gasifier speed—fixed A_n

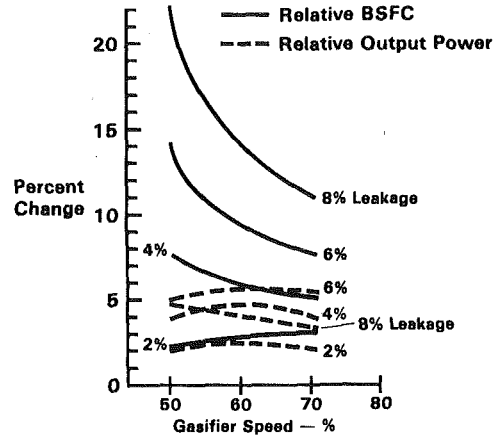

Fig. 6 GT-225 Relative performance with 2–6 leakage versus gasifier speed—fixed A_n

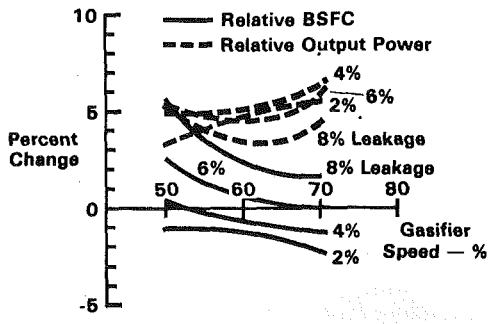

Fig. 7 GT-225 Relative performance with 2–0 leakage versus gasifier speed—fixed A_n

T_4 mode, increasing 3–6 leakage reduced engine output speed at which peak power was obtained (with gasifier speed fixed). This is shown in Fig. 11. The reduction in peak power speed was most severe at 50 percent N_1 with the effects at 60 percent and 70 percent N_1 being about equal (but less than at 50 percent N_1). The large data scatter is due to the output speed-power curves being very flat near the peak region.

Most of the leakage testing was done with the output shaft speed fixed at the peak power speed in the baseline condition. Therefore, some of the performance degradation shown earlier would be due to the power turbine operating at a nonoptimum speed.

The reduction in peak power speed is probably due to the fact that, as the leakage is being increased the PT nozzles must be opened to maintain constant T_4. As the PT nozzle vanes assume a more axial position in the engine, the flow enters the power turbine with less swirl. Also, the increased PT nozzle flow area, coupled with a reduction in mass flow due to the leakage, reduces the flow velocity entering the turbine. Both of these conditions change the relative flow vector approaching the turbine in such a way as to cause negative incidence on

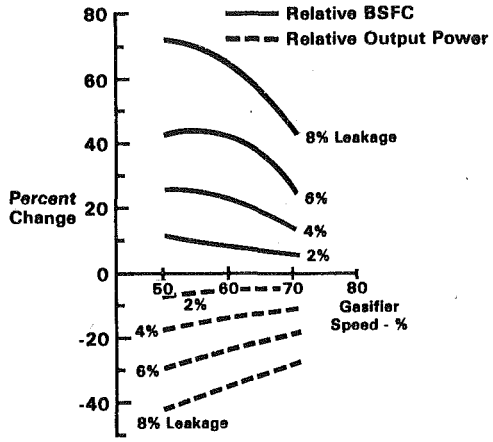

Fig. 8 GT-225 Relative performance with 3–6 leakage versus gasifier speed—fixed T_4

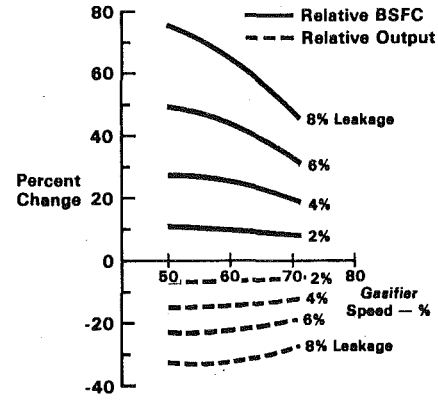

Fig. 9 GT-225 Relative performance with 2–6 leakage versus gasifier speed—fixed T_4

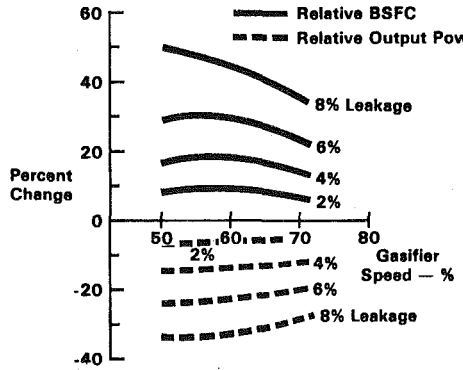

Fig. 10 GT-225 Relative performance with 2–0 leakage versus gasifier speed—fixed T_4

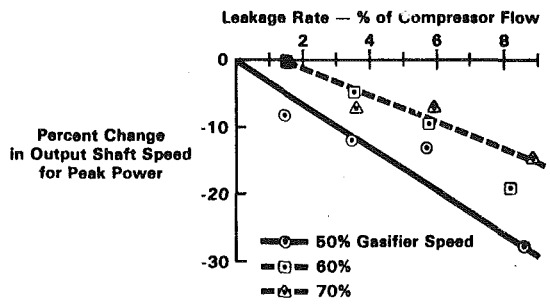

Fig. 11 Effect of 3–6 leakage on output shaft peak power speed—fixed T_4

the PT rotor blades, which is alleviated by a reduction in rotor speed.

Other operating conditions in the fixed T_4 mode would probably differ from this case only to the extent that T_4 is affected by the leakage. Thus, the effect on peak power speed would be expected to diminish at higher gasifier speeds, but would not be appreciably different for other types of leakage.

The effect of leakage on the peak power output speed for the fixed A_n mode should be much less than for the fixed T_4 mode. In this case, the PT nozzles are not changing the flow angle into the turbine, and the smaller reduction in mass flow through the turbines (due to the leakage) should not significantly affect the flow velocity. Therefore, for the fixed A_n mode, the peak power speed should shift only slightly as the leakage increases. This same philosophy would also apply to an engine which operates in the fixed T_4 mode, but without changing the PT nozzle area, such as by using Power Transfer [2]. Hence, using Power Transfer for T_4 control should result in less sensitivity to internal leakage than using variable power turbine nozzles.

Component Performance Interaction. It has been shown that internal leakage can cause very large changes in performance in the GT-225 engine. The performance changes are much larger than would be expected from a simple reduction in flow through the turbines. Additional calculations were performed to show the nature of some of the component interactions as internal leakage increases.

The fixed A_n mode of operation will be covered first. The effect of leakage on turbine inlet temperature, compressor flow rate, compressor pressure ratio, compressor efficiency, turbine flow rate, and regenerator effectiveness is of interest. Figs. 12 and 13 show the effects of leakage on the above parameters at 50 percent N_1 in the fixed A_n mode. Actually, it was found that the type of leakage did not affect the change in compressor flow, pressure ratio and efficiency, or the

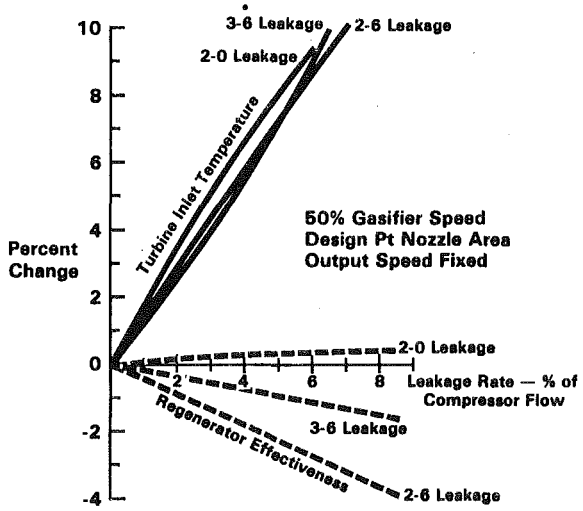

Fig. 12 Effect of leakage on GT-225 component performance—fixed A_n

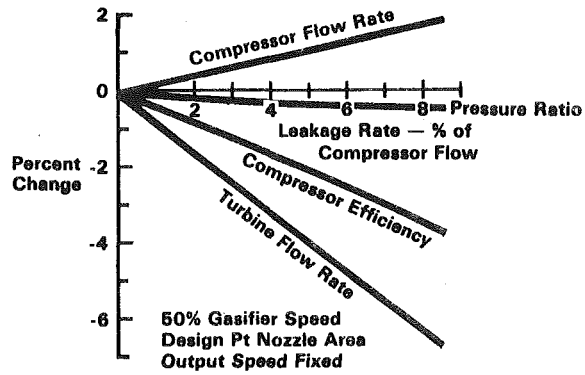

Fig. 13 Effect of leakage on GT-225 component performance–fixed A_n

turbine flow rate, so those curves, shown on Fig. 13, are common for each type of leakage. The effect of leakage on T_4 is nearly the same for the three types of leakage as well, so that the only obvious difference in component performance between the three types of leakage is in regenerator effectiveness.

The most obvious effect of leakage at fixed A_n is the rapid increase in T_4. This is accompanied by a decrease in flow through the turbines. The reduction in turbine flow rate is actually somewhat less than the leakage rate due to a small increase in the compressor flow rate and a change in the fuel flow. The leakage may be considered to be a reduction in the downstream flow restriction, so that the compressor flow increases with a corresponding very small reduction in pressure ratio and a moderate loss in compressor efficiency. The turbine inlet temperature increases much faster than the turbine flow rate decreases, so that the energy flux into the turbines actually increases as the leakage increases. Some of this additional turbine energy input is used by the gasifier turbine to compensate for the increased compressor flow at reduced efficiency. However, the remainder of the increased input energy passes on to the power turbine, resulting in an increase in output power, as shown earlier.

The effect of leakage on component interactions in the fixed T_4 mode is shown in the same way, except that turbine inlet temperature is no longer of interest. Accordingly, curves of compressor flow rate, pressure ratio and efficiency are shown in Fig. 14 for 50 percent gasifier speed at fixed T_4. The changes in compressor pressure ratio and efficiency were not affected by the leakage type, so those curves are common on Fig. 14. Curves of turbine flow rate and regenerator effectiveness are shown in Fig. 15 for the same engine conditions. The compressor flow rate and the turbine flow rate were affected to a small extent by the type of leakage but, again, the most substantial effect of leakage type was in regenerator effectiveness.

The most obvious effect of leakage at fixed T_4 is the rather large increase in compressor flow rate. The increase in compressor flow is nearly equal to the leakage flow, so that the net result is a very small change in turbine flow rate in all cases. The large increase in compressor flow is also accompanied by a moderate decrease in pressure ratio and efficiency as the leakage increases. The turbine inlet temperature is fixed and the turbine flow rate is nearly constant, so that the small loss in inlet pressure results in a small net loss in energy available to the turbines. At the same time, however, the compressor power requirement has increased substantially due to the increased compressor flow and reduced compressor efficiency. Therefore, the gasifier turbine requires a much larger fraction of the available energy than was required previously. The final result is a large reduction in output power with increasing leakage, as shown previously.

Output power is also affected by changes in pressure drop due to the different types of flow leakage. The 2–0 leakage results in reduced pressure drop on both the air and gas sides of the regenerator disk. Compared with the 2–0 leakage, the 2–6 leakage will have the same pressure drop on the air side and slightly more on the gas side, but the 3–6 leakage will have more pressure drop on the air side and much more pressure drop on the gas side. These trends are reflected directly in the output power curves in Fig. 4.

Since T_4 is fixed and turbine flow is nearly constant, the greatest variable affecting fuel flow is regenerator effectiveness. As with the fixed A_n mode, the 3–6 leakage results in a moderate decrease in effectiveness, the 2–6 leakage causes a large decrease in effectiveness, and the 2–0 leakage causes a small increase in effectiveness. These

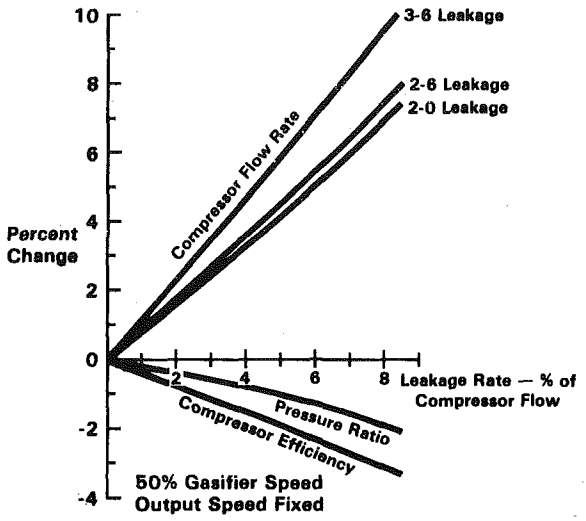

Fig. 14 Effect of leakage on GT-225 component performance—fixed T_4

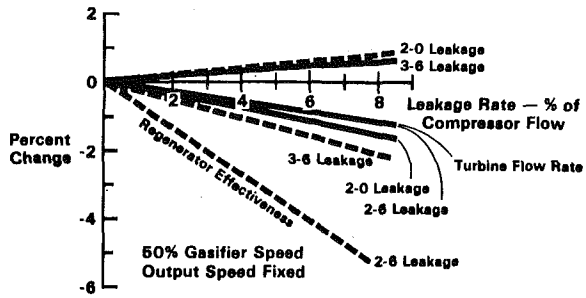

Fig. 15 Effect of leakage on GT-225 component performance—fixed T_4

trends, along with the small differences in output power, are reflected in the BSFC curves in Fig. 4.

The greater engine sensitivity to leakage in the fixed T_4 mode of operation is clearly due to poorer compressor performance. In fact, this entire leakage study has illustrated the importance of good compressor and regenerator performance on overall engine performance. Seemingly small changes in the performance of one component can induce other component changes to cause large changes in engine performance.

Because the engine performance is strongly affected by the leakage-induced component performance changes, the results shown here for the GT-225 engine may be applicable only qualitatively to other vehicular gas turbine engines. The final results will always be dictated by the compressor and regenerator operating characteristics, the type of leakage, the engine speed, and the method of engine control.

References

1 Collman, J. S., Amann, C. A., Matthews, C. C., Stettler, R. J., and Verkamp, F. J., "The GT-225—An Engine for Passenger-Car Gas-Turbine Research," *SAE Transactions*, Vol. 84, Section I, paper No. 750167, 1975.

2 Turunen, W. A., Collman, J. S., "The General Motors Research GT-309 Gas Turbine Engine," *SAE Transactions*, Vol. 74, paper No. 650714, 1966.

S. Fujii
Head, Engine Noise Group
National Aerospace Laboratory
Chofu, Tokyo, Japan
Mem. ASME

Acoustics and Performance of High-Speed, Unequally Spaced Fan Rotors

This paper describes an experimental measurement of the effects of uneven blade spacing on the acoustic and aero-thermodynamic characteristics of high-speed, high-pressure-ratio fan rotors at two selected spacing configurations. A test rig, consisting of inlet guide vanes and transonic rotor blades, was employed to explore the redistribution of harmonic sound energy into a series of multiple tones of lower sound pressure level. The measured data indicated that a ten percent modulated rotor exhibited a six to eight decibel decrease in the sound pressure level as compared with the original first blade passage frequency harmonic. Disadvantages in aerodynamic performance resulting from spacing modulation were not so unfavorable for the ten percent modulated blades. However, with five percent modulated blades, serious deterioration in aerodynamic performance was observed particularly near the blade tip section, which produced an unfavourable acoustic signature. A calculation method, assuming a pulse event for each blade sound pressure, provided agreeable results with the measured data.

Introduction

The frequency of narrow-band noise caused by the rotating blade row depends on the number of blades as well as the speed of rotor rotation, and is tonal in character. This type of noise can be distinguished from the background noise and therefore is very annoying. In the present study, an attempt was made to reduce the tonnal annoyance of the fan rotor preceded by inlet guide vanes through modification of the circumferential spacing of the fan rotor blades.

The investigations of the unequally spaced fans have been actively carried out in recent years, including the U.S. patent [1]. Mellin and Sovran [2] considered the noise generated by steady lift forces on the rotating blades and therein showed a semianalytical, semiempirical method of predicting the relative sound spectrum of an isolated, low-speed fan rotor having any arbitrary circumferential spacing of its blades. Evald, et al. [3] presented three analytical techniques of predicting the noise spectrum resulting from nonuniform spacing. They compared the analyses with the experimental data for a low-speed, 22 blade fan in a 5 hp induction motor, with the reasonable agreements. Shahady, et al. [4] conducted a full-scale static test program in order to evaluate the feasibility of using blade modulation for the helicopter tail rotor. Their measured data demonstrated that all of the blade passage frequency harmonics except the first were significantly attenuated.

The investigations mentioned above are concerned with the steady-lift noise or Gutin propeller noise that can not be propagated through ducts. On the other hand, the rotor-stator interaction produces an efficient propagation of spinning modes down the duct, even with the rotor itself moving at subsonic speeds. For such a case, Duncan and Dawson [5] illustrated the effects of small errors of vane location on the acoustic characteristics, where a small, low-speed axial-flow fan was used.

It is noted that the size, speeds and hence the pressure ratio of the fans for use in most of the investigations documented are considerably small. To author's knowledge, the measured data for a high-speed, high-pressure-ratio, unequally spaced fan have not been available in the open literature. Therefore the main objective of the present paper is to (1) obtain the measured data for high-speed, high-pressure-ratio fan rotors, and (2) elucidate the correlations of acoustic and aerodynamic characteristics for such equally and/or unequally spaced rotors. In this study, the fan rotor blades preceded by inlet guide vanes were employed. The circumferential spacing modulation was made for the rotor blades only. The inlet guide vanes were equally spaced and designed to impart no circumferential velocity component. Such near-zero-loading on the guide vanes was used to minimize both the position and amplitude modulation [6, 7] inherent in shedding wakes. With the guide vane/rotor spacing of 1.5 blade chords, most of interaction noise may be caused by the viscous wakes of vanes.

Test Facility, Hardware and Instrumentation

Description of Test Setup. The experimental apparatus consists of an anechoic room and a fan test rig in which inlet guide vanes and rotor blades were furnished. They are shown in Figs. 1 and 2 respectively. A 1600 kw, variable-speed motor was used to drive the fan. The rotational speed was manually controlled to give a useful range of 7000 rpm to 12,000 rpm.

With the fan operated, air flowed through an inlet silencer and the anechoic room and subsequently entered into a long duct. It was then

Contributed by the Gas Turbine Division and presented at the Gas Turbine Conference and Exhibit and Solar Energy Conference, San Diego, California, March 12–15, 1979 of THE AMERICAN SOCIETY OF MECHANICAL ENGINEERS. Manuscript received at ASME Headquarters November 29, 1978. Paper No. 79-GT-4.

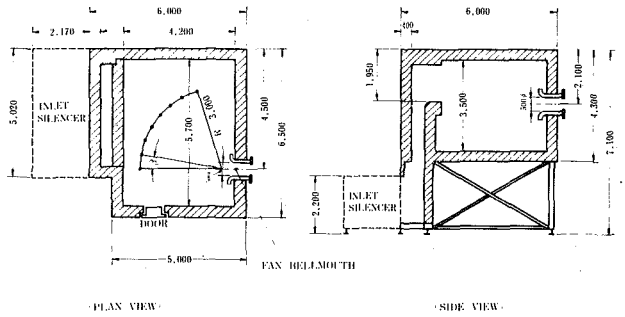

Fig. 1 Anechoic room, units are in mm

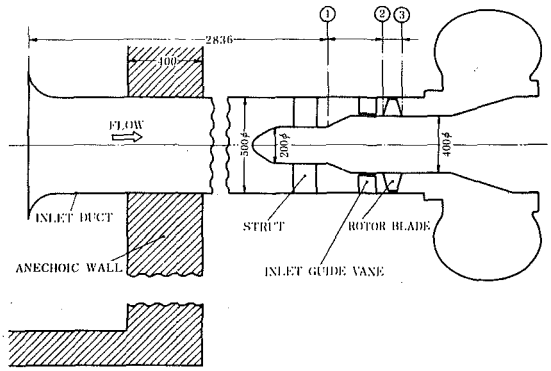

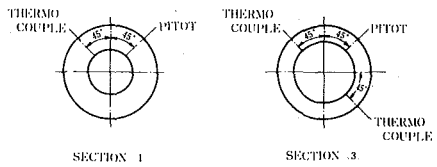

Fig. 2 A schematic of test rig and instrument locations

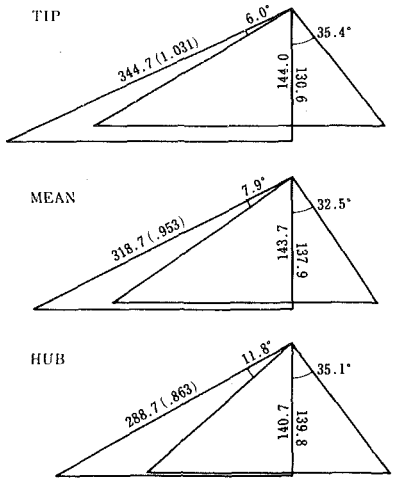

Fig. 3 Velocity triangles, Units are in m/s and numbers in round brackets indicate Mach number

Table 1 Blading details

Location	Stagger Angle	Solidity	Blade Thickness	Camber Angle
Tip	59.0 deg	1.17	4 mm	3.2 deg
Mean	54.1	1.30	6	4.0
Hub	45.4	1.46	8	12.0

Table 2 Baseline fan rotor design characteristics

Corrected Flow Rate	11 kg/s
Rotor Rotative Speed	12000 RPM
Total Pressure Ratio	1.30
Rotor Tip Speed	314 m/s
Rotor Tip Inlet Relative Mach No.	1.02
Rotor Inlet Tip Diameter	500 mm
Inlet Hub-to-Tip Ratio	0.80
Inlet Guide Vane Number	6
Rotor Blade Number	23
Stator Blades	None
Guide Vane-Rotor Tip Spacing	1.5
Guide Vane Chord (Constant)	84 mm
Rotor Blade Chord (Constant)	80 mm

accelerated along a nearly 2:1 contraction to the inlet guide vane section at which a ratio of hub/tip radius was 0.80. Due to space limitation such a long duct was placed to connect the test rig with the anechoic room. The inlet contraction was made in order to minimize the shed wake effect from the structs on the rotor blades. The discharge side of the fan was ducted into a conduit of 600 mm dia and 10,000 mm length. The duct exit was equipped with a remotely controlled throttle.

The test fan had six inlet guide vanes and 23 rotor blades. The vanes and rotor chords remained constant at 84 mm and 80 mm respectively, with a rotor aspect ratio of 1.6. Each guide vane was relatively placed at the same circumferential position as that of the struts which also numbered six. The axial distance between the vanes and rotor blades was kept at the rather high spacing of 1.5 chord length (=120 mm) clear to allow ample room for the wake measurement and to minimize the noise generation of the vane-rotor potential field interaction.

The velocity triangles, designed for the baseline, equally spaced fan rotor, are shown in Fig. 3. The inlet guide vanes did not impart any circumferential momentum to the oncoming flows. The flow leaving from the rotor blades had a swirl angle of about 35 deg along the whole blade height and entered directly into the volute without any outlet straighter equipped. The mass flow rate and overall pressure ratio designed for the original test article were 11 kg/s and 1.3 respectively at 12,000 rpm. The blade profiles had double circular-arc sections, whose design data were obtained from the author's reports [10, 11]. Blading details and design specifications are given in Tables 1 and 2, respectively.

Unequally Spaced Rotors. The circumferential position of rotor blades was determined at its hub radius by the following equation,

$$\theta_i \approx \frac{360°}{23}\left(i + \sum_{i=1}^{i} \alpha \sin \frac{360°}{23} i\right) \quad i = 1, 2, 3 \ldots 23 \qquad (1)$$

where θ_i is ith blade position, and α is the maximum blade angle change (modulation amplitude). Note that the 23 blade position for the original rotor was given by setting $\alpha = 0$ in equation (1). Furthermore two rotor disks were fabricated which permitted the blades

Nomenclature

A_ℓ, B_ℓ = Fourier series coefficients, equation (2)
B = number of blades
$i = 1, 2, \ldots, 23$, equation (1)
$l = 0, \pm 1, \pm 2 \ldots$, equation (2)
n = number of blade-passage-frequency harmonics
n_{max} = noys number at the noisiest band
n_0 = noys, equation (3)
N_0 = modified noys, equation (3)
N = rotational fan speed
Q_c = corrected flow rate
r = radius
r = tip radius
α = modulation amplitude
β = azimuth angle
$f(\theta)$ = sound pressure represented by Fourier forms, equation (2)
θ = (angular frequency) × (time)
θ_i = blade angular position given by equation (1)
BPF = blade-passage-frequency
SPL = sound pressure level
PWL = power level

to be located in the position determined by $\alpha = 0.05$ and 0.10 around the circumference. They are named the five percent and ten percent modulated rotor respectively and their photographs are shown in Fig. 4. The five percent and ten percent spacing changes were selected to reduce the aural detectability while minimizing the problem of balancing the rotor. The dynamic balance of modulated rotors was equalized by reshaping the thickness of inner sides of the disk. The testing were carried out with the 0 percent, five percent and ten percent modulated rotors used while the inlet guide vanes were equally spaced. Note that the equally spaced rotor is sometimes referred to, by different names such as "baseline," "original" and "unmodulated" rotor in the main body of the paper.

Measurements of Flow. Access for flow measurements was through slots on the outer wall at stations ①, ② and ③ as indicated in Fig. 2. In particular, at station ② both radial and circumferential traversings were made to examine the flow uniformities and to determine the wake profiles shed from the vanes. Most of intrablade row measurements were carried out by use of the total pitot tubes, thermocouples and hot-wire probes. Overall flow rates were measured by an orifice located midway in the long outlet duct.

Noise Instrumentation. The noise level measurements depend mostly on the sound pressure readings of 12.5 mm dia field microphones (B & K 4133) which were set up at a circle of 3000 mm radius from the fan bellmouth center in the anechoic room, Fig. 1. They were spaced at ten deg intervals from zero to 70 deg on that circle. The 6 mm dia condenser microphones (B & K 4136) were also mounted flush on the fan outer casing at several axial locations.

All of the sound pressure were recorded on a multi-channel FM tape recorder (AMPEX FIR-1300). The runs were of the order of one minute to permit satisfactory tape recording of the noise data. The overall response of the system from 20 Hz to 10,000 Hz, considered adequate for the blade passing frequency, was almost flat. The tape readings were played back into an A/D converter and the frequency analysis was performed in 20 Hz bandwidth on a digital computer (TIME/DATA TDA-332). The sound pressure levels and fan speeds obtained for different test conditions were accurate within ± 1 dB and ± 13 rpm respectively.

Experimental Results and Discussion

Aerodynamic Performance. Overall performance data from both modulated blade configurations are compared to the original, equal spacing test article, in Fig. 5. The overall pressure ratio was obtained from an arithmetical mean of five point readings of the pitot tube traversing along the radius. Multiplication of the blade rotational speed with the flow circumferential component yielded the temperature rise for use in evaluating the adiabatic efficiency. It is clearly shown that the five percent modulated rotor exhibited the lowest values of overall pressure ratio, adiabatic efficiency and surge limit as compared with the 0 percent and ten percent modulated rotors. This can be regarded as originating in a significant deterioration of the blade element performance at the tip section for the five percent modulation only, as the detailed survey data of Fig. 6 further demonstrate. The design tip clearance was 1.5 mm, which was common to all cases of modulation. On the basis of the measured velocity triangles, it was revealed that the tip section had operated with rather high turning angle (= 14.6 deg at the design speed) and heavy loading in low efficiency. Notice that Shahady's experiments [4] displayed the worst performance of the thrust versus Mach number curve in the six percent modulation case, as compared with 0 percent and ten percent modulation of helicopter blades for an attack angle of ten deg. The exact nature and its causes of this singular appearance are not understood and are under study.

Unsteady Flow Measurements. One revolutional variations of mean velocity and flow angle were obtained using the cross hot-wire probes immersed at the mean radius behind the rotor blades, Fig. 7.

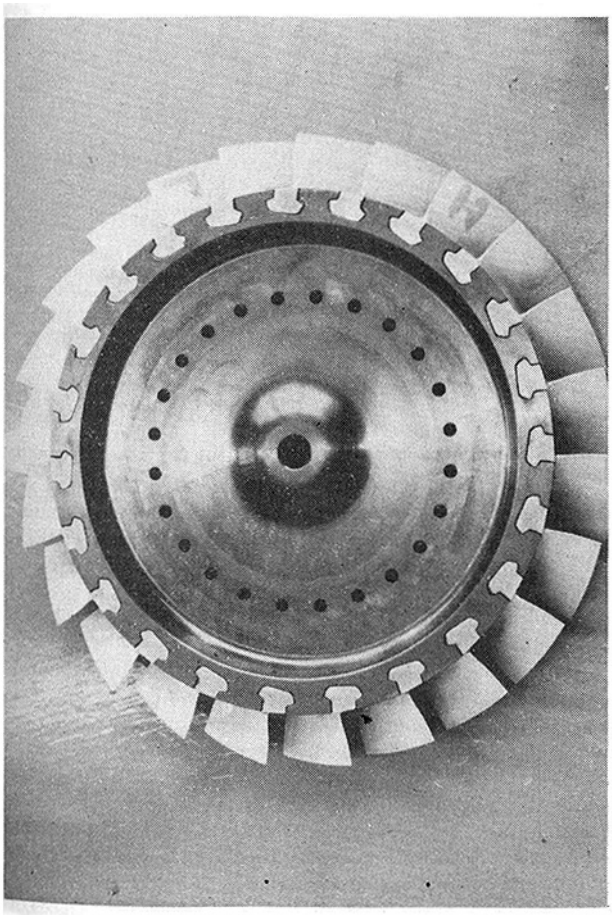

Fig. 4(*a*)

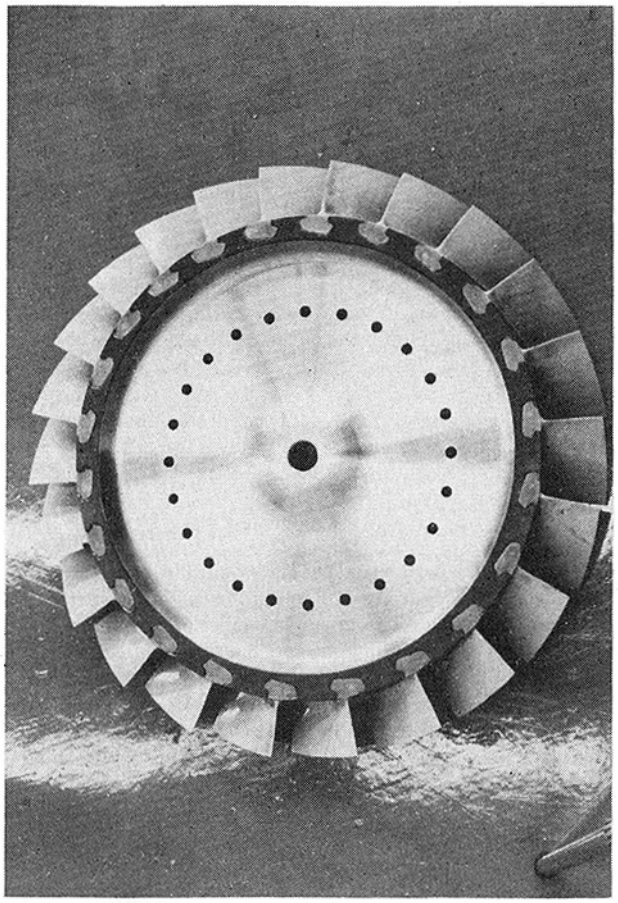

Fig. 4(*b*)

Fig. 4 Modulated rotors

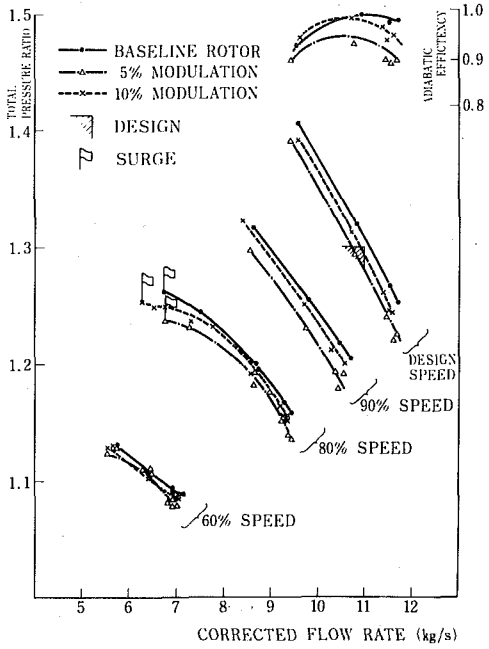

Fig. 5 Overall performance of unmodulated and modulated rotors

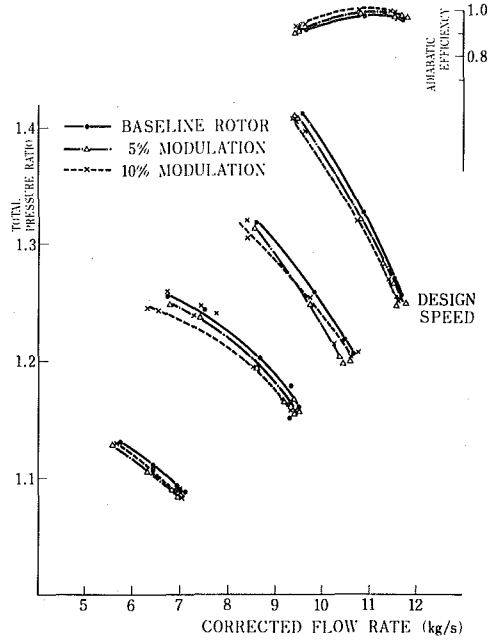

Fig. 6(*b*)

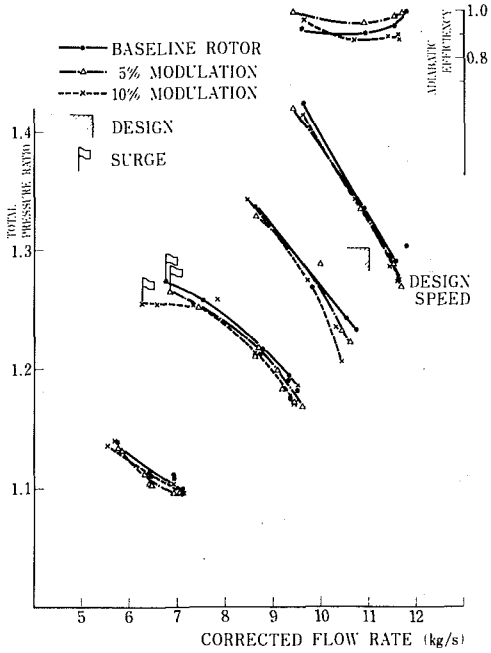

Fig. 6(*a*)

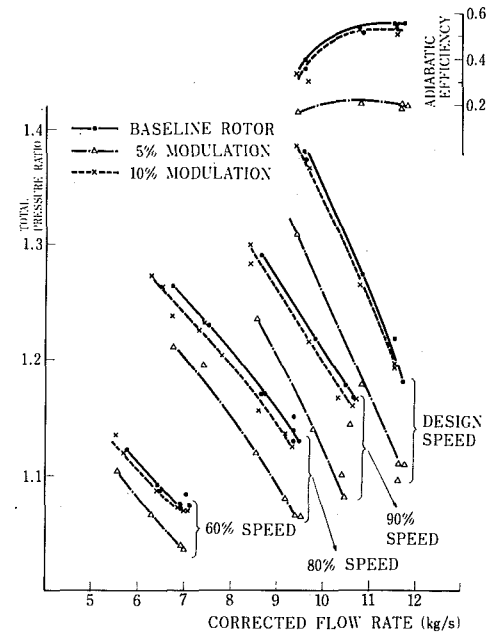

Fig. 6(*c*)

Fig. 6 Blade element performance (*a*) at near hub (*b*) mean (*c*) near tip section

With the trigger of a pulse signal per one revolution, which was optically picked up, the unsteady data were recorded on magnetic tape for off-line data analyses. The ensemble average procedure was taken over the data in order to eliminate random turbulent components. A cosine rule of hot-wire characteristics was assumed in computing the resultant velocities, which were further divided through by the mean value, U_0, of the velocity variations. The absolute flow angles plotted were measured from a reference. It is noticeable that the plateau formed by the measured values between two adjacent wakes became steep as the blades were modulated. The larger the amplitude of modulation became, the higher the exit velocity flowing along the suction side of the blade surface. The same trend was recognized in the flow angle data. It appears that the circumferential asymmetry in blade spacing caused an aerodynamic interaction of one blade with others, so that the peculiar phenomenon was produced.

The hot-wire data were once again analysed in 20 Hz bandwidth, as shown in Fig. 8. The vertical scales are arbitrary, indicating auto-power density. The first and second blade-passage-frequency (BPF), 4.6 kHz and 9.2 kHz respectively at the design speed, were made multiple with the blades modulated. Another spike of the spectral density, which was seen near 2 kHz to 3 kHz, was probably attributed to the turbulent flow coherence.

Fig. 9 illustrates pressure waves captured by the microphones mounted flush on the outer casing in front of and behind the rotor blades. To obtain the photograph shown, the pressure trace displayed on an oscilloscope was triggered once per revolution by a shaft angle reference signal. The camera shutter was left open for several rotor revolutions and the superimposed waves are made by the same blade during succeeding passes. They apparently show periodic nature of the pressure fluctuations in front of the rotor, whereas changes in both amplitude and position can be seen behind one blade. Metzger and Hanson [6] has obtained similar photographs for the wake traces of the subsonic tip speed fan blades.

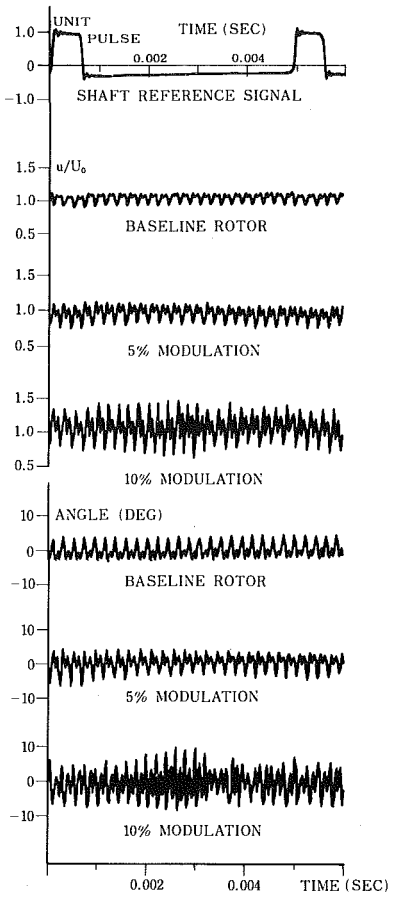

Fig. 7 One revolutional variations of exit resultant velocity and flow angle

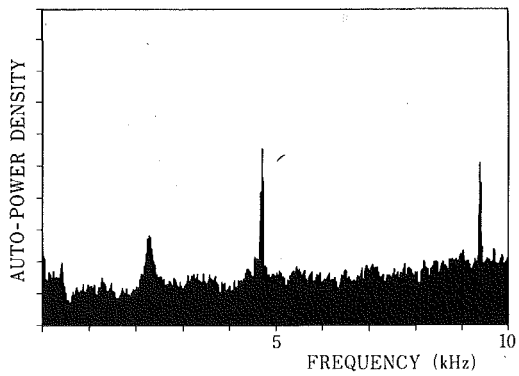

Fig. 8(*a*)

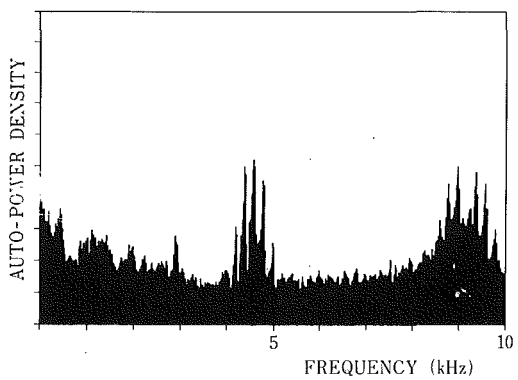

Fig. 8(*b*)

Acoustic Results. The effects of the modulated spacing on the spectral density are typically illustrated in Fig. 10, which were obtained from the sound pressure data measured at an azimuth angle of 30 deg at the design speed. The only parameter varied was the percentage of blade modulation, 0 percent, five percent and ten percent. As excpected, the original first and second BPF were redistributed into a series of multiple tones. A decrease of eight decibel was recognized in the ten percent modulated rotor for the first BPF. But, with the five percent modulation, the peaks of the multiple spectral density were not weaker than those of the original. A series of spikes, seen at the fundamental rotational frequency (=200 Hz at the design speed) and its harmonics, were apparently caused by shock waves at the blade leading-edge, that is, the buzz saw noise. Although the blade modulation altered the magnitudes of each buzz saw tone, the strongest of these peaks was about 15 dB below the highest of BFP because of the fan operation near the sonic velocity at the tip section only.

The radiation patterns of the far-field sound pressure are summarized in Figs. 11–13. They were selected to represent the sound pressure levels (SPL's) at the maximum and the minimum flow rate measured at fan speeds, 12,000 rpm, 10,800 rpm and 9600 rpm. It is defined in the figures that the BPF of modulated rotors is a tone frequency at which the maximum magnitude of sound pressure can be detected around the original BPF. It should be noted that the radiation patterns obtained are proper in the present experiments, because the directivity depends largely on an acoustic impedance of the exit face of the long duct used. But even with this experimental configuration it will be still possible to make a relative comparison of directivity differences noted in the testing where the percentage of spacing modulation is varied.

At the minimum flow rate of each speed, the overall and first BPF SPL's for the five percent modulated rotor were dominant at all directions, Figs. 11(*a*), 12(*a*) and 13(*a*), because the blade tip sections operated with rather heavy loadings in low efficiency. This data trend is similar to the helicopter rotor tests [4], where a moderate increase in overall SPL was reported for the six percent modulated rotor only. With the flow rate increased at 10,800 rpm and 9600 rpm, the blade loading became much light so that any significant difference in the overall SPL's between unmodulated and modulated rotors was not recognized. A six to eight decibel decrease of SPL directivity was obtained for the first BPF of the ten percent modulated rotor. Furthermore it is of interest to note that any singularity of acoustic signature, which was notable in the first BPF of the five percent modulation, was not produced in the second BPF SPL's.

Other acoustic comparisons were made with power levels (PWL's) found by integrating the sound level around the microphone arc, together with the use of a spherical spreading rule. The results are plotted in Fig. 14. The five percent modulation displayed the overall PWL's of about 2 dB higher than other modulations, except at the maximum flow rate point of 9600 rpm and 10,800 rpm. It is again demonstrated that the second BPF harmonic was more attenuated

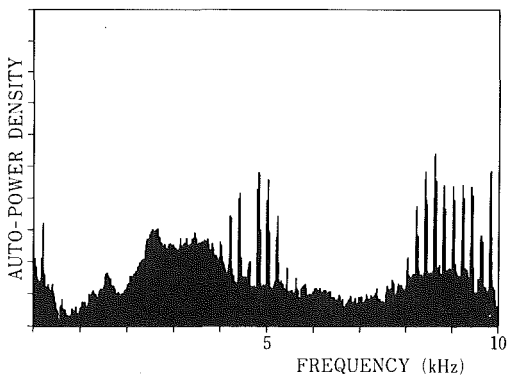

Fig. 8(*c*)

Fig. 8 Autopower spectra of the shedding wake velocity measurements (*a*) baseline (*b*) five percent modulated (*c*) ten percent modulated rotor

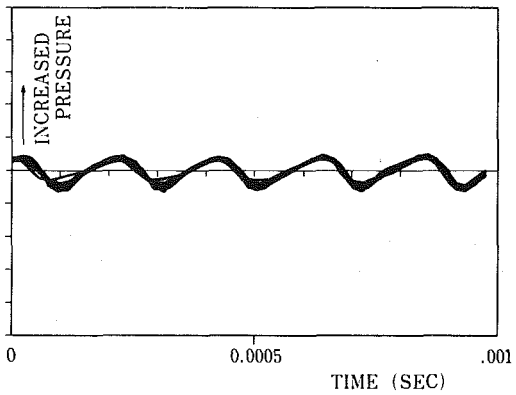

Fig. 9(*a*)

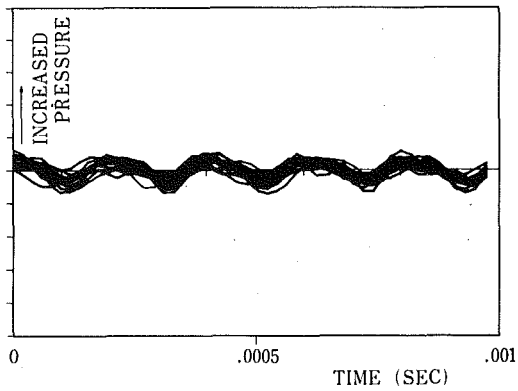

Fig. 9(*b*)

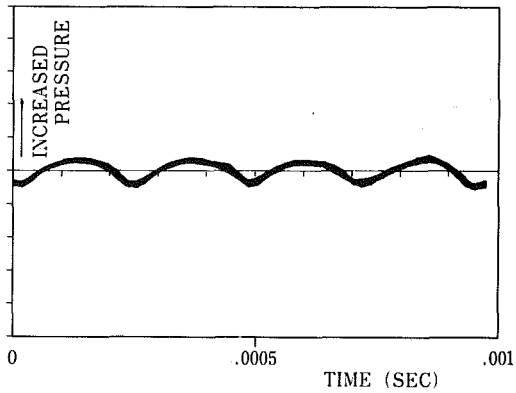

Fig. 9(*c*)

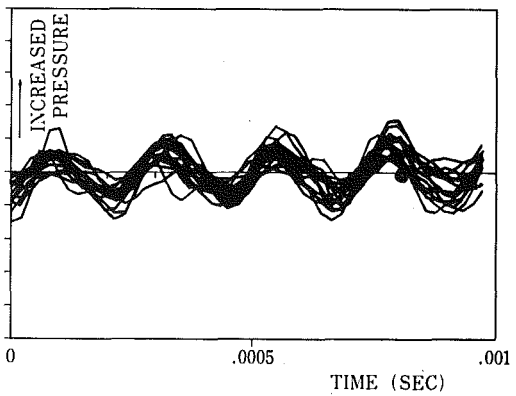

Fig. 9(*d*)

Fig. 9 Pressure fluctuations on the outer casing (*a*) with five percent modulated blades in front of the rotor (*b*) behind the rotor (*c*) with ten percent modulated blades in front of the rotor (*d*) behind the rotor

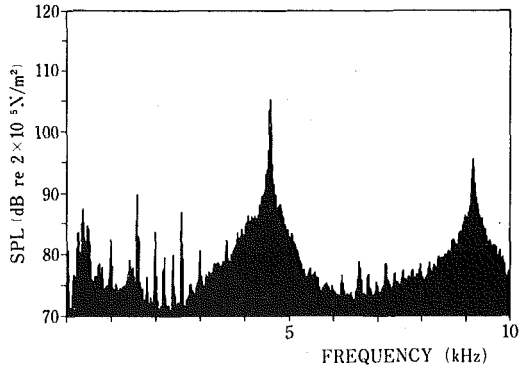

Fig. 10(*a*)

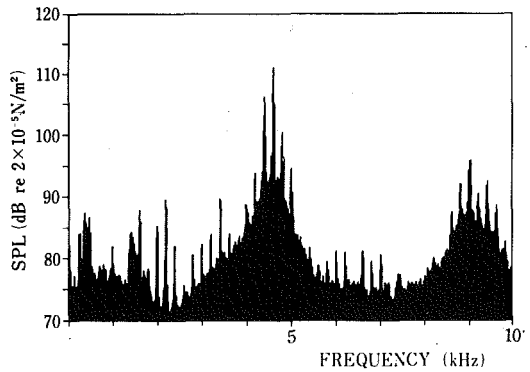

Fig. 10(*b*)

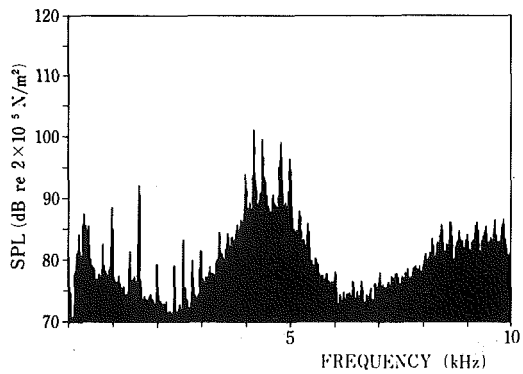

Fig. 10(*c*)

Fig. 10 Typical autopower spectra of the far-field sound pressure measured at $\beta = 30$ deg, $N = 12\,000$ rpm and $Q_c = 10.8$ kg/s (*a*) with unmodulated rotor $\alpha = 0$ (*b*) five percent modulation $\alpha = 0.05$ (*c*) ten percent modulation $\alpha = 0.10$

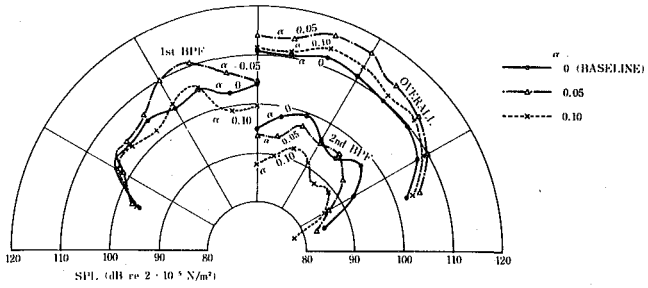

Fig. 11(*a*)

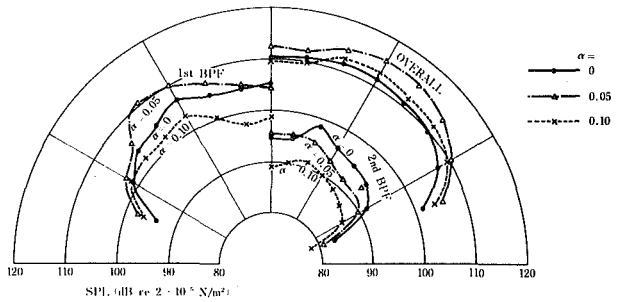

Fig. 11(*b*)

Fig. 11 Overall, first and second blade-passage-frequency noise radiation patterns measured on a three meter radius for three different configurations (*a*) at N = 12000 rpm and Q_c = 9.5 kg/s (*b*) N = 12000 rpm and Q_c = 11.6 kg/s

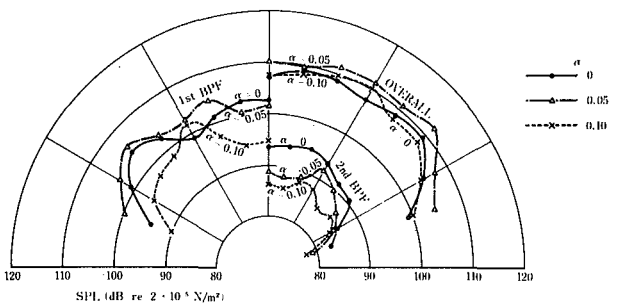

Fig. 12(*a*)

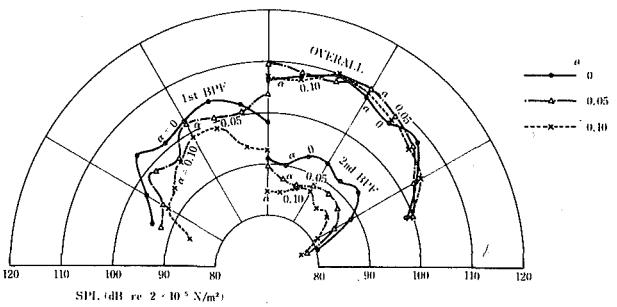

Fig. 12(*b*)

Fig. 12 Overall, first and second blade-passage-frequency noise radiation patterns (*a*) at N = 10800 rpm and Q_c = 8.5 kg/s (*b*) N = 10800 rpm and Q_c = 10.5 kg/s

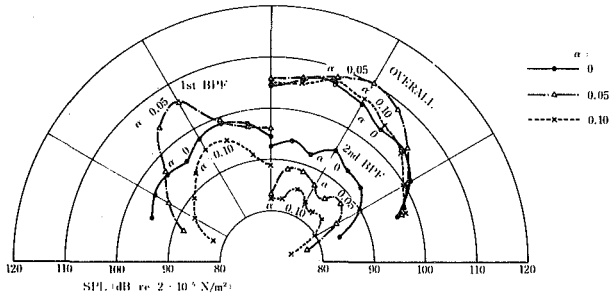

Fig. 13(*a*)

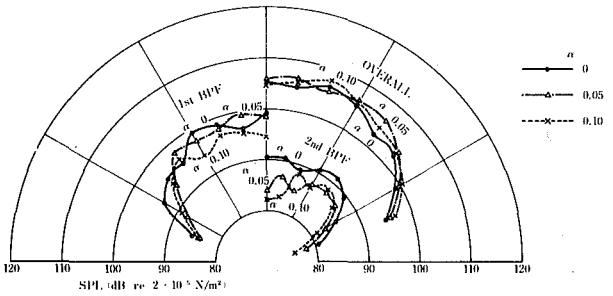

Fig. 13(*b*)

Fig. 13 Overall, first and second blade-passage-frequency noise radiation patterns (*a*) at N = 9600 rpm and Q_c = 7.4 kg/s (*b*) at N = 9600 rpm and Q_c = 9.4 kg/s

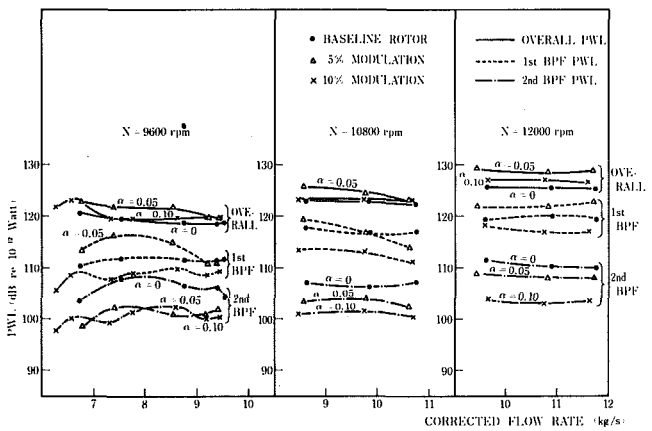

Fig. 14 Overall, first and second power levels versus flow rate at three different speeds for three configurations

than the first BPF by modulating the blade spacing. It can be then surmised that the spacing modulation has a more beneficial influence upon many bladed turbomachine rotors than few bladed. In fact, the BPF high harmonics except the first were attenuated in the six bladed helicopter rotor tests [4].

The acoustic effects of the spacing change may be predicted by comparing the Fourier analyses of the unmodulated and modulated rotors [3, 4]. Assuming that the pressure is periodic over one revolution of the rotor, the pressure fluctuations at a point may be represented by

$$f(\theta) = \sum_{\ell=0,\pm1,\ldots}^{\infty} A_\ell \sin\{(nB + l)\theta\} + \sum_{\ell=0,\pm1,\ldots}^{\infty} B_\ell \cos\{(nB + l)\theta\} \quad (2)$$

where the pressure, $f(\theta)$, attains a maximum value at a blade location $\theta = \theta_i$ given by equation (1). We then assumed the plausible, various shapes of $f(\theta)$, which are summarized in Fig. 15. By use of equations

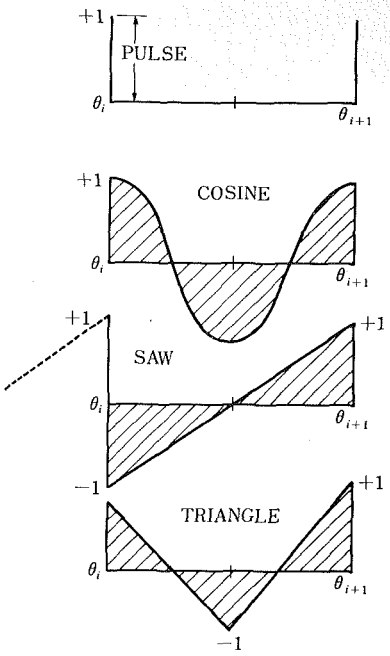

Fig. 15 Assumed shapes of sound pressure event for use in predicting the magnitudes of multiple pure tones

(1) and (2) and assumed shapes for pressure event, the magnitudes of the Fourier coefficients, $\sqrt{A_\ell^2 + B_\ell^2}$, were computed for both unmodulated and modulated cases. They were further expressed in decibels, such that $\Delta\text{SPL} = 20 \log_{10} 1.0/\sqrt{A_\ell^2 + B_\ell^2}$, the 1.0 representing the amplitude of the unmodulated case [4]. The results are shown in comparison to the measured data in Fig. 16.

The figures demonstrate that all of the assumed shapes predicted almost the same value of ΔSPL of the first BPF. The agreements with the measured data were reasonable for $l = \pm 1, \pm 2$; but the discrepancy was serious for the center frequency $l = 0$. Particularly in the five percent modulation case, positive values of the measured ΔSPL might arise due to the change of acoustic characteristics itself with the heavily loaded blades.

With regard to the second BPF, the cosine and triangle shapes did not give agreeable results with the measured data while the impulse-type shape had a reasonable predictive capability.

The main thrust of this study was to attenuate the aural detectability of the tone noise. Making use of the following formula given by Kryter and Pearsons [8]

$$N_0 = n_{\max} + 0.07\,(\textstyle\sum n_0 - n_{\max}) \qquad (3)$$

the SPL's measured in front of the bellmouth ($\beta = 0°$) were converted into the modified noy number, N_0. The results are plotted in Fig. 17. They indicate a difference of about 50 noy numbers between the 0 percent and ten percent modulated rotors at the large flow rate, which in turn implies about a three perceive-noise decibel (PNdB) decrease [9].

Conclusions

The application of modulation principles to high-speed, axial-flow fans was considered as a means to reduce the aural detectability. The 0 percent, five percent and ten percent spacing changes were selected for the acoustic and aerodynamic testing. The test results showed that spectral modifications could be achieved by relatively small blade spacing changes.

The measured data comparisons indicated that the ten percent modulated rotor displayed a six to eight and about a ten decibel SPL decrease in the first and second BPF respectively, as compared with the original, baseline rotor. Disadvantages in aerodynamic performance resulting from spacing modulation were not recognized with the ten percent modulated blades.

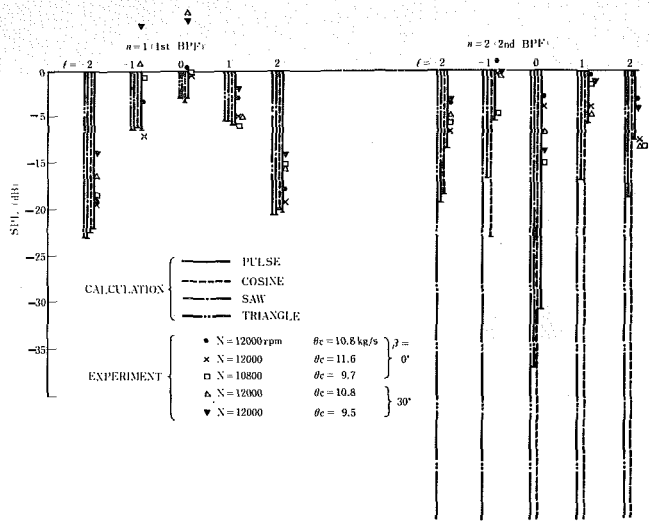

Fig. 16(*a*)

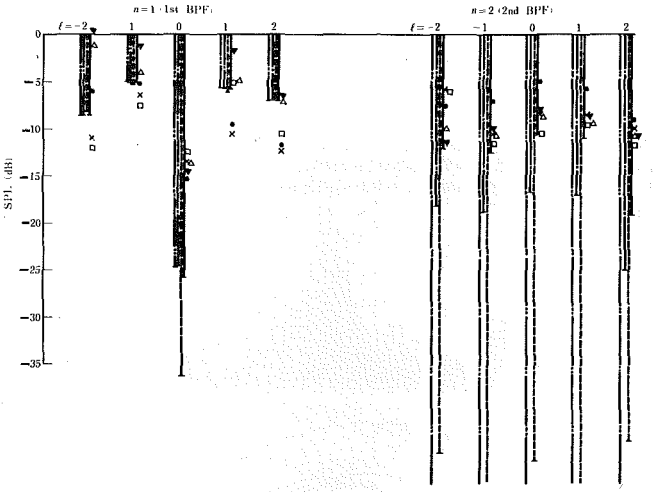

Fig. 16(*b*)

***Fig. 16* Sound-pressure magnitude comparison of experiment and calculation for (*a*) five percent modulation (*b*) ten percent modulation**

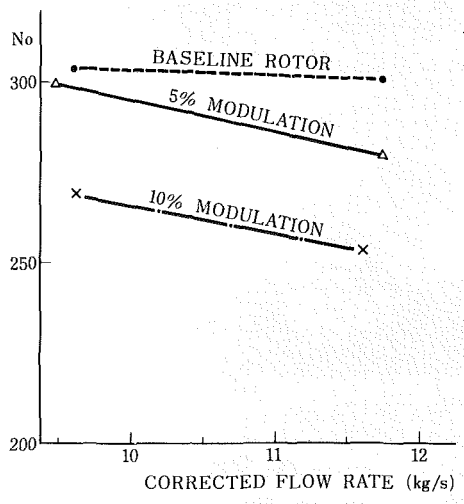

Fig. 17 Modified noy numbers versus flow rate at $N = 12000$ rpm and $\beta = 0$ deg

It was however revealed that the five percent modulated rotor only exhibited a serious deterioration of the aerodynamic performance at the blade tip elements. The peak amplitudes of the first BPF SPL of the five percent modulated rotor were therefore not reduced.

The pressure fluctuations were represented in Fourier forms with various kinds of assumed shapes for pressure events. Comparison to the measured data showed that the calculation method assuming a pulse type had a reasonable capability of predicting the peak magnitudes of redistributed pure tones.

Acknowledgments

The author is indebted to H. Nishiwaki and K. Takeda for their assistance in carrying out the experiments and data reduction for the tests described in this paper. T. Torisaki was the general manager of the project. Support of this research by Environmental Protection Agency of Japan is gratefully acknowledged.

References

1 Caruso, W. J., et al. "Turbo-Machine Blade Spacing with Modulated Pitch," U.S. Patent 3,006,603, Oct. 31, 1961.

2 Mellin, R. C. and Sovran, G. "Controlling the Tonal Characteristics of the Aerodynamic Noise Generated by Fan Rotors," ASME paper No. 69-WA/FE-23, 1969.

3 Evald, D., Pavlovic, A. and Bollinger, J. G. "Noise Reduction by Applying Modulation Princiles," *J. Acous. Soci. America*, Vol. 49, 1971, p. 1381.

4 Shahady, P. A., et al. "The Effects of Modulated Blade Spacing on Stator Rotor Acoustics and Performance," AIAA paper No. 73-1020, 1973.

5 Duncan, P. E. and Dawson, B. "Reduction of Interaction Tones from Axial Flow Fans by Suitable Design of Rotor Configuration," *J. Sound & Vib.*, Vol. 33, 1974, p. 143.

6 Metzger, F. B. and Hanson, D. B. "Low Pressure Ratio Fan Noise Experiment and Theory," ASME paper No. 72-GT-40, 1972.

7 Hanson, D. B. "Unified Analysis of Fan Stator Noise," *Acous. Soci. America*, Vol. 54, 1973, p. 1571.

8 Kryter, K. D. and Pearsons, K. S. "Judged Noisiness of a Band of Random Noise Containing an Audible Pure Tone,". *Acous. Soci. America*, Vol. 38, 1965, p. 106.

9 Kryter, K. D. and Pearsons, K. S. "Modification of Noy Tables," ibid., Vol. 36, 1964, p. 394.

10 Fujii, S. and Matsuki, M. "Several Topics of Axial-Flow Compressors Research at the National Aerospace Laboratory (Japan)," Tokyo Joint International Gas Turbine Conference, JSME-6, 1971.

11 Fujii, S., et al. "Aerodynamic Design and Test Results of Front Fans," National Aerospace Lab. Tech. Report TR-268T, 1972.

12 Fujii, S., et al. "Some Considerations on Pure Tone Noise Generation in an Axial-Flow Fan," *1977 Tokyo Joint Gas Turbine Congress Proceedings, p. 428.*

E. C. Hansen
G. K. Serovy
Iowa State University,
Ames, IA

P. M. Sockol
Research Engineer.
NASA-Lewis Research Center,
Cleveland, OH

Axial-Flow Compressor Turning Angle and Loss by Inviscid-Viscous Interaction Blade-to-Blade Computation

A method for computation of the flow field around an arbitrary airfoil cascade on an axially symmetric blade-to-blade surface was developed which takes into account the development and separation of the blade surface boundary layers and mixing in the wake. The method predicts the overall fluid turning and total pressure loss in the context of an inviscid-viscous interaction scheme. The inviscid flow solution is obtained from a compressible flow matrix method. The viscous flow is obtained from a differential boundary layer method which calculates laminar, transitional and turbulent boundary layers. Provisions for the calculation of laminar and turbulent separation regions were added to the viscous scheme. The combined inviscid-viscous interaction scheme described yields results which are quantitatively consistent with experimental data. This suggests that the physical basis for the interactive system is correct and justifies continued exploration and use of the method.

Introduction

Recent experience in flow field computation for axial-flow compressors has supported the quasi-three-dimensional steady relative flow model. In this model iteration to convergence occurs between solution of the conservation equations on a hub-to-tip surface approximating a mean stream surface in the blade passages, and estimates of the flow on multiple axisymmetric surfaces approximating blade-to-blade stream surfaces. The blade-to-blade stream surface approximations are used to determine airfoil cascade configurations which turn and decelerate the flow and consequently generate a distribution of relative total-pressure losses in the flow field.

At present axial-flow compressor design and analysis is strongly dependent on correlations of measured turning angle and loss from experiments on linear airfoil cascades and annular fixed and rotating rows of blades. In real fan and compressor geometries numerous phenomena exist which influence the flow so as to modify the velocity and property distributions from those based on a strictly interpreted quasi-three-dimensional model. However, considerable gains in design system reliability could be realized by development of a blade-to-blade flow field computation method predicting airfoil cascade local and exit region fluid angles and relative total pressure losses for the type of inlet and exit initial boundary conditions generated in a typical current hub-to-tip surface solution.

In the investigation summarized in this paper an inviscid-viscous flow field interaction method was developed for computation of the fluid turning and loss characteristics of an arbitrary airfoil cascade. The method deals with the flow on an axially symmetric blade-to-blade stream surface approximation. The flow may be compressible, and axial velocity-density product and stream surface radius changes are permitted. A principal objective of the study was to demonstrate that current and reliable inviscid and viscous region solutions could be utilized with an efficient interaction method to generate physically realistic information concerning the flow patterns in the blade-to-blade passage and to adequately model the flow following separation and downstream of the cascade geometry. This first report of the results of the investigation describes the structure of the computation method and demonstrates its effectiveness in several test cases.

Computation Methods for Cascade Flows

The general subject of airfoil cascade flow field computation has been discussed extensively in the literature [1–3]. Alternative procedures range from inviscid field calculation methods through fully viscous solutions. The fully viscous solutions are at present in the initial stages of development and involve numerous subsidiary geometric and aerodynamic problems. For some requirements, inviscid flow field solutions are useful. In cases when cascades are not highly loaded, so that surface velocity diffusion is not excessive, the pressure distribution information developed through inviscid field analyses can be valid.

When airfoil cascade fluid turning angle characteristics are critical,

Contributed by the Gas Turbine Division and presented at the Gas Turbine Conference and Exhibit and Solar Energy Conference, San Diego, California, March 12–15, 1979 of THE AMERICAN SOCIETY OF MECHANICAL ENGINEERS. Manuscript received at ASME Headquarters November 29, 1978. Paper No. 79-GT-5.

Table 1 Summary of inviscid-viscous iterative calculation procedures for airfoil cascades

Inviscid-Viscous Cascade Analysis	Inviscid Flow Calculation Method	Viscous Region Calculation Method		Interaction Method		Cascade Type and Blade Type Tested
		Boundary Layer	Separated Flow Region	Displacement Thickness Effect Included By	New Displacement Thickness Level	
Speidel [9]	Speidel (1954)	Truckenbrodt (1952) Integral	θ Calculated at the trailing edge Speidel (1954)	Modifying the camber line shape only	—	2-D decelerating NACA 0010 0015 0020
Föttner [10]	Schlichting (1955)	Scholz (1960) Truckenbrodt (1952) Integral	None described	Injection	Full displacement thickness	2-D decelerating NACA 65-(12 A_{10})06
Föttner [11]	Shaalan and Horlock (1968)	Scholz (1960) Truckenbrodt (1952) Integral	H = constant, correlation for θ change	Modifying the original profile shape	Full displacement thickness	2-D decelerating NACA 65-0010 with a circular camber line
Geller [4]	Martensen (1959)	Walz (1966) method II Integral	Injection to produce a constant downstream pressure	Injection beginning at separation	—	2-D decelerating NACA 65-($4A_2I_{8b}$)10 65-($8A_2I_{8b}$)10 65-($12A_2I_{8b}$)10 Accelerating, camber angle = 110°
Sanger [12]	Katsanis (1969)	McNally (1970) Integral	Manual extrapolation	Modifying the original profile shape	Full displacement thickness	Compressor stator, double circular arc

inviscid field solutions have limited value. Geller [4], Dodge [5], Ispas [6], Stark and Starke [7] and Miller and Serovy [8] have described attempts to utilize inviscid methods. The limitations are apparent insofar as fluid turning is concerned. Losses are, of course, not associated with the inviscid solution.

Inviscid-viscous flow interaction models have also been suggested frequently as the basis for improved airfoil and cascade performance prediction. For airfoil cascades Table 1 summarizes the published results up to the time of the present study. In these interaction methods an inviscid solution for the actual cascade geometry was first calculated to obtain airfoil surface pressure distributions. These pressures were then used to compute boundary layer development, and the resultant displacement thicknesses were used to modify the original cascade geometry. Beyond this initial similarity, the methods differed in the way the profile was modified, in how the input to the boundary layer flow was obtained from the inviscid flow field, in the closure condition used to obtain the outlet angle, in the way separation was handled, and in the way matched inviscid-viscous solutions were obtained.

The interaction methods listed in Table 1 were all studied during the initial phases of this investigation, and it was decided that a substantial improvement might result by incorporating a more efficient technique for inviscid-viscous region interaction, and by using

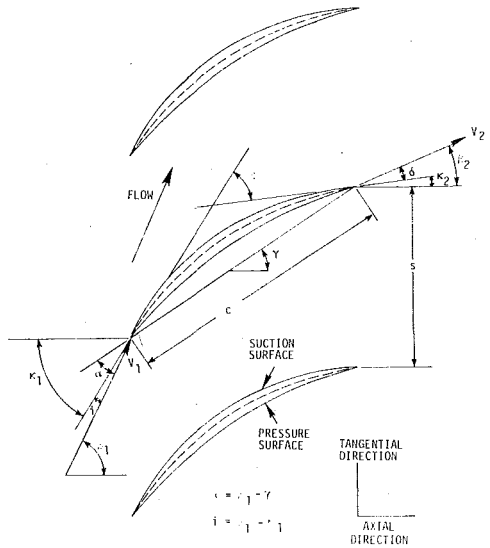

Fig. 1 Cascade notation

Nomenclature

a_{cr} = critical velocity
b = blade to blade streamsheet thickness
c = chord length (Fig. 1)
C_p = pressure coefficient, $P_1 - p/P_1 - p_1$
C_w = wake coefficient [23]
H = boundary layer form factor, δ^*/θ
i = incidence angle (Fig. 1)
ℓ = arc length along the blade surface
M_i = inlet Mach number
P = total pressure
p = static pressure
Re_c = Reynolds number based on the chord length
s = blade spacing in the tangential direction (Fig. 1)
U or V = fluid velocity
X = coordinate parallel to the chord line measured from the leading edge
α = angle of attack (Fig. 1)
β = fluid angle of relative flow measured from axial direction (Fig. 1)
γ = blade-chord angle or stagger angle, angle between blade chord line and axial direction (Fig. 1)
δ = deviation angle, angle between cascade exit relative flow direction and line tangent to camber line at the trailing edge (Fig. 1)
δ^* = boundary layer displacement thickness
η = coordinate normal to the flow direction
θ = boundary layer momentum thickness
κ_1, κ_2 = camber line angles, angles between line tangent to camber line and axial direction at leading and trailing edge (Fig. 1)
κ = curvature of streamline
λ = ratio of the fluid velocity to the critical velocity, a_{cr}
ρ = fluid density
σ = cascade solidity, c/s
τ_w = wall shear stress
ϕ = blade section camber angle, $\kappa_1 - \kappa_2$ (Fig. 1)
ψ = stream function

Subscripts

calc = value calculated from the boundary layer equations
inj = value injected on the surface in the inviscid flow
I = value associated with the inviscid flow
o = outlet flow
p = pressure surface
s = suction surface
v = value associated with the viscous flow
1 = upstream station
2 = downstream station

less restricted computational models for both the inviscid solution and the viscous region. The following section describes the approach used.

Inviscid-Viscous Interaction Method

The inviscid-viscous interaction method developed in this study uses two already existing computer codes, one for the calculation of the inviscid flow field and one for the calculation of the boundary layer flow.

The program for the calculation of the inviscid flow is reported in Katsanis and McNally [13] for compressible flow on an axially symmetric blade-to-blade surface with provision for axial velocity-density product and stream surface radius change.

The boundary layer program used is a revised version of the Albers and Gregg [14] program. This is a differential method with provisions for laminar, transitional, and turbulent boundary layers. The displacement effect of the boundary layer is modeled by injecting fluid (in the inviscid calculation) along the airfoil surface, as suggested by Lighthill. This is done by changing the value of the stream function, ψ, along the airfoil surface by the amount $\Delta\psi = U\rho b\delta^*$, beginning at the first vertical mesh line downstream of the leading edge. This additional fluid then continues downstream (beyond the trailing edge) in the inviscid calculation. The following subsections summarize the major features of the inviscid-viscous interaction technique used. Substantial additional information is included in Hansen (15).

Utilization of Viscous Region Program. First, the boundary layer thickness and velocity profile used to initiate the viscous region calculation are obtained from the solution to the Hiemenz flow given in Schlichting [16]. For the first boundary layer calculation the computation station locations are established empirically. In subsequent boundary layer calculations, the computation station locations along the blade surfaces are determined as follows.

The first ten steps are $\Delta\ell = 4\delta^*$. Between the eleventh point and the midpoint of the blade $\Delta\ell = 18\delta^*$ or $\Delta\ell = c/200$, whichever is larger. On the rear one-half of the blade $\Delta\ell = c/60$.

The transition model in the Albers and Gregg [14] program was used unchanged, but modifications were made to account for laminar and turbulent separation. When laminar separation occurs, momentum thickness growth and reattachment are predicted by the method of Roberts [17]. When Roberts' model predicts no reattachment possible (bursting), a limit is placed on the total separation zone length so that calculations can continue.

The Albers and Gregg program was also extended to calculate small regions of separated flow using some of the suggestions of Carter and Wornom [18]. The convective term in the boundary layer equation, ρU, is set equal to zero in the backflow region and the tridiagonal system of equations is slightly modified to insure diagonal dominance. However, the edge velocity is specified in the Albers and Gregg procedure and not the displacement thickness as in the Carter and Wornom method. When the separated region becomes too large, the method fails. In this case, an estimate of the boundary layer at the trailing edge is obtained by integrating

$$U^2\frac{d\theta}{d\ell} + (2+H)\theta U\frac{dU}{d\ell} = \frac{\tau_w}{\rho}, \tag{1}$$

where $\tau_w/\rho = 0$ and U is known. H is linearly estimated between H_{last}, at the last acceptable boundary layer calculation, and $H = H_{\text{last}} + 1.0$ at the trailing edge.

Interaction Procedure. The object of viscous-inviscid region interaction is to find matched viscous and inviscid solutions, for which the displacement thickness calculated from the boundary layer equations is equal to that injected along the surface in the inviscid flow, and an appropriate trailing edge condition is satisfied.

A summary of the overall computation procedure is as follows. Beginning with an initial guess of outlet angle for the inviscid flow, the outlet angle is varied until the trailing edge suction surface and pressure surface pressures are almost equal. The suction surface boundary layer is then calculated and one-half of the displacement thickness is injected along the surface in the inviscid calculation to obtain the coefficient, $\partial U_s/\partial\delta^*_s$, which is discussed later. Then both the suction and pressure surface layers are calculated. At this point the interaction loop is entered, and changes in the injected suction surface displacement thickness and the outlet angle are made. These changes are made each iteration until convergence or eight iterations. At convergence, the pressure surface boundary layer is calculated using the latest pressure distribution.

The trailing edge condition used establishes a continuous pressure along a line normal to the flow at the trailing edge. Measurements made near the trailing edge of an airfoil by Preston and Sweeting [19] show this to be experimentally true. These measurements also show a pressure gradient through the viscous layer at the trailing edge. Spence [20] suggested that the pressure change could be calculated from the curvature (κ) of the inviscid streamlines and the velocity distribution through the boundary layer by integrating

$$-\kappa U^2 = -\frac{1}{\rho}\frac{\partial p}{\partial \eta} \tag{2}$$

from the edge of the boundary layer to the airfoil surface. This equation was used in this investigation to estimate the actual surface pressures on the rear one-half of the blade and at the trailing edge point. This was not done on the forward one-half of the blade because the boundary layer is small. The technique was applied by using the inviscid velocity derivatives at the edge of the boundary layer to estimate κ and then integrating equation (2) along a normal to the streamline from the edge of the boundary layer to the airfoil surface. Then knowing the inviscid pressure at the edge of the boundary layer and the pressure change through the boundary layer, an estimate of the viscous surface pressure was obtained and a corresponding velocity was computed as input for the boundary layer calculation.

A matched viscous-inviscid solution is reached by iteratively estimating better values of injected suction surface displacement thickness and outlet angle. The method used is somewhat similar to that of Brune, Rubbert, and Nark [21]. Brune, et al. match the viscous and inviscid solution at several points along their simple test case, but because of the much more complex flow, the present method uses the trailing edge location as the only matching location. Fig. 2 shows the advantage of the Brune, et al. scheme, which uses information from both the inviscid and viscous solutions to estimate the next displacement thickness, over other interaction schemes which use only the previously calculated displacement thickness. The inviscid line describes how the trailing edge suction surface displacement thickness changes the velocity at the trailing edge. The viscous line shows how a change in velocity at the trailing edge changes the trailing edge displacement thickness. The slopes of these lines are then estimated and a better guess of the displacement thickness is obtained. Estimating the displacement thickness, as just described, and the outlet angle, to obtain a continuous pressure normal to the flow at the

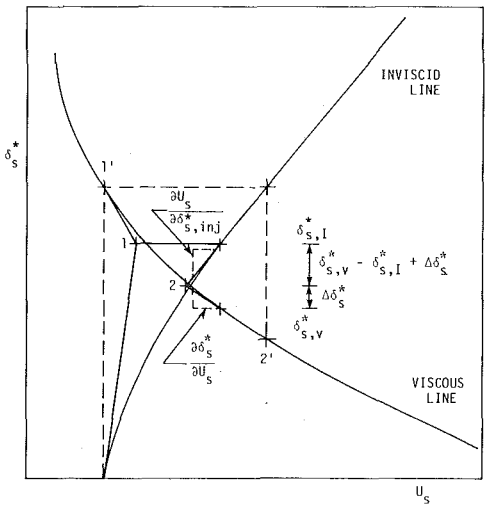

Fig. 2 Interaction between suction surface velocity and boundary layer displacement thickness at the trailing edge

trailing edge, simultaneously is accomplished using equations (3–6).

$$\Delta\delta^*_s = \frac{\partial\delta^*_s}{\partial U_s}\Delta U_s \tag{3}$$

$$\Delta U_s = \frac{\partial U_s}{\partial\beta_{o,I}}\Delta\beta_{o,I} + \frac{\partial U_s}{\partial\delta^*_s}(\delta^*_{s,v} - \delta^*_{s,I} + \Delta\delta^*_s) \tag{4}$$

$$\Delta U_p = \frac{\partial U_p}{\partial\beta_{o,I}}\Delta\beta_{o,I} \tag{5}$$

$$U_p + \Delta U_p = U_s + \Delta U_s \tag{6}$$

This system of four equations has four unknowns, $\Delta\delta^*_s$, ΔU_s, ΔU_p and $\Delta\beta_{o,I}$. The values of $\delta^*_{s,v}$, $\delta^*_{s,I}$, U_p and U_s are readily obtained at the trailing edge from the latest inviscid and viscous calculations as seen in Fig. 2. $\delta^*_{s,v}$ is the value of the suction surface displacement thickness at the trailing edge calculated from the boundary layer equations. $\delta^*_{s,I}$ is the value of the suction surface displacement thickness at the trailing edge injected on the airfoil. $\delta^*_{s,v} - \delta^*_{s,I} + \Delta\delta^*_s$ is the change in the injected displacement thickness and $\Delta\beta_{o,I}$ is the change in the inviscid outlet angle, U_p and U_s are the trailing edge pressure and suction surface boundary layer input velocities. The derivatives $\partial U_s/\partial\beta_{o,I}$ and $\partial U_p/\partial\beta_{o,I}$ are calculated before the interaction begins by observing the velocities near the trailing edge as the inviscid outlet angle is varied. $\partial U_s/\partial\delta^*_s$ is calculated when the first estimate of the suction surface boundary layer is injected on the bare airfoil. $\partial\delta^*_s/\partial U_s$ is obtained from the boundary layer solution as $(d\delta^*_s/d\ell)/(dU_s/d\ell)$ evaluated at the trailing edge. When all the constants are known, the new values of $\beta_{o,I}$ and δ^*_{inj} are calculated by adding one-half of the change predicted by equations (3–6).

Cascade Exit Region. Downstream of the trailing edge, the total pressure loss and the outlet angle are calculated from the inviscid outlet angle and the trailing edge boundary layer displacement and momentum thicknesses using the control volume model for complete mixing due to Lieblein and Roudebush [22].

Cascade Data for Test Cases

It was considered that acceptable cascade test case data for the present work should include measurements of the inlet Mach number, inlet Reynolds number, inlet air angle, inlet turbulence, fluid entrance properties, the geometry of the blade-to-blade passage and the value of the local-to-inlet axial velocity density ratio through the cascade. Necessary dependent or measured quantities included turning or outlet angle, a measure of total pressure loss, and the pressure distribution on the blade surfaces. In addition experiments were sought in which values of the boundary layer displacement and momentum thicknesses along the blade surface were available.

Although the present model is able to calculate cases with axial velocity density ratios other than one,[1] it was felt that two-dimensional experiments would be best for initial test cases because they would probably point to the sources of flaws in the modeling and because the majority of the data for which the axial velocity-density product was controlled were in fact two-dimensional. Airfoil cascades using three blade sections, NACA 65-410, NACA 65-(12)10, and USSR 10A30/27.6 II 45 were selected. The 65-410 airfoil was selected because in addition to the data of Herrig, et al. [23], data from Peterson [24] provided boundary layer information on both sides of the blade for three angles of attack. A 65-(12)10 cascade was chosen because low speed and Reynolds number data were available from Herrig, et al. [23], boundary layer data were available from Milsch [25], and high speed data were available from Dunavant, et al. [26]. Finally, a USSR 10A30/27.6 II 45 cascade was chosen because interior flow field distributions were measured by Bunimovich and Svyatogorov [27]. The airfoil sections were each used for test case computation in one cascade configuration as shown in Table 2.

Results

The inlet flow conditions for the cascade test cases are given in Table 2. Calculations were made using a Univac 1100/42 computer.

NACA 65-410 Airfoil Cascade. Fluid turning, loss, and suction surface transition and separation points as a function of angle of attack for the NACA 65-410 cascade are shown in Fig. 3. The two calculations (1 and 2) shown differ only by the step size ($\Delta\ell$) used on the last one-half of the blade. Calculation 2 uses the same step size in the boundary layer as all other calculations in this work, while calculation 1 uses a larger step size. Notice that up to $\alpha = 18$ deg the two calcu-

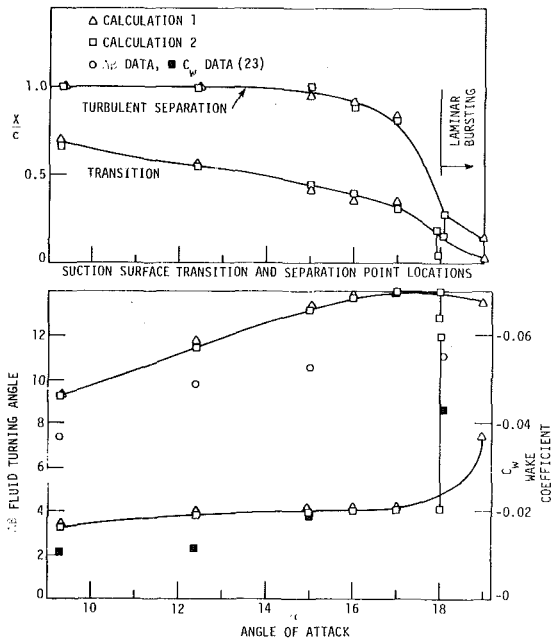

Fig. 3 Fluid turning angle and loss with calculated transition and separation points for two-dimensional 65-410 linear airfoil cascade. c = 124 mm, σ = 0.78, γ = 45 deg, M_i = 0.1, Re_c = 245,000

[1] The Katsanis and McNally [13] program includes the useful feature of being able to vary the axial velocity-density product and the axially symmetric stream surface radius as functions of the meridional distance through the cascade.

Table 2 Independent cascade variables for each test case

Test Case	Inlet Mach Number M_i	Inlet Reynolds Number Re_c	Angle of Attack α deg	Inlet Turbulence Intensity Tu	Axial Velocity Density Ratio
65-410 Cascade γ = 45.0 deg, σ = 0.78					
Low Speed	0.1	245,000	9.3 deg, 12.4 deg 15.0 deg, 16.0 deg 17.0 deg, 18.0 deg 19.0 deg	0.005	1.0
65-(12)10 Cascade γ = 45.7 deg, σ = 1.0					
Low Speed	0.1	245,000	4.2 deg, 17.7 deg 19.2 deg, 20.7 deg 21.7 deg	0.005	1.0
10A30/27.6II45 Cascade γ = 27.4 deg, σ = 1.3					
	0.41	270,000	16.6 deg	0.005	1.0

lations are in agreement. The calculated turning, $\Delta\beta$, has a slope which is quite similar to the experimental data and levels off as the experimental data do. This decrease in turning occurs near the point where laminar separation and bursting occur in the model. However, the values of turning for the experimental data and the calculation differ by about two deg. The calculated wake coefficient is high at low angles of attack and not high enough at high angles of attack. Although at high angles of attack the calculated and experimental wake coefficients do not match, they both show the same trend, with a rapid increase for a small change in angle of attack occurring after the point of laminar separation and bursting. The points of transition and turbulent separation move dramatically near the onset of laminar separation and bursting. This is to be expected, because as the inlet angle is increased, the pressure gradient on the suction surface is steeper and the transition point moves forward until the gradient is so steep that laminar separation occurs. The computation time for the seven incidence cases run consecutively was 2.03 hr (17.4 min per incidence case).

Fig. 4 shows the convergence of the calculations for the NACA 65-410 cascade. All of the calculations were done so that the converged solution from the previous inlet conditions is used as the starting point of the calculation of the next inlet conditions. $U_s - U_p$ is the difference in the viscous surface velocities on the suction and pressure surfaces and indicates the degree to which the trailing edge pressures are equal. $\delta^*_{inj} - \delta^*_{calc}$ is the difference in the injected suction surface trailing edge displacement thickness and suction surface trailing edge displacement thickness calculated from the boundary layer equations. $\beta_{o,I}$ is the angle at the downstream boundary of the inviscid calcula-

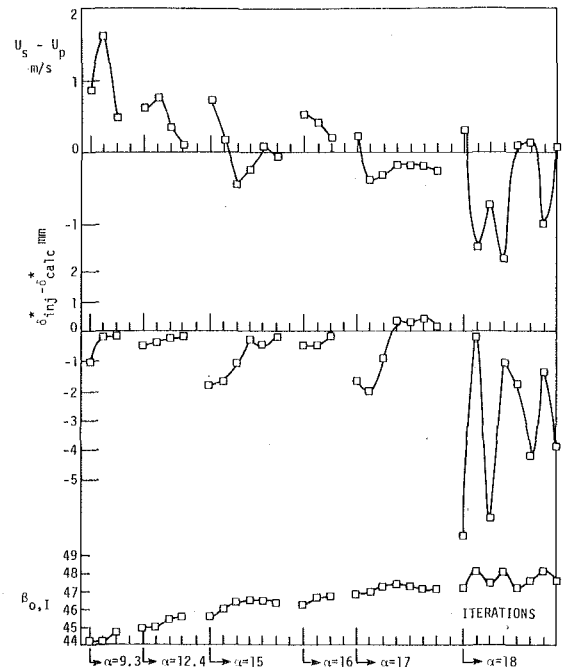

Fig. 4 Convergence of the calculations at several angles of attack for the 65-410 airfoil cascade of Fig. 3

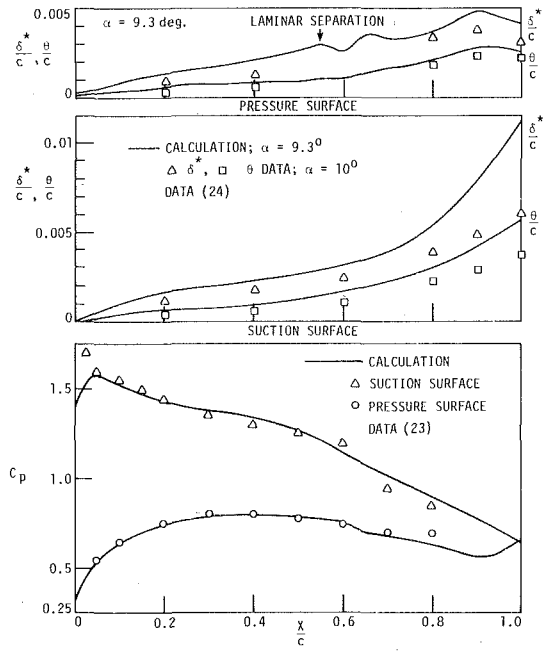

Fig. 5 Surface pressures and boundary layers for the 65-410 airfoil cascade of Fig. 3 at α = 9.3 deg

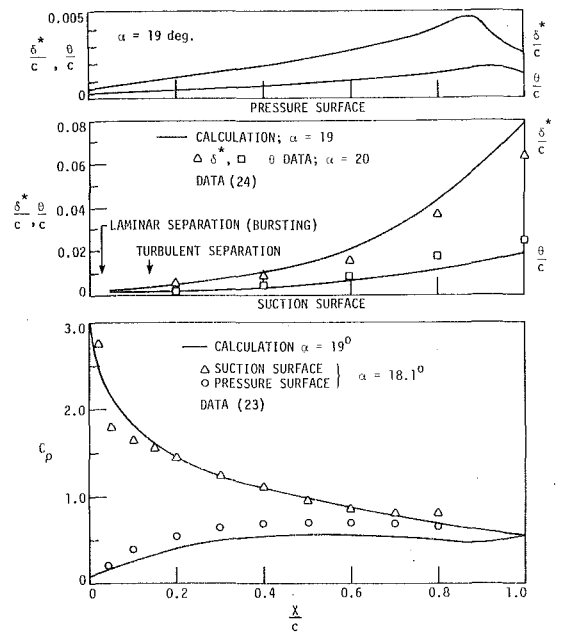

Fig. 6 Surface pressures and boundary layers for the 65-410 airfoil cascade of Fig. 3 at α = 19 deg

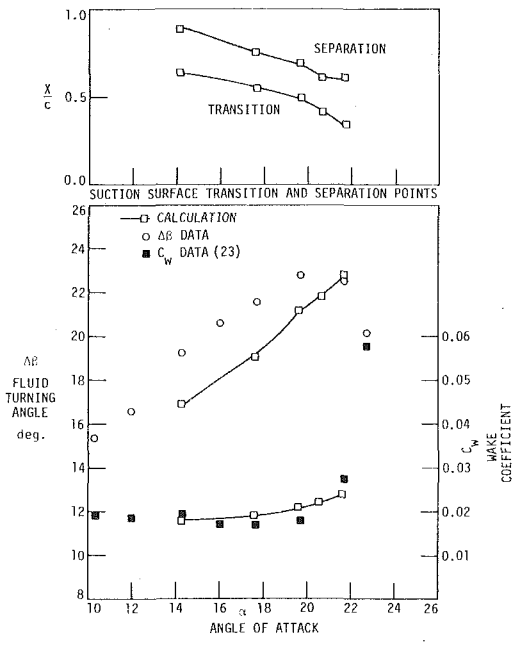

Fig. 7 Fluid turning angle and loss with calculated transition and separation points for two-dimensional 65-(12)10 linear airfoil cascade. c = 124 mm, σ = 1.0 γ = 45.7 deg, M_l = 0.1, Re_c = 245,000.

tion. All the calculations converged except for $\alpha = 18$ deg, which did not converge in eight iterations. The large oscillations in $\delta^*_{inj} - \delta^*_{calc}$ were caused by the boundary layer flow alternating between transition, laminar separation and laminar bursting.

Figs. 5 and 6 show the surface pressures and the displacement and momentum thickness on the suction and pressure surface for two different angles of attack. At $\alpha = 9.3$ deg (Fig. 5), the surface pressures match well with the experimental data, the pressure surface boundary layer also agrees with experimental data, and the suction surface boundary layer is larger than that measured. Convergence was obtained at $\alpha = 19$ deg, because laminar separation near the leading edge was calculated at each iteration. The calculation at $\alpha = 19$ deg was compared with the data of Herrig, et al. [23] at $\alpha = 18.1$ deg and Peterson [24] at $\alpha = 20$ deg in Fig. 6. Though the suction surface pressure peak seems to match, the predicted surface pressure near the trailing edge is lower than the experimental data. The suction surface boundary layer matches fairly well.

NACA 65-(12)10 Airfoil Cascade. The turning, loss, and suction surface transition and separation points plotted against the angle of attack for the NACA 65-(12)10 cascade are shown in Fig. 7. The calculated turning, $\Delta\beta$, has a slope which is similar to the data, but the level of turning is less and at high angles of attack the turning does not decrease. The wake coefficient C_w is at about the right level, but there is no rapid increase in C_w. The transition point and the separation point move forward with increasing incidence as expected. There is no laminar separation on the suction surface in any of the calculations. This may be the reason there is no sudden increase in the displacement thickness with the corresponding increase in C_w and decrease in $\Delta\beta$.

Fig. 8 shows that for $\alpha = 14.2$ deg the surface pressures agree well with the data. At $\alpha = 21.7$ deg, Fig. 9 shows that although the surface pressures match over the leading edge portion of the blade, at the

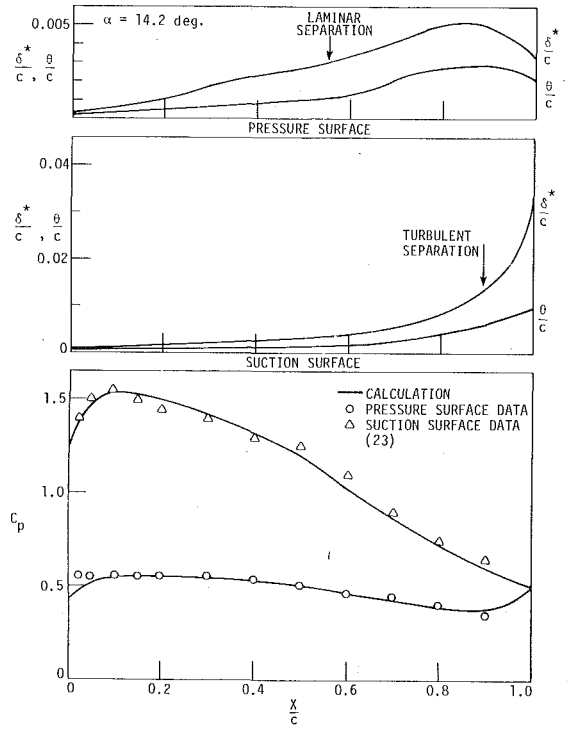

Fig. 8 Surface pressures and boundary layers for the 65-(12)10 airfoil cascade of Fig. 7 at $\alpha = 14.2$ deg. $c = 124$ mm, $\sigma = 1.0$, $\gamma = 45.7$ deg, $M_l = 0.1$, $Re_c = 245{,}000$

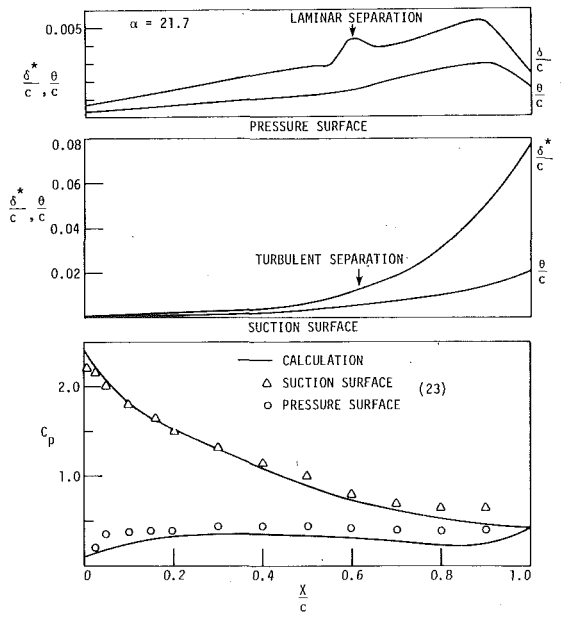

Fig. 9 Surface pressures and boundary layers for the 65-(12)10 airfoil cascade of Fig. 7 at $\alpha = 21.7$ deg. $c = 124$ mm, $\sigma = 1.0$, $\gamma = 45.7$ deg, $M_l = 0.1$, $Re_c = 245{,}000$

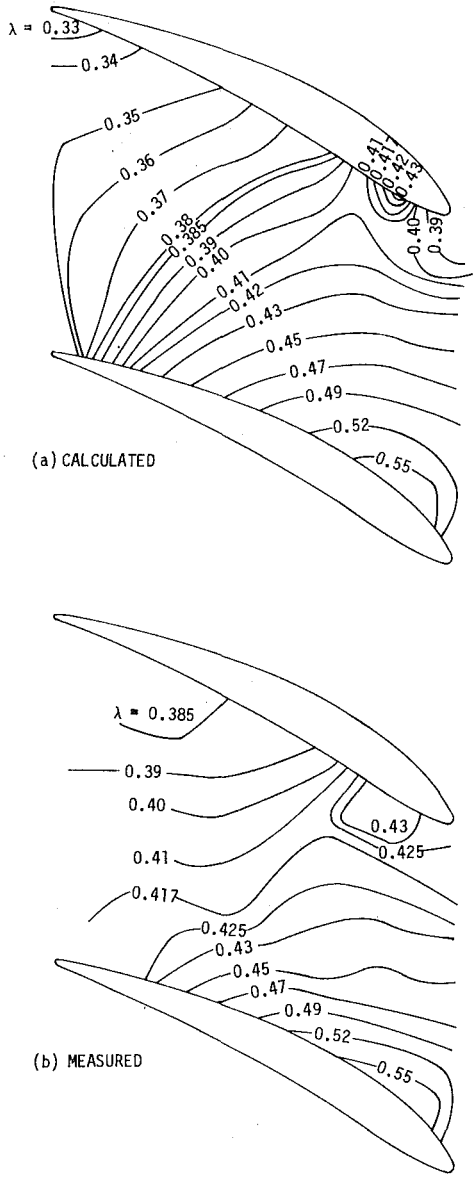

Fig. 10 Calculated and measured [27] velocity fields in a 10A30/27II45 linear airfoil cascade at $i = 0$. $c = 40$ mm, $\sigma = 1.3$, $\gamma = 27.4$ deg, $M_l = 0.412$, $Re_c = 270{,}000$

trailing edge there is too much diffusion.

In addition to these angles of attack, one higher angle, $\alpha = 22.7$ deg, was run for several iterations. Though it did not converge, it yielded some useful information. With an increased incidence angle, the peak velocity from $\alpha = 21.7$ deg to $\alpha = 22.7$ deg remained almost the same and there was no laminar separation predicted. This suggests that it is important to correctly model the peak velocity on the suction surface in the inviscid calculation systems.

USSR 10A30/27.6 II 45 Airfoil Cascade. The 10A30/27.6 II 45 cascade of Bunimovich and Svyatogorov [27] was selected to compare calculated and measured flow field velocities. Fig. 10 shows that the flow fields match fairly well. The higher velocity at the exit of the experimental cascade was probably caused by an axial velocity-density product change. The axial velocity-density ratio in the calculation was 1.0 and in the measured data was reported as 1.0 to 1.15.

Additional test cases have been run at higher Mach numbers (15) and for axial velocity-density ratios other than 1.0 for various types of airfoil section. These results will be discussed in later reports.

Concluding Remarks

Because inviscid flow field solutions are not sufficient for general prediction of airfoil cascade fluid turning angles, inviscid calculations should be combined with an interacting viscous region solution. The viscous region solution must be suited to the computation of combinations of laminar, laminar separated, transitional, turbulent and turbulent separated flows.

The cascade leading and trailing regions are critical in the correct definition of the flow field. The leading edge velocity distribution must be accurately determined, and this is especially necessary in modeling laminar separation. In the trailing edge vicinity, the static pressure distribution across the viscous layer in a direction normal to the streamlines is continuous but not necessarily constant. Pressure distribution through this layer is required for correct determination of the fluid angle throughout the cascade exit region.

It is believed that the inviscid-viscous interaction system developed in this investigation has demonstrated sufficient quantitative consistency between computed and measured flow field characteristics, including fluid turning angles and total pressure losses, to justify the conclusion that the physical basis for the system is correct. Further exploration of the validity of the method is currently in progress, involving the study of test cases at higher Mach number levels and with axial velocity-density product distributions in the through-flow direction.

Acknowledgments

Analysis and computation contributing to this paper was supported by NASA Grant NsG-3033, AFOSR Grant 78-3609 and AFSC/Air Force Aero Propulsion Laboratory Contract F33615-76-C-2090. The major portion of E. C. Hansen's Doctoral program was completed as part of the NASA-Lewis Research Center Graduate Program in Aeronautics. It is a pleasure for the authors to recognize the useful suggestions and ideas resulting from discussions and project reviews with the technical staff members of the supporting groups and agencies.

References

1 Scholz, N., *Aerodynamik der Schaufelgitter*, Karlsruhe, Verlag G. Braun, 1965. Translated and revised by Dr.-Ing. A. Klein as *Aerodynamics of Cascades*, AGARDograph 220, 1977.

2 Hansen, Elmer C., "A Study of the Methods for Analysis of the Flow Field in Cascades," Iowa State University, Engineering Research Institute, ISU-ERI-Ames-77065 (TCRL-6), 1976.

3 Gostelow, J. Paul, "Review of Compressible Flow Theories for Airfoil Cascades," ASME JOURNAL OF ENGINEERING FOR POWER, Vol. 95, 1973, pp. 281–292.

4 Geller, W., "Incompressible Flow Through Cascades with Separation. *In* Boundary Layer Effects in Turbomachines." AGARDograph 164, 1972, pp. 171–186.

5 Dodge, Paul, "The Use of a Finite-Difference Technique to Predict Cascade, Stator and Rotor Deviation Angles and Optimum Angles of Attack," ASME JOURNAL OF ENGINEERING FOR POWER, No. 95, 1973, pp. 185–190.

6 Ispas, I. *Berechnung der Kompressible Reibungsfreien Unterschallströmung durch Turbomaschinengitter mit Hilfe eines Differenzverfahrens*, Brenstoff-Warme-Kraft, Vol. 26, 1974, pp. 435–441.

7 Stark, U. and Starke, J., "On the Turning Characteristics of Plane Compressor Cascades with NACA 65-Profiles in Quasi Two-Dimensional Incompressible Flow," Report 74/2, Institute of Fluid Mechanics, T. U. Braunschweig, 1974.

8 Miller, Max J. and Serovy, George K., "Deviation Angle Estimation for Axial-Flow Compressors Using Inviscid Flow Solutions," ASME JOURNAL OF ENGINEERING FOR POWER, No. 97, 1975, pp 163–168.

9 Speidel, L., "Berechnung der Strömungsverluste von ungestaffelten ebenen Schaufelgittern," Dissertation, T. H. Braunschweig, 1953. Ingenieur-Archiv. Vol 22, 1954, pp. 295–322.

10 Föttner, L., "A Semi-Empirical Approach of the Transonic Flow Past Cascades Including Shock and Viscous Effects," *AGARD Conference Proceedings*, Vol. 34, 1968, pp. 11-1–11-18.

11 Föttner, L., "Analytical Approach for the Loss and Deflection Behavior of Cascades in Transonic Flow Including Axial Mass Flow Variation," In *Boundary Later Effects in Turbomachines.* AGARDograph 164, 1972, pp. 121–139.

12 Sanger, N. L., "Two-Dimensional Analytical and Experimental Performance Comparison for a Compressor Stator Section with D-Factor of 0.47," U. S. NASA TN D-7425. 1973.

13 Katsanis, T. and McNally, W. D., "FORTRAN Program for Calculating Velocities and Streamlines on a Blade-to-Blade-Stream Surface of a Tandem Blade Turbomachine," U. S. NACA TN D-5044, 1969.

14 Albers, J. and Gregg, J., "Computer Program for Calculating Laminar, Transitional, and Turbulent Boundary Layers for a Compressible Axisymmetric Flow," U. S. NACA TN D-7521, 1974.

15 Hansen, E. C., "Blade-Surface Boundary Layer and Wake Computational Models for Estimation of Axial-Flow Compressor and Fan Blade-Row Fluid Turning Angles and Losses," Unpublished Ph.D. Dissertation, Iowa State University, Ames, Iowa, 1978.

16 Schlichting, H., *Boundary Layer Theory.* 6th Edition. McGraw-Hill, New York. 1968, pp. 87–90.

17 Roberts, W. B., "Effect of Reynolds Number and Laminar Separation on Axial Cascade Performance." ASME JOURNAL OF ENGINEERING FOR POWER, No. 97, 1975, pp 261–273.

18 Carter, J. E. and Wornom, S. F., "Forward Marching Procedure for Separated Boundary-Layer Flows," *AIAA Journal.* 13(8), 1975, pp. 1101–1103.

19 Preston, J. H. and Sweeting, N. E., "The Experimental Determination of the Boundary Layer and Wake Characteristics of a Simple Joukowski Aerofoil, with Particular Reference to the Trailing Edge Region," Aeronautical Research Council Reports and Memoranda No. 1998. 1943.

20 Spence, D. A., "Prediction of the Characteristics of Two-Dimensional Airfoils," *Journal of Aeronautical Sciences*, Vol. 21(9), 1954, pp 557–620.

21 Brune, G. W., Rubbert, P. E. and Nark, T. C., Jr., "A New Approach to Inviscid Flow/Boundary Layer Matching," AIAA Paper 74-601, 1974.

22 Lieblein, S. and Roudebush, W., "Theoretical Loss Relations for Low-Speed Two-Dimensional Cascade Flow," U.S. NACA TN 3662, 1956.

23 Herrig, L. J., Emery J. C. and Erwin, J. R., "Systematic Two-Dimensional Cascade Tests of NACA 65-series Compressor Blades at Low Speeds," U. S. NACA TN 3916, 1957.

24 Peterson, C. R., "Boundary Layer on an Airfoil in a Cascade," Massachusetts Institute of Technology Gas Turbine Laboratory Report 49, 1958.

25 Milsch, R., "Systematische Untersuchung über den Einfluss der Rauhigkeit von Verdichterschaufeln auf den Gitterwirkunsgrad," Dissertation, Der Technischen Universität, Hannover, 1971, 118 pp.

26 Dunavant, J. C., Emery, J. C., Walch, H. C. and Westphal, W. R., "High Speed Cascade Tests of the NACA 65-($12A_{10}$)10 and NACA 65($12A_2I_{8b}$)10 Compressor Blade Sections," U. S. NACA RM L55I08, 1955.

27 Bunimovich, A. I. and Svyatogorov, A. A., "Aerodynamic Characteristics of Foil Compressor Cascades at High Subsonic Speed," FTD-MT-24-69-68, April 26, 1968. Translation of Lopatochnyye Mashiny i Struynyye Apparaty, Sbornik Statey. Vypusk 2, Moscow, Izdatel' stvo Mashinostroyenie, 1967, pp. 5–35.

I. G. Rice
P. E.
Consultant.
P.O. Box 233
Spring, Texas
Mem. ASME

The Combined Reheat Gas Turbine/ Steam Turbine Cycle

Part I—A Critical Analysis of the Combined Reheat Gas Turbine/Steam Turbine Cycle

The reheat gas turbine cycle combined with the steam turbine Rankine cycle holds new promise of appreciably increasing power plant thermal efficiency. Apparently the cycle has been overlooked and thus neglected through the years. Research and development is being directed towards other gas turbine areas because of the world energy crunch; and in order to focus needed technical attention to the reheat cycle, this paper is presented, using logic and practical background of heat recovery boilers, steam turbines, gas turbines and the process industry. A critical analysis is presented establishing parameters of efficiency, cycle pressure ratio, firing temperature and output. Using the data developed, an analysis of an actual gas generator, the second generation LM5000, is applied with unique approaches to show that an overall 50 percent efficiency power plant can be developed using today's known techniques and established base-load firing temperatures.

Introduction

The reheat gas turbine cycle when coupled with the Rankine cycle offers interesting prospects of improving cycle efficiency and at the same time markedly increasing the gas turbine output per unit air flow. The size of the gas turbine and thus the cost should also be improved.

The reheat gas turbine cycle itself is well known and received attention in years gone by—particularly in Europe and more recently in the USSR. The thrust of the reheat cycle was to use a regenerator to heat the compressor discharge air to improve cycle efficiency. Intercooling along with regeneration was also suggested for the same reason. It is well established that reheat will increase power output by 35 to 40 percent but without the complication of regeneration and intercooling the cycle efficiency is degraded over the simple cycle.

Another example of the reheat gas turbine cycle presently being employed is the afterburner of the jet engine for aircraft use—particularly for the military and, to a limited extent, for commercial planes, namely the Concorde SST. The jet reheat cycle has been developed to give reliable service where augmented output is required for a short or limited time. The greatly increased thrust comes at the expense of markedly increased fuel consumption. Commercial applications, because of the fuel consumption, have gone to efficient high bypass ratio fan jets for subsonic flight which in turn has made available the second generation high-ratio high-firing temperature gas generators for industrial applications.

Perhaps it has been thought that the degradation in efficiency of the reheat cycle would not offer an advantage to combined cycle power plants. Attention has not been given to the cycle because of the gas turbine increased fuel consumption. Thought must be given to the extra higher level heat that is available in the exhaust and the overall entropy aspect as well as the concept of extracting maximum work at as high a working fluid temperature level as possible to obtain the highest efficiency.

Another explanation of the apparent overlooking of the cycle is the feeling, particularly in the U. S., that the extra complication and cost of more controls, another burner, compatibility of nozzle area, start-up procedures, etc., would offset any advantage offered in terms of specific power output (reduction in physical size), particularly at a higher fuel consumption.

There is another reason that can be cited. The aircraft derivative gas turbines offer an advantage in potential physical arrangements for the reheat cycle such that a reheat combustor can be readily added between the gas generator and the power turbine; whereas the more conventional industrial (heavy duty) gas turbines are mostly single shaft units for power generation and do not readily lend themselves to the addition of a reheat burner. Yet the knowledge of applying combined cycles rests, to a great extent, with those who furnish the industrial units; and the aircraft manufacturers to a certain extent have followed the lead of the industrials—those who also manufacture steam turbines.

It can also be said that the second generation aircraft gas turbines fire at elevated temperatures and utilize high compression ratios suitable for reheat cycles, whereas the industrial units because of their single shaft configuration are limited to lower ratios.

Contributed by the Gas Turbine Division and presented at the Gas Turbine Conference and Exhibit and Solar Energy Conference, San Diego, California, March 12–15, 1979 of THE AMERICAN SOCIETY OF MECHANICAL ENGINEERS. *Manuscript received at ASME Headquarters December 7, 1978. Paper No. 79-GT-7.*

With the advent of the increasing number of high-temperature/high-pressure-ratio gas turbines on the market, such as the LM2500, LM5000, JT9, RB-211, Spey, and the Mars which lend themselves to reheat cycles, it is timely to examine in detail the reheat cycle and the combined reheat gas/steam cycle.

In today's gas turbine industrial state of improved proven basic controls (solid state), computer control, better sensing devices, better auxiliaries, etc., the complication argument is greatly nullified. Gas turbine controls and steam turbine controls have become sophisticated and use space-age solid state technology.

The reheat gas turbine combined cycle is not in competition with the high-temperature research and development work being carried forward. Improvement in techniques such as better convection cooling of blades, better film cooling of blades, transpiration blade cooling, liquid blade cooling and ceramics can all be applied to the reheat cycle. The reheat cycle supplements and extends the other cycles already being developed. Likewise, work on coal gasification and liquification can be integrated with the reheat combined cycle.

It is interesting to trace the history of the steam turbine for power generation. Pressures were increased and temperatures were increased. Then reheat was introduced (complications accepted) to improve cycle efficiency by obtaining more specific work per pound of steam and per pound of boiler combustion air flow. Development continued to supercritical pressures, but practicality of cost and boiler operation has stabilized steam conditions to the typical 2400 psig (16.55 MPa) with 1000 FTT (838°C) initial temperature and 1000 FTT (838°C) reheat temperature.

The reheat gas turbine can be applied to greatly increase the specific work of the air side of the cycle and thus again improve cycle efficiency. It seems logical to consider reheat and follow the course of the steam turbine industry. Therefore an analysis of the reheat gas turbine cycle and the combined reheat gas turbine/steam turbine cycle will be presented.

Reheat Gas Turbine Cycle

The reheat gas turbine cycle is represented by the T-S and P-V diagrams, Fig. 1. Air at atmospheric pressure is compressed from State 1 to State 2. Fuel is added in the first combustion chamber to increase the temperature at constant pressure to State 3. The hot gas is then expanded to State 4 where again fuel is added in a second combustor to heat the gas to State 5. Gas is then expanded to State 6—atmospheric pressure.

In the case of a simple cycle gas turbine, the gas is only heated once and expands from State 3 to atmospheric pressure, State 6′. The diagram is also representative of a gas generator where the gas is exhausted to the power turbine at State 4, assuming the total expansion power is so divided.

A schematic diagram of the reheat gas turbine cycle is shown in Fig. 2 where the numbers on the schematic correspond with the numbers of the T-S and P-V diagrams. The fuel added to the two combustion chambers is indicated as f_1 for the first burner and f_2 for the second. A simple cycle gas turbine would not incorporate the second combustor and would only show fuel f_1.

Analysis of the Simple Cycle Gas Turbine

As a starting point and to serve as a benchmark for comparison purposes, the simple cycle gas turbine must be analyzed. Parameters of efficiency, specific work, firing temperatures and pressure ratios are all important factors to consider in the analysis. Appropriate assumptions have been made such that the results obtained will closely approximate actual data from known gas turbines. It is important also to select appropriate firing temperatures used in today's turbines. Firing temperatures from 1600 to 2400°F (871 to 1316°C) have been used along with cycle pressure ratios of 6–38. The assumptions for the simple cycle are listed in Table 1.

Fig. 3 shows a plot of cycle efficiency versus net output (work) in terms of BTU/lb of air. This plot gives a good representation of what takes place when the firing temperature is increased and when the pressure ratio is allowed to vary.

The curve shows optimum efficiencies and optimum pressure ratios

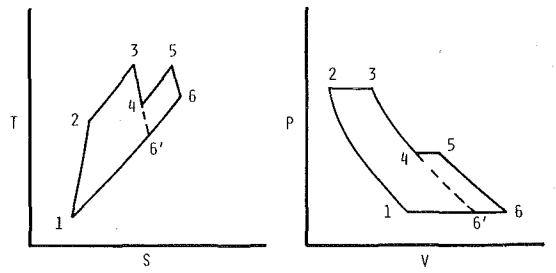

Fig. 1 Temperature-Enthalpy and Pressure-Volume reheat gas turbine cycle diagrams

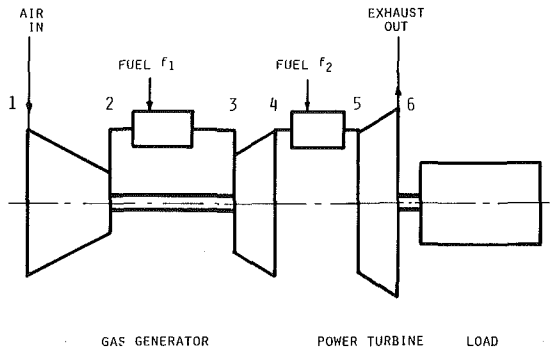

Fig. 2 Schematic diagram of reheat gas turbine cycle

Table 1

	Assumption	Constant Used		Assumption
1	Compressor Efficiency	85 percent	11	Keenan and Kaye Gas Tables for Air Compression
2	Turbine Efficiency	87 percent		
3	Combustion Pressure Loss	4 percent	12	Kennan and Kaye Gas Tables for 400 percent Theoretical Air for Expansion
4	Combustion, Radiation and Mechanical Loss	3 percent		
5	Air Leakage	0.5 percent	13	All Calculations based on one pound of air with 0 percent relative humidity (KW can be calculated by multiplying air flow in lb./HR and dividing by 3413)
6	Inlet Pressure psia(KPa)	14.7 (101.36)		
7	Exhaust Pressure psia(KPa)	14.9 (102.74)		
8	Fuel Burned	$(CH_2)n$		
9	Fuel Value BTU/lb. LHV(MJK_g)	18,400 (428)		
10	Inlet Air Temp. °F (°C)	60°(15.6°)		

for different firing temperatures and it can be noted that the optimum efficiency for a given firing temperature occurs at a higher pressure ratio than the optimum net output. Table 2 tabulates these optimum values.

It then follows that an actual gas turbine must be a compromise between the two optimum values or specifically designed for one particular optimum value depending upon its purpose.

Figure 3 also indicates that increasing the firing temperature increases both output and cycle efficiency. Each 100°F increase in firing temperature increases the output by about 10 percent and the efficiency by 1.25 to 1.50 percentage points for the optimum pressure ratios. Therefore, there is decided reason to increase firing temperatures and pressure ratios of simple cycle gas turbines.

Industrial gas turbines now fire at base load temperatures of 1800 to 2000°F (982 to 1093°C) with pressure ratios of 10 to 12. The second generation aircraft derivatives fire at 2000 to 2130°F (1093 to 1166°C)

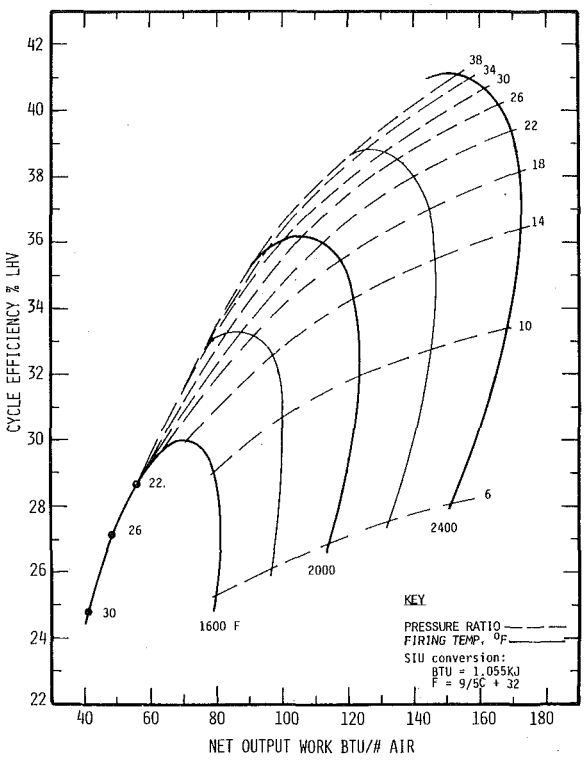

Fig. 3 Plot of simple cycle gas turbine cycle efficiency versus net output as a function of cycle pressure ratio and firing temperature

base load and incorporate compressors with pressure ratios of 16 to 29. It is worthy of noting that the aircraft derivatives are designed for take-off temperatures considerably higher in the order of 2400°F (1316°C) and the 2400°F top curve Fig. 3 gives some insight as to the selection of the higher pressure ratios.

Compressor and Gas Generator Exit Temperatures. As the pressure ratio is increased the compressor discharge temperature, t_2, increases also. At the same time the gas generator exit temperature decreases. These relationships are shown in Fig. 4.

It can be noted that the compressor discharge temperature line crosses the gas generator exhaust temperature line for a given firing temperature. For 1600°F (871°C) t_2, this compression ratio is about 21 and at 2000°F (1093°C) the ratio is 36. However, because of the losses in compression and expansion, the breakover point of incremental power increase over incremental compressor power required is less than these values and is reflected in the efficiency curves of Fig. 3 and Fig. 4.

It can be seen that a high ratio cycle of 30 has a compressor discharge temperature of about 1000°F (538°C) whereas the gas generator exit temperature for a firing temperature of 2000°F (1093°C) is about 1170°F (632°C).

Exhaust Temperature for Heat Recovery. It is important to understand the relationship of compression ratio, firing temperature, and exhaust temperature when dealing with any type of heat recovery, particularly boilers. Exhaust temperature (the availability of energy) is a prime factor in the selection of equipment, the design of the equipment and, in the case of the combined cycle, the overall cycle to select.

Figure 5 is a plot of exhaust temperature, t_6' versus cycle pressure ratio for 1600°F, 2000°F, and 2400°F (871, 1093, and 1316°C) firing temperatures.

This diagram illustrates that the low ratios provide the higher exhaust temperatures whereas going to higher ratios to optimize simple cycle efficiency produces a lower exhaust temperature which can be detrimental for heat recovery cycles. The data presented in Table 2 for optimum ratios is superimposed on Fig. 5.

The second generation gas generators, having high pressure ratios, produce relatively low exit temperatures leaving the power turbine.

Table 2

Firing Temperature °F (°C)	*Optimum Pressure Ratios*	
	Cycle Efficiency	*Output*
1600° (871°)	14	8
2000° (1093°)	26	12
2400° (1316°)	38	16

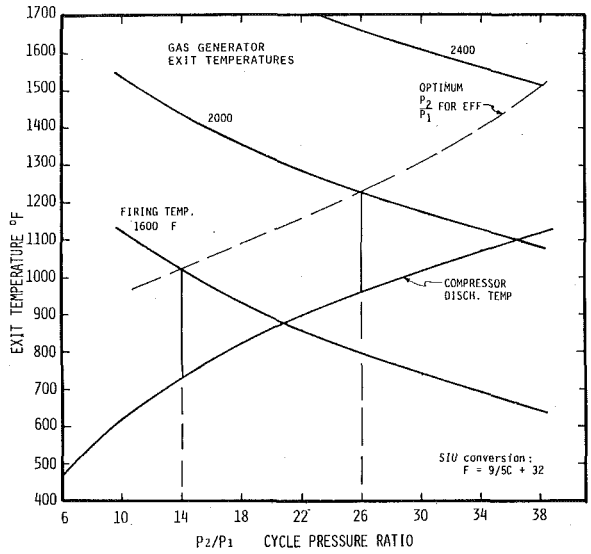

Fig. 4 Gas generator exit temperature and compressor discharge temperature versus cycle pressure ratio as a function of firing temperature

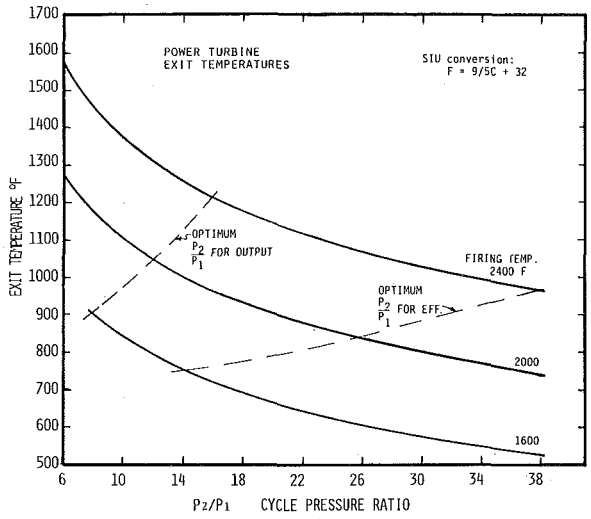

Fig. 5 Power turbine exit temperature versus cycle pressure ratio as a function of firing temperature

The LM5000, for instance, with a ratio of 29, is shown to produce about 810°F (432°C) for a 2000°F (1093°C) firing temperature which is low for heat recovery boilers. A lower ratio industrial unit that fires at 1800°F (982°C) with a ratio of 12 has an exhaust temperature of about 970°F (521°C) which is much better for boiler heat recovery. These conflicts will be discussed later when analyzing heat recovery for the reheat cycle.

Analysis of the Reheat Cycle Gas Turbine

In the analysis of the reheat cycle, the second combustion pressure loss was assumed to be 3 percent. A lower pressure drop combustor is assumed where weight and size are not as critical as for an aircraft unit and where the split shaft does not impose shafting restrictions. Also, to be on the safe side, 400 percent theoretical air was used to simplify the interpolation even though the fuel/air ratio would indicate a slightly lower theoretical air. All the other assumptions used for the simple cycle are retained.

A map of cycle efficiency versus net output (work) is presented in Fig. 6. This plot is an extention of the simple cycle graph, Fig. 3, and illustrates what happens to efficiency and output when reheat is increased from zero to full temperature ($t_5 = t_3$).

It is interesting to note that for full reheat, the optimum cycle ratio for output is also the optimum ratio for cycle efficiency. The output and efficiency both rise to a point and then fall off sharply. These optimum values are given in Table 3.

In the case of partial reheat the optimum ratios again change and for the case of $t_5 = (t_3 - 200°F)$ the points have been plotted. Pressure ratio lines which show what happens from no reheat to full reheat are superimposed on the graph. The curves move from left to right and help visualize how the cycle efficiency drops off as the net output increases.

It can be seen that the efficiency declines more for the 1600°F firing temperature and less for 2000°F and still less for 2400°F. At the same time, the output increases at a greater rate as the firing temperature increases.

Table 4 presents optimum comparisons of cycle efficiency and output for the simple and reheat cycle. The table tabulates decreases and increases in cycle efficiency and output respectively.

The increase in output at modest sacrifices in efficiency for future trends firing temperatures of 2000 to 2400°F (1093 to 1316°C) are significant. Yet there is a far more beneficial effect of reheat on the combined cycle as will be shown later.

Power Turbine Expansion Ratios. Expansion ratios available for reheat cycles are important from a practical standpoint of combustor size and pressure drop. Without adequate ratio to work with, the practicality of a reheat cycle is questioned. Therefore the effect of firing temperature and cycle pressure ratio is presented for evaluation in Fig. 7.

The effect of firing temperature is more dominant than cycle pressure ratio. At 1600°F t_3 (871°C) the expansion ratio available is only about 2.5 whereas when the firing temperature is increased to 2000°F (1093°C), the expansion ratio increases to 3.75. At a still higher firing temperature of 2400°F (1316°C) the ratio rises further to 5.25.

As a means of comparing the expansion ratios obtained to the ideal ratios for an equal split of power between the gas generator and the power turbine, a comparison line is plotted for the square root of the total expansion ratio. The 2400°F (1316°C) firing temperature expansion ratio is seen to approach more closely the ideal power split.

Whereas the first generation gas generators firing at 1600°F (871°C) produced a rather low expansion ratio, the second generation gas generators that fire at 2000 to 2100°F (1093 to 1149°C) hold the promise of making the reheat cycle more practical.

Gas Generator Exit Temperature. Another factor to consider in the reheat cycle is the temperature level of the gas generator exhaust. Figure 8 presents exit gas generator temperature, t_4, as dashed lines for the three firing temperatures of 1600, 2000, and 2400°F (871, 1093, and 1316°C). As can be expected, the gas generator exit temperature is noticeably affected by firing temperature. Also, as the cycle pressure ratio is increased, the exit temperature drops off appreciably.

When considering a combustor to reheat the gas, both the inlet temperature to the combustor and the final temperature leaving the combustor are important. With the second generation gas generators with cycle pressure ratios of 18 to 30 having a 2000°F (1093°C) firing temperature the exit temperature ranges from 1350°F (732°C) for an 18 ratio to 1170°F (632°C) for a 30 ratio. These values are within practical limits for a reheat cycle.

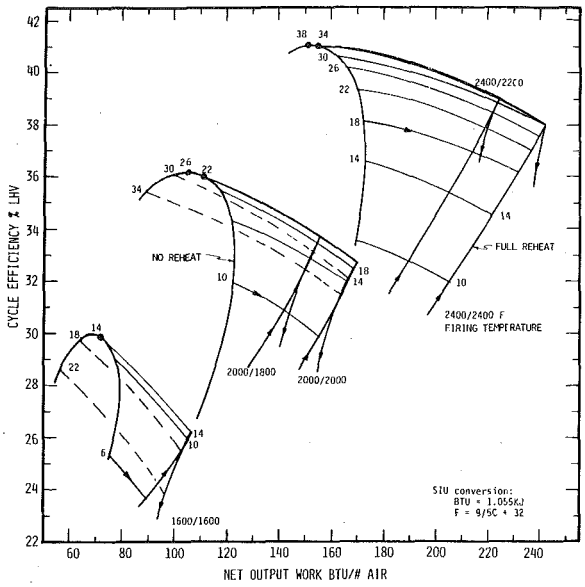

Fig. 6 Map of simple and reheat gas turbine cycle efficiency versus net output as a function of cycle pressure ratio and firing temperature

Table 3

Firing Temperature °F (°C)	*Optimum Pressure Ratio*	
	Cycle Efficiency	*Output*
1600° (871°)	14	14
2000° (1093°)	26	26
2400° (1316°)	38	38

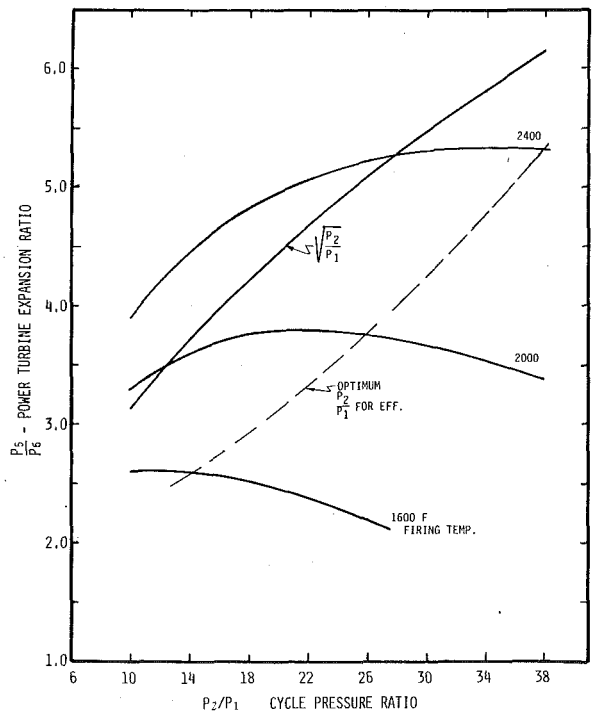

Fig. 7 Power turbine expansion ratio versus cycle pressure ratio as a function of firing temperature

Table 4

	Optimum Simple Cycle		*Optimum Reheat Cycle*			
Firing Temp. °F (°C)	*Efficiency percent*	*Output BTU/LB (KJ/Kg)*	*Efficiency Percent*	*Percent Decrease*	*Output BTU/LB (KJ/Kg)*	*Percent Increase*
1600° (871°)	30.0	78 (18.1)	26.2	12.7	107 (24.9)	37.2
2000° (1093°)	36.2	123 (28.6)	32.7	9.7	171 (39.8)	39.0
2400° (1316°)	41.0	173 (40.2)	38.1	7.1	243 (56.5)	40.1

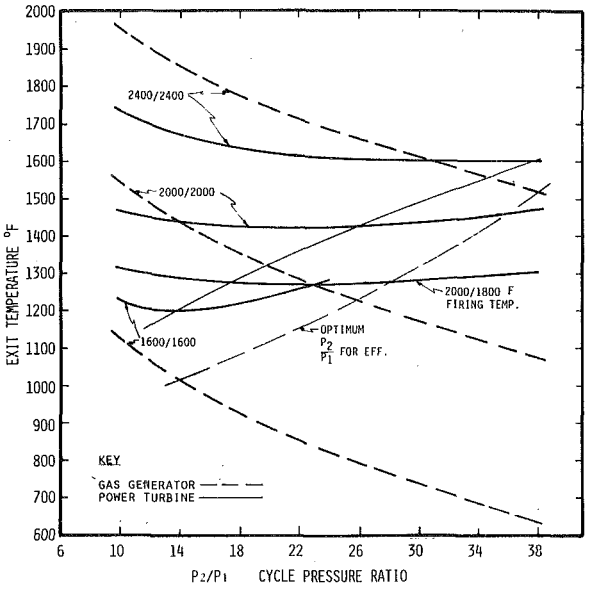

Fig. 8 Gas generator and power turbine exit temperatures versus cycle pressure ratio for different firing temperatures

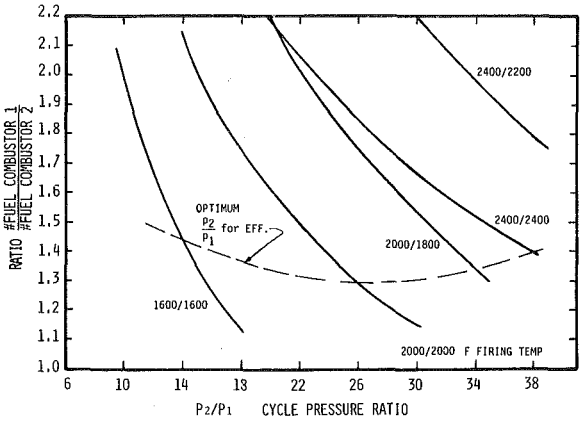

Fig. 9 Fuel ratio of the two combustors versus cycle pressure ratio for various firing temperatures

Looking forward, a 2400°F (1316°C) firing temperature will result in exit temperature of about 1520°F (827°C) for a cycle ratio of 38.

Power Turbine Exhaust Temperature. When considering heat recovery, the power turbine exhaust temperature is most important. Many times it becomes necessary to supplementary fire the exhaust gases to raise the exhaust temperature to an acceptable level. It is important to know what these temperatures are. Exhaust temperatures for various firing temperatures are shown as solid lines in Fig. 8. Note that the temperatures remain rather constant over a broad working range of cycle pressure ratios.

It can be seen that the exhaust temperature for the 2000/2000°F (1093/1093°C) reheat firing temperature is a little over 1400°F (760°C) for cycle pressure ratios of 14 to 34. Likewise, for 2000/1800°F (1093/982°C) firing temperature, the exhaust temperature remains about constant at approximately 1275°F (691°C).

It is important to note that these power turbine exhaust temperature ranges are ideal for heat recovery and the combined cycle. It has been shown by others as well as the author that the best range for heat recovery boilers is between 1200 and 1400°F (649 and 760°C).

The power turbine exhaust temperature for 2400/2400°F (1316/1316°C) is shown to be about 1600°F (871°C) which is higher than necessary but not detrimental to a combined cycle.

When considering a reheat cycle power turbine, it must be noted that the exhaust temperatures discussed are high and the exhaust plenum would require expensive high temperature materials. The plenum would also be much larger, as the exit volume (and velocity) would vary directly in response to the absolute temperature according to the formula $PV = WRT$. Also the power turbine blading would require adequate cooling for the reheat firing temperatures suggested.

Fuel Ratios. Another factor to consider is the amount of fuel to be burned in the reheat combustor compared to the first combustor. To evaluate the relative fuel split for the reheat cycle, Fig. 9 is included. In general it can be noted that the reheat burner would require less fuel than the primary or first burner. In the working range of ratios of 18 to 30 and for firing temperatures of 2000/2000°F (1093/1093°C) and 2000/1800°F (1093/982°C) the ratio of f_1/f_2 runs between 1.2 and 1.8.

NO_x Control. An important consideration in today's gas turbines is emission control. The emission of NO_x is particularly problematic. Development work is being carried out with dual combustion systems and with water/steam injection to help temper the high flame temperatures inside the primary flame for NO_x control. Several technical papers have been written on this subject.

In the case of the reheat gas turbine, two combustors would be required and a distinct possibility exists that, with this cycle, the first chamber could be run rich and the second lean or visa-versa to control NO_x. Development work based on studies and tests already run on the rich/lean system would have to be conducted to evaluate the reheat cycle and the advantage of having two burners.

The prospects of water/steam injection can be readily applied to the reheat cycle as to the simple cycle to control NO_x and development work already done can be applied directly.

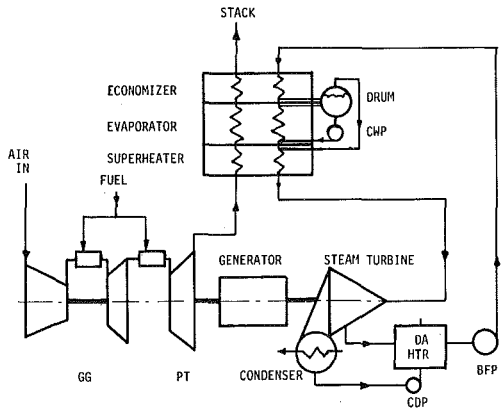

Fig. 10 Schematic diagram of combined reheat Gas/Steam cycle

Analysis of Combined Reheat Gas Turbine/Steam Turbine Cycle

The fundamentals of the reheat gas turbine cycle presented earlier in this paper can now be applied to the steam (Rankine) cycle to form a combined cycle. A simplified schematic diagram of this combined cycle is presented in Fig. 10 where the gas turbine exhausts into a heat recovery boiler to generate steam. In turn, the steam is run to a conventional condensing steam turbine. The steam turbine is mechanically connected to a generator (in tandem, as shown, or to a separate generator). The condensate out of the condenser is pumped through feedwater heaters (not shown) to a deaerator and then pumped by the boiler feed pump (BFP) to the economizer, then through the evaporator coils (boilers) and finally through the super heater to complete the closed loop.

The boiler can be a dual drum boiler and the steam turbine can be an admission design to accept the incremental steam generated by the second drum but for the purposes of establishing trends and parameters, a single drum configuration is assumed to simplify the calculations and to avoid overly complicating the analysis.

Heat Recovery Boiler. The heat recovery boiler has been developed over the past two decades to adapt to the recovery of heat in the form of steam from the large gas turbine exhaust flows at relatively modest temperatures. Such boilers were the outgrowth of process

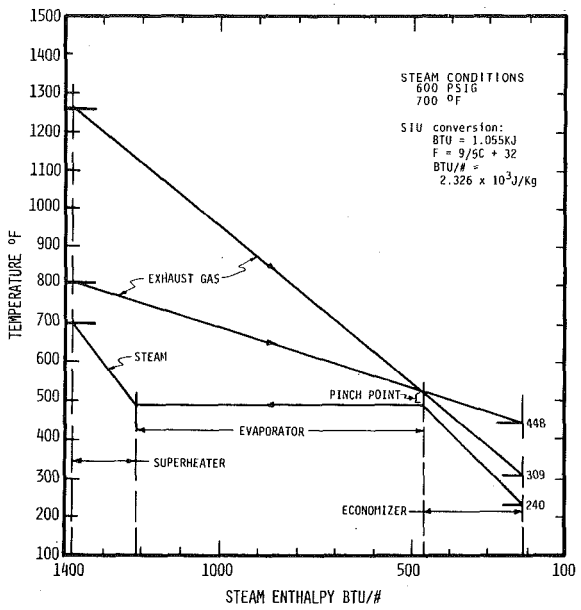

Fig. 11 Plot of temperature-enthalpy showing both steam heat/temperature relations and gas turbine exhaust temperatures with a 40°F boiler pinch point

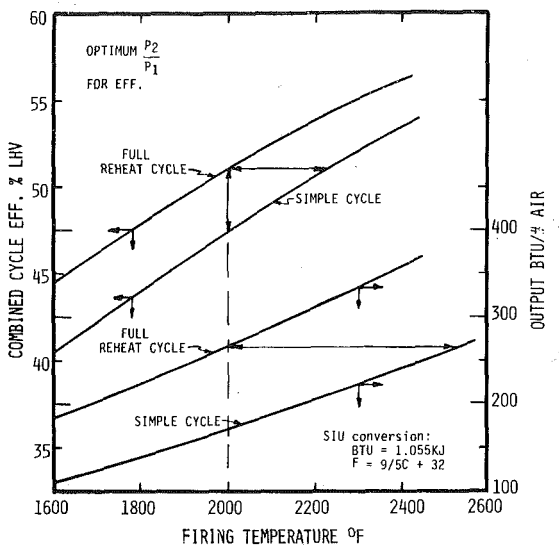

Fig. 12 Combined cycle efficiency and output versus firing temperature for both simple and reheat gas turbines

heaters where extended surface (finned tubes) were applied for convection heat transfer whereby a close approach temperature of the gas to the saturated steam temperature could be obtained and still maintain a low pressure drop of the near atmospheric gas turbine exhaust.

The process of generating steam is given schematically in Fig. 11. Two cases are shown, one for a gas turbine exhaust temperature of 800°F (427 °C) and the other for 1250°F (677°C) to illustrate a point. Typical steam conditions of 600 psig (4.14 MPa) 700°F (371°C) with a feed water temperature of 240°F (116°C) have been selected.

Water enters the economizer at 240°F (116°C) on the right side and is heated to the saturation temperature of 485°F (252°C). Then the water is boiled at constant temperature to 100 percent quality where the saturated steam is superheated to 700°F (371°C).

The gas turbine exhaust gives up its heat to the steam/water until the approach or so called "pinch point" is reached. (With such boilers the delta or approach is generally 30 to 50°F (16.6 to 27.8°C) for economical designs.) This pinch point then determines the stack or boiler exit temperature. The exhaust gas has an almost constant specific heat (C_p) for the temperature/pressure ranges encountered; and therefore a straight line temperature drop is encountered as shown on the diagram.

In the case of the 800°F (427°C) gas turbine exhaust, the minimum stack temperature reached is 448°F (231°C) whereas for the 1250°F (677°C) exhaust the temperature is considerably lower—309°F (154°C). In the latter case it can be readily seen that a much lower stack loss will occur and a greater percentage of the heat will be converted to steam. This example points to one of the chief advantages of the reheat cycle.

Many times, as has been stated earlier, the gas turbine exhaust is supplementary fired to raise the temperature as there is ample excess air for this purpose. It is readily reasoned that if the exhaust has to be supplementary fired, why not supplementary fire before the power turbine and in so doing generate extra incremental power which is obtained at topping power efficiency (3413 BTU/KWH)? The overall cycle would be thus improved and a lower stack temperature would result.

Combined Reheat Gas Turbine/Steam Turbine Cycle. The analysis of the combined cycle has been simplified by arbitrarily preselecting appropriate steam conditions and steam turbine expansion efficiencies. In so doing, good results can be obtained without being diverted by over-complication or trying to optimize each cycle. The assumptions selected apply equally to the simple cycle and the reheat cycle and perhaps favor the simple cycle as being conservative in regard to reheat cycle gains. The assumptions used are given in Table 5.

Effect of Firing Temperatures on Efficiency. Firing temperature has a decided effect on combined cycle efficiency and a plot of cycle efficiency is shown in Fig. 12. Increasing the firing temperature

Table 5

		Simple Cycle	*Reheat Cycle*
1	Feedwater Temp. °F (°C)	240 (116)	240 (116)
2	Deaerator Press. Psia (KPa)	25 (173)	25 (173)
3	Boiler Approach Temp. °F (°C)	40 (22)	40 (22)
4	Steam Pressure Psig (MPa)	600/850*(4.14/5.86)	850/1250**(5.86/6.62)
5	Steam Temp. °F	700/900*(371/482)	900/900**(482/482)
6	Condenser Pressure in. Hga	2.5	2.5
7	Steam Turbine Expansion Eff. Percent***	75	75
8	Cycle Pressure Ratio for		
	1600°F Firing Temperature	8 and 14	14
	2000°F Firing Temperature	12 and 26	26
	2400°F Firing Temperature	16 and 38	38
9	Boiler Radiation and Leakage Loss Percent	0	0
10	Water Make-up Percent	0	0
11	No Gas Turbine Inlet and Exhaust Loss	—	—
12	Exhaust Enthalphy Keenan and Kaye Gas Tables for 400 Percent Theo Air	—	—
13	Calculations Based on One Pound of Air Flow KW can be calculated by multiplying air in lb./HR flow and dividing by 3413)		
14	Data Developed by Gas Turbine Cycle Analysis		

* For 2400°F (1316°C) Simple Cycle
** For 2400°F (1316°C) Reheat Cycle
*** Includes Losses and Auxiliary Power

from 1600°F to 2400°F raises the efficiency from a little over 40 percent to about 53.5 percent for the combined simple cycle and from about 45 percent to a little over 56 percent for the combined reheat.

It can be seen that at 2000°F firing temperature the reheat cycle has an efficiency point advantage of 3.5 percent (7.4 percent increase) which can be equated to an increase of about 200°F firing temperature for the simple cycle (see the arrow on the graph). This gain is significant and is worthy of note considering the high cost of fuel today and projected cost in future years.

An overall picture of what takes place in the two cycles in terms of cycle efficiency is presented in Fig. 13. The left side shows the simple cycle gas turbine efficiency for the two optimum conditions of compression ratio (CR) for output and efficiency. Efficiency increases as the heat is absorbed by the boiler and converted to work where 100 percent of the heat obtainable is recovered. At this point, the simple cycle gas turbine is slowly changed to a full reheat cycle by adding increasing amounts of fuel in the second combustor until both firing temperatures are equal. The cycle efficiency rises as the efficiency lines run from left to right.

Effect of Firing Temperature on Output. To illustrate what happens to output for the combined cycle, a plot of the output of the two gas turbine cycles versus firing temperature is also given in Fig. 12. As can be seen, output is also substantially increased as the firing temperature rises. Note that the reheat output has a slightly sharper rise than the simple cycle.

This curve is useful in evaluating size and potential cost of equipment. In an example of 2000°F firing temperature, the reheat cycle is shown to develop some 95 more BTU/LB of air flow than the simple cycle which is equal to approximately 56 percent more output. This figure indicates the relative physical size of the steam and gas turbine of the two cycles and points out potential cost advantages. This assertion is made in light of the relatively small change in the output ratio of the gas turbine to the steam turbine as shown in Fig. 14.

Another point of interest on this plot is that the simple cycle would have to fire at approximately 2600°F to equal the same output as the 2000°F reheat cycle as can be seen by the arrow on the graph.

Combined Cycle Reheat Gas Turbine/Reheat Steam Turbine. There is a further advantage in cycle efficiency and output per unit air flow by also incorporating reheat in the steam side of the cycle. This potential will be explored in the second of these papers where the LM5000 will be used as a basis for obtaining realistic results using data of actual gas turbine hardware available today.

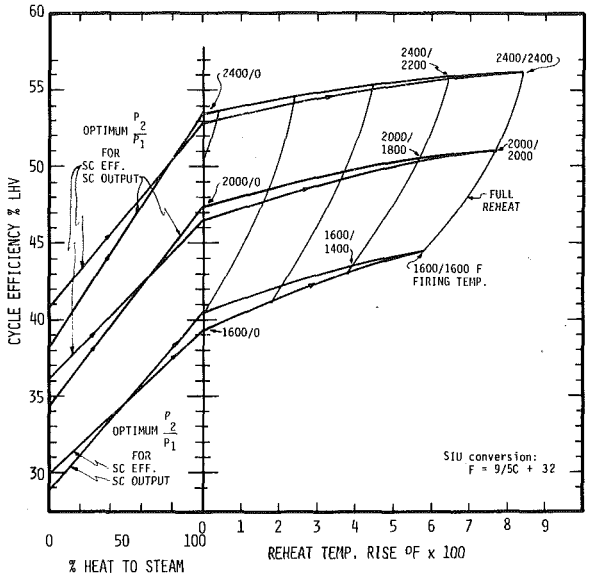

Fig. 13 Cycle efficiency for simple and reheat gas turbines when combined with the steam turbine

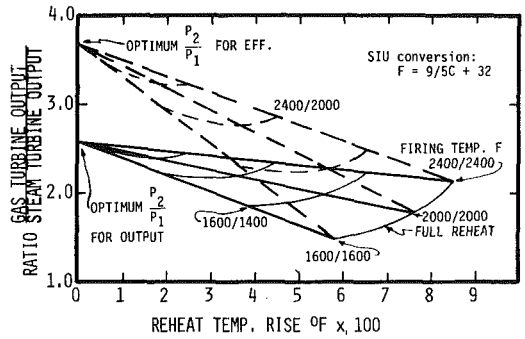

Fig. 14 Ratio of gas turbine output/steam turbine output versus reheat temperature rise

Conclusions

Based on the assumptions made and the graphs presented in this paper, the following conclusions are drawn:

1 The reheat cycle gas turbine efficiency is degraded slightly (approximately 6 percent) over the simple cycle for equal firing temperatures.
2 The reheat cycle gas turbine output is increased significantly by about 40 percent.
3 The reheat gas turbine cycle optimum pressure ratios run higher than for the simple cycle by significant amounts and both the optimum output and the efficiency points take place simultaneously at this elevated pressure level.
4 The combined cycle incorporating the reheat gas turbine offers significant cycle efficiency improvements for equal firing temperatures.
5 The output per unit air flow is significantly greater for the combined cycle utilizing the reheat gas turbine which points to potential cost savings for such a cycle.
6 The reheat combined cycle favors the second generation gas turbines and primarily the aircraft derivative gas generator because of their higher firing temperatures and pressure ratios.
7 The possibility of developing the reheat gas turbine/steam turbine cycle is within the framework of existing equipment when coupled with development work on the second combustion chamber, the high temperature power turbine, and added controls.

The graphs presented can serve as background information for further study of the reheat gas turbine as well as the combined cycle. They also can provide further input to the gas turbine manufacturer when studying the development of future gas generators, gas turbines and power turbines.

References

1 Sawyer, J. W., *Gas Turbine Engineering Handbook,* 1st ed., Gas Turbine Publications, Stamford, Conn., 1966.
2 Saywer, J. W., *Sawyer's Gas Turbine Engineering Handbook,* 2nd ed. Three Vol., Gas Turbine Publications, Stamford, Conn., 1972.
3 Sawyer, J. W., *Sawyer's Gas Turbine Catalog,* Gas Turbine Publications, Stamford, Conn., Vol. 9–14, 1970–78.
4 *Diesel and Gas Turbine Worldwide Catalog,* Diesel and Gas Turbine Progress, Milwaukee, Wisc., Vol. 36–39, 1970–74.
5 Rice, I. G., "Case Study as a Key to Gas Turbine Evaluation," *Oil and Gas Journal,* April 15, 1968, pp. 67–71.
6 Plumley, D. R., and Rice, I. G., "Balance Your Gas Turbine Heat," *Hydrocarbon Processing,* April, 1968, pp. 154–160.
7 Puyper, H. P., and Rice, I. G., "Steam and Gas Turbines in Tandem Can Pay Dividends," *Oil and Gas Journal,* Oct. 11, 1965, pp. 199–207.
8 Rice, I. G., "Don't Waste That Gas Turbine Heat," *Oil and Gas Journal,* June 19, 1959, pp. 66–70.
9 Uvarov, V. V.; Beknev, V. S.; and Manushin, E. A., "100s and 1000s Mw Open and Semi-closed Cycle Gas Turbines for Base and Peak Operation," ASME Paper No. 74-GT-160.
10 Keenan, J. H., and Keyes, F. G., *Theoretical Steam Rate Tables,* ASME, 1938.
11 Keenan, J. H., and Keyes, F. G., *Thermodynamic Properties of Steam, John Wiley and Sons,* 1947.
12 Keenan, J. H., and Kaye, J., *Gas Tables* John Wiley and Sons, 1956.
13 Vincent, E. T., *The Theory and Design of Gas Turbines and Jet Engines,* McGraw-Hill, New York, 1050.
14 Cohen, H.; Rogers, G. F. C.; and Saravanmuttoo, H. I. H., *Gas Turbine Theory,* Longman Group, London, 1972.

I. G. Rice

P.E.
Consultant.
P.O. Box 233
Spring, Texas
Mem. ASME

The Combined Reheat Gas Turbine/ Steam Turbine Cycle

Part II—The LM 5000 Gas Generator Applied to the Combined Reheat Gas Turbine/Steam Turbine Cycle

Part I presented an analysis of the simple and reheat gas turbine cycles and related these cycles to the combined gas turbine Rankine cycle. Part II uses the data developed in Part I and applies the second generation LM5000 to a combined cycle using a steam cycle with 1250 psig 900 FTT (8.62MPa and 482°C) steam conditions; then the reheat gas turbine is combined with a reheat steam turbine with steam conditions of 2400 psig and 1000/1000 FTT (16.55 MPa and 538/538°C). A unique arrangement of the superheater is discussed whereby part of the steam heat load is shifted to the reheat gas turbine to obtain a minimum heat recovery boiler stack temperature and a maximum cycle efficiency. This proposed power plant is projected to have a net cycle efficiency of 50 percent LHV when burning distillate fuel.

Introduction

The data presented in Part I give good insight into what takes place in the reheat gas turbine and its combined reheat cycle. The numbers and curves were presented to show parameters and trends and to be the basis for selecting the proper cycle pressure ratio and reheat firing temperature.

The temperature of the power turbine and the expansion ratio available are important considerations in designing a power turbine. The exhaust temperature discharging from the power turbine to the heat recovery boiler is another factor that must be given proper consideration in designing both the power turbine exhaust plenum and the steam end of the cycle.

In today's state of the art, it seems reasonable to select an inlet temperature of 1800°F (982°C) to the power turbine as an upper limit for convection cooling of the blading using investment casting techniques and trailing-edge cooling of the first two nozzles. If the temperature is extended to 2000°F (1093°C), then film cooling would have to be employed which is more expensive and would require additional development cost and time.

Looking at the exhaust plenum of the power turbine, an 1800°F (982°C) reheat temperature would result in approximately 1275°F (691°C) exit temperature. This temperature is high. At 1275°F (691°C) expensive high-temperature materials would be required. Also the size would have to be increased relative to the absolute temperature to maintain an exhaust velocity deemed reasonable for an ordinary gas turbine with a 1000°F (538°C) exhaust temperature. Going above 1800°F (982°C) reheat would increase the design and material problems involved in the exhaust end of the turbine. The exhaust temperature must also be considered for its effect on the exhaust duct to the boiler, the bypass—if there is one—the expansion joints and the insulation.

Then there is the consideration of the boiler itself and the thermodynamics of the cycle. A power turbine exit temperature of 1275°F (691°C) would be almost optimum for generating steam at the right temperature and pressure for the steam turbine. At the same time a minimum stack temperature of 300°F (149°C) could be obtained to minimize the stack gas loss.

All of these factors indicate that the LM5000 gas generator with a firing temperature of 2100°F (1149°C) and a pressure ratio of about 29 would be well suited for the combined reheat cycle. A cross section of the LM5000 is shown in Fig. 1.

Therefore, Part II of this paper will be based on the LM5000 with a reheat temperature of 1800°F (982°C). An analysis will be presented using data from a gas generator that is available today. This method will give more credibility to the cycle and will eliminate some of the unknowns. The greatest development cost of the cycle is the gas generator which has already been developed. Development work on the aircraft version of the high-temperature, high-efficiency power turbines for the LM2500, RB211-24 and the JT-9 is behind us and an

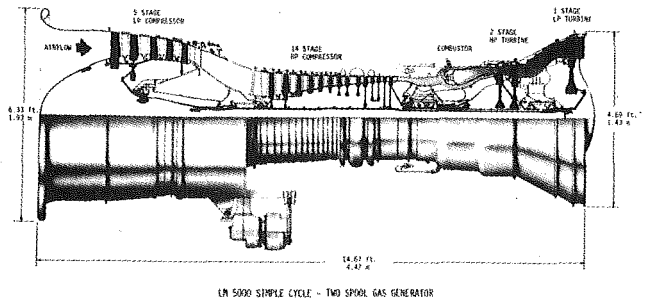

Fig. 1 Cross section of GE LM5000 gas generator giving overall dimensions

Contributed by the Gas Turbine Division and presented at the Gas Turbine Conference and Exhibit and Solar Energy Conference, San Diego, California, March 12–15, 1979 of THE AMERICAN SOCIETY OF MECHANICAL ENGINEERS. Manuscript received at ASME Headquarters December 7, 1978. Paper No. 79-GT-8.

1800°F (982°C) low-ratio power turbine is well within our reach right now.

Figure 2 shows the first LM5000 coupled to a conventional power turbine undergoing tests in Japan.

Second Generation Gas Generators

There are now several second generation gas generators on the market for industrial applications. It might be interesting to compare these units with curves developed in Part I of this paper to see where they might fit for potential reheat applications. The tabulation, Table 1, contains pertinent information comparing the estimated performance for base load operation.

It can be noted that the figures in Table 1 agree very closely with the curves for the simple cycle gas turbine presented in Part 1.

Reheat Gas Turbine

The LM5000 was selected for reasons explained in the Introduction. However, there are a few additional points to consider in the design regarding the second combustion chamber and the power turbine that should be mentioned. No attempt is made to lay out any specific design; rather a conceptual approach is presented with ideas that will serve as guidelines.

In the conventional gas generator/power turbine arrangement, the power turbine nozzle area and resulting pressure resistance is selected to match the gas generator output so both can operate properly in unison with so-called fixed nozzles. The gas generator can be started, run up to speed and operated with the power turbine following the gas generator.

In the case of the reheat gas turbine, the first-stage power turbine nozzle area would be designed for the greater volume at the elevated temperature—the area varying directly with the absolute temperature—to maintain proper velocity. This situation, which must be considered, leads to two possible solutions: (1) variable first-stage nozzles or, (2) start-up with both burners operating under a programmed controlled temperature rise.

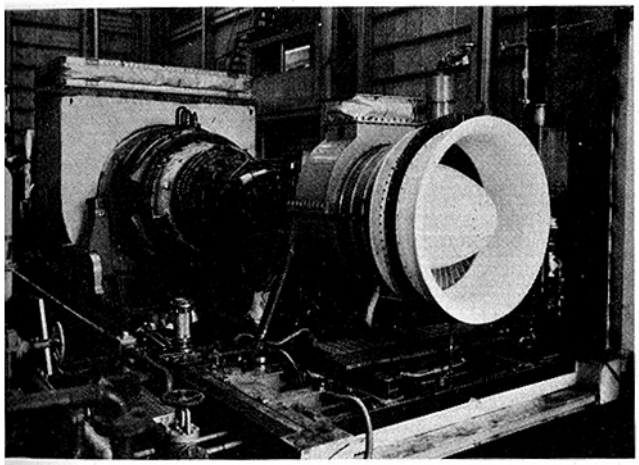

Fig. 2 First LM5000 gas generator coupled to an industrial IM5000 power turbine after completing tests at the IHI shop in Japan in June, 1978

In the case of the variable nozzles, development work would have to be done and such nozzles would be expensive. There are many two-shaft turbines operating with variable second-stage nozzles but they operate at about 1200°F (649°C), not 1800°F (982°C). The second approach with both burners operating might be more acceptable (practical and economical).

The second combustor should not present a design problem because the heat release would be rather modest and there is ample oxygen present. However, because of the higher temperature and lower pressure the combustor would be much larger—again following the law PV = WRT and other aerodynamic scaling. There are many low-pressure gas turbine burners in operation today.

Controls would have to be designed for double fuel operation and perhaps would be similar in nature to the controls for a single or double automatic extraction steam turbine. Experimental reheat gas turbines have already been run for test automobile evaluation and some control development has already been accomplished. Reheat gas turbines have also been built in Europe where experience exists to draw upon.

Nozzle and Blading Cooling Air. In the sample case using the LM5000, the cooling air for the power turbine nozzles and blades can be supplied by an electric driven air compressor with intercooling or a small gas turbine; or steam might possibly be used. Considering 3 percent air required the power needed would be about 700 HP for atmospheric air, but this power loss would be more than recovered as the extra heated air passes through the power turbine. In case of steam, the specific heat would be about twice that of air and half as much flow would be needed, (1½ percent, or 15,000 lb./HR). This steam could be extracted from the steam turbine at the proper pressure level. No attempt is made in this paper to evaluate these effects or alternate methods.

Effect of Inlet and Back Pressure. Inlet drop and back pressure affect all gas turbines, but the second generation turbine as well as high-temperature industrial gas turbines where considerably less air flow is required for a given output are affected less. In the case of the reheat gas turbine, the effect becomes even more pronounced.

Inlet power loss is the direct result of the pumping power required to draw X number of pounds of air through a restriction. The loss is directly proportional to the mass of the air flow. Also the amount of air flow is directly proportional to the density, and therefore the output capability is proportional to the absolute inlet pressure.

Exhaust loss, similarly, is a result of the expansion power lost when a given flow of hot gas is not allowed to expand all the way to atmospheric pressure. The loss is a function of exit temperature also and the higher the temperature, the more potential energy is lost. All losses, considering a constant firing temperature which results in extra fuel and extra pumping power, must show up as higher exhaust en-

Table 1

	Base Load Ratings—60°F and 14.7 Psia Inlet						
	GG4C-1	*GT 200*	*LM2500*	*LM5000*	*Mars*	*RB-211-24*	*Spey*
Cycle Press. Ratio P_2/P_1	14.9	16	18	29	16	18	18
PT Output BTU/lb Air	84.2	89.5	132.3	114	92.5	107.2	93.2
Exhaust Flow lb./s	312	815	145.5	272	82.2	196	128
IGHP × 10^3	43.50	115.60	31.30	50.00	12.18	34.0	19.10
Cycle Eff. (IGHP) LHV percent	35.6	38.8	41.5	43.0	38.4	40	40
Firing Temp. °F	—	—	2,138	2,100	—	1,925	1,820
GG Ex Press. Psia	—	—	57.6	56.0	—	47.5	46.0
GG Ex Temp. °F	—	—	1,400	1,215	—	1,292	1,141
PT Ex Temp. °F	933	842	950	802	785	849	842

Note: SI Conversion Factors:
BTU/lb. = 2.326 KJ/Kg
lb./s = 4.536 KG/s

$$IGHP = \frac{IKW}{.746}$$

$$°F = \frac{9}{5}°C + 32$$

Abbreviations:
PT—Power Turbine
IGHP—Isotropic Gas Horsepower
GG—Gas Generator
EX—Exhaust

Table 2

	Constant t_4 and PT Speed *Simple Cycle Gas Turbine*	*Reheat Gas Turbine*
Inlet		
Power Loss per 1 in. H_2O—percent	0.425	0.371
Reduction in Fuel per 1 in. H_2O—percent	0.275	0.267
Specific Fuel Consumption per 1 in. H_2O—percent	0.150	0.104
Reduction in Air Flow—percent	0.250	0.250
Exhaust		
Power Loss per in. H_2O—percent	0.175	0.121
Reduction in Fuel per 1 in. H_2O—percent	0.025	0.017
Increase in Specific Fuel Consumption per 1 in. H_2O—percent	0.150	0.103

SIU conversion: 1 in. H_2O = 249Pa

Table 4

1	Ambient Temperature °F	60
2	Inlet Pressure psia	14.7
3	Steam Pressure psig	1250
4	Steam Temperature °F	900
5	Feed Water Temperature to Boiler °F	250
6	Steam Turbine Efficiency, percent	80
7	Power Turbine Efficiency, percent	87
8	Reheat Gas Turbine Combustor Loss, percent	3
9	Reheat Combustor Pressure Drop, percent	3
10	Power Turbine and Generator Loss, percent	2
11	Steam Turbine and Generator Loss, percent	3
12	Boiler Radiation and Blowdown Loss, percent	2
13	Constant Reheat Firing Temperature °F	1800
14	Inlet & Back Pressure Loss ″H_2O	4/10
15	Condenser Pressure ″Hga	2
16	Keenan & Kaye Gas Tables for 400% Theoretical Air	

Note: SIU Conversion Factors:

thalpy to maintain a heat balance.

To illustrate inlet and exhaust losses of a second generation gas turbine and reheat gas turbine, Table 2 is shown.

The figures in Table 2 for the reheat gas turbine were derived from Fig. 6, Part I, where the values for nonreheat were multiplyed by the BTU/lb. output ratio of 100/145 which is a measure of the air flow. In other words, there is an increase of some 45 percent power for the same pumping loss. Note that the effect of inlet air density loss is independent of pumping loss and remains the same.

Considering the inlet loss of 4 in. H_2O in the application of the LM5000 and the back pressure to the boiler of 6 in. and, alternately, 10 in. H_2O, the losses would be as given in Table 3.

It can be noted that the reheat gas turbine output is reduced by about 2.5 percent and the specific fuel consumption increased by about 1.25 percent. Yet the added fuel flow and the pumping losses all go to the boiler where they are recovered in the steam turbine at about 40 percent efficiency. Therefore the apparent increases in specific fuel consumption of the reheat gas turbine would be less if credit were given for the incremental power generated by the steam turbine.

Table 2 shows that for 4 in. H_2O inlet drop the air flow (and exhaust) is reduced by 1 percent because of the density change. Therefore the output of a nonsupplementary fired boiler would also be reduced by 1 percent. The steam flow, then, should not change much, if at all, for no supplementary firing. In the LM5000 application

Table 3

	GT Power Loss percent		*GT Fuel Flow Red. percent*		*Change in S.F. Consump. percent*	
4 in. H_2O Inlet	1.48	1.48	1.07	1.07	.416	.416
6 in. H_2O Exhaust	.73	—	.10	—	.618	—
10 in. H_2O Exhaust	—	1.21	—	.17	—	1.030
Total	2.21	2.69	1.17	1.24	1.034	1.446

SIU conversion: 1 in. H_2O = 249Pa

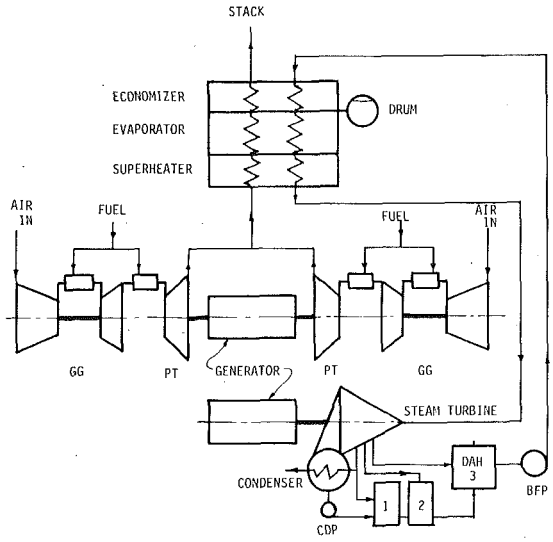

REHEAT GAS/STEAM CYCLE

Fig. 3 Schematic diagram of two LM5000 gas generators with reheat power turbines driving an electric generator in tandem in a combined cycle

and assuming a separately driven air compressor for the power turbine cooling air, the exhaust flow would increase by the amount of the cooling air used. In order to simplify the calculations, however, and to be within the accuracy of the data available, no changes of exhaust flow and temperature to the boiler will be considered. Greater accuracy would require data from an actual reheat power turbine.

Reheat Gas Turbine/Steam Turbine Cycle

Theoretical data presented in Part I is now applied to an actual gas generator to investigate and project the cycle efficiency of the reheat combined cycle from a more practical and realistic standpoint. Up-to-date figures of the LM5000 which were obtained from the manufacturer after the first unit was thoroughly tested have been used in the cycle. The cycle was calculated on the basis of (1) Continuous Operation, (2) Electric Base and (3) Peak. The new International Standard ISO/DIS-3977 for gas turbines defines these modes of operation as follows:

1 *Continuous* Continuous or base load operation typical of pipeline service, process applications or electric power generation up to 8700 hr per year with infrequent starting greater than 100 hr/start,

2 *Electric Base* Longer duration of mid-range electrical power

Table 5

Mode	*Half Plant Capacity* GG Fuel Input LHV BTU/HR × 10^6	RH Fuel Input LHV BTU/HR × 10^6	GT Net Output KW	ST Net Output KW	Total Net Output KW	Net Cycle Eff, percent
Continuous	296.24	171.57	43,002	23,442	66,444	48.69
Electric Base	320.16	162.57	45,969	23,814	69,783	49.34
Peak	336.72	155.90	48,083	23,734	71,817	49.76

SIU conversion: BTU = 1.055 KJ

generation: application up to 4000 hr per year with up to 8 hr/start,

3 *Peak* Short duration intermittent type of operation as occurring typically in electric power generation for peak load demands. Operation should normally be limited to 500 hr per year and up to 2 hr/start.

Table 4 presents the assumptions applied in the calculations of the cycle.

Two LM5000s are coupled end to end to one hydrogen-cooled generator as shown in Fig. 3. The steam generated by the two boilers feed one hydrogen-cooled steam turbine generator set. Boiler stack temperatures were calculated on the basis of a 40°F (22.22°C) pinch approach temperature. Stack temperatures are given in Table 9.

The results of the calculations are presented in Table 5.

It can be noted that the gas turbine power output increases when going from continuous operation to peak operation. However, because the reheat firing temperature is arbitrarily kept constant at 1800°F (982°C) the steam turbine output does not change much and the full benefit of peaking is not realized. The higher expansion ratio of the power turbine lowers the temperature of the boiler which affects boiler steam output and tends to offset the increased air flow. If the reheat temperature is increased along with the gas generator, additional peaking power could be realized from both the power turbine and the steam turbine.

The cycle efficiencies shown in Table 5 correlate well with the first of these papers and are appreciably higher by about 10 percent above what could be obtained with a nonreheat gas turbine combined cycle.

Heat balances were calculated and close closures of about 0.5 percent were obtained to check the validity of the fuel safety factors used in calculating fuel consumption, the use of the gas table figures, and the steam calculations.

It is interesting to note that the method presented above correlates very closely with the method Richard Foster-Pegg presented in his recent ASME paper where 23,622 KW net (continuous mode) is developed using 545 psia and 1000°F (3.76 MPa and 538°C) steam conditions versus 23,442 KW net above.

Reheat Gas/Reheat Steam Cycle

Boiler Considerations. The cycle efficiency advantages of the steam turbine reheat cycle were adopted a number of years ago. Reheating the steam results in greater output per pound of steam which in turn reduces both the stack loss and the condenser loss percentage-wise. Yet little attention, if any, has been given to the reheat gas turbine.

A heat recovery boiler for a reheat steam turbine complicates matters because considerably more surface is required and low temperature differentials are encountered. Also the greater surface creates more back pressure and additional gas turbine power loss.

Attention over the past years has been directed to the outlet end of a heat recovery boiler where dual drums have been incorporated to lower the stack temperature. The reason for doing so was presented in the first part of these papers.

There is, however, another way to lower the stack temperature for high-pressure boilers with the advent of the reheat gas turbine combined cycle: The superheat boiler heat load can be shifted to the gas turbine. The exhaust enters the boiler directly without any superheater.

Fig. 4 illustrates what takes place regarding the reheat, superheat and boiler sections. Considering 2400 psig 1000/1000°F (16.55 MPa 538°C) steam conditions, and if all sections are in the heat recovery boiler, the stack temperature would be approximately 410°F (210°C) in the case of a 1290°F (698.9°C) gas turbine exhaust temperature. If the boiler only had the superheater, the stack would be about 310°F (154.4°C). However if the boiler had nothing but the evaporator and economizer, a 300°F (148.9°C) could be readily reached as can be seen in Fig. 4. The gas turbine temperature gradient shifts to the right.

It is significant that the temperature differential between the gas and the steam is considerably greater for both the evaporator and the economizer sections. Considerably less boiler surface would be required which would reduce the cost and the back pressure. It is believed that such a boiler could be designed for 6 in. of water back pressure.

Cycle Considerations. If the superheat and reheat heating is accomplished by the reheat burner of the gas turbine, a cycle would result as shown in Fig. 5. It can be noted that the burner not only heats the gas turbine air but also heats the steam vapor for the reheat steam turbine. The burner fulfills two functions. A conceptual design of such a burner/heater will be presented later in the paper.

The dry and saturated steam from the boiler is run to the gas turbine superheater, heated to 1000°F (537.8°C) and then piped to the steam turbine. The cold reheat steam would be rerun to the reheat gas turbine coils and then readmitted to the steam turbine like a conventional reheat steam cycle. The pipe runs would be short to and from the steam turbine and the steam pressure drop should be less than for a conventional steam cycle. Piping costs should be reduced.

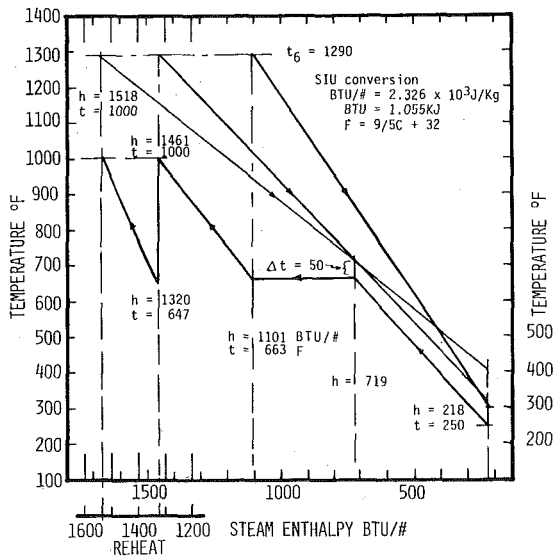

Fig. 4 Temperature/enthalpy diagram for reheat steam turbine (2400 psig—1000/1000°F) showing gas turbine exhaust temperature gradients

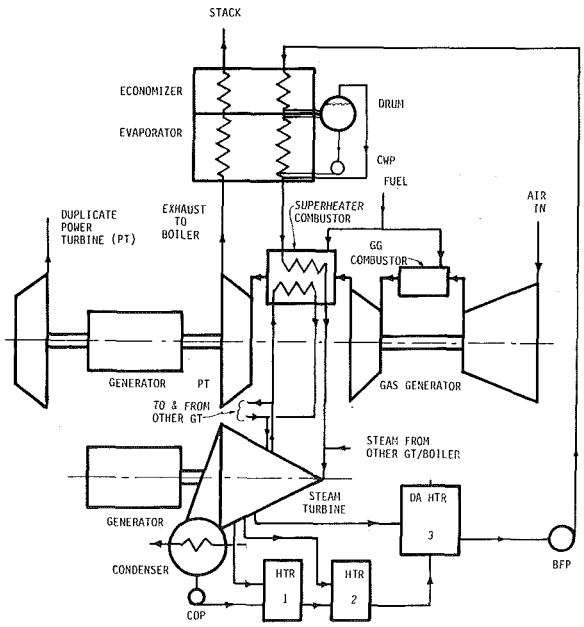

REHEAT GAS/REHEAT STEAM CYCLE

Fig. 5 Schematic diagram of reheat gas turbine combined with a reheat steam turbine with the steam superheat and reheat taking place in the reheat combustor

A compact power plant would result which would be easy to lay out and design. The piping would be simplified and the heat recovery boiler would be smaller and more economical.

A conventional reheat steam turbine heat balance can be used and accurate steam flow heat balances can be directly applied with good accuracy to eliminate many of the unknowns. A practical approach to this method was presented at an ASME meeting by Richard Foster-Pegg last Winter [1].

Application. It has been shown previously that the reheat gas turbine can be applied to the conventional boiler for nonreheat steam conditions of 1250 psig and 900°F (8.62 MPa 482.2°C). A decided cycle efficiency gain resulted. Further gains can be realized with steam reheat which will now be discussed.

Two LM5000s are twin-mounted to one hydrogen-cooled generator of 100,000 KW capacity. (The power turbines would have counter rotation.) The steam turbine would also be a 100,000 KW size so that both would produce about the same power as will be shown. The steam output for the two boilers and the two gas turbine superheaters would feed the one steam turbine.

Steam Turbine Heat Balance. Fig. 6 presents a steam path heat balance of a conventional reheat steam turbine with steam conditions of 2400 psig and 1000/1000°F (16.55 MPa 537.8/537.8°C) for reference. Fig. 7 presents the reheat turbine bottoming cycle for the same steam conditions. The numbers in Fig. 7 were used for the calculations *in this paper.*

The steam turbine heat balance takes into account the boiler feed pump input but a loss of 3 percent should be applied to take into consideration steam leakage, mechanical losses and the hydrogen-cooled generator losses.

Cycle Efficiency and Heat Balance. The assumptions used in the calculations are given in Table 6.

Table 7 presents the results of the cycle analysis for the three modes of operation.

A heat balance for the electric base mode of operation is presented in Fig. 8. The heat balances were checked for each mode and very close closures resulted which indicated that the assumed losses were reasonable and the steam turbine heat balance is compatible with the gas turbine cycle.

The firing temperature to the power turbine was kept constant at 1800°F (982.2°C) for the three modes of operation; by doing so, the superheat and reheat temperatures to the steam turbine would also remain about constant.

Heat Release. It is interesting to note that the heat release for the gas generator and the power turbine are about equal which results in a balanced control system and compatible fuel control values and piping.

Also the overall air/fuel ratio calculation is 28.34 and based on a 100 percent theoretical air/fuel ratio of 14.5, the overall theoretical air of the cycle is 195 percent for the heat balance of Fig. 8. Therefore, the use of the 200 percent theoretical Air Table of Kennan and Kaye gives accurate results directly without interpolation.

Economics. The reheat combined gas/steam turbine will require detailed in-depth studies and the design of the power turbine, combustor and the reheat heat exchanger need further investigation, far beyond the scope of this paper. Other than engineering, there are the development and test costs associated with such a cycle.

The power turbine could possibly take the form of the fan jet high bypass pressure ratio power turbines with their lightweight blading, honey-comb air seals, anti-friction bearings, multi staging and cradled bearings/shafting. These turbines would be well adapted to provide

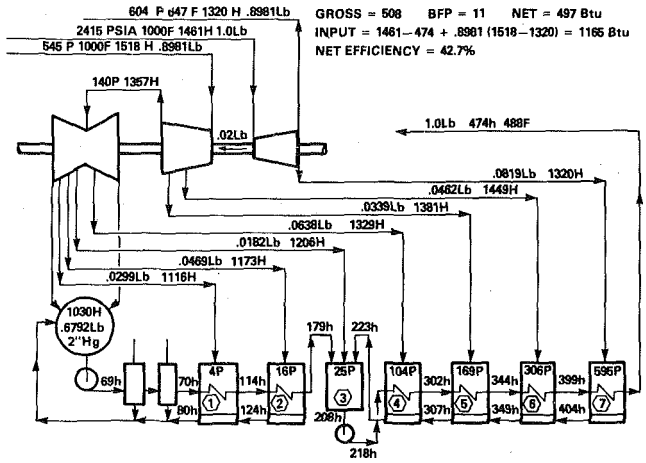

Fig. 6 Heat balance diagram of a typical conventional steam power plant cycle

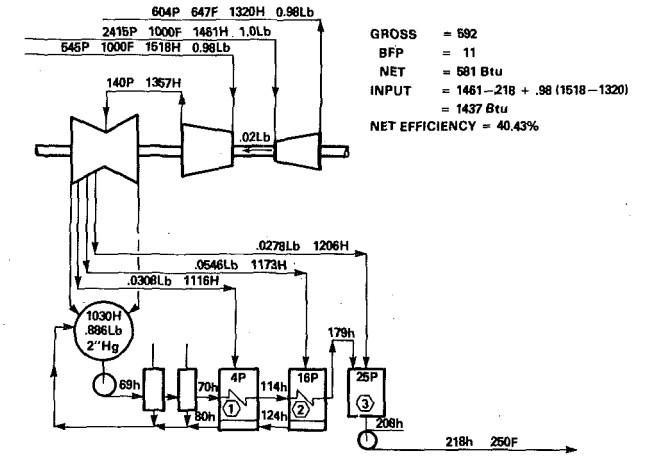

Fig. 7 Heat balance diagram of a 2415 psia—1000/1000°F—reheat steam turbine cycle with three feedwater heaters

Table 6

1	Inlet Pressure psia	14.7
2	Ambient Temperature °F	60
3	Power Turbine Efficiency, percent	87
4	Reheat Gas Turbine Combustion Loss, percent	3
5	Steam Superheater Combustion Loss, percent	1
6	Steam Reheat Combustion Loss	1
7	Reheat Combustor Pressure Drop	3
8	Power Turbine & Generator Loss, percent	2
9	Steam Turbine & Generator Loss, percent	3
10	Boiler Radiation & Blowdown Loss, percent	2
11	Constant Reheat Firing Temperature °F	1800
12	Inlet & Back Pressure Loss in H_2O	4/6
13	Condenser Pressure in. Hga	2
14	Liquid Fuel with 18,400 BTU/lb. LHV	
15	Keenan and Kay Gas Tables for 200 percent Theoretical Air	
16	Steam Heat Balance, Fig. 7	

Note: SIU Conversion Factors:
in. H_2O = 249Pa
BTU = 1.055KJ
in. Hg = 3.388 KPa
PSI = 6.895KPa
°F = 9/5°C + 32

Table 7

	Half Plant Capacity					
Mode	GG Fuel Input LHV BTU/Hr × 10^6	RH Fuel Input LHV BTU/Hr × 10^6	GT Net Output KW	ST Net Output KW	Total Net Output KW	Net Cycle Eff, percent
Continuous	296.24	337.75	43,608	48,234	91,842	49.44
Electric Base	320.16	334.14	46,601	49,313	95,914	50.03
Peak	336.72	328.22	48,750	49,561	98,311	50.46

Note: SIU Conversion: BTU = 1.055KJ

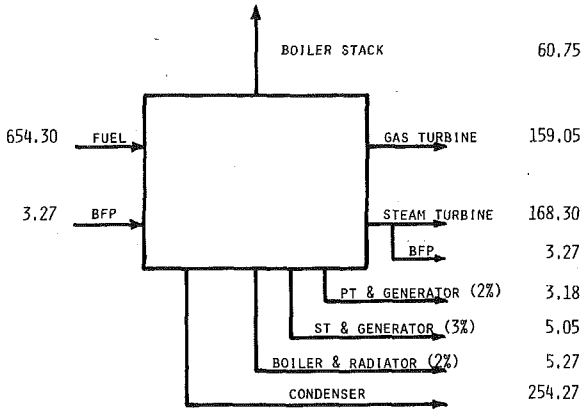

FUEL INPUT & ASSUMED LOSSES

	TOTAL INPUT		LOSSES
GAS GENERATOR	320.16		--
REHEAT GT	167.03	334.14	5.01 (3%)
INITIAL STEAM SH	108.58		1.09 (1%)
STEAM REHEAT	58.53		.58 (1%)
BOILER FEED PUMP	3.27		--
TOTAL	657.57		6.68

CYCLE EFFICIENCY = $\frac{159.05 + 168.30}{654.30} = 0.5003$

NOTE: FUEL INPUT BTU/HR X 10^6 LHV
SIU CONVERSION BTU = 1.055×10^3J

ELECTRIC BASE OPERATION HEAT BALANCE

Fig. 8 Heat balance tabulation of reheat gas/reheat steam cycle for electric base operation

high efficiency at high inlet temperature. Nevertheless, the development costs would be substantial.

The rapid rise in fuel costs, limited future oil supply, coal fuel development, high interest rates, power rate increases, and other uncertainties make it difficult for engineers today to apply economics properly. Engineers are going through a change in approach using new economic standards where the simple five year payout rule of thumb for utility applications may not be fully valid. The economics of developing the reheat cycle, therefore, must be viewed with an open mind because in this paper the old rule of thumb is applied for a broad first look.

In a simplified economic evaluation, the standard combined cycle available today is considered to have a cycle efficiency of 44 percent LHV, the reheat gas turbine/steam turbine 48.5 percent, and the reheat gas turbine/reheat steam turbine 49.5 percent. It is assumed that fuel will cost 2.50 dollars per million BTU LHV. The unit size is assumed to be 100,000 KW, the hours per year of operation, 8000, and the load factor, 80 percent. Table 8 presents this data.

Table 8 indicates that there would be 5,750,000 dollars generated in five years from the fuel savings. These savings would be applied to the added cost of the reheat power turbine. Similarly, 1,150,000 dollars per power plant would be made available to pay for the reheat steam turbine combustor/heat exchanger. It should be noted that there would be a savings in the heat recovery boiler as it would be simpler and have less surface (greater mean temperature difference). Also the two superheaters would not be duplicated in the heat recovery boiler which would be a saving. Yet it is not known what the costs would be to develop reheat equipment and what the market for such cycles is. Any projection is beyond the scope of this paper. These figures, however, look attractive and are worth further investigation.

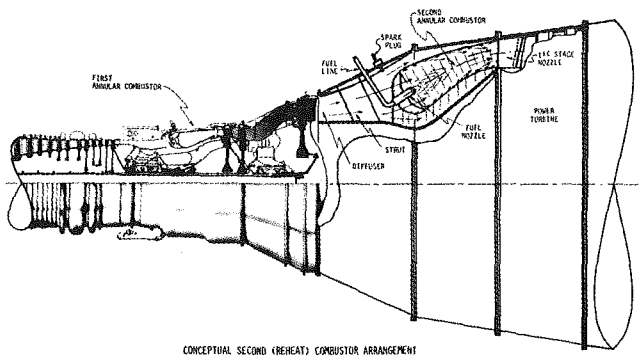

Fig. 9 View of reheat combustor showing relative size and location in respect to the LM5000 gas generator combustor

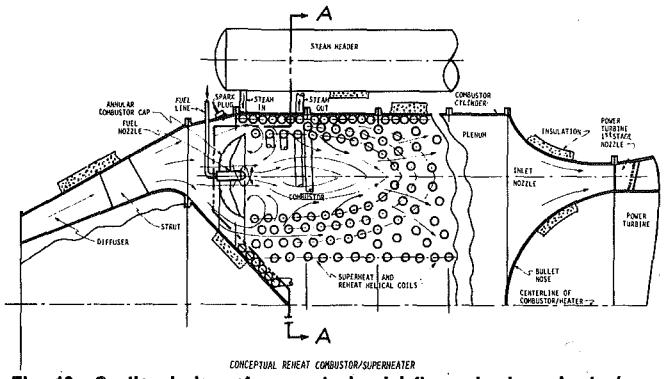

Fig. 10 Sectional view of conceptual axial flow reheat combustor/superheater showing helical tube arrangement to form annular combustion cavity and to mix and distribute combustion/gas generator gasses

Reheat Gas Turbine Combustor and Power Turbine. A conceptual layout of the proposed combustion chamber and power turbine coupled to the LM5000 is presented in Fig. 9.

The combustor is shown to incorporate an annular liner with multiple burners similar to the LM5000. The cord and pitch line diameter have been increased to follow the law PV = WRT where 2100°F (1149°C) and 30 atmospheres were related to 1800°F (982°C) and 3.75 atmospheres to obtain a square root value of 2.6 for equal volumes (velocities) and this value was increased slightly to provide a lower pressure drop combustor. Similarly the power turbine nozzle area related to the last stage of the gas generator was increased by a square root value of 1.16.

The length of the diffuser and combustor would be about 60 percent greater than the diffuser to a conventional power turbine not incorporating the second burner. This length penalty is not very great considering the potential power gain. The power turbine diameter might be slightly greater and the nozzle cord width adjusted to give approximately 1.35 times the area.

Reheat Gas Turbine Combustor Superheater/Reheat/Superheater. A conceptual layout of an axial flow combustor/su-

Table 8

	Cycle Eff. LHV	Percent Inc.	Percent Fuel Consump.	Fuel Cost dollar/yr × 10^6	Savings dollar/yr × 10^6	Savings dollar × 10^6/5 yrs	Savings dollar × 10^6/5 yrs
Conventional Combined Cycle	44	Base	100	12.41	Base	Base	...
Reheat G.Turb./ S.Turb.	48.5	10.2	90.7	11.26	1.15	5.75	Base
Reheat G.Turb./ Reheat S.Turb.	49.5	12.5	88.9	11.03	1.38	6.90	1.15

perheater/reheater for the steam turbine is shown in Fig. 10. The required diameter of the reheat cylinder was determined to be about 10 ft when considering a velocity of 100 ft/s and a 70 percent increase in area to accommodate the superheater tubes assuming an average gas temperature of 2000°F (1093°C). The length would be determined by the surface area required for the superheater and an estimate might be 18 ft.

The outer shell would be made in sections about two ft long and bolted together so that the superheater coils could be inserted properly. The superheater tubes are wrapped around and around to form helical coils of specific configurations. These coils would form an annular combustion cavity and would control air flow to the burner. Downstream from the burner they would then temper the hot combustion gasses and distribute them to more superheater coils.

An annular combustion cap, or ring, would be used to control the air flow (swirl) to multiple burners. A cross section, A-A of Fig. 10 is shown in Fig. 11 where the superheater coils and the combustion cap can be seen.

Section A-A also shows the four superheater headers required to distribute and gather the heated steam. Note that the cold steam enters the bottom and goes around and around and then exits at the top for each superheater.

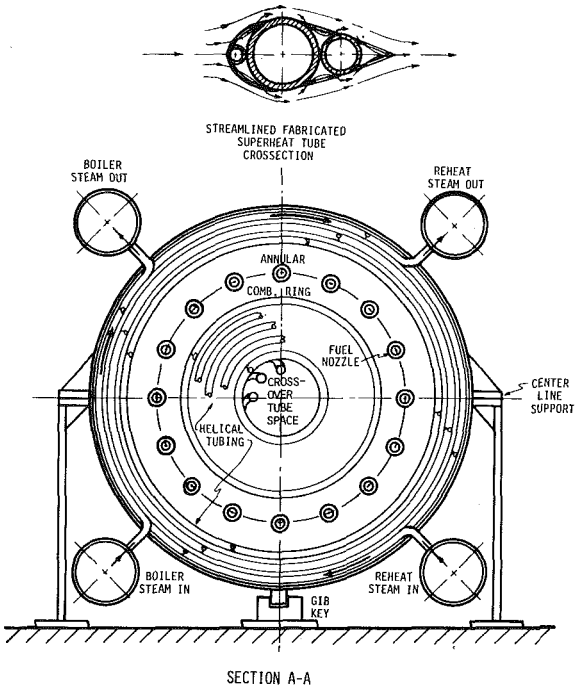

Fig. 11. Cross section of reheat combustor/superheater showing helical tube arrangement, annular combustor cap, fuel nozzles and steam headers. At top is shown streamlined fabricated superheat tube cross section.

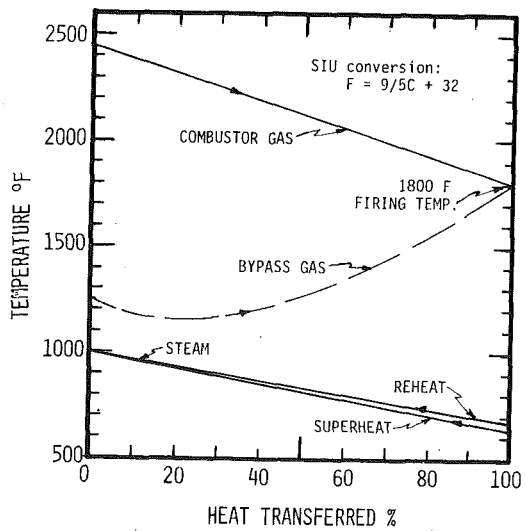

Fig. 12 Temperature curve showing large temperature differences between steam and gas for excellent heat transfer

The heat exchanger shell could be center-line supported to control expansion and to maintain a reasonable centerline elevation with respect to the foundation in order to satisfy alignment of the gas generator and power turbine. Also it should be noted that the gas generator can be quickly and readily removed to service the combustor and superheater.

The heat transfer should be very high with a high heat flux at the temperature levels, radiant conditions and the density of hot gas at about 3.75 atmospheres. A temperature difference curve is shown in Fig. 12 where the equivalent temperature of the hot gasses at approximately 2400°F (1316°C) is cooled to the specified preselected power turbine inlet temperature of 1800°F (982°C). Note that the temperature entering the superheater combustor is already at approximately 1250°F (677°C) which provides a good temperature differential for the 1000°F (538°C) steam temperature. The conditions of temperature and radiation would be very similar to superheaters of conventional boilers.

Each superheater coil should be configured so that each tube length is balanced for (1) steam pressure drop and (2) equal radiant and convection heat absorption area. Equal pressure drop is needed for flow distribution and the balance of radiation/convection heat absorption should provide good superheater temperature control—particularly at part load conditions.

The gas side pressure drop of conventional superheaters is about 2 in. H_2O per superheater which amounts to less than 1 percent drop for the two superheaters for an atmospheric aspirated boiler. Therefore, with careful design, the pressurized superheaters and scaling, if applicable, should be of the same magnitude (1 percent loss).

The tubes could be made in three different pipe sizes and streamlined with perforated leading and trailing edge overlays to minimize pressure drop and to control the hot gas flow as illustrated at the top of Fig. 11. The perforations would allow proper temperature gas to reach the interior surfaces of the tubes and the effective heat transfer area would be increased considerably.

The diffuser from the gas generator to the combustor would have to be very carefully designed to recover as much of the velocity pressure as possible before dumping to the lower velocity region. Fig. 10 shows extra length. Also it can be noted that the gas generator exit gas has a swirl to it that will give the flow a longer path to help the diffusion.

Figure 10 also shows a power turbine nozzle consisting of an outer bellmouth cone and an inner bullet nose similar to the inlet of the LM5000 itself to reduce inlet loss from the reheater to the power turbine as the velocity is again increased.

The gas pressure loss of the combustor/superheater, with proper innovations, is considered to be 3 percent in the analysis. Further study would have to be made to arrive at more accurate values using specific designs.

Nonreheat Steam Turbine Versus Reheat Steam Turbine

Data comparing the cycles incorporating the nonreheat steam turbine and the reheat steam turbine are presented in Table 9 where pertinent data on the gas generator power turbine and boiler are included.

Conclusions

The data presented in Part II of this paper lead to the following conclusions based on the assumptions used:

1 two tandem LM5000s when combined with a nonreheat steam turbine (1250 psig—900°F) (8.62 MPa 482°C) will produce 132.88 MW net power baseload at an efficiency of 48.69 percent LHV,

2 two tandem LM5000s when combined with a reheat steam turbine (2400 psig 1000/1000°F) (16.5 MPa 538/538°C) will produce a 183.68 MW net power baseload at an efficiency of 49.44 percent LHV,

Table 9

Half Plant Capacity
Non-Reheat ST Steam Conditions 1250 psig—900°F
Reheat ST Steam Conditions 2400 psig—1000/1000°F
Average GG Figures Presented

		Base		*Electric Base*		*Peak*	
		No STRH	STRH	No STRH	STRH	No STRH	STRH
1	GG IHP × 10^3	50.0		55.0		59.1	
2	GG Firing Temperature °F	2100*		2250*		2400*	
3	GG Exhaust Flow lb./s	272		283		289	
4	GG Exhaust Temperature °F	1215		1262		1295	
5	GG Exhaust Pressure psia	56.00		58.60		61.00	
6	GG Fuel Cons. BTU/Hr × 10^6LHV	296.24		320.16		336.72	
7	Fuel Cons. BTU/Hr × 10^6LHV	169.55	337.75	162.57	334.14	155.90	328.22
8	Tot. Fuel Cons. BTU/Hr × 10^6LHV	465.79	633.99	482.73	654.30	492.62	664.94
9	PT Ex. Flow to Boiler lb./s	274.5	277.2	285.4	288.1	291.3	294.0
10	PT Ex. Temp. to Boiler °F	1269	1281	1253	1266	1240	1252
11	PT Expansion Ratio	3.702		3.867		4.025	
12	PT Net Output BTU/lb. Flow	151.3	152.2	155.8	156.5	159.7	160.4
13	Steam Flow lb./Hr × 10^3	197.5	292.1	200.5	298.6	199.9	300.1
14	Boiler Stack Temp. °F	328	300	335	300	341	300
15	Air/Fuel Ratio lb. Air/lb. Fuel	38.40	28.21	38.42	28.34	38.32	28.39
16	PT New MW Output	43.00	43.61	45.97	46.60	48.08	48.75
117	ST New MW Output	23.44	48.23	23.81	49.31	23.73	49.56
18	Total Net MW Output	66.44	91.84	69.78	95.91	71.81	98.31
19	Cycle Efficiency LHV percent	48.69	49.44	49.34	50.03	49.76	50.46

* Estimated Values

Note: SIU Conversion Factors:
in. H_2O = 249Pa
BTU = 1.055KJ
in. Hg = 3.388KPa
PSI = 6.895KPa
°F = 9/5°C + 32

Abbreviations:
GG—Gas Generator
PT—Power Turbine
ST—Steam Turbine
Ex—Exhaust

3 the reheat combustor/heat exchanger offers a way to shift the superheater load and reduce heat load away from the heat recovery boiler to (a) reduce the stack temperature to a mininum of 300°F, (b) reduce the boiler surface and back pressure and (c) reduce the cost of the boiler and steam piping,

4 the nonreheat steam cycle superheater could be incorporated in the gas turbine combustor to lower the stack temperature and improve the nonreheat steam turbine combined cycle efficiency; it is noted that the efficiency levels of both non and reheat steam cycles are relatively close together,

5 the combined reheat gas turbine/reheat steam turbine appears to be possible with proper development work on the reheat combustor/heat exchanger and the low pressure ratio high temperature power turbine,

6 growth in size and cycle efficiency is possible by increasing the power turbine and gas generator firing temperatures. The paper leads to the possibility of further innovations such as early intercooling of the gas generator air compressor and NO_x control with the two burners,

7 the reheat combined cycle could renew interest in the "Gatlin Gun" approach (Cincinnati Gas and Electric Company 100 MW installation) where perhaps ten gas generators would exhaust into one large cylindrical combustor/superheater (Approximately 35 feet in diameter.); the hot gasses would then expand through a low speed power turbine (900 to 1200 RPM) to develop 500 MW; the steam turbine would also develop some 500 MW to form a 1000 MW power plant,

8 the reheat combined cycle makes it possible to develop a hybrid system where a relatively good grade distillate is burned in the gas generator combustor and an equal amount of low-grade fuel (low BTU coal gas, coal derived liquid, or shale derived liquid, etc.) could be burned in the second combustor under lower pressure and temperature conditions; the power turbine blading would be larger and more adaptable to the latest cooling techniques and at the same time more durable for such low-grade fuels.

The lower pressure could be more compatible with the coal gasification process in the case of LBTU coal gas and less parasitic compression power would be required. A further study of such a cycle is suggested.

Acknowledgments

Appreciation is expressed to my devoted wife, Carolyn, who is also my loyal secretary, for her assistance in editing and typing these two papers. Without her support and diligence this project could not have been undertaken.

Appreciation is also extended to Mr. Richard Foster-Pegg of Westinghouse Electric Corporation for the use of his steam turbine heat balances and to Mr. Hans Lanz and General Electric Company for use of the data on the LM5000 gas generator.

References

1 Foster-Pegg, R. W., "Steam Bottoming Plants for Combined Cycles," ASME JOURNAL OF ENGINEERING FOR POWER, Vol. 100, No. 2, April 1978.

2 Caruvana, A, Day, W. H., Manning, G. B., and Sheldon, R. C., "Evaluation of a Water-Cooled Gas Turbine Combined Cycle Plant," ASME Paper No. 78-GT-77.

3 Fraize, W., Lay, R., and Sharp, E, "Advanced Power Conversion Systems," ERDA, April, 1977.

4 *Steam, Its Generation and Use,* Babcock and Wilcox Company, 1955.

5 *DeLaval Engineering Handbook,* McGraw-Hill, 1970.

6 Mark, L. S., *Mechanical Engineers' Handbook,* McGraw Hill, 1951.

B. Lakshminarayana
Professor.

R. Davino
Graduate Assistant.

Department of Aerospace Engineering,
The Pennsylvania State University,
University Park, Penn. 16802

Mean Velocity and Decay Characteristics of the Guidevane and Stator Blade Wake of an Axial Flow Compressor

Pure tone noise, blade row vibrations, and aerodynamic losses are phenomena which are influenced by stator and IGV blade wake production, decay, and interaction in an axial-flow compressor. The objective of this investigation is to develop a better understanding of the nature of stator and IGV blade wakes that are influenced by the presence of centrifugal forces due to flow curvature. A single sensor hot wire probe was employed to determine the three mean velocity components of stator and IGV wakes of a single stage compressor. These wake profiles indicated a varying decay rate of the tangential and axial wake velocity components and a wake profile similarity. An analysis, which predicts this trend, has been developed. The radial velocities are found to be appreciable in both IGV and the stator wakes. This wake data as well as the data from other sources are correlated in this paper. Appreciable static pressure gradient across the wake is found to exist near the trailing edge of both stator and IGV.

1 Introduction

The investigation of inlet guide vane (IGV) and stator blade wakes is important for providing adequate design criteria for multistage axial-flow turbomachinery used in aircraft, marine, space, and land vehicles. IGV and stator blade wake production, decay, and interaction influence phenomena such as pure tone noise, blade row vibrations, and aerodynamic losses and inefficiencies which occur in an axial-flow compressor. The mixing and dissipation of the blade wakes with the free stream of the flow produces a loss of energy which corresponds to a reduction in efficiency of the turbomachine. The three-dimensional velocity profile of the wake and the trajectory of the wake center as a function of the distance from the trailing edge of the IGV and stator blade is of important consideration in the design of subsequent blade rows. This information is also essential for prediction of the aerodynamic and acoustical properties of a turbomachine. Through an adequate understanding of the IGV and stator blade wake the turbomachinery aerodynamicist can minimize losses and accurately determine blade row geometries for the IGV, rotor, and stator. Also, the acoustician can predict and minimize broadband and pure tone noise levels.

A large number of parameters influence the production, decay and interaction of the IGV and stator blade wake. The nature of the flow at the exit of the IGV and stator blades is three-dimensional and turbulent having axial, tangential, and radial velocity components. The development and nature of this flow is illustrated in Fig. 1. This velocity profile is produced as a result of the boundary layer development along the surface of the blade. As the boundary layers from both surfaces of the blade meet at the trailing edge of the blade, they form a defect in the velocity profile behind the blade which decreases in magnitude as the wake progresses downstream. The radial component of the velocity profile in the wake develops due to an imbalance of the centrifugal and pressure forces near the surface of the blade. This radial flow also decreases in magnitude as the wake progresses downstream.

The objective of this investigation is to study the characteristics

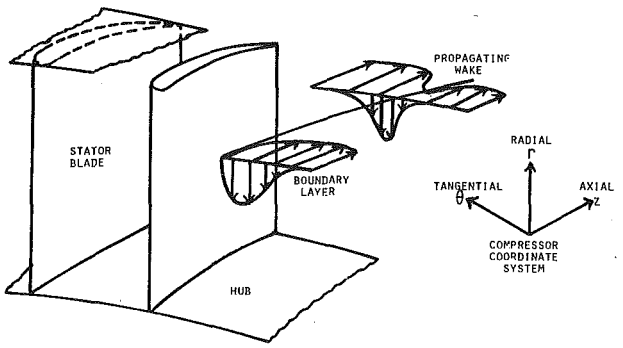

Fig. 1 Stator blade wake production and development

Contributed by the Gas Turbine Division and presented at the Gas Turbine Conference and Exhibit and Solar Energy Conference, San Diego, California, March 12–15, 1979 of THE AMERICAN SOCIETY OF MECHANICAL ENGINEERS. Manuscript received at ASME Headquarters December 7, 1978. Paper No. 79-GT-9.

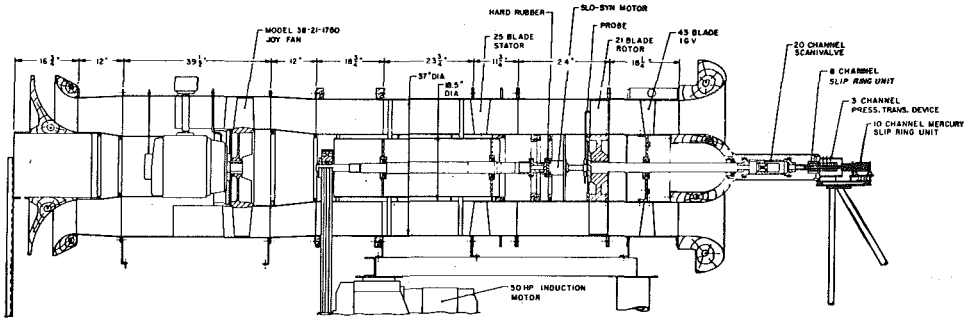

Fig. 2 PSU axial-flow compressor facility

of the wake of IGV and stator blades. Wake measurements were performed with a single sensor hot wire probe in a stationary reference frame. The wake was surveyed in the tangential direction at various axial distances behind the IGV and stator blade. Using the above experimental procedure the mean velocity components of the wakes were determined. From these experimental results the IGV and stator blade wake mean velocity profile, decay, and trajectory were determined.

The effects of the streamline curvature in a swirling turbulent flow has been reviewed by Bradshaw [1]. Streamline curvature was found to produce large changes in the turbulence structure of the shear layers. These changes were found to be an order of magnitude more important than the normal pressure gradient. Thus the wakes of IGV and stator are likely to be different from the cascade and isolated airfoil wakes due to the presence of swirl or the curvature in the flow. This prompted the investigation reported in this paper.

2 Experimental Equipment and Procedure

2.1 Facility and Operating Condition. The research compressor facility of the Department of Aerospace Engineering at the Pennsylvania State University was used for all measurements in this investigation. This single-stage, axial-flow compressor facility is shown schematically in Fig. 2. This compressor has a hub-tip ratio of 0.5 and OD of 91 cm. The inlet guide vanes, rotor blades, and the stator blades are of aluminum casting and number 43, 21 and 25 blades, respectively. All measurements were obtained under constant operating conditions. The IGV and stator blade row geometry and the operating characteristics of the facility are tabulated in Table 1. The performance of this compressor facility is discussed in [2]. The stage was designed by Smith [3].

Table 1 Blade row geometry and operating characteristics

	IGV	Stator
R	0.82	0.75
Blade Chord	90 mm (3.54 in.)	103 mm (4.05 in.)
Blade Spacing	56 mm (2.2 in.)	85 mm (3.35 in.)
Solidity	1.60	1.22
Rotor Speed	1060 rpm	1060 rpm
Blade Pressure Coefficient (ψ_s)	−0.13	0.376
Blade Drag Coefficient (C_D)	0.024	0.0172
Blade Lift Coefficient (C_L)	0.51	0.73
Flow Coefficient (ϕ)	0.56	0.56
Stage Loading Coefficient (ψ)	0.52	0.52
Inlet Velocity	29.2 ms (96 fps)	40 ms (131 fps)
Inlet Flow Angle	0 deg	42.5 deg
Camber Angle	23 deg	—
Outlet Flow Angle (Mean)	20 deg	21 deg

2.2 Probe, Instrumentation and Data Processing. A single-sensor hot wire measurement technique developed by Whitfield, et al. [4] and improved by Schmidt and Okiishi [5] and Hirsch and Kool [6] was used in this investigation. The hot wire probe configuration used in this investigation is shown in Fig. 3. The hot wire probe was

Nomenclature

$C_p = (p_\ell - p_1)/1/2\,\rho V_1^2$
C_L, C_D = lift and drag coefficient based on cascade mean velocity
c = blade chord
e = instantaneous voltage of the hot wire
E = hot wire voltage
E_0 = hot wire voltage at zero flow velocity
f = frequency
L = wake width $[2(L_s + L_p)/S]$
L_s, L_p = length scales corresponding to the suction and pressure sides of the wake
p = static pressure
PS = pressure surface
Δp = difference in static pressure between free stream and the wake location
R = nondimensionalized radius (r/r_t)
$\mathcal{S}$ = streamwise distance normalized by blade chord
S = blade spacing
SS = suction surface
s, n, r = streamwise, normal, and radial probe directions, respectively (Fig. 2)
T = turbulence intensity (RMS value of the fluctuation divided by local total velocity)
V = velocity
v = defect in velocity $(V_{\max} - V_{\min})$
v_c = defect in velocity at the wake center line
$V_{\min}$ = minimum velocity in the wake
V_e = effective cooling velocity
$\overline{V}$ = total velocity vector
τ_b, τ_d = probe turning angle increments ($\tau_b = \tau_d = 120$ deg)
z, θ, r = axial, tangential, and radial coordinates, respectively
Y = tangential distance from the wake the center line nondimensionalized by semi blade spacing ($2r\theta/S$, $\theta = 0$ at wake center)
Z = axial distance normalized by the blade chord ($Z = 0$ at the trailing edge)
α = sensor yaw angle
β_2 = air outlet angle
η = normalized tangential distance ($r\theta/L_s$, $r\theta/L_p$)
ψ_s = blade pressure rise coefficient (based on inlet dynamic head)
ϕ, ψ = flow and stage loading coefficients (normalized by $\frac{1}{2}\rho U_t^2$)
θ_n = probe yaw angle
θ_0 = probe angle
θ_p = probe pitch angle
Λ = nondimensionalized velocity defect at the wake center (v_c/V_0)—except in the case of radial velocity, where it is equal to $|(V_r)_m|/V_{z_0}$

Subscript

a, b, d = values corresponding to the three probe angle orientations
0 = values in the free stream
z, θ, r = values corresponding to the axial, tangential, and radial coordinates, respectively
t = tip
m = maximum
P, S = pressure and suction surfaces, respectively
1 = upstream values
ℓ = local
c = values at the wake centerline

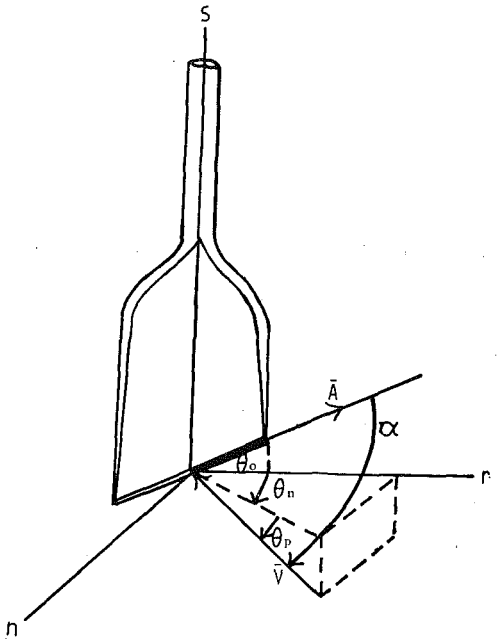

Fig. 3 Hot wire configuration

fixed in a holder and a support which was positioned incident to the IGV and stator blade wake. This hot wire probe holder and support as well as orientation of the probe are illustrated in Fig. 4.

A probe angle θ_0 of 35.3 deg and probe turning angles τ_b and τ_d of 120 deg were chosen so that the probe would be orientated in three mutually perpendicular directions. At each measurement station the hot wire was rotated through three orientations. Utilizing this technique the IGV and stator wakes were surveyed in the tangential direction with the probe axis aligned in an approximate streamwise direction (s) (Fig. 3). The location of the measurement stations are tabulated in Table 2. Thus, at each measurement station the hot wire probe surveyed the IGV and stator blade wake in the tangential direction and at each location of the survey the probe was rotated through its three orientations. The hot wire voltages at these orientations were recorded and then processed into the mean velocity components of the wake at that location. The hot wire sensor is represented in Fig. 3 by the unit vector $\bar{A}$ slanted at the angle θ_0 to the r axis, the velocity vector is denoted by $\bar{V}$. The probe coordinates s, n and r are fixed to the probe. The probe yaw angle θ_n will change by the amount of turning while the pitch angle θ_p will remain constant as the probe is rotated about its axis. The sensor yaw angle α can be expressed in terms of the angles θ_0, θ_p, and θ_n as follows:

$$\cos \alpha = \cos \theta_0 \cos \theta_p \cos \theta_n + \sin \theta_0 \sin \theta_p \quad (1)$$

The above probe geometry was developed by Schmidt and Okiishi [5].

The hot wire velocity calibration was made in the typical manner with the sensor yaw angle α equal to 90 deg. The flow velocity V is related to the bridge voltage E by the empirical equation:

$$E^2 = E_0^2 + BV^m \quad (2)$$

where the constants B and m were determined by fitting equation (2) to the calibration data. E_0 is the hot wire voltage at zero velocity. In the flow measurements the sensor yaw angle did not equal 90 deg and the velocity indicated by the sensor was not the actual velocity but an effective cooling velocity, V_e. Schmidt and Okiishi [5] have developed a second order empirical correlation to express the effective cooling velocity as a function of sensor yaw angle, pitch angle, and velocity as follows:

$$V_e/V = b_0 + b_1\alpha + b_2\theta_p + b_3V + b_4\alpha^2 + b_5\theta_p{}^2 + b_6V^2 + b_7\alpha\theta_p + b_8\alpha V + b_9\theta_p V \quad (3)$$

The coefficients b_0 through b_9 were determined through a least squares fit of the effective cooling velocity data.

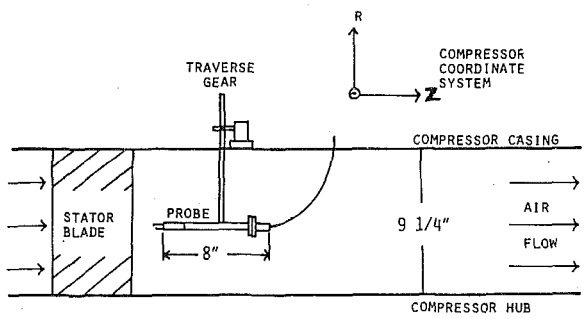

Fig. 4 Probe orientation behind the stator vane

Table 2 Measurement stations for IGV and stator wake

IGV		STATOR	
R = 0.75	Z = 0.019, 0.037, 0.075, 0.147, 0.290, 0.600	R = 0.75	Z = 0.013, 0.026, 0.053, 0.106, 0.160, 0.211, 0.317, 0.423, 0.634, 0.846
R = 0.514, 0.53, 0.55, 0.63, 0.72, 0.80, 0.88, 0.96, 0.97, 0.98	Z = 0.08 and 2.3 (Values vary slightly from one radii to another).		

Measurements were obtained at the flow field measurement points by positioning the hot wire sensor at three probe angle orientations (a, b and d). These orientations correspond to probe yaw angles of $\theta_{n,a}$, $\theta_{n,b}$, and $\theta_{n,d}$ which are:

$$\theta_{n,a} = \theta_n \quad (4)$$

$$\theta_{n,b} = \theta_n - \tau_b \quad (5)$$

$$\theta_{n,d} = \theta_n - \tau_d \quad (6)$$

where τ_b and τ_d are constant probe turning angle increments. For every wire orientation an expression for the yaw angle α similar to equation (1) and a relationship for this effective cooling velocity similar to equation (3) can be expressed. These equations were solved modifying a computer program developed by Gorton [7]. This program determined the coefficients (b_0, b_1, $b_2 \cdots b_9$) in equation (3) by empirically fitting the calibration data. The effective velocities $V_{e,a}$, $V_{e,b}$, and $V_{e,d}$ were known as a result of measurement. This velocity vector was then transformed to the compressor coordinate system. The above procedure was repeated for every flow field measurement station. The resulting velocity vectors determined the mean velocity profiles which defined the structure and the decay of the IGV and stator blade wake.

3 Experimental Data and Interpretation

3.1 **Mean Velocity Profiles.** As indicated earlier, mean velocity profile measurements in the wake of the IGV and the stator blade were carried out at various axial locations of the flow passage. Figs. 5–9 illustrate the axial, tangential, and radial velocity profiles of the IGV and stator wake as the wakes propagate downstream. These mean velocities are normalized with respect to the local free stream axial velocity V_{z_0}. These normalized velocities are plotted as a function of the normalized tangential location Y given by

$$Y = \frac{2r\theta}{S}$$

Here r is the radial location of the measurement, θ is the tangential location of the measurement station, and S is the blade spacing (θ = 0 at the wake center).

Figs. 5 and 7 illustrate the axial velocity profile of the IGV and stator wakes, respectively, as the wake propagates downstream. The defect in the velocity profile of the IGV wake is approximately 40

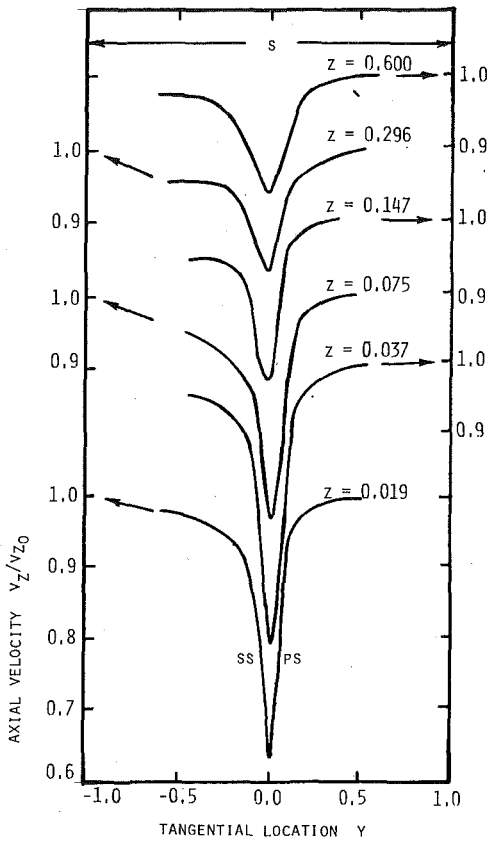

Fig. 5 IGV wake axial velocity profiles, R = 0.82 (Trailing Edge V_{z_0} = 30.2 m/s, Far Wake V_{z_0} = 31.2 m/s)

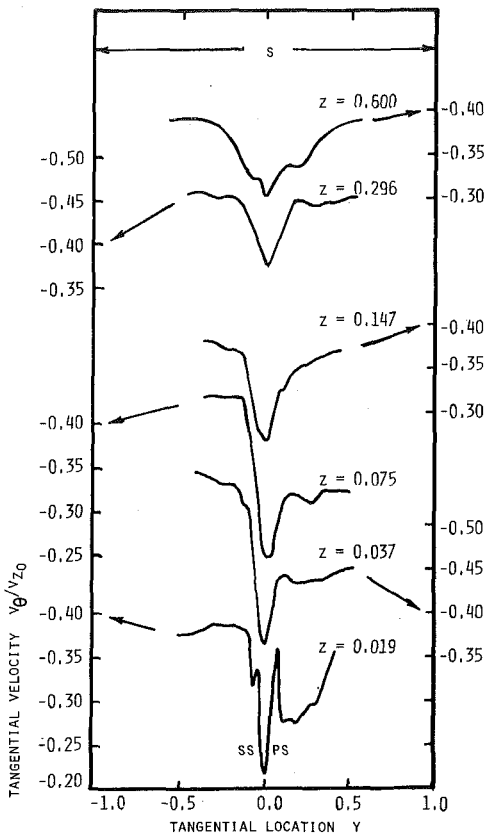

Fig. 6 IGV wake tangential velocity profiles, R = 0.82

percent of the free stream value near the trailing edge of the blade (Z = 0.019) where the stator wakes show a defect of approximately 60 percent (at Z = 0.013). The pressure and suction sides of the axial velocity profile correspond to the pressure and suction surfaces of the respective blade. The IGV and the stator axial velocity profiles shown in Figs. 5 and 7 indicate varying boundary layer and wake development between the IGV and the stator blade wakes. The IGV wake velocity profiles show a larger boundary layer growth on the suction side of the wake whereas the stator wake velocity profiles indicate a larger growth of the blade boundary layer on the suction side of the blade only at the first station. Subsequent wake development shows larger thickness on the pressure side. This may have been caused by intense mixing between the two shear layers. The velocity gradients are steep near the trailing edge for both the cases.

Figs. 6 and 8 show the development of the tangential velocity profiles of the wakes as they propagate downstream of the IGV and the stator. These velocity profiles also indicate the curvature of the wake centerlines and the variance in the boundary layer development. The tangential velocity in the wake center close to the trailing edge of the blade is approximately 25 percent of the free stream axial velocity behind the IGV and approximately 10 percent of the free stream axial velocity behind the stator. The tangential velocity inside the wake is not only a function of its free stream value but also the radial velocity. The radial velocity influences the decay of the tangential velocity. In the case of IGV, the free stream value (V_{θ_0}) increases slightly between the first and second station (Z = 0.019 and 0.037, respectively) and remains nearly constant downstream of Z = 0.037. The IGV wake shows a tendency to become symmetrical, about the wake centerline, beyond Z = 0.147 (see Figs. 5 and 6). Initially there is substantial difference between the pressure and suction surface free stream values of tangential velocity for the IGV wake and Fig. 6 shows that these eventually equalize at Z = 0.147. This effect can be attributed to inviscid effects as well as the curvature of the blade surface, which persists downstream of the blade. The suction surface part of the wake is again thicker than the pressure surface for the IGV (Fig. 6).

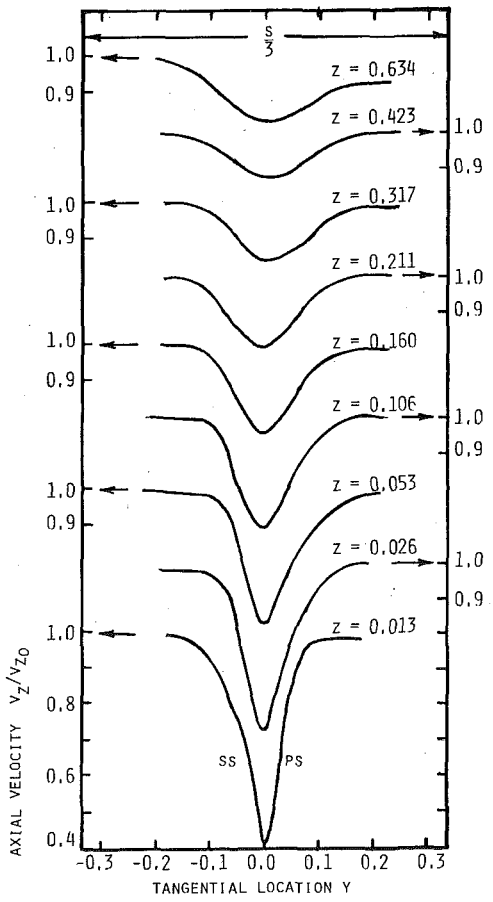

Fig. 7 Stator wake axial velocity profiles, R = 0.75 (Trailing Edge V_{z_0} = 32.7 m/s, Far Wake V_{z_0} = 29.4 m/s)

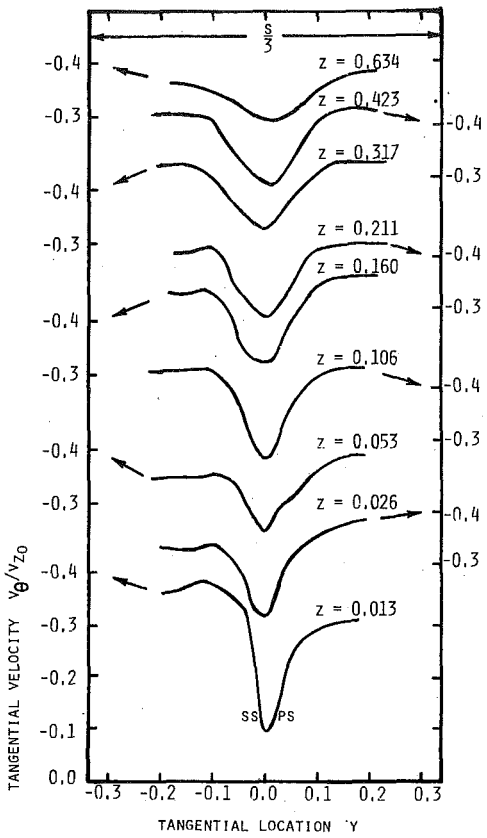

Fig. 8 Stator wake tangential velocity profiles, $R = 0.75$

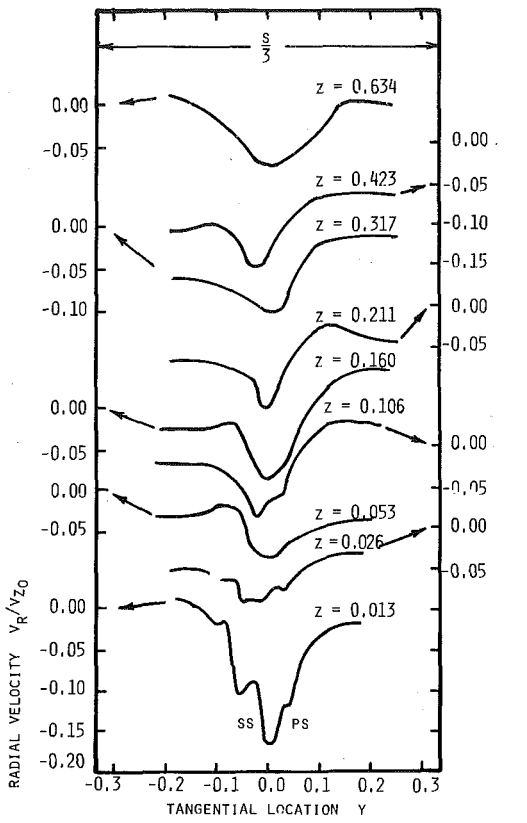

Fig. 9 Stator wake radial velocity profiles, $R = 0.75$

The tangential velocity distribution in the stator blade wake also shows a trend similar to the IGV. The free stream tangential velocity increases near the trailing edge up to $Z = 0.160$ and stays nearly constant beyond $Z = 0.211$. This seems to imply that the outlet angle, both the local and the mean values, change appreciably from trailing edge to about quarter chord and remain nearly constant beyond this station. The pressure surface has a thicker wake than the suction surface, except at the first station ($Z = 0.013$). One possible explanation is larger accumulation of the wake flow on this surface due to radial inward velocity. The decay of the defect in the tangential velocity is slower than the corresponding axial velocity. This will be discussed further in a later section.

Radial flow occurs in the wake due to an imbalance of centrifugal and pressure forces close to the surface of the blade inside the blade boundry layers. As the surface of the stator blade row is approached, the tangential velocity decreases and, therefore, the centrifugal forces diminish in this region, while the radial pressure gradient is nearly constant. This imbalance between the centrifugal force and the radial pressure gradient sets up a radial inward flow. This inward flow persists even in the wake. This can be clearly seen in Fig. 9, where the radial velocities for the stator wakes are plotted. The maximum radial inward velocities are about 15 percent of the axial free stream velocities decreasing to less than 1 percent within 5 percent of the chord length. The radial velocities decay very rapidly in this region. Existence and persistence of radial velocity beyond $Z = 0.106$ may be due to large hub to tip redistribution of flow (through radial equilibrium equation) that occurs downstream in the wake between the hub and annulus. Presence and effect of three-dimensional flows are thus evident.

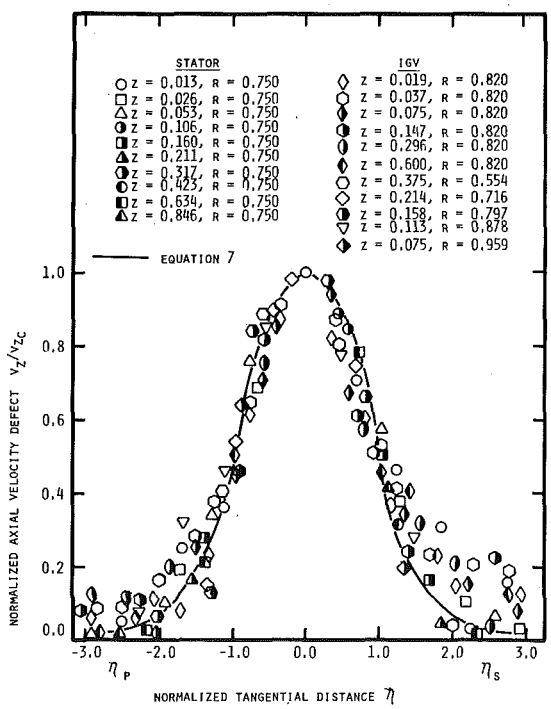

Fig. 10 Similarity in axial velocity profiles for IGV and stator wakes

3.2 **Similarity in the Mean Velocity Profile.** A similarity in the mean velocity profiles of the wakes behind flat plates, isolated airfoils, and rotor blades has been established by previous investigators. This similarity was also found to exist for the velocity profiles of the wakes behind the IGV and stator blades examined in this investigation.

In Fig. 10, the axial component of velocity for the IGV and stator blade is reduced to a single curve using the velocity defect at the centerline as the scaling velocity and two different length scales, L_s and L_p. L_s and L_p are distances on the suction and pressure sides of the wake centerline from the point of minimum velocity to a point where the velocity defect is $v_c/2$. v_c is the velocity defect at the centerline and v is the velocity defect of the wake at the measuring point.

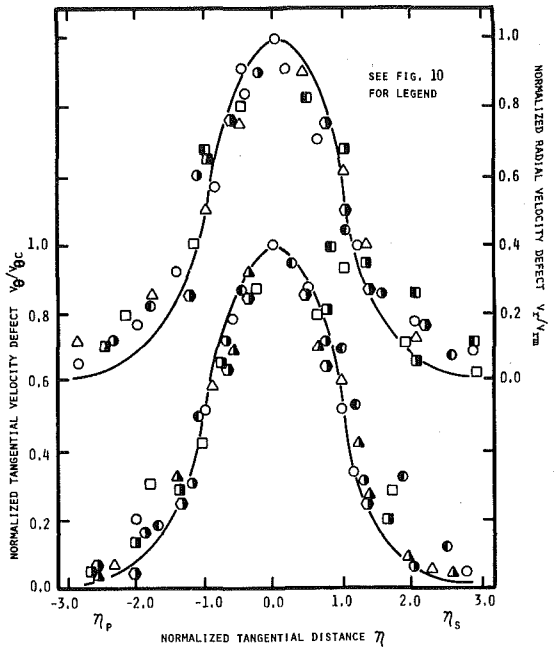

Fig. 11 Similarity in tangential and radial velocity profiles for IGV and stator wakes

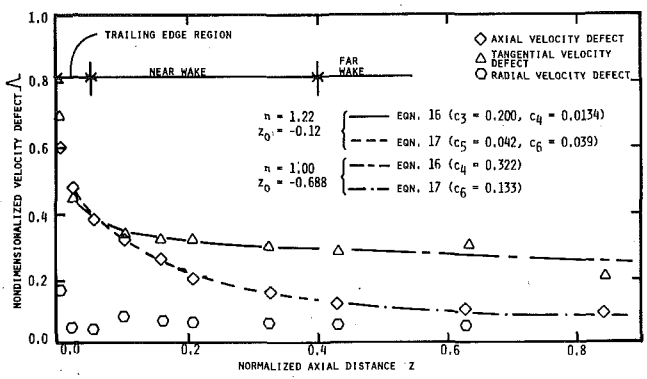

Fig. 13 Decay of axial, tangential, and radial velocity defects behind the stator vane, $R = 0.75$

The similarity in the velocity profiles of the IGV and the stator blade wake shown in Fig. 10 indicates that the profiles are nearly symmetric (when normalized by suitable velocity and length scales) about the wake centerline. The axial velocity profiles show good agreement with the Gaussian distribution near the wake centerline. This correlation is expressed as,

$$\frac{v}{v_c} = \exp(-0.693\,\eta^2) \tag{7}$$

where η is the ratio of the tangential distance $r\theta$ and the proper length scale L_p or L_s. At the wake edge, however, this correlation breaks down as is evidenced particularly in the IGV velocity profile. The correlation is also poor in IGV wakes near the annulus and hub walls (not shown).

The tangential velocity defect as well as the radial velocity, plotted in a similar way and shown in Fig. 11, also reveal the existence of similarity even in the near wake region.

The stator data due to Bitterlich and Rubner [8] and Daneshyar [9] and the cascade data due to Pollard and Gostelow [10] are plotted in Fig. 12. Both the cascade and the stator data follow the Gaussian function (equation (7)).

The data shown in Figs. 10, 11 and 12 and discussed here indicate that similarity in profile exists for IGV, stator and cascade wakes. The influence of curvature on the wake profile is not appreciable. The deviation of the defect from the Gaussian function (equation (7)) is appreciable only near the hub and annulus walls and the trailing edge region. Perhaps this is one of the important conclusions of this paper

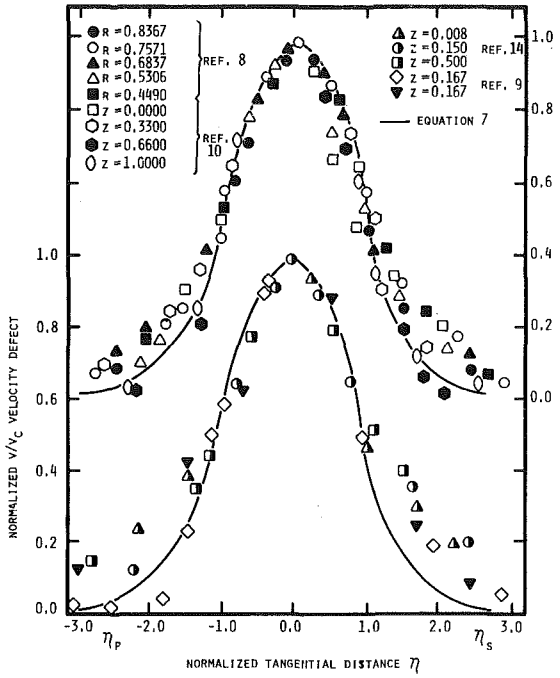

Fig. 12 Similarity in velocity profiles for cascade and stator wakes

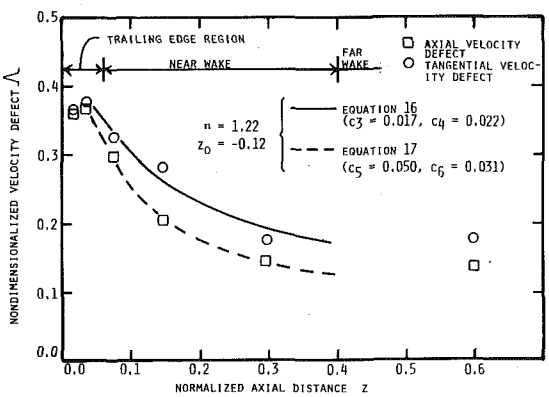

Fig. 14(a) Decay of axial and tangential velocity defects behind the IGV, $R = 0.82$

and should greatly aid the unsteady aerodynamicists and acousticians to model the flow for the prediction of the aerodynamic transfer function and noise radiation.

3.3 **Decay of the Velocity Defect.** The wake velocity defect is normalized by the free stream velocity as follows:

$$\Lambda = \frac{v_c}{V_0} = 1 - \frac{V_m}{V_0}, \quad \Lambda_z = \frac{v_{zc}}{V_{z0}}, \quad \Lambda_\theta = \frac{v_{\theta c}}{V_{\theta 0}}, \quad \Lambda_r = \frac{|V_{rm}|}{V_{z0}}$$

The decay rate of the axial, tangential, and radial components of the velocity defect of the wakes behind the stator and the IGV blade are presented in Figs. 13 and 14(a), respectively. Three regions of decay can be distinguished in the wake. These regions are: (1) trailing edge region ($0.0 < Z < 0.06$), (2) near wake region ($0.06 < Z < 0.4$), and (3) far wake region ($z/c > 0.4$).

[1] *Trailing Edge Region.* In this region the wake defect decays very rapidly and the bounded shear flow is transformed into free shear flow. Major causes of rapid decay are pressure gradient, high turbulence intensity and wake centerline curvature. This region is common to axial, tangential, and radial velocities in both the IGV and the stator blade wakes. The stator wake defect decay (Fig. 13) shows a large decay rate for all the components, the radial component being the most rapid at this location. In both the IGV and the stator wake the axial defect decays more rapidly than the tangential component. Possible reasons for this phenomena are explained later.

[2] *Near Wake Region.* In this region the decay rates of the wake defects are appreciably slower. In both cases, the tangential component of the wake defect decays slower than the axial component. The radial component, however, shows a distinctly different trend in this region. The radial velocity increases slightly and decreases again. This may be caused by three-dimensional effects such as the distribution of the free stream velocity components and interaction in the radial direction.

[3] *Far Wake Region.* In this region the decay rate of the wake defects are very slow and approach an asymptotic value. In the IGV wake, the axial and tangential components of the wake defect are approximately the same, but in the stator wake the axial component decays at a slightly faster rate. Both wakes show a slow decay rate approaching a constant value. This is the region where interaction between the adjoining wakes causes appreciable slowdown in the decay rate.

The differential decay rates of the tangential and the axial velocity defects may be attributed to the curvature, presence of the radial velocity and the radial pressure gradient. The fact that the tangential velocity defect is decaying slower than the axial velocity defect seems to indicate the change in outlet angle as the flow proceeds from the trailing edge of the blade to the next blade row. Reasons for the differential decay of the axial velocity and tangential velocity defects as well as the quantitative description of the decay rate can be derived from the analysis presented below.

In [11], an analysis of the rotor wake was carried out to predict the decay rates for the axial, the tangential and the radial velocities. The same analysis can be employed to describe the trend observed for the IGV and the stator wake reported here. The approach used in [11] is based on the momentum integral technique and is valid for wakes where the defect is not large and similarity in profiles exist. The equations of [11][1] can be simplified to provide the following expressions for the decay rates for the radial velocity, and the defect in tangential and axial velocity,

$$H\frac{d}{dz}(LV_{rm}) = -2\frac{V_{\theta_0}}{V_{z_0}}\frac{L}{r}v_{\theta c}G \tag{8}$$

$$G\frac{d}{dz}(Lv_{\theta c}) = \frac{2}{r}\left[\frac{d}{dr}(rV_{\theta_0})\right]L\frac{V_{rm}}{V_{z_0}}H \tag{9}$$

$$F\frac{d}{dz}(Lv_{zc}) = \frac{d(V_{z_0})}{dr}\frac{LV_{rm}H}{V_{z_0}} \tag{10}$$

where

$$F = \int_0^1 (v_z/v_{zc})d\eta$$

$$G = \int_0^1 (v_\theta/v_{\theta c})d\eta$$

$$H = \int_0^1 (V_r/V_{rm})d\eta$$

It is clear from the above expressions that the radial velocity is dependent on the centrifugal acceleration in the free stream ($V_{\theta_0}^2/r$). Hence the radial velocity should decay rapidly in a blade row with higher V_θ or lower r. The decay of the axial velocity is dependent on the radial velocity as well as the radial gradient in axial velocity in the free stream, while the tangential velocity defect depends on V_{θ_0} distribution in the radial direction and the radial velocity. Thus, for a free vortex stage, the tangential and axial velocity should decay at the same rate. For the present case, both IGV and stator wakes, the gradient (dV_{z_0}/dr) is negative, while $d(rV_{\theta_0})/dr$ is positive. Thus, in this particular case, the axial velocity defect should decay more rapidly than the tangential velocity and this is consistent with the trends indicated by measurements.

A solution of equations (8, 9) and (10) is attempted assuming $L \ll r$. Since $G = H = F$ from the correlation of the profile (equation (7), Figs. 10–12), the equations reduce to

$$\frac{d}{dZ}(LV_{rm}) = 0 \tag{11}$$

$$\frac{d}{dZ}(Lv_{\theta_c}) = 2\left[\frac{c}{r}\frac{d}{dr}(rV_{\theta_0})\right]L\frac{V_{rm}}{V_{z_0}} \tag{12}$$

$$\frac{d}{dZ}(Lv_{z_c}) = \frac{cd(V_{z_0})}{dr}\frac{LV_{r_m}}{V_{z_0}} \tag{13}$$

where

$$Z = z/c$$

Solution of equation (11) is

$$LV_{r_m} = C_1$$

Let,

$$L = C_2(Z - Z_0)^n \tag{14}$$

Then,

$$V_{r_m} = C_1(Z - Z_0)^{-n}/C_2 \tag{15}$$

$$v_{\theta_c} = C_3(Z - Z_0)^{-n+1} + C_4(Z - Z_0)^{-n} \tag{16}$$

$$v_{z_c} = C_5(Z - Z_0)^{-n+1} + C_6(Z - Z_0)^{-n} \tag{17}$$

are solutions of equations (11–13). The value of the exponent n will be derived empirically.

In these equations, C_1, C_2, C_4, C_6 and Z_0 are constants which depend on the initial properties of the wake through such parameters as C_D, c/S, etc., and

$$C_3 = \frac{2C_1c}{C_2rV_{z_0}}\frac{d}{dr}(rV_{\theta_0}) \tag{18}$$

$$C_5 = \frac{C_1}{C_2}\frac{c}{V_{z_0}}\frac{d}{dr}(V_{z_0}) \tag{19}$$

It is thus evident that the decay characteristics of the IGV and stator blade wake depend not only on the initial property of the wake, but also on the radial distribution of V_{θ_0} and V_{z_0}.

The predictions from the above theory are compared with the stator wake data and IGV wake data in Figs. 13 and 14(*a*), respectively. The exponent in equation (14) was derived from the wake width data described later. The constants C_3, C_4, C_5, and C_6 (these include the terms dV_{z_0}/dr and $d/dr(rV_{\theta_0})$) were derived from the data on decay

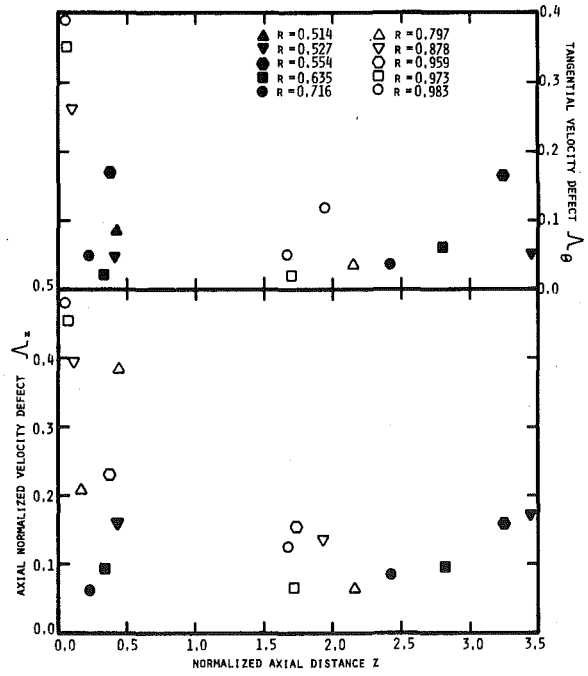

Fig. 14(*b*) Radial variation of defect in axial and tangential velocity for the IGV

[1] Some of the errors in the analysis presented in [11] are corrected. These corrections are included in equations (8, 9) and (10) of this paper.

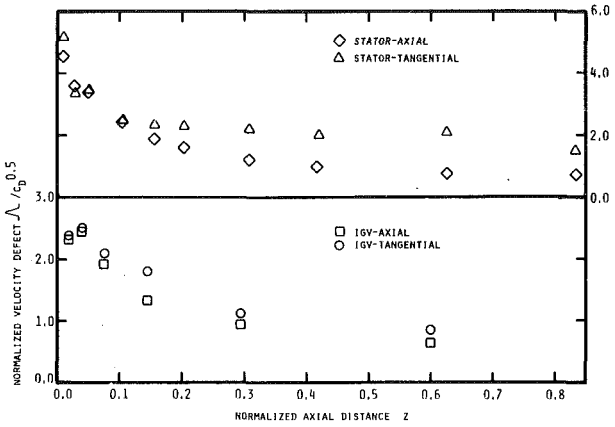

Fig. 15(*a*) Correlation of the velocity defects for the IGV and stator

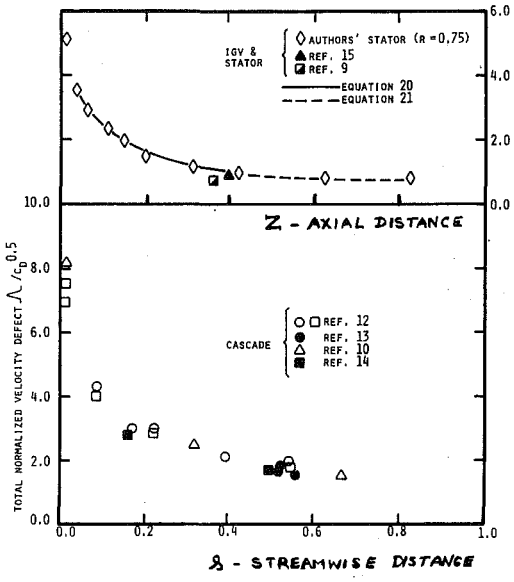

Fig. 15(*b*) Correlation of total velocity defect for IGV, stator and cascade

of velocity defect. The value of n is found to be 1.22 in the near wake and 1.0 in the far wake. Other constants are shown in respective plots. Since the scatter in the radial velocity is appreciable, no attempt was made to compare the theory with data. The predicted trend in the stator blade wake decay, as shown in Fig. 13, agrees very well with the data. The tangential velocity defect decays slower than the axial velocity defect in the near wake, giving rise to appreciable curvature to the wake centerline trajectory. Both the axial and tangential velocity defects are predicted to decay at the same rate far downstream and this agrees very well with the data. Similar conclusions can be drawn from the comparison of predicted and experimental values of IGV wake decay (Fig. 14(*a*)). Since only one data point is available in the far wake region, no comparison with the theory is made in this region.

The decay in the defect of axial and tangential velocity at various radii are shown plotted in Fig. 14(*b*). Caution should be exercised in interpreting this data. Since the wake belongs to different blade elements, with variation in C_D and C_L values as well as chordwise growth of the boundary layer, the curve shown in Fig. 14(*b*) should not be interpreted as the decay rate. The variation in wake defect at different radii is clear from this plot. The defect is largest at the tip of the blade decreasing continuously towards the mid-radius (where it is lowest) and then increasing again towards the hub. This trend is clear in both the axial and tangential velocity defects. This trend also persists far downstream, even up to three to four chord lengths downstream. This differential decay rate as well as the magnitude of the wake defect can be attributed to the three-dimensional effects caused by radial inward

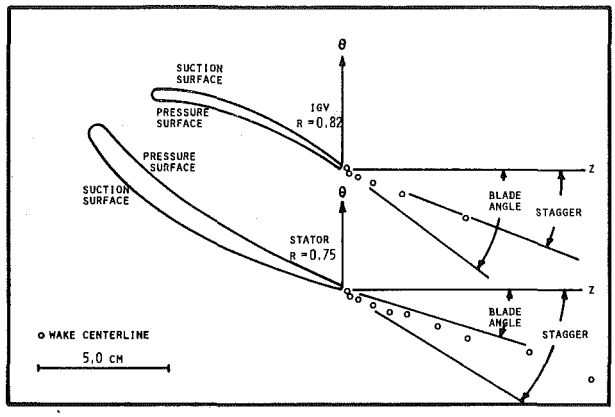

Fig. 16 Curvature of the IGV and stator wake centerline

flow in these blade wakes, except in the hub and tip region. Hence, three-dimensional effects (through radial velocity) tend to diffuse the wakes more rapidly away from the hub and wall regions.

The maximum defect in velocity is related to the blade element, through the drag coefficient. The correlation of the defect, assuming $\sqrt{C_D}$ dependency, is shown in Figs. 15(*a*) and 15(*b*) for the authors' as well as others' data. The cascade, IGV as well as stator data seem to follow $\sqrt{C_D}$ correlation (Fig. 15(*b*)). In the trailing edge region, both the cascade as well as the annular cascade (IGV and stator) wakes decay very rapidly. The decay in the near wake seems to be rapid in the case of stator and the IGV wake.

The decay rate of the total velocity shown in Fig. 15(*b*) can be represented by the following expressions:

$$\text{Near Wake: } \Lambda/\sqrt{C_D} = \frac{v_c}{V_0\sqrt{C_D}} = 0.168\,(Z + 0.12)^{-0.22} + 0.353\,(Z + 0.12)^{-1.22} \quad (20)$$

$$\text{Far Wake: } \Lambda/\sqrt{C_D} = \frac{v_c}{V_0\sqrt{C_D}} = 0.9792/(Z + 0.688) \quad (21)$$

These decay laws for the total velocity have exactly the same form as those for the axial and tangential velocity defects (equations (17) and (16), respectively).

It is thus clear that the stator wake decays faster than the cascade wake (12). As there are insufficient data points, no attempt has been made to derive the correlation for the trailing edge region, where it should vary as Z^{-n}, with large value for n [11].

3.4 **Wake Curvature and Flow Angles.** The curvature of the IGV and stator blade wake centerline is shown in Fig. 16. The wake centerline is shown at the location of the maximum streamwise velocity defect. Both the IGV and stator blade wake centerlines were found to deflect rapidly toward the suction surface of the blade in the trailing edge region of the wake. This deflection is appreciable as compared to the near and far wake regions.

The curvature of the wake center line trajectory is quite large in the trailing edge region for both the IGV and the stator. The stator wake centerline reaches an asymptotic value, with very small curvature, rather quickly ($Z < 0.05$), while the IGV wake center line trajectory seems to change its curvature continuously until $Z = 0.296$. Thus the IGV wake undergoes a much more gradual change in outlet angle.

The flow outlet angle variation downstream of the trailing edge, for both the IGV and the stator, at the wake centerline as well as wake edges on the pressure and the suction surfaces are shown in Fig. 17. For the stator wake, the flow angles are lowest on the wake center and highest on the suction side of the wake edge. It increases continuously until $Z = 0.2$ and decreases slightly beyond this station. This indicates that the angle variation across the wake is substantial (caused by differing decay rates for axial and tangential velocity defect) and this persists even downstream. Allowing for such a variation in the design of subsequent blade row is important in order to avoid off design operation. The angle variation downstream of the IGV shows the same trend as the stator. Initially the difference between the values at the

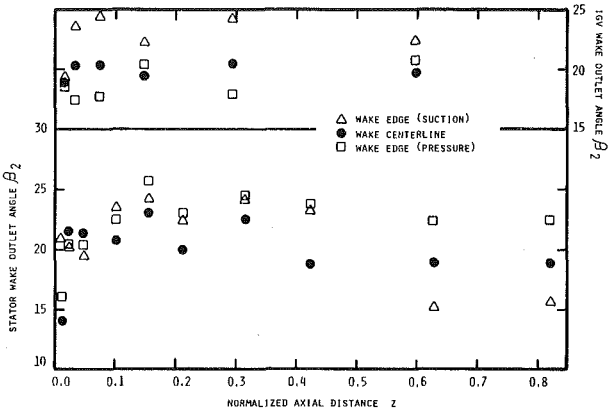

Fig. 17 Variation of IGV and stator blade wake outlet angle

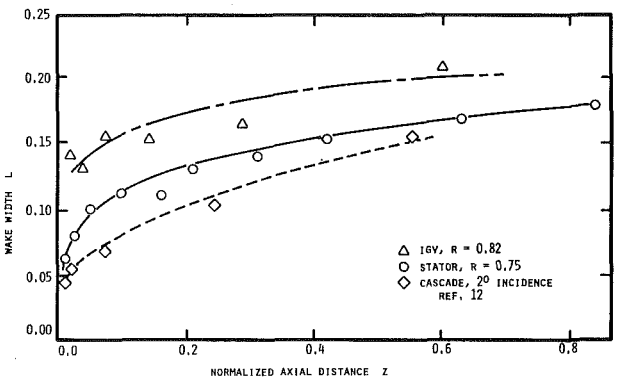

Fig. 18 Variation of wake width of IGV, stator, and cascade blades with downstream distance

free stream and the wake center line is small, this difference increases up to $Z = 0.3$ and decreases to small values at far downstream.

3.5 **Wake Width.** The variation of the width of the wake (near mid-radius) behind the IGV and the stator blades is shown in Fig. 18 as a function of the axial distance behind the blades. L is the characteristic width defined by

$$L = 2[L_s + L_p]/S$$

The growth of the wake width near the trailing edge region is seen to be substantially different behind the IGV and the stator blades. The wake width behind the IGV assumes a nearly constant value ($L = 0.14$) in the trailing edge region and the near wake region and increases to the value of 0.20 at the end of the survey in the axial direction. The development of the stator wake width indicates a more gradual development. The width of this wake increases rapidly in the trailing edge region of the wake and then increases at a slower rate in the near and far wake regions. The spreading rate of the stator wake is compared with the cascade data of [12] in Fig. 18. It is clear that the stator wake grows much more rapidly than the cascade wake in the trailing edge and near wake region, while the cascade wake grows faster in the far wake region. One can argue that the diffusion of the stator wake is influenced by radial velocities which are small far downstream. This may account for the trend observed in Fig. 18.

The wake width depends on the blade element performance, through such parameters as C_D, C_L, as well as the radial distribution of V_{θ_0} and V_{z_0}. Both the IGV and the stator wake show a dependence of $\sqrt{C_D}$ on the wake width correlation shown in Fig. 19. The collapse of both the sets of data seems to confirm such a correlation. The expressions for the wake width at various regions of the wake, based on the theory of Section 3.3 and equation (14), are as follows:

$$\text{Near Wake: } \frac{L}{\sqrt{C_D}} = 1.39\,(Z + 0.55)^{1.22} \tag{22}$$

$$\text{Far Wake: } \frac{L}{\sqrt{C_D}} = 1.18(Z + 0.688) \tag{23}$$

3.6 **Turbulence Intensity and Spectrum.** The turbulence

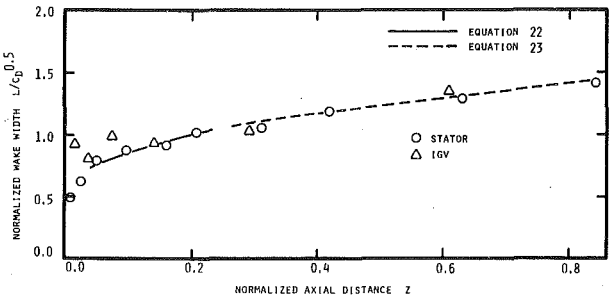

Fig. 19 Correlation of IGV and stator wake width

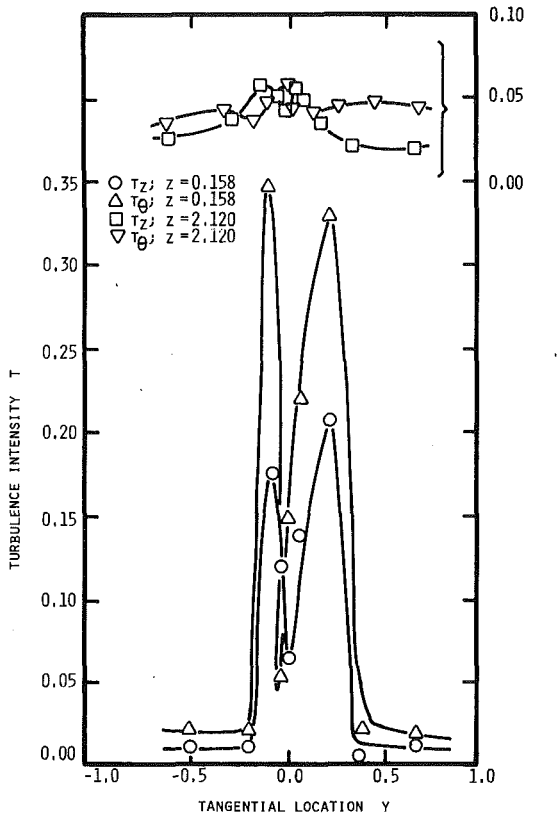

Fig. 20(*a*) Turbulence intensities in the IGV wake, $R = 0.80$

intensity and spectrum were measured at several radii at two downstream locations for the IGV, one very near and one very far from the trailing edge, using an "x" hot wire. The tangential and axial component of intensities at $R = 0.80$ and at $Z = 0.158$ and 2.12 are shown in Fig. 20(a). Both the axial and tangential intensities are high in the center of the wake and decrease rapidly to about one percent in the free stream. Furthermore, the characteristic dip in the distribution at $Z = 0.158$ can also be seen. This arises due to the blade boundary layer (where intensities are zero on the surface and maximum slightly away from it) being transformed into a free shear layer. Furthermore, the intensities decay rapidly to very small values at $Z = 2.12$.

The spectrum of the total turbulent energy in the stator wake measured using a spectrum analyzer is shown in Fig. 20(b) for $R = 0.75$ at $Z = 0.013$. Two spectra, one taken at the center of the wake and the other taken outside the wake, are shown in Fig. 20(b). It is evident that all the energy in turbulence outside the wake is confined to low frequencies (less than 1 KHZ) with a peak at 360 HZ, this corresponds to the blade passing frequency of the upstream rotor. Hence, these peaks represent the rotor wake. Even though the rotor is located at least six chords upstream of the stator, its effect still persists in the stator passage. The velocity defect in the wake of the rotor is seen by a stationary hot wire probe as unsteady velocity and hence its effect appears in the spectrum. The energy spectrum inside the wake shows

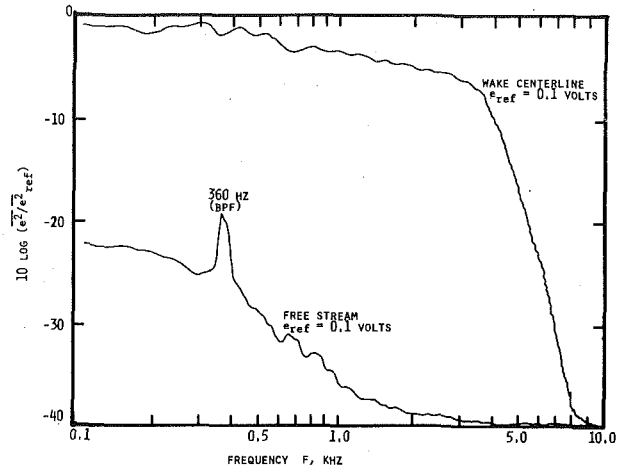

Fig. 20(*b*) Spectrum of turbulent energy in the stator wake; $Z = 0.013$, $R = 0.750$

no such peaks, indicating the substantial change in the rotor wake transport properties through a stator passage. Furthermore, the spectrum at the wake center shows the typical energy distribution that exists in turbulent flow, with most of the energy contained within 10 KHZ. The outer part of the curve follows the power law (f^{-n}) distribution of the energy for frequency > 3 KHZ.

3.7 **Static Pressure Distribution Across the Wake.** The static and stagnation pressures across the wake were measured using a Prandtl pitot tube of 1.6 mm outside diameter aligned in the direction of the flow. The static pressure data is shown plotted in Fig. 21(*a*) in the form of static pressure rise coefficient ($C_p = (p_\ell - p_1)/1/2\,\rho V_1^2$, where p_ℓ = local static pressure and p_1 and V_1 are upstream values of static pressure and velocity, respectively) for both IGV and stator blade at various values of Z. For the stator wake at $Z = 0.053$, the static pressure at the center of the wake is about 15 percent higher than the free stream value on the pressure side and 25 percent higher than the free stream value on the suction side. It should be remarked here that part of this difference may be due to the error in the static pressure measurement caused by the turbulence in the flow, which is likely to be high at this region. The difference in static pressure across the wake vanishes rapidly downstream reaching to less than 10 percent at $Z = 0.211$ to negligible values at $Z > 0.423$. The inviscid effects downstream of trailing edge or the presence of pressure gradients due to inviscid turning is evident at $Z = 0.053$. Inviscid effects are negligibly small for $Z > 0.053$. Probable cause of static pressure gradients across the wake are: streamwise curvature, high turbulence intensity gradients across the wake and large velocity gradients that exist in these regions.

The static pressure distribution across the IGV wake also shows a similar trend, but the static pressure drop across the blade row is much smaller in the wake centerline region as compared to the free stream region. Here again, the static pressure in the wake is higher than the free stream values. The gradients in static pressure vanish beyond $Z = 0.3$.

It is thus evident that the classical assumption of constancy in static pressure across the wake is not valid in the trailing edge region.

The static pressure difference (Δp) across the wake normalized by its value at the center line [$(\Delta p)_c$ or Δp_{max}] is plotted against nondimensional distance (η_s or η_p) in Fig. 21(*b*). It is evident that this distribution shows a trend towards similarity, even though it is not as good as the velocity profile similarity. One reason for the scatter in the data near the wake center is the error in static pressure (which is a function of the local turbulence intensity) measurements at these locations. Additional work in this area is needed. Existence of similarity, if proved, should greatly simplify the problem of predicting the stator and IGV wakes.

Conclusions

The following conclusions can be drawn from the measurement and

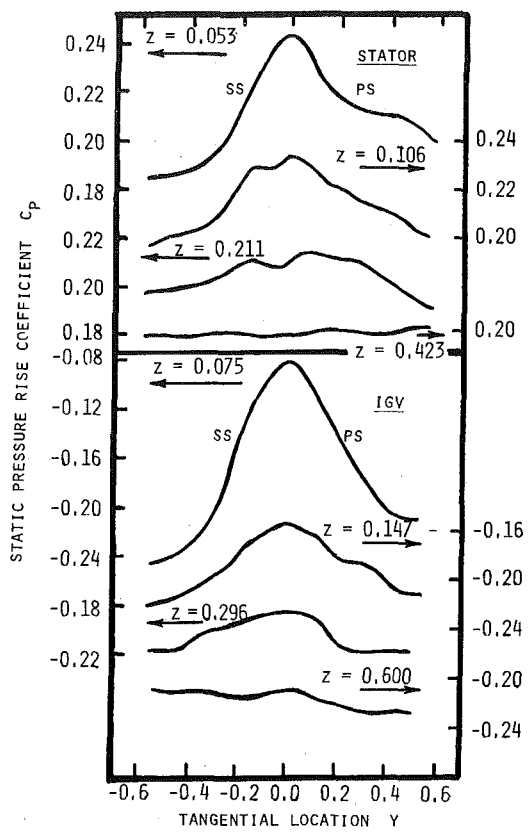

Fig. 21(*a*) Distribution of static pressure coefficient across the wake for IGV ($R = 0.82$) and stator ($R = 0.75$) blade at various axial locations

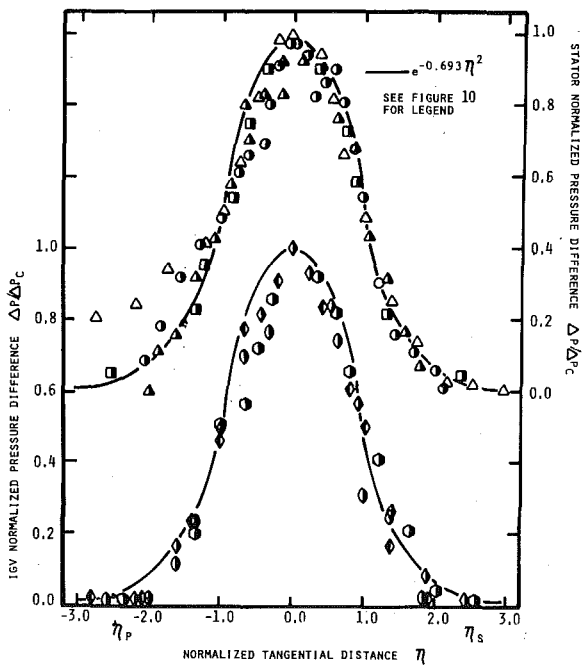

Fig. 21(*b*) Similarity in static pressure profile across the wake for the IGV and stator blade

correlation of the IGV and the stator wake data reported in this paper.

[1] The mean velocity measurements indicate that both the IGV and the stator wakes are three-dimensional in nature with appreciable radial inward flow inside the wake. Initially the profiles are asymmetrical, but show a tendency towards symmetry as the flow proceeds far downstream.

[2] Both the local and mean outlet angles in the wake change appreciably in the trailing edge region and this persists for at least 1/4

to 1/2 chord from the trailing edge. Appreciable change in outlet angle across the wake is also observed.

[3] The axial, tangential and the radial velocity profiles not only become symmetrical but also similar when the defect is normalized by its value at the center line and the length by their respective length scales (L_s and L_p). The resulting profile follows a Gaussian function [exp $(-K\eta^2)$].

[4] The axial and tangential velocity defects, and the radial velocity decay differentially. The radial velocity at the exit of the stator decays rapidly and then increases once again downstream. The tangential velocity defect decays less rapidly than the axial velocity for both cases. The free stream velocity gradients in the radial direction, it is shown, are responsible for this phenomena. The decay is very rapid in the trailing edge region, and this decay slows down as the flow progresses downstream.

[5] The defect in axial and tangential velocity of the IGV and the stator wake measured by the authors as well as the data from other sources correlate well with $\sqrt{C_D}$.

[6] The decay of axial and tangential velocity defects, as well as the wake width predicted from momentum integral type of analysis, agree well with the data.

[7] The defect in the velocity is minimum near the mid-radius and increases towards the hub and annulus wall for the IGV.

[8] The wake width increases rapidly in the trailing edge region for the stator wake and this rate of spread is larger than that of a cascade or IGV wake.

[9] Expressions given for the velocity defect, the wake width and the profile should enable complete description of the wake as well as the flow distortion caused by them.

[10] The turbulence intensities are found to be high, the maximum value occurring slightly away from the wake center line. This is characteristic of the near wake. The turbulence spectrum indicates that the energy content in the free stream is limited to low frequencies, while the energy in the wake is contained up to 5 to 10 KHZ.

[11] Appreciable static pressure gradients across the wake exist in the trailing edge region and these gradients decay rapidly to almost zero within half a chord. The static pressure in the wake are found to be higher than the free stream.

[12] The IGV and stator wakes show substantial enough differences from an isolated or cascade wake to warrant the development of a three-dimensional analysis.

Acknowledgments

The research reported in this paper is a by-product of the project on rotor wake study supported by NASA Grant NsG 3012. Partial support from this grant as well as NASA Grant NsG 3032 is gratefully acknowledged. The authors wish to thank N. Sitaram and A. Ravindranath for their help in the acquisition and correlation of some of the wake data reported in this paper.

References

1 Bradshaw, P., "Effects of Streamline Curvature on Turbulent Flow," AGARDograph No. 169, 1973.

2 Ravindranath, A. and Lakshminarayana, B., "Mean Velocity and Decay Characteristics of the Near and Far Wake of a Compressor Rotor Blade of Moderate Loading," submitted for publication to ASME.

3 Smith, L. H., "Three-Dimensional Flow in Axial Flow Turbomachinery," WADC Tech. Rept. 55-348, Vol. II, Johns Hopkins University, March 1956.

4 Whitfield, C. E., Kelley, J. C., and Barry, B., "A Three-Dimensional Analysis of Rotor Wakes," *Aeronautical Quarterly*, Nov. 1972, pp. 285–300.

5 Schmidt, D. P. and Okiishi, T. H., "Multistage Axial-Flow Turbomachine Wake Production, Transport, and Interaction," *AIAA Journal*, Vol. 15, No. 8, Aug. 1977, pp. 1138–1145.

6 Hirsch, C. H. and Kool, P., "Measurement of the Three-Dimensional Flow Field Behind an Axial Compressor Stage," ASME JOURNAL OF ENGINEERING FOR POWER, Vol. 99, April 1977, pp. 168–179.

7 Gorton, C. A., "Analytical and Experimental Study of Three-Dimensional Mean Flow and Turbulence Characteristics Inside the Passages of an Axial Flow Inducer," M.S. Thesis, Department of Aerospace Engineering, The Pennsylvania State University, 1974.

8 Bitterlich, W. and Rubner, K., "Annulus Wall Boundary Layer in Axial Flow Turbomachines," AGARDograph 164, 1972, pp. 397–413.

9 Daneshyar, M., "Annulus Wall Boundary Layer in Turbomachines," Ph.D. Thesis, Cambridge University, 1974.

10 Pollard, D. and Gostelow, J. P., "Some Experiments at Low Speed on Compressor Cascades," ASME JOURNAL OF ENGINEERING FOR POWER, July 1967, pp. 427–436.

11 Lakshminarayana, B., "Nature of Flow Distortions Caused by Rotor Blade Wakes," AGARD CP 177, 1976.

12 Raj, R. and Lakshminarayana, B., "Characteristics of the Wake Behind a Cascade of Airfoils," *Journal of Fluid Mech.*, Vol. 61, Part 4, 1973, pp. 707–730.

13 Lieblein, S. and Roudebush, W. H., "Low Speed Wake Characteristics of Two-Dimensional Cascade and Isolated Airfoil Sections," NASA TN 3771, 1956.

14 Satyanarayana, B., "Unsteady Wake Measurements of Airfoils and Cascades," *AIAA Journal*, Vol. 15, No. 5, May 1977, pp. 613–618.

15 Welsh, J. K., "Experimental Investigation of the Effect of Tip Clearance and End Losses on Axial Compressor Performance," M.S. Thesis, Department of Aeronautics, U.S. Naval Postgraduate School, 1973.

to 1/2 chord from the trailing edge. Appreciable change in outlet angle across the wake is also observed.

[3] The axial, tangential and the radial velocity profiles not only become symmetrical but also similar when the defect is normalized by its value at the center line and the length by their respective length scales (L_s and L_p). The resulting profile follows a Gaussian function [exp $(-K\eta^2)$].

[4] The axial and tangential velocity defects, and the radial velocity decay differentially. The radial velocity at the exit of the stator decays rapidly and then increases once again downstream. The tangential velocity defect decays less rapidly than the axial velocity for both cases. The free stream velocity gradients in the radial direction, it is shown, are responsible for this phenomena. The decay is very rapid in the trailing edge region, and this decay slows down as the flow progresses downstream.

[5] The defect in axial and tangential velocity of the IGV and the stator wake measured by the authors as well as the data from other sources correlate well with $\sqrt{C_D}$.

[6] The decay of axial and tangential velocity defects, as well as the wake width predicted from momentum integral type of analysis, agree well with the data.

[7] The defect in the velocity is minimum near the mid-radius and increases towards the hub and annulus wall for the IGV.

[8] The wake width increases rapidly in the trailing edge region for the stator wake and this rate of spread is larger than that of a cascade or IGV wake.

[9] Expressions given for the velocity defect, the wake width and the profile should enable complete description of the wake as well as the flow distortion caused by them.

[10] The turbulence intensities are found to be high, the maximum value occurring slightly away from the wake center line. This is characteristic of the near wake. The turbulence spectrum indicates that the energy content in the free stream is limited to low frequencies, while the energy in the wake is contained up to 5 to 10 KHZ.

[11] Appreciable static pressure gradients across the wake exist in the trailing edge region and these gradients decay rapidly to almost zero within half a chord. The static pressure in the wake are found to be higher than the free stream.

[12] The IGV and stator wakes show substantial enough differences from an isolated or cascade wake to warrant the development of a three-dimensional analysis.

Acknowledgments

The research reported in this paper is a by-product of the project on rotor wake study supported by NASA Grant NsG 3012. Partial support from this grant as well as NASA Grant NsG 3032 is gratefully acknowledged. The authors wish to thank N. Sitaram and A. Ravindranath for their help in the acquisition and correlation of some of the wake data reported in this paper.

References

1 Bradshaw, P., "Effects of Streamline Curvature on Turbulent Flow," AGARDograph No. 169, 1973.

2 Ravindranath, A. and Lakshminarayana, B., "Mean Velocity and Decay Characteristics of the Near and Far Wake of a Compressor Rotor Blade of Moderate Loading," submitted for publication to ASME.

3 Smith, L. H., "Three-Dimensional Flow in Axial Flow Turbomachinery," WADC Tech. Rept. 55-348, Vol. II, Johns Hopkins University, March 1956.

4 Whitfield, C. E., Kelley, J. C., and Barry, B., "A Three-Dimensional Analysis of Rotor Wakes," *Aeronautical Quarterly*, Nov. 1972, pp. 285–300.

5 Schmidt, D. P. and Okiishi, T. H., "Multistage Axial-Flow Turbomachine Wake Production, Transport, and Interaction," *AIAA Journal*, Vol. 15, No. 8, Aug. 1977, pp. 1138–1145.

6 Hirsch, C. H. and Kool, P., "Measurement of the Three-Dimensional Flow Field Behind an Axial Compressor Stage," ASME JOURNAL OF ENGINEERING FOR POWER, Vol. 99, April 1977, pp. 168–179.

7 Gorton, C. A., "Analytical and Experimental Study of Three-Dimensional Mean Flow and Turbulence Characteristics Inside the Passages of an Axial Flow Inducer," M.S. Thesis, Department of Aerospace Engineering, The Pennsylvania State University, 1974.

8 Bitterlich, W. and Rubner, K., "Annulus Wall Boundary Layer in Axial Flow Turbomachines," AGARDograph 164, 1972, pp. 397–413.

9 Daneshyar, M., "Annulus Wall Boundary Layer in Turbomachines," Ph.D. Thesis, Cambridge University, 1974.

10 Pollard, D. and Gostelow, J. P., "Some Experiments at Low Speed on Compressor Cascades," ASME JOURNAL OF ENGINEERING FOR POWER, July 1967, pp. 427–436.

11 Lakshminarayana, B., "Nature of Flow Distortions Caused by Rotor Blade Wakes," AGARD CP 177, 1976.

12 Raj, R. and Lakshminarayana, B., "Characteristics of the Wake Behind a Cascade of Airfoils," *Journal of Fluid Mech.*, Vol. 61, Part 4, 1973, pp. 707–730.

13 Lieblein, S. and Roudebush, W. H., "Low Speed Wake Characteristics of Two-Dimensional Cascade and Isolated Airfoil Sections," NASA TN 3771, 1956.

14 Satyanarayana, B., "Unsteady Wake Measurements of Airfoils and Cascades," *AIAA Journal*, Vol. 15, No. 5, May 1977, pp. 613–618.

15 Welsh, J. K., "Experimental Investigation of the Effect of Tip Clearance and End Losses on Axial Compressor Performance," M.S. Thesis, Department of Aeronautics, U.S. Naval Postgraduate School, 1973.

DISCUSSION

T. H. Okiishi[2]

The attempt by the authors to correlate the streamwise development of turbomachine inlet guide vane and stator wakes is appreciated by this discussor. Some clarification about the measurement method used by the authors is requested. In using a single slanted hot-wire sensor to obtain three-dimensional velocity data in a turbomachine, several investigators [4, 6, 16] have indicated that careful selection of the reference yaw position of the sensor $\theta_{n,a}$, is required. Further, while a value of 120 deg was suggested for τ_b and τ_d in [4], more care in selecting values of τ_b and τ_d was proposed in [6] and [16]. Schmidt [16] concluded that it was important to select the values of $\theta_{n,a}$, $\theta_{n,b}$ and $\theta_{n,d}$ to correspond to regions of high sensor yaw angle sensitivity. Although the use of hot-wire probes as reported in [4, 6] and [16] involved aligning the probe axis radially and the probe related to this paper was operated with its axis parallel to the turbomachine axis, it is of interest to know if any of the above mentioned considerations were judged to be important by the authors.

[2] Professor, Department of Mechanical Engineering, Iowa State University, Ames, Iowa 50011

Additional References

16 Schmidt, D. P., and Okiishi, T. H., "Multistage Axial-Flow Turbomachine Wake Production, Transport, and Interaction," AFOSR-77-0720 TR. 1976. (NTIS accession No. N77-31173).

Authors' Closure

The authors wish to thank T. H. Okiishi for his comments. We do not find any prior investigation aimed at a systematic study of the optimum yaw position ($\theta_{n,a}$) of the probe. To make sure that the error is small, one complete set of measurements was duplicated using conventional pitot probe. The mean velocity measured from the hot wire and the pitot probes was found to be identical. The choice of the probe alignment was based on the least aerodynamic interference. The probe was aligned such that the axis is nearly aligned with the flow streamwise direction. This arrangement provides least angularity error as well as least aerodynamic interference.

W. J. Lewis
Assistant Chief Engineer,
Advanced Projects,
Rolls-Royce Limited,
Bristol, England

R. Hurd
Manager,
Military Installations (Bristol),
Rolls-Royce Limited,
Bristol, England

Augmented Vectored Thrust Engines and the Problem of Avoiding Hot Gas Recirculation

It can be argued that the vectored thrust engine is one of the best propulsion systems for V/STOL combat aircraft. The next step is to consider the problems to be overcome in integrating such a powerplant into the airframe. A critical installation issue, and one which is not unique to vectored thrust systems, is that of hot exhaust gas recirculation. In this paper some of Rolls-Royce's hot gas recirculation experience is described, covering, in particular, the creation of a specialized recirculation test facility and some sample test results. The application of the results to a vectored thrust installation is discussed, together with some of the implications for the aircraft designer. Finally, some comments are made regarding the requirements of other V/STOL propulsion systems to avoid excessive hot gas recirculation.

Introduction

The Rolls-Royce Pegasus 11 vectored thrust turbofan is now in operational service in the Harrier (AV-8A) and there are planned developments of both the engine and aircraft to improve the payload/range performance and engine life. All the studies carried out indicate that to improve payload/range performance still further, for a given aircraft gross take-off weight, some form of thrust augmentation is desirable as this reduces the basic engine size and hence fuel consumption for the subsonic cruise condition, leading to an overall reduction in engine-plus-fuel weight for a given mission. Augmentation has also been shown to be the most effective way of achieving a high thrust for maneuvering and combat, and to achieve supersonic flight speeds. Fig. 1 shows how the aircraft gross weight is reduced as the thrust boost due to reheat is increased; this is for three completely different missions with different thrust sizing points and different times spent at fully and part boosted thrust.

As the vectored thrust concept has proved so successful, Rolls-Royce has spent much effort studying the best way of providing augmentation to a vectored thrust engine. The method chosen has been to introduce a combustion system in the fan exhaust plenum chamber (Fig. 2) which permits augmentation at any position of the vectored nozzle, thus achieving thrust boost both for V/STOL operations and in conventional flight.

Augmentation of the fan exhaust flow is chosen, rather than augmenting the core flow, for the following reasons:

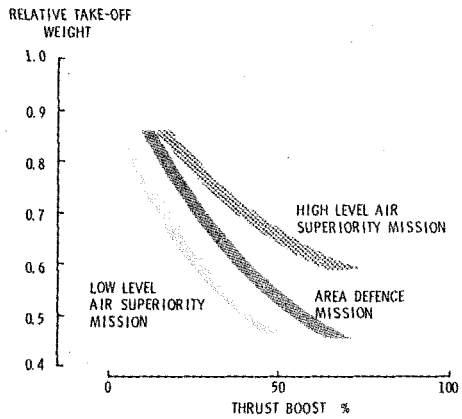

Fig. 1 Effect of thrust boost on aircraft weight

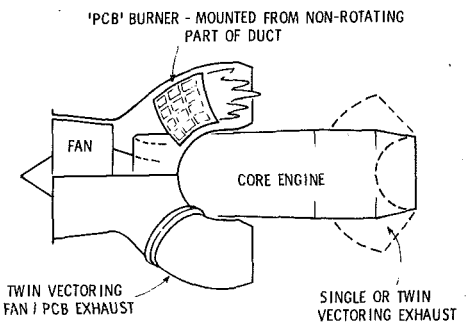

Fig. 2 Augmented vectored thrust engine layout

Contributed by the Gas Turbine Division and presented at the Gas Turbine Conference and Exhibit and Solar Energy Conference, San Diego, California, March 12–15, 1979 of THE AMERICAN SOCIETY OF MECHANICAL ENGINEERS. Manuscript received at ASME Headquarters December 7, 1978. Paper No. 79-GT-10.

1 The thrust center with the nozzles vertical is kept well forward and consequently the engine does not have to be installed too far forward in the airframe.

2 A given temperature rise and hence thrust boost is achieved with lower final gas temperature, thus reducing potential ground footprint problems.

3 There is ample cooling air readily available.

4 As the main engine combustor outlet temperature increases the engine bypass ratio also tends to increase (to avoid the need for cooling the core exhaust system) and hence a greater airflow is available for augmentation.

A substantial amount of full scale development work on a fan exhaust boost system (Plenum Chamber Burning or PCB) has already been carried out by Rolls-Royce. This has shown the system is practical from an engineering standpoint, and performance studies have shown the resulting powerplant is very competitive with other systems, e.g., lift plus lift/cruise powerplants [1 and 2].

One of the disadvantages of augmenting the fan exhaust flow is that the four-poster nozzle layout of the vectored thrust engine, as it is known at present, encourages recirculation of the exhaust gases from the front nozzles and so, when this exhaust gas temperature is high, special measures have to be taken to obtain an acceptable level of intake temperature rise and distortion.

Previous work, including both theoretical and experimental studies (model and full scale), indicated that as much as 15–20 percent of the flow leaving the front nozzles on the existing Pegasus installation could return to the intake during certain stages of VTOL operations. It is emphasized that this high level of recirculation does not present a problem since the engine is a turbofan and the front nozzle exhaust gas temperature is low (<100°C, 210°F) and 20 percent of the front nozzle flow represents only 11 percent approximately of the total intake flow. Thus the maximum mean intake temperature rise does not exceed 11°C (20°F), or 11 percent of the front nozzle temperature rise, during VTOL maneuvers, and generally the intake temperature rise is much less than this. There is also a temperature distortion, the maximum local values being approximately 2 to 2.5 times the mean value. Again, it is emphasized that the engine operates perfectly satisfactorily in the aircraft and no problems due to hot gas recirculation have been encountered with Harrier (AV-8A) in operational service.

When the thrust of a vectored thrust engine is boosted by burning in the fan exhaust, the temperature of the front nozzle flow is raised significantly. If the same 20 percent of the front nozzle flow is again reingested and the exhaust gas temperature is say 1000°C (1800°F) then the mean intake temperature rise would be, in the worst case, over 100°C (180°F). All things being equal this would imply peak local temperatures of over 200°C (390°F) and, even assuming that the engine could run under the associated distortion conditions, the thrust loss would be enormous. In fact, as Fig. 3 shows, the thrust increase by augmentation is more than offset by the loss of thrust due to hot gas recirculation, even with a uniformly distributed inlet temperature rise.

This problem was identified several years ago and much work has been carried out since then to achieve solutions. This paper outlines

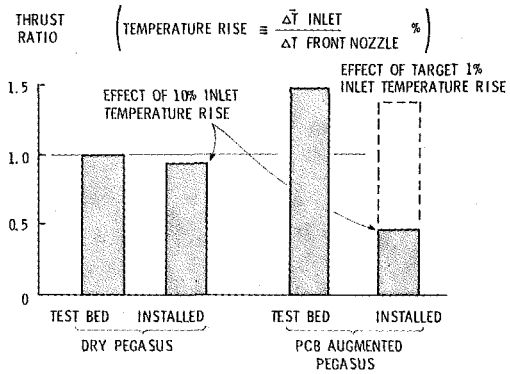

Fig. 3 Thrust loss due to hot gas recirculation

Rolls-Royce studies and experience on:

1 Understanding the four-poster Pegasus installation recirculation flow mechanisms.

2 The selection of suitable experimental techniques and the creation of a special hot gas recirculation test facility.

3 Methods of reducing hot gas recirculation effects to an acceptable level in a PCB-augmented Pegasus engine installation.

In this last respect the aim at Rolls-Royce has been to achieve inlet temperature rise and distortion effects in the augmented installation which are no worse than for the dry Pegasus in Harrier (AV-8A). This has meant reducing the amount of hot exhaust gas which can recirculate by a factor of 10 approximately, giving peak values of mean ΔT (inlet)/ΔT (nozzle) no greater than 1 percent.

Basic Insights

The earliest Pegasus recirculation studies centred on the Hawker P1127 prototype vectored thrust aircraft. From the nature of the four-poster lift jet arrangement set up by the Pegasus engine it was possible to foresee the various ways in which the exhaust flow might recirculate back to the inlets, i.e.,

1 The separate lift jet flows would meet on the ground creating up-flows or "fountains" aligned longitudinally and transversely beneath the aircraft.

2 The remainder of the exhaust flow would travel outwards to recirculate on a longer time scale, and after much mixing with ambient air, driven by the effects of buoyancy and entrainment.

3 Some of the forward arc ground flow would be blown back to, or overtaken by, the inlets to be reingested when there was relative movement between aircraft and the ambient air mass.

These three forms of recirculation were dubbed "near field," "far field," and "intermediate" or "thrust reverser" recirculation, respectively, and are illustrated in Fig. 4.

For vertical take-offs and landings it was considered that the near field recirculation system, consisting of longitudinal and transverse fountains, would be the dominant one. This route back to the inlets was short and direct, with little opportunity for mixing to take place, and so the exhaust gas would be reingested with minimal loss in temperature. However, it was also felt that the really hot exhaust gas fountains from the rear jets would be held back by the forward nozzle efflux, so that only relatively cool fan exhaust air would find its way up to the inlets.

A simple theoretical model was set up to check these hypotheses. It was assumed that the ground flow from each lift jet was initially radial and that a "slice" of this flow from the two forward lift jets would reach the inlets. The size of this slice, in angular terms, was defined by a simple intuitive geometric projection back from the inlets. Having established a quantity for the gas reingested it was a simple matter to perform a heat balance sum and calculate the resulting inlet temperature rise. The results obtained agreed well with test results from the P1127 aircraft and this gave a first confirmation of the validity of our view of the recirculation process during VTOL maneuvers.

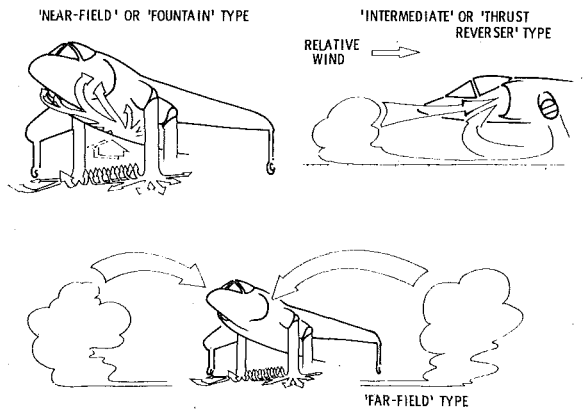

Fig. 4 Four-poster Pegasus hot gas recirculation mechanisms

Subsequently, a variety of flow visualization and measurement tests were carried out with laboratory models using air or water, and tracers such as helium gas, CO_2 particles, liquid dye etc. These confirmed, in a very convincing way, the importance of the forward jet longitudinal fountain in a "four-poster" recirculation system. Fig. 5 shows an example of a water tank test with dye injected into the nozzle flows at two different points. This shows quite clearly that gas from the forward inboard quadrants of the nozzles flows very readily to the simulated inlet via the longitudinal fountain.

Fountain Deflection Experiments

When work began in earnest on finding a way to limit recirculation to the very low levels necessary for a PCB-augmented vectored thrust powerplant, it was felt this might be achieved by interposing physical barriers, or carefully placed jets of cool air from the engine compressor, between the lift jets and the inlet to act as fountain deflectors. An assessment using the simple theoretical method described indicated this would be a fruitful approach and consequently an experimental test program was launched.

This program was carried out in a 6 ft × 4 ft (1.8 m × 1.2 m) (working section) hot gas recirculation wind tunnel which had been set up to test half models of vectored thrust fighter aircraft. The half model arrangement was chosen because it permitted a reasonably large model scale (1/9th to 1/6th) and because it made the mechanics of mounting the model, rotating the nozzles, and supplying hot exhaust gas and inlet suction particularly easy.

Figure 6 shows a summary plot of the results achieved with a wide variety of shields and airjets during simulated vertical lift-off or touch-down conditions (i.e., jet vertical, no forward speed, wheels touching ground). Clearly, a large reduction in recirculation was achieved and certain of the devices came close to achieving the target recirculation level, ΔT (inlet)/ΔT (nozzle) = 1 percent, necessary to keep within the P1127/Harrier inlet temperature rise range. This showed that the front jet longitudinal fountain could be influenced, and that it was indeed the dominant exhaust recirculation path for a four-poster vectored thrust engine installation. However, the results also indicated that the shields tested were less effective under forward speed conditions, or when the aircraft was jet-borne some distance above the ground, and it was concluded that more work and a better test rig were necessary.

Recirculation Rig Development

Although the Rolls-Royce half model recirculation test facility had proved satisfactory for static (hover) tests on some prototype recirculation control devices, it was not suitable for the wider range of test conditions considered necessary for a proper PCB-boosted engine installation development program. Its main shortcomings were:

1 Inadequate flow simulation—half model testing against a tunnel wall stabilizes the fountains thereby inhibiting beneficial mixing with the surrounding air, and it introduces a spurious boundary layer under forward test conditions. A further limitation is that half models cannot be tested under crosswind conditions.

2 Unsuitability for tests simulating the aircraft vertical motion; the 6 ft × 4 ft (1.8 m × 1.2 m) working section was too small for tests with a reasonable scale "whole" aircraft model which could be moved up and down to simulate jet-borne ascents and descents.

It was therefore decided to construct a new rig. Fortunately the existing one was located in a large empty room (70 ft (21.3 m) long × 22 ft (6.7 m) wide × 12 ft (3.7 m) high) capable of accommodating almost any type of scale model test rig. The two main options were as follows:

(*a*) A whole aircraft model mounted and supplied from above, suspended from a carriage with vertical travel only, located in a new, larger wind tunnel working section.

(*b*) A whole aircraft model mounted and supplied from a carriage with both horizontal and vertical travel such that it could be "flown" through simulated V/STOL maneuvers (no wind tunnel required).

The advantages in each case were as follows:

Option (*a*)

1 relatively simple carriage and supply system,

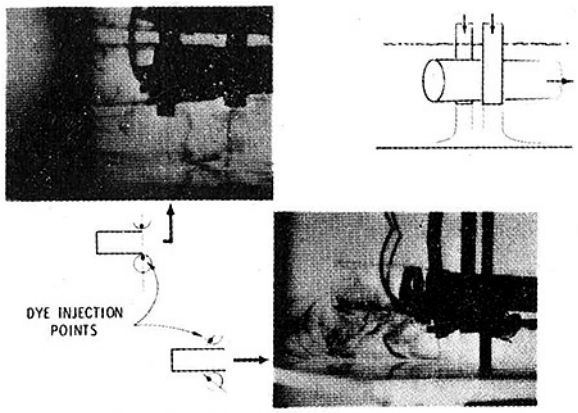

Fig. 5 Water flow simulation of fountain type recirculation

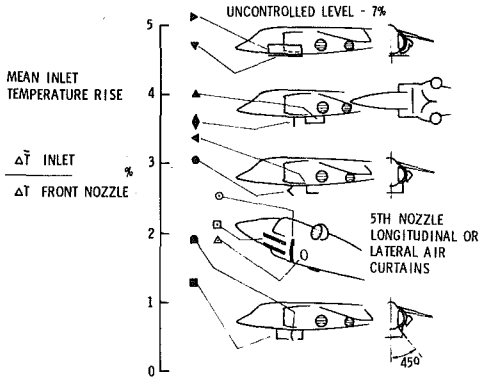

Fig. 6 Effectiveness of various fountain deflection devices

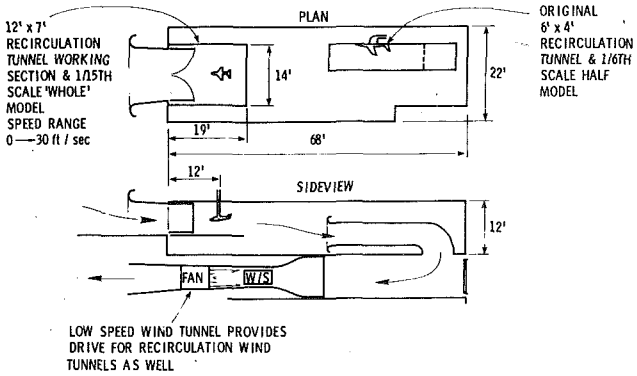

Fig. 7 Rolls-Royce recirculation test facility

2 used minimum clear space,

3 could use existing tunnel drive,

4 simulates atmospheric, or moving ship, wind effects,

5 easy to purge hot air from test cell.

Option (*b*)

1 most realistic simulation of jet-borne take-off and landing maneuver trajectories.

2 maximum freedom from cell wall interference effects.

The disadvantages, on the other hand, were:

Option (*a*)

1 tunnel floor boundary layer had to be tolerated or removed when simulating aircraft forward speed.

2 prone to tunnel wall interference.

Option (*b*)

1 relatively complex carriage and model supply system,

2 required maximum clear space,

3 wind effects not easily simulated,

4 hot air purging slightly more difficult.

Since the work was to be of a general nature with approximate aircraft configurations, compromise flow scaling, and with a need for an easily operated, flexible, reliable rig, it was decided that the key advantage of option (*b*), the ability to fly realistic V/STOL maneuvers, was not important enough to warrant the extra cost and complexity involved. Consequently the wind tunnel option (*a*) was chosen.

Figure 7 shows the layout of the facility with the revised tunnel working section. A scale model investigation of the flows into, and within, the building was carried out, and this showed that the existing tunnel could be left in place and that only a large bell-mouthed opening was required at the upstream end of the cell to provide a large open jet working section with the desired flow characteristics.

Flow scaling is an essential requirement for recirculation testing. It simply means that although the absolute flow pressures, velocities and temperatures used in the test rig may not be the same as at full scale, the ratios between relevant properties of the various flows are the same as at full scale so that the recirculatory flows are reproduced as realistically as possible. The scaling laws for Pegasus recirculation tests derive from fundamental studies in the United Kingdom, involving full scale and model tests [3 and 4], and are as follows:

$$\text{Geometry } \frac{L \text{ model}}{L \text{ full scale}} = k_1$$

$$\text{Momentum } \frac{(P_J - p_W) \text{ full}}{(P_J - p_W) \text{ scale}} = \frac{(P_I - p_I)\, m}{(P_I - p_I)\, f} = \frac{(P_W - p_W)\, m}{(P_W - p_W)\, f}$$

model

$$\text{Excess Temperature } \frac{(T_J - T_W) \text{ full}}{(T_J - T_W) \text{ scale}} = k_2$$

$$\text{Buoyancy/Momentum } \left(\frac{(T_J - T_W)}{(P_J - p_W)} \frac{D_J}{T_J^{1/2}}\right) \text{ model} = \left(\frac{(T_J - T_W)}{(P_J - p_W)} \frac{D_J}{T_J^{1/2}}\right) \text{ full scale}$$

$$\text{Time Ratio } (\dot{\tau}) = \frac{t_{\text{full scale}}}{t_{\text{model}}} = \frac{(D_J/(P_J - p_W)^{1/2})f}{(D_J/(P_J - p_W)^{1/2})m}$$

where J refers to jet flow, I refers to inlet flow and W refers to the free stream or wind flow. Figure 8 shows comparisons between scaled model and full scale test results obtained for the P1127 aircraft configuration and shows that excellent agreement between the real and simulated recirculation flows is achieved.

In applying these laws to the sizing of the rig working section a number of other constraints had to be taken into account:

1 The rig was primarily for studies of fighter aircraft in jet-borne flight between 0 and 50 ft altitude.

2 The model had to be large enough to accommodate multiple arrays of inlet temperature sensors for measuring distortion effects.

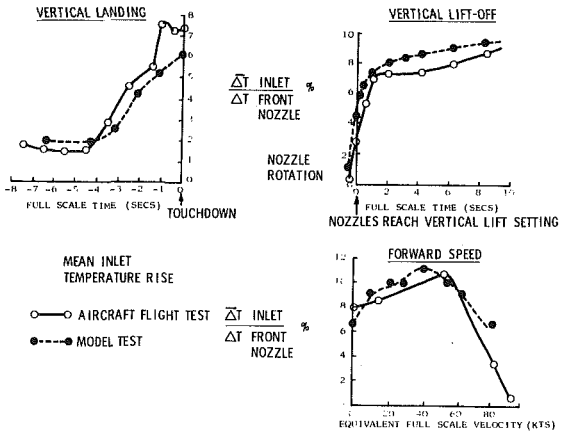

Fig. 8 Comparison of model and full-scale recirculation test results (P1127 aircraft)

3 To avoid problems with the model and carriage actuation arrangements and with transient temperature sensor response rate the recirculation time was to be kept reasonably long.

4 The tunnel working section speeds should not be so low as to be sensitive to spurious draughts or wind gusts.

The resulting working section design (Fig. 7) was 12 ft × 7 ft (3.7 m × 2.1 m) and the speed range, using the drive system already existing, was 0 to 35 ft/sec (10.7 m/s). This can accommodate V/STOL fighter models up to about 1/15 th scale, and, by suitable flow scaling, it can simulate actual flight speeds up to about 100 knots.

Figure 9 shows the model carriage and supply system adopted. A simple vertical strut protruding from the tunnel ceiling was chosen because it allows the model to be yawed very easily—the whole assembly rotates on a turntable in fact. The vertical motion is powered by an electronically controlled hydraulic system. This has been set up to permit a range of ascent accelerations and descent velocities to be simulated as follows:

	Model Carriage	*Full scale equivalent*
Ascent acceleration g	0.03–0.18	0.05–0.3
Descent velocity ft/s	0.4–3.0	2–15

Figure 10 shows a typical model assembly attached to the carriage strut.

One other important rig design topic is the business of starting the various flows and the intended V/STOL maneuver in a realistic manner and with no premature heating of the air around the model. Two significant problems are:

1 the time taken to set up the nozzle air heater, and

2 the time taken to heat up the connecting pipes so the air reaches the nozzles at the required temperature.

The solution adopted was to allow the heater to discharge to an overboard dump while conditions were being set up, and to use rota-

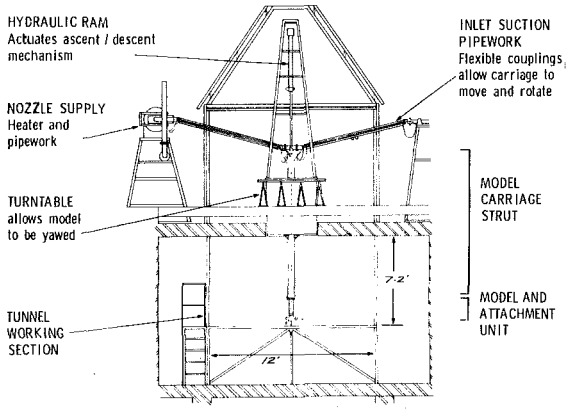

Fig. 9 Reingestion tunnel—model carriage

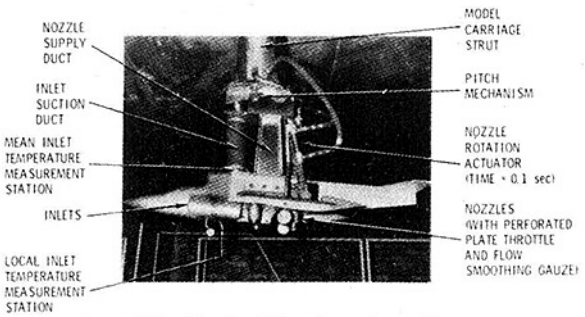

Fig. 10 One-fifteenth scale model

table nozzles on the model which discharge the flow aft, to be carried away by the tunnel airflow, while the connecting pipes warmed up. When this was achieved the nozzles could be rotated downwards and the particular aircraft maneuver was then initiated. Static air tests, i.e., vertical maneuvers, presented a slight problem in that there was no air flow to purge away the hot air used to heat the pipes. However, it was found that once the pipes had been heated in the way described they remained hot and so VTOL tests could be carried out after a series of STOL tests with no difficulty.

The commissioning trials which followed rig completion showed it to be up to expectations in every respect and since then rather more than 2000 test runs, i.e., V/STOL maneuvers, have been made.

Model Inlet Temperature Measurement Systems

Two types of temperature measurement system were evolved, as illustrated in Fig. 11. These were:

1 An analogue system for recording *mean* inlet temperature rise—the results being continuously recorded on a pen trace UV recorder. The sensor in this case is a resistance thermometer consisting of 20 thin tungsten wires (time constant = 0.01 seconds) stretched across the inlet duct. These are arranged as 10 individual loops to give some redundancy as a protection against foreign object damage.

2 A digital system for recording *local* inlet temperature rise using a multiple array of thermocouples. 36 rapid response "DISA" thermocouples are arrayed across the inlet duct close to where the engine entry would be, and their output is sampled frequently and rapidly to pick up the localized and short duration hot gas streaks which characterize recirculation. Temperature distribution plots and distortion coefficients can thus be obtained at any instant during the ascent or descent.

The turbulent or unsteady nature of recirculating exhaust flows means that the ingestion of hot gas streaks tends to be a variable phenomenon. As a consequence it has been found necessary to repeat each test maneuver at least three times to obtain a reliable overall measure of the likelihood and magnitude of recirculation occurring. Fortunately this does not noticeably affect the cost of testing because the time for each run is a matter of seconds, which is negligible compared with the total tunnel occupancy costs of a test program.

Jet Convergence Experiments

Although the attempts made to control recirculation by deflecting the hot gas fountain were partially successful, there was a significant residual recirculation effect which was about twice that experienced in Harrier and which was considered to be too large for satisfactory V/STOL operations. Consequently an alternative method was evolved. Instead of allowing the fountain to form and then deflecting it away from the inlets, it was proposed that the fountain should be prevented from forming altogether. By keeping the hot gas entirely on the ground it was considered that very low levels of recirculation should be experienced at all heights and forward speeds.

It was hypothesized that to eliminate the fountain the two front jets should be directed inwards towards the engine center line so that they met at or just above ground level. Some crude water flow tests (Fig. 12) were carried out which showed that the fountain was suppressed, and this was followed by some simple fixed height aerodynamic tests, with hot exhaust jets, with measurements of mean intake temperature rise. Figure 13 shows some results from these tests comparing the intake temperature rise for parallel front jets with the converged system. These results showed that, provided the correct point of jet confluence was obtained in relation to the ground, very low levels of intake temperature rise were possible.

The encouraging results from these two preliminary experiments gave sufficient confidence in the converged jet technique for a program of tests to be undertaken in the moving model test rig described in this paper. The aim was to test a fairly representative aircraft model over a wide range of carefully simulated jet-borne ascents and descents to check that the converged nozzles method remained effective over an adequate V/STOL maneuver envelope, and to identify any flight conditions where the residual recirculation effects might prove to be prohibitive. The test model used for this program was the one shown in Fig. 10.

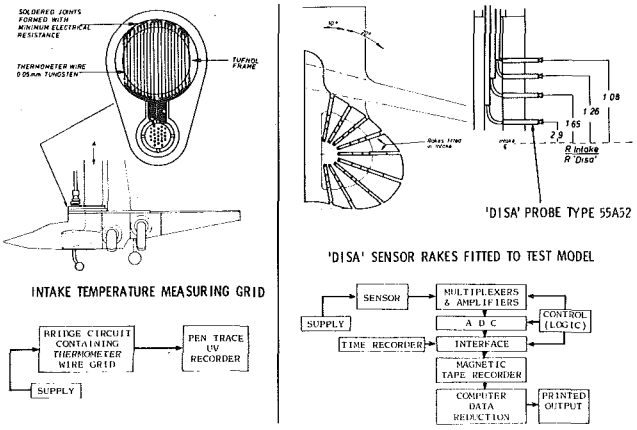

Fig. 11 Inlet temperature instrumentation

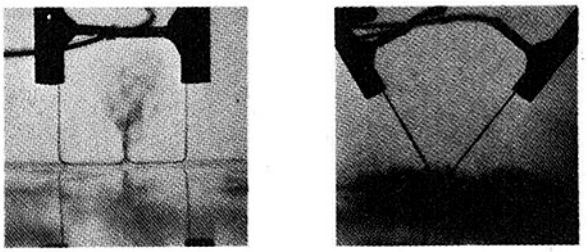

FLOW VISUALISATION USING DYE INJECTION
TESTS SHOW EFFECT OF JET CONVERGENCE ON FOUNTAIN

Fig. 12 Water flow simulation of converged lift jets

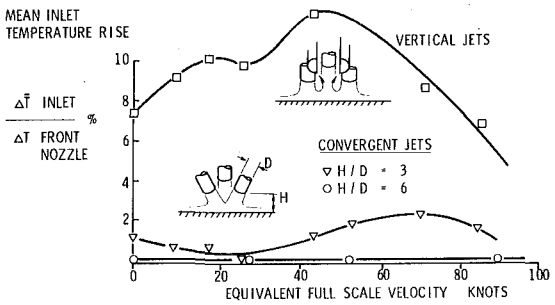

Fig. 13 Effect of jet convergence on inlet temperature rise

Both the mean and local inlet temperature measurement systems were used and some typical results are given in Figs. 14 to 16. Figure 14 shows typical traces of inlet temperature as a function of aircraft height, recorded for particular take-off and landing maneuvers. From such traces it is possible to plot charts, as shown in Fig. 15, displaying the highest value of mean inlet temperature rise encountered in any given maneuver (defined by ascent acceleration or descent velocity, and the relative wind speed). Similar displays showing the highest local temperature, or the highest temperature distortion coefficient can also be produced. For assessing the likely effects of inlet temperature rise on the engine performance and handling it is also necessary to know where any hot gas streaks are located and Fig. 16 shows typical, illustrative, inlet duct temperature distribution plots.

Application of the Results

From the data shown on Fig. 15, and other similar curves for different nozzle angles and wind directions, predictions can be made of the likely intake temperature rise due to hot gas reingestion during any take-off or landing maneuver. Provided the aircraft characteristics are sufficiently well known so that the relationship between speed, nozzle angle and ground roll can be defined, the variation of intake temperature during the maneuver can be predicted. The maximum value for each take-off run or landing can then be plotted as a function

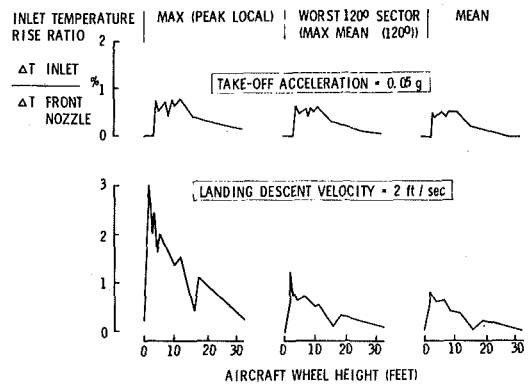

Fig. 14 Converged lift jets—typical inlet temperature traces

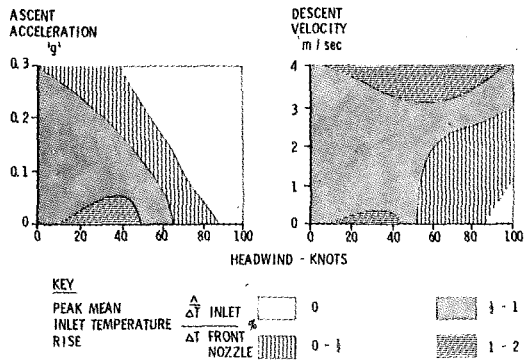

Fig. 15 Converged lift jets—peak recirculation levels

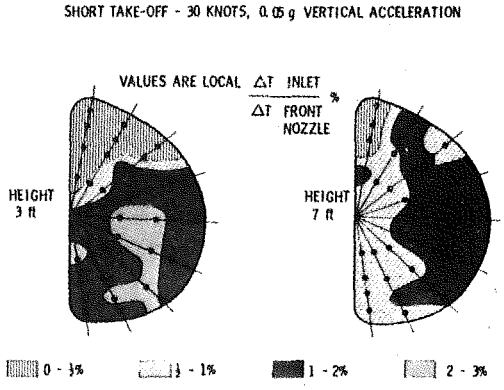

Fig. 16 Typical inlet temperature distributions

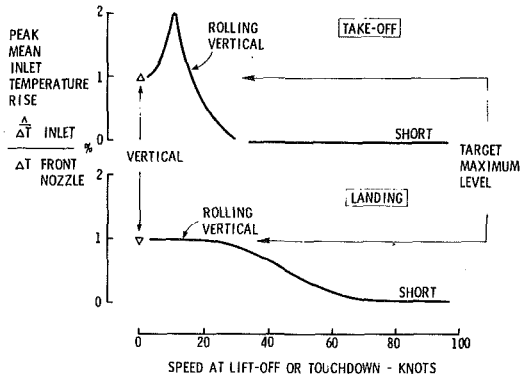

Fig. 17 Converged lift jets—typical V/STOL maneuver peak recirculation levels

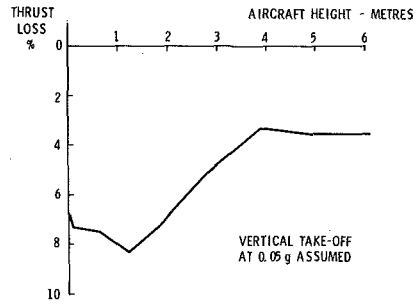

Fig. 18 Overall lift loss with converged jets

of the ground speed. Figure 17 shows that for an aircraft powered by an augmented vectored thrust engine, the intake temperature rise due to hot gas reingestion is less than the target level set for all take-off and landing maneuvers except in the case of very short take-off runs. Under these particular conditions the combination of nozzle angle and forward speed produces a significant amount of intermediate or thrust reverser recirculation. It will be noted that a purely vertical take-off is acceptable and it is considered possible to avoid the high levels of intake temperature rise for the very short ground runs by the selection of suitable operational procedures.

Although the measurements of intake temperature rise indicate that acceptably low levels of hot gas recirculation can be achieved there are other factors to be taken into account. The total weight that can be lifted vertically will be reduced by other losses which are incurred as a result of achieving low recirculation levels. These are:

1 The loss of thrust due to the inwardly angled jets, which will be equal to (1-cos Θ) where Θ is the angle the jet makes with the vertical. This loss is only applied to the front nozzle thrust so the overall loss of thrust will depend on the front: rear nozzle thrust split. The angle also depends on the height of the nozzles above the ground and the distance between them.

2 The effect of the converged jets is to eliminate the longitudinal fountain created between the front jets of the normal four-poster without convergence. Losing this fountain reduces a favorable lift effect near the ground.

3 The elimination of the fountain without excess convergence angles may require a longer undercarriage than could otherwise be used, so there may be a weight penalty or a retracted undercarriage stowage problem.

Figure 18 shows the variation of total lift loss versus height taking the above factors into account. It includes the effect of intake temperature rise on engine thrust, the thrust loss due to nozzle convergence, the ground effect lift losses, and the weight penalty of an increased undercarriage length.

For the particular configuration chosen the total lift loss for a VTO is shown to have a maximum value of about 8 percent. Additional losses, such as the air intake total pressure recovery have to be accounted for, but it is suggested that an engine uninstalled thrust: aircraft gross weight of 1.2 to 1.25 will provide a sufficient margin for vertical acceleration after all the installation effects have been incorporated.

Finally, it is considered that the results obtained from these recirculation tests can be interpreted in a broader way, and some general rules can be generated which would apply to other V/STOL propulsion system layouts with high temperature exhaust jets. These are as follows:

1 The jet effluxes should be arranged such that they impinge on the ground along a single line disposed longitudinally under the aircraft; the likelihood of severe reingestion occurring increases when the exhaust jets are arranged transversely.

2 Fountains must not be completely eliminated unless quite large suck-down forces (≃25 percent of the lift) can be tolerated; aligning the impingement pattern longitudinally can create fountains which are transverse and these will be situated between the extreme nozzle positions.

3 The engine air intake entries should be beyond the limits of the exhaust jets in a fore and aft sense. That is, for a lift plus lift/cruise or bleed and burn propulsion system, the lift/cruise engine intake should be ahead of the forward lift jets; this then allows the forward lift jet exhausts to entrain residual hot gas flows from the transverse fountain and prevent hot fountain gas reaching the air intake.

This last recommendation obviously means a long air inlet duct, which increases weight and volume, and pressure loss, and is a penalty to pay relative to the compact vectored thrust engine layout. An additional penalty of the bleed and burn system is the size and weight of the duct to the forward lift jets.

Figure 19 shows diagrammatically a number of different jet impingement layouts for different V/STOL propulsion systems and categorizes them into those prone to high levels of hot gas reingestion and those that are not. The selection is not intended to be exhaustive and only reingestion due to fountain flows has been considered, i.e., that occurring for true vertical take-offs and landings. For STO operation the "intermediate" or "thrust reverser" reingestion may be important but this has not been considered.

Concluding Remarks

[1] and [2] have shown how the augmented vectored thrust engine is competitive with other types of V/STOL propulsion system and has the advantages of simplicity and flexibility. It is also a natural successor to the unboosted Pegasus/Harrier for a V/STOL aircraft which has a supersonic performance and better maneuverability. Work carried out by Rolls-Royce has indicated that a potential problem of the augmented engine—that of hot gas recirculation—may be avoided provided the appropriate features are incorporated into the installation.

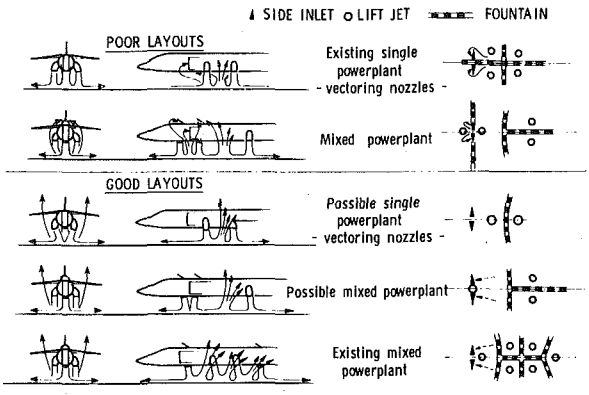

Fig. 19 Comparison of alternative configurations

References

1 Lewis, W. J., and Hurd, R., "Propulsion Systems for Supersonic V/STOL Combat Aircraft," Rolls-Royce paper presented at 23rd Annual Gas Turbine Conference, ASME, London, April 1978.

2 Hooper, J. A., "The Choice of Propulsion System for a Future V/STOL Combat Aircraft," Rolls-Royce Note GN 17397, June 1974.

3 Kemp, E. D. G., "Studies of Exhaust Gas Recirculation for VTOL Aircraft," AIAA Paper 67-439, July 1967.

4 Abbott, W. A., "Estimation of Intake Temperatures during V/STOL Operation from Model Tests," Unpublished material.

E. Schmidt

Research Engineer.
Institut für Aerodynamik und Gasdynamik,
Universität Stuttgart,
Pfaffenwaldring 21,
D-7000 Stuttgart 80,
W. Germany

Computation of Supercritical Compressor and Turbine Cascades with a Design Method for Transonic Flows

The development of supercritical cascades follows experience with supercritical single profiles. In cascade arrangement strong inter-blade influences exist in the transonic region, so that a desired pressure distribution, starting from the contour shape, is not easy to realize. For these cases, a design method has been developed in which the boundary conditions can be prescribed in a simple and clear manner. Thickness and deflection are not restricted, since the full potential equation is treated. Variation of the axial velocity density ratio is provided for. The solution by relaxation leads to short computing times. Experimental comparisons for turbine and compressor cascades show the applicability of the method.

Introduction

Modern turbomachines will be equipped with blades which have supercritical profiles. However, our knowledge of the most efficient design is at present limited. In the past decade, much experience has been gathered about favorable shockfree flows around supercritical single profiles and this indeed can serve as a basis. But the velocity distributions so found require other contours for cascades, since the boundary conditions differ greatly in the two cases. For compressor cascades, even for those of large pitch and low deflection, in the transonic region, the influence of the adjacent profiles is appreciable because of the vicinity of the mass flow maximum. In turbine cascades the supersonic regions can extend to the adjacent profiles, so that a comparison with single profile flow is no longer possible.

For the design of low-loss cascades one suitably should start from the velocity distribution, since one has a much more exact knowledge of it—mainly from boundary layer investigations—than of the respective contour shape. That is true especially near the sonic velocity location, since at this condition large changes of the velocities are caused by small modifications of the contours. Therefore for this domain, design methods are of greater importance than for the subsonic region, where one can also get good cascade designs in an iterative manner with analysis methods.

While most transonic cascade computation methods treat the analysis problem [1–5] only a few methods for transonic design exist, [6, 8]. Difficulties with the application of design methods often result from the use of the hodograph plane, which is not easily grasped by the engineer due to the use of velocity coordinates. The physical plane cannot be used for design problems, since its coordinates are the result of the computation.

The method presented for the computation of transonic plane potential flows [9] uses the more clearly arranged potential-streamfunction-plane. Because of the sensitive cross-section dependence of the transonic flow a channel between two blades will be always considered. The boundary conditions thereby are prescribed as velocity magnitudes on the stagnation streamlines of the suction and pressure sides of a flow channel. Since the prescription is given over the arc length, pressure gradients determined from boundary layer calculations can be considered exactly. The boundary conditions are transformed into the computational plane by integration. Then the flow field is computed by the solution of the full potential equation by means of a relaxation method. Subsequently the field is back transformed into the physical plane by combined differentiation and integration. From this the blade profile coordinates and the geometry of the cascade result. For the profile thickness and the turning angle no restrictions are required since no linearization assumptions are made. The potential-streamfunction-coordinates provide for a rectangular grid in the computing plane and for a contour adapted grid in the physical plane, so that no interpolations are necessary on the boundaries. Moreover the asymmetric difference formulas of the supersonic regions are automatically orientated correctly in the flow direction without special arrangements.

The method was tested on several interferometric measured flow fields, from which a transonic turbine cascade flow will be shown here. In addition several compressor cascades were designed with it and

Contributed by the Gas Turbine Division and presented at the Gas Turbine Conference and Exhibit and Solar Energy Conference, San Diego, California, March 12–15, 1979 of THE AMERICAN SOCIETY OF MECHANICAL ENGINEERS. Manuscript received at ASME Headquarters December 8, 1978. Paper No. 79-GT-30.

partly tested at the DFVLR, Cologne. An expansion of the method allows consideration of the axial velocity-density-ratio, permitting a better approximation to the real physical conditions.

Governing Equations

For a steady, two-dimensional, compressible flow, the equations of continuity and irrotationality, transformed to the potential-streamfunction-coordinates are valid in the form

$$\frac{1}{\rho^2 w}(\rho w)_\varphi + \vartheta_\psi = 0 \tag{1}$$

$$\frac{\rho}{w} w_\psi - \vartheta_\varphi = 0 \tag{2}$$

By differentiation and elimination of the flow angle ϑ one obtains in logarithmic form the flow differential equation

$$(\ln \rho)_{\varphi\varphi} + (\ln w)_{\varphi\varphi} + ((\ln \rho)_\varphi)^2 + (\ln \rho)_\varphi (\ln w)_\varphi + \rho^2 (\ln \rho)_\psi (\ln w)_\psi + \rho^2 (\ln w)_{\psi\psi} = 0, \tag{3}$$

which reduces to the Laplace equation for incompressible flow (ρ = const.). By normalization of the velocities with the critical velocity

$$\mathrm{La} = \frac{w}{a^*}$$

and introduction of the isentropic relation

$$\frac{\rho}{\rho_0} = \left(1 - \frac{\gamma - 1}{\gamma + 1}\mathrm{La}^2\right)^{1/(\gamma-1)} \tag{4}$$

one obtains the full potential equation in the potential-streamfunction plane

$$C_1(\ln \mathrm{La})_{\varphi\varphi} + C_2(\ln \mathrm{La})_{\psi\psi} + C_3((\ln \mathrm{La})_\varphi)^2 + C_4((\ln \mathrm{La})_\psi)^2 = 0 \tag{5}$$

with the coefficients

$$C_1 = \frac{1 - \mathrm{La}^2}{K_1^{(\gamma+1)/(\gamma-1)}} \qquad C_3 = \frac{K_2(1 + \mathrm{La}^2)}{K_1^{2\gamma/(\gamma-1)}}$$

$$C_2 = 1 \qquad C_4 = \frac{K_2}{K_1}$$

where

$$K_1 = 1 - \frac{\gamma - 1}{\gamma + 1}\mathrm{La}^2 \qquad K_2 = -\frac{2}{\gamma + 1}\mathrm{La}^2.$$

The type of this nonlinear partial differential equation of second order changes in dependence of the sign of the coefficient C_1: For C_1 positive (subsonic flow) it is elliptic, for $C_1 = 0$ (sonic velocity) parabolic and for C_1 negative (supersonic flow) it is hyperbolic. For pure subsonic flow it was solved by Stanitz [10], in the most cases, however, by means of a linearized pressure-density-relation, which reduces the problem to the solution of the Laplace-equation, but fails in the near sonic region.

For transonic flow computations a finite difference method was developed, which uses distinct difference equations in the different domains of dependence, as was done first by Murman and Cole [11] for a small disturbance form of the potential equation.

A conservative formulation of the problem was not sought, since the advantages of this formulation lie in the treatment of discontinuities like shocks. However, supercritical profiles are intended to avoid shocks, so none need be prescribed in a design method. The disadvantage of the higher expense—finer grids for the same accuracy and therefore more storage and computing time requirement [12]—would not be justified. Good agreement with experimental results was obtained for the treatment of weak shocks by the above method.

Numerical Solution

In the elliptic domain, because of the all around dependence of every fieldpoint, centered difference formulas with a truncation error of second order are used. For instance, for the second derivative in the flow direction, one has

$$(\ln \mathrm{La})_{\varphi\varphi}|_{i,j} = \frac{1}{(\Delta\varphi)^2}(\ln \mathrm{La}_{i+1,j} - 2 \ln \mathrm{La}_{i,j} + \ln \mathrm{La}_{i-1,j}). \tag{6}$$

According to the linear theory these implicit systems are not liable to stability conditions.

In the hyperbolic domain, for the prevention of upstream travelling disturbances, upwind difference formulas of implicit form are used. In explicit systems the CFL-stability-condition requests the step size to be zero in the flow direction at sonic velocity and therefore makes them useless for transonic calculations. Calculations with formulas of first and second order were carried out. For example, for the second derivative in the flow direction, one has with

1 first order accuracy: $(\ln \mathrm{La})_{\varphi\varphi}|_{i,j}$

$$= \frac{1}{(\Delta\varphi^2)}(\ln \mathrm{La}_{i,j} - 2 \ln \mathrm{La}_{i-1,j} + \ln \mathrm{La}_{i-2,j}) \tag{7}$$

2 second order accuracy: $(\ln \mathrm{La})_{\varphi\varphi}|_{i,j}$

$$= \frac{1}{(\Delta\varphi)^2}(2 \ln \mathrm{La}_{i,j} - 5 \ln \mathrm{La}_{i-1,j} + 4 \ln \mathrm{La}_{i-2,j} - \ln \mathrm{La}_{i-3,j}) \tag{8}$$

In comparison to analytical solutions, the system of second order showed the higher accuracy expected with, of course, a greater expenditure in computing time. Crosswise to the flow direction centered equations are valid also in the hyperbolic domain. The orientation in the flow direction, important in unsymmetric systems for the correct reproduction of the domain of dependence, occurs automatically, owing to the chosen computational plane contrary to other transonic methods [13], where such an alignment has to be especially introduced. Passing through the sonic velocity a parabolic point was inserted, if supersonic velocity followed from elliptic computation and subsonic velocity from hyperbolic computation. Therefore, the coefficient of the second derivative in the flow direction of equation (5) was set equal to zero.

The nonlinear difference equation system with tridiagonal coefficient matrices is solved by relaxation. This method is especially suited for transonic computations, since it allows much independence in the choice and modification of the boundary conditions at the change of type of the governing equation in the progress of computation. For

Nomenclature

a^* = critical sonic velocity
A = Area
d = flow cross section width
l = blade chord length
La = Laval number, normalized velocity, w/a^*
n = arc length along potential-lines
s = arc length along streamlines
t = pitch
w = velocity
x = physical coordinate, see Fig. 1
y = physical coordinate, see Fig. 1
β_1 = upstream flow angle, see Fig. 1
β_2 = downstream flow angle, see Fig. 1
β_S = stagger angle
γ = ratio of specific heats
Γ = circulation
ϑ = local flow angle
ρ = density
ρ_0 = stagnation density
φ = potential function
ψ = stream function
ω = axial velocity density ratio function
Ω = axial velocity density ratio

Subscripts

1 = upstream station
2 = downstream station
i = numbering of field points in φ-direction
j = numbering of field points in ψ-direction
BW = blade wake
SW = side wall
LE = leading edge
TE = trailing edge
PS = pressure side
SS = suction side
φ = partial differentiation referring to φ
ψ = partial differentiation referring to ψ

short computing time the relaxation factors were optimized in the elliptic and hyperbolic domain. More details are contained in [9].

Boundary Conditions and Transformations with Consideration of Axial Velocity Density Variation

As in the field computation, also in the prescription of the boundary conditions, the different domains of dependence must be considered. The design task in the elliptic domain leads to a Diriclet problem requiring the prescription of the field quantity—here the modulus of the velocity vector—on the whole boundary of the integration domain. The combined initial-value-boundary-value-problem of the hyperbolic domain, however, needs the velocity prescription on a noncharacteristic initial-value-curve as well as on the lateral boundaries. In the second case, no values may be prescribed across the downstream streamlines. In transonic flows the sonic line—as part of the elliptic boundary and as initial-value curve of the hyperbolic domain—is unknown, since it belongs to the result. Here the iterative solution process with its continuously changing values of the field points aids, since this process provides for a provisional shape of the sonic line, until this line is established at convergence of the computation.

A difficulty arises at the prescription of the velocity distribution in local supersonic regions, since this is the question of not a well posed problem. Thus, not every prescription is physically meaningful, so that not in every case convergence of the numerical solution is assured. Therefore one is dependent on results from single profiles, until there exists more experience in the cascade sector. According to the experience of the author to date, however, this problem seems to be not too serious, since non-converging design computations have been the exception up to now. The acceleration of the whole channel flow from subsonic to supersonic velocity poses no problem for the convergence of the computation.

For the explanation of the boundary condition prescription it is necessary to show a cascade in the physical plane, although its shape is only the result of the computation, Fig. 1. Up- and downstream values La_1, β_1, La_2, β_2 are coupled because of the periodicity of the cascade flow. They must yield constant pitch-chord-ratio, so that double covering of the flow field or unclosed profiles are avoided. Indeed, for the consideration of the displacement effect of the blade profile wake the flow field may remain partly uncovered, so that the axial velocity-density ratio is to be chosen

$$\Omega = \frac{A_1}{A_2} = \frac{\rho_2 w_2 \sin \beta_2}{\rho_1 w_1 \sin \beta_1} > 1 \tag{9}$$

Additionally for the consideration of the displacement effect of the side wall boundary layers an $\Omega_{SW} > 1$ can be chosen, which together with the Ω_{BW} of the blade wake yields the whole axial velocity-density ratio

$$\Omega = \Omega_{BW} \cdot \Omega_{SW}. \tag{10}$$

The consideration of the side wall boundary layers will be treated further below.

For a chosen upstream flow La_1, β_1 and a chosen downstream velocity La_2 one obtains from the continuity equation for the downstream flow angle

$$\beta_2 = \arcsin \frac{\Omega \cdot La_1 \sin \beta_1 \left[\frac{1}{2}(\gamma + 1 - (\gamma - 1)La_1^2)\right]^{1/(\gamma-1)}}{La_2 \left[\frac{1}{2}(\gamma + 1 - (\gamma - 1)La_2^2)\right]^{1/(\gamma-1)}} \tag{11}$$

The circulation along the boundaries of a control surface around a blade yields at strict periodicity ($\Omega = 1$):

$$\Gamma = t(La_2 \cos \beta_2 - La_1 \cos \beta_1). \tag{12}$$

For axial velocity density ratios $\Omega \neq 1$ the first term in parentheses has to be divided by Ω.

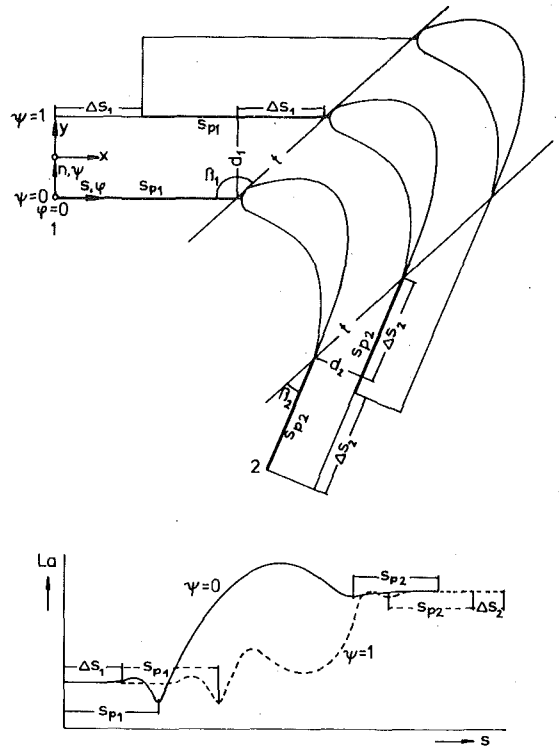

Fig. 1 Prescription of boundary conditions

Up and downstream cross sections 1 and 2 for the prescription of constant flow conditions (constant velocity magnitude and direction, constant potential) must be chosen sufficiently distant from the cascade, whereas in cross section 2 only for subsonic flow may values be prescribed. An extension of the flow field of 1.5 to 2 pitches has proved to be sufficient.

On the periodic boundaries s_{p1} and s_{p2} of the stagnation streamlines of the up- and downstream flow the velocity distributions must coincide. The shifting distances Δs_1 and Δs_2 on the pressure side streamline follow from

$$\Delta s_1 = \frac{-d_1}{\tan \beta_1} \quad \text{and} \quad \Delta s_2 = \frac{d_2}{\tan \beta_2} = \frac{d_1 \cos \beta_2}{\Omega \sin \beta_1}. \tag{13}$$

Integrated with constant velocities La_1, La_2, respectively, they correspond to equation (12). In the calculations all distances are normalized with the upstream cross section

$$d_1 = t \cdot \sin \beta_1. \tag{14}$$

At the front stagnation points the prescribed velocities cannot be reduced to zero, since the numerical method does not permit this singular point. The necessary smoothings, however, produce no great deviations, as experimental comparisons show. At the rear stagnation points the problem does not appear, since they do not exist physically owing to the wake.

The prescription on the parts of the stagnation streamline, which form the cascade contour, first of all depends on boundary layer aspects. Limits are given by the maximum pressure gradients which the boundary layer can tolerate without separation. If at the design condition local supersonic regions are provided for, the distributions have to be chosen suitably in such a manner that by isentropic recompression the strength of the final shock will be reduced in order to avoid boundary layer separation.

Problems with contour intersections can only arise in very thin profiles. These profiles result from velocity distributions which have a relative low level in comparison with the upstream and downstream flow. These problems are easy to remove by increasing the velocities at the appropriate positions. The velocity distribution, which is given along the arc length of the boundary stream- and potential lines,

$$\text{La} = \text{La}(s) \qquad \text{La} = \text{La}(n)$$

for the transformation on φ,ψ-coordinates will be integrated

$$\varphi(s) = \int_{\psi=\text{const.}} \text{La}(s)ds \qquad \psi(n) = \int_{\varphi=\text{const.}} \frac{\rho}{\rho_0}\text{La}(n)dn \quad (15)$$

From this integration the circulation computed around the profile

$$\Gamma = \oint_{\substack{\text{blade}\\ \text{contour}}} \text{La}(s)ds$$
$$= (\varphi_{TE} - \varphi_{LE})_{SS} - (\varphi_{TE} - \varphi_{LE})_{PS} \quad (16)$$

serves together with equation (12) for the adjustment of the potentials of the suction and pressure sides.

Then for the boundaries of the computation plane follows

$$\text{La} = \text{La}(\varphi),$$

in the same way

$$\text{La} = \text{La}(\psi).$$

The last generally is presumed constant. Therefore the potential- and the streamfunction are normalized with

$$\Delta\psi_1 = \frac{\rho_1}{\rho_0}\text{La}_1.$$

After the computation of the velocity field from the numerical solution of the potential equation by relaxation, the transformation into the physical plane requires the determination of the direction field of the velocity. The direction of the velocity vector follows from the integration of the continuity equation (1) along potential lines:

$$\vartheta(\psi) = -\int_{\varphi=\text{const.}} \frac{\rho_0^2}{\rho^2\text{La}}\left(\frac{\rho}{\rho_0}\text{La}_\varphi + \text{La}\left(\frac{\rho}{\rho_0}\right)_\varphi\right)d\psi. \quad (17)$$

Analogous the integration of the equation of irrotationality (2) along streamlines yields

$$\vartheta(\varphi) = \int_{\psi=\text{const.}} \frac{\rho}{\rho_0\text{La}}\text{La}_\varphi d\varphi. \quad (18)$$

At first, the turning of the middle streamline has to be computed by equation (18) and adapted to the presumed turning ($\beta_2-\beta_1$) by iterative modification of the velocity distribution. Then for

$$x = -\int_{\varphi=\text{const.}} \frac{\rho_0 \sin\vartheta}{\rho\text{La}}d\psi = \int_{\psi=\text{const.}} \frac{\cos\vartheta}{\text{La}}d\varphi \quad (19)$$

$$y = \int_{\varphi=\text{const.}} \frac{\rho_0 \cos\vartheta}{\rho\text{La}}d\psi = \int_{\psi=\text{const.}} \frac{\sin\vartheta}{\text{La}}d\varphi \quad (20)$$

The integration along the middle streamline first yields its physical coordinates and the following integration along potential lines gives the coordinates of the contour.

In cascade experiments a small cross-section variation normal to the computing plane can occur by side wall boundary layers growing in the flow direction. A simple approximation for the consideration of this three-dimensional phenomenon was inserted into the two-dimensional method. Since an increase of the axial velocity-density ratio Ω by side wall boundary layers in the two-dimensional computation adds this side wall effect to the profile boundary layers, this effect must be cancelled by a corresponding spreading of the streamtubes in the computation plane normal to the flow direction. The development of the displacement effect of the side wall boundary layers in the blade region can be optionally prescribed by a function

$$1.0 \le \omega \le \Omega_{SW},$$

in the simplest case linear. The spreading of the streamtubes then occurs by a distortion of the integrands in equation (19) and (20) in the integration along potential lines:

$$x = -\int_{\varphi=\text{const.}} \frac{\omega(\varphi,\psi)\rho_0 \sin\vartheta}{\rho\text{La}}d\psi \quad (21)$$

$$y = \int_{\varphi=\text{const.}} \frac{\omega(\varphi,\psi)\rho_0 \cos\vartheta}{\rho\text{La}}d\psi \quad (22)$$

The overall progress of the method is outlined as a block diagram in Fig. 2.

Results

For the verification of the method in addition to analytical examples (in [9]) experimental results were referred to, in which the whole velocity field could be compared. A very good possibility therefore is offered by interference exposures, which reproduce transonic flow fields measured without disturbing instrumentation in the flow. For this purpose accelerated flows are preferable. Since the method computes the potential flow boundary, for the thin boundary layers of these flows, checking of the contour calculation has less uncertainties than for decelerated flows with thick boundary layers.

One test case presents the velocity distribution of a transonic turbine cascade flow shown in Fig. 3. In this example both situations—

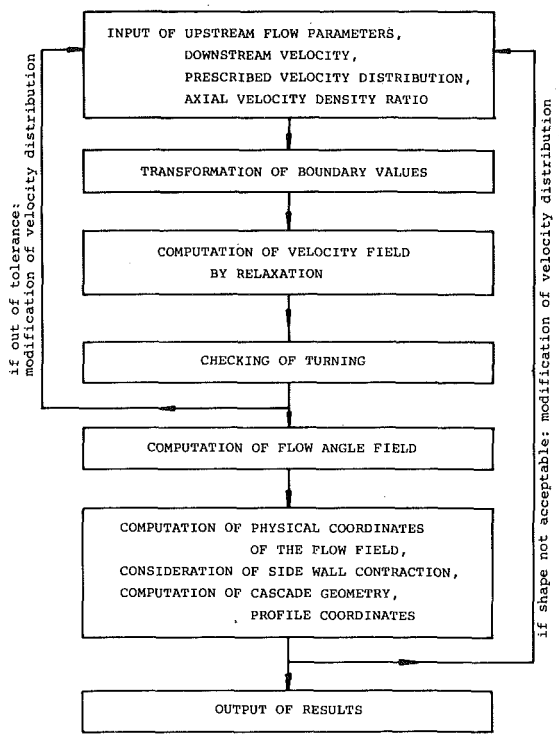

Fig. 2 Block diagram of the numerical method

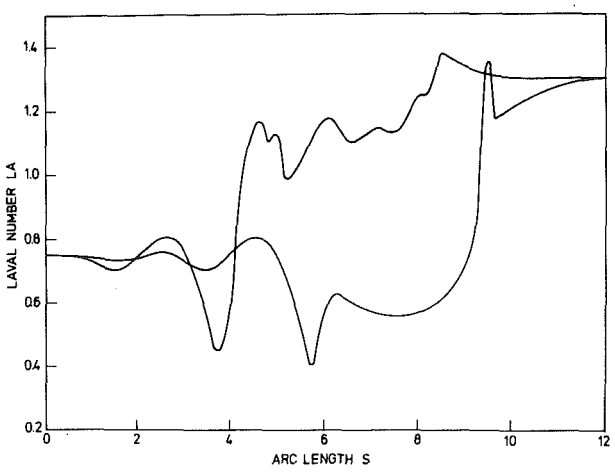

Fig. 3 Prescribed velocity distribution for a turbine cascade (from experiment)

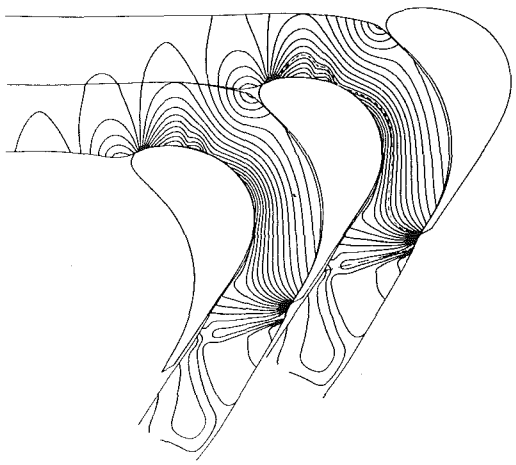

Fig. 4 Calculated contours and isotachs of the turbine cascade flow (dashed line: sonic line, dash-dotted line: shock)

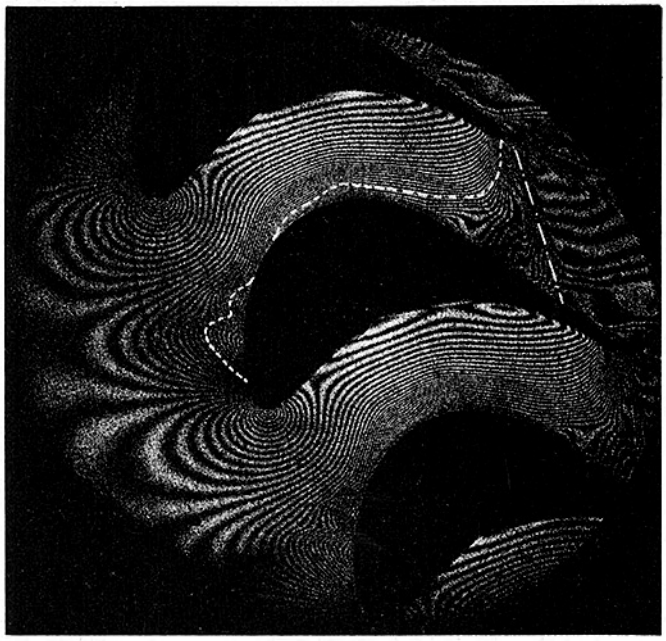

Fig. 5 Interference exposure of the turbine cascade flow (dashed line: sonic line, dash-dotted line: shock)

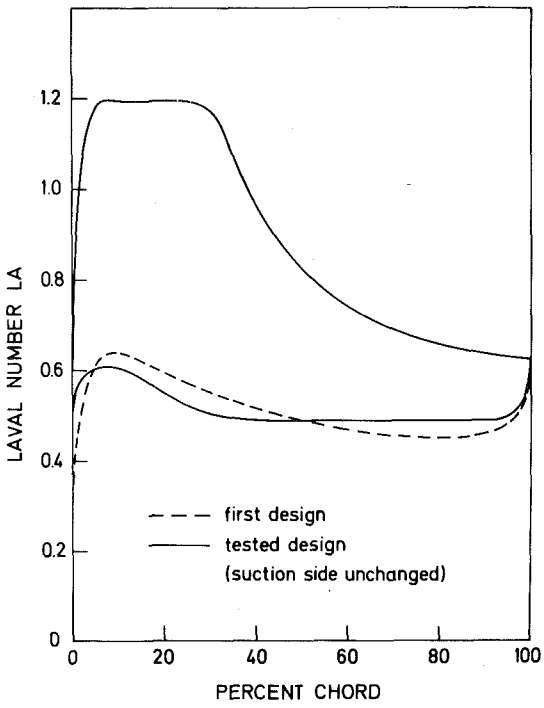

Fig. 6 Prescribed velocity distribution for a compressor cascade (SKG 1.3)

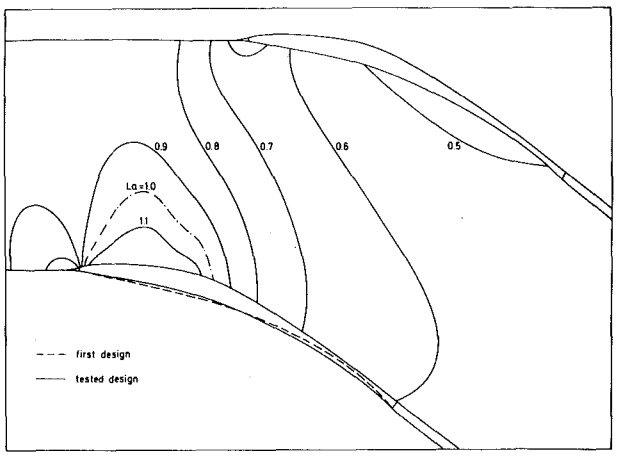

Fig. 7 Calculated contours and isotachs of the compressor cascade SKG 1.3

local supersonic region and acceleration from subsonic to supersonic velocity of the whole channel flow—appear in the same field. The upstream flow with $La_1 = 0.75$, $\beta_1 = 153$ deg is turned through 123.5 deg to the downstream flow with $La_2 = 1.30$, $\beta_2 = 29.5$ deg with an axial velocity density ratio $\Omega = \Omega_{BW} = 1.05$, which only considers the blade wake. Fig. 4 shows the result of the computation, the blade contours and the field of constant velocity lines (isotachs). Also drawn in are the previously manufactured cascade contours, with which the later computed values agree very well. With exception of the region at the blade nose, which is not exactly treated, the deviations correspond to the development of the boundary layer along the blade contour, which was taken into account at the evaluation. The flow field shows the typical characteristics of high loaded strong turning cascades. The local supersonic region at the beginning of the suction side results from leading edge blockage, which is clearly explained by the development of the channel width between the suction side and the stagnation streamline of the adjacent profile above it: In spite of the curvature of the stagnation streamline the cross section behind the lower stagnation point reduces significantly and extends only in the region of the upper stagnation point, where the local supersonic region breaks down with two weak shocks. Subsequently the flow accelerates to supersonic velocity with a wide extended sonic line caused by the high channel turning with weak contraction. On the pressure side, sonic velocity is only reached by a strong expansion around the trailing edge of the blade, where the flow is at once adapted with an oblique shock to the pressure and direction of the adjacent flow channel.

The interference exposure, Fig. 5, shows the same shape of the isotachs, especially of the sonic lines. Also the direction of the oblique shock agrees well with the isentropic computation.

Korn [7] calculated and Stephens [14] tested a compressor cascade with a shockfree supercritical velocity distribution. For a high turning compressor cascade a similar velocity distribution was prescribed, which shows the characteristics of supercritical single profiles: The suction side consists of a supersonic roof top with following strong pressure rise without a shock. The pressure side has a pronounced rear loading (Fig. 6). The upstream flow occurs with $La_1 = 0.824$, $\beta_1 = 126.8$ deg, the downstream flow with $La_2 = 0.590$, $\beta_2 = 90$ deg, the axial velocity-density ratio considering only the blade wake amounts to $\Omega_{BW} = 1.04$. The original velocity distribution (pressure side dashed) exhibited very low velocity over the rear of the pressure surface in comparison to the downstream flow due to significant rear loading. This led to a very thin profile in the rear part (0.6 percent including the boundary layer at 80 percent of the profile chord, see Fig. 7, dashed line). Since the suction side should remain unchanged, the pressure

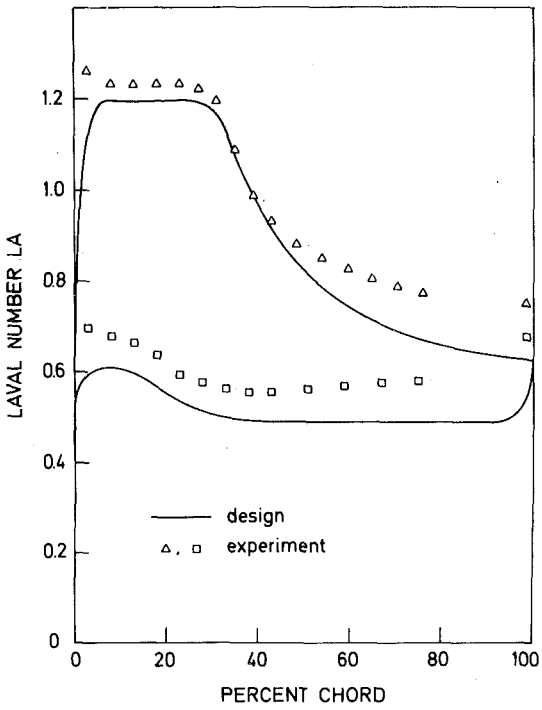

Fig. 8 Comparison between experimental and prescribed velocity distribution at the design point (SKG 1.3)

side had to be changed in such a manner that the circulation remained constant (Fig. 6, full line). Thereby an increase of the profile thickness at this position to 1.8 percent was achieved (Fig. 7, full line), which was also after substraction of the boundary layer displacement thickness sufficient for fabrication. For this design the pitch-chord-ratio amounts to $t/l = 0.826$, the stagger angle $\beta_S = 103.7$ deg.

This cascade was tested in the cascade tunnel of the DFVLR, Cologne. These experiments will be reported in [15]. Here for comparison only the experimental result for the design point is shown (Fig. 8). Deviations are evident first of all at the blade nose and in the rear part of the profile. The nose peak with great probability could be traced back to several curvature jumps in the manufactured contour in this region. Strongly growing side wall boundary layers are responsible for the increase of the velocity level in the rear part of the profile. The channel contraction caused by the side wall boundary layers was not considered in the computation.

For the investigation of this deviation the potential flow boundary was computed from the measured velocity distribution, which was taken as prescription for the computation. The dashed lines around the lower profile of Fig. 9 shows the result of the fully two-dimensional computation. Without consideration of the contraction normal to the computation plane the side wall boundary layers are added to the profile boundary layers, so that these appear of exaggerated thickness. Therefore the approximation described in the last chapter for the consideration of the side wall contraction was provided for. For the new computation of the potential flow boundary the whole axial velocity density ratio $\Omega = 1.094$ was partitioned into the linear growing portion of the side wall $\Omega_{SW} = 1.05$ and into the portion of the blade wake $\Omega_{BW} = 1.042$, which corresponds roughly to experimental experience.

The result is shown on the upper profile in Fig. 9. The boundary layer thickening in comparison with the design indeed is still considerable, but much more probable than in the lower profile of Fig. 9. At the profile leading edge, however, it is certainly too thick, since here the side wall boundary layer displacement thickness was considered to be zero. Since the side wall boundary layer suction of the cascade tunnel works with constant pressure level over the side wall plane there exists the possibility that, owing to the low pressure in the local supersonic region of the potential flow, there inflow takes place instead of suction, so that the velocities are increased in comparison

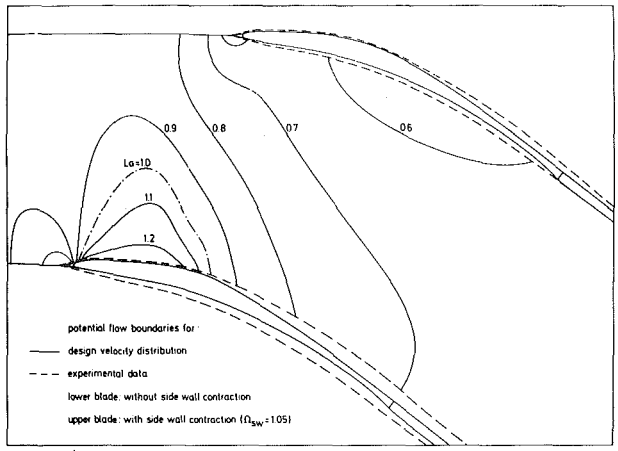

Fig. 9 Effect of the consideration of side wall contraction (SKG 1.3)

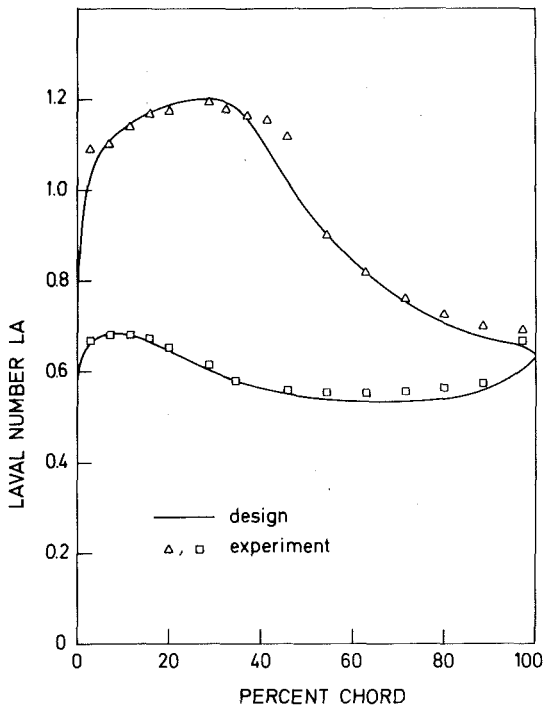

Fig. 10 Prescribed and measured velocity distribution for the compressor cascade SKG 2.7

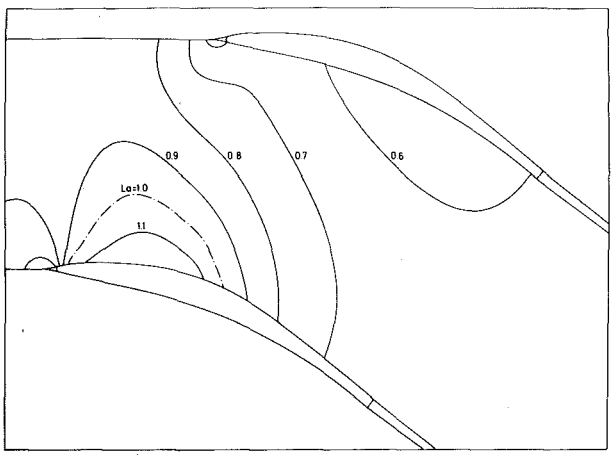

Fig. 11 Calculated contours and isotachs of the compressor cascade SKG 2.7

to the design. The simulated profile boundary layer thickness therefore really belongs to the side wall boundary layer.

This cascade showed, as described in detail in [15], a very small working range, since for the boundary layer calculation of the design distribution a too optimistic assumption about the position of the transition point was made.

Therefore a new velocity distribution was prescribed, which was less critical from the viewpoint of the boundary layer development, Fig. 10. The supersonic plateau at the beginning of the suction side is distorted by reducing the leading edge gradient, and the local supersonic region as well as the pressure rise are shifted backwards. The pressure side velocity distribution is increased and the rear loading is eliminated. The upstream values La_1, β_1 were retained, and also the downstream flow angle β_2. The downstream velocity now amounts to $La_2 = 0.625$, since the axial velocity density ratio was increased to $\Omega = 1.09$ including the side wall boundary layers with $\Omega_{SW} = 1.05$.

Fig. 11 shows the cascade shape. Pitch-chord-ratio and stagger angle remained unchanged. The maximum thickness ratio now amounts to 8 percent as compared with 5.7 percent in the former design. Additionally the thickness distribution is considerably smoothed.

In Fig. 10 also the experimental result for the design point is given. Good agreement with the prescribed velocity distribution is evident. On the suction side at the beginning and the end of the local supersonic region there exist slightly stronger expansions than prescribed. The deviations at the leading edge are possibly due to the limitations of the computation method. At the end of the supersonic region a laminar separation bubble appears. Possibly there, the flow returns with a weak shock to subsonic flow. On the pressure side only in the trailing edge region just as on the suction side end the velocities are slightly increased. Interference exposures are expected to clarify further details of the compressor cascade flows.

Conclusion

A method for the design of transonic cascade flows has been developed. The boundary value prescription used is very simple and clear in comparison to other design methods. The results showed good agreement for a turbine cascade flow, even in the presence of shocks which are of less importance for design methods, since one wants to avoid them. With the inclusion of the axial velocity-density ratio good agreement with experiments was obtained also for compressor cascades.

References

1 McDonald, P. W., "The Computation of Transonic Flow through Two-Dimensional Gas Turbine Cascades," ASME Paper No. 71-GT-89, 1971.

2 Gopalakrishnan, S., Bozzola, R., "A Numerical Technique for the Calculation of Transonic Flows in Turbomachinery Cascades," ASME Paper No. 71-GT-42, 1971.

3 Delaney, R. A., Kavanagh, P., "Transonic Flow Analysis in Axial-Flow Turbomachinery Cascades by a Time-Dependent Method of Characteristics," ASME JOURNAL OF ENGINEERING FOR POWER, Vol. 98, No. 3, 1976, pp. 356–364.

4 Dodge, P. R., "A Non-Orthogonal Numerical Method for Solving Transonic Cascade Flows," ASME Paper No. 76-GT-63, 1976.

5 Ives, D. C., Liutermoza, J. F., "Second Order Accurate Calculation of Transonic Flow Over Turbomachinery Cascades," AIAA Paper 78-1149, AIAA 11th Fluid and Plasma Dynamics Conference, Seattle, Wash., July 1978.

6 Legendre, R., "Ecoulement d'un Fluide Compresible au Travers d'une Grille d'Aillettes de Turbine," *La Recherche Aérospatiale*, No. 125, 1968.

7 Korn, D., "Numerical Design of Transonic Cascades," *ERDA Research and Development Report* C00-3077-72, Courant Inst. Math. Sci., New York University, Jan. 75.

8 Garabedian, P., Korn, D., "A Systematic Method for Computer Design of Supercritical Airfoils in Cascade," *Comm. Pure Appl. Math.*, Vol. XXIX, 1976, pp. 369–382.

9 Schmidt, E., "Numerische Berechnung und experimentelle Untersuchung des transsonischen Strömungsfeldes in stark umlenkenden Schaufelgittern," Dissertation, Universität Stuttgart, 1976.

10 Stanitz, J. D., "Design of Two-Dimensional Channels with Prescribed Velocity Distributions along the Channel Walls," NACA Rep. No. 1115, 1953.

11 Murman, E. M., Cole, J. D., "Calculation of Plane Steady Transonic Flows," AIAA-Paper 70-188, 1970.

12 Jameson, A., "Transonic Potential Flow Calculations Using Conservation Form," *Computational Fluid Dynamics 2nd Conference Proceedings*, Hartford, Conn., 1975, pp. 148–161.

13 Bauer, F., Garabedian, P., Jameson, A., Korn, D., "Supercritical Wing Sections II, "*Lecture Notes in Economics and Mathematical Systems*, Vol. 108, Springer, New York 1975.

14 Stephens, H. E., "Application of Supercritical Airfoil Technology to Compressor Cascades: Comparison of Theoretical and Experimental Results," AIAA Paper 78-1138, AAIA 11th Fluid and Plasma Dynamics Conference, Seattle, Wash., July 1978.

15 Rechter, H., Schimming, P., Starken, H., "Design and Testing of Two Supercritical Compressor Cascades," to be presented at the 24th Annual International Gas Turbine Conference, San Diego, California, March 12–15, 1979.

N. Venkatrayulu
Assistant Professor.
Assoc. Mem. ASME.

D. Prithvi Raj
Professor and Head.
Mem. ASME
Thermal Turbomachines Laboratory,

Department of Mechanical Engineering,
Indian Inst. of Technology,
Madras 600 036, India.

R. G. Narayanamurthi
Director.
Indian Institute of Technology,
Madras 600 036, India.

Influence of Freely Rotating Inlet Guide Vanes on the Return Flows and Stable Operating Range of an Axial Flow Fan

This paper presents the results of experimental investigations on the three-dimensional flow and performance characteristics of a free vortex axial flow fan rotor, with a freely rotating and braked inlet guide vane row. The influences of axial distance between the inlet guide vane row and the rotor inlet, inlet guide vane setting angle and shape, partial omission of guide vanes at the hub and tip regions on the return flows have been studied and optimum axial distance and setting angle that will improve the useful operating range of the fan were determined. Use of freely rotating inlet guide vanes at high flow volumes and braked inlet guide vanes at low flow coefficients resulted in a reduction of return flows and an increase of the stable operating range of the axial fan rotor by more than 35 percent and this combination has yielded higher efficiencies as well in the extended region of stable operation.

Introduction

Axial flow fans and compressors, in spite of high peak efficiencies obtainable in modern designs, are limited in their application because of their narrow operating range. Most axial flow fans and compressors show an unstable characteristic for small delivery volumes. The specific work-volume characteristic of an axial flow fan shows that the specific work increases with a decrease of volume starting from the maximum discharge point until what is known as the stalling point is reached. The discontinuity in the characteristic curve is a symptom of instability and serious flow disturbances with return flows occurring at rotor inlet tip region and near the hub region at rotor outlet.

The relation between the performance and return flows has been discussed by Scheer [1], Toyokura and Kubota [2], Ida [3], and Pfleiderer [4]. Several attempts have been made in the past to extend the useful operating range of axial flow machines. An obvious remedy for the limitations on the operating range is to change the vane angle setting with changes in operating conditions to maintain optimum lift coefficients [5, 6]. An appreciable stabilizing effect in the operating range was reported by Scheer [1] when fixed straight radial baffles were installed in front of the rotor. Ponomareff [7] obtained an improvement of the stability of the characteristic of an axial flow compressor stage, by using a concentric guide bell at the inlet nozzle. A concentric ring before the rotor in the vicinity of the casing and a separator (with vanes) between the ring and external casing also produced a stabilizing effect [8].

The objective of the present investigations is to find out whether the speed controlled adjustable inlet guide vanes (freely rotating and braked) can be used to eliminate or minimize the region of instability of the axial fan characteristic and improve the performance of the fan at low flow coefficients with a reduction in the size of return flows. The reason for this attempt of using an additional member, namely the inlet guide vane row, is due to the fact that a major change in the flow pattern takes place at rotor inlet if the operation is changed from stable to unstable operating range, as shown in Fig. 1 and [1, 9].

Experimental Set-Up

A general schematic lay-out of the single stage axial flow fan designed for the present investigations is shown in Fig. 2. The inlet guide vane row was mounted such that it could freely rotate while the fan

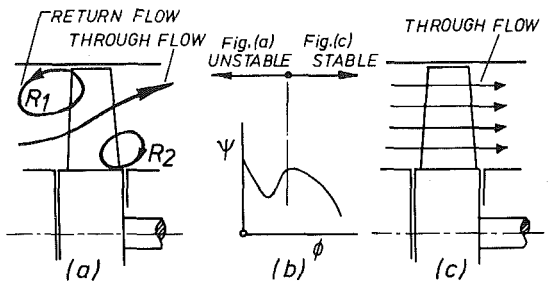

Fig. 1. Flow lines in the meridian section of the axial flow fan for stable and unstable operation of the fan

Contributed by the Gas Turbine Division and presented at the Gas Turbine Conference and Exhibit and Solar Energy Conference, San Diego, California, March 12–15, 1979 of THE AMERICAN SOCIETY OF MECHANICAL ENGINEERS. Manuscript received at ASME Headquarters December 8, 1979. Paper No. 79-GT-31.

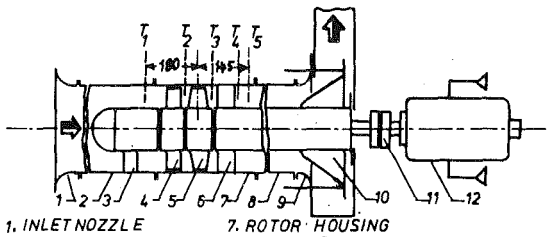

Fig. 2 Schematic lay-out of an axial flow fan

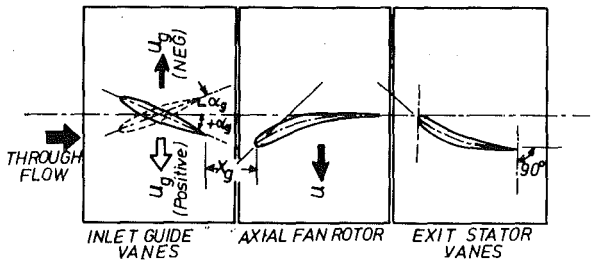

Fig. 3 Schematic arrangement of inlet guide vane, rotor and exit stator vanes at the hub section

was running and the rotation could be regulated through a braking mechanism. Provision was made for traversing the two-dimensional and three-dimensional probes at planes T_1, T_2, T_3, T_4 and T_5, for a radial survey of flow condition. The speed of the fan and freely rotating inlet guide vane row was measured with the help of contactless magnetic pick-ups and universal electronic counters.

A 10 kW cradle type d-c dynamometer capable of running from 2000 to 9000 rpm was used as a drive motor for the fan. The volume flow was regulated by means of a throttle cone and the inlet nozzle was used for the measurement of volume flow. Three hole wedge type probes were used for measuring the flow condition at upstream and downstream of the fan (planes T_1 and T_4) and five hole probes were used to measure the three-dimensional flow condition at the inlet and outlet of the axial fan rotor (planes T_2 and T_3).

The inlet guide vanes were fixed at an angle α_g and at an axial distance X_g, upstream of the rotor as illustrated in Fig. 3. Four sets of inlet guide vanes were used for the present studies. The first set of guide vanes were straight uncambered and of thickness distribution according to NACA 0015. A cambered guide vane derived from NACA 65 (12)10 was used for the second set of guide vanes. Sets III and IV of inlet guide vanes had the same blade section as that of set I, but with a reduced blade height not fully occupying the annulus (Partial guide vanes) [10].

The axial fan rotor used in the current investigations was designed for free vortex flow condition, for a hub-tip ratio of 0.4 and a tip diameter of 250 mm, flow coefficient of 0.4 and the energy coefficient 0.3. Untwisted exit stator vanes of circular arc camber were provided at the rotor outlet to remove the rotational component of velocity present in the flow leaving the rotor.

Experimental Program

The performance of the fan was first studied without inlet guide vanes and later with a guide vane row at rotor inlet for the two cases (1) freely rotating and (2) fully braked. The experimental investigations with uncambered inlet guide vanes (IGV), comprised of the determination of the following curves; viz. $\psi = f(\phi)$, $\gamma = f(\phi)$ and $\eta = f(\phi)$, at a constant rotor speed and a detailed flow measurement at different stations T_1, T_2, T_3, T_4 and T_5. Five axial distances X_g, namely 33, 28, 23, 18 and 13 mm and three guide vane settings 0 deg and ±10 deg for each of the X_g have been studied. Optimum value of X_g was obtained. For $X_{g\text{opt}}$ tests were conducted for α_g values 0 deg., ±10 deg, ±20 deg and ±30 deg also and the value of the optimum setting angle was determined after analyzing the performance characteristics. The tests for determining $X_{g\text{opt}}$ and $\alpha_{g\text{opt}}$ were made with uncambered IGV. Tests with cambered guide vanes and partial guide vanes were conducted only for the optimum distance and setting angle. The critical flow coefficients marking incipience of return flows at rotor inlet and outlet were determined from the axial velocity measurements and the extent of blade height affected by return flows was also determined.

Determination of Flow Parameters

The different parameters used to evaluate the performance and flow condition are determined in the following way:

1 Volume Flow = $V = \alpha_n \cdot A_n \cdot \sqrt{\frac{2}{\rho} \cdot \Delta p_n}$, m^3/s (1)

where

α_n = discharge coefft. of inlet nozzle
A_n = area of cross section of the nozzle, m^2
ρ = density of air, kg/m^3
Δp_n = static pressure difference across the nozzle, N/m^2

Flow coefficient = $\phi = c_m/u_t$ (2)

c_m = mean axial velocity = V/A_0
u_t = blade tip speed: $2 \cdot \pi r_t \cdot n$
A_0 = annulus area at rotor inlet $\pi(r_t^2 - r_h^2)$

2 Specific work = $W = (p_D - p_S)/\rho$ (3)

where

p_D = average static pressure at the discharge side of the fan, N/m^2
p_S = average static pressure at the suction side of the fan, N/m^2

Energy Coefficient = $\psi = 2W/u_t^2$ (4)

3 Fluid power $N_{\text{eff}} = \rho VW$ (5)

4 Coupling Power = $N_c = 2\pi nT$, Watts (6)

where the torque, T, is measured at the dynamometer, Nm

Power coefficient = $\gamma = \left(N_c \Big/ \frac{\rho}{2} \cdot A_0 \cdot u_t^3\right)$

Nomenclature

A_n = area of the inlet nozzle, m^2
A_0 = annulus area at rotor inlet, m^2
c = absolute velocity, m/s
c_m = axial velocity, m/s
c_u = tangential velocity, m/s
n = speed of the fan, rpm, rps
n_g = speed of inlet guide vane row, rpm, rps
N_c = coupling power, Watts
N_{eff} = Fluid power: ρVW, Watts
p = static pressure, N/m^2, mm of water
p_0 = stagnation pressure, N/m^2, mm water
r = radius, mm
T = torque, Nm
u = peripheral velocity, m/s
V = volume flow, m^3/s
W = specific work, Nm/kg
X_g = inlet guide vane axial distance from rotor inlet, mm
α_g = inlet guide vane setting angle with respect to axial direction, deg
α_y = yaw angle with respect to axial direction, deg
γ = power coefficient: $N_c \Big/ \left(\frac{\rho}{2} \cdot A_0 \cdot u_t^3\right)$
η = efficiency
θ = pitch angle, deg
ρ = density, kg/m^3
ϕ = mean flow coefficient: c_m/u_t
ψ = energy coefficient
IGV = inlet guide vanes
Coefft. = coefficient

Subscripts

1 = conditions at rotor inlet
2 = conditions at rotor outlet
c = critical condition
h = hub of rotor
t = tip of rotor
S = suction side of the fan
D = delivery side of the fan

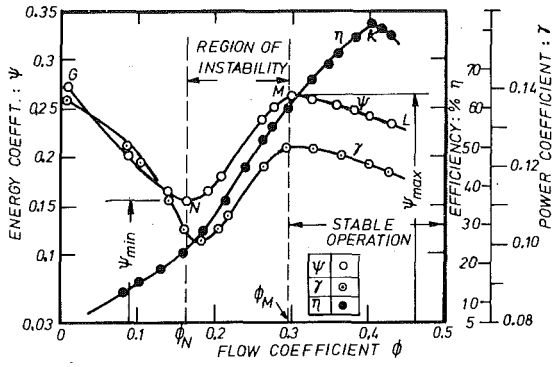

Fig. 4(*a*) Performance characteristics of axial flow fan without inlet guide vanes

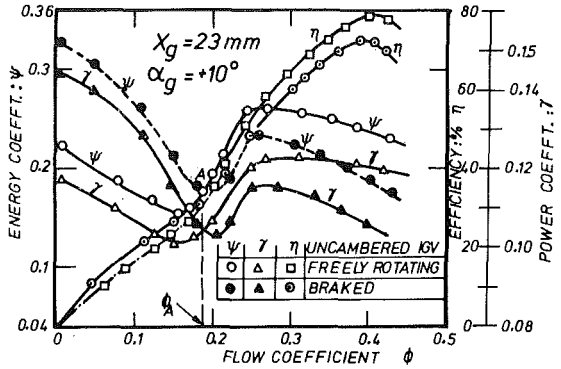

Fig. 4(*b*) Axial flow fan characteristics with inlet guide vanes X_g = 23 mm; α_g = 10 deg

5 Efficiency = $\eta = \rho VW/N_c$ (7)

6 Flow velocity = $c = \sqrt{\frac{2}{\rho} \cdot q}$

where q = dynamic pressure, N/m^2

7 Axial velocity = $c_m = c \cdot \cos\theta \cdot \cos\alpha_y$
Tangential velocity = $c_u = c \cdot \cos\theta \cdot \sin\alpha_y$
Radial velocity = $c_r = c \cdot \sin\theta$
α_y = yaw angle; θ = pitch angle (8)

Results and Discussion

Influence of IGV on the Characteristics. Figure 4(*a*) shows the performance characteristics of the fan without inlet guide vanes. As the flow is throttled, the energy coefficient gradually increases to a maximum value of 0.26 at about $\phi = 0.3$ and then gets reduced suddenly to reach a value $\psi = 0.15$ at $\phi = 0.15$, marked MN on the characteristic. For $\phi < 0.15$, the value of ψ increases much faster to reach a value of 0.27 at $\phi = 0$. The drop MN in the performance characteristic is attributed to the stalling of rotor blades and indicates the unstable operation of the machine.

The phenomenon of rotor blade stalling is understood as a result of flow separation on the blades in consequence of too large angles of incidence, as well as due to changes in radial equilibrium leading to strong radial flow velocities and finally accompanied by two return flow areas R_1 and R_2, Fig. 1. At zero delivery G, the two vortices R_1 and R_2 increase so much that the suction and pressure sides are filled up. In spite of lack of main flow, often the highest pressure rise occurs at G, which could be due to the flow passing the rotor more or less radially and therefore pressure rising as in radial blades. From the study of typical variations of meridional loadings, it was observed that away from the maximum efficiency point, K, the axial velocity c_m distribution is no longer uniform.

Figure 4(*b*) shows the characteristic curves of the fan with an inlet guide vane row for X_g = 23.mm and α_g = +10 deg. It is observed that the characteristics for freely rotating and braked inlet guide vanes cross at a point A and the conditions at this point are denoted by ψ_A and ϕ_A. At high flow coefficients in the stable operating region the direction of rotation of inlet guide vanes was opposite to the rotation of the rotor for $+\alpha_g$ [10]. As the flow was throttled, the speed of the freely rotating guide vane row gradually reduced and reached zero at $\phi = \phi_A$ and for flows below ϕ_A, the rotation of the guide vanes reversed to that of rotor rotation. For $\phi < \phi_A$, the speed of the inlet guide vanes increased at a much faster rate towards the zero volume. For negative setting angles $-\alpha_g$ the rotation was in the same direction as the fan rotor. The speed got reduced as the flow was throttled and reached a minimum value at a particular flow coefficient and further reduction in volume flow resulted in an increase of the speed of rotation of guide vanes without any change in the sense of rotation. At high flow coefficients the rotation of inlet guide vanes is induced by the main flow passing through the guide vane channels, but at reduced volumes the return flows from the rotor at inlet with strong peripheral components have a predominant influence on the rotational behavior of the inlet guide vanes and hence under this influence they rotate at high speed in the direction of rotor rotation.

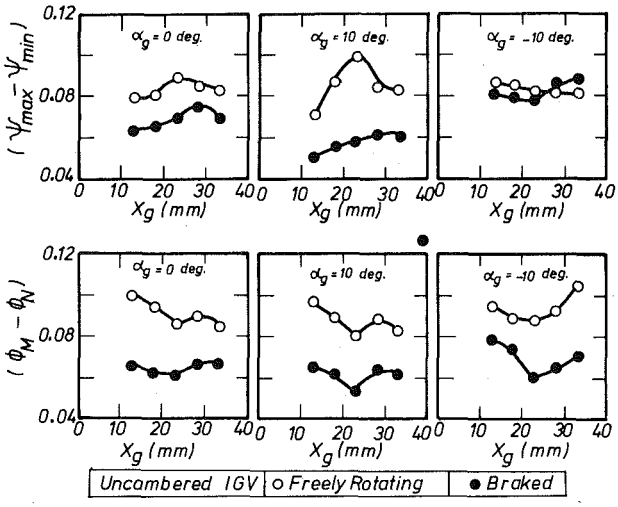

Fig. 5 Influence of X_g and α_g on $(\psi_{max} - \psi_{min})$ and $(\phi_M - \phi_N)$

Point A in Fig. 4(*b*) for $+\alpha_g$ and a similar point for $-\alpha_g$, refer to similar flow condition inside the fan, when rotor blades are stalled and ϕ_A indicates the limit below which the return flow has a marked influence on the rotational behavior of the guide vanes. For the sake of brevity of the paper, the performance characteristics and the results of flow surveys for all X_g and α_g are not included in this paper, but were presented in detail by the author in his report [10]. The variation of ϕ_A, $(\phi_M - \phi_A)$, $(\psi_{max} - \psi_{min})$, and $(\phi_M - \phi_N)$ were plotted as a function of axial distance X_g for different values of α_g. The region of instability given by $(\phi_M - \phi_N)$, Fig. 5, has a smaller value for the axial distance X_g = 23 mm and α_g = +10 deg. Considering the value of maximum ψ and the corresponding efficiency the performance characteristic for X_g = 23 mm and α_g = +10 deg are found to have ψ_{max} and efficiency higher in magnitude and occurring at a smaller ϕ_M indicating an improvement in stable operating range compared to the fan without inlet guide vanes.

Three-Dimensional Flow Surveys

In order to explain more precisely the state of flow near the axial fan rotor blades at various flow rates, the axial velocity components of the through flow at points near the hub and tip of rotor inlet and outlet of rotor are shown as a function of mean flow coefficient, Fig. 6(*a*), for the fan without inlet guide vanes. The flow coefficients at which the backflow occurs at inlet and outlet are referred to as critical flow coefficients ϕ_{c1} and ϕ_{c2}. From figures similar to Fig. 6, for different X_g and α_g, ϕ_{c1} and ϕ_{c2} were obtained for different cases under study and the variation of inlet and outlet critical flow coefficients for uncambered inlet guide vanes are shown in Fig. 6(*b*). It could be seen that the optimum conditions, X_g = 23 mm, and α_g = +10 deg established from the performance characteristics are in good agreement with regard to the critical flow coefficients also.

It was found by the author [10] that the axial distance X_g of the

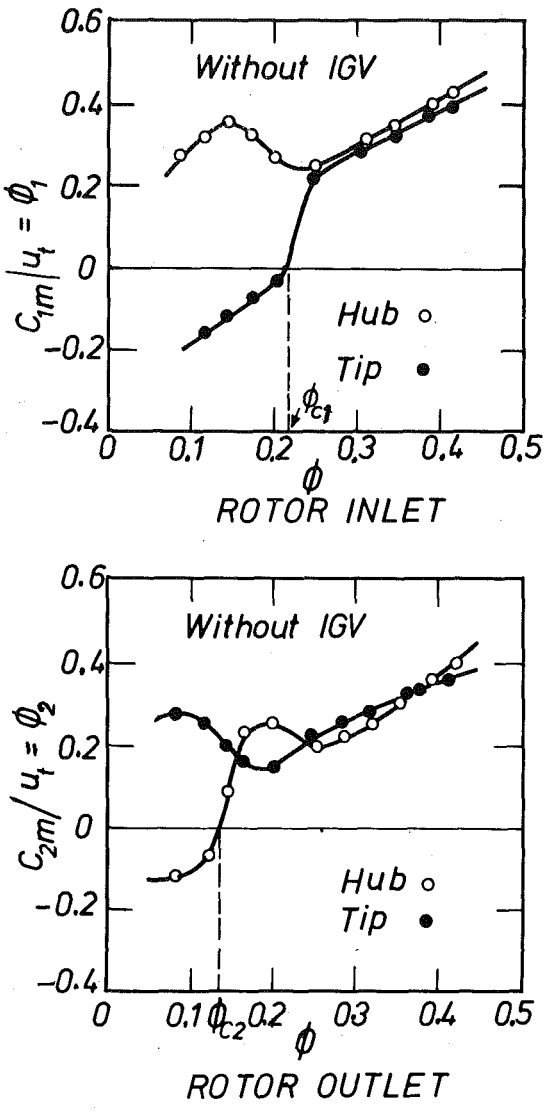

Fig. 6(*a*) Variation of axial velocity components at inlet and outlet of fan rotor without inlet guide vanes

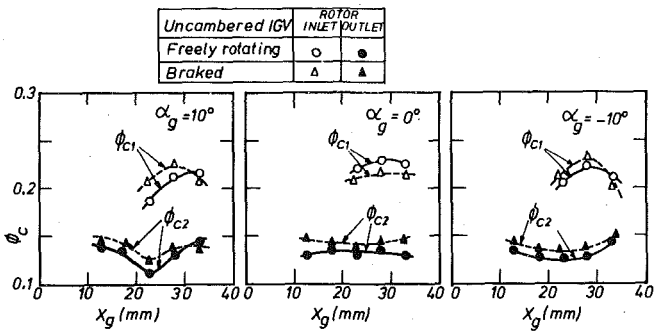

Fig. 6(*b*) Variation of critical flow coefficient ϕ_c (incipience of return flow) with inlet guide vane axial distance X_g

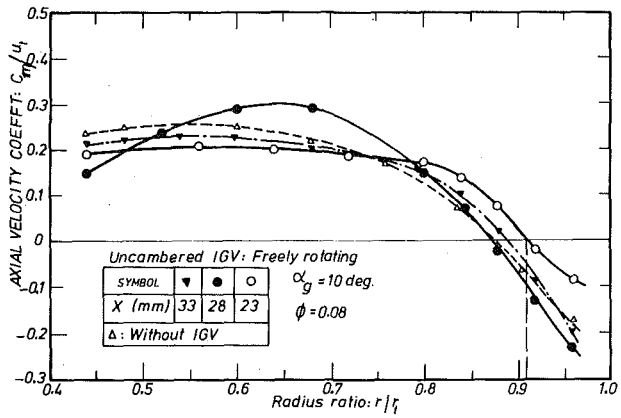

Fig. 7(*a*) Rotor inlet axial velocity distribution for stalled flow—influence of X_g

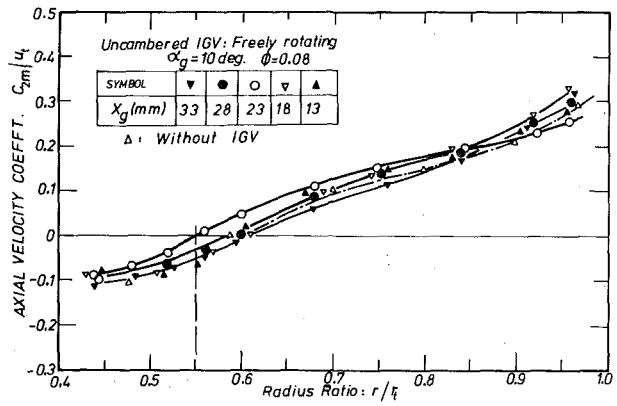

Fig. 7(*b*) Rotor outlet axial velocity distribution for stalled flow—influence of X_g

inlet guide vanes exerted a considerable influence on the return flow velocities. A slight reduction in the magnitude of return flow velocities was noted with a decrease of X_g and with an increase of X_g the magnitude of return flow velocities was found to increase. To a certain extent the reduction in X_g means the backflow fluid hits the guide vanes soon and is made to flow back into the rotor, but all the same it is observed that bringing the guide vanes too close to the rotor inlet resulted in disturbing the flow condition at entry to the rotor, whereas moving the inlet guide vane row away from the rotor, the influence of guide vanes in guiding the return flow fluid effectively into the rotor gets reduced.

The radial distribution of axial velocity at rotor inlet and outlet is shown in Fig. 7(*a*) and (*b*), for one flow coefficient in the stalled flow region for freely rotating inlet guide vanes for five distances and one vane setting $\alpha_g = 10$ deg. Of the five distances again, the arrangement of guide vanes with $X_g = 23$ mm and $\alpha_g = 10$ deg has resulted in the reverse flow occupying a smaller length of blade height as compared with the other distances. The return flow at rotor inlet occupied about 15 percent and at outlet about 25 percent of blade height with freely rotating inlet guide vanes; about 20 percent at inlet and 30 percent at outlet with braked inlet guide vanes and about 22 percent at inlet and 32 percent at outlet without inlet guide vane row. Thus the freely rotating inlet guide vanes are seen to reduce the extent of return flow areas at inlet and outlet compared to the fan without inlet guide vanes.

The variation of axial velocity components at rotor inlet and outlet for several flow coefficients and the radial distribution of axial velocity components in the stalled flow range for one typical flow coefficient are plotted in Fig. 8(a) to 8(*d*) for the different cases under study. A comparison of flow condition at rotor inlet and outlet from Fig. 8 reveals that the use of uncambered inlet guide vane row reduces the extent of return flows with respect to the fan without IGV. Freely rotating uncambered inlet guide vanes have a smaller value of critical flow coefficient compared to all other cases, Fig. 8(*a*) and (*b*). Fig. 9 shows the axial velocity distributions at different stations, 10, 25, and 35 mm upstream of the rotor for the fan without IGV indicating the extension of return flows over a longer distance upstream of the rotor, which are reduced in the presence of inlet guide vane row.

From the results of the investigations, it has been found that an appreciable increase in the useful operating range of the fan is obtained with freely rotating inlet guide vanes. Besides retaining higher specific work in the extended region of stable operation, the power coefficient was reduced obtaining higher efficiency for the corresponding volumes when compared to the fan without inlet guide

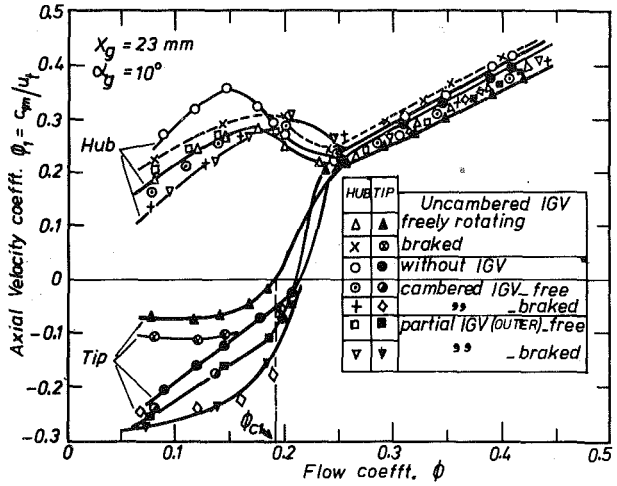

Fig. 8(*a*) Axial velocity variation at rotor inlet

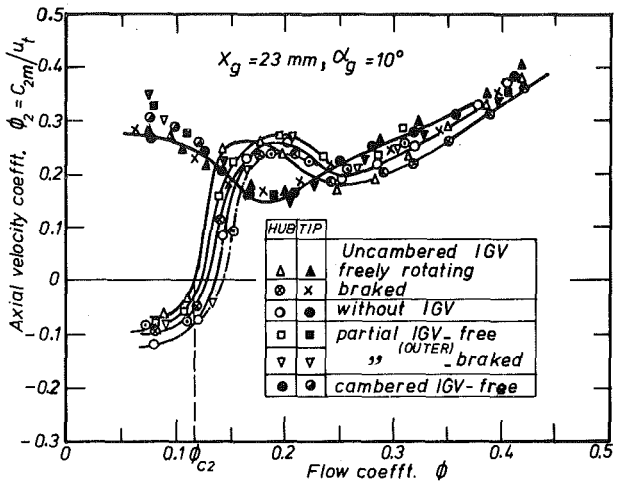

Fig. 8(*b*) Axial velocity variation at rotor outlet

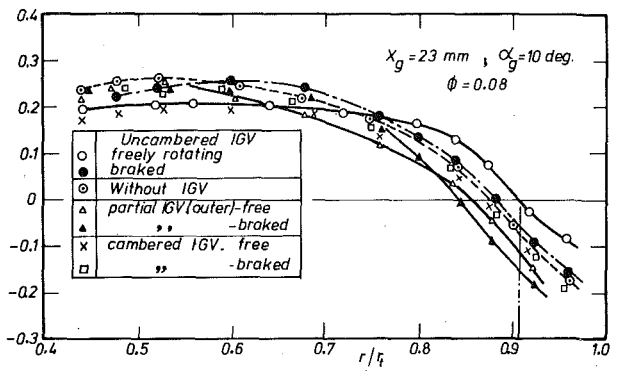

Fig. 8(*c*) Inlet axial velocity distribution for stalled flow

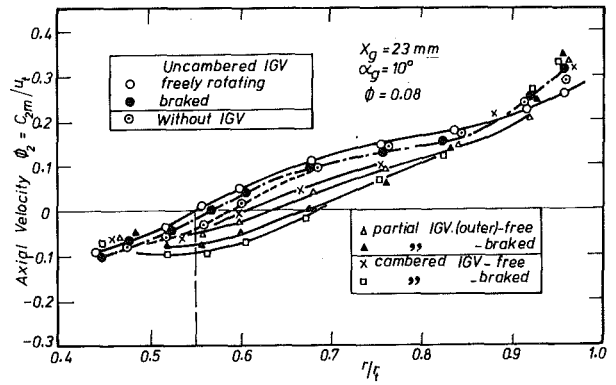

Fig. 8(*d*) Outlet axial velocity distribution for stalled flow

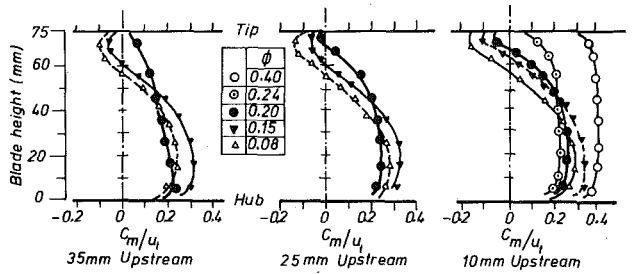

Fig. 9 Axial velocity distributions upstream of axial fan rotor without inlet guide vanes

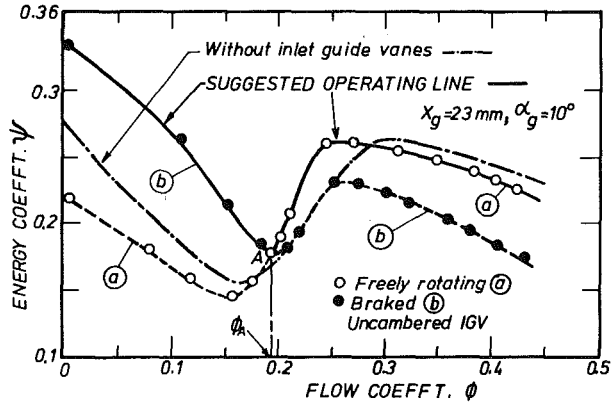

Fig. 10 Intersection of the characteristics of the fan with (*a*) freely rotating and (*b*) braked uncambered inlet guide vanes

vanes. For operation in the stalled flow range of the characteristic, higher specific work and efficiencies were obtained with braked inlet guide vanes compared to the fan without IGV as well as with freely rotating IGV, see Fig. 4(*a*) and (*b*). The region of instability as determined from the quantity $(\phi_M - \phi_N)$ is reduced from 0.14 for the fan without IGV to 0.09 with freely rotating IGV, the reduction in the region of instability being 35 percent. Better results in the performance of the fan with an essential improvement in the stalled working range could be obtained by the combined use of freely rotating and braked inlet guide vanes, if the IGV are allowed to rotate freely at higher volumes and are braked fully at lower volumes, see Fig. 10. The suggested characteristic of operation is shown by a full line, whereby the region of instability $(\phi_M - \phi_A)$ is reduced with the above combination by about 45 percent as compared to the $(\phi_M - \phi_N)$ of the fan without IGV.

Conclusions

1 An appreciable increase of 35 percent in the useful operating range of the fan is obtained with freely rotating IGV compared to the fan without inlet guide vanes.

2 For the operation of the fan in the stalled flow range, braked inlet guide vanes improve the performance better than the other two cases.

3 Essential improvement in the stable operating range is noted by the combined use of freely rotating and braked IGV.

4 An axial distance of X_g of about 40 percent (23 mm axial distance) of rotor blade chord and $\alpha_g = +10$ deg, giving prewhirl in the direction of rotation of the fan rotor were found to be the optimum values for the rotor tested.

5 The extent of return flows are reduced by the use of an inlet guide vane row.

Remarks

A method of improvement of stable operating range of an axial fan rotor and reduction of return flows has been suggested with the help

of the present work. But in order to make generalizations it is necessary to conduct tests on more rotors of varying designs.

References

1 Scheer, W., "Untersuchungen und Beobachtungen uber die Arbeitsweise von Axialpumpen unter besonderer Berucksichtigung des Teillastbereiches," *B.W.K.*, 11, 1959, pp. 503–511.

2 Toyokura, T., and Kubota, N., "Studies of the Backflow Mechanism of Turbomachines," Part 1, *Bulletin of JSME.*, Vol. 11, No. 43, 1968, pp. 147–156.

3 Pfleiderer, C., "Die Kreiselpumpen," 4 Aufl, Springer, 1955, pp. 383.

4 Ida, T., "Characteristics and Flow Conditions of a Forced Vortex Impeller of an Axial fan," *Bulletin JSME.*, Vol. 13, No. 60, June 1970.

5 Keller, C., *The Theory and Performance of Axial Flow Fans*, McGraw Hill, New York, (1937), pp. 100–104.

6 Bell, B. E., "Test of a Single state Axial Flow Fan," NACA Rep. No. 729, 1942.

7 Ponomareff, A. I., "Axial Flow Compressors for Gas Turbines," *Trans ASME.*, Vol. 70, 1948, pp. 295–306.

8 Tanaka, S., and Murata, S., "On the Partial Flow Rate Performance of Axial Flow Compressor and Rotating Stall," *Bulletin JSME.*, Vol. 18, Nov. 1975, pp. 1277–1284.

9 Pfleiderer, C., "Vorausbestimmung der Kennlinien Schnelläufiger Kreiselpumpen," Berlin, 1938.

10 Venkatrayulu, N., "Some Investigations on the Off-design Performance of an Axial flow fan," Ph.D. Thesis Indian Institute of Technology, Madras, India, June 1974.

R. P. Dring
Supervisor.
Gas Turbine Technology

M. F. Blair
Research Engineer.
Mem. ASME

H. D. Joslyn
Research Engineer.

United Technologies Research Center
East Hartford, Conn.

An Experimental Investigation of Film Cooling on a Turbine Rotor Blade

Film cooling has been studied on the rotor blade of a large scale (low speed) model of a high pressure turbine first stage. Film coolant was discharged from single holes on the pressure and suction surfaces of the airfoil. For each blowing site the coolant to free stream mass flux ratio and density ratio were varied from 0.5 to 1.5 and from 1.0 to 4.0 respectively. Both surface flow visualization and local film cooling adiabatic effectiveness data were obtained. The observation was made that although it can have a strong radial component, the trajectory of the film coolant was very insensitive to coolant flow conditions. The existence of the radial component of the film coolant trajectory was found to have a strong impact on the nature of the effectiveness distribution. The data have been compared with data taken by other investigators on flat surfaces and in plane cascades. Agreement between the flat plate data and the suction surface data was reasonably good. However, the pressure surface results showed a much faster decay of the effectiveness than did the flat plate data due to effects thought to be related to both curvature and radial flow.

Introduction

With the evolution of gas turbine cycles with higher turbine inlet temperatures has come the need for increasingly effective means of cooling the turbine airfoils. One such cooling technique currently receiving wide application is film cooling. During recent years, many parameters affecting film cooling have been intensively studied. A survey of work up to 1971 has been published by Goldstein [1]. Although the bulk of the discussion is related to slot injection, there was some discussion of isolated hole injection. Ericksen [2] investigated film cooling behind a row of inclined holes, and among other things found that the effect of Reynolds number was relatively small. A simple analytical model of the effectiveness pattern produced by a jet has been published by Ericksen, et al., [3]. Pedersen [4] also looked at a row of inclined holes including mainstream to coolant density ratio as a prime variable. This permitted him to vary the mass and momentum flux ratios independently. He presented a correlation of his results including the effects of all these variables. Liess, et al., [5] examined the effects of free stream acceleration and Mach number and found them to be small. Lander, et al., [6] measured film cooling effectiveness on a first vane cascade in an attempt to include realistic geometry and flow conditions (including free stream turbulence). Finally, Muska, et al., [7] confirmed the additive nature of the effectiveness of multiple rows of film cooling holes. Although film cooling has been applied to many turbine rotor blades, there is no background at all on the impact of rotation and radial flow on the film coolant trajectory or film effectiveness.

There are, however, numerous aerodynamic mechanisms present in a turbine rotor blade passage which can give rise to radial flows. Aside from end effects such as tip leakage and end wall boundary layer vortices there are the following: three-dimensional inviscid flow (both irrotational and rotational) and three-dimensional boundary layer flow on the airfoils. With film cooling the potential exists for an additional effect due to rotation since the density of the coolant fluid can be as high as three times that of the free stream fluid. In the absence of any information on these effects they are ignored in the typical design system. Historically it has been assumed that the radial velocity in the film is zero. Any shortcoming of this approach has been compensated for by calibrating the design system on engine experience.

Description of Test Equipment and Techniques

Test Equipment. The experimental program was carried out in a 5 ft dia rotating rig with a 1½ stage turbine model having a 0.8 hub/tip ratio. This is a low speed facility which draws ambient air (from out-of-doors) through a series of screens and flow straighteners prior to reaching the inlet guide vanes. The axial chords of the airfoils in each row of the turbine model are all approximately 6 in. (0.15 m) or approximately five times engine scale. At a typical running condition, the axial flow velocity in the test section is 75 ft/s (23 m/s) and the shaft speed is 405 rpm. Airfoil Reynolds numbers are approximately 5.6×10^5 which is typical of high pressure turbine airfoils. Because the rig also has velocity triangles typical of those of a high

Contributed by the Gas Turbine Division and presented at the Gas Turbine Conference and Exhibit and Solar Energy Conference, San Diego, California, March 12-15, 1979 of THE AMERICAN SOCIETY OF MECHANICAL ENGINEERS. Manuscript received at ASME Headquarters December 8, 1979. Paper No. 79-GT-32.

pressure turbine, it provides an excellent simulation of the centrifugal and Coriolis effects as they would occur in the boundary layers of an actual engine scale turbine airfoil. The two-dimensional aerodynamic design of the rotor and its radial stacking are typical of current turbine designs.

For these film cooling tests coolant to free stream density ratios from 1.0 to 4.0 were produced using mixtures of air and sulfur hexafluoride, SF_6 (molecular weight = 146) as the coolant fluid. A trace amount of ammonia was included in some tests for flow visualization purposes. As previously mentioned, the turbine free stream fluid was air at ambient conditions. The coolant mixtures were heated above the free stream temperature and adiabatic effectiveness was determined by measuring the free stream and coolant temperatures and the adiabatic recovery temperature distribution on the airfoil surface with a matrix of thermocouples downstream of each blowing site.

Two coolant hole locations were chosen for this study, one at midspan and ten percent axial chord on the suction surface and one at midspan and 16 percent axial chord on the pressure surface. These holes are sufficiently far aft so as to be relatively uninfluenced by the details of the leading edge flow, and yet far enough forward so as to be uninfluenced by the suction surface endwall vortices and by the strong acceleration toward the trailing edge on the pressure surface. At the suction surface location the local flow velocity is roughly five times that at the pressure surface location. It was expected that at the low free stream velocity locations, such as on the pressure surface, that the radial flow effects would be much more strongly felt than on the high velocity locations, such as on the suction surface.

A flow metering system consisting of four calibrated glass rotameters was assembled to provide precise flows of the film coolant mixture to the blowing sites at various coolant blowing rates, M, and various coolant to free stream fluid density ratios, R. The error expected from these meters is ±1½ percent on the average and ±3 percent maximum.

Blade Pressure Distribution Measurements. In order to set the coolant flow rate, it was necessary to know the free stream velocity at each blowing site. For this purpose the rotor blade midspan pressure distribution was measured at a nominal (design) value of (C_x/U_m) of 0.78. The data taken included (1) airfoil midspan surface pressures at twenty-two locations around the perimeter of the blade, (2) rotor inlet relative total pressure at midspan (from a rotor mounted Kiel probe) and (3) rotor exit tip static pressure measured on the rotor casing. The rotating frame pressures were measured using a rotor-mounted scanivalve and transducer.

When comparing measured pressures to computed pressure distributions, it is convenient to use a pressure coefficient based on the blade exit midspan static pressure ($P2$) as a reference pressure and the difference between the inlet total pressure and the midspan exit static pressure as a normalizing pressure difference ($PT1$-$P2$). It was found in all cases that the measured pressure surface maximum pressures were slightly lower than one would expect from the measured rotor inlet total pressures. This difference, however, is only about one percent of the rotor exit relative dynamic pressure. This effect is probably related to radial flows in the rotor channel shifting the location of the high and the low total pressure fluid between the inlet total pressure probe (which is at the rotor leading edge plane) and the 30 percent chord location where the pressure surface pressure is near its maximum. In all cases the total pressure that was inferred from the pressure surface was used in evaluating the airfoil distributions. The midspan exit static pressure was determined by applying a correction to the static pressure measured on the rotor exit tip casing. This correction was based on the assumption of free-vortex flow. This is a very small correction (roughly one percent of the rotor exit relative dynamic pressure) and hence the slight inaccuracy associated with the assumption of free-vortex flow is negligible. The results are shown as data points in Fig. 1.

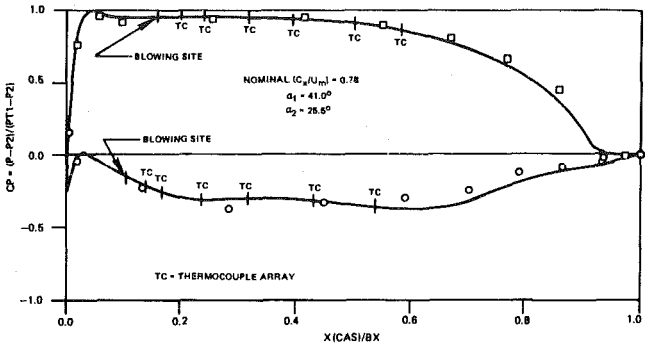

Fig. 1 Rotor midspan pressure distribution

The computed curve in Fig. 1 is based on an inviscid potential flow calculation [8]. The inlet and exit flow angles (α_1 and α_2 measured from tangential) were adjusted to give best agreement with the measurements. The predicted trailing edge stagnation point singularity has been eliminated in favor of the more physically realistic trailing edge condition of a base pressure equal to the downstream static pressure ($C_p = 0$). This affects the pressure distribution over less than the aft-most ten percent of the airfoil, i.e., X/BX from 0.9 to 1.0.

In general the measured and computed pressure distributions are in excellent agreement. The agreement is especially good in the leading edge region where the film coolant blowing sites are located. The suction and pressure surface blowing sites are 10 and 16 percent axial chord respectively from the leading edge as indicated in Fig. 1. From these results it has been determined that the local surface flow velocities at the suction and pressure surface blowing sites are (as a fraction of rotor midspan wheel speed) 2.05 and 0.40 respectively at the design point value of (C_x/U_m). This corresponds to 196 and 38 ft/s at a typical running condition of 405 rpm. The error expected in these velocities is ±1 percent for the suction surface and ±5 percent for the pressure surface. These results were used to compute the various film coolant mass flow rates required to achieve the desired values of the coolant to free stream mass flux ratio, M and the coolant to free stream density ratio, R.

Flow Visualization Tests. The first phase of the film cooling test program consisted of a series of flow visualization tests employing ammonia and Ozalid paper. The objective of these tests was to qualitatively determine the nature of the film coolant footprint on the airfoil surface downstream of each blowing site for the full range of density ratios, R, and blowing rates, M, to be studied in the program. These flow visualization film cooling patterns could then be employed to determine the effectiveness instrumentation arrays.

Both the flow visualization and effectiveness test airfoils were fabricated by casting duplicates of machined aluminum rotor blades (B_x = 6.34 in., 16.6 cm) with rigid urethane foam. This particular foam material was selected for its extremely low thermal conductivity (0.02

Nomenclature

B_x = airfoil axial chord
C_x = axial component of flow velocity
D = discharge hole diameter
I = momentum flux ratio: $(\rho V^2)_c/(\rho V^2)_f$
M = mass flux ratio: $(\rho V)_c/(\rho V)_f$
R = density ratio: (ρ_c/ρ_f)
Re_D = blowing site Reynolds number: $(\rho_f V_f D/\mu)$
S = surface arc length
T = temperature
U_m = wheel speed at midspan
V = flow velocity
X = axial distance
β = angle between the discharge hole axis and a plane tangent to the airfoil surface
δ^* = boundary layer displacement thickness
η = cooling effectiveness: $(T_s - T_f)/(T_c - T_f)$
ρ = fluid density
μ = fluid absolute viscosity

Subscripts

c = coolant
f = free stream
s = surface

to 0.03 Btu/hr ft °F). While this property is unimportant to the flow visualization tests it is important in the measurement of local film effectiveness [9].

The foam airfoils were fabricated using the following procedure. First holes (⅛ in. dia, 3.2 mm) were drilled into the aluminum rotor blade. The hole locations are known to within 0.3 percent of axial chord which is a relatively small fraction of the hole diameter. Each hole is inclined at an angle of 30 deg to the surface. The plane of each hole was set such that the axis of the hole is tangent to a cylindrical surface intersecting the airfoil at the location. The result is that all of the holes are oriented in the streamwise direction with no radial component. Next a hydrocalic cement mold was cast around the metal blade with drill rods inserted in the coolant holes. Finally the rigid foam was cast in the concrete mold producing a precise copy of the original metal blade.

With the flow visualization airfoils mounted on the rotor and a piece of Ozalid paper mounted on the airfoil surface behind the blowing site the rig was brought up to the desired running conditions of through flow velocity (C_x) and midspan wheel speed (U_m) such that the nominal design point velocity triangles (i.e., C_x/U_m) were obtained. The flow metering device was then connected to one of the blowing sites and the air and sulfur hexafluoride (SF_6) flow rates were adjusted until the desired coolant to free stream density ratio R, and coolant to mainstream mass flux ratio, M, were obtained. When the flow was established, a trace amount of ammonia was introduced into the film coolant flow. The amount of ammonia was always less than one percent of the total coolant mass flow so it had a negligible effect on both the R and M ratios. A strobe light triggered with a once per revolution pulse from the rotor shaft was used to observe the flow trace on the ozalid paper. After a trace of suitable darkness had been achieved, the ammonia was turned off and the lines were flushed with ammonia free flow. The flow metering device was then connected to the rotary union channel leading to the other blowing site and the process was repeated.

Figure 2 is a typical example of the flow visualization results. Traces are shown for a low M ratio and for both the suction and pressure surface blowing sites at nominal density ratios, R of 1 and 4. In all cases the suction surface film coolant trajectory is narrow, straight and has only a slight radial displacement. The pressure surface trajectory on the other hand is much wider, displays noticeable curvature, and has a strong radial displacement (roughly 30 deg radially outward). In comparing the various traces, it must be kept in mind that the relative darkness of each trace is primarily a function of how long the ammonia was allowed to flow. It should not be related directly to film coolant effectiveness. The trace width is also a function of the ammonia flow time but to a much lesser degree.

In order to gain additional insight into the flow mechanisms occurring in the experiment, a very small amount of pure ammonia was passed through both blowing sites. It was expected that this would indicate the nature of the flow over the blade in the absence of film coolant discharge. The results were virtually identical to those of Fig. 2. This indicates that it is unlikely that the pressure surface radial flow is due to a three-dimensional boundary layer since if this were the case the flow visualization trace direction would be expected to change somewhat when going from very low to very high blowing rates as the coolant jet penetrated the free stream. Such a change in direction was not observed to occur. The suction and pressure surface film coolant trajectories appear to be simply following the three-dimensional inviscid flow over the airfoil. Without a fully three-dimensional rotating frame cascade flow analysis, it is difficult to say with certainty what aspects of the rotor design have produced the radial flows.

Effectiveness Measurement. Upon completion of the flow visualization tests, the fabrication of two instrumented effectiveness airfoils was initiated. The two airfoils were cast using the previously discussed low thermal conductivity urethane foam. One airfoil had the suction surface blowing site (at ten percent chord) and the other airfoil had the pressure surface blowing site (at 16 percent chord). These airfoils were cast with thermocouples (TC's) mounted internally in the film coolant supply lines so that the coolant temperature could be measured immediately prior to ejection at the airfoil surface. Airfoil surface TC arrays located downstream of each blowing site were determined on the basis of the flow visualization results. The streamwise positioning, the radial extent and the locations where TC's were concentrated were all based on the flow visualization results. Figure 3 shows the array on the airfoil with the pressure surface blowing site. Six rows of hole pairs (two for each TC) can be seen with 8 to 12 thermocouples mounted in each row. The TC rows have been shown in relation to the airfoil pressure distribution in Fig. 1. One mil (0.025 mm) dia chromel-alumel thermocouples were welded to three mil (0.075 mm) dia chromel-alumel wires in internal chambers on each airfoil. These heavier leads then passed out of the airfoils through the hub attachment buttons. When all the TC's were mounted, a thin coat of varnish was applied to the test surfaces to hold the TC's firmly in position and to restore the surface smoothness.

For the effectiveness tests the "coolant" fluid passed from the calibrated metering system through the rotary union, through an electrical heater, and into each airfoil. The heater was used to bring the coolant gas flow to a temperature approximately 50°F above that

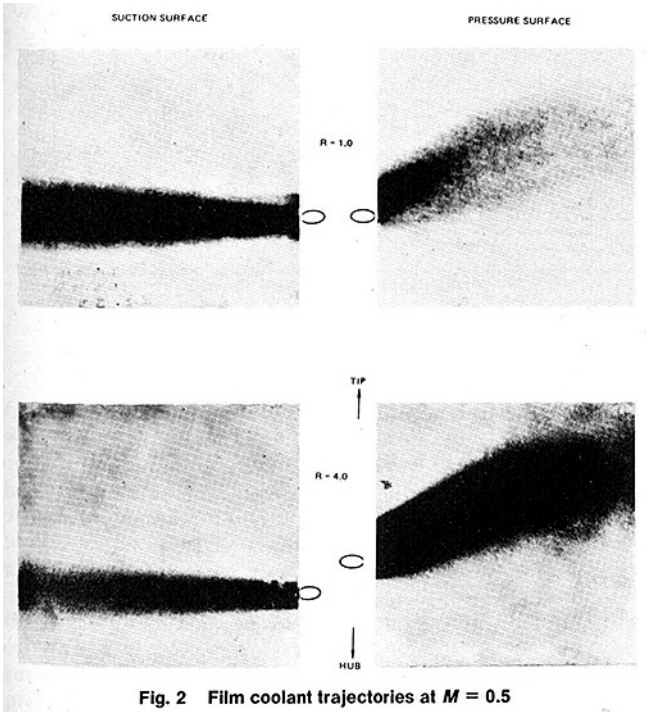

Fig. 2 Film coolant trajectories at $M = 0.5$

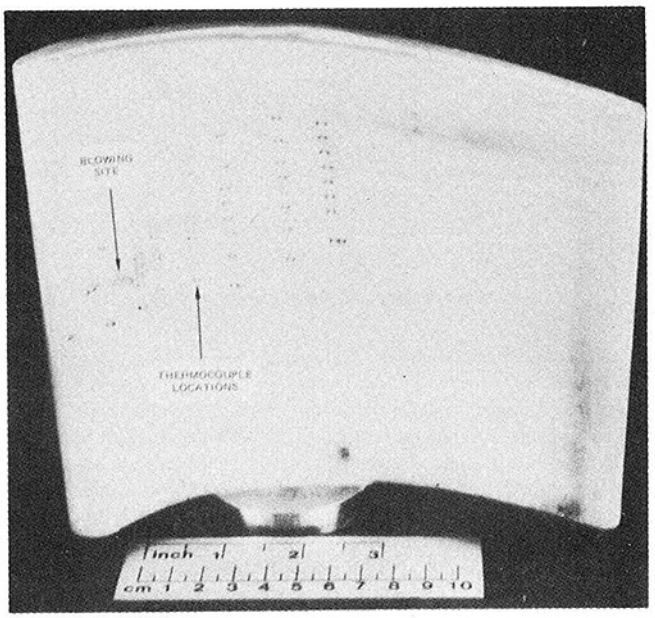

Fig. 3 Thermocouple array locations on the pressure surface

of the mainstream fluid. The *TC* lead wires from both airfoils were connected to a 144 channel *TC* scanning system mounted on the rotor (near the rig axis). The *TC* scanner communicated digitally with the rig data acquisition system computer. This digital communication eliminated all difficulties associated with slip-ring noise on analog signals.

The coolant supply system was designed to provide a coolant mixture to one blade at a time. For each flow condition, one blade was film cooled and the other blade provided a convenient and accurate station to measure the free stream adiabatic wall recovery temperature. Individual thermocouples on the film-cooled blades were calibrated by recording indicated temperatures with no cooling air flowing. All *TC* calibration corrections were less than or equal to 0.5°F.

Discussion of the Results

Typical results of the testing on the suction and pressure surfaces for twelve combinations of M and R ratios on each surface are shown in Figs. 4–7. A complete presentation of all the results is available in [10]. The figures illustrate the profiles across the film coolant footprint at each array of *TC*'s. Sketched below them are iso-effectiveness contours that have been inferred from the profiles. Several thermocouples became inoperative during the final stages of model fabrication, during installation in the rig and during testing. In total, six out of the total of 130 *TC*'s were inoperative. All of the bad *TC*'s were on the suction surface, and they have been indicated in Figs. 4 and 5. Due to this loss of instrumentation, some interpolation had to be employed in constructing the effectiveness profiles on the suction surface. In areas where this was done, the profiles have been drawn with dashed lines. The uncertainty in all measured temperatures is estimated to be 0.7°F. This can be shown by the method of [11] to result in an uncertainty in the effectiveness of at most 0.02. As a result of this the locations of the 0.02 contours, and also, but to a lesser degree, the 0.05 contours, are not considered precise. For this reason, they have been drawn in as dashed lines in all of the figures. The degree to which most of the effectiveness profiles return to zero on either side of the footprints is indicative of the uncertainty in the results.

The film cooling patterns obtained from the separate flow visualization and film effectiveness tests were consistent for all tests on both the suction and pressure surfaces. As an example, the effectiveness patterns (Figs. 4–7) can be seen to bear close resemblance to the flow visualization patterns (Fig. 2). The suction surface effectiveness footprint is narrow and has only a slight radially outward deflection. Even though the maximum effectiveness and the footprint width vary markedly over the range of M and R tested, the location of the centerline of the footprint appeared to be insensitive to these variables. As in the flow visualization tests, the pressure surface effectiveness footprint was wide and exhibited a large radial deflection. The maximum effectiveness and the footprint width on the pressure surface, however, both appear to be far less sensitive to M and R than on the suction surface.

The different widths of the suction and pressure surface coolant patterns are somewhat analogous to the differences in film coolant coverage that can be achieved through the use of compound angled blowing holes as opposed to simple streamwise blowing. Generally speaking, compound blowing can result in a much wider film coolant effectiveness footprint than simple streamwise blowing [12, 13]. On the suction surface the major axis of the cooling hole is parallel to the film coolant trace, and the result is a relatively narrow trace which is typical of simple streamwise blowing. In contrast to this, the major axis of the pressure surface hole is at an angle of approximately 30 deg to the film coolant trace, and this has produced the much wider film coolant footprint characteristic of compound blowing. As mentioned in the discussion of the flow visualization tests, it appears that the film coolant trajectory is governed primarily by the nature of the undisturbed flow over the airfoil, i.e., in the absence of film cooling. Centrifugal and Coriolis forces may be important in determining the nature of the undisturbed flow, but beyond that, they appear to have no significant impact on film coolant trajectory.

The basic conclusions of the experiment are that there is a strong radial component to the pressure surface film coolant trajectory and that both the suction and pressure surface trajectories are very insensitive to both the density ratio, R, which was varied over a range from 1 to 4 and the mass flux ratio, M, which was varied over a range from 0.5 to 1.5.

The fact that film coolant trajectory is insensitive to coolant flow conditions eliminates one of the concerns of the turbine designer. However, one must keep in mind that the pressure surface coolant

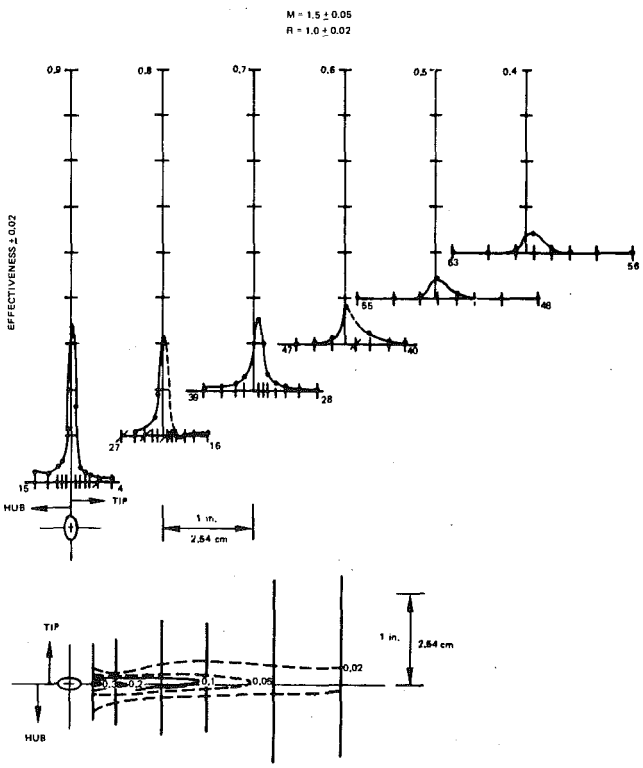

Fig. 4 Suction surface film cooling

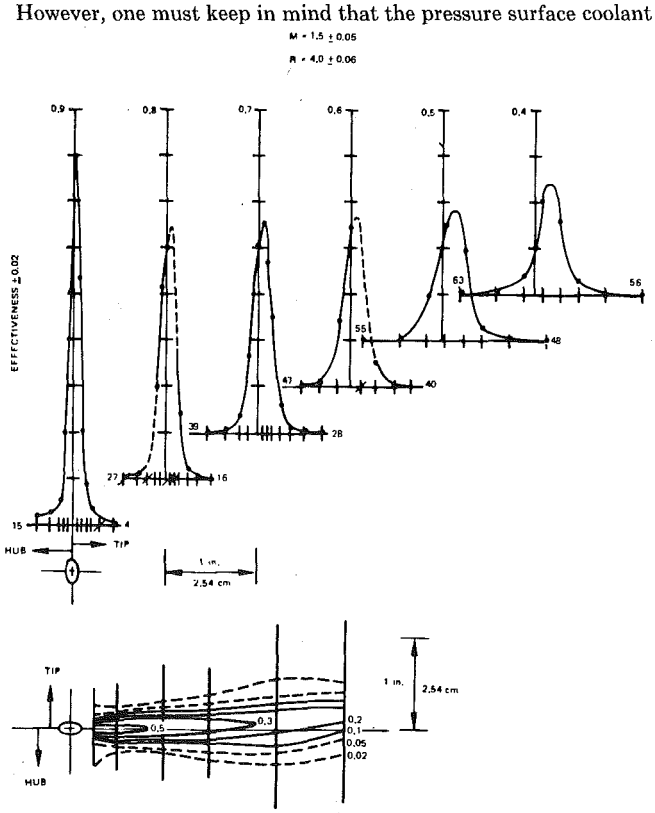

Fig. 5 Suction surface film cooling

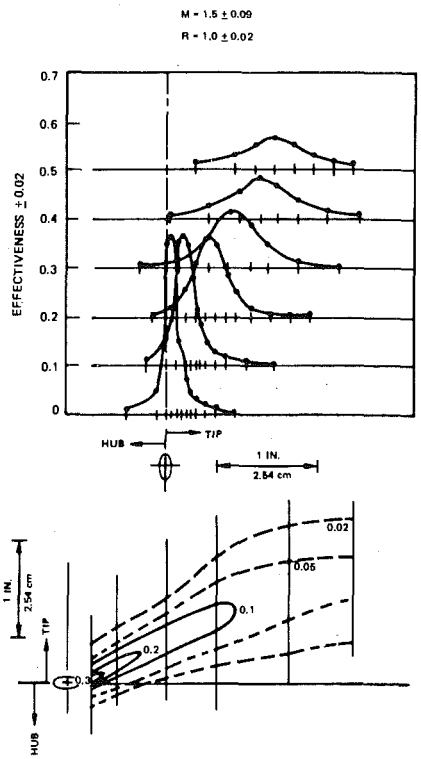

Fig. 6 Pressure surface film cooling

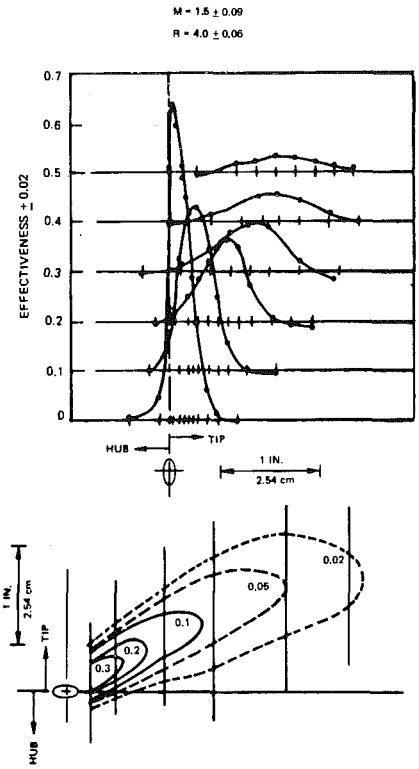

Fig. 7 Pressure surface film cooling

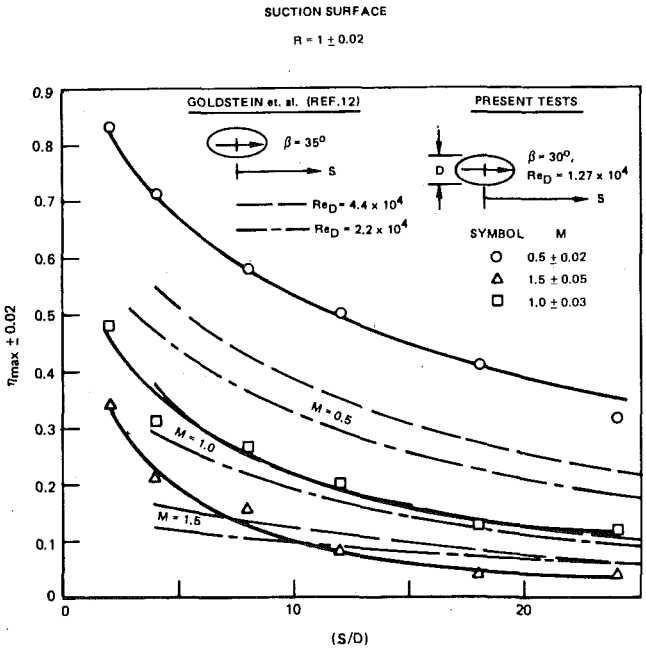

Fig. 8 Decay of maximum effectiveness

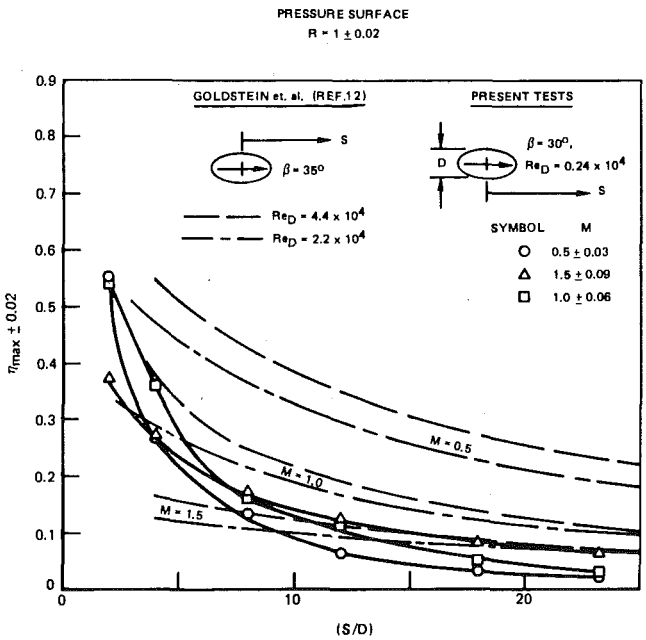

Fig. 9 Decay of maximum effectiveness

trajectory represents a wide departure from typical design system assumptions. This can give rise to two problems. First, large portions of the airfoil surface downstream (axially) of the coolant discharge hole will be starved of film coolant since this air will have moved radially outward toward the tip of the airfoil. The second problem arises in that compound angled holes are frequently used to achieve improved film cooling coverage on turbine airfoil surfaces. These holes are generally oriented under the assumption of purely axial flow on the airfoil surface. If the radial flow occurring on the blade pressure surface was aligned with the compound hole angle, the enhanced film coverage would not be achieved. The result of both of these possible problems would be burning near the airfoil pressure surface trailing edge in the region downstream of the blowing sites experiencing maximum radial flow.

The effectiveness data taken during the present program have been compared to flat plate wind tunnel data reported by Goldstein, et al. [12]. There were, however, some differences between the present film cooling test conditions and those of [12]. For the present program, the suction and pressure surface holes are at 30 deg to the surface, but in the tests of [12], the holes were at 35 deg to the surface. For the present program, the pressure and suction surface blowing site Reynolds numbers (Re_D) are 0.24×10^4 and 1.27×10^4, respectively, whereas for the tests of [12] values of 2.2×10^4 and 4.4×10^4 were employed. This difference is not believed to be important since the data of [1,

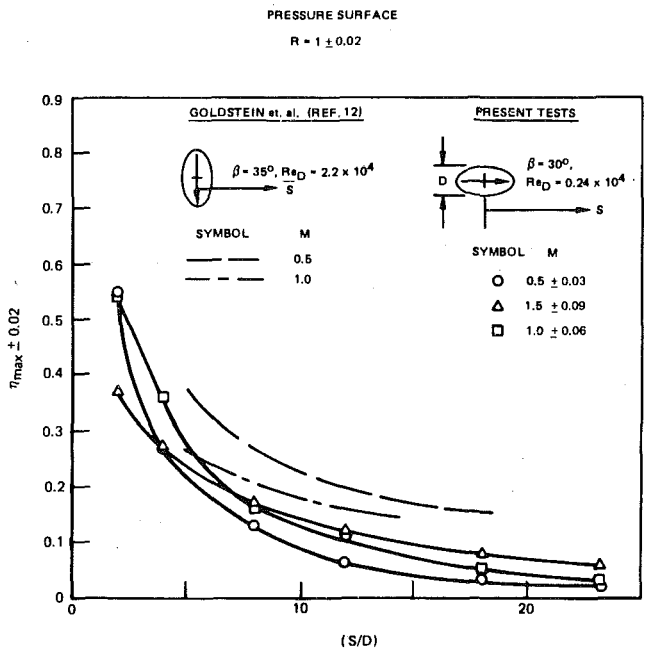

Fig. 10 Decay of maximum effectiveness

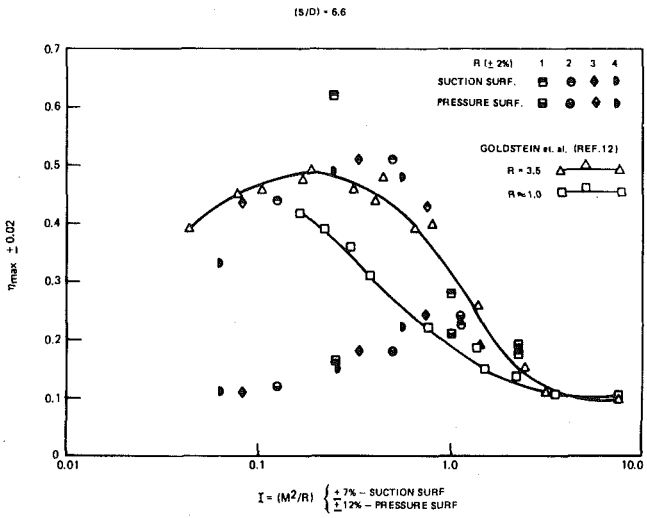

Fig. 11 Maximum effectiveness as a function of momentum flux ratio and density ratio

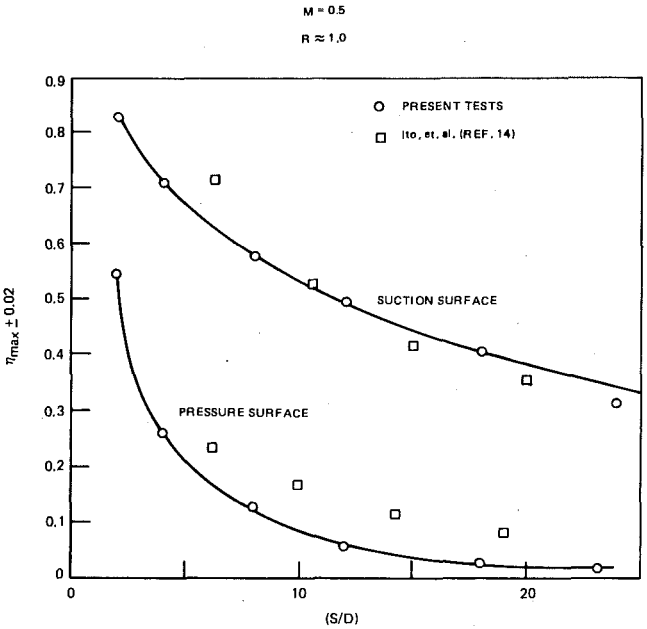

Fig. 12 Decay of maximum effectiveness

5] indicate that film effectiveness is insensitive to Reynolds number. Most of the data reported in [12] are for a normalized displacement thickness (δ^*/D) of 0.116. For the present tests, (δ^*/D) is 0.036 and 0.059 on the suction and pressure surfaces respectively. The reduced coolant injection angle and (δ^*/D) ratio of the present tests would both be expected to produce effectivenesses slightly higher than those of [12]. This generally did not turn out to be the case as shall become apparent in the following paragraphs.

The suction surface data are compared with the data of [12] in Fig. 8. For a density ratio, R, of 1.0 the decay of the maximum effectiveness is shown as a function of normalized distance aft of the center of the blowing site. For blowing rates, M, of 1.0 and 1.5, the present data are in reasonably good agreement with the data of [12]. At $M = 0.5$, there is a significant difference. The reason for this difference is unclear at present, but it may be due to the effects of curvature as shall be discussed below. The pressure surface data are compared with the same flat plate data of [12] in Fig. 9. As can be seen, significant differences exist between the two sets of data for all conditions. The effectiveness data of the present program are, in general, much lower and less sensitive to M than those of [12]. The pressure surface data, however, show a greater similarity to other data of [12] which were obtained with the hole oriented at right angles to the flow direction (Fig. 10). The lower level of maximum effectiveness and its relative insensitivity to M appear to be partially a result of the radial flow over the blowing site causing the hole to behave as a compound angled hole. A final comparison with the data of [12] is given in Fig. 11, where the maximum effectiveness is plotted as a function of the momentum flux ratio ($I = M^2/R$) at a normalized distance downstream of the hole center (S/D) of 6.6. Although the suction surface results are in reasonably good agreement with those of [12], the pressure surface results are distinctly different. The conclusion drawn from these comparisons is that although the suction surface film coolant behavior is similar in many respects to what one would have expected from the flat plate results of [12], the pressure surface results are both qualitatively different (i.e., a strong radial component to the coolant trajectory) as well as quantitatively different (i.e., the effectiveness levels are, in general, much lower than one would have expected from flat plate results).

The difference between the data presented here and those of Goldstein, et al. [12] may partially result from the effects of surface curvature. In a recent paper, Ito, et al. [14] have reported film cooling data taken on a turbine blade in a plane cascade with rows of blowing sites on both the suction and pressure surfaces. Their holes were at 35 deg to the surface and had a center-to-center distance of three diameters. In all other respects, their configuration was very similar to that of the present program. Their facility being a plane cascade, however, had no radial flow effects. Most of the data they present is laterally averaged, but some local effectiveness data is reported for a density ratio of 0.95 and a mass flux ratio of 0.5, for the pressure and suction surfaces. These data, on the hole centerlines, ([14], Figs. 4 and 5) are almost identical with those of the present program on the suction surface, and they are also quite close on the pressure surface (Fig. 12). The pressure surface effectiveness data of [14] are higher by 0.05 to 0.10 than those of the present program. This difference is probably due to both the effects of the row of holes as opposed to the single hole employed in the present program and also the effect of the radial flow. Ito, et al. [14] attribute most of the difference between suction and pressure surface film cooling behavior to the effects of surface curvature. The effects of high and low blowing rate and concave and convex surface curvature are summarized by Ito et al., in Fig. 10 of that work. This figure is for laterally averaged effectiveness, but the results it illustrates are similar in many respects to those of Fig. 11 of the present work. The high effectiveness on the suction surface at low momentum flux ratios, I, is attributed by Ito et al., to the effect of curvature causing the coolant jet to be close to the wall. At higher

values of I, the curvature effects cause the jet to lift off the surface resulting in lower effectiveness. On the pressure surface, the effects were shown in [14] to be reversed. Low values of I caused low effectivenesss, but the effectiveness increased gradually as I increased. It was suggested by Ito et al., and indeed it is confirmed by their data as well as by that of the present work (Fig. 11), that the suction (convex) and pressure (concave) surface data should cross at a value of I equal to or somewhat greater than unity.

Conclusions

Both qualitative and quantitative differences were seen to exist between the behavior of film coolant on the suction and pressure surfaces of a turbine rotor blade. On the suction surface, the film coolant had only a small radial displacement and was in many respects similar to existing data taken on flat surfaces with streamwise oriented holes. Where comparisons were possible, the suction surface data was also nearly identical with film cooling data taken by other investigators on a plane cascade airfoil of very similar geometry.

On the pressure surface, the film coolant had a large radial displacement and, in general, very low levels of effectiveness were measured. The radial displacement was a result of the radial component of the free stream flow over the blowing site. The low level of effectiveness appears to be due both to the effectively compound orientation of the hole, due to the radial flow, and surface curvature effects which tend to reduce coolant effectiveness on concave surfaces at momentum flux ratios, I, less than approximately unity.

Finally, the film coolant trajectories for each blowing site are virtually uninfluenced by the coolant blowing rate, M, and by the coolant to free stream density ratio, R.

Acknowledgments

This program was sponsored by the Air Force Aero-Propulsion Laboratory (AFSC) United States Force. The authors are indebted to the efforts of many people for the completion of this program and in particular to Mr. Charles Coffin for his skill and patience in building the models, Mr. Raymond Whitmore for developing the TC scanning system, and finally Mr. Joel Wagner and Mr. John Kostic for helping in acquiring the data.

References

1 Goldstein, R. J., "Film Cooling" in *Advances in Heat Transfer.* Academic Press, New York and London, Vol. 7, 1971, p. 321.

2 Ericksen, V. L., "Film Cooling Effectiveness and Heat Transfer with Injection Through Holes," Ph.D. Thesis, University of Minnesota, 1971.

3 Ericksen, V. L., Eckert, E. R. G., and Goldstein, R. J., "A Model for the Analysis of the Temperature Field Downstream of a Heated Jet Injected into an Isothermal Crossflow of an Angle of 90°." NASA CR72990, 1971.

4 Pedersen, D., "Effect of Density Ratio on Film Cooling Effectiveness for Injection Through a Row of Holes and for a Porous Slot," Ph.D. Thesis, University of Minnesota, 1972.

5 Liess, C., "Film Cooling with Ejection from a Row of Inclined Circular Holes, An Experimental Study for the Application to Gas Turbine Blades," von Karman Institute for Fluid Dynamics, Technical Note 97, March 1973.

6 Lander, R. D., Fish R. W., and Suo M., "External Heat Transfer Distributions on Film Cooled Turbine Vanes," *Jour. Aircraft,* Vol. 9, No. 10, Oct. 1972, pp. 707–714.

7 Muska, J. F., Fish, R. W., and Suo, M., "The Additive Nature of Film Cooling From Rows of Holes," ASME Paper No. 75-WA/GT-17, 1975.

8 Caspar, J. R., Hobbs, D. E., and Davis, R. L., "Calculation of Two-Dimensional Potential Cascade Flow Using Finite Area Methods," to be published in the *AIAA Journal,* Vol. 17, No. 12, Dec. 1979.

9 Blair, M. F. and Lander, R. D., "New Techniques for Measuring Film Cooling Effectiveness," ASME JOURNAL OF HEAT TRANSFER, Vol. 97, No. 4, Nov. 1975, pp 539–543.

10 Dring, R. P., Blair M. F., and Joslyn H. D., "Research on Centrifugal Effects on Turbine Rotor Blade Film Cooling," AFAPL (TBC), AFSC, Report No. AFAPL-TR-78-63, Aug. 1978.

11 Kline, S. J. and McClintock, F. A., "Describing Uncertainties in Single Sample Experiments," *Mech. Eng.,* Vol. 75, No. 1, 1953, pp. 3–8.

12 Goldstein, R. J., Eckert E. R. G., Eriksen, V. L., and Ramsey, J. W., "Film Cooling Following Injection Through Inclined Circular Tubes," NASA CR-72612, Nov. 1969.

13 Colloday, R. S. and Russell, L. M., "Flow Visualization of Discrete Hole Film, Cooling for Gas Turbine Applications," ASME 75-WA/HT-12, Dec. 1975.

14 Ito, S., Goldstein R. J., and Eckert, E. R. G., Film Cooling of a Gas Turbine Blade," ASME, *Journal Engineering for Power,* Vol. 100, July 1978, pp. 476–481.

D. A. Bailey
Research Engineer.
United Technologies Research Center,
East Hartford, Conn.
Assoc. Mem. ASME

Study of Mean- and Turbulent-Velocity Fields in a Large-Scale Turbine-Vane Passage

Laser-Doppler velocimetry was used to investigate the secondary flow in the endwall region of a large-scale turbine inlet-guide-vane passage. The mean and turbulent velocities were measured for three different test conditions. The different test conditions consisted of variations in the blade aspect ratio and the inlet boundary-layer thickness or all three cases, a passage vortex was identified and its development documented. The turbulent stresses within the vortex were found to be quite low in comparison with the turbulence in the inlet boundary layer.

Introduction

It has been recognized for some time that an important portion of turbine loss and heat transfer is associated with the passage secondary flow in the endwall region. This secondary flow is related to the curvature of the inviscid streamlines, which produces a lateral pressure gradient. In response to this pressure gradient, the low-momentum flow in the endwall boundary layer develops a lateral-velocity component, which convects low-momentum fluid toward the convex surface of the passage, developing into a longitudinal vortex. This vortex has a significant influence on the flow in that region, since it convects high-momentum, freestream fluid to the near-wall region, thereby increasing viscous losses and heat transfer.

Since endwall losses are significant to overall gas turbine performance [1], efforts have been under way to understand these flows, to predict their behavior, and eventually to minimize passage losses through optimally-designed passage contours. A number of investigations of three-dimensional flows have provided some elucidation of the features of the flow. Rohlik and others [2] measured a concentration of passage losses near the suction surface-endwall junction. Herzig, Hansen, and Costello [3] observed the roll-up of the flow near the suction surface and the eventual formation of a passage vortex. An indirect measure of the influence of the vortex was provided by Blair [4], who observed high heat-transfer rates on a passage endwall near the suction surface. Pressure-loss measurements within a passage were recently obtained by Sjolander [5], and a detailed picture of the passage vortex has been provided by Langston, Nice, and Hooper [6]. The development of the passage vortex, as well as the total-pressure defect within the vortex, was well documented in both of these experiments. Aside from these fundamental studies, many tests have been conducted on cascades where only the inlet and exit conditions were measured and the losses determined for the specific test case. Examples of these tests are mentioned by Dunham [7] and Ainley [1].

In addition to the experimental effort, there have also been several analytical studies of this phenomenon. The original analytical efforts were restricted to laminar passage flow, even though the endwall flow in a turbine passage is normally turbulent. This direction proved fruitful, since, as Hansen and Herzig [8] concluded, after comparing the turbulent and laminar flows, the turbulent effects are not qualitatively dominant in curved channel flows. Although laminar boundary-layer theory has provided insight into the nature of flows through an idealized passage, it is not applicable to the important region of the passage vortex.

Another method of considering the generation of secondary flow in curved channels has been extensively developed by Hawthorne [9]. He disregarded viscous effects within the curved section of the channel and considered the convection of vortex lines in the channel. However, this method is not applicable to endwall boundary layers, since inviscid solutions will not predict local skin-friction and heat-transfer rates. Therefore, to attack the important questions of loss and heat transfer, computational procedures for predicting three-dimensional, viscous flows have been initiated.

Computational procedures have been developed for the prediction of viscous secondary flows by Briley [10], Patankar and Spalding [11], and Ghia, Ghia and Studerus [12]. In fact, both Dodge [13] and Briley, Kreskovsky, and McDonald [14] have attempted to solve the endwall flow through a typical turbine vane. The evaluation of these studies has been limited, however, because of the lack of data for turbine endwall flows. This is especially so for the turbulence within a developing passage vortex.

The goals of this experimental program were, therefore, two-fold. The primary goal was precise measurement of mean-velocities of the secondary flow through a turbine-vane passage. These results could be used in the evaluation of analytical and computational procedures, which have been or may be developed for the prediction of such secondary flows. The other goal of this program was documentation of

Contributed by the Gas Turbine Division and presented at the Gas Turbine Conference and Exhibit and Solar Energy Conference, San Diego, California, March 12–15, 1979 of THE AMERICAN SOCIETY OF MECHANICAL ENGINEERS. Manuscript received at ASME Headquarters December 8, 1978. Paper No. 79-GT-33.

the turbulence of the flow as the passage vortex developed. These data, if obtained in sufficient detail, could be used to evaluate a turbulence model, such as a two-equation turbulence model, for use in a numerical prediction procedure.

The experimental approach used to satisfy the above goals was to simulate a turbine-passage flow in a large-scale test section, thus permitting high spatial resolution for velocity measurements. In this test section, the horseshoe vortex that develops at the blade leading-edge was suppressed. This resulted in an isolated passage vortex. Within the test section, mean velocities and turbulent stresses were measured, providing evidence of the development of a passage vortex from a turbulent inlet boundary layer. Most of the measurements were obtained with a laser-Doppler velocimeter, thus eliminating the uncertainty associated with intrusive sensors. Three different test conditions, consisting of variations in inlet boundary-layer thickness and test-section aspect ratio (span/axial chord), were studied.

Wind Tunnel

The experiment was conducted in a low-speed, general-purpose wind tunnel. The tunnel, illustrated in Fig. 1, had a uniform inlet flow with less than one percent deviation of either the core-flow velocity or total pressure from the centerline values. The total turbulence, $\sqrt{1/3(\overline{u'^2} + \overline{v'^2} + \overline{w'^2})}/U_\infty$, of the core flow was measured upstream of the test section and found to be 0.007. The integral length scale of the longitudinal turbulence component was 52 mm. The power-spectral density [15] of the longitudinal component of turbulence was measured and found to be in good agreement with the Liepmann spectrum, indicating the turbulence was in a normal state of decay and that the above measurements were free from spurious signals.

The test-section approach duct had three adjustable bleed slots on each of the four surfaces. These removed the distorted boundary layer caused by the contraction and permitted control of the inlet boundary-layer thickness. To obtain a thin inlet boundary layer all three sets of the bleed slots were used; to obtain a thick inlet boundary layer only the first set was used. Two additional bleed slots were located between the test-section approach duct and the leading edge of the vanes. These were used to remove the boundary layers that would have impinged on the vane leading edges; especially important was the elimination of the boundary layers in the region of the endwall-vane leading edges where a corner vortex would have formed. A more detailed discussion of the wind tunnel is given by Bailey [16].

Test Conditions

The experiment was conducted at a test-section Reynolds number of 4.6×10^5, based on the axial chord and the inlet velocity. This Reynolds number is typical of sea-level, take-off conditions for modern gas-turbine engines. No attempt was made to simulate compressibility effects; the maximum Mach number in the test section was 0.3. The test fluid was atmospheric air.

The experiment consisted of three different test conditions; "TKBLSS", a thick inlet boundary layer with a short span (blade aspect ratio of 0.617); "TNBLSS", a thin inlet boundary layer with a short span (blade aspect ratio of 0.617); and "TNBLLS", a thin inlet boundary layer with a long span (blade aspect ratio of 1.87). Comparison between flow conditions "TKBLSS" and "TNBLSS' shows the effect of variation in the inlet boundary-layer thickness, while comparison between flow conditions "TNBLSS" and "THBLLS" shows the effect of variation in the blade aspect-ratio on the secondary flow.

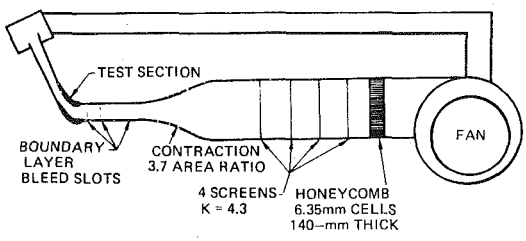

Fig. 1 UTRC low-speed wind tunnel

The lower aspect-ratio geometries were obtained using splitter plates to simulate the endwall. The plate extended just upstream of the test section for condition "TNBLSS", while for condition "TKBLSS", it extended the full length of the test-section approach duct. Boundary-layer trip wires were used to insure fully turbulent boundary layers. For both thicknesses of the boundary layers the trip wires were more than one hundred wire-diameters upstream of the test section, thus insuring that the flow distortion caused by the wire was completely diffused. The Reynolds number, based on the wire diameters, was more than adequate to obtain a turbulent boundary layer. Identical trip wires were used at the same locations on the splitter plate as on the fixed endwall, so that the inlet boundary layers to the test section would be symmetrical about the mid-span.

Test Section

The turning-passage test section was approximately ten times larger than typical first-stage, turbine-inlet-guide vanes for modern gas-turbine engines. The surface coordinates of the actual test section are given in [16]; the surface shapes are shown in Fig. 2. The test section was made of two-dimensional vane surfaces with parallel endwalls. The span and pitch were 508 mm and 210 mm. The mid-span, wall, static-pressure distribution was measured and compared to the pressure distribution for the calculated [17] potential flow in an equivalent cascade. After adjustment of the exit tail-boards and the inlet bleed slots, excellent agreement was obtained between the measured and calculated flow, as shown in Fig. 3. The wall, static-pressure distribution was identical for the three test cases.

The test section was a channel passage rather than a cascade passage. This permitted the removal of the boundary layers that would impinge on the leading edges of the test section near the endwall, thus eliminating the intense vorticity normally observed in this area [5, 6]. The resulting vortices, sometimes called horseshoe vortices, have an extreme effect on the endwall flow near the leading edge of the passage airfoils. Eliminating these vortices simplified the flow and permitted the study of an isolated passage vortex. Although this elimination of horseshoe vortices also eliminates some of the practical aspects of the flow, the difficulty in understanding and predicting passage vortices justifies this simplification.

The measurement locations are shown in Fig. 2.

Instrumentation

General. A combination of laser-Doppler velocimetry and hot-wire/hot-film anemometry was utilized to measure the mean and fluctuating velocities through the passage. Hot-wire/hot-film anemometry was used to measure the upstream inlet flow and the endwall boundary layers just inside the passage. This was done to utilize the best features of anemometers, such as the high spatial resolution and

Nomenclature

C_p = static pressure coefficient $P - P_i/1/2\rho U_i^2$
K = pressure loss coefficient $\Delta p/1/2\rho U^2_{\text{Total}}$
P = static pressure
U,V,W = mean velocities in the directions of x,y, and z
u',v',w' = fluctuating velocities in the directions x,y, and z
x = spatial coordinate in the direction of the core flow
y = spatial coordinate in the direction from the pressure surface to the suction surface and perpendicular to the core flow
z = spatial coordinate in the direction from the endwall to the passage midspan
ρ = density of the fluid

Subscripts

∞ = undisturbed velocity at the edge of the shear layer
i = inlet flow conditions, such as the undisturbed inlet-flow velocity

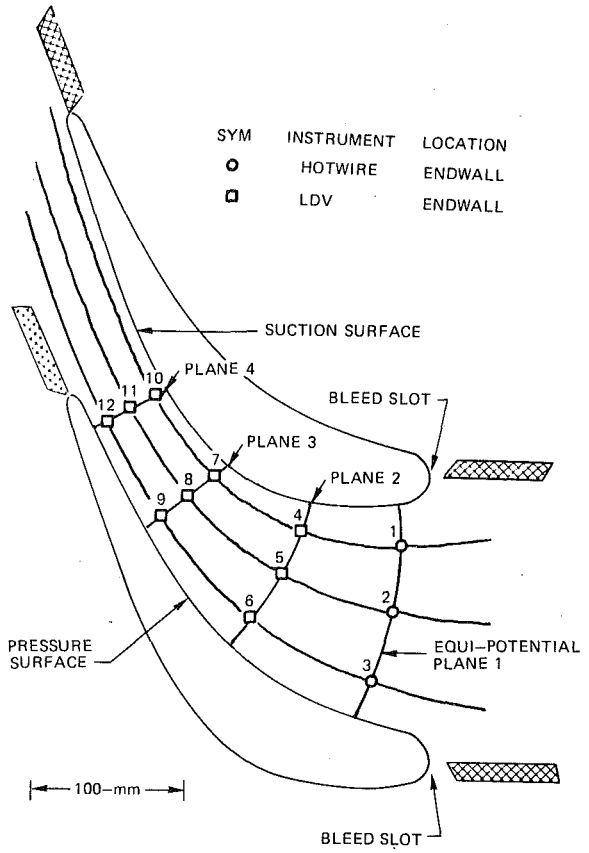

Fig. 2 Test-section geometry and measurement locations

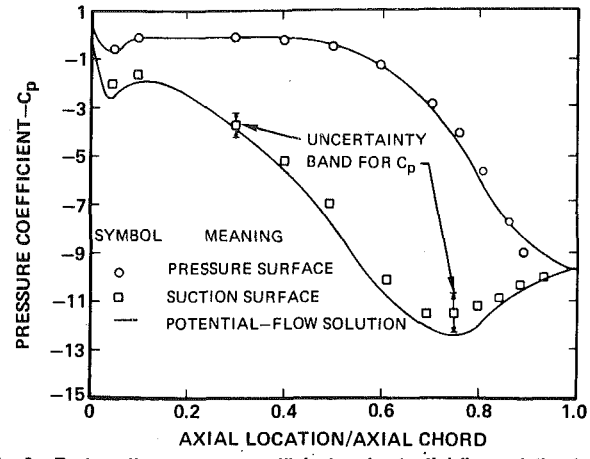

Fig. 3 Test-section pressure coefficient and potential-flow solution for an equivalent cascade (showing 20:1 uncertainty estimates)

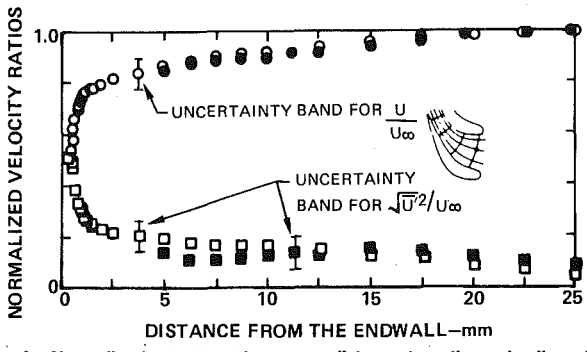

Fig. 4 Normalized velocity ratios versus distance from the endwall, position 2, flow condition TKBLSS (showing 20:1 uncertainty estimates)

SYMBOL	MEANING	INSTRUMENT
○	U/U_∞	Hot wire
●	U/U_∞	LDV
□	$5\sqrt{\overline{u'^2}}/U_\infty$	Hot wire
■	$5\sqrt{\overline{u'^2}}/U_\infty$	LDV

the rapid rate of data acquisition. In the regions where the passage vortex had developed, laser-Doppler velocimetry (LDV) was used because of the high precision in velocity measurements required to resolve the secondary flow. An additional advantage of LDV and requirement for the experiment was the elimination of the disturbances associated with intrusive sensors in secondary flows.

The hot-wire/hot-film measurements were obtained with TSI sensors (1218G-T1.5 and 1210-60). For flow condition "TKBLSS", the boundary-layer measurements at positions 1, 2, and 3 were obtained while the signal was being monitored periodically with an auto-correlator. This insured that no anomalous signals, such as those encountered from probe vibration, were biasing the output.

Laser-Doppler Velocimetry. Since the work reported here was not considered an instrumentation development program, a detailed description of the laser-Doppler velocimeter is not appropriate. But, a description of the system is available in [16].

LDV Seeding. When LDV measurements are obtained in air, seeding particles are normally required to obtain a rapid data rate. If these particles are sufficiently small and of low density, their velocities will closely match the fluid velocity. However, as the particle size or density increases, the tendency of the particles to follow the flow decreases. Therefore, careful attention must be directed to the seeding problem. This is especially true in turbulent flows, where the particles must follow the individual eddies, as well as the mean flow.

Several theoretical studies have been conducted on the response of a seeding particle to a turbulent eddy. These studies are summarized by Melling and Whitelaw [18]. Based on those results, it was determined that sub-micron particles were required for this experiment to obtain particle velocities within one percent of the fluid velocity. Merely obtaining small particles, however, is by no means the complete solution to the seeding problem. A further difficulty arises because the bonding forces of sub-micron particles are such that they are rarely found as single particles; hence, de-agglomeration of the particles is of major importance.

Particles are usually dispersed by passing compressed air through a fluidized bed containing the seeding material, but Marteney [19] has pointed out that this method seldom has the necessary energy to overcome the agglomeration forces. Marteney found that the shearing stresses in a capillary tube, with a large pressure drop, would provide the required energy to de-agglomerate sub-micron particles. It was also mentioned in this study that one of the forces of agglomeration is the capillary junction between liquids absorbed on the surface of the particles; therefore, dry air should be used for the particle seeding.

Therefore, a seeding system was designed, incorporating the above information. Titanium dioxide particles were used because of their small diameter, 0.22 μm, and the uniformity of their size. Dry, compressed air was used in a fluidized bed to obtain a suspension of the particles. The air-particle mixture was passed through a capillary tube and then entered the wind tunnel upstream of the honeycomb with the jet normal to the wind tunnel wall. No direct measurements of de-agglomerated particle size were obtained, but the agreement between hot-wire and LDV turbulence measurements for position 2, flow condition "TKBLSS" (Fig. 4) indicates that the particles were following the turbulent eddies.

Results and Discussion

Mean Measurements. Before discussion of the particular measurements that were acquired, it is appropriate to define the coordinate system and the associated velocity components. The x-axis and the velocity component U were in the direction of the undisturbed core flow. The y-axis and the velocity component V were parallel to the plane of the endwall, from the pressure to the suction surface, and perpendicular to the x-axis. The z-axis and the velocity component W were perpendicular to the endwall, in the direction from the endwall to the mid-span.

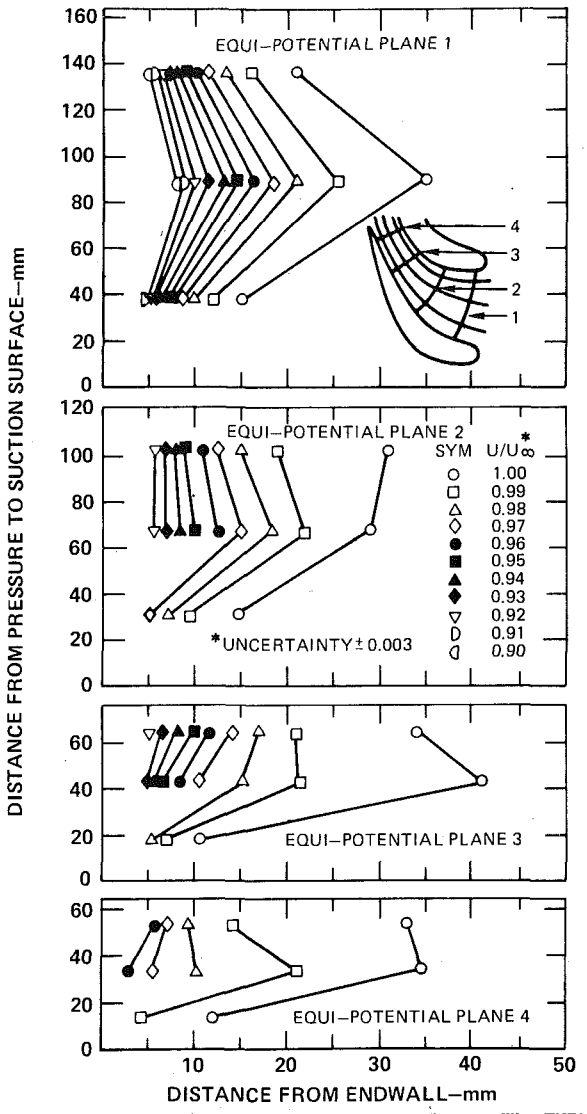

Fig. 5 Longitudinal velocity ratios for different planes, flow condition TKBLSS (showing 20:1 uncertainty estimates)

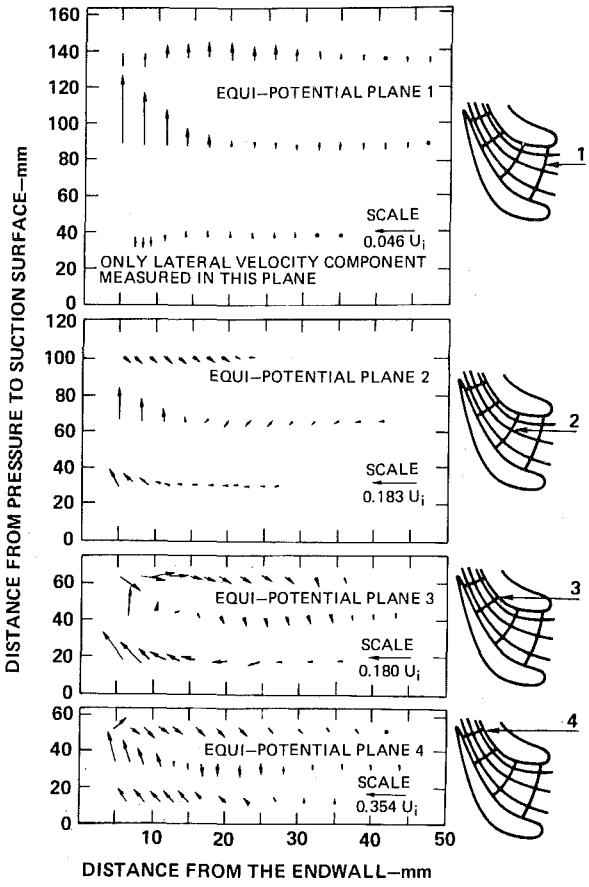

Fig. 6 Lateral velocity for different planes, flow condition TKBLSS

Complete results, as well as a more detailed description of the facility and equipment are available in [16].

Flow condition "TKBLSS". The mean-longitudinal and mean-lateral velocities measured at the four planes, specified in Fig. 2, are shown in Figs. 5 and 6. The uppermost figures represent the first plane of measurement, while the lower figures show the velocities farther through the test section. The ordinate on each of the four inserts corresponds to the distance between the suction and pressure surface at that particular location; the abscissa corresponds to the distance from the endwall. In Fig. 6, the arrows represent the direction and magnitude of the lateral velocity at the locations corresponding to the base of the arrows, except in the first figure, where only the lateral-velocity component parallel to the endwall is shown.

The longitudinal velocities, shown as contour plots in Fig. 5, were nondimensionalized by the local core-flow velocities. In consequence, the core-flow velocity variations across the passage, from the pressure to the suction surface, do not dominate the figure. Hence, only the local velocity defect of the longitudinal component is shown in Fig. 5. The lateral velocities for the same location were similarly treated and are shown in Fig. 6. These lateral velocities were normalized through division by the test-section inlet velocity. Note that the scales are different for each of the four portions of this figure.

At the first plane of measurements, a distortion of the shear layer is evident, as shown in Fig. 5. The location at which U/U_∞ (where U_∞ is the undisturbed core-flow velocity) equals 0.95 is approximately 1.5 mm at the center of the passage, but only 9 and 7 mm near the suction and pressure surfaces. This distortion of the shear layer may have been due to the contraction of the flow between the test-section approach duct and the first plane of measurement. Such a contraction could have distorted the boundary layer, causing secondary flow [20]. The lateral velocities in plane 1 (Fig. 6) indicate that the endwall shear layer has developed a strong cross-passage flow, from the pressure to the suction surface, in the mid-passage. Near the pressure and suction surfaces there is some lateral flow, but it is quite weak in comparison with the lateral flow that develops farther through the passage, as can be seen by comparing the different scales in Fig. 6. At the downstream locations, (planes 2, 3 and 4) Fig. 5 shows an accumulation of low-velocity fluid near the suction surface-endwall corner (the upper left-hand corner of the plots). The overall extent of the low-velocity region also decreased with downstream location. This effect may have been due to the acceleration of the core flow through the passage, which would have had a greater influence on the low-velocity fluid.

The passage vortex gradually developed as the flow was turned through the passage, as shown by the lateral velocities in Fig. 6. At the first equipotential plane, only a weak cross-passage flow existed. In plane 2, a passage vortex had started to form. The flow at the near mid-pitch location was generally toward the suction surface, as in plane 1, but farther from the endwall the flow developed lateral velocities in the sense of a clockwise passage vortex. Near the pressure surface the lateral velocity was toward the endwall; near the suction surface it was toward mid-span. At planes 3 and 4 the lateral velocity continued to develop into a longitudinal vortex. The measurements at plane 4, the passage throat, show that the passage vortex extended from one vane surface to the other and was centered approximately halfway between the surfaces, 12 to 15 mm from the endwall.

In the suction surface-endwall corner of planes 3 and 4 there appeared to be a complicated flow pattern that may have been due to a counter-rotating vortex. Additional evidence of this is shown in Figs. A4 and A7 of [16]. Aside from this corner region, the general lateral-flow field was of a relatively simple nature, appearing similar to a

concentrated vortex. This was in contrast to the measurements obtained by Langston, Nice and Hooper [6] of the secondary flow in a rotor cascade. They observed a longtudinal vortex that was considerably smaller than the passage width. In their passage, the vortex developed on the endwall and was convected toward the suction surface. As it approached the suction surface, it was convected toward the center of the span. This type of vortex motion is somewhat similar to that of a potential vortex near a corner.

The reason for the smaller, more localized vortex, observed in [6], is not completely clear. For both experiments, the ratio of the inlet boundary-layer thickness to the passage pitch was near 0.12. However, the degree of turning and the acceleration were quite different in the two experiments, and these two parameters could have a strong influence on the extent of the longitudinal vortex within the passage. The difference in the size of the vortices in the two experiments may, therefore, be related to differences in the turning angle and the acceleration of the flow. The rotor cascade used by Langston, Nice and Hooper turned the flow 107 deg, while accelerating it to 1.6 times the inlet velocity. In this study the flow was turned only 72 deg, but accelerated to 3.24 times the inlet velocity.

It could be hypothesized that this difference is due to the presence of horseshoe vortices in their experiment and the absence of them in this experiment. However, in a test section similar to this one (except for a lower Reynolds number and the presence of horseshoe vortices) Marchal and Sieverding [21] observed a concentration of lateral velocities similar to that found in this study. These results, in comparison with Langston, Nice and Hooper's, are shown in Fig. 7. This figure shows a passage vortex centered halfway between the suction and pressure surface in a turbine inlet-guide vane, but concentrated near the suction surface-endwall region in a turbine-rotor blade. These results indicate that the region of the pressure surface, near the endwall, may not be a two-dimensional flow for a turbine inlet-guide vane, with thick endwall boundary layers, even though this may be the case for a turbine rotor blade.

Another observation that can be drawn from Figs. 5 and 6 is that the secondary flow extends further from the endwall than the region of the low-velocity fluid. This is in contrast to the results of Langston, Nice and Hooper.

Flow Condition "TNBLLS". The test arrangement for flow condition "TNBLLS" consisted of a thin inlet boundary layer and the high aspect-ratio test section. Figure 8 shows that the boundary layer at position 2 was approximately 3 mm thick, based on the location at which $U/U_\infty = 0.95$. This is considerably thinner than the 10 to 15-mm thick boundary layer measured for flow condition "TKBLSS". Measurements at planes 2, 3, and 4 were treated the same as those for flow condition "TKBLSS", except that only one lateral component, V, of the mean velocity was measured. The lateral and longitudinal velocities are shown for each plane in Figs. 9 and 10.

Figure 9 shows a rapid thickening of the boundary layer between the first and second planes. Figure 10 shows a lateral velocity toward the suction surface at the second plane, except near the suction surface where the lateral velocities indicate the possible presence of a weak counter-rotating vortex. This is similar to the results for flow condition "TKBLSS" shown in Fig. 6 (note that the scales are different in Figs. 6 and 10 for both the velocity vector and distance from the endwall).

The third equi-potential plane of Fig. 10 shows a passage vortex in the suction surface-endwall region. Figure 9 shows an accumulation of low-momentum fluid in this area. At mid-passage and near the pressure surface locations, there was general cross-channel flow toward the suction surface (Fig. 10), and a thinning of the low-velocity region (Fig. 9). At the passage throat, equi-potential plane 4, the low-momentum fluid was concentrated near the suction surface (Fig. 9), extending approximately 12 mm from the endwall. Near the pressure surface there is only slight evidence of low-momentum fluid.

As also noted for flow condition "TKBLSS," Figs. 9 and 10 show that at the exit plane (plane 4) significant lateral velocities existed in regions with no velocity defect.

Based on the above, it can be concluded that the difference in the

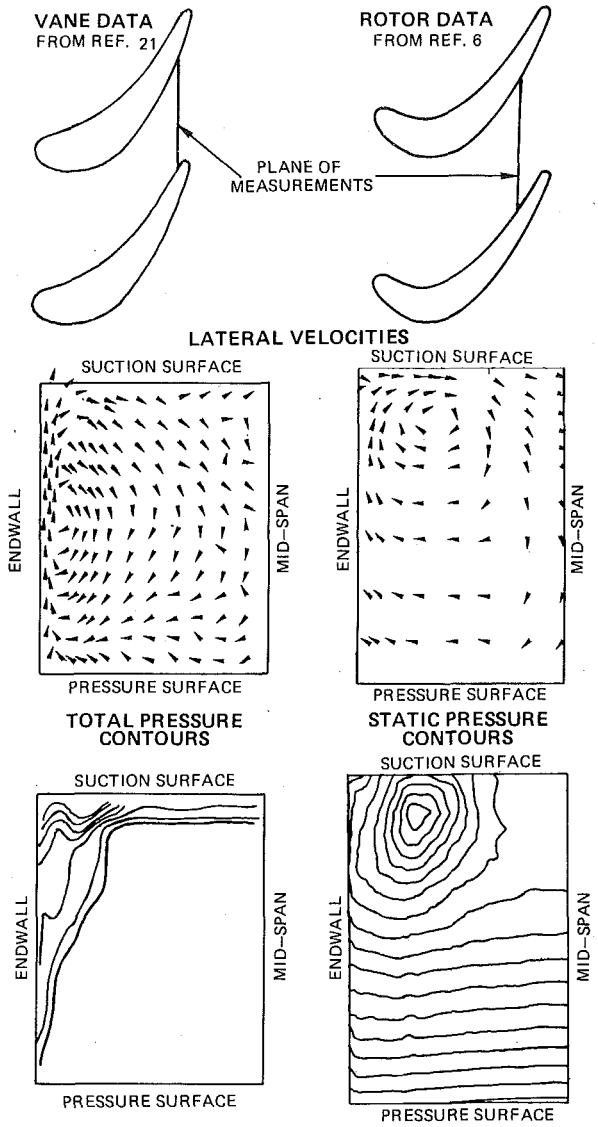

Fig. 7 Comparison of flows through turbine vanes and rotors

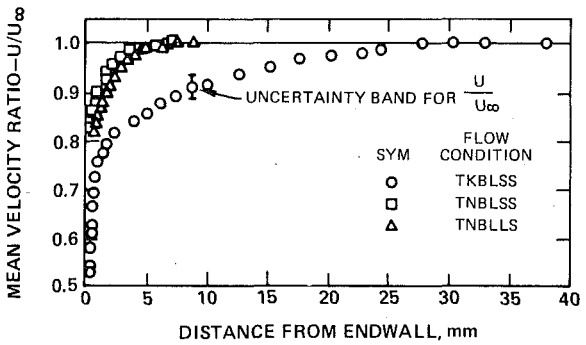

Fig. 8 Inlet boundary layer velocity profiles, position 2 (showing 20:1 uncertainty estimates)

boundary-layer thicknesses at the first equi-potential plane for flow conditions "TKBLSS" and "TNBLLS" (Fig. 8) had a significant effect on the exit flow. For flow condition "TNBLLS" the passage vortex was located in the suction surface-endwall region. This is in contrast to flow condition "TKBLSS" in which the passage vortex appeared to be centered halfway between the pressure and suction surfaces and farther from the endwall.

The results for flow condition "TNBLLS" indicate that most of the low-velocity fluid in the passage exit was generated within the test

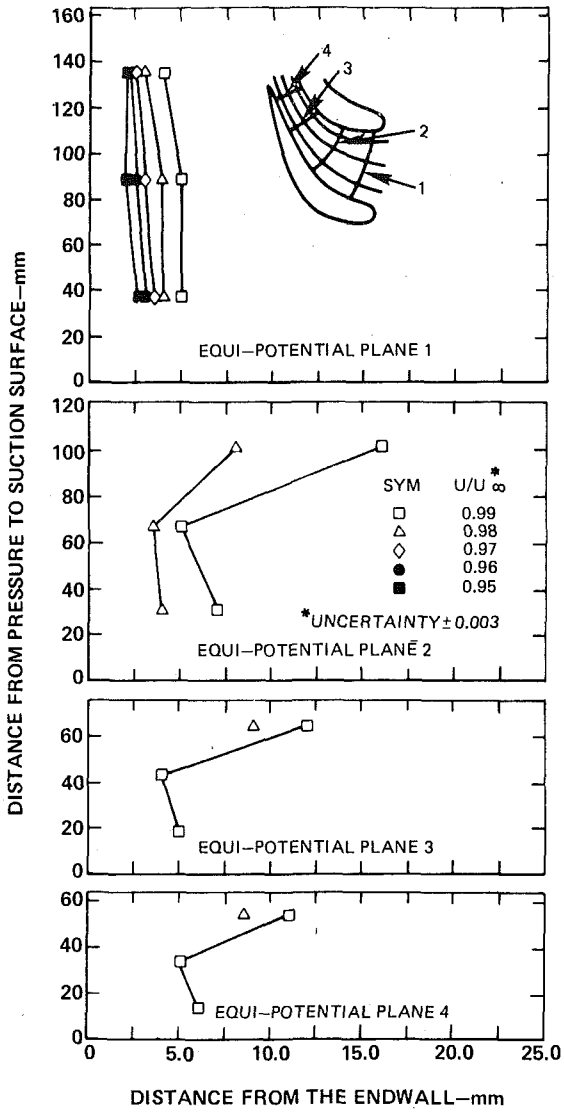

Fig. 9 Longitudinal velocity ratios for different planes, flow condition TNBLLS (showing 20:1 uncertainty estimates)

section, rather than being convected through the passage. The evidence to support this inference is that the endwall boundary layer was produced, just downstream of a bleed slot, by a 0.51-mm wire. This wire was located 50 mm upstream of the vane leading edge, yet the boundary layer was already 5 mm thick at measurement plane 1. This would also suggest that an inlet-guide-vane passage with no inlet shear flow would still have a significant amount of shear flow and secondary flow at the exit of the passage.

Flow Conditions "TNBLSS" and "TNBLLS". The isolated effect of blade aspect-ratio variation can be observed by comparing the results of flow conditions "TNBLSS" and "TNBLLS". Condition "TNBLSS" was nearly identical to condition "TNBLLS" except that the aspect ratio (span to axial chord) was decreased from 1.87 to 0.617, a factor of approximately three. The inlet boundary layers were similar for the two cases, as can be seen in Fig. 8.

A direct comparison of the three mean-velocity components is possible for downstream locations, near the suction surface, such as Position 7, as shown in Fig. 11. The uppermost part of the figure shows the lateral velocities W; the middle part, the lateral velocities V; and the lower part, the longitudinal velocities U. The figure shows a stronger secondary flow, lateral component V, and an altered longitudinal flow for condition "TNBLSS". In fact, the lateral velocity in the plane of the endwall was nearly twice the value for conditions "TNBLSS" as compared to condition "TNBLLS." Also, the passage vortex appeared to be closer to the endwall for condition "TNBLSS", as inferred from the location where V equaled zero. The velocities

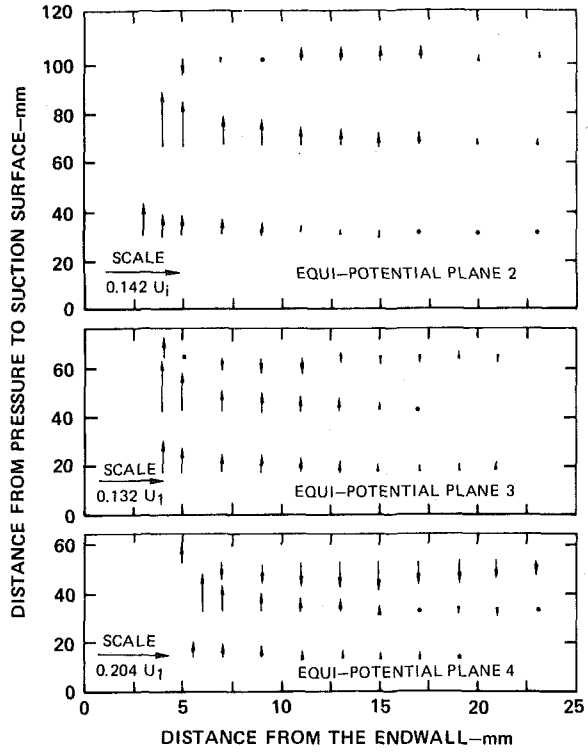

Fig. 10 Lateral velocity ratios for different planes, flow condition TNBLLS

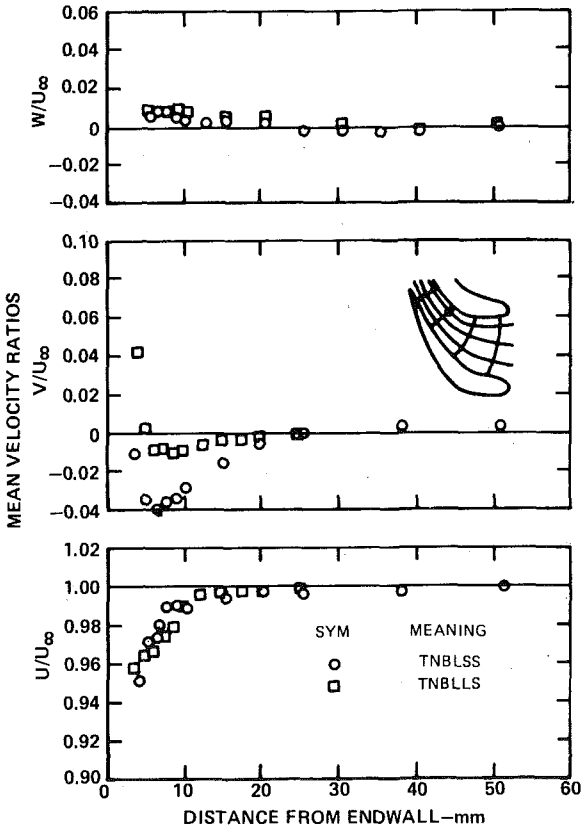

Fig. 11 Mean velocity ratios versus distance from the endwall, position 7, flow conditions TNBLSS and TNBLLS (size of symbols indicate 20:1 uncertainty estimate)

normal to the endwall, W, were insignificant in comparison to the other lateral component, and almost identical for the two cases. The longitudinal component had a smaller velocity defect for condition "TNBLSS", but this may have been a result of the passage vortex being centered at a different location for the two cases.

Two possible mechanisms exist for altering the secondary flow through a change in the passage span. The first is blockage due to the low-velocity shear layer next to the endwall. However, from the more complete measurements for flow condition "TNBLLS", the blockage effect was estimated and found to be insignificant for the two aspect ratios considered in this study. This estimate was based on the displacement thicknesses of the endwall shear layers being 2.5 mm at plane 1 and 5 mm at plane 4. From the results shown in Fig. 9 these would be conservative estimates. Since the test-section spans for the two cases were 168 and 508 mm, the acceleration of the core flow, due to viscous blockage, would be approximately 1 and 3 percent. The other possible mechanism, through which a change in the aspect ratio could alter the secondary flow, is induced vortex motion. Although it is impossible to obtain quantitative estimates of this effect from the data, it is possible that a change in the value of the velocities induced by the mirror image vortices could result from changes in aspect ratio. Although these velocities may be quite small, only a small change in the location of the passage vortex would be necessary to cause a significant change in the results of Fig. 11. This is especially so when the measurements are obtained near the center of the passage vortex.

In summary, the qualitative features of the two flows were similar, with quantitative variations in the mean velocity. These variations could be the result of a slight relocation of the passage vortex, which would preserve the global features of the flow, but change the velocities at fixed locations near the suction surface.

In comparison, the difference in the extent of the secondary flow for flow conditions "TKBLSS" and "TNBLLS" were quite significant, as is shown in Fig. 12. Aside from the larger region of secondary flow for flow conditions "TKBLSS", the lateral velocity V indicates that the center of the vortex was near position 11. This was inferred from the change in the direction of the lateral velocity at 14 mm from the endwall. The results for case "TNBLLS" only show flow from the pressure to the suction surface. This indicates that the location of the passage vortex was between position 11 and the suction surface.

Turbulence Measurements. *Flow condition "TKBLSS".* Measurement of the turbulence within the passage vortex was one of the principal problems this experiment was intended to address. Prior to this study no information existed for turbulent stresses within a passage vortex. Since the turbulent stresses at a particular location are dependent on the upstream flow history, as well as local diffusion, production and dissipation, it is difficult to estimate the qualitative nature of the turbulence in the vane-passage exit plane, let alone infer the quantitative distribution of the turbulent stresses. A turbulence model that includes these effects will have empirical constants as a result of the scaling law arguments used to simplify the turbulence model. The practical method by which these simplifications can be tested and the empirical constants evaluated is through comparison with experimental results.

To address the above problem, the turbulent stresses were measured at the same locations as the mean velocities (see Fig. 2). At the first measurement plane of Fig. 2, only the longitudinal normal stresses were measured. An example of these results was shown in Fig. 4 with the data for the mean measurements. The data indicated there was normal behavior for accelerating boundary layers. At the downstream measurement locations (positions 4–12) all six turbulent stresses were measured for this flow condition. Complete results are given in [16]. A sample of these results is shown in Fig. 13 as nondimensionalized normal stresses (based on the local core-flow velocity) versus distance from the endwall. These results represent the maximum turbulent stresses measured within the passage vortex. As is shown, the maximum stresses measured were approximately four percent at a location 5 mm from the endwall. This 5 mm was the spatial resolution of the instrument when measuring next to the endwall. These turbulence levels rapidly decreased to core-flow levels within 20 mm of the endwall. Since the passage vortex extended 30 to 40 mm from the endwall it can be concluded that, in large regions of the passage vortex, the turbulent stresses were insignificant. This observation is considered to be the most important finding of the present study. It suggests that a laminar-flow computational procedure may provide a reasonably accurate prediction of the secondary

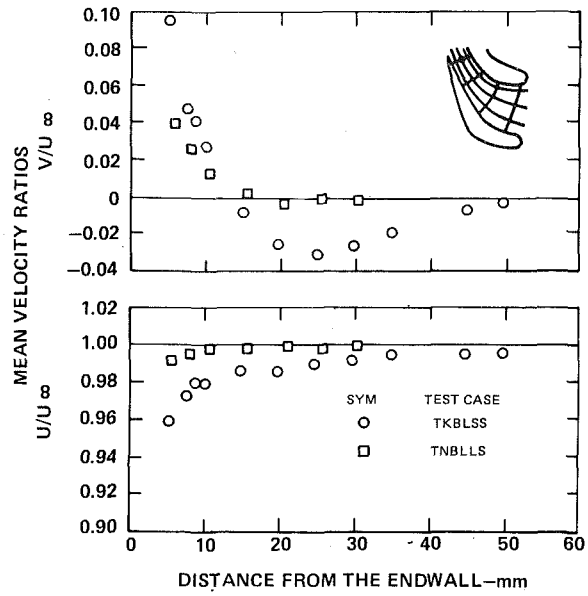

Fig. 12 Mean velocity ratios versus distance from the endwall, position 11, flow conditions TKBLSS and TNBLLS (size of symbols indicate 20:1 uncertainty estimates)

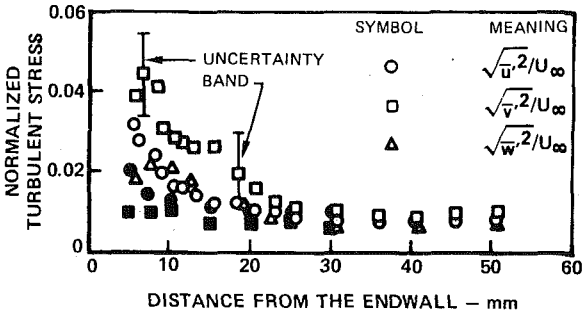

Fig. 13 Normalized turbulent stress versus distance from the endwall position 10 (showing 20:1 uncertainty estimates):

Open symbols—position 10, TKBLSS
Solid symbols—position 11, TNBLLS

flow structure far from the endwall.

Flow Condition "TNBLLS". The turbulence data provided little insight into understanding flow condition "TNBLLS", since the most interesting regions of the flow were within 5 mm of the endwall, which was beyond the limit of the LDV. The nondimensionalized turbulent normal stresses were found to be generally between 0.02 and 0.03 near the endwall with a decrease to core-flow values within 10 or 15 mm of the endwall. Near the pressure surface and at mid-span in planes 3 and 4 there was little evidence of turbulent flow to within 5 mm of the endwall, indicating that the shear layer was quite thin. An example of the turbulent stresses measured at position 11 is shown in Fig. 13. These results are in agreement with the mean-velocity measurements, which showed an accumulation of the low-momentum fluid near the suction surface and little evidence of shear flow near the pressure surface.

Flow Conditions "TNBLSS" and "TNBLLS"—Comparison. The turbulent stresses measured for flow conditions "TNBLSS" and "TNBLLS" were essentially identical, as can be seen in [16].

In summary, although the passage vortex was generated by highly-turbulent, low-velocity fluid from the endwall region, this experiment has shown that this high turbulence did not exist in the passage vortex. In fact, large regions of the passage vortex were shown to be non-turbulent.

Experimental Uncertainty

The estimated uncertainty for the pressure distribution of Fig. 3

was obtained using the method of Kline and McClintock [22]. The uncertainty band for C_p is for 20:1 odds. The uncertainty in axial location is smaller than the size of the symbols.

The uncertainty in the mean-velocity hot-wire measurements of Figs. 4 and 8 was estimated from the drift in the calibrations of the sensors, which were performed before and after each measurement. An attempt was made to use this same method to evaluate the uncertainty in the turbulence measurements, but the change in the slope of the calibration curve was insignificantly small. Therefore, the uncertainty was estimated to be ten percent based on Bradshaw's [23] discussion of this problem. The uncertainty of the mean-velocity measurements obtained with laser-Doppler velocimetry was evaluated using a calibrated flow. From these results the uncertainty was estimated to be 0.3 percent. For the turbulence measurements the estimated uncertainty was based on the observed background noise. The biasing effect noted by McLaughlin and Tiederman [24] was not applicable because of the low turbulence levels.

In all of the preceding figures the uncertainty in the measured distance from the endwall was smaller than the size of the symbols.

Conclusions

1 Using laser-Doppler velocimetry techniques, a longitudinal vortex was identified and its formation was investigated in a turbine inlet-guide-vane passage for one variation in inlet endwall boundary-layer thickness and one variation in the blade aspect ratio. For all three cases, the horseshoe vortex was suppressed in this experiment.

2 Maximum turbulence intensities within the longitudinal vortex were found to be between 2 to 4 percent. Large regions in the vortex were non-turbulent, with intensities approaching free stream values. Since a turbulent wall boundary layer was the source of vorticity that produced the passage vortex, these low turbulence levels were not anticipated.

3 The lateral-velocity fields, generated by the passage vortex, extended significantly beyond the region of the longitudinal-velocity defect. This is in contrast to previous measurements obtained in a rotor cascade.

4 The primary effects of reducing the inlet endwall boundary-layer thickness, by a factor of approximately five, were to reduce the maximum lateral velocities, by a factor of approximately two, and to change the spatial extent of the vortex. The apparent vortex was located closer to the endwall, by a factor of approximately two.

5 The effect of changing blade aspect ratio by a factor of three was small. Measured turbulent stresses were essentially identical for the two cases. Observed changes in the mean velocity at selected locations near the suction surface, may have been caused by a difference in the location of the passage vortex for the two cases.

References

1 Ainley, D. G., "Performance of Axial-flow Turbine," *Proceedings of the Institution of Mechanical Engineers,* Vol. 159, 1948, pp. 230–244.

2 Rohlik, R. E., et al., "Secondary Flows and Boundary-Layer Accumulations in Turbine Nozzles," NACA Rept. 1168, 1953. (Supersedes NACA TN 2871, 2909 and 2989.)

3 Herzig, H. Z., Hansen, A. G., and Costello, G. R., "A Visualization Study of Secondary Flows in Cascades," NACA Rept. 1163, 1954. (Supersedes NACA TN 2974.)

4 Blair, M. F., "An Experimental Study of Heat Transfer and Film Cooling on Large-Scale Turbine Endwalls," *Trans ASME,* Vol. 96, No. 4, Dec. 1974, pp. 524–529.

5 Sjolander, S. A., "The Endwall Boundary Layer in an Annular Cascade of Turbine Nozzle Guide Vane," Tech. Rept. No. ME/A 75-4, Dept. Mech. and Aero Engr., Carleton Univ., Ottawa, Canada, Dec. 1975.

6 Langston, L. S., Nice, M. L., and Hooper, R. M., "Three-Dimensional Flow Within a Turbine Cascade Passage," *Trans ASME,* Vol. 99, No. 1, Jan. 1977, pp. 21–28.

7 Dunham, J., "A Review of Cascade Data on Secondary Losses in Turbine," *Journal of Mechanical Engineering Science,* Vol. 12, No. 1, Feb. 1970, pp. 48–59.

8 Hansen, A. G., and Herzig, H. Z., "Cross Flow in Laminar Incompressible Boundary Layers," NACA TN 3651, 1956.

9 Hawthorne, W. R., "Secondary Circulation in Fluid Flow," *Proceedings of the Royal Society of London,* Vol. 206, Series A, May 1951, pp. 374–387.

10 Briley, W. R., "Numerical Method of Predicting Three-Dimensional Steady Viscous Flow in Ducts," *Journal of Computational Physics,* Vol. 14, No. 1, Jan. 1974, pp. 8–28.

11 Patankar, S. V., and Spalding, D. B., "A Calculation Procedure for Heat, Mass and Momentum Transfer in Three-Dimensional Parabolic Flows," *International Journal of Heat and Mass Transfer,* Vol. 15, Oct. 1972, pp. 1787–1806.

12 Ghia, U., Ghia, K. N., and Studerus, C. J., "A Study of Three-Dimensional Laminar Incompressible Flow in Ducts," Preprint 76-424, AIAA, July 1976.

13 Dodge, P. R., "Numerical Method for 2D and 3D Viscous Flows," *AIAA Journal,* Vol. 15, No. 7, July 1977, pp. 961–965.

14 Briley, W. R., Kreskovsky, J. P., and McDonald, H., "Computation of Three-Dimensional Viscous Flow in Straight and Curved Passages," Rept. R76-911841-9 (Contract Rept. NASC Contract N00019-74-C-0302) United Technologies Research Center, August 1976.

15 Hinze, J. O., *Turbulence: An Introduction to Its Mechanism and Thoery,* 1st ed., McGraw-Hill, New York, 1959.

16 Bailey, D. A., "Study of Mean- and Turbulent-Velocity Fields in a Large-Scale Turbine-Vane Passage", NASA CR-3067, 1979.

17 Caspar, J. R., Hobbs, D. E., and Davis, R. L., "The Calculation of Two Dimensional Compressible Potential Flow in Cascades Using Finite Area Techniques," Preprint 79-0077, AIAA, Jan. 1979.

18 Melling, A., and Whitelaw, J. H., "Seeding of Gas Flow for Laser Anemometry," DISA Information, No. 15, Oct. 1973, pp. 5–14.

19 Marteney, P. J., "Experimental Investigation of the Opacity of Small Particles," NASA CR-211, Apr. 1965.

20 Bansod, P., and Bradshaw, P., "The Flow in S-shaped Ducts," *The Aeronautical Quarterly,* Vol. 23, May 1972, pp. 131–140.

21 Marchal, Ph., and Sieverding, C. H., "Secondary Flow Within Turbomachinery Bladings," *Secondary Flows in Turbomachinery,* AGARD-CP-214, The Hague, Netherlands, Mar. 28–30, 1977.

22 Kline, S. J., and McClintock, F. A., "Describing Uncertainties in Single-Sample Experiments," *Mechanical Engineering,* Vol. 75, No. 1, Jan. 1953, pp. 3–8.

23 Bradshaw, P., *An Introduction to Turbulence and its Measurement,* 1st ed., Pergamon Press, New York, 1971.

24 McLaughlin, D. K., and Tiederman, W. G., "Biasing Correction for Individual Realization of Laser Anemometer Measurements in Turbulent Flows," *Physics of Fluids,* Vol. 16, No. 12, Dec. 1973, pp. 2082–88.

J. Martinon
Office National d'Etudes et de Recherches Aérospatiales (ONERA)
92320 Châtillon
France

Use of the Characteristic Method for the Prediction of the Three-Dimensional Flow Field in High Transonic Compressors

The strong pressure gradients that take place in high performance transonic axial flow compressors induce important viscous interaction effects. In order to estimate these effects and to calculate the flow field in the inviscid core, the perfect gas approach is necessary. A three-dimensional stationary characteristic method is used for such an approach, and numerical results are given for the flow field in: • the blade channel of a supersonic cascade with converging side walls, • the blade channel of an annular supersonic cascade, • the inlet region of a linear supersonic blade cascade with converging side walls.

1 Introduction

The strong axial, radial and tangential pressure gradients that take place in high performance transonic axial flow compressors induce important viscous interaction effects. However, the perfect gas approach is necessary for the determination of these effects and the flow field in the inviscid core.

As early as 1952, Wu [1] gave a quasi-three-dimensional theory of flow in turbomachines; two-dimensional calculations have to be made on two families of stream surfaces, and the solution is obtained after an iterative process in which the results on each family are used for the solution of the equations on the other one. But most of analytical studies of flow in turbomachines consist in an axisymmetric mean flow calculation, followed by a blade-to-blade calculation; such a method does not allow for a correct consideration of three-dimensional effects, which may be expected to be important for turbomachines with low hub-to-tip ratio or with convergent hub and/or casing.

The determination of stationary flow fields in domains comprising subdomains where the velocity of the gas is subsonic and other subdomains where it is supersonic is a rather uneasy work, because the mathematical nature of the partial differential equation system to be solved is either elliptic or hyperbolic. One can use time-dependent equations and look for the solution at infinite times, as did Carrière and Capelier [2], Veuillot [3], and Delaney and Kavanagh [4] for two-dimensional flow fields; but the addition of one more independent variable and the need for many iterations in time make these calculations very lengthy for three-dimensional flows.

The present work is only concerned with supersonic subdomains, so that the stationary equations remain everywhere hyperbolic. We chose to solve these equations with a three-dimensional method of characteristics rather than a finite-difference scheme, for the first method adheres more closely to the physical model and may be expected to have a greater accuracy.

A feature of the flow in supersonic axial flow compressors is the fact that most often the axial component of the fluid velocity is subsonic, so that the blades influence the flow field in front of the blade row, and the calculations must start several chord lengths upstream.

The purpose of this work is the determination of stationary supersonic inviscid three-dimensional flows in cascades and turbomachine rotors or stators, including the inlet region of the blade channel. The capability of predicting strong shock waves has not been yet developed, for shock losses across leading edge shocks are often small.

After a rapid description of the method of characteristics and of the numerical schemes we use, we will present three applications. Using a *direct method* we will first determine:

- the flow field in the blade channels of a linear cascade with converging side walls,
- the flow field in the blade channels of an annular cascade.

Then by means of an *inverse method* we will describe:

- the flow field in the inlet region and the blade channels of the same linear cascade with converging side walls.

2 The Method of Characteristics

2.1 General. Hyperbolic systems in three independent variables have the property that particular linear combinations of the partial differential equations yield *compatibility relations* involving differentiation in only two independent directions, which locally define a *characteristic plane.*

In the case of the equations of the steady perfect gas flow, particular combinations even lead to differential operators tangent to the local streamline. The envelope of the characteristic planes passing through

Contributed by the Gas Turbine Division and presented at the Gas Turbine Conference and Exhibit and Solar Energy Conference, San Diego, California, March 12–15, 1979 of THE AMERICAN SOCIETY OF MECHANICAL ENGINEERS. Manuscript received at ASME Headquarters December 8, 1978. Paper No. 79-GT-34.

a given point P comprises:

- the straight line through P, the direction of which is given by the velocity at P,
- a circular cone, called the *characteristic cone,* the axis of which is this straight line.

Characteristic cones are tangent to the corresponding characteristic planes along *bicharacteristic lines.*

The situation is quite similar for transient two-dimensional perfect gas flow equations, and numerical schemes are easily transposed from one case to the other. Such numerical schemes have been proposed by Sauerwein [5], Chu, Niemann, and Powers [6], Strom [7], Katskova and Chushkin [8], Borisov and Mikhailov [9], Ransom, Hoffman and Thompson [10], Camarero [11]. Frühauf [12] applied a subsidiary characteristic method to the calculation of steady isentropic supersonic flows in blade channels of annular cascades without upstream influence.

Practically it is not necessary to use the whole characteristic cone for the calculations; we have used a network of four bicharacteristic lines and the streamline through a single point P, together with the method proposed by Butler [13] for the elimination of cross-derivative terms.

2.2 Compatibility Relations. The system to be solved is

$$\underline{\nabla}\cdot(\rho\underline{q}) = 0$$
$$(\underline{q}\cdot\nabla)\underline{q} + 2\underline{\Omega}\times\underline{q} + \underline{\Omega}\times(\underline{\Omega}\times\underline{x}) + (\underline{\nabla}p)/\rho = 0$$
$$\underline{q}\cdot\underline{\nabla}s = 0 \qquad (1)$$

where p, ρ, $\underline{q}$, s, $\underline{x}$ are the dimensionless static pressure, density, velocity, specific entropy, position of the considered point P. $\underline{\Omega}$ is the (dimensionless) rotational speed; the origin of the relative coordinate system is located on the axis of rotation.

Dimensionless variables are defined as follows: let Λ, ρ_∞, q_∞ be reference length, density, and velocity, and let $\underline{\tilde{x}}$, $\tilde{\rho}$, $\underline{\tilde{q}}$, $\tilde{p}$, $\underline{\tilde{\Omega}}$ be dimensioned variables. Dimensionless variables are:

$$\rho = \tilde{\rho}/\rho_\infty; \quad \underline{x} = \underline{\tilde{x}}/\Lambda$$
$$\underline{q} = \underline{\tilde{q}}/q_\infty; \quad p = \tilde{p}/\rho_\infty q_\infty^2; \quad \underline{\Omega} = \underline{\tilde{\Omega}}\Lambda/q_\infty$$

If S_∞ is the specific entropy $\tilde{S}$ of the gas in the state ($\tilde{\rho} = \rho_\infty$, $\tilde{p} = \rho_\infty q_\infty^2$), s is given by:

$$s(p,\rho) = \frac{\tilde{S}(\tilde{p},\tilde{\rho}) - S_\infty}{c_p}$$

The equation of state of the gas is:

$$\rho = p^{1/\gamma}e^{-s} \qquad (2)$$

Setting (2) into (1) so that p, $\underline{q}$, s become the dependent variables, one obtains, with Cartesian orthogonal coordinates:

$$(\partial q_j/\partial x_j) + (q_j/\gamma p)(\partial p/\partial x_j) = 0$$
$$q_j(\partial q_i/\partial x_j) + \rho^{-1}(\partial p/\partial x_i) + 2\epsilon_{ijk}\Omega_j q_k + (\Omega_j x_j)\Omega_i - \Omega^2 x_i = 0 \qquad i = 1,2,3$$
$$q_j(\partial s/\partial x_j) = 0 \qquad (3)$$

We assume that, if a is the local speed of sound:

$$q^2 > a^2$$

It may be shown that the direction of any bicharacteristic line at point P is given by the vector

$$\underline{L} = \underline{q} + c(\underline{\zeta}\cos\varphi + \underline{\eta}\sin\varphi)$$
$$c = aq/\sqrt{q^2 - a^2} \qquad (4)$$

A possible set of compatibility relations is:

$$d_{\underline{q}}s = 0 \qquad (5a)$$
$$d_{\underline{q}}[a^2/(\gamma-1) + q^2/2 - \Omega^2 r^2/2] = 0 \qquad (5b)$$
$$\rho c(\zeta_j\cos\varphi + \eta_j\sin\varphi)d_{\underline{L}}q_j + d_{\underline{L}}p + \rho c^2(\eta_j\cos\varphi - \zeta_j\sin\varphi)(\eta_i\cos\varphi - \zeta_i\sin\varphi)(\partial q_j/\partial x_i) + 2\rho c q\Omega_i(\eta_i\cos\varphi - \zeta_i\sin\varphi) + \rho c^2[(q_i/q^2) - c^{-1}(\zeta_i\cos\varphi + \eta_i\sin\varphi)](\Omega^2 x_i - \Omega_i x_j\Omega_j) = 0 \qquad (5c)$$

Where operator $d_{\underline{q}}$ indicates derivation along a streamline and $d_{\underline{L}}$ derivation along a bicharacteristic.

φ is a parameter, $0 \leq \varphi < 2\pi$, and $\underline{\zeta}$ and $\underline{\eta}$ are orthonormal reference vectors lying in the plane normal to the vector $\underline{q}$. The degree of freedom in the choice of $\underline{\zeta}$ and $\underline{\eta}$ is used to maintain φ constant along each bicharacteristic line: if $\underline{\zeta}$ and $\underline{\eta}$ are given at a point P, using the orthogonality relations and the condition:

$$[q_i + c(\zeta_i\cos\varphi + \eta_i\sin\varphi)]\cdot[q_iq_j - (q^2 - a^2)\delta_{ij}]\partial x_j/\partial\varphi = 0 \qquad (6)$$

they may be determined at any point of the bicharacteristic passing through P and corresponding to the value of φ. Note that equations (5c) and (6) are simpler for

$$\varphi = 0, \quad \varphi = \pi/2, \quad \varphi = \pi, \quad \varphi = 3\pi/2$$

and equation (5c) only involves the term of cross-derivatives

$$\rho c^2\eta_i\eta_j(\partial q_j/\partial x_i) \quad \text{or} \quad \rho c^2\zeta_i\zeta_j(\partial q_j/\partial x_i)$$

In order to eliminate these two terms, we will use another linear combination of equations (3):

$$q_j(\partial p/\partial x_j) + \rho c^2(\zeta_i\zeta_j + \eta_i\eta_j)(\partial q_j/\partial x_i) + \rho(c^2/q^2)q_j(\Omega^2 x_j - \Omega_j x_i\Omega_i) = 0 \qquad (7)$$

One can easily show that:

$$\zeta_i\zeta_j + \eta_i\eta_j = \delta_{ij} - q_iq_j/q^2 \qquad (8)$$

where $\delta_{ij} = 1$ if $i = j$ and $\delta_{ij} = 0$ if $i \neq j$.

3 Numerical Scheme

We intend to calculate the values of $\underline{q}$, p, s at a certain number of points on a surface (Σ_2), knowing their values at points on a surface (Σ_1) upstream of (Σ_2). Hereafter, we will assume component q_3 of the velocity to be supersonic and choose for (Σ_1) and (Σ_2) parallel planes, normal to the coordinate direction x_3 (this direction is not necessarily the axis of the turbomachine, but for instance it may be the chord of a blade).

We use the following notation (Fig. 1): P_2 is the solution point on (Σ_2); P_1 is the point at the intersection of the streamline through P_2 with (Σ_1); P_3, P_4, P_5, P_6 are the points at the intersections with (Σ_1) of the bicharacteristics through P_2 for which $\varphi = 0$, $\varphi = \pi/2$, $\varphi = \pi$, $\varphi = 3\pi/2$.

3.1 Finite Difference Form of the Equations. Let Δx_3 be the distance between planes (Σ_1) and (Σ_2). The differential equations of the streamline and of the bicharacteristics through P_2 may be

Nomenclature

a = local speed of sound
c = length of vector $\underline{L} - \underline{q}$; $c = aq/\sqrt{q^2 - a^2}$
$\underline{L}$ = vector tangent to a bicharacteristic
p = static pressure
$\underline{q}$ = velocity vector of the fluid (magnitude q)
r = distance from a point to the axis of rotation
s = dimensionless specific entropy ($S - S_\infty)/c_p$
x_i = rectangular cartesian coordinates
X, Y = unknown terms of cross-derivatives (equations (11) and (12))
γ = ratio of specific heats
δ_{ij} = Kronecker delta
ϵ_{ijk} = 1 if $(i,j,k) = (1,2,3)$ or $(2,3,1)$ or $(3,1,2)$; -1 if (i, j, k) = (1, 3, 2) or (2, 1, 3) or (3, 2, 1); 0 in all other cases
$\underline{\zeta}$, $\underline{\eta}$ = orthonormal reference vectors in the plane normal to $\underline{q}$
ρ = static density
σ = parameter along streamlines
τ = parameter along bicharacteristics
φ = parameter of a bicharacteristic
$\underline{\Omega}$ = rotational speed (magnitude Ω)
$d_{\underline{v}}f = \underline{V}\cdot\underline{\nabla}f = V_i(\partial f/\partial x_i)$
$f(P_k)$ or $(f)_k$ Value of function f at point P_k
$(f)_{\overline{k_1,k_2}} = (f(P_{k_1}) + f(P_{k_2}))/2$

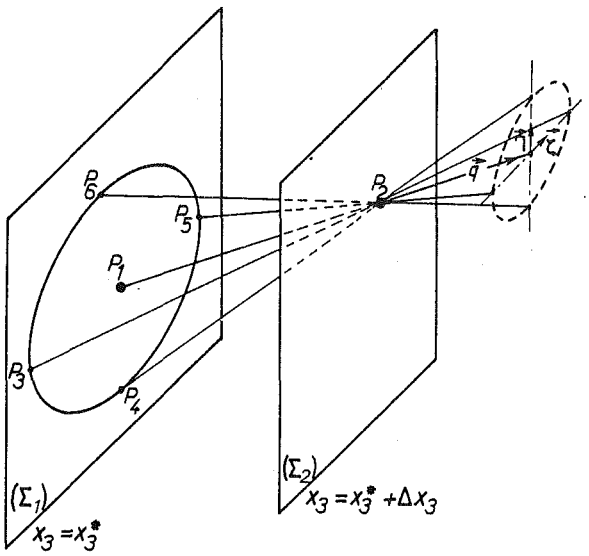

Fig. 1 Bicharacteristic scheme

discretized with third-order accuracy to yield:

$$x_i(P_2) - x_i(P_1) = \sigma(P_2)(q_i)_{\overline{1,2}}$$
$$x_i(P_k) - x_i(P_2) = \tau(P_k)(q_i + c(\alpha\zeta_i + \alpha'\eta_i))_{\overline{2,k}} \quad (9)$$
$$i = 1, 2, 3 \qquad k = 3, 4, 5, 6$$

where: $\alpha = \cos((k-3)\pi/2)$, $\alpha' = \sin((k-3)\pi/2)$ and symbol $(\ )_{\overline{1,2}}$ indicates mean values. Equations (5*a*) and (5*b*) yield:

$$s(P_2) = s(P_1)$$
$$a^2(P_2)/(\gamma-1) + q^2(P_2)/2 - \Omega^2 r^2(P_2)/2 = a^2(P_1)/(\gamma-1) + q^2(P_1)/2 - \Omega^2 r^2(P_1)/2 \quad (10)$$

Equation (5*c*) becomes, with third-order accuracy:

$$(\rho c(\alpha\zeta_j + \alpha'\eta_j))_{\overline{2,k}}(q_j(P_k) - q_j(P_2)) + p(P_k) - p(P_2) + \tau(P_k)\{(\alpha^2 X + \alpha'^2 Y)/2 + 2\Omega_i(\rho c q(\alpha\eta_i - \alpha'\zeta_i))_{\overline{2,k}} + (1/2)[\rho c^2(\alpha^2\eta_i\eta_j\partial q_j/\partial x_i + \alpha'^2\zeta_i\zeta_j\partial q_j/\partial x_i)]_k + (\rho c(cq_i/q^2 - \alpha\zeta_i - \alpha'\eta_i)(\Omega^2 x_i - \Omega_i x_j\Omega_j))_{\overline{2,k}}\} = 0 \quad (11)$$

with: $X = (\rho c^2\eta_i\eta_j\partial q_j/\partial x_i)_2$, $Y = (\rho c^2\zeta_i\zeta_j\partial q_j/\partial x_i)_2$

Similarly, (7) yields:

$$2(p(P_2) - p(P_1)) + \sigma(P_2)\{X + Y + (\rho c^2(\delta_{ij} - q_i q_j/q^2)\partial q_j/\partial x_i)_1 + 2(\rho c^2 q_j/q^2(\Omega^2 x_j - \Omega_j x_i\Omega_i))_{\overline{1,2}}\} = 0 \quad (12)$$

We also use a finite-difference form of (6), $\underline{\zeta}(2)$ being parallel to the vector:

$$\underline{q}(P_2) \times \underline{\nabla}p(P_1) + [(\underline{q}(P_2)/q(P_2))\cdot\underline{\nabla}p(P_1)]\underline{q}(P_2) - q(P_2)\underline{\nabla}p(P_1)$$

There are now as many equations as unknown variables (among which one must not forget the two terms of cross derivatives, X and Y). Obviously the values of the dependent variables at point P_2 can be calculated with a third-order accuracy, without iterations to determine the partial derivatives in plane (Σ_2).

3.2 Interpolation Process. We only know the solution $\underline{q}, p, s$ of (3) at discrete points belonging to (Σ_1), but we need to calculate the values of $\underline{q}, p, s$ and their derivatives at any point of (Σ_1), for P_3, P_4, P_5, P_6 (and perhaps P_1) are not necessarily known points. The selected interpolation scheme uses second-order polynomials in x_1 and x_2, locally fitted by a least-square method to the known data at nine points. It has been verified that the error introduced by this scheme is at most of the same order as the truncation error.

3.3 Direct and Inverse Scheme. *Direct Scheme.* In the direct scheme, the position of the solution point P_2 is not known in advance, but has to be determined with the complete solution on (Σ_2). The streamline is projected downstream from a known point P_1, and the four bicharacteristics are projected upstream from the intersection of the streamline with (Σ_2), to their intersections with (Σ_1). In this method the computation proceeds along streamlines passing through the points chosen as the nodes of a network in the initial plane.

The nine points used as base points for the interpolation in the determination of the solution at point P_2 are P_1 and its eight neighbours in the network of plane (Σ_1).

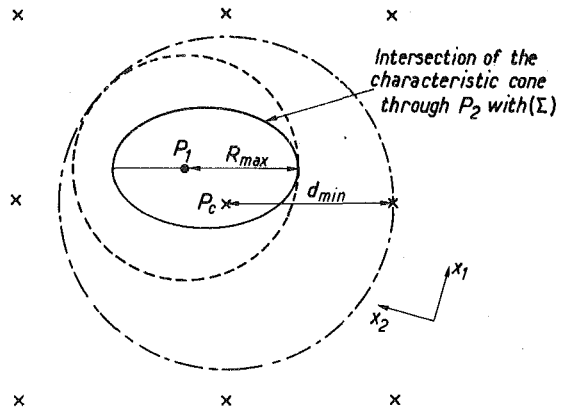

Fig. 2 Stability criterion for the inverse scheme

Although the values $\underline{q}(P_1)$, $p(P_1)$, $a(P_1)$ are known, the linear stability analysis shows that they must be re-calculated by the interpolation scheme for solving (12); this analysis also gives the maximum value for Δx_3 at point P_1:

$$\Delta x_{3M} = (q_3/q)(q_3/c - \sqrt{q_1^2 + q_2^2}/q)d_{\min} \quad (13)$$

where $d_{\min}$ is the distance from P_1 to the nearest of its eight neighbour points. The distance between (Σ_1) and (Σ_2) must be the smallest Δx_{3M} calculated for all points P_1 belonging to (Σ_1).

Inverse Scheme. In the inverse scheme, the position of the solution point P_2 is chosen in advance, and the streamline and the four bicharacteristics through P_2 are projected upstream toward (Σ_1).

The nine base points of the interpolation scheme are the data point which is nearest to P_1 and its eight neighbour points.

The stability criterion is as follows: let $R_{\max}$ be the distance from P_1 to the farthest point on the intersection of the characteristic cone through P_2 with (Σ_1), and let $d_{\min}$ be the distance from the central point of the interpolation P_c to the nearest of its neighbour points; the circle with center P_1 and radius $R_{\max}$ must be inside the circle with center P_c and radius $d_{\min}$ (Fig. 2).

Boundary Points. The points on the blades or the casing walls are calculated with the same scheme as the interior points, except that the slip condition is used instead of the compatibility relation (11) corresponding to point P_6. The vector $\underline{n}(P_2)$ is chosen parallel to the outer normal.

As for the points situated at the edge of two different walls, both corresponding slip conditions are used instead of the compatibility relations corresponding to points P_5 and P_6 when the angle of the normal vectors is at least equal to $\pi/2$ (and $\Omega = 0$).

4 Applications of the Direct Scheme

The direct scheme (code name CACTES) has, so far, been applied to examples such as nozzles, linear blade cascades, and annular blade rows. At the end of the calculations, the numerical solution is known along streamlines; this provides information in the same form as calculations based on Wu's [1] theory would but our calculation is really three-dimensional and needs no iterations between two streamsurface families.

4.1 Flow Field in a Linear Blade Cascade with Converging Side Walls. Some experimental data on a linear blade cascade with converging side walls have been presented by Meauzé [14]. Table 1 gives geometrical parameters of the cascade.

Table 1 Geometrical parameters of the linear cascade

Blade chord	6.7 cm
Pitch	2.58 cm
Stagger angle	39.3 deg
Aspect ratio:	
—inlet	1.493
—outlet	1.045

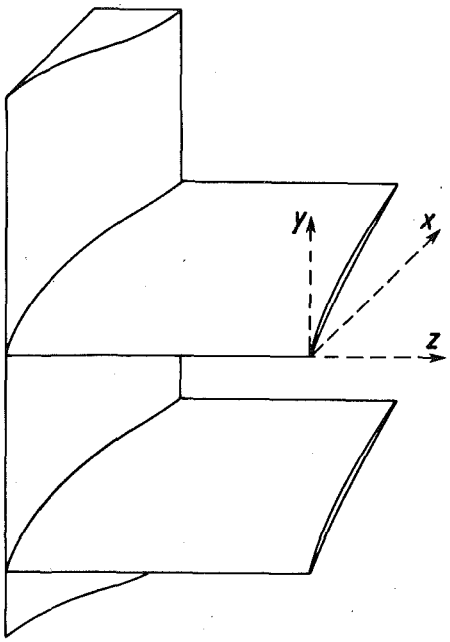

Fig. 3 Linear blade cascade with converging side walls

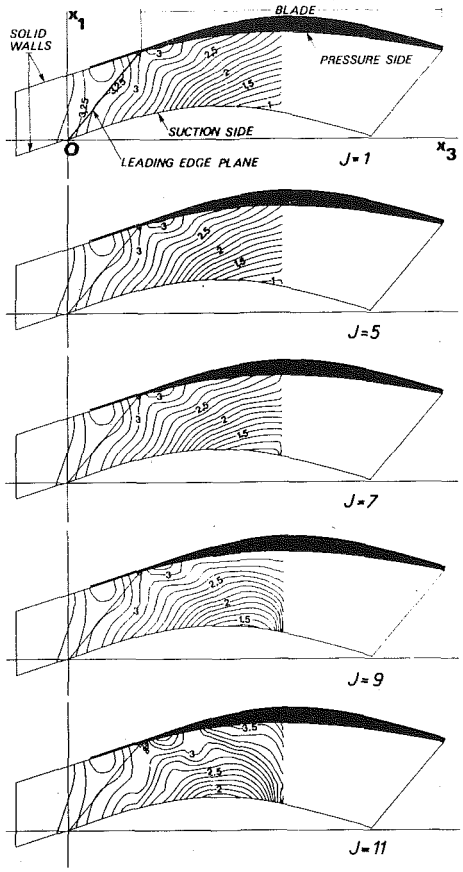

Fig. 4 Projection on plane x_3Ox_1 of constant static pressure lines on stream surfaces between the symmetry plane ($J = 1$) and the converging side wall ($J = 12$). (Static pressure unit = 0.1 atm)

The nontwisted, constant section blades are parallel to a direction Oz, the leading edge plane is parallel to Oy and the side wall convergence is defined by a function $z(x)$ (Fig. 3). The xOy plane is a symmetry plane and the calculation only accounts for the upper part ($z \geq 0$). The coordinates x_1 x_2, x_3 are chosen in such a way that x_2 coincides with z and Ox_3 be parallel to the blade chord. In this calculation the periodicity condition in front of the cascade is not taken into account but the channel is extended upstream to the plane $x_3 = -1.152$ (length unit = 1 cm) in the following manner: consider the pressure side characteristic through the leading edge in a two-dimensional calculation, and its intersection with the suction side of the adjacent blade; we choose the direction of the velocity in the initial plane to be the same as that at this intersection.

The experimental stagnation conditions are 0.8 atm and 330 K ($\gamma = 1.4$), and the upstream Mach number is 1.26.

With reference length, density and velocity respectively equal to $\Lambda = 10^{-2}$ m, $\rho_\infty = 1$ kg/m^3 and $q_\infty = 10^2$ m/s (so that the reference static pressure is $\rho_\infty {q_\infty}^2 = 10^4$ Pa), the dimensionless initial values are: $p = 3.047$, $s = 1.654$, $q_1 = 1.215$, $q_2 = 0$, $q_3 = 3.807$.

The representation of the numerical results is difficult since the stream surfaces are not plane. Therefore we give here diagrams representing on various planes projections of constant static pressure lines, in order to help the reader to understand the physical phenomenon.

Fig. 4 represents, in a plane parallel to the plane of symmetry of the test set-up, projections of the constant static pressure lines on the stream surfaces that divide the space between this plane of symmetry ($J = 1$) and the converging side wall ($J = 12$) into constant mass fluid domains. Only the stream surfaces corresponding to $J = 1, 5, 7, 9$ and 11 are presented. The calculation has been stopped near the sonic domain. It can be seen that the leading edge shock waves have been replaced by continuous compression areas. Near the plane of symmetry the constant pressure lines are nearly independent of J and the flow is locally two-dimensional; the fluid is expanded all along the suction side. On the contrary, near the converging wall the flow is strongly three-dimensional, and along the suction side the fluid expansion is followed by a compression and eventually by a strong shock wave.

Fig. 5 represents, in a plane perpendicular to both the leading edge plane and the plane of symmetry, projections of constant static pressure lines on the stream surfaces that divide the space between the pressure side ($I = 1$) and the suction side ($I = 7$) into constant mass fluid domains. Only the stream surfaces corresponding to $I = 2$, 4 and 6 are presented. Near the plane of symmetry, the constant pressure lines are straight lines perpendicular to this plane; this again shows that in the calculated domain the wall convergence does not influence the flow in the middle region of the test set-up. The highly three-dimensional nature of the flow near the converging wall can be seen again.

The duration of the calculation is very short; from $x_3 = -1.152$ to $x_3 = 4.769$ it takes less than 28 min with a C.I.I. IRIS 80 computer (less than one min with a CDC 7600—all calculations in double precision). It is possible, instead of determining the vectors $\underline{\zeta}$ and $\underline{\eta}$ at points P_3, P_4, P_5, P_6, to set them equal to $\underline{\zeta}(P_2)$ and $\underline{\eta}(P_2)$; then the results are essentially the same and the computer time is even shorter.

In order to check the accuracy of the calculations, a computation has also been made with thirteen (instead of seven) stream surfaces between the pressure side and the suction side, and fifteen (instead of twelve) between the symmetry plane and the converging wall; it has shown that the accuracy of the presented results is quite satisfactory.

4.2 Flow Field in an Annular Blade Row. An annular cascade made of twelve constant section blades has been investigated; the corresponding test set-up is described in [15]. It was designed to yield a nearly two-dimensional flow; we intend to verify this assumption. Table 2 gives some cascade parameters.

Table 2 Data for an annular cascade

Hub radius	9.6 cm
Hub to tip ratio	0.85
Blade chord	6.0 cm
Stagger angle	29.42 deg
Rotational speed	0

We use eleven stream surfaces between the pressure side ($I = 1$) and the suction side ($I = 11$), and five between the hub ($J = 1$) and

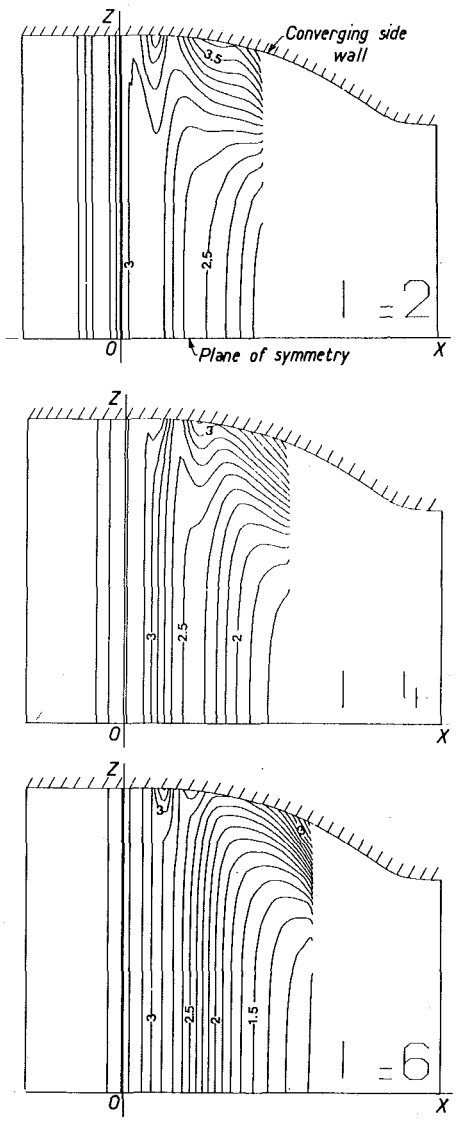

Fig. 5 Projection on plane xOz of constant static pressure lines on stream surfaces between the pressure side ($I = 1$) and the suction side ($I = 7$). (Static pressure unit = 0.1 atm)

the outer casing ($J = 5$). With an assumption similar to that used for the linear cascade, the calculation domain is extended upstream, 0.8 chord length.

Stagnation conditions are 5.2 atm and 330 K ($\gamma = 1.4$) and for an upstream Mach number equal to 1.43, the dimensionless initial values are:

$$\begin{cases} p = 15.681 \\ s = 1.119 \\ q = 4.384 \end{cases}$$

$$(\Lambda = 6 \times 10^{-2}\ \text{m},\ \rho_\infty = 1\ \text{kg/m}^3,\ q_\infty = 10^2\ \text{m/s})$$

The downstream pressure is low enough for the flow to remain started in the whole blade channel.

Figure 6 represents on a plane perpendicular to the radius midway between the leading edges of two adjacent blades, the projection of constant static pressure lines on the mean stream surface ($J = 3$). The two branches of the leading edge shock wave can be seen; their approximate locations are indicated by the interrupted lines. The internal shock wave is stronger than the outer one.

Figure 7 represents the variations of the static pressure along the eleven streamlines on the mean stream surface ($\bar{z} = 0$ at the leading edge, $\bar{z} = 1$ at the trailing edge). Again one can see the two branches

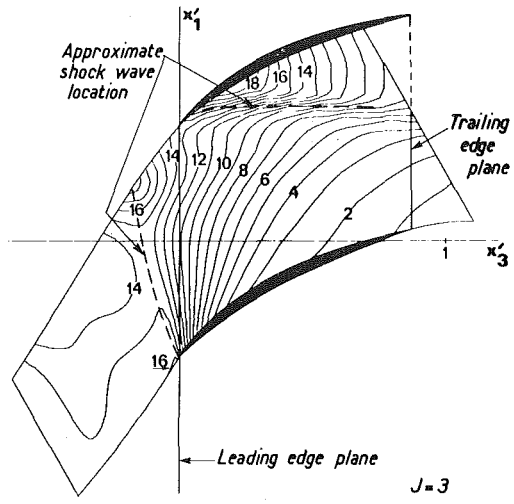

Fig. 6 Projection on $x'_3Ox'_1$ plane of constant static pressure lines on the mean stream surface (Static pressure unit = 0.1 atm). Annular blade row

of the leading edge shock wave and the expansion along the suction side. The shock system is sketched in Fig. 8.

The calculation took approximately 28 min with a C.I.I. IRIS 80 computer (all calculations in double precision).

Experimental results are available for this case and a two-dimensional calculation has been carried out in the past (see Paulon, Reboux, Sovrano [15] for a similar case). The two-dimensional calculation at the mean radius used a plane characteristic, shock fitting method. Comparison between numerical and experimental results is presented on Figs. 9 and 10. We have plotted the results of the present calculation on the mean streamsurface ($J = 3$) and on the two adjacent surfaces ($J = 2$ and $J = 4$), as well as the results of the plane calculation and the experimental results at mean radius. It can be seen that inside the blade channel the three-dimensional effects are not very important. This confirms the assumption made at the time of the design of the test set-up. The agreement between two- and three-dimensional results is quite good; this also proves that the development of shock prediction by a shock-fitting method was not necessary for the three-dimensional scheme, for the method of characteristics takes sufficiently well into account the effects of moderate shock waves (as was also shown by other authors [16]).

5 Applications of the Inverse Scheme

The inverse scheme (code name SICTES) has been applied to the calculations of linear three-dimensional blade cascades with sharp leading edges, including the inlet region and a domain upstream of the cascade. Its extension to similar calculations in rotating or nonrotating annular blade rows is straight forward.

As an example we have chosen the same cascade as in Section 4.1. We have seen in 4.1 that if one does not account for the real flow configuration upstream of the cascade, initial conditions have to be guessed, by using assumptions that are not completely satisfactory. To account for the upstream influence of the blades, we carry out the calculation on a semi-infinite cascade. In front of each blade channel we define a domain which is limited by two planes parallel to $0x_3$ and a plane normal to $0x_3$ (Fig. 11). The calculation of the first domain is made with the assumption that the upstream boundary conditions are those of a uniform flow field. The calculation of the second domain is carried out with the results of the previous calculation along the common boundary of the first two domains, and so on; we use uniform flow field conditions along the upstream boundary. The calculation is stopped when the differences between the results in the inlet region of the n^{th} domain and those of the $(n-1)^{\text{th}}$ domain are small enough.

In the present case, the angle of the incoming flow with the tangential direction Oy has an experimental value equal to 30 deg, so that there is an expansion fan at the suction side leading edge of the first domain. The other leading edges all induce a shock wave, with a rather

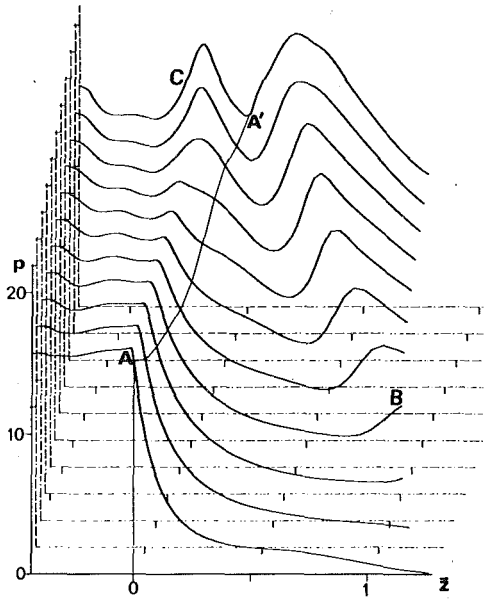

Fig. 7 Static pressure along streamlines on the mean stream surface (Static pressure unit = 0.1 atm.). Annular blade row

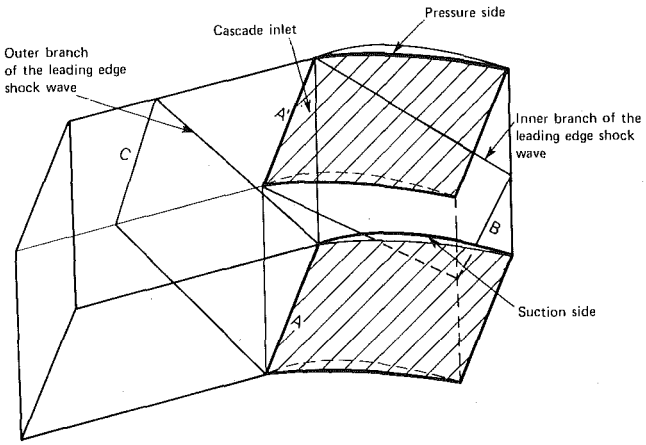

Fig. 8 Shock wave system. Annular blade row

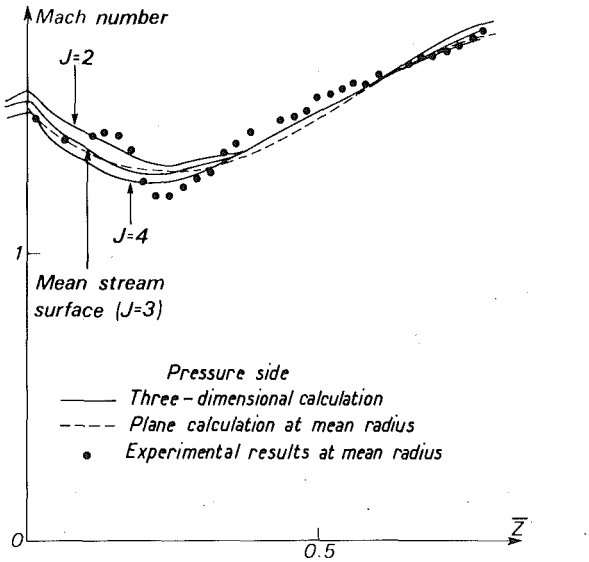

Fig. 9 Mach number distribution along the pressure side. Annular blade row

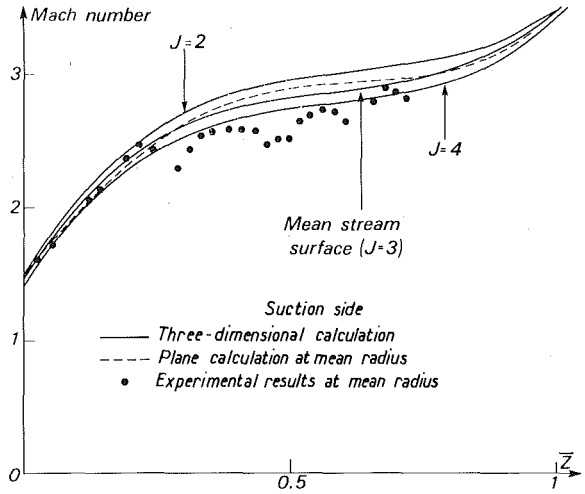

Fig. 10 Mach number distribution along the suction side. Annular blade row

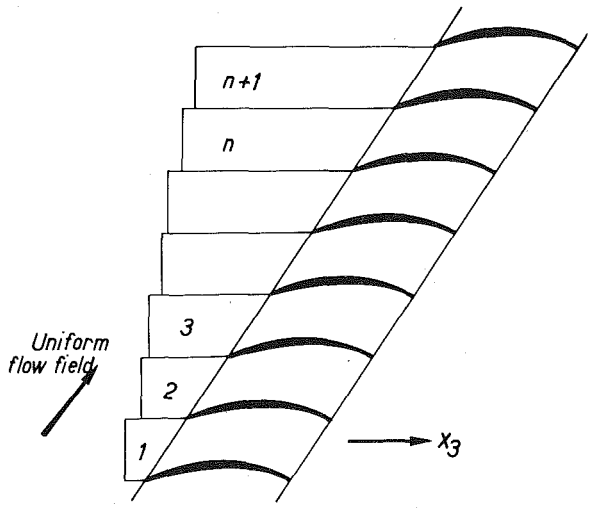

Fig. 11 Computational domain for a semi-infinite three-dimensional linear cascade

small flow deviation angle (less than 5 deg) on both sides of the blades.

In order to study the convergence of the iterations, we calculate the maximum absolute value of the pressure differences between similar points in domain n and domain $(n-1)$, in the inlet plane to the channel. This value is as low as 0.2 percent in the second domain ($n = 2$) and 0.02 percent in the fifth one ($n = 5$). Figure 12 represents constant static pressure lines in the five computational domains, at 90.9 percent of the domain height, i.e., near the converging wall.

The calculation was carried on in the third domain, downstream of the inlet region, in the blade channel. Figure 13 shows the projection on the symmetry plane of constant static pressure lines in the symmetry plane ($J = 1$) and at 54.5 percent ($J = 7$), 72.7 percent ($J = 9$), 81.8 percent ($J = 10$) and 90.9 percent ($J = 11$) of the channel height between the symmetry plane and the converging wall. Figure 14 represents the static pressure along the seven streamlines at 90.9 percent of the channel height, as a function of x_3; the different expansion and compression areas can be seen clearly; the leading edge plane is represented by line AA'. Figure 15 represents on a plane perpendicular to the plane of symmetry and to the leading edge plane the projection of constant static pressure lines on the surface midway between two blades ($I = 4$) and on a surface near the suction side, at 83.3 percent of the channel width ($I = 6$).

Conclusions similar to those of the case described in 4.1 can be drawn from these results, however the perturbations due to insufficiently accurate inlet conditions have disappeared in the present calculation.

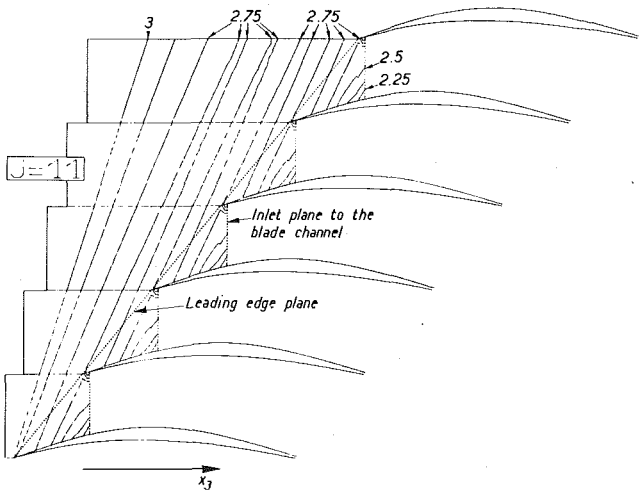

Fig. 12 Projection on plane x_3Ox_1 of constant static pressure lines, at 90.9 percent of channel height. (Static pressure unit = 0.1 atm)

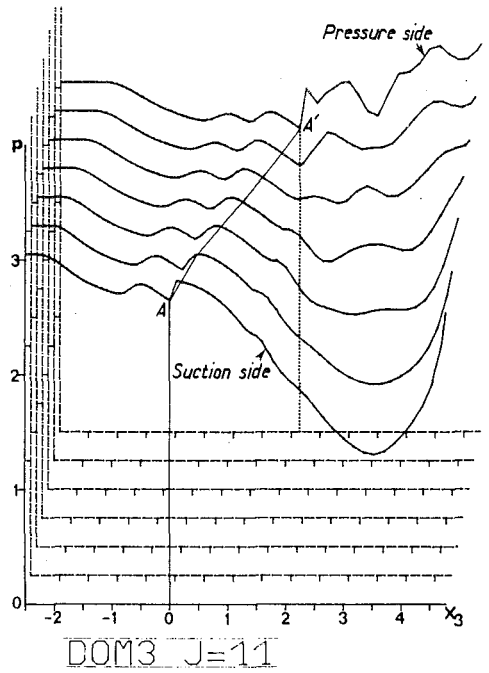

Fig. 14 Static pressure along streamlines at 90.9 percent of channel height. (Static pressure unit = 0.1 atm). Third domain

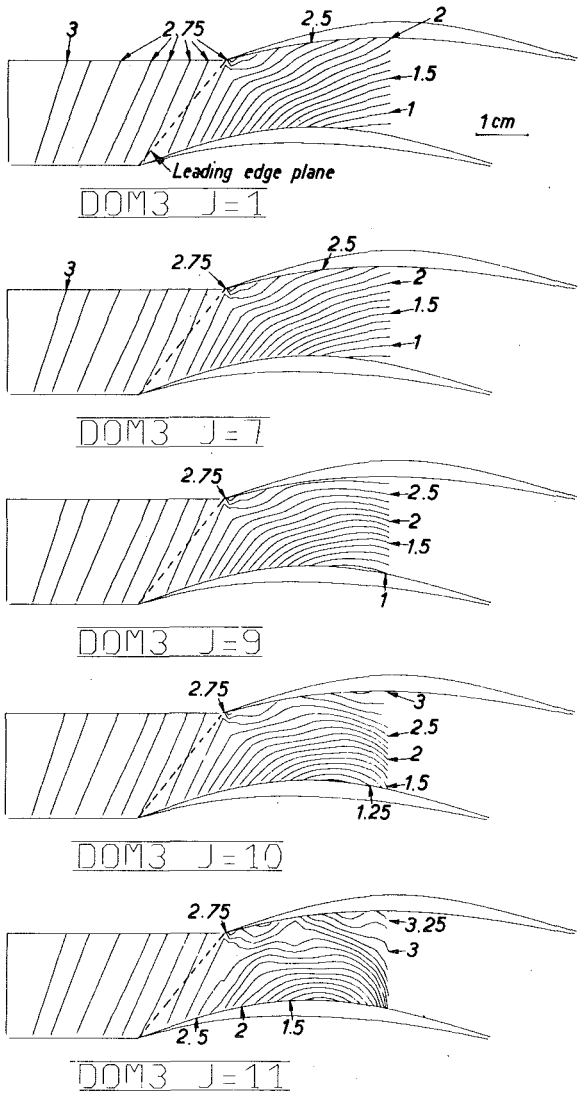

Fig. 13 Projection on plane x_3Ox_1 of constant static pressure lines in the symmetry plane ($J = 1$), and at 54.5 percent ($J = 7$), 72.7 percent ($J = 9$), 81.8 percent ($J = 10$), 90.9 percent ($J = 11$) of channel height. Third domain. (Static pressure unit = 0.1 atm)

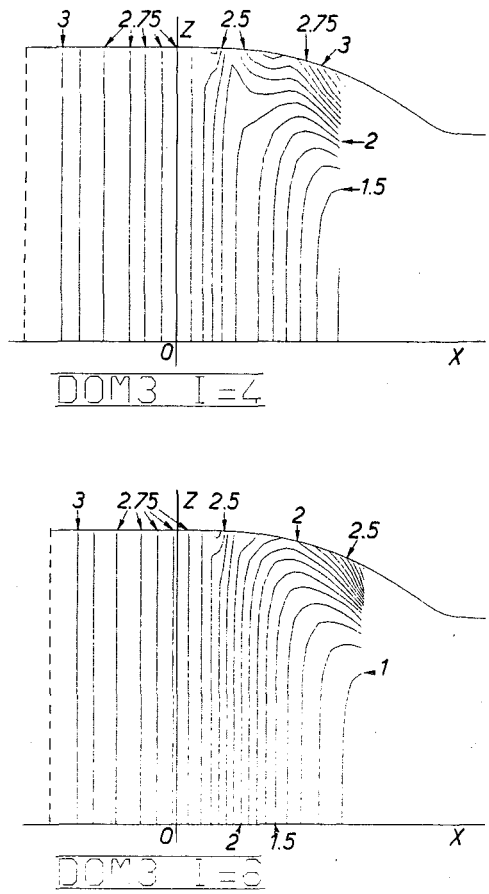

Fig. 15 Projection on plane xOz of constant static pressure lines at 50.0 percent ($I = 4$) and 83.3 percent ($J = 6$) of domain width. (Static pressure unit = 0.1 atm). Third domain

The computation time of the first five domains down to $x_3 = 1.8$ and of the third domain down to $x_3 = 4.78$ is 61 min with a CII IRIS 80 computer (about 2 min with a CDC 7600 computer). This time is of course longer than the time required for the calculation of a single blade channel, but its reward is the accuracy of the description of the inlet region.

6 Conclusion

A characteristic scheme has been developed for the calculation of three-dimensional supersonic flows in blade cascades and turbomachinery. Computation appears to be much less time-consuming than time-dependent three-dimensional schemes, and to have a high degree of accuracy. It can be used for completely supersonic domains or coupled with transient schemes to calculate the supersonic part of a transonic flow.

In its present state none of the codes used takes into account the actual shock waves, but in the encountered range of Mach numbers, this approximation seems quite sufficient.

This scheme was applied for the description of the flow field in a linear cascade with converging side walls, for which the supersonic inlet flow has a subsonic axial component. The strong three-dimensional effects that eventually lead to flow separation near the converging wall have been correctly described.

In the case of an annular blade cascade of high hub-to-tip ratio, the three-dimensional calculations confirmed the two-dimensional nature of the flow.

References

1 Wu, C. H., "A General Theory of Three-Dimensional Flow in Subsonic and Supersonic Turbomachines of Axial-, Radial-, and Mixed-Flow Types," NACA TN 2604, Jan. 1952.

2 Carrière, P., Capelier, C., "Application de la Méthode des Caractéristiques Instationnaires au Calcul Numérique d'un Ecoulement Permanent Compressible," AGARD CP35 *Transonic Aerodynamics*, Sept. 1968.

3 Veuillot, J. P., "Calcul Numérique de l'Ecoulement Transsonique d'un Fluide Parfait dans une Grille d'Aubes," *La Recherche Aérospatiale*, No. 1975–6, pp. 327–338.

4 Delaney, R. A., Kavanagh, P., "Transonic Flow Analysis in Axial-Flow Turbomachinery Cascades by a Time-Dependent Method of Characteristics," ASME JOURNAL OF ENGINEERING FOR POWER, Vol. 98, No. 3, July 1976, pp. 356–364.

5 Sauerwein, H., "Numerical Calculations of Arbitary Multidimensional and Unsteady Flows by the Method of Characteristics," AIAA Paper, No. 66-412, 1966.

6 Chu, C. W., Niemann, A. F., Jr., Powers, S. A., "Calculation of Multiple Rocket Engine Exhaust Plumes by the Method of Characteristics," AIAA Paper No. 66-651, Part I, June 1966, pp. 1–25.

7 Strom, C. R., "The Method of Characteristics for Three-Dimensional Real-Gas Flows," Cornell Aeronautical Laboratory, Inc., Buffalo, N.Y. 14221, Technical Report AFFDL-TR-67-47, July 1967.

8 Chushkin, P. I., "Numerical Method of Characteristics for Three-Dimensional Supersonic Flows," *Progress in Aeronautical Sciences*, Vol. 9, Pergamon Press, 1968, pp. 41–122.

9 Borisov, V. M., Mikhailov, T. E., "Stationary Three-Dimensional Irrotational Motion of a Gas at Supersonic Velocity," *USSR Computational Mathematics and Mathematical Physics*, Vol. 10, No. 4, 1970, pp. 253–264.

10 Ransom, V. H., Hoffman, J. D., Thompson, H. D., "A Second-Order Bicharacteristics Method for Three-Dimensional, Steady, Supersonic Flow," *AIAA Journal*, Vol. 10, No. 12, Dec. 1972, pp. 1573–1581.

11 Camarero, R., "Reference Plane Method for the Solution of Three-Dimensional Supersonic Flows," *The Aeronautical Quarterly*, Vol. 27, Part 1, Feb. 1976, pp. 75–86.

12 Fruehauf, H. H., "A Method of Characteristics for Three-Dimensional, Steady, Supersonic Flow in Rotating and Stationary Annular Cascades," ESRO TT-44, July 1975.

13 Butler, D. S., "The Numerical Solution of Hyperbolic Systems of Partial Differential Equations in Three Independent Variables," *Proceedings of the Royal Society*, Series A, Vol. 255, No. 1281, April 1960, pp. 232–252.

14 Meauzé, G., "Effets des Ecoulements Secondaires dans les Grilles d'Aubes Rectilignes," in *Secondary Flows in Turbomachines, AGARD Conf. Proc.* 214 (1977), paper No. 10.

15 Paulon, J., Reboux, J., Sovrano, R., "Comparison of Test Results Obtained on Plane and Annular, Fixed or Rotating Supersonic Blade Cascades," ASME JOURNAL OF ENGINEERING FOR POWER, April 1975, pp. 245–253.

16 Frühauf, H. H., Förster, K., "Numerical Computation of Multi-shocked supersonic cascade flows," Contribution to the 6th International Conference on Numerical Methods in Fluid Dynamics, Tiblisi, June 20–24, 1978.

N. R. Lindblad
W. F. Schilling
General Electric Company
1 River Road, Bldg. 53-316
Schenectady, NY 12345

H. J. Aeschbacher
ARAMCO Overseas Company
55 Laan Van Meerdervoort
The Hague
The Netherlands

W. H. Knoll
ARAMCO
P.O. Box 5000
Dhahran, Saudi Arabia

Gas Turbine Bucket Corrosion Protection Developments

This paper describes a joint General Electric/ARAMCO program for improving rotating gas turbine parts lives in desert environments with high concentrations of alkali salts and sulfur-containing fuels. A description of the environment is given along with a definition of the hot corrosion problem. A series of buckets coated with experimental or developmental coatings produced by a variety of processes such as pack cementation, physical vapor deposition, plasma spray and sheet claddings are described and results from actual field trials are discussed. Pt-Cr-Al pack cementation coatings were observed to perform well. Next generation overlay coatings of the MCr-AlY-type applied by plasma spraying electron beam and sheet cladding processes also performed well.

Introduction

ARAMCO Environment and Operation. The Arabian American Oil Company (ARAMCO) operates in the Arabian desert and off-shore area, in the Eastern Province of Saudi Arabia. It produces oil from an area nearly 500 km in length and 300 km in width. Gas turbines are used extensively for mechanical drives and power generation. The total installed horsepower to date is approximately 1.5 million with another 1.5 million now in the installation phase. ARAMCO uses no natural gas wells, but fuels these engines with the associated gas released from the oil, after its pressure is reduced. Thus all fuel gas is a high BTU saturated gas with large quantities of H_2S, 1 to 12 mole percent.

These engines are scattered throughout the total area from the sea coast to far within the desert. Alkali earth salts, particularly chlorides, sulfates and carbonates are found in large quantities deposited in the desert sands as well as the sea coast. Studies by C. C. Carson of the General Electric Company show as great a concentration as two percent sodium salts in the sands with most of these salts concentrated in the very fine particles. During the frequent sand storms, air borne particles were found to contain about ten times as much salt. All units, both power generation and mechanical drives are designated to operate under continuous base load conditions. However, the pump drive units because of the driven systems properties, experience a large number of full load trips. The units are started almost immediately, thereby accumulating over 8000 h/yr, but the running hours to starts ratio is about 50 to 1. The power generation and compressor drive turbines fare much better with about 1000 to 1.

These engines are designed for a summer ambient of 45 to 50 °C depending on the area of application; to allow no reduction of power during the summer months, therefore, nine to ten months a year, most units operate below full base load.

A serious limitation in the use of industrial gas turbines is an accelerated attack of the high temperature parts by what is commonly referred to as hot corrosion. This hot corrosion of turbine parts is an extremely rapid form of oxidation attack that occurs when liquid sodium sulfate (Na_2SO_4) or other alkali metal salts have condensed on airfoil surfaces from the gas stream. These deposits are formed in the combustion process due to the reaction between sulfur, oxygen, and alkali metals. The presence of only a few parts per million (ppm) of sodium and sulfur is sufficient to cause extensive hot corrosion damage to high temperature alloys. Sulfur is present as a natural contaminant in the fuel, while sodium can be introduced in a multitude of ways such as a natural contaminant in the fuel, as salt water in liquid fuel, or through the turbine air inlet at sites located on or near salt water or other contaminated areas. The source of sulfur for the results described in this paper is H_2S in natural gas while sodium comes from the turbine site terrain which contains up to two percent sodium in the desert sand.

Specific ARAMCO Bucket Corrosion Experience with Non-General Electric Turbines. Between 1961 and 1969 ARAMCO installed two mechanical drive single shaft units of 15,000 HP output and three units in power generation service of 22,000 HP output supplied by one turbine manufacturer. Firing temperatures on these units is 730 °C and they are operated without inlet air filters. Heavy sulfidation attack was found in the first unit after approximately 50,000 hr of operation (Fig. 1(a)). The heaviest attack was on the uncooled blades of Nimonic 80 A base material. For this reason, an extensive program was started to evaluate different base materials and coatings under ARAMCO operating conditions.

Various individual test blades and rainbow[1] sets have been installed

Contributed by the Gas Turbine Division and presented at the Gas Turbine Conference and Exhibit and Solar Energy Conference, San Diego, California, March 12–15, 1979 of THE AMERICAN SOCIETY OF MECHANICAL ENGINEERS. Manuscript received at ASME Headquarters December 13, 1978. Paper No. 79-GT-47.

[1] The term rainbow is used to designate a set of buckets containing a mixture of buckets which have either different base materials and/or types of protective coatings.

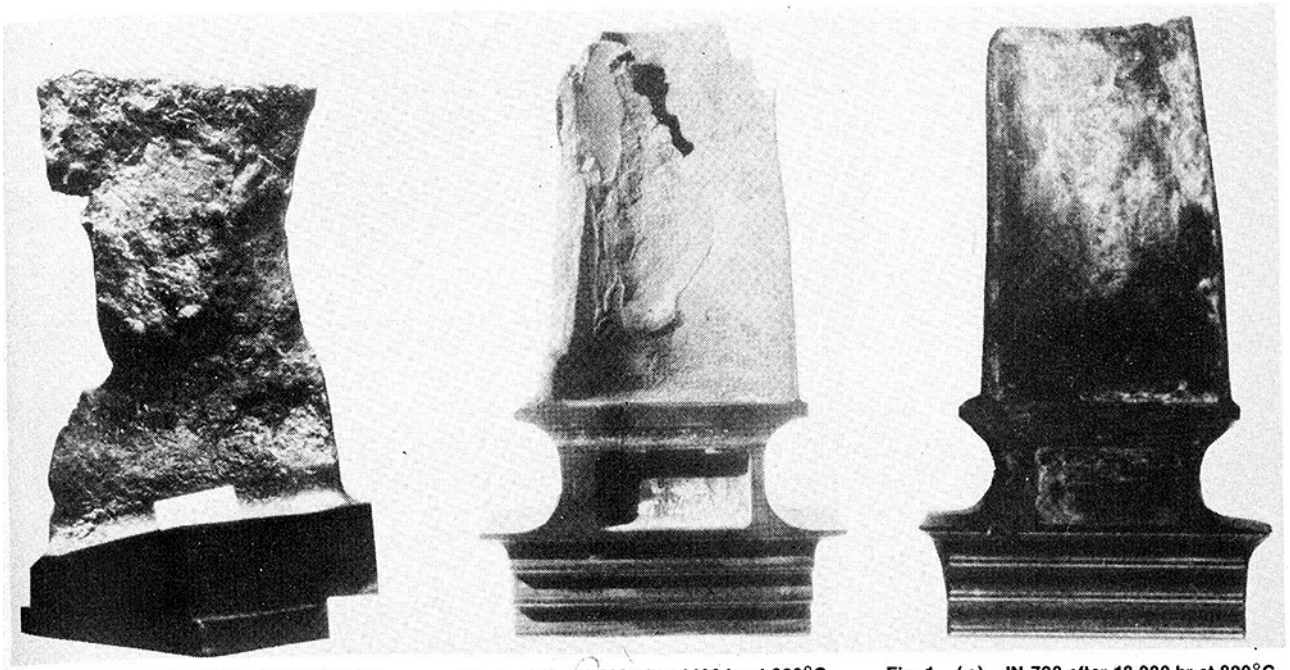

Fig. 1 (*a*) Nimonic 80A after 50,000 hr

Fig. 1 (*b*) U-700 after 4400 hr at 820°C

Fig. 1 (*c*) IN-738 after 18,000 hr at 820°C

Fig. 1 Typical hot corrosion attack on three bucket alloys in ARAMCO turbines

and tested. Following are some details of one test on turbine stator blades which ran for 18,400 hr between 1970 and 1973. The rainbow set consisted of the following base materials.

ATS2	In 738
Nimonic 80 A	MN 421
Nimonic 81	MM 432
IN 713 LC	X 40

Five different coatings, all originating from European sources, were applied to the ATS-2 and Nimonic 80 blades only. The remaining base materials were uncoated during this test. The results after 18,400 hr are summarized below.

Base Materials	
High Corrosion resistance	X-40, Nimonic 81
Adequate corrosion resistance	In 738, MARM 421, MARM 432
Low corrosion resistance	ATS-2
Not adequate corrosion resistance	Nimonic 80 A
No corrosion resistance	IN 713 LC

The behavior of these coatings (listed numerically) is outlined in Table 1. In general, the coating performance in Nimonic 80 A base material was inferior to that on ATS-2.

Based on the results on this test it was decided to use Nimonic 81 base material with corrosion protective coating No. 2 (DEW-Cr) for future use in these units. All units are now equipped with these materials and show good corrosion resistance. One of these units is now equipped with a further test set of first stage stator blades which had been installed during 1977. The following materials are included in this set: X-40, IN 738LC, IN 792, IN 939 and ATS-2. The first scheduled inspection is expected to take place the end of 1978.

One of the 22,000 HP units is equipped with several blades consisting of ATS-2 base material with a modified No. 2 (DEW-Cr) coating. These blades have now been operated for approximately 70,000 hr and will be removed during 1978. The above example demonstrates that slight modifications on coating compositions may give tremendous improvements on corrosion resistance. Therefore, it is most important that the original coating manufacturer receives complete feedback on all field results.

Specific ARAMCO Bucket Corrosion Experience with General Electric Turbines. In December 1970, an Arabian American Oil Company (ARAMCO) MS 5001 Turbine at Abqaiq, Saudi Arabia, was shut down for inspection as a result of a power loss which occurred over a two or three month period. This turbine burned natural gas containing 3.5 percent H_2S and had operated 4400 hr.

Table 1 Results of early rainbow rotor testing

Coatings	On ATS-2	On NIM 80 A
No. 1*	partially corroded	partially corroded
No. 2 (DEW-Cr)	partially corroded	mainly corroded
No. 3*	completely corroded	mainly corroded
No. 4*	mainly corroded	
No. 5*		no resistance

* Coating proprietary to ARAMCO

Inspection revealed that the power loss was due to tip corrosion of the first stage U-700 buckets. The missing inch to inch and one half of the pressure side of the airfoil shown in Fig. 1(b), as well as the heavy oxide buildup extending to about an inch above the platform, clearly demonstrate the severity of the attack on the buckets.

A metallographic examination using the optical microscope revealed severe surface attack characteristic of "hot corrosion" on the pressure side of the airfoil. It is typified by excessive oxidation above the surface with a depleted zone containing particles (gray) of a sulfide (e.g. CrS_X) between the base metal and the oxide as seen in Fig. 2. It was evident that corrosion had reduced the airfoil cross-section to a thickness which could not support much load and was the probable cause of failure.

The turbine was rebucketed with U-500C to prevent a recurrence of the catastrophic hot corrosion attack if U-700 material were used. This was an interim solution, since U-500C is a weaker alloy although it has about ten times more corrosion resistance than U-700 in highly corrosive environments. Alloy IN 738, when it became available, replaced U-500C to get the desired creep life while maintaining good hot corrosion resistance.

In order to evaluate potentially improved corrosion resistance, the rotor was rebucketed with IN 738 buckets, 16 of which were coated, thus producing a test "rainbow rotor." 15 of these buckets, were coated with four "first generation" coatings. These coatings consisted of:

1 one aluminide coating normally used for oxidation resistance in aircract engines,
2 one chromium coating similar to that used by a heavy-duty gas

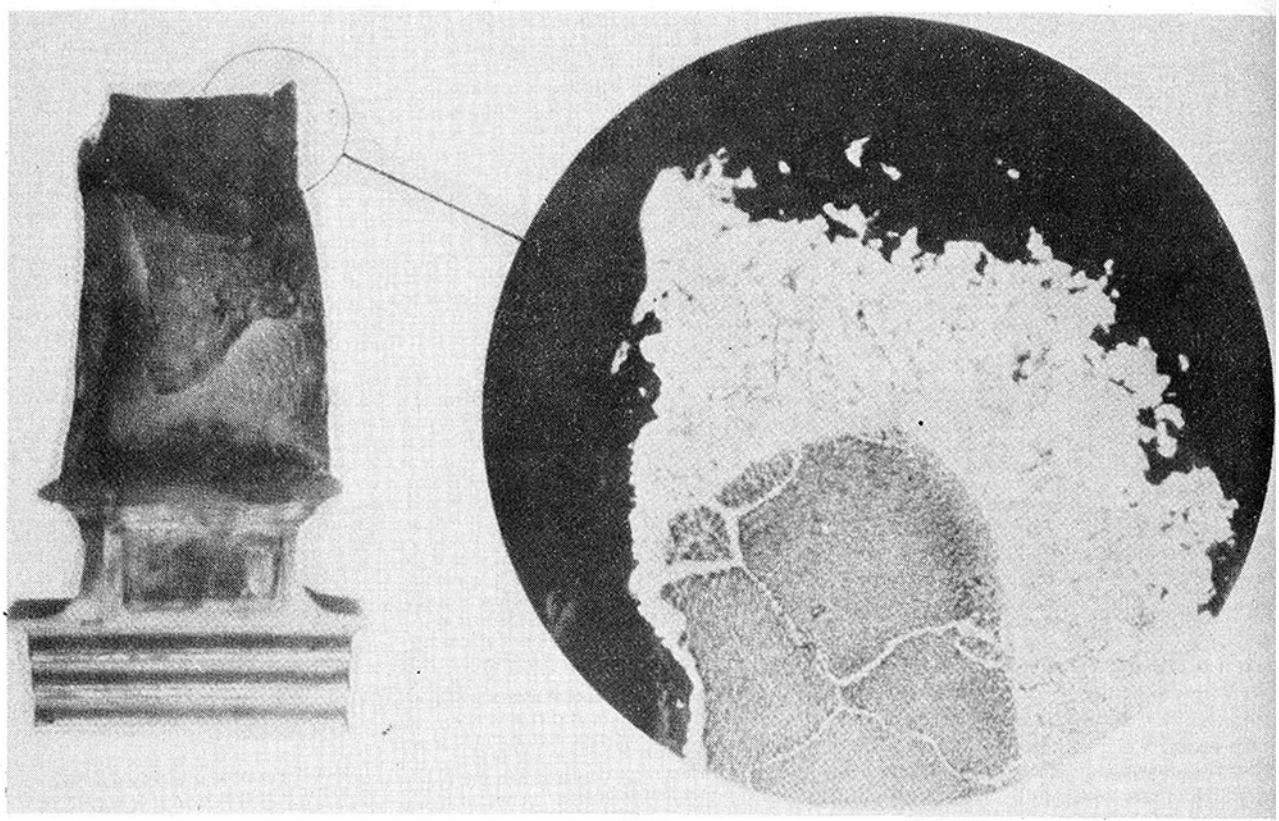

Fig. 2

turbine manufacturer, but at a much lower temperature,

3 two chromium/aluminum coatings which lasted twice as long in the burner rigs as either the aluminum or chromium coatings.

The sixteenth bucket was coated with a then-experimental electron-beam deposited coating capable of much longer burner rig life.

After 18,000 hr of service, the buckets were removed, cleaned and examined to determine the amount of coating and base metal attack. An uncoated bucket is shown in Fig. 1(c). All the coatings added life to the bucket airfoil surfaces. The aluminide, chromide, and the Cr-Al coatings added only 2000 to 4000 hr to the life of the IN 738 buckets, and weren't worth further consideration for long life buckets. The second generation coating (MCrAlY) had much greater protection capability, but was nonadherent or failed through localized defects in several critical areas. It was concluded that this type of coating composition would be outstanding when improved processing techniques for application were developed.

It was also observed that tips of the buckets exhibited extensive distress and corrosion. But the uniformity of tip distress on the uncoated and all coated buckets suggested that tip loss was not a corrosion phenomenon only. Significant amounts of corrosion were observed on the tips of all buckets on both the pressure and suction sides. A knife-shaped profile and lack of internal corrosion products at the tip of the pressure side suggested attack was due to the combined effect of corrosion and erosion.

The turbine atmosphere is both corrosive and erosive. It appeared that corrosion began as the protective oxide on the bucket surface was stripped away and bare metal exposed. Hot corrosion attack then began in the bare base metal. Then the corrosion products were also stripped away by the particulate matter in the gas stream, thus causing the base metal to corrode at an even faster rate. Corrosion and erosion thus combined to produce a degree of corrosion attack which was greater than if only corrosion were present. The results indicated that the combination of second generation coatings and added tip protection held the promise of giving substantial added bucket lives in ARAMCO environments. These systems were incorporated into the four phase advanced rainbow rotor program.

ARAMCO—General Electric Rainbow Rotor Program. ARAMCO's original purchase of mechanical drive turbines for their water flood program consisted of 22 Frame 5, two shaft General Electric turbines rated at 22,500 HP. These turbines were widely scattered in remote desert areas and controlled by microwave telemetry. The original concept involved unmanned stations, but problems in the telemetry, water piping and coordination between the sites required manning of the plants. These problems accounted for the low running hours per start.

From ARAMCO's experience with the earlier lower firing units they expected hot gas corrosion on their newer turbines and set 40,000 running hours between major overhauls and bucket change outs as a realistic goal to be achieved. Cleaning of the fuel was determined to be uneconomical. Each water flood site consisted on an average of two or three turbines and each gets its fuel from the nearest GAS/OIL Separation Plant. An ASME paper [1] showed that salt ingestion could be reduced by high efficiency air filters and all new turbines are equipped with these. A program also was set up to retrofit the water flood turbines with filters.

Still, ARAMCO felt that from its earlier experience with various metals and coatings that much, if not all its goals could be achieved with protective bucket coatings. ARAMCO approached General Electric and suggested a jointly funded program to develop the most practical bucket protection. Testing of various available coatings and any experimental coatings which appeared promising were to be done in the G.E. Frame 5 turbines in actual operating conditions. ARAMCO accepted and bore all responsibility for a failure due to any experimental coating, a very minimal risk and up to date none have occurred. Buckets were to be removed at various running hours and returned to General Electric for extensive laboratory testing.

Program Overview

The bucket coating development program identified by General Electric's Gas Turbine Department and ARAMCO consisted of four distinct phases which were established largely on the basis of machine availability, duty cycle and the ability of the various state-of-the-art coating processes to produce meaningful quantities of (i.e. 10–20) coated hardware for field evaluation. Further, as improvements in

this state-of-the-art for large industrial hardware were realized both from a compositional and process standpoint, it was the intent of this program to retain flexibility in order to incorporate these improvements as they occurred. Thus, the following program phases were identified over a two year period and are shown in Table 2.

While hot corrosion of bucket tips was a concern for the MS 5001 machine no such distress has been observed for the MS 5002 and thus tip protection will not be discussed in this paper. Currently, only the Pre-Phase I and Phase II coatings have been evaluated and results are reported here. Field testing of Phase I has just been completed while Phase III is continuing.

As can be seen from the above chronology, both improved processing capability and coating compositions based on laboratory burner rig testing were included in each successive Phase of the program.

Detailed descriptions of the processes utilized in this program can be found elsewhere in the literature [2–6]; a brief description of each of the coating processes is given here for completeness.

Pack Cementation. This is one of the oldest and most well established methods for producing a protective, corrosion resistant layer on a superalloy surface. The method generally requires the embedding of the part in a mixture of alumina, aluminum halide & surface activator. The subsequent application of temperature and time results in Al deposition and subsequent diffusion/reaction to form a thin (50–100 μm) layer of βNiAl at the part surface. Recently the incorporation of precious metals such as Pt or Rh into the diffusion coating has spawned a whole new generation of this class of coatings.

Physical Vapor Deposition. This process has been actively investigated over the past 10–15 years and is currently used as a production coating process for aircraft and industrial gas turbine overlay coatings. The process utilizes an electron beam to produce a molten metal pool where vapor pressure will produce the desired coating composition. Due to the high beam temperatures a high metal vapor pressure is produced from the alloy elemental species. This gas is then deposited directly on the colder workpiece in a line of sight manner. In most instances the workpiece is preheated prior to coating. The advantages of this method include a high degree of coating compositional flexibility, capability to coat complex geometries such as turbine buckets and relatively high coating rates. Disadvantages include structural control, inability to use elements with low vapor pressures and moderately high cost.

Plasma Spray Coatings. This process utilizes a high temperature, high velocity plasma gas (Ar, He) stream into which fine metal powders of the desired composition are injected. The powders are heated in the plasma stream and in some instances melted, accelerated and deposited on the substrate or workpiece. Proper control of the plasma gun motion relative to the workpiece motion allows for good overall coating thickness control. Recently, modifications to the plasma spray process have been made to allow spraying in an enclosed chamber at low particle pressures of inert gas. These modifications permit the application of adherent oxide-free coatings with compositions containing highly reactive elements. Advantages include compositional flexibility, good structural control, moderate cost and high rates.

Sheet Claddings. Sheet claddings require the forming and diffusion bonding of thin (175–375 μm) highly corrosion-resistant sheet alloys to the high strength superalloy bucket substrate. The technique utilizes conventional sheet forming to technology and hot isostatic pressing (HIP) to produce a diffusion bonded overlay coating of uniform thickness with excellent control of coating structure. The technique is limited to compositions which can be produced in sheet form. In some instances, both PVD coatings and sheet claddings were subjected to pack aluminization after coating as a means of further increasing the surface aluminum content of the overlay coatings.

Pre-installation Procedures. First stage MS 5002 production buckets were obtained and sent to various coating vendors for coating. Sheet claddings are a General Electric Gas Turbine Division (GTD) development and as such were applied by the Schenectady, NY Material and Process Laboratory since vendor capability did not exist at the time this program was conducted. The as-coated and heat treated buckets were returned to GTD and sample buckets were sectioned and metallographically checked for coating quality, bondline structure, thickness and surface finish where required. Coating identities were stamped on the bucket shanks after which the buckets were moment weighed and charted for wheel position prior to shipment to ARAMCO for turbine insertion in the field.

Table 2 Coating/process summary

Phase	Processes	Coating Compositions
Pre-Phase I	Pack Cementation	PtCrAl
Phase I	Pack Cementation	PtCrAl
	Plasma Spray	CoCrAlY
	PVD	CoCrAlY
Phase II	Pack Cementation	PtCrAl
	Plasma Spray	CoCrAlY
	PVD	CoCrAlY
	Sheet Cladding	NiCr, FeCrAlY, CoCrAlY
Phase III	Pack Cementation	PtCrAl
	Plasma Spray	NiCrSi, CoCrAlY
	PVD	CoCrAlY

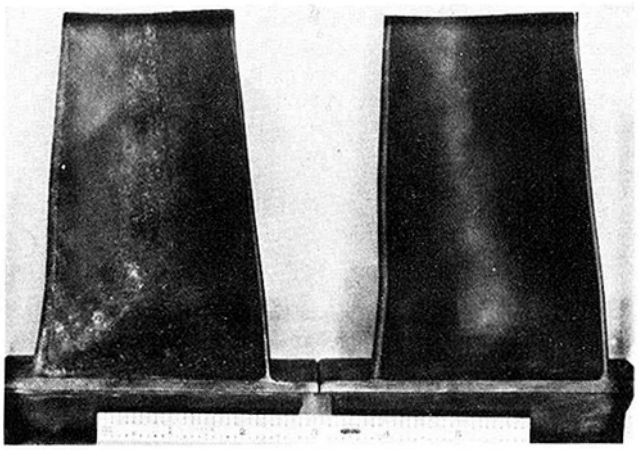

Fig. 3 (*a*) Uncoated IN-738 Fig. 3 (*b*) Pt-Cr-Al coated IN-738

Fig. 3 The visual appearance of a Pt-Cr-Al coated IN-738 bucket compared with an uncoated IN-738 after 25,000 hr of service at a metal temperature of 830°C in an ARAMCO MS-5002 turbine

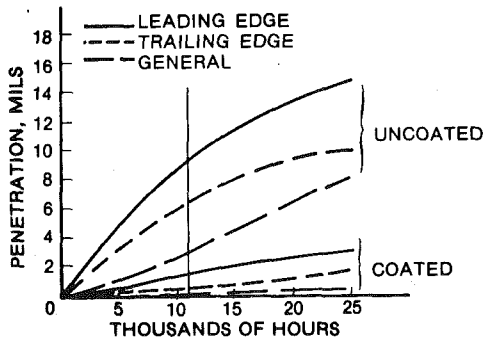

Fig. 4 Comparison of the penetration of Pt-Cr-Al coated and uncoated IN-738 buckets

Pre-Phase I—Results and Discussion

Coated and uncoated IN-738 buckets were removed from an ARAMCO MS 5002 gas turbine to evaluate the protectiveness of the platinum-chromium-aluminum coating compared with the uncoated IN-738 base alloy. Buckets were removed after 11,271 hr of service (289 fired starts) and after 25,000 hr of service (600 fired starts). Operation was base load at 930°C firing temperature.

The coated and uncoated bucket airfoils after 25,000 hr of service are shown in Fig. 3 (similar *but better* after 11,271 hr). Most of the coated airfoil and platform surfaces were very smooth and shiny, essentially devoid of built-up scale, deposits, or crusty residues. Some surface roughness, but much less in comparison with the uncoated bucket, was noted at the pressure and suction face fillets and along the pressure face side of the leading edge.

In contrast, the uncoated buckets exhibited corrosion and extreme surface roughness over most of the airfoil pressure face and platform surfaces. The leading edges of the uncoated buckets were quite rough and blunted in several areas. Profile measurement at the leading edges revealed 250–3755 μm of surface recession.

The Pt-Cr-Al coatings was extremely protective for 25,000 hr on IN-738 and was unpenetrated except for a very small area on the leading edge. A graphic comparison of the penetration of the coated and uncoated buckets is shown in Fig. 4 at the leading and trailing edges and for the airfoil in general. Even on the leading edge where the coating was penetrated, however, no attack of the IN-738 base metal was observed as shown in Fig. 5(a). In contrast, the uncoated bucket, Fig. 5(b), showed extensive oxide penetration to a depth of 375 μm. This massive oxide attack is a form of low temperature hot corrosion which occurs at temperatures of 705°C and below and was found only at the leading edge and on the platform. This type of corrosion was not observed after 11,000 hr of service when the turbine operated at full load; during the last 14,000 hr of operation, the turbine ran at 83 percent of full power with a resultant significant drop in metal temperatures.

The trailing edge area of the buckets showed the next most severe attack. The coating was partially penetrated in this location with losses to the diffusion zone (25—50 μm) as shown in Fig. 6(a). At the same location on the uncoated bucket, classical hot corrosion occurred to a depth of about 250 microns as shown in Fig. 6(b). Globular sulfides are located in depleted regions below the surface oxide and intergranular penetration of sulfides forms spikes or stress-risers into otherwise good base metal.

Most of the coated bucket had very little attack of the coating and appeared as shown in Fig. 7(a). After 11,000 hr, the uncoated bucket also revealed little hot corrosion attack, but after 25,000 hr appeared as shown in Fig. 7(b) with about 200 μm of penetration. Again, intergranular attack was present which may act as a notch and reduce fatigue properties.

As a result of this evaluation, it was determined that the Pt-Cr-Al coating will protect IN 738 buckets for 25,000 hr in this environment and operating conditions. Furthermore, the hot corrosion resistance of IN-738 will contribute additional life before bucket failure. Turbines operating under similar conditions should have 40,000 to 60,000 hr of bucket life.

Phase II Macroscopic Examination

The Phase II buckets were removed from the turbine after 13,051 fired hr and 225 starts. The buckets were subjected to a macroscopic examination including charting of the service condition of each bucket prior to sectioning and macroscopic preparation. At the time of the preparation, the detailed evaluation of all parts was still in progress, however, the preliminary stages of the program are complete and reported here.

The macroscopic appearance of the buckets removed from the Phase II turbine were similar to those shown in Fig. 3.

Uncoated IN-738. Duplicate buckets were removed from the turbine for evaluation and were found to be very similar in appearance. The concave face displayed light to moderate attack (surface roughening/scaling) near the trailing edge which transitioned to heavier scaling near the bucket mid-chord and then to little or no corrosion near the leading edge. The bucket leading edge, however, was extremely roughened. The bucket platform sections were heavily scaled. The convex face showed moderate to heavy corrosion near the leading edge which transitioned to little or no attack towards the trailing edge.

Pack Diffusion Coatings. As we observed in the Pre-Phase I section of this paper, the NiPtCrAl coated bucket also performed extremely well in the turbine environment utilized for the Phase II exposures. Except for some very light surface roughening on the concave face near the trailing edge and on the fillet (root) radius this coating was essentially unattacked after the exposure.

Plasma Spray Coatings. These coatings all appeared by macro-examination not to have suffered environmental degradation. An objective assessment of the surface condition was difficult due to

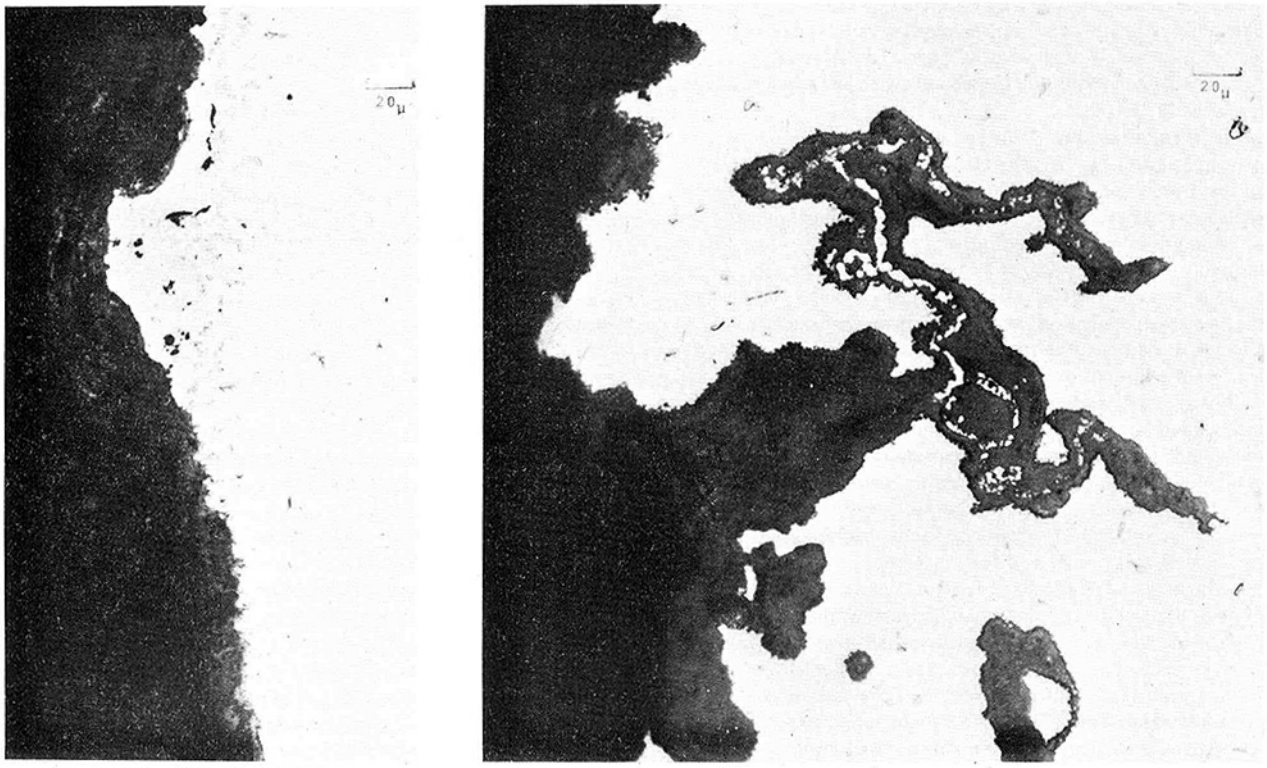

Fig. 5 (a) Pt-Cr-Al coated IN-738

Fig. 5 (b) Uncoated IN-738

Fig. 5 Comparison of the leading edge of uncoated and Pt-Cr-Al coated IN-738 buckets after 25,000 hr of service. The coating was penetrated to the base metal while the uncoated leading edge was penetrated 375 μm into the base metal.

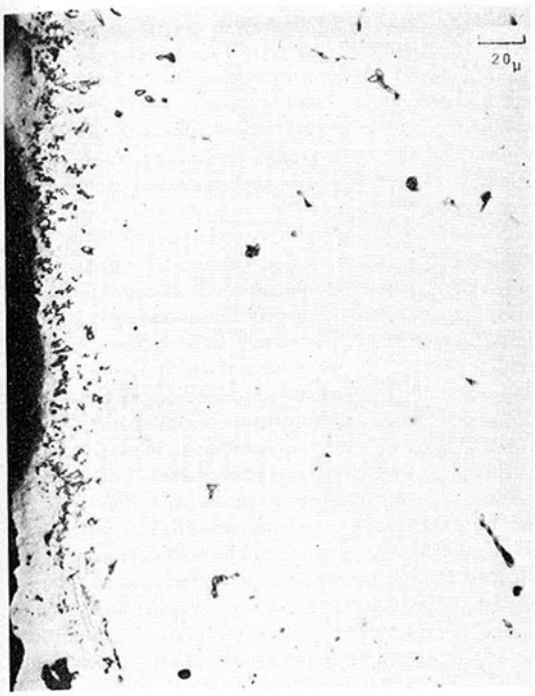

Fig. 6 (*a*) Pt-Cr-Al coated IN-738

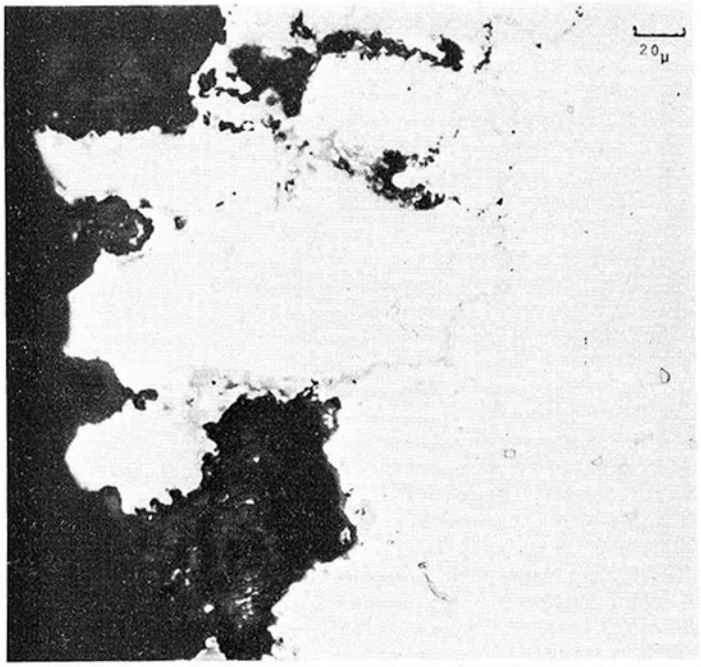

Fig. 6 (*b*) Uncoated IN-738

Fig. 6 Comparison of the trailing edge area of the uncoated and Pt-Cr-Al coated IN-738 buckets after 25,000 hr of service. The coated bucket was unpenetrated while the uncoated bucket showed 250 μm of surface intergranular attack.

Fig. 7 (*a*) Pt-Cr-Al coated IN-738

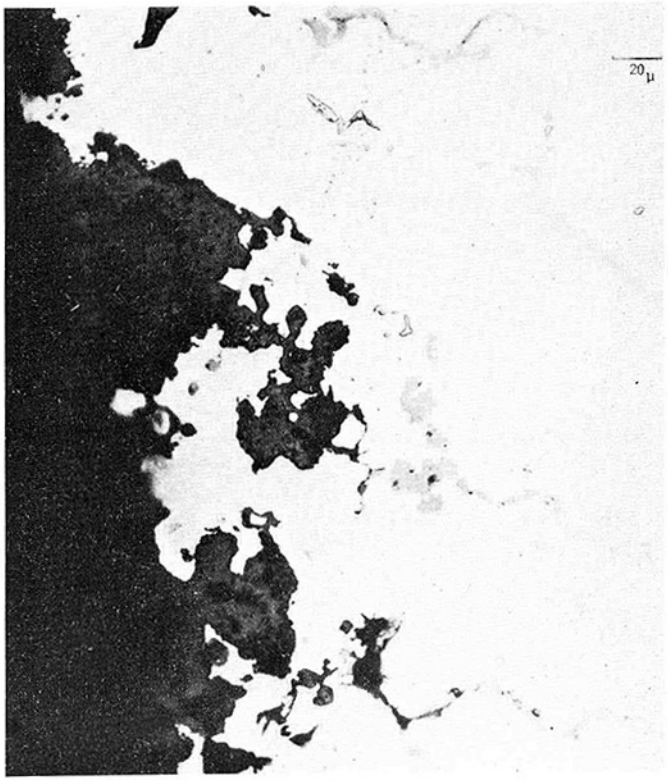

Fig. 7 (*b*) Uncoated IN-738

Fig. 7. Comparison of most of the uncoated and Pt-Cr-Al coated IN-738 buckets after 25,000 hours of service. The coated bucket surfaces were essentially unattacked while the uncoated bucket showed 200 μm of surface and intergranular attack.

the initially high surface roughness associated with the finish on the original as-sprayed buckets. In general, surface roughness was observed to decrease from an average of about 7.5 μm to about 3.0–4.0 μm after turbine exposure. Additionally, the bucket pressure face was observed to have higher roughness than the suction face after exposure. No difference was observed for the two coating compositions evaluated.

Sheet Claddings. As indicated in Table 2, Fe, Ni and Co-based alloy composition were evaluated. In general, the Ni-based compositions both as-clad and clad + pack aluminided showed the severest degradation. The as-clad NiCr bucket possessed moderate to heavy surface roughening on the pressure face near the bucket mid-chord region and variations of light to heavy attack on the suction face near the bucket trailing edge.

In strong contrast to the results described above, the Fe and Co based clad compositions appeared to be in excellent condition. Except for a few localized spots generally near the bucket trailing edge these compositions appeared to be virtually unattacked.

Electron Beam Coatings. The two buckets which were electron beam coated with a Co-based composition were also in excellent condition. One bucket which had been pack aluminided after EB coating displayed a small amount of spallation at the bucket trailing edge, but otherwise undamaged. In general, the electron beam deposited coatings were much smoother after turbine exposure than any of the other overlay coatings evaluated.

Phase II Metallographic Evaluation

A detailed metallographic evaluation of the uncoated IN-738 was conducted and the results are reported below. The preliminary metallographic evaluation of the coated buckets was then confined to the corresponding uncoated bucket region which displayed the greatest amount of hot corrosion attack. As indicated earlier, a detailed investigation of each coating's performance over the entire bucket surface is in progress.

Uncoated IN-738. Metallographic examination of the uncoated IN-738 pitchline section indicated that the most severe corrosion occurred at the leading edge. 100–180 μm of sulfide penetration was observed at this location. This attack (Fig. 8) was mainly in the form of intergranular hot corrosion. Relatively little surface oxide was observed. Similar areas on the pitchline section were also observed on the trailing edge half of the concave face and on the convex face near the leading edge. Surface roughening was found to occur in both the presence and absence of intergranular attack. No evidence of intergranular penetration was found on the lower airfoil section where, however, surface roughening had occurred. As observed on IN-738 buckets from other ARAMCO machines the fillet/platform areas exhibited low temperature hot corrosion. The metallographic examination confirmed the earlier visual observations that blistering, surface distortion, heavy oxide formation and bucket wall thinning had not occurred as a result of this exposure. All coatings were evaluated at the bucket leading edge, pitchline section for direct com-

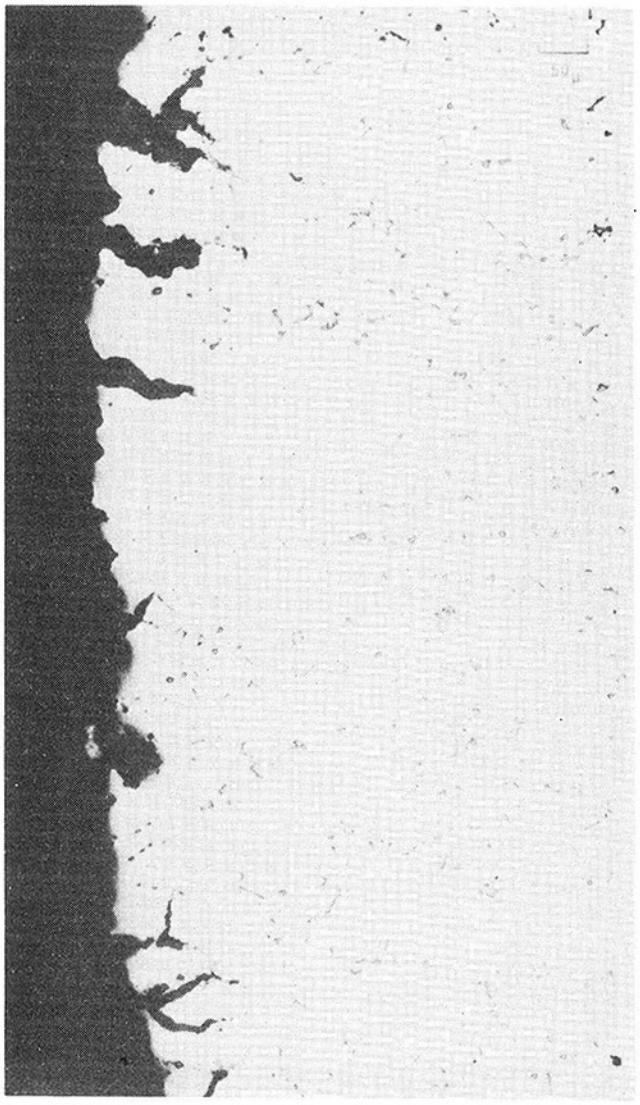

Fig. 8 Uncoated IN-738

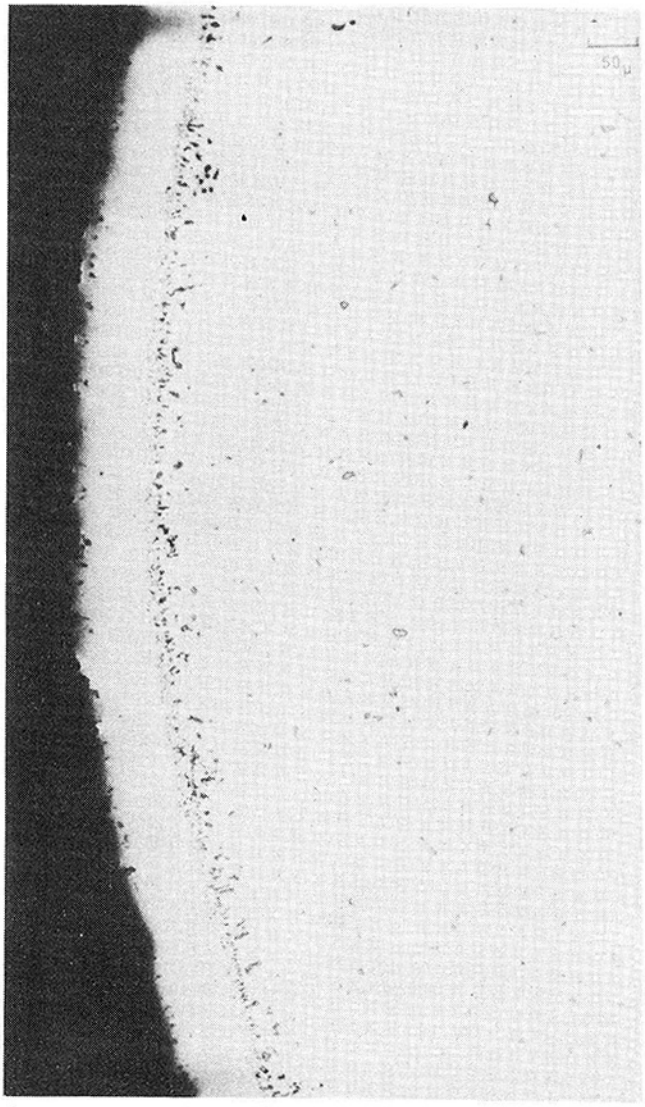

Fig. 9 Pt-Cr-Al at leading edge

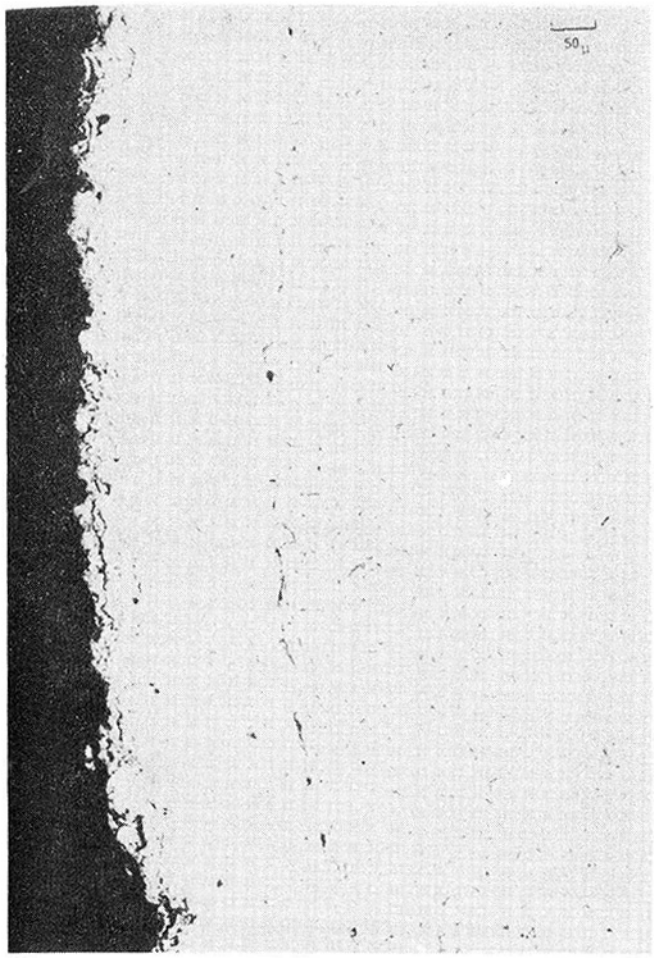

Fig. 10 Plasma sprayed CoCrAlY coating

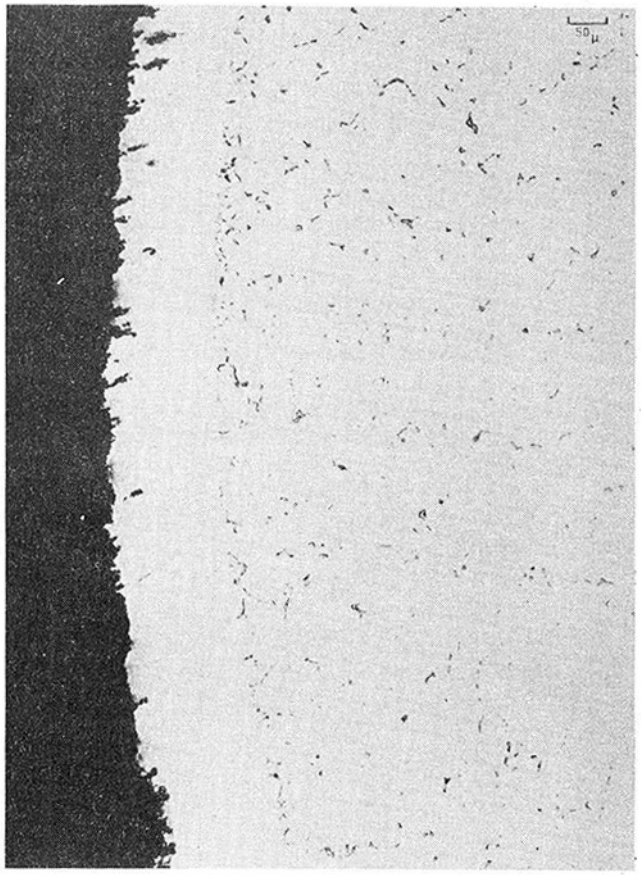

Fig. 11 Electron beam CoCrAlY coating after 13,051 hr turbine service

parison with uncoated IN-738 since this location displayed the most severe hot corrosion attack.

Pack Cementation Coatings. The Pt-Cr-Al coating (Fig. 9) was entirely intact and showed no evidence of distress at the bucket leading edge where evaluated. The coating was about 65 μm thick at this location which favorably compares with an as-coated thickness of 65–80 μm.

Plasma Sprayed Coatings. The plasma sprayed CoCrAlY coatings were observed to be in excellent conditioon (Fig. 10). The coating thickness was 210 μm at the bucket leading edge. Approximately 50 μm of hot corrosion attack was observed at this location. This attack appeared to be associated with the layer of interparticle oxide stingers which had been formed during the spraying process. The coating was adherent despite a semi-continuous oxide layer or other contaminant at the coating/substrate interface. No IN-738 base metal attack was observed.

Electron Beam Coatings. A thin layer of oxide scale as well as about 30 μm of hot corrosion attack was apparent on the coating (Fig. 11). The overall coating thickness was about 160 μm compared to an as-coated thickness of 175 μm. The coating/substrate interface was extremely clean and no evidence of coating spallation or cracking was observed. Overall the coating was in excellent condition and base metal attack had not occurred.

Sheet Claddings. The nickel based Ni-Cr cladding showed evidence of significant hot corrosion attack. The pitch section leading edge suffered cladding loss down to the IN-738 substrate alloy. A small amount (10 μm) of substrate attack was observed primarily in the diffusion zone region. Approximately 50 μm of cladding remained compared to a starting thickness of 200 μm. The Ni-Cr cladding which was pack aluminided also suffered considerable attack. In this case, approximately 125 μm of the original 200 μm of cladding remained and heavy oxide/sulfide scaling was present. Base metal attack had not occurred.

The Fe and Co base claddings, in sharp contrast to the nickel base composition performed extremely well. The Fe base composition showed a small amount of surface roughening and less than 15 μm of oxide scale. The original 250 μm of cladding still remained (Fig. 12(a)). The cobalt based cladding which had been pack aluminided after cladding (Fig. 12(b)) was virtually unattacked after turbine exposure.

Summary

Early ARAMCO field experience identified the need for improved bucket surface stability. A "rainbow rotor" concept was chosen by General Electric and ARAMCO as the means for evaluating a variety of bucket coating compositions and processes under identical field conditions. Initial (Pre-Phase I) results on Pt-Cr-Al coatings indicated that an additional 25,000 hr of bucket life can be obtained by their use. In no instance was base metal (IN-738) attack observed on the Pt-Cr-Al coated buckets after this exposure.

The uncoated In-738 Phase II bucket suffered 180 μm of hot corrosion attack after the 13,051 hr turbine exposure. In contrast all of the Phase II coatings succeeded in preventing base metal attack. The Cr-Al pack cementation coating and the Ni-Cr cladding were nearing the end of their useful life while the Ni-Cr cladding which had been over-aluminided by pack cementation was observed to be attacked at a faster rate than any other coatings. The Pt-Cr-Al, plasma sprayed CoCrAlY, electron beam CoCrAlY, clad FeCrAlY and CoCrAlY were all in excellent condition. Additional turbine exposures are required (and are in progress) in order to discriminate between the remaining coating systems.

Acknowledgments

The authors would like to acknowledge H. M. Fox, K. L. Kettler, General Electric Co., and T. L. Flowers, ARAMCO for their conscientious attention to this program.

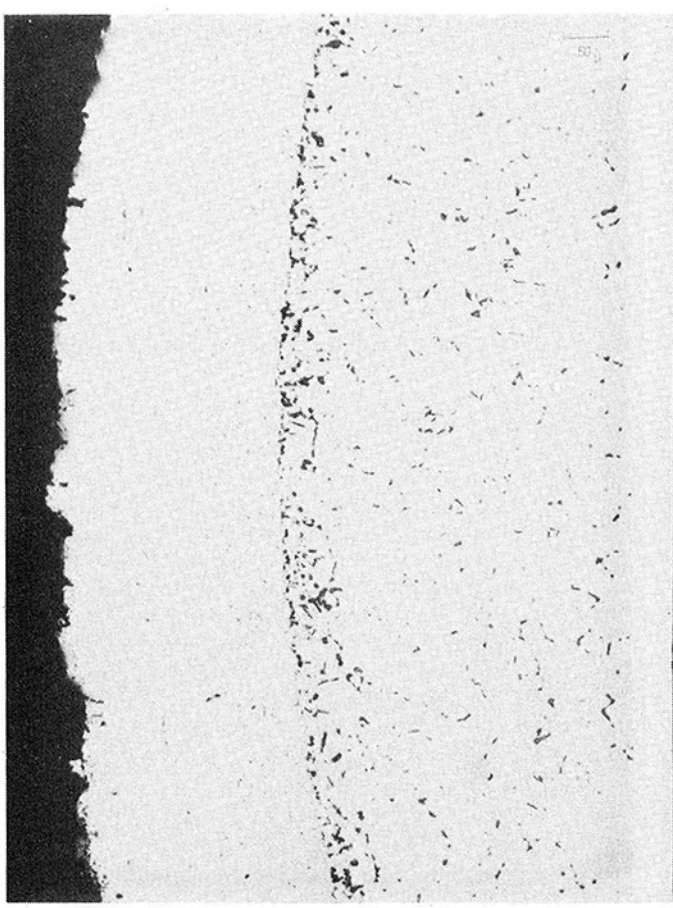

Fig. 12 (*a*) FeCrAlY cladding on IN-738

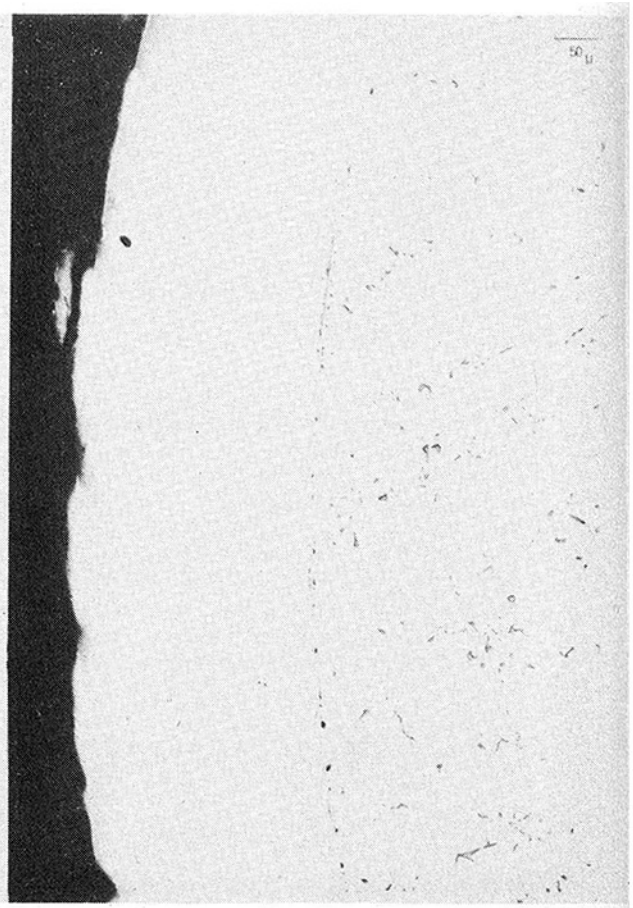

Fig. 12 (*b*) CoCrAlY cladding on IN-738

References

1 ASME Paper No. 75-GT-105.

2 Lindblad, N. R., *Oxidation Met.*, 1, 1969.

3 Mehlberger, E., Seventh International Metal Spraying Conference, London, Sept. 1973, Paper No. 58.

4 Powell, C. F., et al., *Vapor Deposition,* John Wiley & Sons, Inc., New York.

5 Gedwill, M. A. and Grisaffe, S. J., *Metals Engineering Quarterly,* May, 1972.

6 Beltran, A. M. and Schilling, W. F., "Superalloys: Metallurgy and Manufacture," *Proceedings of the Baton Rouge,* p. 425.

J. W. Vogan
Senior Research Engineer.

A. R. Stetson
Chief-Materials Engineering.

Solar Turbines International,
2200 Pacific Highway, P.O. Box 80966,
an Operating Group of
International Harvester
San Diego, CA 92138

Application of Abrasive Coatings to Clearance Control in the Gas Turbine

Efficiency of a gas turbine is reduced by vane tip losses in the compressor section; also, vane tip/rotor rubs can produce catastrophic failure of a gas turbine engine. This paper describes a test rig and experimental data obtained evaluating abrasive coatings for clearance control between the vanes and the rotor in a gas turbine compressor. Plasma/flame sprayed oxides, carbides and bonded abrasives were tested under conditions duplicating those encountered in the compressor section. The effectiveness of the coatings in grinding away the vane tips to provide minimum clearance without damage to the vane or rotor was determined. Coatings with rough, sharp abrasive grains were most effective. The laboratory tests were confirmed in engine development tests and by application to a compressor rotor now in operation.

Introduction

With rising fuel costs and increasing shortages, improved efficiency in gas turbine engines is essential. The large tip clearances currently in use in stationary turbine compressors to prevent contact due to shaft eccentricities and other factors are no longer acceptable.

The problem is best illustrated by reference to a schematic of a modern industrial gas turbine (Fig. 1). The vanes in the engine are static about the rotor. Spacing between unshrouded vanes and rotor should be minimal for greatest efficiency, i.e., clearance to permit assembly and to allow for rotor thermal and mechanical growth and thermal growth of the vane and tolerance stackup. Under ideal operating conditions this minimal spacing could be used. However, experience has shown that some eccentricities in the shaft can develop and clearance must be opened to allow for this possibility; also, the condition of operation can tighten clearance, e.g., hot restarts or liquid or ice ingestion.

Vane/rotor contact can produce bowing and imbalance by uneven heating of the rotor. Frictional heat in the vanes accentuates the initial contact by additional incursion resulting from thermal expansion transfer of the vane material to the rotor (scabbing). When extremely severe, vane/rotor contact can produce rotor or vane failure and thus catastrophic engine damage. Calculations and experience have also shown that the initial vane/rotor interference rate can be as high as 25 μm/s (0.001 in./s) and can last for up to 30 s in the engine studied. Other engines may differ due to design or operational factors.

Increasing vane tip clearance to eliminate rub is a very unsatisfactory approach to minimizing vane/rotor rub problems. It results in an overall decrease in engine performance (output power and thermal efficiency).

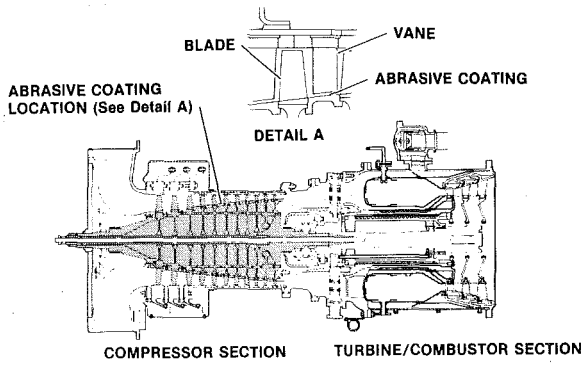

Fig. 1 Typical modern axial flow commercial gas turbine

To effect near-net clearance, a system was developed that permits vane/rotor tip rub without excessive heating of either component. An abrasive coating applied to the rotor was the means of achieving this objective. To be effective, the coating had to meet the following requirements:

1 remove the vane tips without generating excessive temperature rise either in the rotor or the vane,

2 be unaffected by thermal cycling between anticipated ambient temperature and 427°C (800°F),

3 application as a part of the normal manufacturing sequence without subsequent finishing operations,

4 compatible with an AISI 410 rotor material.

Essentially, no quantitative data were available on the performance of abrasive coatings under the anticipated operating conditions. Aluminum oxide applied by plasma or flame spraying has been used on compressor cases, with some success, to serve as an abrasive coating for removal of blade tips in the event of rub. However, no data were available as to its use on the rotor. To obtain the required data on coatings, a test rib was designed and built. The rig duplicated those

Contributed by the Gas Turbine Division and presented at the Gas Turbine Conference and Exhibit and Solar Energy Conference, San Diego, California, March12–15,1979 of THE AMERICAN SOCIETY OF MECHANICAL ENGINEERS. Manuscript received at ASME Headquarters December 13, 1978. Paper No. 79-GT-48.

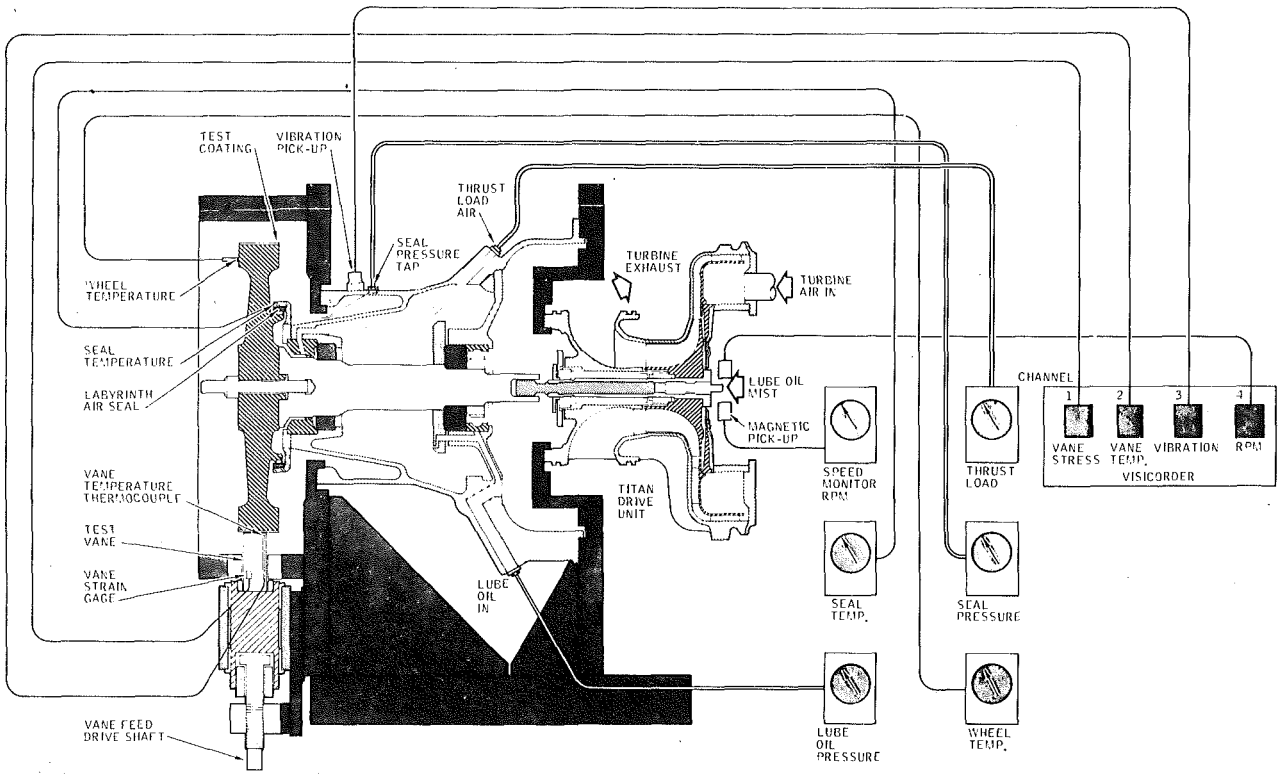

Fig. 2 Schematic and cross section of the rub test rig for evaluation of abrasive rotor coatings

conditions predicted in compressor operation. Oxides and carbides were selected as the primary abrasives because of their stability, hardness, sharp cutting edges, low cost and availability; although consideration was given to other materials during the test program.

Test Facility Design and Operation. The rub test rig is described in detail since it is relatively unique and its operation was essential to the study. The test rig design was based on a Solar axial flow compressor. During operation, gas in the compressor discharge end is at a temperature of 427°C (800°F) and the surface velocity of the rotor is 305 mps (1000 fps). When a rub occurred, the vane to rotor intrusion rate was calculated to be 0.025 mm per second (0.001 in. per second) with the maximum anticipated interference being 0.75 mm (0.030 in.). The test rig was designed to duplicate these conditions.

The completed rig, illustrated in Fig. 2, is powered by an air-driven turbine adapted for this application from one of Solar's standard production engines. Air to drive the turbine is supplied at a pressure of 0.69 MPa (100 psi) with a mass flow of 1.35 kg (3.0 lbs) per second. This value may vary from test to test depending upon the coating tested and the configuration of the test rotor.

The turbine is directly coupled to the rotor shaft through a flexible coupling. The relatively slow turbine speed (20,000 rpm versus 60,000 rpm plus in normal operation) reduces drive efficiency; however, this is more than offset by the elimination of the gearbox of an electric motor driven unit. The test rig has been essentially maintenance-free after literally hundreds of test runs.

The basic test rotor used in abrasive rub testing is a nominal 31 cm (12 in.) in diameter, machined from an AISI 410 forging. Several of these were made to minimize downtime while the disk is being coated between tests. Over 50 material systems have been tested to date with this equipment.

The vane used for testing the coatings is located immediately below this disk on a platform advanced by a variable speed drive calibrated to produce an advance rate of 0.025 mm (0.001 in.) per second.

During elevated-temperature operations, the rotor disc is heated by an oxygen-MAPP gas torch and the vane by the hot gas generated in the cavity during of the disk.

The initial instrumentation used to monitor the tests consists of:

- Vane temperature thermocouples
- Vane stress strain gauges
- Disk speed sensing pickups

These outputs were recorded by an oscillograph. Wheel temperature was monitored by a standard strip chart recorder. In addition to this basic test data, vibration levels, oil pressure, and bearing temperatures were monitored to warn of potential equipment failure.

The basic test procedure used to evaluate rotor coatings with this equipment is as follows. The periphery of the rotor is processed with the test coating, checked for thickness and roughness and balanced. Similarly, the test vane is instrumented, weighed and measured. The components are assembled to the test rig, as shown in Fig. 2, and the disk accelerated to 5000 rpm. At this time the heating torch is ignited and the rotor again accelerated to test speed. Temperature and speed are stabilized at the desired test conditions and the vane advance mechanism is initiated at the predetermined rate. The time of initiation of rub is noted and the vane ingression is continued past this point to produce the desired interference. Vane travel is then reversed to prevent unplanned rub from thermal soakback or other factors by providing a positive end point. Typical test conditions used in this program were:

- Rotor surface speed 305 mps (1000 fps)
- Rotor temperature 427°C (800°F)
- Incursion rate 0.025 mm/s (0.001 in./s)
- Incursion depth 0.75 mm (0.03 in.)

After evaluation the rotor is stripped and recoated while new vanes are used for each test.

The test rig has been in operation for four years without significant operational problems. Numerous modifications have been made to increase its versatility. Tests now in progress utilize multiple vanes with additional instrumentation and an instrumented thin wall rotor for measuring temperature and strain with information being transmitted to a data acquisition system by telemetry.

Testing

Selection of Materials. Because of the lack of literature data on abrasive coatings for the proposed application, it was decided to test as many different material systems as were practical. Initial selection of the materials for testing was made on the following basis:

1 The material system must be potentially capable of prolonged operation at 427°C (800°F) in an oxidizing atmosphere.

2 Testing would be limited to materials that were commercially available.

3 The abrasive grain would be of a composition of demonstrable hardness with sharp, cutting edges.

4 The coating must be applied to a finish dimension without subsequent processing.

5 Application of the coating was to be compatible with our standard compressor fabrication methods.

Using these guidelines the following materials were selected for initial testing as the abrasive constituent in the coating:

- Aluminum oxide
- Chromium carbide
- Tungsten carbide
- Silicon carbide
- Chromium sesquioxide

Plasma spraying (PS) was selected as the primary method of application for these materials. The processes were well advanced at Solar and could be used to apply the coatings to the close tolerances required. Nickel aluminide was chosen as the primary bonding agent in the composite coatings since it is self-bonding to most alloys, including the AISI 410 substrate. Cobalt and nickel-chromium bonding alloys were also used in a few composities, as were coatings of the pure abrasive materials.

In addition tothe plasma sprayed materials, a Solar developed abrasive coating (RC-1) was applied by conventional spray techniques and cured at 538°C (1000°F), i.e., at a point significantly below the standard tempering temperature.

Test Procedures. The material systems evaluated and tested for the following characteristics:

- Thermal shock resistance
- Thermal stability
- Adherence
- Surface roughness
- Abrasiveness, as determined on the rub test rig

Thermal Shock. Coatings were tested for their ability to withstand repeated thermal cycling by applying the coating to a test panel of AISI 410 steel, 77 mm × 103 mm × 1.53 mm (3 in. × 4 in. × 0.060 in. thick). These panels were heated to 538°C (1000°F), removed and quenched in water. This cycle was repeated ten times or until failure occurred, as evidenced by spalling of the coating.

Thermal Stability. The effect of prolonged exposure to elevated temperatures was determined using panels prepared in the same manner as those used in the thermal shock tests. These panels were heated in a furnace for 500 hr at 850°F. After testing the panels were removed and examined visibly for any evidence of attack due to the prolonged exposure to the elevated temperature.

Adherence. The adherence of the coating was evaluated in two ways—bend testing and tensile bond tests. For bend testing, coated panels similar to those used in the previous test, differing only in size (51 mm [2 in.] square), were bent over a 12.7 mm (0.50 in.) dia mandrel for a total bend of 180 deg. Performance was judged on the basis of percent of material lost.

The second test for adherence, or bond strength, utilized tensile strength. The coating to be evaluated was applied to the end of a 2.54 cm (1 in.) dia rod. A similar rod was then bonded to the caoting using a high-strength epoxy adhesive. After curing the adhesive to its maximum strength, the cemented rod was placed in a tensile testing machine and the tensile force required to rupture the coating-substrate bond was measured. Bond strength was then calculated. This test is more fully described in ASTM.

Surface Roughness. Surface roughness of the coating was measured using the same samples as were used in the test. A conventional profilometer was used to make these measurements. Similar measurements were also made on the coated rotors to assure consistency of the coating process.

Rub Testing. The periphery of the test rotor was coated to a thickness of 0.25 mm (0.010 in.) and the rotor mounted on the test rig. The test vane was instrumented with a thermocouple attached 2.5 mm (0.10 in.) from its tip and strain gauges cemented to the vanes, 32 mm (0.125 in.) from the base. The rig was brought up to an operating speed of 304 mps (1000 fps) at 427°C (800°F) and stabilized. The vane was then advanced into the coated disk at a rate of 0.025 mm (0.01 in.) per second. After the vane contacted the disk, it was allowed to advance for an additional 30 s at which point the feed mechanism was reversed

Table 1 Initial screening test results for rotor abrasive coatings applied to AISI 410 base

Abrasive System	Ease of Application	Surface Roughness (μ metre-μ in.)	Microstructure Appearance	Adherence		Abrasive Grain Appearance
				Bend Test (% Material Lost)	Tensile Bond Strength (MPa - psi)	
Nickel Aluminide Bonded Aluminum Oxide	Difficult	4.4 - 175	Laminar with approximately 10 percent abrasive	30	29 - 4200	Rounded edges
Plasma Sprayed Aluminum Oxide (53 > 15 microns)	Moderate	5.0 - 200	Laminar with discontinuous voids	20	47 - 6800	Flat with rounded corners
Flame Sprayed Aluminum Oxide (75 > 30 microns)	Difficult to control thickness	5.7 - 225	Similar to plasma sprayed with larger voids	15	52 - 7500	Ovoid
RC-1	Easily applied to required thickness	10.6 - 425	Projecting abrasive grains bonded to substrate	5	N/A	Sharp blocky grains
Cobalt Bonded Tungsten Carbide (43 > 30 microns)	Moderate	4.5 - 180	Fine uniformly dispersed abrasive grains in metal matrix	5	52 - 7600	Metallic coating on abrasive
Cobalt Bonded Tungsten Carbide (53 > 30 microns)	Moderate	8.8 - 350	Uniform structure with evenly dispersed grains	10	45 - 6600	Rounded abrasive grains
Cobalt Bonded Tungsten Carbide (74 > 30 microns)	Easily applied to finish dimension	14.4 - 575	Open structure with approximately 20 percent voids	10	58 - 8400	Large round grains
Nickel-Chromium Bonded Chromium Carbide	Moderate	6.3 - 250	Fine fused appearance	90	64 - 9300	Fine grains dispersed in metal matrix
Nickel Aluminide Bonded Chromium Carbide	Moderate	4.4 - 175	Laminar structure with discontinuous voids	10	30 - 4300	Fine rounded grains

and the vane withdrawn from contact. The unit was then shut down and the vane and disk removed for examination. Data recorded during this test were the strain on the vane, the temperature indicated by the thermocouple located 2.5 mm (0.10 in.) from the tip, and the change in wheel speed. Both the coating and the vane were examined visually for burning, metal transfer and overall appearance. Representative vanes were also sectioned for metallographic examination.

Results and Discussion

Over 50 material systems were tested. Typical results are presented in Table 1 for the initial screening tests of various coatings. These results have been limited to those obtained with aluminum oxide, tungsten carbide, chromium carbide and chromium sesquioxide abrasives. As is evident in the table, the baseline abrasive was aluminum oxide. It was tested (1) as a pure plasma sprayed coating, (2) with various binders, and (3) applied by flame spraying. Tungsten carbide was limited to a cobalt binder. Attempts to bond tungsten carbide to the substrate chemically were unsuccessful. Chromium sesquioxide was tested only as a pure material and showed little promise. Chromium carbide was tested both with a nickel-chromium alloy binder and with nickel aluminide as the bonding agent.

The first criteria used for evaluating the coating was the ease of reliability with which it could be applied. Materials showing poor deposit efficiency were discontinued since they were not considered suitable for the end application. Chromium sesquioxide and nickel aluminide bonded aluminum oxide were dropped at this point.

Surface roughness values ranged from 3.1 μm (110 μmin.) for the chromium sesquioxide to 14.1 μm (575 μin.) for tungsten carbide which was the coarsest material tested. The majority of the abrasive materials were found to lie between 5 μm (200 μm) and 11 μm (425 μin.). Plasma sprayed coarse aluminum oxide, which is one of the most common abrasive materials used in this and similar applications, gave a surface roughness of 5.1 μm (225 μin.). The RC-1 coating had a surface finish of 11 μm (425 μin.). Both materials appeared to be adequately rough for the proposed application.

Metallographic sections were taken of all coating types and examined visually at a magnification of 100×. The comments in the table are largely self-explanatory. Of particular note is the typical difference between plasma sprayed and chemically bonded abrasive (RC-1). This is illustrated in the scanning electron micrographs in Figs. 3 and 4. The *PS* coatings exhibited a relatively dense structure with rounded grains and thus retained little of the structure required to grind and accommodate the grinding debris. With the RC-1 abrasive coating, the structure is open and the grains retain the majority of their "as crushed" sharpness. As will be noted subsequently, sharp grains and an open structure are required in an effective self-cleaning abrasive coating. Attempts to obtain this structure by plasma or flame spraying were unsuccessful. As power was reduced to the plasma gun, for example, to decrease rounding of the edges of the abrasive grains to improve cutting efficiency, the weak, porous structure was readily wiped away during a rub. Co-spraying of a nickel aluminum bonder alloy with the abrasive grains also did not produce adequate retention of the abrasive unless plasma power was high enough to melt edges of the abrasive grains.

The final test in this phase was for the adherence of the coatings to the substrate. Except for the chromium carbide, none of the coatings was severely damaged by the bend test. The material loss indicated in the table was largely on the edges where more severely stressed conditions exist. The nickel aluminide bonded oxide and the conventional fine grained aluminum oxide had relatively high spalling tendencies but losses were not sufficient to discontinue use of the materials on this basis. Tensile testing for bond strength showed that all of the materials were capable of meeting the low centrifugal stresses expected during operation (<680 kPa [100 psi]).

Data obtained from the bend test and bond strength test were confirmed in the thermal shock test. Thermal shock results were not tabulated. All materials passed and no significant differences were found in performance during thermal shock.

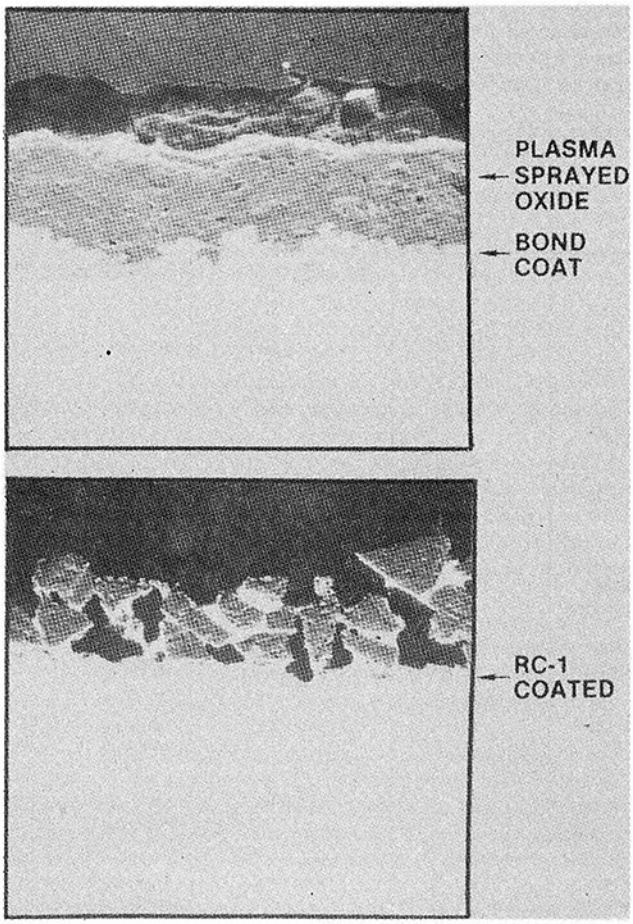

Fig. 3 Coating cross sections

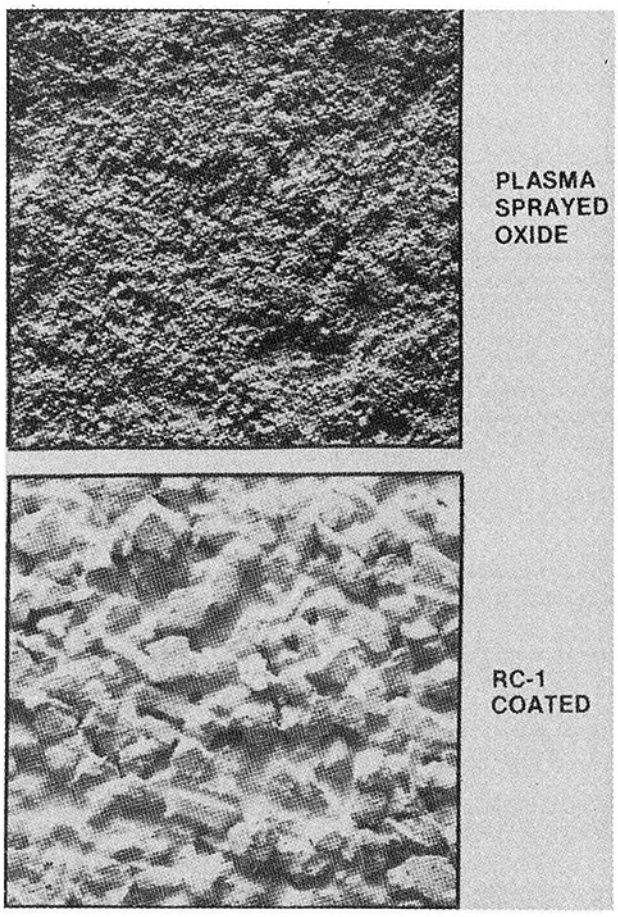

Fig. 4 Coating surfaces

Similar tests were conducted on chemically bonded tungsten carbide abrasive grains. These data are not included. The binder under consideration did not adequately wet the tungsten carbide abrasive grains. Tensile bond strengths are not reported for the RC-1 coating since the epoxy adhesive used in these tests did not adhere consistently to it.

The rub characteristics of representative coatings tested in this series are reported in Figs. 5–7. In addition, a rub on a bare, uncoated disk is included in each to serve as a baseline. Uncoated rotor data represent the situation in a conventional vane/rotor rub and should be used as a guideline in evaluating subsequent results.

Typical appearance of rotors after a vane rub is shown in Figs. 8, 9 and 10. Figure 8 is an uncoated disk. Chatter marks from the vane are evident. These are the result of localized metal buildup and are a source of very high vibration levels generated in the vane during rub with the bare disk. Figure 9 is a rotor plasma sprayed with a conventional aluminum oxide abrasive. Although chatter marks have been eliminated, the metal transfer (scabbing) to the disk is excessive, indicating limited service life and potential problems in rubs with multiple vanes. Figure 10 is a photograph of an RC-1 abrasive coated disk. This disk has been through the same rub test as the two previous disks but no evidence of metal transfer or coating damage can be observed. In Fig. 11 the appearance of this rub is shown in actual operation. To the left of the picture is a steady stream of sparks similar to those generated by a grinding wheel. This steady grinding operation

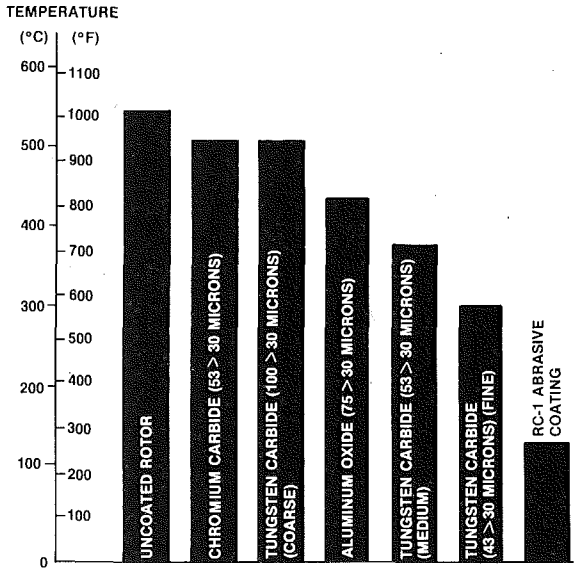

Fig. 5 Temperature rise generated in the vane during rub

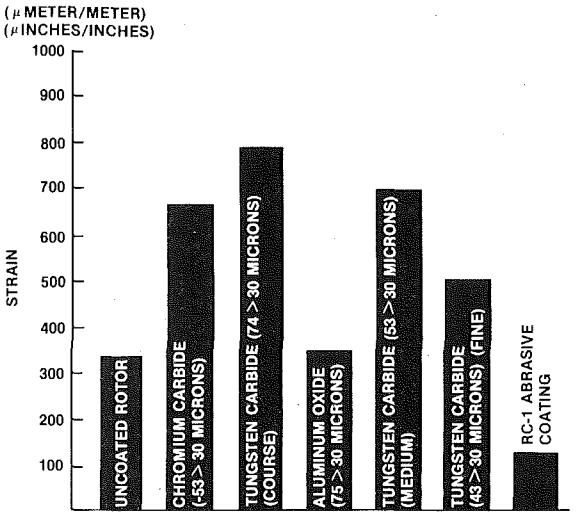

Fig. 6 Comparative maximum vane strain values generated during abrasive rub

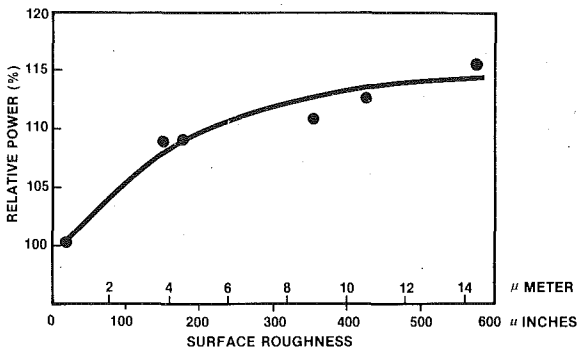

Fig. 7 Relative power to drive coated and uncoated rotors as a function of surface finish

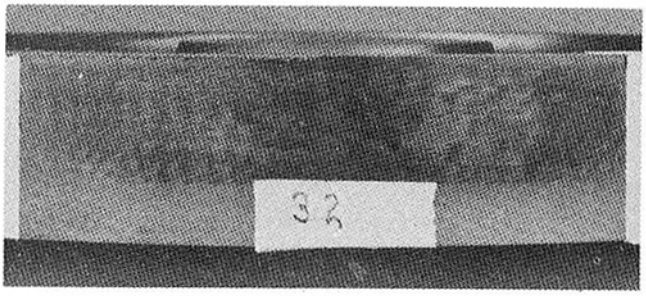

Fig. 8 Uncoated rotor after 30 s rub

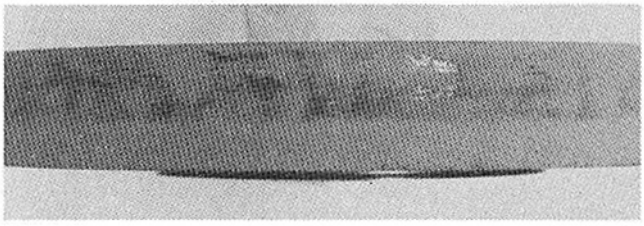

Fig. 9 Appearance of the aluminum oxide coating after vane rub

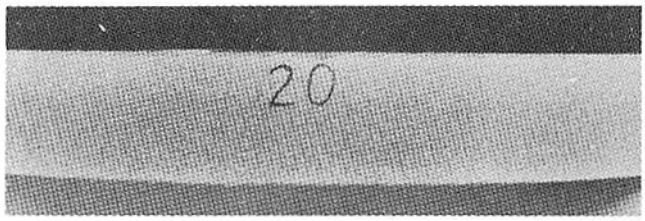

Fig. 10 Rotor coated with RC-1 after rub test

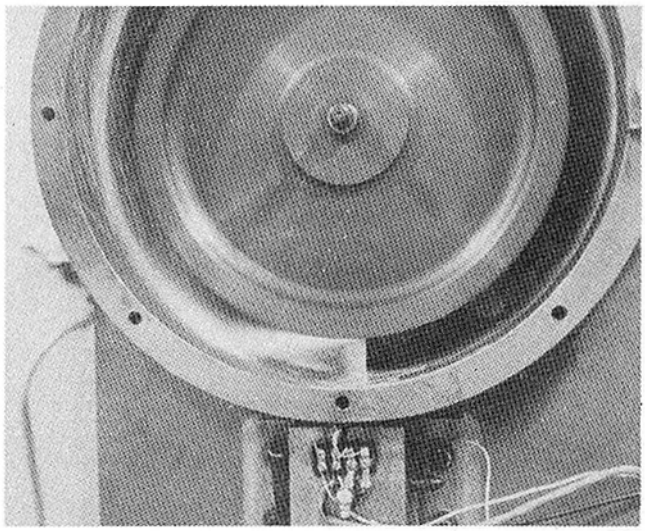

Fig. 11 Appearance of RC-1 during rub test

continues throughout the rub. When uncoated discs, or discs coated with plasma sprayed aluminum oxide, are tested in this manner, the stream is intermittent, indicating that the thermal growth occurs during rub until sufficient heating occurs to melt the tip of the vane. At this point the molten metal is thrown clear and the rub is interrupted until the vane has advanced sufficiently to resume contact. This is an undesirable situation since it tends to create a destructive rub mode and gives considerable excess vane wear, amounting to 0.25 mm (10 mils) in most cases due to thermal expansion of the vane resulting from frictional heating.

Three grades of tungsten carbide were tested and, as predicted upon examination of the coating prior to test, the coarser the grain, the better the cutting action and the less metal transfer. The chromium carbide coating showed heavier transfer than any of the other materials tested and was dropped from the program.

The next criteria used in evaluating the coatings's effectiveness was the temperature recorded by a chromel-alumel thermocouple located 2.5 mm (0.10 in.) from the tip of the vane at the time of initial contact. These data are reported in Fig. 5. The temperature indicated by this thermocouple lagged the contact temperature due to the mass of the vane and the distance to the rub area. Actual vane tip temperature was sufficient to generate melting in most tests. An indication of the magnitude of this delay is the discrepancy between the temperature readout of 543°C (1010°F) for the vane rub on the bare disc in comparison with the probable tip temperature in excess of 1482°C (2700°F) as indicated by the melting of the vane tip. In all cases, the application of a coating to the rotor reduced the temperature observed on the vane. However, with the exception of the RC-1 coating, all coatings tested still created melting of the vane tip. Increasing the grain size of the tungsten carbide abrasive did not reduce the indicated vane temperature. The reverse occurred with the tungsten carbide abrasive, giving an indicated vane temperature of 301°C (573°F) for the coarser material. This represents a nominal grain size variation of −325 mesh for the fine material as opposed to −150 mesh for the coarse material. The chromium carbide gave a slight temperature reduction of 21°C (60°F). These temperatures are almost identical with those obtained with the coarse tungsten carbide coating. The coarse aluminum oxide coating reduced the measured temperatures to 435°C (820°F), again indicating some improvement in performance.

Strain data, Fig. 6, generally paralleled the temperature data, indicating the effectiveness of the coating. The correlation was qualitative, not quantitative, as was the speed lost during rub. The data obtained from the bare disk were inconsistent with those obtained from the coated disk, with regard to strain and speed, and this discrepancy has not been resolved. The disk coated with sharp abrasive grain (RC-1 coating) showed an increase in speed during rub caused by a slight smoothing of the disc during initial contact. The reduction in air drag was greater than the frictional drag on the disk due to rub. An overall acceleration of the disk was thus recorded for a constant driving force on the turbine.

The air drag imparted to the disk by the rough abrasive coatings is calculated from the power required by the driving turbine. The bare uncoated disk was used as a baseline and given an arbitrary value of 100. Increased mass flow required through the turbine to stabilize at operating speed was calculated and converted to relative percentage as compared with the bare uncoated disk. On this scale the increase in power amounted to between 10 and 15 percent. The data obtained are presented in Fig. 7. This measurement is useful in assuring reproducible testing and comparing overall coating roughness. It is not applicable to axial compressor operation where the effect is not detectable due to relatively small percentages of area.

Appearance of the vane tips after a rub is very revealing as to the effectiveness of a coating in preventing over-heating and excess stock removal. The appearance of a metal-metal rub, also characteristic of essentially all of the plasma sprayed coatings, is shown in Fig. 12. The alloy reaches a temperature near the melting point at which it is readily extruded. This extension of the material is relatively symmetric, showing essentially no preference to move to material in the direction of the motion of the disk. With an efficient cutting material,

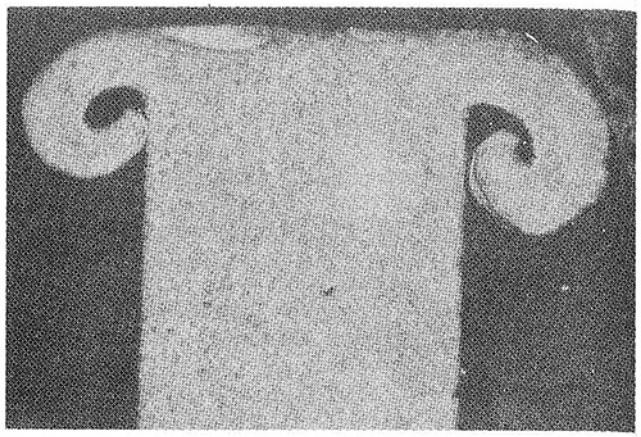

Fig. 12 Cross section of a typical vane after rub with a plasma spray coated rotor

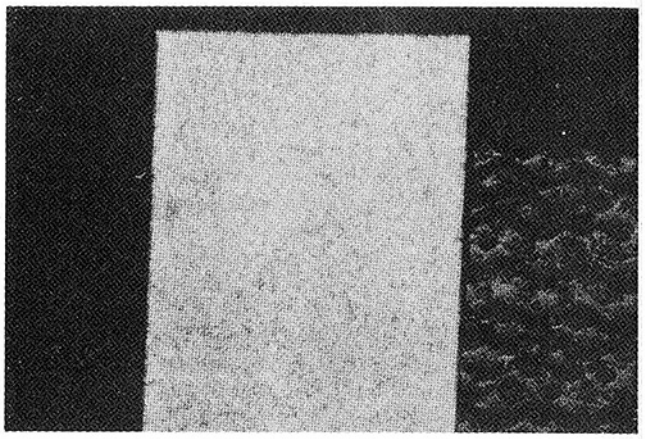

Fig. 13 Cross section of a typical vane after rub on RC-1 coated rotor

e.g., the RC-1 coating, this extrusion of material does not occur, as shown in Fig. 13. The vane is uniformly ground with minimum heating. Essentially no burr is formed that would interfere with blade aerodynamics or increase scabbing.

In ranking of abrasive coatings by this test, the two most significant test parameters appear to be temperature rise and maximum strain during a rub. These data for representative coatings are illustrated in Figs. 5 and 6. The results show that many of the plasma sprayed coatings are little, if any, better than the uncoated alloy with regard to vane reaction. The RC-1 coating with the retained sharp abrasive is the outstanding coating. This coating was selected for a full-size compressor test rig.

The comparison of coated versus uncoated rotors during vane tip/rotor rub is clearly shown in Fig. 14. These tests were conducted on a full-size rotor to confirm the results obtained in the laboratory. The vanes to the left have been rubbed against the RC-1 coated rotor. Except for a very thin wire edge, no vane deformation or burning has occurred. The vanes rubbed against heavy burrs on these vanes can easily be seen. It is also evident that the vanes rubbed against the uncoated rotor have a burr both on the leading edge and the trailing edge, as in the laboratory tests.

A compressor rotor installed in a development test engine is now in service and is shown in Figs. 15 and 16 after a periodic inspection. The coated rotor has been in use for approximately two years without any problems associated with the coating and no evidence of coating failure has been detected. The coated rotor was installed after an exceptionally severe rub had occurred during test. The scabbing in the rotor surface that generates excessive vane wear is evident in Fig. 17. Under abnormal operating conditions, generated during test, more severe damage has been observed on rotor wear of up to 0.25 mm (0.01 in.). The coated rotor has exhibited none of these problems and is still in service. As expected, no aerodynamic effects on engine performance due to the coating have been detected.

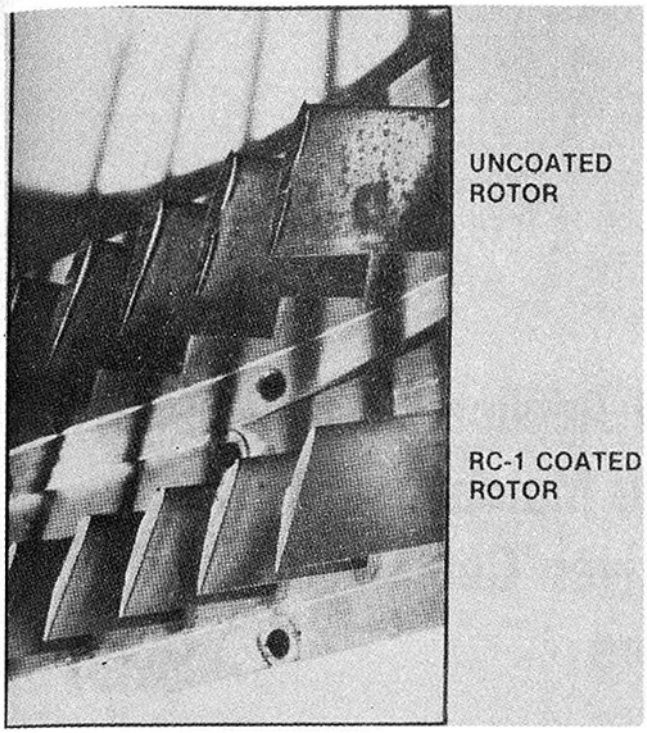

Fig. 14 Vane segments rubbed against a full scale rotor during advanced engine development tests

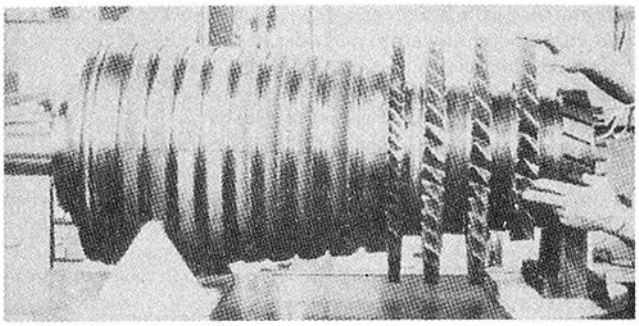

Fig. 15 Overall view of RC-1 coated mars 10,000 hp engine compressor rotor showing the eight stages receiving the coating

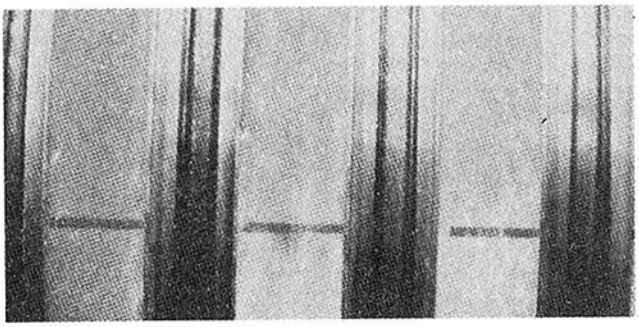

Fig. 16 Closeup view of RC-1 coated mars 10,000 hp engine compressor rotor indicating lines of potential rubbing

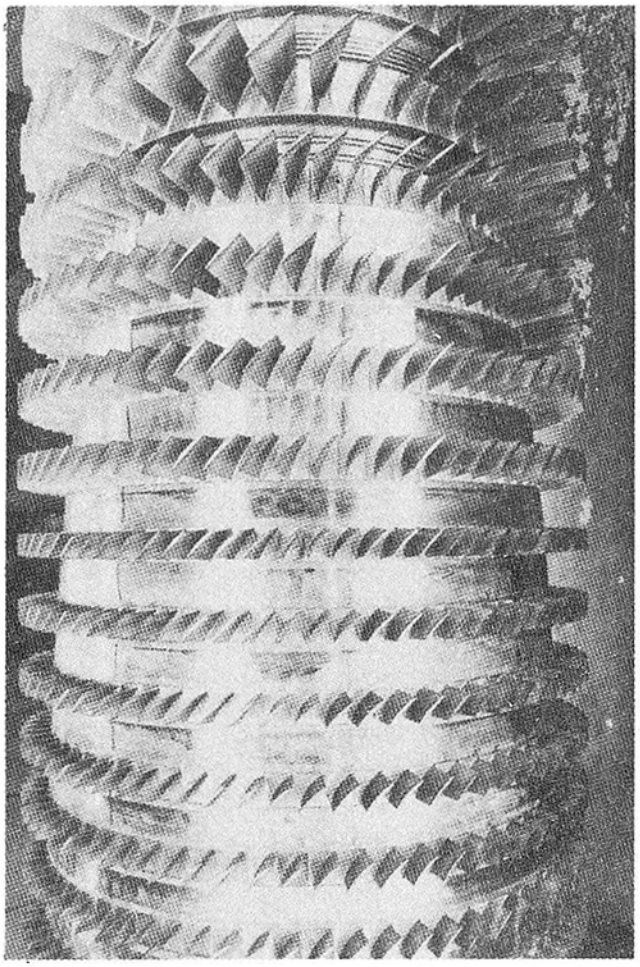

Fig. 17 Uncoated mars compressor rotor showing severe rub and metal transfer

Conclusions

Properly engineered abrasive coatings applied to turbine compressor rotors are an effective means of reducing temperature increase during rub and eliminating excessive vane strain. These coatings can be applied with sufficient reliability for production usage on compressors operating up to 427°C (800°F). Some loss of efficiency might be expected due to the increased surface roughness of the rotor. However, this represents only a small percentage of the total wetted rotor area and the effect is not detectable in normal operation. The increase in efficiency due to operating with minimum vane clearances can far more than offset this slight increase in aerodynamic drag.

Testing of the various coatings showed that conventional flame and plasma sprayed coatings lose much of their effectiveness due to a rounding or melting of the sharp edges of the abrasive grain during application. When the sharp edges of the grain were maintained by other bonding methods, cutting efficiency was greatly increased and the overheating or melting of the vane tips was eliminated. Inorganic low temperature bonds for the abrasive, e.g., the one used in RC-1, afforded the best grain sharpness retention. The specific composition was developed for use on AISI 410 and further development may be required for application to other alloys.

Further work will be conducted with these coatings, not only for use on the turbine compressor rotor, but also on blade tips to overcome rub problems in the blade housing area. The use of the reduced running clearances allowed through application of abrasive coatings to parts that may come in high speed contact during operation is expected to reduce overall fuel consumption of the turbine engines significantly.

In evaluating an abrasive coating, the visual examination of the specimens after tests for burrs, melting and metal transfer is one of the most reliable means of evaluating their performance. Instrumented data, such as strain gauges and thermocouples, are helpful in this evaluation but the data generated are insufficient for a final decision. The test rig built for this program, because of its versatility and the speed with which it may be adapted to other configurations and the rapid test turn-around, has proven invaluable for gaining practical insight into the behavior of high-speed rotating components during rub. Its reliability has been demonstrated by engine operation over a long time period utilizing the coating developed in this study.

D. W. Wood
Market Manager.
Cooper Rolls Incorporated,
North Sandusky St.
Mount Vernon, OH 43050
Mem. ASME

R. G. Reid
Station Engineer.
Union Gas Limited.
50 Keil Drive North,
Chatham, Ontario
Canada N7M 5M1
Mem. ASME

Design and Application of a Single Gas Turbine Matched with Two Tandem Driven Centrifugal Compressors

This paper deals with the design and application of a 29,000 bhp (21,625 KW) gas turbine-compressor unit to perform the duties of high pressure ratio/low volume (storage) and low pressure ratio/high volume (transmission). To achieve this wide range of requirements, a single gas turbine was matched with two tandem driven centrifugal compressors. The paper describes the considerations and the techniques used to select the gas turbine, compressor aerodynamic performance and match the gas turbine and compressors.

Introduction

Gas transmission companies have practiced gas storage for many years in order to satisfy varying seasonal demand levels, while maintaining a relatively constant supply level from the gas producers. This is accomplished by storing natural gas in underground formations during low demand periods and withdrawing the stored gas during high demand periods.

The typical injection and withdrawal (storage) cycle experiences a wide range of pressure ratios and flows as a result of the application. Historically, reciprocating compressors, in the majority of cases, have been selected for injection/withdrawal applications due to their inherent pressure ratio and loading flexibility that is accomplished by varying the compressor cylinder clearance volume with built-in pockets. Reciprocating compressors of the integral engine compressor design have been available for the last two decades with ratings that were generally under 5000 bhp (3,730 kW). A trend was, therefore, established to utilize multiple integral engine compression sets and add to these with similar or like equipment as system demands grew.

This pattern was followed by many natural gas companies, due primarily to equipment availability and economics associated with steady nonsporadic growth. However, the cost associated with the purchase, installation and maintenance of this multi-unit reciprocating equipment becomes less attractive if a single gas turbine-compressor set can be used. In the case discussed in this paper, the requisites for the gas turbine compression package included:

1 Nominal 30,000 bhp (22,370 kW) rating in a single unit to operate in place of equivalent reciprocating units and take advantage of the "economy of scale" principle,

2 low specific fuel consumption so as to equal or better that of available reciprocating equipment,

3 low weight and small space requirements to reduce installation costs,

4 compressor design to maximize flexibility that would be available in multiple reciprocating units while maintaining high compression efficiency.

These requirements are basically an attractive economic alternate to the historical multi-unit reciprocating compressor precedence. The gas turbine power with an RB.211 gas generator satisfied the first three requisities. Unique tandem driven centrifugal compressor arrangement was designed to satisfy the last requisite.

Station Location and Configuration

The Dawn Compressor Station is located approximately 40 mi (64 km) southeast of Sarnia in Southern Ontario, as shown in Fig. 1. By definition, it is a multipurpose station in that the station stores, withdraws, and transmits natural gas. To accomplish the storage of the gas, underground formations located in the general geographical area surrounding the station are utilized. The station location with the storage reservoirs and piping network can be found in Fig. 1. Referring to Fig. 1, the major lines running off to the north-east are the primary pipelines that service the heavily industrialized Ontario market. The major line running south services the Windsor area. As can be seen, this is the focal point for the gas companies' complete system.

The station piping consists basically of three headers with the existing compressors piped and valved to the headers such that several modes of operation are available

The station compression equipment consisted of twelve recipro-

Contributed by the Gas Turbine Division and presented at the Gas Turbine Conference and Exhibit and Solar Energy Conference, San Diego, California, March 12–15, 1979 of THE AMERICAN SOCIETY OF MECHANICAL ENGINEERS. Manuscript received at ASME Headquarters December 18, 1978. Paper No. 79-GT-81.

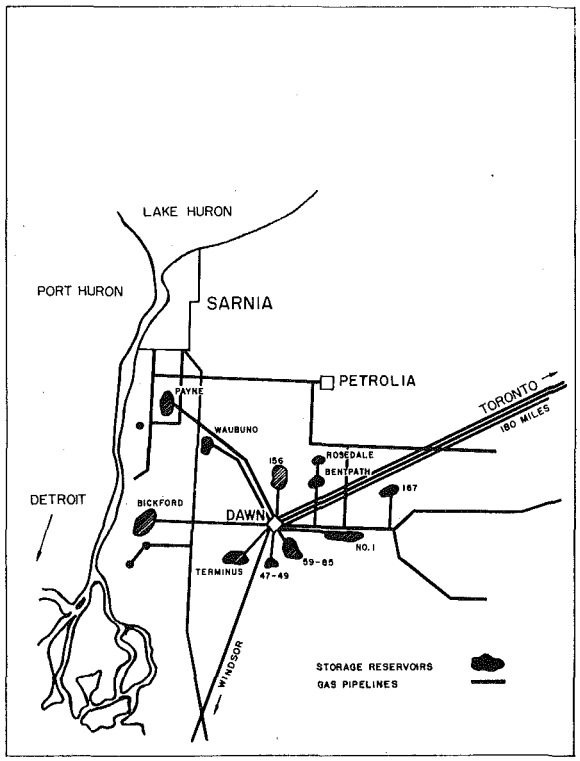

Fig. 1 Station location (storage pools and pipe network)

cating engine compressor sets prior to the addition of the new equipment. Of these twelve, seven are below 500 bhp (373 kW) and five in the 2000 to 3400 bhp (1490 to 2540 kW) range. There is a total of 15,700 bhp (11,700 kW) of reciprocating equipment.

The station was experiencing growth in peak day and average day throughput. The existing horsepower for peaking was becoming fully extended. Thus, because of the growth, more horsepower in a transmission application was needed to compress the gas for the pipelines. Also, because this gas came in part from the reservoirs, and more of it was needed to satisfy growth, the gas had to be withdrawn to lower reservoir pressures. This occurred at the same time as the transmission requirement and thus the need for more horsepower in a storage application existed.

It is this transmission/storage operation that the tandem driven centrifugal compressors satisfied.

Performance Requirements

From the foregoing and the projected flow rates demanded by the system, the modes of operation were set as found in Table 1.

In order to arrive at criteria that would allow the purchaser to evaluate performance, two sets of guarantee conditions were specified—one for high pressure ratio/low flow and one for low pressure ratio/high flow.

In Table 2, Condition 1 represented the requirements for transmission service and Condition 2 the requirements for storage service. In addition to the pressure and flow parameters, other gas characteristics were specified. The suction temperature was given as 67°F (19.4°C), specific gravity 0.594, ratio of specific heat 1.295. The actual gas analysis was given to verify specific gravity (molecular weight) ratio of specific heat (K value) and determine the super compressibility at the given conditions. Computer analysis was an aid in the rigorous calculations of gas conditions.

Conditions 1 and 2 were analyzed by calculating the work required to raise the pressure of the gas from suction to discharge. The work is often referred to as head, which is work per unit weight or foot-pounds per pound (kilojoules per kilogram). Also, it was necessary to determine the actual volume rate of gas at the suction for both

Table 1

Transmission Service	Flow (MMCFD)	Suction Pressure (PSIG)	Discharge Pressure (PSIG)	Compressor* Operation
Peak	2,000	700	900	Parallel
Off-Peak	1,500	700	900	Parallel
Off-Peak	400/800	400/450	800/850	Series
Storage Service				
Peak	400/600	300	700	Series

1 PSI = 6.89×10^{-2} Bar
1 MMCFD = 1.116×10^{3} NM³/Hr.

* Tandem compressor operation with respect to each other

Table 2

Condition	Suction Pressure (PSIG)	Discharge Pressure (PSIG)	Flow (MMCFD)
1	700	900	2,000
2	300	700	450

1 PSI = 6.89×10^{-2} Bar
1 MMCFD = 1.116×10^{3} NM³/Hr.

Table 3

	Condition 1	Condition 2
Specific Gravity	0.5935	0.5935
K Value (Cp/Cv)	1.295	1.295
Compressibility	0.9057	0.9590
Capacity (MMCFD)	2,000	450
Inlet Flow (ACFM)	26,268	14,214
Inlet Temperature (°C)	19.4	19.4
Inlet Pressure (PSIA)	714	314
Discharge Pressure (PSIA)	914	714
Head (ft-Lb/Lb)	10,888	42,110
Compressor Efficiency (percent)	75*	75*
Power Required (HP)	27,718	24,101

1 MMCFD = 1.116×10^{3} NM³/Hr
1 ACFM = 4.72×10^{-4} M³/S
1 PSI = 6.89×10^{-2} Bar
1 ft-Lb/Lb = 2.99×10^{-3} KJ/KG
1 HP = 7.46×10^{-1} KW

* Assumed value for preliminary calculation.

conditions. The volume rate is referred to as actual cubic feet per minute (actual cubic meters per second). Table 3 represents the results of the calculations.

As can be seen from Table 3, there was a significant shift in inlet flow and head requirements between Condition 1 and Condition 2. The power required at each condition was compatible with a single gas turbine driver of 26,400 bhp (19,690 kW) ISO. Condition 1 is a winter, cold ambient temperature, transmission requirement and Condition 2 is a summer, warm ambient temperature, storage requirement. The gas turbine output characteristic power curve allows for increased output at the colder ambient temperature condition.

Gas Turbine and Compressor Selection

Because of the shifts in inlet flow and head, a decision was made to use compressors that could operate in either a parallel configuration (Condition 1) or a series configuration (Condition 2). In making this decision, it was recognized that a gas turbine of this size driving two centrifugal compressors in tandem had not been attempted before. Although this arrangement was unique, the principle was sound and all major components (gas turbine and compressors) were field proven.

Fig. 2 shows the arrangement of gas turbine and tandem compressors. Both compressors are connected to the same shaft through couplings and must, therefore, operate at the same speed. Thus, while operating in parallel for Condition 1, both compressors must accomplish the same head at the same speed while flowing the 2000 MMCFD (2.232×10^{6} NM³/hr). Also of prime consideration was the staging of the two compressors due to the volume reduction of the gas while operating in the series configuration. Still a further consider-

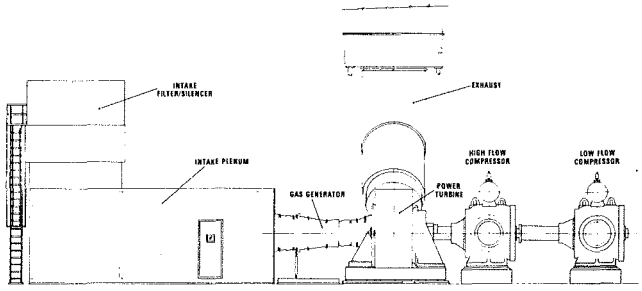

Fig. 2 Arrangement of gas turbine compressors

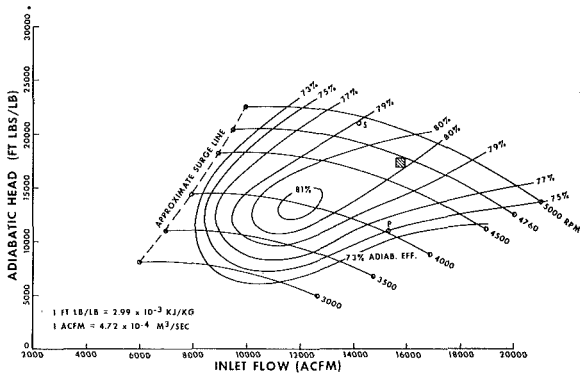

Fig. 3 Performance map of high flow compressor

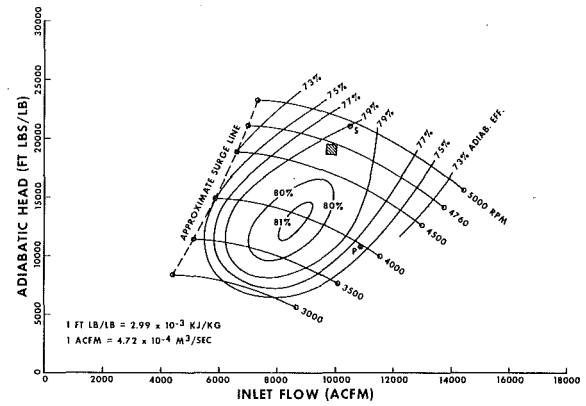

Fig. 4 Performance map of low flow compressor

ation was to make compressor performance selection so that both operating conditions could be achieved in the stable range of operation at compressor efficiencies that would allow the power required to stay within the limits of the driver. Referring again to Table 3, note that the compressor effieiency was assumed as 75 percent. This compressor efficiency became the target value.

The compressor performance maps found in Fig. 3 and Fig. 4 were derived through a trial and error, cut and fit process. Fig. 3 exhibits the operating characteristics of the high flow compressor which becomes the first stage for series operation. Fig. 4 is the performance for the low flow, second stage compressor. The speeds indicated demonstrate variations in head with inlet flow and constant compressor efficiency lines are superimposed. The point marked S is the operating point on each figure showing series operation. The point marked P is that for the parallel operation. The cross-hatched square on each figure represents the compressor design. The significant points to be observed are: the design head of both compressors is roughly the same, the design volume of the low flow compressor, with respect to the high flow compressor, is related to the volume reduction as a result of the pressure rise through the first stage compressor in the series mode, the efficiencies (verified through testing) exceeded the goal.

The selection of the series or parallel mode is accomplihsed by manipulation of the valves in the gas piping. When the compressors are operated in the series mode, each compressor will absorb approximately half the gas turbine driver output. However, in the parallel mode, the high flow compressor will absorb approximately 40 percent higher flow and gas turbine output than the low flow compressor. The combined flow of both compressors achieved the specified flow of 2000 MMCFD (2.232×10^6 NM^3/hr).

The lower operating speed in the parallel mode resulted in a reduced gas turbine output of 95 percent of the output at rated speed. This was a result of lower power turbine efficiency. It was determined that at ambient temperatures below 0°F (−17.8 °C) the gas turbine could produce sufficient power to match that required by the compressors. This met the operational requirements of the gas transmission company, due to higher natural gas demands at colder temperatures.

Fig. 5 illustrates the overall flexibility of the gas turbine compression system. To demonstrate its use, enter with gas flow rate at lower left corner to inlet pressure line, follow to lower center section for gas inlet temperature, follow vertically to arrive at the inlet flow co-or-

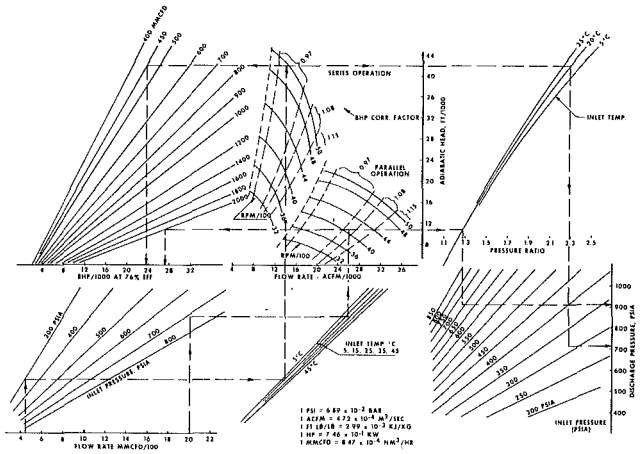

Fig. 5 Nomogram overall compression performance

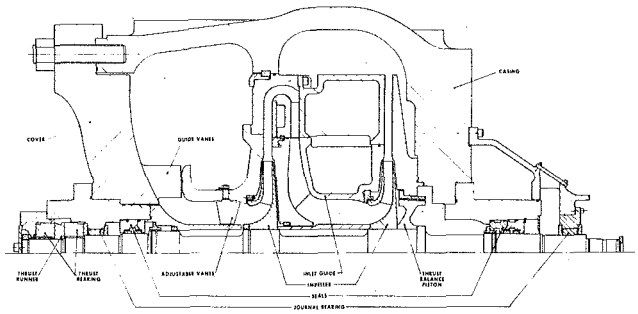

Fig. 6 Centrifugal compressor cross section

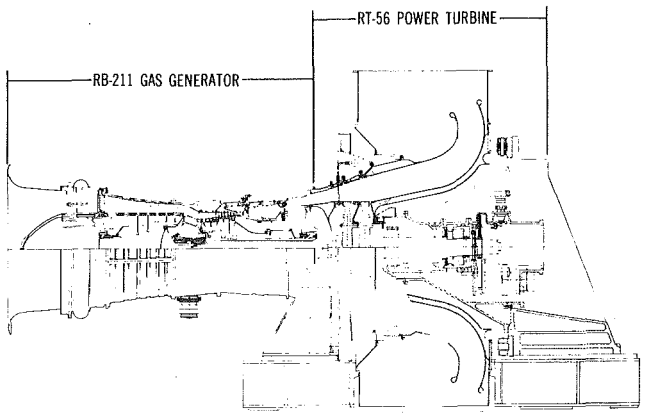

Fig. 7 Gas turbine cross section

dinate. Enter lower right section with required discharge pressure to inlet pressure line, follow vertically to inlet temperature and then horizontally for head co-ordinates. Power required for operating condition can be determined by use of upper left section using flow rate and power correction factor. Note that the operating maps drawn on this chart combine both compressors; i.e., one map for series operation and one for parallel operation.

Fig. 6 shows a quarter section of the outboard gas compressor. Two impellers were used in each compressor with the supporting bearing arrangements to allow a "drive through" of the inboard compressor.

Fig. 7 illustrates the gas turbine design employed. Note the gas generator coupled to a free power turbine. This two shaft design with independent power turbine speed allows for a wide range of driven equipment speed with corresponding high output torque that was mandatory for this application.

Field Operation

In March of 1978, after one month commissioning, the unit was put into operation. The unit was continuously operated for two weeks and field data were logged. The data were then used to verify the performance of the gas turbine and centrifugal compressors. It was found that the actual gas turbine fuel flow was lower than that predicted at the specifiied full load value (34 percent thermal efficiency). It was also found that the compresssor designs exceeded the specified condition of pressure ratio and flow.

Summary

A unique gas turbine compression arrangement was installed to satisfy a complicated need. The required duty of high volume/low pressure ratio and low volume/high pressure ratio was achieved with the tandem driven centrifugal compressors matched to a single high efficiency gas turbine driver. The unit has achieved the economic benefits and performance criteria that were predicted.

Acknowledgments

The authors acknowledge the able assistance of the Union Gas organization, especially D. W. Patterson, and the aid of Cooper Energy Services, particularly R. H. Meier.

V. Kulle
D. J. Cornies
L. E. Courterelle

Alberta Gas Trunk Line,
205 Fifth Ave., S.W. Box 2535,
Calgary, Alberta,
Canada T2P 2N6

Field Testing and Modifications of Pipeline Compression Equipment

Introduction

Field performance testing of Gas Turbine and Centrifugal Compressors is of prime importance to natural gas transmission companies using large numbers of diverse types of gas turbine/compressor installations.

As of July 1, 1978 the Alberta Gas Trunk Line Company Limited (AGTL) operated approximately 6500 mi of pipeline, 600 receipt meter stations and 32 compressor stations, mostly powered by gas turbines, totalling almost half a million installed HP. Total system receipts for the first half of 1978 were close to 950,000 MMcf. This complex system is remotely controlled from one central control point located at Calgary (See Fig. 1).

Efficient operation has always been a prime concern of AGTL. Recently soaring fuel gas prices have emphasized the need to recognize the most efficient drivers combinations that best fit the operational requirements of the system at any given time.

To meet this objective it is essential to have accurate gas compressor performance data (See Fig. 2) regarding the efficiency and head-flow characteristics at various speeds. It is important to know the limitations such as maximum and minimum operational speeds, surge, horsepower output at a given ambient temperature, vibration characteristics of the engine.

Of equal importance to the user however, is to know what could prevent him from achieving the required performance or efficiency. Correlating data, establishing the trend (comparing the results from various tests), and finally setting the maximum allowable deviations from the "normal" conditions for each particular type of unit and even each engine, thus becomes one of the prime requirements for sound preventive and predictive maintenance programs.

1 Data Acquisition Equipment Description

The need for a large volume of accurate data soon led to the development of the portable programmable Data Acquisition System (DAS) package, which is mounted in a trailer type vehicle. The system is presented schematically in Fig. 3.

(a) Instrumentation Points of Measurement. It is recognized that the accuracy of the measurement is directly related to the quality of sensors used. For pressure measurements high quality transducers are used and are calibrated before each test using dead weight testers, with pressure gauges of laboratory standards, for comparisons. Temperatures are measured by platinum resistance temperature detectors (RTD) and thermocouples (T/C).

The temperature rise measurement across the compressor, being the most critical, utilizes matched platinum RTD's with matched signal conditioners. The same equipment is used for measurement of the gas flowing temperature at the orifice plate. These are periodically checked in a laboratory standard temperature bath.

A type J thermocouple is used to measure outside air temperature and a type KT/C for measuring turbine inlet (TIT) or exhaust gas (TEX) temperature.

Speed is measured by a standard magnetic reluctance type pick-up mounted in close proximity to toothed wheels mounted on the gas generator, N_{GG}, and Free Power Turbine (N_{PT}) shafts.

The transducers are mounted on stands and are connected by cables to the designated outlets on an externally mounted panel for easy access. Typical measurement points are shown in Fig. 4.

(b) DAS Controller. This is a desk top programmable calculator. AGTL in-house developed programs are used to direct all activities of its peripheral equipment (i.e., scanner, analog to digital converter, X-Y plotter, cassette tape recorder, and line printer). The calculator has a total memory of 1473 registers with its capability enhanced by the use of three plug-in ROM's (Read only memories pre-programmed for a dedicated purpose). The calculator memory is "volatile," in that a loss of power requires reloading from a permanent record (cassette tape or magnetic card).

(c) DAS Scanner. It consists of a set of relays that can be closed or opened via directions sent in from the Controller. The Scanner is "addressed" to select the desired input parameter and, by relay closure, input the signal from the transducer to the analog to digital converter.

(d) Analog/Digital Converter (ADC). It receives instructions from the Controller. The signal received from the Scanner is sampled and converted to the digital form. The Controller accepts and stores the converted information in its registers.

The speed counter information is received and stored in a similar manner.

(e) DAS Cassette Memory, X-Y Plotter and Line Printer. The Controller converts electrical analogs of pressure, temperature, speed etc. to the appropriate units for use in the computations. These and results of the computations are stored in the cassette memory, and printed out, or displayed on the X-Y Plotter.

A set of parameters measured and used at a typical location is shown in Fig. 4.

Other parameters and constants include barometric pressure, composition of natural gas at the location and related computed constants, orifice data, etc. These are entered into the calculator via keyboard.

Contributed by the Gas Turbine Division and presented at the Gas Turbine Conference and Exhibit and Solar Energy Conference, San Diego, California, March 12–15, 1979 of THE AMERICAN SOCIETY OF MECHANICAL ENGINEERS. Manuscript received at ASME Headquarters December 18, 1978. Paper No. 79-GT-82.

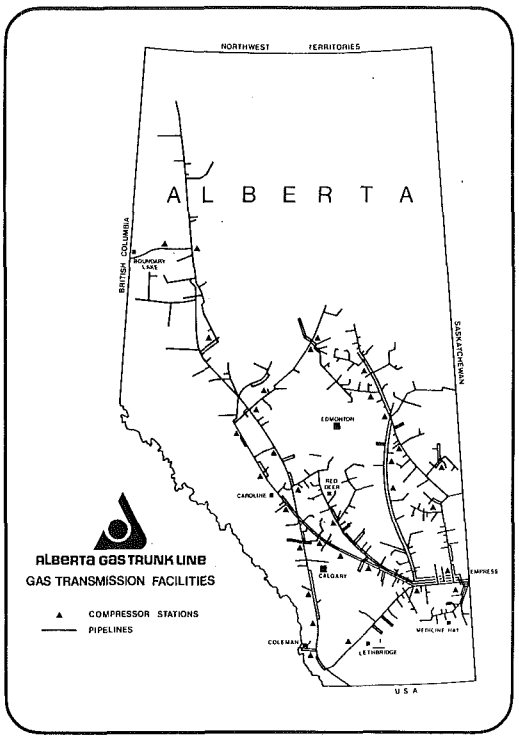

Fig. 1

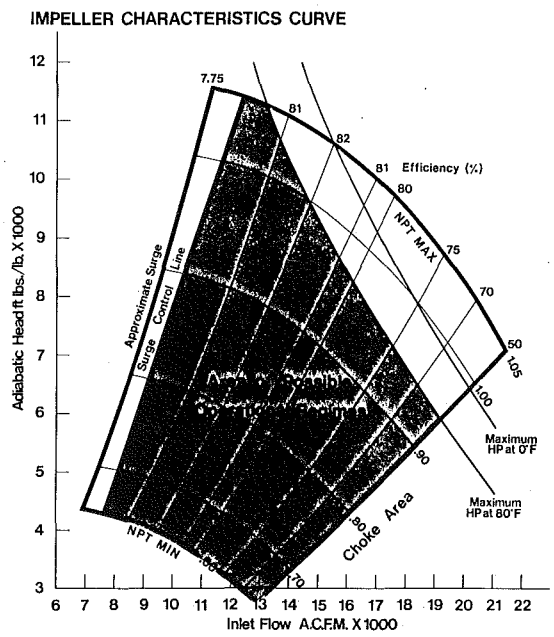

Fig. 2

2 Procedures

The actual test procedures will vary depending upon the purpose of the test but typical steps are:

- set up of the equipment
- initializing with base information
- varying of one parameter to cover the operational range

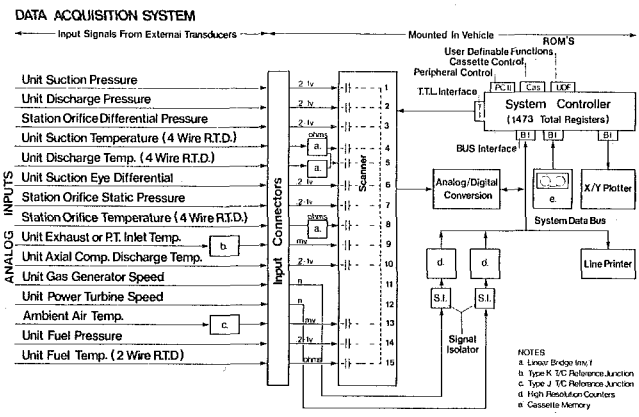

Fig. 3

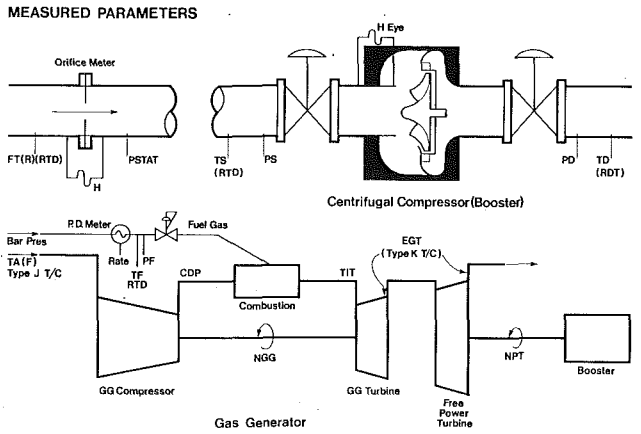

Fig. 4

- stabilization after each change in operating condition
- calculation and storage and/or display data.

The data acquired are utilized to calculate adiabatic head, gas horsepower, adiabatic efficiency using the following equations:

$$Head = \frac{(1545.2)\,(Z)\,(TS)}{(MW)\,(GAMR)}\left[\left(\frac{R_D}{Ps}\right) GAMR - 1\right] \tag{1}$$

$$Gas\ hp = \frac{1.5744}{1000}\,(Grav)\,(Q)\,(Head) \tag{2}$$

$$AD\ EFF = \frac{\left(\frac{P_D}{Ps}\right) - 1}{\left(\frac{T_D}{Ts}\right) - 1} \tag{3}$$

More accurate efficiency can be obtained by using the Benedict-Webb-Rubin equations of state for real gases. The program is lengthy and unsuitable for the present DAS. Experimental correlation was established to give the empirical equation

$$[2]\ \text{BWR}\ EFF = 0.0306 + 0.5466\,(AD\ EFF) + 0.5715\,(AD\ EFF)^2 \tag{4}$$

from that finally

$$\text{BWR shaft hp} = \frac{\text{GAS hp}}{\text{BWR}\ EFF} \tag{5}$$

Nomenclature

BAR PRES = barometric pressure, psia
PD = discharge pressure (booster), psia
PS = suction pressure (booster), psia
PSTAT = orifice pressure absolute, psia
H = orifice flow differential, in. water
TS(R) = suction temperature, °R
DELT(F) = difference between suction and discharge temperatures, °F (or °R)
TD(R) = discharge temperature, °R
FT(R) = orifice flow temperature, °R
H EYE = suction to eye differential, in. water
CDP = compressor discharge pressure, psig
NGG = gas generator speed, rpm
NPT = (free) power turbine speed, rpm
EGT/TIT = exhaust gas/turbine inlet temperature, °F
Z = compressibility factor,
HEAD = head (adiabatic), ft lbs f/lb m
ACFM = actual cubic feet/min booster flow, cfm
Q = gas flow, mmscfd (14.73 psia 520°R

Table 1 Typical data arrangement from the test

SITE DATA (UNCORRECTED)
LOCATION STAT.UNIT 8464.2
DATE D/M/Y 190978

TEST	EGT	CDP	NGG	NPT	TAMB	F/PRESS	F/TEMP	F/RATE	DWR-HP
5.00	957.74	103.01	7973.12	3622.71	45.88	761.43	124.84	23.80	6376.73
52.00	1021.00	110.46	8098.22	3834.35	57.96	750.94	116.94	21.53	7631.65
26.00	1078.02	123.31	8201.00	4213.03	56.33	691.49	112.20	17.50	9379.32
49.00	1142.30	132.74	8306.12	4330.39	60.12	731.49	108.08	16.73	10793.25
41.00	1193.20	142.37	8397.65	4537.03	57.96	730.98	105.30	15.63	12147.03
13.00	1272.54	161.99	8525.25	5026.10	51.61	665.66	98.09	11.80	15469.87
45.00	1316.81	164.02	8615.22	4969.45	58.25	714.58	99.19	12.43	15897.31
18.00	1353.51	177.68	8708.53	5383.32	51.39	627.90	93.47	10.00	18397.66

ISO CORRECTED DATA
LOCATION STAT.UNIT 8464.2
DATE D/M/Y 190978

TEST	TAMB	EGTC	CDPC	NGGC	NPTC	BWRHPC	SEC1 SCF/HPC-HR	SFC2 BTU/HPC-HR	V SCFD*1000
5.00	45.88	994.53	131.88	8075.93	3669.42	7162.09	10.66	10202.28	1832.77
52.00	57.96	1023.99	140.36	8106.38	3838.22	8673.35	9.76	9340.88	2032.11
26.00	56.33	1085.96	154.98	8222.15	4223.90	10642.86	9.06	8667.27	2313.73
49.00	60.12	1138.85	165.71	8297.16	4325.72	12292.11	8.80	8416.88	2595.07
41.00	57.96	1196.53	176.66	8406.11	4541.60	13805.07	8.43	8068.30	2793.78
13.00	51.61	1297.57	198.99	8586.63	5062.28	17473.37	8.12	7765.26	3403.33
45.00	58.25	1319.40	201.29	8621.50	4973.07	18072.29	8.02	7676.00	3479.52
18.00	51.39	1380.49	216.83	8773.09	5423.23	20775.94	7.65	7316.63	3812.79

Another part of the program reduces such data as *EGT, CDP,* N_{GG}, and N_{PT} and *hp* to the standard *ISO* conditions.

Specific fuel consumption measurement is still to a certain degree manual. The fuel flow rate is determined from a positive displacement meter. A stop watch is used to measure the rate of consumption of a measured volume of gas. Fuel pressure and temperature are monitored by the scanner simultaneously. Some typical test results are shown in Table 1 and Fig. 5.

The system as described provides almost instantaneous results, with all the calculations performed and available in the field. Test results were found essential to the Gas Control, Operations and Maintenance Departments. The information is beneficial also in the System Planning and Engineering Departments.

3 Application of Test Results to Equipment Modifications

The rapidly increasing cost of natural gas and a need to conserve natural resources has caused a considerable shift in the pipeline operation philosophy over the past few years.

(a) It became economically feasible in some cases to use looping to reduce the required hp. The effect of this at the compressor station is to reduce head while maintaining the same or higher flow rates. Usually restaging of the gas compressors becomes necessary. This can frequently be accomplished through modification of existing hardware.

Prior to any such restaging attempt it is imperative to have an accurate compressor characteristic map in order to tailor the hardware to the new conditions. Field testing of the unit provides the required data which can be used to predict the performance after restaging to verify compatibility with new requirements.

Post modification tests establish actual characteristics which are then used in gas control daily operations. The data also verify the accuracy of our predictions. Several restagings have been completed successfully. In one case the restaging involved the conversion of a two stage compressor into a single stage unit, producing half the original head. This required relocation of the first stage centrifugal wheel assembly into the second stage position, as the first stage wheel is generally wider to accommodate the higher volume of gas at the lower first stage pressure. The discharge diaphragm assembly was adjusted to accommodate the wider wheel and diffusor. A suction spool piece was installed to carry the gas through the unused first stage area to the eye of the impeller. The balance piston has been checked and adjusted as required. We have realized some improvement in operation efficiency from this restaging.

(b) Field testing has proved very beneficial in another problem which occurs from time to time, i.e., gas generator-free power turbine mismatching. This has occurred in originally supplied equipment and after intensive tests and studies it was eventually corrected by manufacturers.

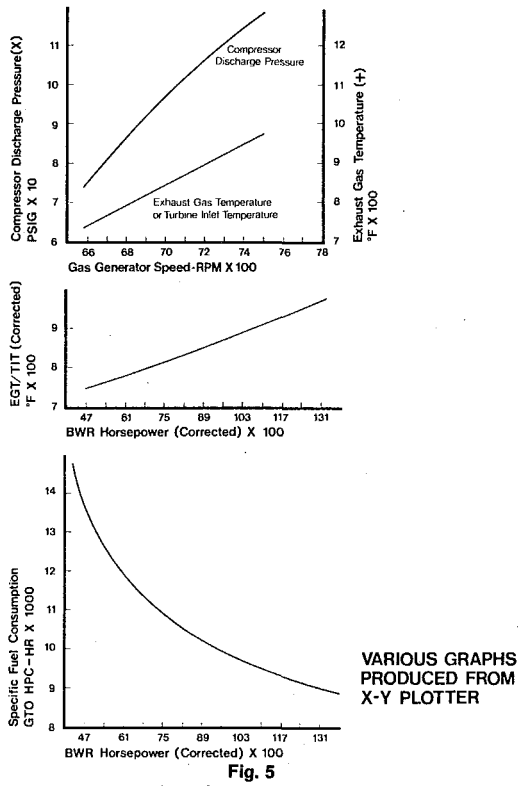

Fig. 5

Replacement or repairs of turbine stators can result in a change in flow area sufficient to cause a change in the engine match and can result in large deviations from the expected performance. A reduction in flow area will produce high compressor discharge pressure, but the engine will reach temperature limits prematurely at a lower gas generator speed than expected. Horsepower output is lower and fuel consumption is increased. In severe cases even the starting of the engine is impaired, the acceleration rate being much slower than expected. In this extreme case the start should be interrupted immediately and mismatching corrected at once.

An increase in flow area will produce lower firing temperatures but also low compressor delivery pressure and correspondingly will again result in a loss of power and lower efficiency.

Therefore field testing of a unit in new condition to establish base line performance data and testing before and after every overhaul is essential in order to ensure that the unit is maintained at the correct

match point. A lower exhaust temperature after overhaul could be a result of a cleaner compressor, but could also be caused by an increase in flow area. Plotting the gas producer speed against power output will establish whether correct engine match has been maintained.

In one instance, no major changes were made to a gas generator during a routine inspection. The free power turbine required a first stage stator change due to a creep problem. (Stator vanes were gradually "dishing" toward the first stage blades, thus reducing the axial clearance between stator and rotor.)

On reinstallation the unit reached its turbine inlet temperature limit at a considerably lower gas generator speed than just prior to repair. Analysis of the performance data revealed that the compressor discharge pressure had increased at a given gas generator speed. Horsepower output had also increased at a given speed. Exhaust temperature was higher at a given power. All indications pointed to a reduction in flow area of the new first stage power turbine stator. A check back to early engine logs indicated that the original engine match was almost identical to the new engine match.

The inference is that deformation due to creep of the stator vanes increased the exit angles of the vane trailing edges especially at the inner diameter, thus increasing the flow area. This particular example illustrates the importance of establishing detailed base line information to provide accurate performance monitoring. The intriguing detail from this last case was that we also encountered slightly increased fuel consumption with the new stator vanes.

(c) Field testing played its role as an early indicator of some problems in the following maintenance case.

Two 2000 hp reciprocating units were experiencing a high incidence of vibration related failures. Vibration spectrum analysis indicated two main sources of vibration. One source was ultimately traced to unbalanced forces in the engine which are inherent to the engine design. These forces produced a rocking motion of the engine frame and generated vibration levels as high as .050 in. on the turbocharger mounted on the top of the engine. Elimination of vibration of the engine mounted turbocharger was accomplished by removing it from the source of vibration.

The second source of vibration was found to involve pulsation in suction and discharge piping which caused failures in the compressor area. The pulsation frequency was equal to the natural frequency of the piping. This frequency was also in resonance with the fifth harmonic of the engine speed, which had a significant effect on the amplitudes. Even with restricted engine speed compressor flange bolts failed and pipe nozzles cracked due to the fatigue. These occurred within 400–500 hr since start-up. On one unit vibration has been attenuated to an acceptable level by installation of several orifice plates in the pulsation vessel nozzles.

Conclusions

1 The DAS System has proven to be a valuable and reliable tool for measuring the performance of gas turbines.
2 The test results are being directly applied in the following areas,
   (a) Gas Control—in controlling the day to day pipeline system operations.
   (b) Field Operations—in helping to troubleshoot various operational problems.
   (c) Technical Services—in assuring a quality control over repairs and modifications.

Reliable test data are also beneficial in the System Planning and Engineering activities.

References

1 Alberta Gas Trunk Line Files and Papers.
2 Pott, M., "An Empirical Correlating Function to compute BWR HP from Adiabatic Data," AGTL 1974 Paper.
3 Mirosh, E. A., "Centrifugal Compressor Maps and Surge Control," AGTL 1972 Paper.
4 Urban, L. A., "Condition Monitoring of Turbine Engines and Gas Compressors or Gas Line Pumping," National Research Council Canada Associate Committee on Propulsion, Oct. 1974.
5 Hewlett Packard Model 3050A—Data Acquisition Syste Manuals.
6 American Gas Association, "Orifice Metering of Natural Gas," Report No. 3. "Manual for determination of Supercompressibility Factors for Natural Gas."

H. K. Lorösch
J. Vay
R. Weigand
Kugelfischer Georg Schäfer & Co.,
Schweinfurt,
W. Germany

E. Gugel
H. Kessel
Annawerk
8633 Rödental-Oeslav,
W. Germany

Fatigue Strength of Silicon Nitride for High-Speed Rolling Bearings

Use of ceramic materials in bearings is deemed attractive for high speed bearings because of the low density of ceramic rolling elements but also to meet high hot strength requirements of other bearing applications. Production methods of various rough shapes of hot pressed silicon nitride (HPSN) are being discussed. Material comparison within the HPSN family was made on the basis of results obtained with a number of methods of testing materials. HPSN balls with low surface roughness have been produced for high speed bearing applications. Rolling fatigue tests have been performed in bearings with AISI M50 VIM Var rings at full hydrodynamic lubrication and at stresses within the elastic range. Results show these balls as being suitable for high speed bearings.

In some applications steel bearing parts, even of high-alloy steel, reach their fatigue limit too early under extreme operating conditions. This limit is dictated either by the insufficient heat resistance of steel beyond approximately 400 °C or the high unit weight of the steel rolling elements at high speeds.

In the last decade many industrial countries have tried anxiously to overcome these limits set by current materials. It turned out soon that besides their low specific weight sintered ceramic materials have many other interesting characteristics, e.g., high hot hardness and relatively favorable wear characteristics. Consequently various institutes carried out systematic researches on the promising non-oxide ceramic material Si_3N_4. High precision rolling elements of this material Si_3N_4 show good cycling results. This is an essential prerequisite for employing this material in rolling bearings.

This article does not discuss the use of ceramic materials at elevated temperatures. The scope shall cover chiefly the possibilities of using hot-pressed silicon nitride in high-speed bearings.

1 Application Possibilities of Balls from Hot-Pressed Silicon Nitride

In high-speed, reliably lubricated bearings service life is dictated by material fatigue strength. If service life is to be increased, the forces between the bearing parts as well as the unit loads in the material have to be minimized. Hot-pressed silicon nitride has not only a lower unit weight but also a higher modulus of elasticity than steel. The use of silicon nitride brings the reduction of the centrifugal forces which are predominant in high-speed bearings, but at the same time increases the material stressing. Fig. 1 shows the assets of ceramic balls used; e.g., in high-speed conventionally designed angular contact ball bearings, the use of Si_3N_4 will be effective with increasing thrust load only at higher speeds. This figure will only show trends. It would be wrong to start from conventional bearings when evaluating the usefulness of ceramic balls. Raceway conformity and ball diameter would have to be optimized using a ceramic-steel combination. Although it can be realized that in the range of speed reference values of $d \times n$ of $2 - 3 \times 10^6$ mm min^{-1} ceramic balls are equivalent to a considerable degree to steel balls even under high loads on relatively large bearings. If the following conditions are given, the use of ceramic balls can be considered:

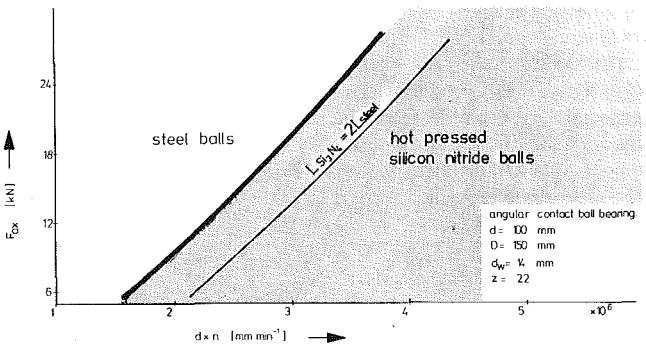

Fig. 1 Zones of higher bearing life with steel balls and silicon nitride balls

(a) Ceramic balls of specified quality can be manufactured with the same reliability as steel balls.
(b) The cycling strength of ceramic balls reaches the same reliability under the same specific stressing.
(c) The propagation of the fatigue damage is as slow and nonmalignant as of bearings completely made of steel.

2 Manufacture of Balls

2.1 Making the Material. Comparing both material variations of silicon nitride the reaction bonded silicon nitride is to be excluded

Contributed by the Gas Turbine Division and presented at the Gas Turbine Conference and Exhibit and Solar Energy Conference, San Diego, California, March 12–15, 1979 of THE AMERICAN SOCIETY OF MECHANICAL ENGINEERS. Manuscript received at ASME Headquarters December 18, 1978. Paper No. 79-GT-83.

for this application due to its porosity entailing low strength and hardness. Only a dense silicon nitride is considered which according to the latest state of the art is manufactured by hot pressing. Hereby a silicon nitride powder made by nitriding of silicon powder is mixed with a flux powder, generally magnesium oxide, and compressed at 1700 to 1740 °C with 25 bis 35 MN/m^2 in controlled atmosphere or compressed in vacuum between graphite dies.

The nature and grain size of the powder as well as the percentage of flux additive are essential as they influence the characteristics of the structure. To obtain the desired surface characteristics and dimensional accuracy during grinding a homogenous structure with a small grain size is mandatory whose development requires a thoroughly controlled hot-pressing cycle.

Two hot-pressed materials used for the subsequent examination are described in Section 4.

2.2 Blank Making. Blank making in hot pressing is a special challenge. This blank should approach as close to the shape of the final ball as possible. To insure a high strength- and wear-resistant quality, the percentage of flux additive should be minimized. This, however, means that the mass becomes less fluid so that hot-pressing becomes increasingly difficult as the shape of the blank approaches the final ball shape.

The simplest hot-pressing process is the manufacturing of plane and parallel plate which were cut to cubes and ball blanks made therefrom. This method is favorable for the homogeneity of the material. The processing of the balls, however, is very time-consuming and expensive, since approximately one half of the material has to be removed by grinding.

The next step was to make grooved plates (Fig. 2). They were sawed to cylindrical blanks, which have to be deburred by grinding but the stock removed only amounts to one third of the blank volume.

The manufacture of plates with grooves in two directions is very critical. On one hand very complicated graphite press dies are required, and on the other hand the compound to be hot-pressed is not sufficiently fluid to reach the required homogenous material quality. This can be controlled more easily by single blank pressing. The higher pressing cost for the single piece pressing is compensated by the lower grinding cost compared to the previously mentioned blanks, i.e. cubes and cylindrical pieces. The economical aspect, however, cannot be fully evaluated. Probably the making of balls starting from a single ball blank will be only preferable from a certain diameter on. Figure 3 shows single hot-pressed blanks for balls with a diameter of 20 mm.

The balls used for the FAG cycling tests were made from grooved plates.

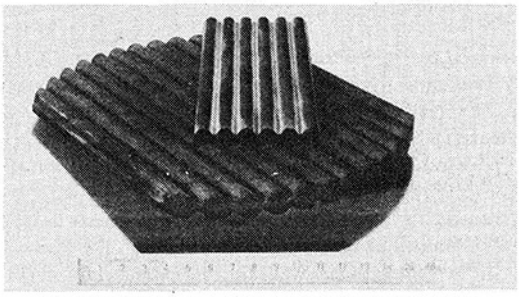

Fig. 2 Multi-grooved disk for ball blank production

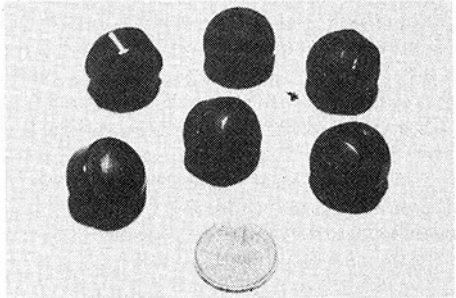

Fig. 3 Hot-pressed blank for a 20 mm dia ball

2.3 Rough Machining. Before finishing the ball blanks from hot-pressed silicon nitride are preshaped by machining between plane and parallel plates, the blanks being cubes, cylinders or preshaped balls. After machining their accuracy is within ±0.05 mm and their out-of-roundness 0.03 mm. Compared with the machining of metallic ball blanks the machining of hot-pressed silicon nitride is extremely difficult, especially the optimum abrasive material and grinding methods have not yet been finalized.

2.4 Finishing. The finishing of the ball blanks comprises two lapping operations. The first one of rough lapping is conducted between multi-grooved plates at low speeds and medium loads using boron carbide suspensions. The second lapping operation, the finish lapping, is conducted between single-grooved cast plates at low speeds and loads using diamond suspensions.

3 Accuracies

All balls used in the test bearings were subjected to metrological and visual examination. During the visual examination the ball surfaces were examined for damages under the microscope. During measuring the shape deviations, the diametrical tolerances of the individual type and the surface roughness (according to DIN5401) were determined. The balls corresponded at least to AFBMA 10; the surface roughness tended to be in the range of AFBMA 3 and 5. Scanning electron microscopic (SEM) photographs have been taken of some balls in order to determine the surface texture (Fig. 4). Balls according to AFBMA 10 are generally used in high-speed bearings for drives.

4 Material Examinations

By checking through pertinent literature, we attempted to find out the technical state of the art in establishing material characteristics

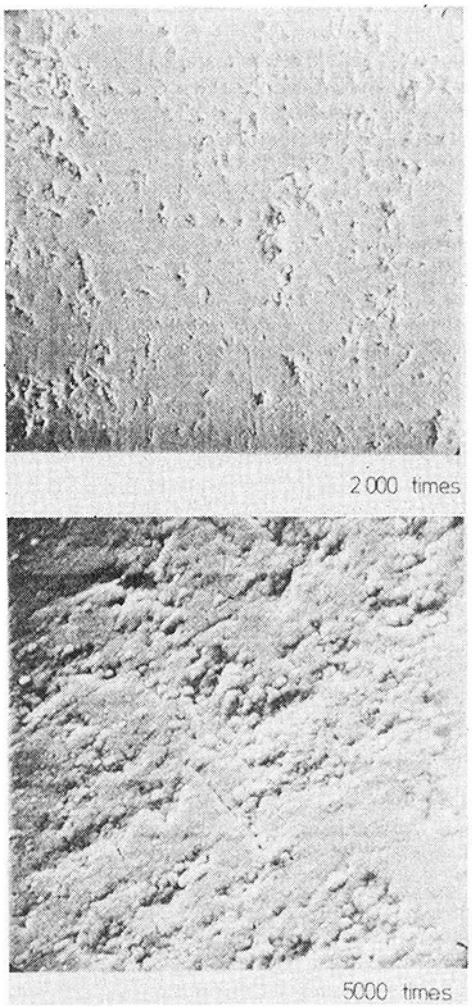

Fig. 4 Surface of a silicon nitride ball

Materialcharacteristics		Norton Range of Test Heats **	Annawerk - Ceranox NH 200	NH 205
Analysis of Major Metallic Constituents (WT-%)	Al	0,26 to 0,8	0,45 - 0,55	0,25 - 0,35
	Ca	0,04 to 0,5	0,1 - 0,2	< 0,05
	Fe	0,52 to 1,86	0,8 1,0	0,45 1,5
	Mg	0,42 to 1,5	1,0 1,1	1,25 1,47
	Ti	0,04 to 0,06	Trace	
	W	0,1 to 1,9		
	Zr	0 to 2,4		
Density (g/cm³)		3,24 to 3,28	3,19 ± 0,006	3,25 ± 0,01
Hardness Vickers HV 10 (MN /m²)			16 670	17 660
Crushing Load Test (N)			17 500	8950
Bendstrength (MN /m²) Four-Point Bending / Weibull Module		674 to 918	700*/m=8-10	657 /m=13
Critical Stress Intensity Factor (MN /m²) Four-Point Bending				5,43
Three-Point Bending		5 to 7,5 Notched Beam Test		5,73
Microstructure α-Si_3N_4(%)			13	
β-Si_3N_4(%) (without amorphous Si_3N_4)			87	- 100 Inclusions of Zirkon Compounds 30 µm
			Grain size see SEM Takings	

*according to Manufacturer's specification **Norton Rep. 19-74-C-0157

Fig. 5 Comparison of material characteristics

of hot-pressed silicon nitride in order to compare it to the values of batches available to us. Chemical composition, density, hardness, structure (grain size, Si_3N_4 phases, foreign particle inclusions) bending strength, pressure resistance and fracture toughness were examined (Fig. 5).

The examination revealed that the examined batches were generally within the range indicated in literature.

The following differences between two qualities were noticed: Quality NH205 had a considerably lower Ca-content, higher density values, 50 percent lower breaking load values during ball pressure test, lower bending strength values and different percentages of α- and β-Si_3N_4 than quality NH200. As to the different structures see SEM taken from the etched surface (Figs. 6 and 7).

Though a clear relation between cycling strength and determined material characteristics cannot be established because of insufficient experience, it can be said that both batches have different strength characteristics and structure. The subsequent cycling test results made it clear that several material characteristics together do allow predictions regarding the cycling strength.

5 Cycling Behavior

Angular contact ball bearings 25/52 mm ϕ × 15 mm with rings of M50 were used for the fatigue test. A glass fiber reinforces polyamide cage was used. The bearings were axially loaded in the test rig (Fig. 8). The loads were selected so that during the test runs no plastic deformation of the raceways occurred.

Test conditions:

Speed	$n = 12\,000\ \text{min}^{-1}$
Thrust Load	$P_{ax} \approx 9\,418$ N
Maximum unit pressure between inner ring and ball	$p_0 = 2\,932\ \text{N/mm}^2$
Lubricant	Shell Tellus 133
	$\nu_{50} = 36\ \text{mm}^2/\text{s}$
Oil inlet temperature	45 °C
Flow rate	160 cm³/min and bearing
Outer ring temperature	95 to 110 °C
Rated minimum thickness of lubricant film referred to outer ring temperature of 110 °C	$0.167 \cdot 10^{-3}$ mm

Under these conditions a separation of the surfaces by the hydrodynamic lubricant film can be assumed. The raceways and the balls did not show any wear after the test runs.

The test runs were stopped immediately by a sensitive vibration pick-up device as soon as first symptoms of damage were developed. Thus it was possible to replace fatigued inner rings, if necessary, and to continue to run the roller assembly until failure. With conventional bearing material the inner rings are the weakest component of the bearing under testing conditions. Eight ball complements with 13 balls each were tested. The statistical percentage of ball complements failures is shown in the diagram in Fig. 9. The ordinate is scaled according to Weibull. The L10 life is 380 hr; i.e., with this load 30 times the rated life according to ISO R281 for bearings of same design made of AISI 52100 high carbon chromium ball bearing steel. Under the same test conditions the balls have a longer life in steel rings because of the unit pressure with steel-steel contact ($p_0 = 2\,607\ \text{N/mm}^2$) is lower, by the factor of 1.12, than with steel-ceramic contact ($p_0 = 2\,932\ \text{N/mm}^2$). On the same test rigs and under the same conditions numerous batches of bearings with steel balls were loaded so that the same unit loads between rolling elements and raceways occurred as in test bearings with ceramic balls. An average L10 life of approximately 400 hr was reached by the steel ball complements.

The comparison reveals that under same unit load ceramic balls can be considered equal to steel balls. Under the conditions mentioned in Section 1, the use of ceramic balls is advantageous at high $d \times n$ values.

To prove the uniform cycling strength of different batches further

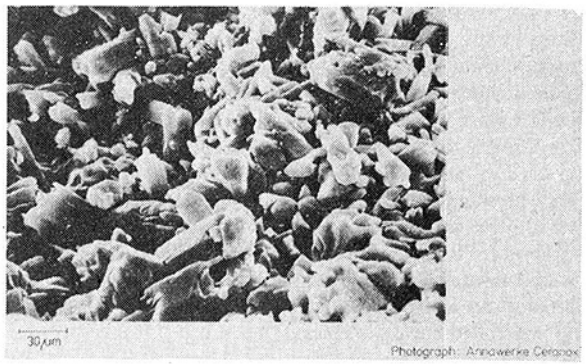

Fig. 6 SEM-micrograph of an etched surface (batch NH200)

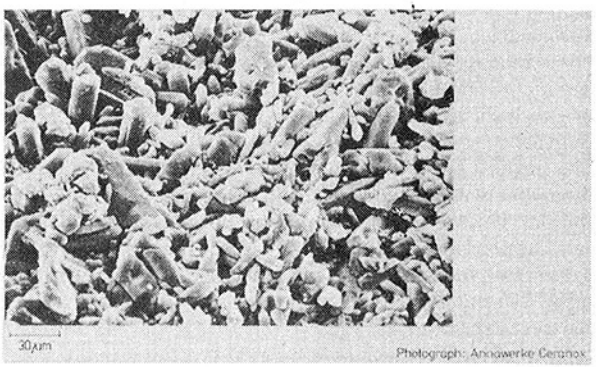

Fig. 7 SEM-micrograph of an etched surface (batch NH205)

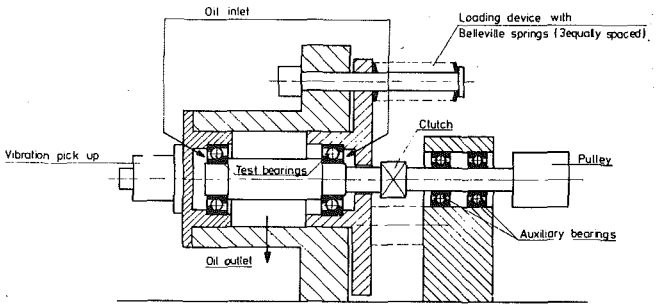

Fig. 8 Scheme of test rig L17

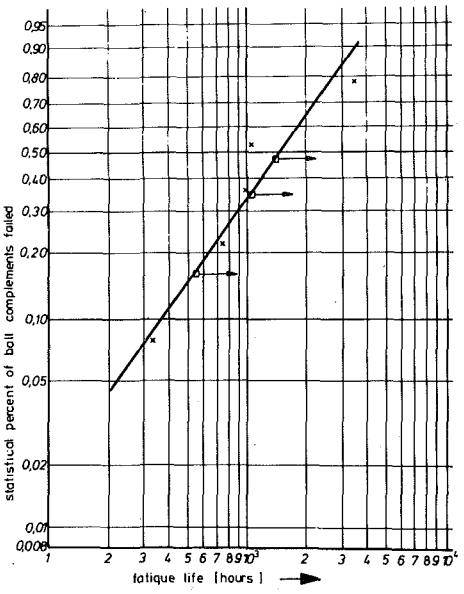

Fig. 9 Fatigue life of ball complements from hot-pressed silicon nitride

examinations are necessary before hot-pressed silicon nitride rolling elements can be assembled in series. Further examinations with balls from a material with more unfavorable characteristics revealed that the basic material influences the cycling strength considerably. Ball complements from a test batch of material quality NH205 when compared to quality NH200, only reached $^1/_{50}$ of the rated life. The cause of this drop of rated life could be the zirconia inclusions or the smaller grain size with which a good coalescence cannot be reached so easily.

The phenomena of failure are similar to that of steel balls. No fractures but spalling occur. The spalling depth is less than that of steel balls.

In practical use the damage propagation speed and the kind of damages are also of great importance. During the first sensor test—the tests are to be continued—one bearing with two fatigued balls and intact rings was kept on running under the same conditions. Figure 10 shows that after a further five hours the damage of the balls increased inconsiderably. The inner ring began to show fatigue wear after two hr. After five hr the bearing noise had increased to an extent that the test run had to be stopped. The result shows that the damage propagation does not hamper the use of ceramic balls.

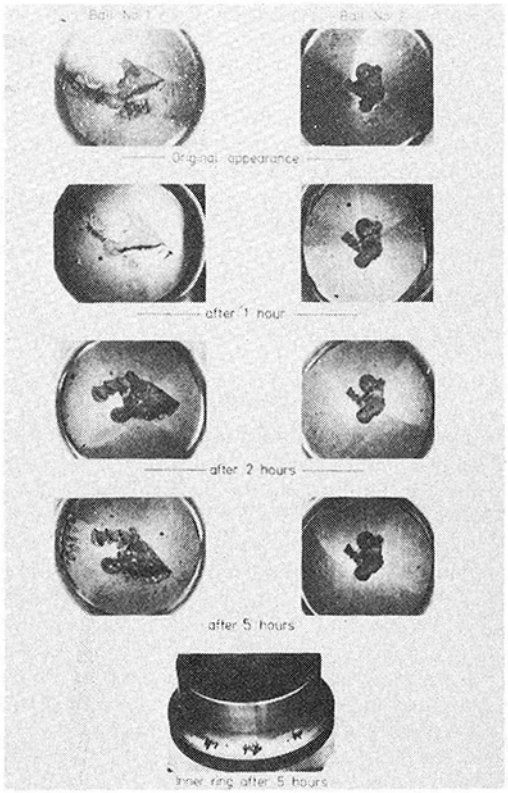

Fig. 10 Advanced damage in a bearing with ceramic balls

T. T. Brown
J. K. Hubbard

Dresser Clark Division
600 Lincoln Ave.
P.O. Box 560
Olean, N.Y. 14760

Application of Gas Turbine/ Compressors in LNG Plants

The objective of this paper is to discuss key considerations associated with selection of Gas Turbine Driven LNG (Liquefied Natural Gas) Turbo Compressors. The selection of any compressor and the ultimate performance is greatly affected by the gas turbine driver chosen. The selection of gas turbine/compressor packages is even more critical when the compressor is to operate on refrigeration service such as in an LNG plant. The selection, performance and operation will be discussed for complete gas turbine compressor packages.

Introduction

Discussion will be limited to the major gas turbine/compressor packages involved in a baseload LNG plant. Smaller compressors and drivers also utilized in an LNG plant will not be considered.

This paper will point out the areas requiring more careful consideration in compressor application utilizing gas turbine drivers in LNG plants. At the present time gas turbines are available only in specific horsepower and speed combinations. For example, from Table 1 it can be seen that if a nominal 30,000 site hp gas turbine were required, it would be available only at two speeds; namely, 3600 or 5000 RPM. On the other hand, steam turbines are presently available with wide horsepower and speed capabilities since in the sizes required for compressor drivers in LNG plants, steam turbines are normally custom designed, as are the compressors.

Notwithstanding the wide range of horsepowers and speeds available with steam turbines, gas turbine drivers for LNG plant applications should not be overlooked since the installed capital cost of gas turbines will be from 10 percent to 30 percent less than for steam turbines when boilers, condensers, etc. are included. In LNG plants the input product is used for fuel and has considerable value. A medium pressure steam plant (approximately 850 psig) will have a thermal efficiency of 24 percent to 25 percent; whereas a gas turbine plant would be 27 percent to 31 percent. Waste heat can be more readily utilized from gas turbines to enhance the thermal efficiency. For example, considering a total plant of 216,000 hp without waste heat utilization and fuel at 1 dollar per million BTU, the fuel cost differential would be 3.1 to 4.1 million dollars per year.

In view of the potential savings, the additional considerations for compressors and potential compromises required in the design stage could prove very profitable.

LNG Plant and Module Sizes

Prior to discussion of processes available for liquefaction of natural gas and gas turbine drivers, it is necessary to define the terminology to be used and limit discussions to certain sized baseload plants.

LNG plants are designed in terms of the volume of gas handled (i.e., MMSCFD) and vary greatly in size, however, world scale plants are normally in sizes of 300 MMSCFD and larger. As a result the total compression requirements dictate extremely large gas turbines and compressors which are beyond the sizes with which manufacturers have experience at this time. As a result, plants are broken down into modules. For example, a 675 MMSCFD LNG plant would have three modules, each of 225 MMSCFD size.

For this paper, discussions will be limited to LNG modules in the range of 150 MMSCFD to 225 MMSCFD which are module sizes

Table 1 Typical Available Gas Turbines* ISO and Approximate Site Ratings at 38°C, Sea Level, Normal Losses and Five Percent Deration

		ISO		SITE	
GAS TURBINE MODEL	POWER TURBINE SPEED RPM	KW (BHP)	HEAT RATE KJ/KW-HR (BTU/HP-HR)	KW (BHP)	HEAT RATE KJ/KW-HR (BTU/HP-HR)
DJ-270G	5600	19,990 (26,800)	10,320 (7,300)	14,980 (20,080)	11,650 (8240)
DJ-290R	5000	22,680 (30,400)	10,400 (7,360)	16,800 (22,520)	11,850 (8380)
FT4C-3F	3600	29,090 (39,000)	11,260 (7,968)	21,560 (28,900)	12,060 (8530)
M5332(B)	4670	25,030 (33,550	12,600 (8,910)	18,700 (25,070)	13,490 (9540)
M7652	3020	48,790 (65,400)	13,080 (9,250)	36,400 (48,800)	14,010 (9910)
CW-352	5000	29,690 (39,800)	12,230 (8,648)	22,190 (29,740)	12,960 (9170)
SOME PLANNED FUTURE GAS TURBINES					
DJ-450	3600	33,570 (45,000)	9890 (7,000)	25,065 (33,600)	10,605 (7500)
OLYMPUS 593	3000/3600	39,760 (53,300)	11,700 (8,280)	29,690 (39,800)	12,540 (8870)

* Data from *Turbo Machinery Catalog and Work Book*, 1978–79 Edition

Contributed by the Gas Turbine Division and presented at the Gas Turbine Conference and Exhibit and Solar Energy Conference, San Diego, California, March 12–15, 1979 of THE AMERICAN SOCIETY OF MECHANICAL ENGINEERS. Manuscript received at ASME Headquarters December 18, 1978. Paper No. 79-GT-85.

utilized in the most recent plants built.

Table 1 is a partial list of dual shaft gas turbines suitable as drivers for LNG compressors for these module sizes.

The site rating in Table 1 of 100°F and sea level was selected as a basis for determining gas turbine performance since many of the most recent LNG plants have been in locations with similar site conditions.

LNG plant module size dictates compression requirements and since compressors are manufactured in basic case sizes with definite speed range parameters, the easiest solution to compressor selection is to have many driver speed and horsepower combinations available. This capability is available with steam turbines but much more restricted with gas turbines. Even though gas turbines have operational speed flexibility, when making a compressor selection it is necessary to operate at the gas turbine design speed as given in Table 1 to obtain the maximum horsepower. Alternatively, when selecting the compressor for a steam turbine driver, the compressor is selected at its optimum running speed and that speed is given to the steam turbine manufacturer around which the turbine is designed.

Both gas turbines and steam turbines have operational speed variation, however, the compressor design speed and horsepower flexibility is limited when using gas turbine drivers.

Process Considerations

Since the first major baseload LNG plant was put into service in the early 1960's, two major types of processes have been utilized for facilities built to date. There are several processes utilized for liquefying natural gas, however, for simplicity purposes, they can be categorized into two: the cascade process and mixed refrigerant process. Refrigeration is key to LNG processing since, when liquefied, natural gas is reduced in volume by approximately 600 times, thereby greatly reducing the capacity requirements of storage and transportation facilities.

For discussion of gas turbine driver requirements, a 225 MMSCFD LNG module was considered since the largest LNG module operating today is of this capacity.

In the cascade process, a series of refrigerant gases are used to remove heat from the natural gas for liquefaction and storage at approximately −260°F. The compression equipment required for one LNG module consists of a propane compressor, one or two ethane or ethylene compressors and usually two or three methane compressors. The gas turbine/compressor matchups are difficult since the power requirements for the methane service can be as much as 10 percent below the propane requirements at a speed of 7000–8000 RPM while the propane compressor would operate at 3000–4000 RPM. The ethylene compressor usually operates at an intermediate speed with similar power requirements to that of the methane compressors. It is obvious that selection of gas turbines of similar sizes without use of high speed gearing is difficult.

In the mixed refrigerant process a mixture of nitrogen, methane, ethane, and propane is usually used. This gas is compressed and used in cooling the feed gas to the storage temperature of approximately −260°F. Certain processes utilize a propane refrigeration cycle to pre-cool the feed gas in addition to the mixed refrigerant cycle. The compression equipment usually consists of a propane refrigerant compressor and two compressors on mixed refrigerant service since the pressure ratio in this service is high.

Table 2 outlines the requirements for a 225 MMSCFD LNG module utilizing the mixed refrigerant cycle with propane pre-cooling. This Table represents the performance parameters for one of the two modules installed in an Indonesian LNG plant with a total plant capacity of 450 MMSCFD.

During selection of gas turbine/compressor packages, the process contractor must keep in mind that plant output is based on LNG contract delivery requirements which usually call for constant output to be maintained continuously year round. Thus, the 450 MMSCFD is a constant daily output requirement each day of the year. The total horsepower requirement per Table 2 for each of the three services involved is approximately 72,000.

Table 2 Requirements per 225 MMSCFD LNG Module

Gas	Mixed Refrigerant Low Stage	Mixed Refrigerant High Stage	Propane
*ACFM	100,000	25,000	100,000
M^3/Min	(2830)	(708)	(2830)
Speed-RPM	4000–5000	5000–6000	2500–3500
*Horsepower	36,000	36000	36,000
KW	(26,856)	(26,856)	(26,856)

* Approximate values

Table 3

	Site H.P.	RPM	Service* HP Reqd	Number of Turbines Required
DJ-270G	20,080	5600	72,000	3.59 (4)
DJ-290R	22,520	5000	72,000	3.20 (4)
FT4C	28,900	3600	72,000	2.49 (3)
M5332 (B)	25,070	4680	72,000	2.87 (3)
M7652	48,800	3020	72,000	1.48 (2)
CW352	29,740	5000	72,000	2.42 (3)

* Plant service horsepower requirements for 2–225 MMSCFD modules per Table 2 is: Low Stage Mixed Refrigerant 72,000 HP, High Stage Mixed Refrigerant 72,000 HP, Propane Refrigeration 72,000 HP

Power Match Considerations

The number of turbines required in Table 3 represents the total number of gas turbine compressors required for each service in the LNG plant and shows that a number of alternatives are available. For example, if the DJ-270G is selected as the driver for the compression equipment, a total of 12 turbines would be required (four low pressure mixed refrigerant, four high pressure mixed refrigerant and four propane drivers). This selection would result in more horsepower being installed than is actually required. The plant output could be raised from 450 MMSCFD to a level which would accommodate the total power produced by the 12 DJ-270G's or the plant designed for future increase in output to the full capability of the 12 DJ-270G's. Alternatively, another turbine combination could be selected such as nine CW-352 turbines and while this reduces the number of turbines, the power available is again more than that required.

Another consideration might be to mix various gas turbine models, however, this results in obvious equipment dissimilarities leading to operational difficulties and expensive spare parts stocking programs. Obviously compromises are required.

Speed Considerations

After the gas turbines are selected, the next consideration is the operating speed. The most desirable solution is for the gas turbine and compressor to operate at a common speed, eliminating the use of high speed gears with their attendant additional cost, risk, and efficiency loss.

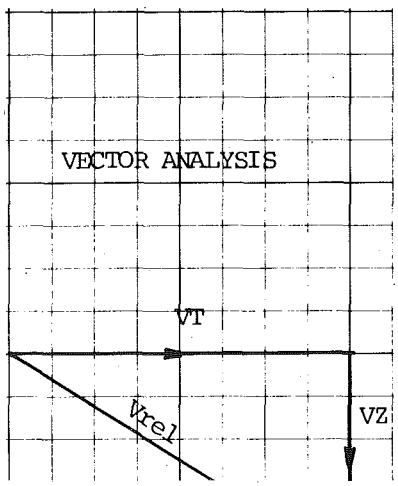

Fig. 1 Vrel = the relative velocity of the gas using a radial guide vane to direct the gas at the impeller cover

Table 1 indicates the optimum speeds at which the compressors should operate from a gas turbine point of view, however, many factors in the compressor design limit this speed.

The first design criteria which must be considered when evaluating compressor speed is impeller tip speed or peripheral velocity as calculated from the following equation:

$$U = \frac{\pi DN}{720} \tag{1}$$

where: U = peripheral velocity (ft/s)[1] (tip speed), D = diameter of impellers (in.), N = rotational speed of the impellers (rev/min)

Recalling that module size dictates compressor case size and consequently maximum impeller diameter the maximum gas turbine speeds to provide acceptable compressor impeller tip speeds are:

Service	*Maximum Impeller Diameter (in.)*	*Maximum Turbine Speed RPM*
Low Stage Mixed Refrigerant	50	4584
High Stage Mixed Refrigerant	40	5730
Propane Refrigeration	60	3820

The gas turbine speed selection for both mixed refrigerant compressors is 4600–5500 RPM. This selection does not fit the propane service without a speed reduction gear. Another selection might be a 3600 RPM turbine for both low stage mixed refrigerant and propane compressor and a speed increaser for the high stage mixed refrigerant compressor.

Other solutions are available but all require compromises.

Another aspect of the correct speed selection is the relationship between the inlet gas velocity generally to the first stage impeller of the compressor and the sonic velocity of the gas compressed. This relationship is a major consideration in the selection of refrigerant compressors since low inlet temperatures and heavy molecular weights are involved.

The sonic velocity of any gas can be calculated as follows:

$$Vs = (k \times g \times R \times T \times Z)^{0.5} \tag{2}$$

where: k = isentropic exponent of the gas, g = gravitational constant (32.2 ft/s^2), R = gas constant of gas (1545/$M.W.$ gas) measured in lb ft/lb, T = absolute temperature of the gas (°R), Z = compressibility factor for the gas at inlet.

For example, the molecular weights and temperatures encountered in mixed refrigerant LNG process are 44 and −35°F for the propane service. In the cascade process temperatures can be as low as −175°F.

After calculating the sonic velocity of the gas from the above equation it must be related to the gas velocity in the impeller. In order to calculate this velocity, tangential and absolute velocities must be calculated as follows:

$$VT = \frac{\pi \times D \times N}{720} \tag{3}$$

Where: VT = tangential velocity (ft/s), D = diameter of the impeller eye (in.), N = operating speed of the compressor (RPM).

$$VZ = \frac{Q \times 144}{A \times 60} \tag{4}$$

where: VZ = absolute velocity of gas entering the impeller (ft/s), Q = inlet capacity to the impeller (CFM), A = area of the eye of the impeller (in.^{2}).

The tangential velocity as listed above results from the rotational speed of the impeller at the point where the gas meets the impeller blade. The absolute velocity of the gas as calculated above is the velocity of the gas as it enters the impeller. Vector analysis of the tangential and absolute velocities result in the relative velocity of the gas to the impeller blade is determined as shown by Fig. 1. The above

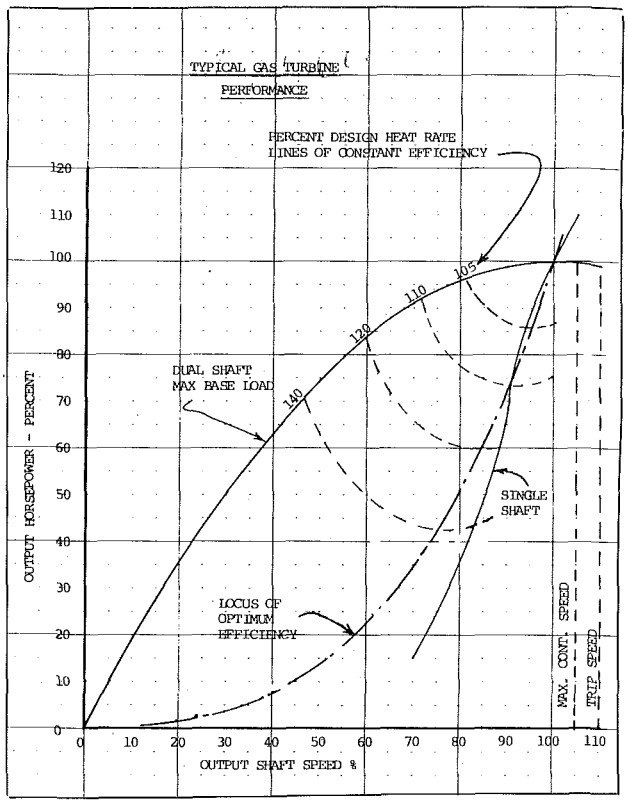

Fig. 2 Typical gas turbine performance

analysis is based on utilization of a radial guide vane directing the gas into the impeller. Many other guide vane arrangements directing the flow of the gas into the impellers are also available and similar vector diagrams can be drawn.

The relative velocity is then compared to the sonic velocity to ensure it does not exceed 85 percent of sonic velocity.

Selection of proper refrigeration compressors must include evaluation of relative velocity to sonic velocity. Since the flow to the compressor is fixed by module size and the gas molecular weight and inlet temperatures are fixed by the process conditions, the operating speed plays a major part in this evaluation. The speed of the propane compressor is very critical because it not only operates at a low temperature, but it also handles a high molecular weight gas. This evaluation is an important consideration since if sonic velocity is reached by the gas in the impeller, shock waves may occur causing excessive noise and resulting vibrations in the compressor attendant with a marked reduction in efficiency.

In selecting the design operating speed of the compressor, the compressor's first and second lateral critical speeds must be considered. Operation near a critical speed is undesirable since high vibration and unstable operation may occur resulting in potential mechanical failure.

API-617 dictates that for "flexible shaft" compressors, (i.e., compressors operating between the first and second lateral critical speeds) the type of compressor used for LNG service, the first actual critical speed must be 15 percent below any compressor operating speed. The second lateral critical speed must be at least 20 percent above the maximum continuous speed of the turbine/compressor package.[2]

Lateral critical speed analysis is also done to determine that the critical speeds of the turbine are compatible with those of the com-

[1] Approximately 1,000 ft/s is considered an industry standard for refrigeration services.

[2] *American Petroleum Institute Standard 617,* 3rd Edition, Washington, D.C., p. 11.

pressor for the operating speed range required.

Suitable matching of driver and compressor is mandatory and matching compromises may be required.

The gas turbine speed and horsepower operating characteristics (Fig. 2) should also be considered in proper selection of compressor speed. Figure 2 demonstrates that gas turbine horsepower output decreases as speed decreases. Thus, if the maximum turbine horsepower at site conditions is required to fulfill the plant horsepower requirements, it is essential that the turbine be rated near 100 percent rated speed.

Other Considerations

Consideration must be given to off-design operating conditions. The turbine horsepower must be compatible to the compressor horsepower requirements at reduced operating speeds. Start-up conditions with regard to torque, speeds, and horsepower produced must also be considered in the selection of gas turbine/compressor packages.

If a point less than full rated horsepower is selected for design, then an effort should be made to match the speed for optimum turbine/compressor efficiency. This logic is seen in Fig. 2. Note the lines of constant turbine efficiency versus horsepower and speed and the line defining the optimum efficiency.

One of the other parameters that must be considered is that of compressor sidestream operating conditions that must be met. For example, the propane refrigerant compressor or the mixed refrigerant compressor may have two or three incoming streams in the cooling cycle. These incoming streams are at specified pressure levels which are often requested to be guaranteed within a minimal tolerance. A driver with a variable design speed such as a steam turbine eases selection of the proper impeller configuration to meet the designated sidestream levels.

Gas turbine drivers have fixed design speeds indicated in Table 1. Thus the sidestream levels must be met by other means such as cutting impeller diameters or selecting impellers at off-peak design points. The flexibility in selecting the compressor is decreased considerably with one of the selection variables (design speed) removed.

Even though it is not common practice to change operating conditions during engineering by the manufacturer, occasionally certain necessary changes by the process contractor must be considered. Often the new operating conditions can be met by design speed changes to the compressor, however, in the case of a gas turbine driver, other changes must be made.

Revised compressor impeller selection may become a viable solution to meet the new requirements. The worst condition might be that the speed requirement of the compressor would fall outside the speed capability of the selected driver.

Summary

The application of turbo compressors with gas turbine drivers for LNG plants may require more study and engineering than with steam turbine drivers. Some of the areas requiring serious consideration have been discussed but the specifics of a particular installation may require study in areas not considered by the writer. However, the potential savings should not be overlooked for any installation and gas turbine drivers should not be ruled out without thorough evaluation.

A. F. Criqui
Product Engineer.
Development

P. G. Wendt
Chief Engineer.
Gas Compressors
Mem. ASME

Solar Turbines International
An Operating Group of International Harvester
2200 Pacific Highway
P.O. Box 80966.
San Diego, CA 92138

Design and Closed Loop Testing of High-Pressure Centrifugal Gas Compressors for the Suppression of Subsynchronous Vibration

The causative phenomena of subsynchronous vibration, or re-excitation of the critical speed of a rotor, are discussed. Two rotor systems designed to control this type of vibration are presented. One system employs tuned, oil film damper bearings while the other features a stiffened rotor geometry. Stability thresholds of each design are compared based on high-pressure closed loop testing.

Background

As modern turbomachinery practice extends to areas of higher speeds and increased fluid pressures, the incidence of rotor dynamic instabilities has also increased significantly. The designer is faced with the task of accommodating greater process pressure levels and greater head requirements in machine envelopes which, for best efficiency and economy, are becoming increasingly compact. The inescapable result is higher horsepower-to-volume density machines operating above one or more critical speeds and characterized by long, slender rotors featuring built-up construction. For a time, tilting pad journal bearings, with their improved damping and low cross-coupling terms provided an answer to marginal stability applications. Now, however, better solutions are needed to keep pace with the evolution of the process machine.

It is the goal of this paper to outline the approach taken and results obtained by one manufacturer of centrifugal gas compressors to produce improved mechanical operation in the face of the increasingly hostile operating environment.

Rotor Construction

The rotor construction of the compressors under observation is shown in Fig. 1. In order to achieve the highest possible lateral stiffness, a stacked construction is used. The impellers and stub shafts are assembled with short, tight pilot fits and held together with a central tie bolt. Thus, it is the impeller hub diameter which dictates the rotor stiffness. This arrangement results in a much stiffer design than one with impellers shrunk on a shaft, since the stiffness is a function of the fourth power of the stiffness diameter.

Subsynchronous Vibration—Symptoms and Causes

Numerous types of rotor instability phenomena have been reported. The widespread occurrence of these ailments is underscored by the fact that virtually all of the mechanisms predicted to cause instabilities have, in fact, been observed [1].

Perhaps the greater number of instabilities are those that are the subject of this paper: a type of subsynchronous vibration (SSV) caused by a re-excitation of a critical speed.

A flexible rotor machine (that is, one that must pass through one or several rotor resonances to reach operating speed) is vulnerable if the damping in the rotor and its support system is insufficient to suppress the tendency of the rotor to vibrate at one of its natural

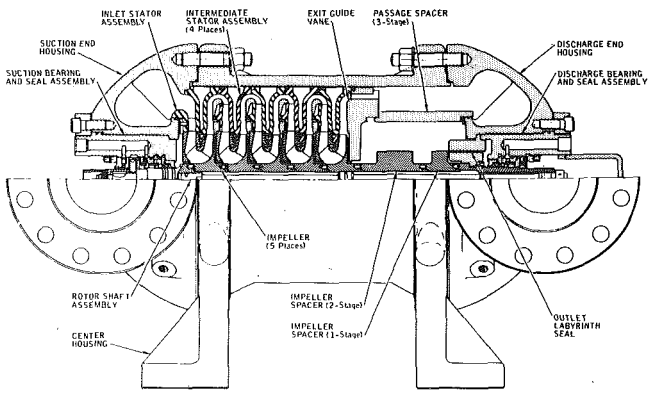

Fig. 1 Compressor construction

Contributed by the Gas Turbine Division and presented at the Gas Turbine Conference and Exhibit and Solar Energy Conference, San Diego, California, March 12–15, 1979 of THE AMERICAN SOCIETY OF MECHANICAL ENGINEERS. Manuscript received at ASME Headquarters December 18, 1978. Paper No. 79-GT-86.

frequencies or critical speeds. An asynchronous driving force must be present, of course, and this is conveniently provided in the wide band fluid dynamic "noise" surrounding the rotor. The disturbance can be generated by turbulence at impellers, balance pistons and labyrinth seals as well as by liquid bushing or oil film type shaft seals.

A typical situation is illustrated by the undamped critical speed map (Fig. 2). System criticals are represented by the intersection of the rotor critical speed lines (shown as a function of bearing stiffness), and the bearing line (which is a function of rotational speed). In this figure, a single bearing stiffness characteristic is shown, although often the stiffnesses are anisotropic such that different characteristics are exhibited in the vertical and horizontal directions. Also, damping, always present to some degree, generally increases the critical speed lines.

Such a rotor would have an unbalance response characteristic as shown in Fig. 3. A response peak would be present corresponding to the first critical speed (bounce, or translatory whirl mode) at 6400 rpm and, for this rotor, there would be little amplification when passing through the second critical speed (rock, or conical whirl mode) at 14,000 rpm. As Fig. 2 shows, the second intersection point is on the straight portion of the second critical speed line. This means that the bearing oil film stiffness is controlling the value of the second critical with very little deflection of the rotor itself. With little rotor deflection, most of the vibration amplitude occurs at the bearings. A relatively large motion at the bearings produces good damping and the damping gives the desirable result of a low amplification factor.

The frequency domain presentation of the vibration would be a single peak at the running speed frequency of 333 H_z caused primarily by rotor unbalance. Under the influence of the aforementioned wide band noise, the vibration spectrum might include a subsynchronous component corresponding to the value of the first critical speed. The rotor is rotating at one speed (running speed) but is excited to vibrate at its natural frequency at a lower frequency; thus, the term re-excitation of the critical speed. Note that once the instability is triggered, the subsynchronous vibration persists at a fixed frequency irrespective of variations in running speed.

It should be noted that the subsynchronous frequency could also be that of the second critical (typical for overhung rotors having greater response to the conical mode) or the third critical speed (the first bending critical) for a rotor operating above that speed. Occasionally more than one mode is exhibited.

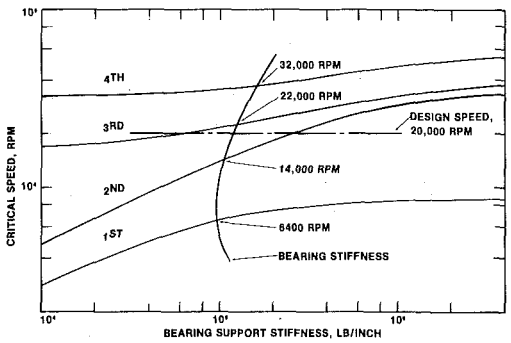

Fig. 2 Typical undamped critical speed map

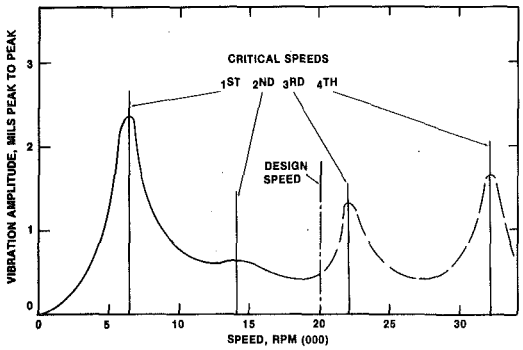

Fig. 3 Typical unbalance response curve

Operating Experience

Subsynchronous vibration was reported on several units when operated at high-pressure levels and was first revealed during factory closed loop load testing. The closed loop test arrangement is shown in Fig. 4. Typically, the vibration amplitude would increase dramatically as the discharge pressure was increased. Figure 5 shows the spectrum from a unit which showed a drastic increase in the subsynchronous vibration at 100 H_z as the discharge pressure was increased to 1550 psi (10,700 kPa).

The onset was sometimes violent enough to be heard and felt in the vicinity of the machine. Damage was fortunately confined to bearing babbitt wiping and light rotor-stator rubs. Experiences with other machines include extensive internal damage when the amplitudes are unbounded. A treacherous characteristic of instability is the suddenness and violence with which it can occur.

Analytical Evaluation

An analytical study was undertaken to determine corrective action. For this, a computer instability program was used [2].

The analysis consists of modeling the rotor and its supports, including fluid film bearings and structure; linearized stiffness and damping values are used. Fluid dynamic excitation is represented at the rotor locations where they occur, such as the impellers, seals, and balance piston. The rotor internal material (hysteretic) damping and damping due to interference fits are also modeled. The complex Eigenvalues of the system dynamic matrix are determined by an extension of the Myklestad-Prohl method [3, 4]. Any operating speed of interest may be examined and for each, the damped natural frequencies of the rotor and the effective damping associated with each natural frequency are displayed. The damping value indicates the degree of stability present for each natural frequency.

The magnitude of the destabilizing influences was first approximated by empirical methods [5]. For an existing machine, whose

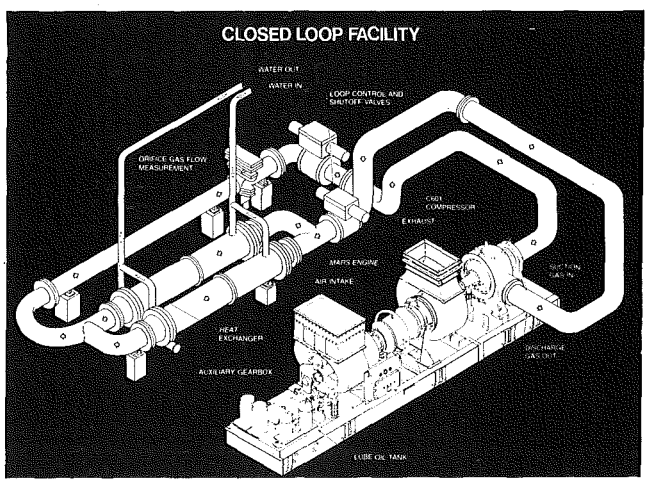

Fig. 4 Closed loop test facility

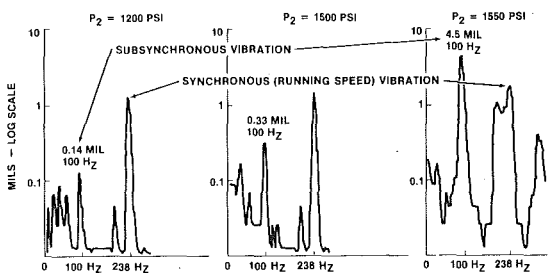

Fig. 5 Vibration spectra showing increasing subsynchronous vibration with increasing discharge pressure

characteristics can be evaluated by testing, the computation can be calibrated by adjusting the cross-coupling coefficients to produce a predicted instability at operating conditions known from testing to be at the threshold of instability.

First Solution—The Damper Bearing

Since the objective of the program was a speedy yet effective solution, the main effort was directed at adding supplemental damping to the system in the form of a squeeze film damper to be located between the journal bearings and their supports [6].

The damper may be regarded as a kind of suspension system consisting of a spring and shock absorber which, when properly tuned, discriminates against the unwanted frequency of vibration.

One measure of the system's ability to damp out vibration is the log decrement. This is the natural logarithm of the ratio of the amplitudes of successive excursions. Thus, any positive value signifies decreasing amplitudes, that is, stability. In practice, a somewhat greater value is needed, and a log decrement of 0.4 has been used as the stability threshold. This is equivalent to 6.4 percent of critical damping or a "Q" of about 8.0. Figure 6 shows the relationship between the log decrement, δ, and amplitude-time behavior.

After conservatively modeling the destabilizing influences, a parametric study was made to determine the optimum location and value of the dampers. Figure 7 shows several important results. Analytically, an optimum value exists such that poorer performance is predicted for either smaller or larger values. Also, the location is decisive. In this case, a suction end damper is predicted to be more effective than a discharge end damper or even dampers at both bearings.

Having identified the damper characteristics required, two special bearings were constructed: one, a five-pad mechanically pivoted tilting pad design; and the other, a propriatary three-pad, fluid pivot bearing. Each was designed with an oil squeeze film damper surrounding the bearing as illustrated in Figs. 8 and 9. Space constraints were severe since the bearing-damper assembly was to be retrofitted into existing units.

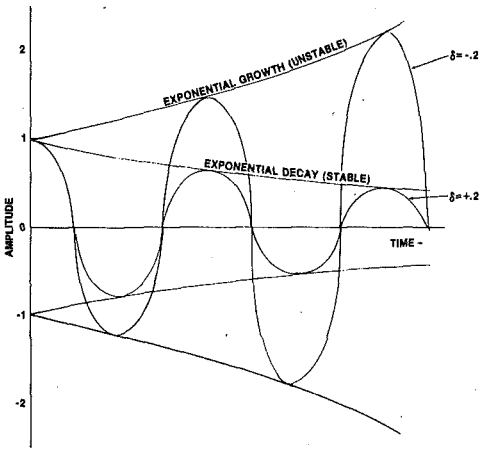

Fig. 6 Vibration amplitude versus time for different values of log decrement

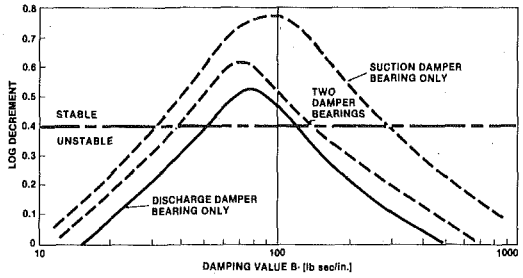

Fig. 7 Compressor damper bearing optimization

Closed Loop Testing

Before introducing the damper bearing in the field, an extensive testing program was carried out to prove the design and to explore the stability limits with and without the damper bearings.

An eight-stage high-pressure (4000 psi (27,600 kPa) maximum) compressor was installed in a gas turbine driven, closed nitrogen test loop.

Over 600 data points were taken over a period of several months under closely controlled conditions.

Test Variables. The following parameters were varied singly and in combination to reveal empirically the factors influencing the instability:

- Suction Pressure
- Pressure Ratio
- Speed
- Journal Bearings

a No Dampers
b Dampers
c Type: 5-pad TPJ and 3-pad Fluid Pivot
d Clearance
e Clearance Symmetry

- Balance Piston Diameter
- Impeller Staging
- Rotor Tie Bolt Tension

Correlation of the test data revealed the threshold of instability [taken for test to be the point at which the subsynchronous vibration reached 0.75 mils (19 μm)] was most influenced by suction pressure and pressure ratio, although almost all of the other factors had some effect.

The effectiveness of the damper, for an otherwise identical rotor, is shown in Fig. 10.

As a control, a low-pressure full speed run preceded the test of each new configuration to verify the mechanical integrity of the compressor and to check that rotor balance had not changed.

Attempts were also made to correlate compressor discharge pressure pulsation frequencies to the frequency of the subsynchronous

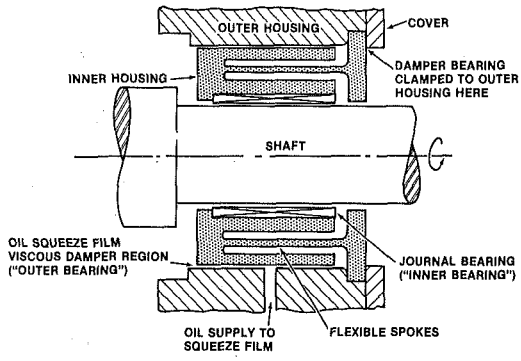

Fig. 8 Schematic damper bearing

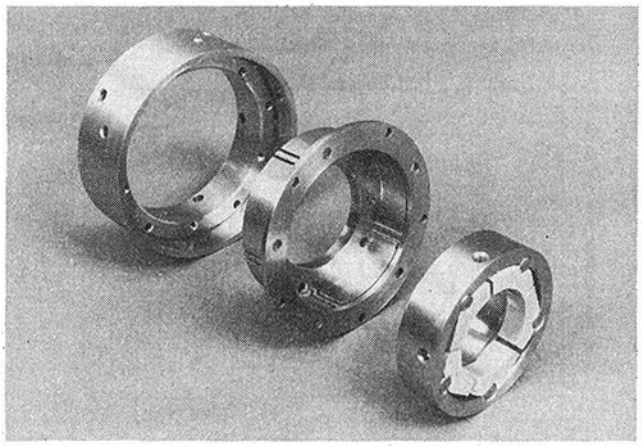

Fig. 9 Damper bearing assembly

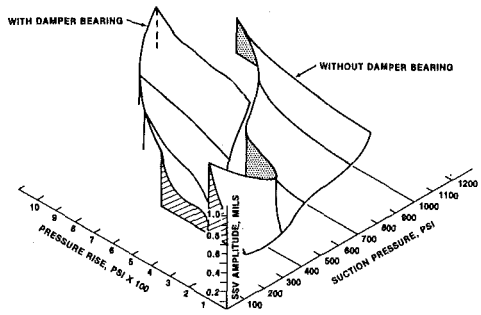

Fig. 10 Subsynchronous vibration versus suction pressure and pressure rise showing the effect of the damper bearing

vibration. The thought was that there might be an aerodynamic disturbance coincident with the rotor critical speed which, of course, would have aggravated the subsynchronous vibration. Other investigators have observed this to be the case [7].

To accomplish this, pairs of dynamic pressure transducers were fitted at the stator housing exit and at the last stage impeller discharge tip. The pairs were located 90 degrees apart so that phase analysis of the transducer output signals might detect the presence of any rotating stall condition.

No rotating stall condition was found. Frequency analysis of the signals showed a number of peaks in the low frequency range (20 to 200 H_z) but none of these coincided with the subsynchronous frequency of the rotor. In addition to the discrete peaks, there was a rather uniform level of noise througout this frequency range. It is likely that this white noise, which surrounded the subsynchronous frequency, provided, or at least contributed to, the destabilizing influence on the rotor.

Test Conclusions. Analysis of the extensive data led to a number of conclusions regarding the influence of the different factors which were varied. These are discussed individually below and summarized in Table 1.

Suction Pressure. Varied from 300 to 1550 psig (2070 to 10,700 kPa). Generally higher SSV occurred with increasing suction pressure but this was not uniformly true. Figure 10 shows a "saddle point" at moderate suction pressure above and below which SSV was more severe.

Pressure Ratio. Varied from choke to surge, numerically, 1.1 to over 3.0. This was the most sensitive of the operating conditions and the SSV trend was uniformly upwards with increasing pressure ratio. As shown in Fig. 10, the trend is slight at first tending toward asymptotic as pressure ratio is further increased.

Speed. Varied from 16,000 to 22,300 rpm. SSV was generally more severe at higher speeds but evidently because higher pressure ratios were attainable rather than being an effect of speed per se.

Journal Bearing. Conventional versus Damper Type. As predicted, the damper bearing (Fig. 10) produced a significant shift in the threshold conditions. An improvement of about 35 percent was noted in maximum pressure ratio attainable with the damper bearing.

Type of Damper Bearing. Little change was noted between the mechanically and fluid-pivoted tilting pad journal bearings for similar operating conditions. Clearly, the improvement resulted from the squeeze film damper surrounding the journal bearing.

Journal Bearing Clearance. Varied from a clearance ratio of 0.0012 to 0.0020. Generally, lower SSV amplitudes were obtained with tighter clearances, although the suction pressure-pressure ratio combination at which the rise became asymptotic was little affected. This can be rationalized in that the tighter bearings are stiffer, yielding lower response to a given stimulus.

Clearance Symmetry. The closely fitted pivot pins in the mechanically pivoted bearing in Fig. 9 allows variation of the horizontal and vertical clearance values independently. These tests revealed a small advantage in favor of the asymmetrical bearing. However, this may be merely a reaffirmation of the effect of stiffness on response as stated in the previous paragraph.

Table 1 Summary of Cause-Effect Relationships on SSV

	Variable	Effect on SSV
1.	Suction Pressure	More severe at higher pressures
2.	Pressure ratio	More severe at higher ratios
3.	Speed	More severe at higher speeds
4.	Damper bearing	Much improved with damper bearing
5.	5-Pad versus 3-Pad TPJ	Little change
6.	Bearing clearance	More severe with larger clearances
7.	Clearance symmetry	Somewhat improved with asymmetrical clearance
8.	Balance piston diameter	More severe with larger balance piston diameter
9.	Compressor staging	More severe with low flow staging
10.	Tie bolt tension	No change

Balance Piston Diameter. Varied from 3.75 to 4.4 in. (95.25 to 111.76 mm) diameter. A distinct improvement in the threshold conditions was observed with the smaller diameter balance piston. A likely explanation is that the magnitude of the destabilizing forces is proportional to the circumference of the balance piston labyrinth seal.

Impeller Staging. The eight-stage rotor was alternately fitted with "A" and "B" impellers on the final stages. The "A" impeller has a discharge port axial width of 0.170 in. (4.32 mm) while that of the "B" stage is 0.260 in. (6.60 mm). As predicted by Alford [8] and Rodgers [9], the instability threshold occurred at more moderate operating conditions with the smaller "A" stages. The shift was about 10 percent in terms of the limiting pressure ratio.

Rotor Tie Bolt Tension. Varied to produce a range of axial clamping force from 38,000 to 50,000 pounds (169,000 to 222,400 N). Essentially no change was noted supporting the prior contention that the stacked and piloted rotor acts as a monolithic structure as long as the axial preload is sufficient to maintain tight contact at the impeller faces.

Several secondary test conclusions were found:

- Oil supply temperature (and thus viscosity, running clearance, and bearing stiffness) effects were significant and the temperature had to be closely controlled to avoid confusion of the results. The SSV threshold was lower (i.e., instability occurred at lower suction pressure-pressure ratio combinations) with higher oil supply temperatures. This effect had been predicted analytically.
- The damper and other improvements never entirely eliminated the SSV, although the amplitude for given conditions was markedly lower, typically by a factor of 20.
- Construction of the damper bearing requires a degree of care and a level of workmanship similar to those of the bearing itself. Part tolerances are of the same order and, since the oil film clearances are about the same, the filtration level customary in modern lube systems serves to keep the damper functioning properly.

Second Solution—Redesigned Rotor

The addition of the damper bearing corrected the occurrence of subsynchronous vibration in most of the applications of the compressor. However, a few units were to operate in the region when the damper alone would not provide enough stability. Moreover, the trend of operating conditions pointed clearly to even more severe pressure for the future.

The second, or long range part of the program centered around a completely new rotor configuration, but with the constraints that the compressor design point speed remain unchanged and rotor and stators be mechanically interchangeable with the original design to facilitate field changeout and maintain commonality of the housing.

Based upon an evaluation of the factors which influence the instability, the rotor was redesigned to achieve:

- Increased lateral stiffness so as to raise the critical speeds
- Relocation of the bearing centerlines to improve modal damping

- Bearing preload and clearance relationships to produce optimum bearing damping.

In addition, the redesign included the provisions for squeeze film dampers, should future conditions require them.

The stiffened rotor was the result of a new series of impellers featuring increased hub diameter. By applying the latest design techniques, this resulted in aerodynamic performance essentially equal to that of the original impeller design despite the change in hub-tip ratio.

The second change, that of repositioning the journal bearings, allowed the designer to obtain plenty of motion at the journal with the rotor mode shape corresponding to the critical speed. This motion increases damping (amount is proportional to the velocity of vibration at the journal) and enables the bearing to more effectively suppress the tendency to vibrate.

Optimizing the bearing damping in consideration of the shaft-to-bearing stiffness ratio further enhances the stability of the system [10].

Redesign Test Results

The redesigned compressor was then tested in the closed loop previously described at about 200 operating points. Here, it was subjected to a broad range of operating conditions to explore the limits of stability.

Results were excellent. No trace of subsynchronous vibration was found over most of the performance map and never more than 0.1 mil (2.5 μm) of SSV was induced at any conditions.

A comparison of the performance of the three rotor systems, original, original with damper bearing, and redesigned rotor, is shown in Fig. 11.

Summary and Conclusions

Fluid dynamic disturbances are known to cause re-excitation of a critical speed in many flexible shaft rotating machines, principally those operating at high pressures and high-pressure ratios.

This instability is very strongly influenced by the operating conditions and can be treacherous in its abruptness and severity.

The precision of analytical investigations of this phenomenon are only as good as the assumptions made for the magnitude of the aerodynamic disturbing forces. Further work is needed on the prediction of these forces.

Auxiliary damping, judiciously applied, can significantly extend the stable operating range of the system. However, a more effective approach involves optimizing the relationships of rotor stiffness, bearing location and bearing stiffness and damping to produce an inherently insensitive design.

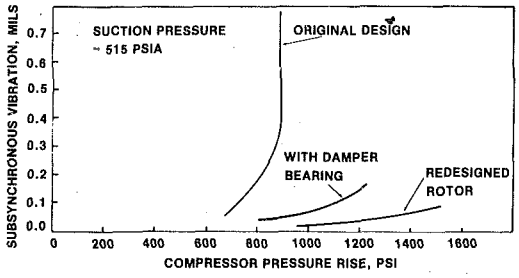

Fig. 11 Subsynchronous vibration versus pressure rise showing the further effects of the stiffened rotor design

References

1 Ek, M. C., "Solution of the Subsynchronous Whirl Problem in the High Pressure Hydrogen Turbomachinery of the Space Shuttle Main Engine," Paper 78-1002 presented at the AIAA/SAE 14th Joint Propulsion Conference, Las Vegas, Nev., July 25–27, 1978.

2 Lund, J. W., "Stability and Damped Critical Speeds of a Flexible Rotor in Fluid Film Bearings," ASME *Journal of Engineering for Industry*, May 1974, pp. 509–517.

3 Myklestad, N. O., "A New Method of Calculating Natural Modes of Uncoupled Bending Vibration of Airplane Wings and other Types of Beams," *Journal of the Aeronautical Sciences*, Apr 1944, pp. 153–162.

4. Prohl, M. A., "A General Method of Calculating Critical Speeds of Flexible Rotors," ASME *Journal of Applied Mechanics*, Vol. 12, Vol. 67, 1945, pp. A-142-A-148.

5 Thompson, W. E.: "Fluid Dynamic Excitation of Centrifugal Compressor Rotor Vibrations," ASME paper No. 77-SE-22.

6 Gunter, E. J., Barrett, L. E. and Allaire, P. E., "Design and Application of Squeeze Film Dampers for Turbomachinery Stabilization," *Proc. 4th Turbomachinery Symposium*, Gas Turbine Laboratories, Texas A & M University, Oct. 1975.

7 Abdelhamid, A. N., Colwill, W. H. and Barrows, J. F., "Experimental Investigation of Unsteady Phenomena in Vaneless Radial Diffusers," ASME paper No. 78-GT-23.

8 Alford, J. S.: "Protecting Turbomachinery from Self-Excited Rotor Whirl," ASME JOURNAL OF ENGINEERING FOR POWER, Vol. 87, Oct 1965, pp. 333–344.

9 Rodgers, C., "Impeller Stalling as Influenced by Diffusion Limitations," ASME *Journal of Fluids Engineering*, March 1977, Vol 99, pp. 84–97.

10 Barrett, L. E., Gunter, E. J., and Allaire, P. E.: "Optimum Bearing and Support Damping for Unbalance Response and Stability of Rotating Machinery," ASME Paper No. 77-GT-27.

P. M. Chapple
P. F. Flynn
J. M. Mulloy

Cummins Engine Co.
Mail Code 50165
Columbus, IN 47201

Aerodynamic Design of Fixed and Variable Geometry Nozzleless Turbine Casings[1]

A design method has been developed to produce nozzleless turbine casings which provide a centrifugal turbine wheel with a uniform inlet state. The analysis includes the effect of wall friction and has been found to accurately predict the mass flow versus pressure ratio characteristics of nozzleless casings. The uniform inlet state provided by this design approach provides turbine wheel/casing configurations with near optimum efficiency and a very low aerodynamic blade vibration excitation level. The model has been extended to produce variable area casings to simulate a simplified variable casing geometry. Testing has verified the accuracy of the approach both in the design point and variable geometry cases. Also depicted are new insights into turbine wheel design constraints discovered when using a variable geometry turbine casing.

Introduction

Improvement in turbocharger component efficiencies is an important design goal for all turbomachinery designers. Presented within this paper is a design method for nozzleless turbine casings to be used with radial turbines, which although simple in its analysis and approach, has provided excellent results. In order to highlight the differences between the present approach and those approaches previously used, a review of the historically used approaches and experimental results derived from such approaches will be outlined. With the results of these approaches as a background, the formulation of the new approach to presenting a radial turbine wheel with a desired entrance state will be presented. Although the approach presented is based upon very fundamental first principle arguments, the experimental results depict the relative worth of such a design procedure compared to previously applied procedures.

With the analysis and presentation of data pertaining to fixed geometry turbine casings as a background, the application of the same approach to two optional configurations of mechanically simple variable geometry casings will be shown. Experimental data depicting the performance of such casing configurations over an approximately two to one turn down in mass flows at a constant wheel speed and pressure ratio will be portrayed. From the data obtained during these experimental studies, a series of conclusions about what lies ahead for turbine casing and wheel designers when making applications to turbochargers will be derived.

Present Methods

A variety of approaches has been used to specify the specific mechanical configurations of nozzleless turbine casings for radial turbines. Fig. 1 depits the general shape used for previous turbine casing designs. As can be noted in the cross-sectional view, the turbine casing is essentially a nozzle made up of a volute shaped conical section which is wrapped around the turbine wheel. The cross-sectional area of this cone has been determined by several different methods. The two most prominent methods used to date relate to the distribution of a decreasing area or A/R around the circumference of the casing. These methods are adequately described in literature for incompressible flow by Hawthorne [1], Wislicenus [2, 3], and Brown [4]. Depending upon which approach is used, the casing size, or in other words, the casing's capability to accelerate a given mass flow is depicted either by the casing area or the casing A/R. If casing area is the design parameter used to describe a configuration, the controlled area is usually wrapped around a relatively constant diameter vaneless space into which the turbine wheel fits. The cross-sectional area of this passage, sometimes relatively circular in shape, is distributed so as to decrease at a uniform rate from the casing entrance through 360 deg of travel about the given vaneless space. In this case, the voluted portion of the casing can be pictured as a single nozzle having a shape of an essentially conical passage with converging sidewalls.

In the other popular approach where casings are labeled with an A/R value, the A/R value has a correspondence with the casing's ca-

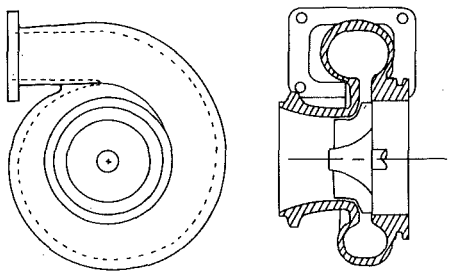

Fig. 1 Typical turbine casing designed using *A/R* method

[1] Patents applied for.

Contributed by the Gas Turbine Division and presented at the Gas Turbine Conference and Exhibit and Solar Energy Conference, San Diego, California, March 12–15, 1979 of THE AMERICAN SOCIETY OF MECHANICAL ENGINEERS. Manuscript received at ASME Headquarters December 18, 1978. Paper No. 79-GT-87.

pability to accelerate a mass flow. An arbitrarily defined cross-sectional area divided by the radius to the centroid of that cross-sectional area provides the starting information for the design of the volute scroll. In this case, the area is distributed about the casing periphery so that the casing A/R value at any angular position is made to decrease uniformly through an angle of 360 deg. This type of configuration also normally gives an essentially conical volute wrapped around the turbine casing vaneless space. The exact same area distribution cannot precisely satisfy both sets of above relationships concurrently, unless the radius to the local area centroid is held constant around the casing. Within our organization at various times and by various design groups, both approaches have been used for the specification of turbine casing volute shapes. Fig. 2 depicts a map of a turbocharger turbine using a turbine casing configuration in which the distribution of A/R about the periphery of the wheel has been the design criteria. The scales upon the map are self-explanatory. One point worth noting is that the scales chosen for the turbine map representations are normalized to an arbitrary inlet pressure of 99.6×10^3Pa and 922 K inlet temperature. The 922 K temperature chosen as a standard representation is a temperature that represents the order of typical exhaust temperatures that might be expected at full load on the diesel engines to which these turbochargers are matched. The map shown represents the optimum match of turbine casing size to turbine wheel configuration. It is a standard practice in matching turbochargers to vary overall turbocharger characteristics by changing turbine casing configurations while using the same turbine wheel configuration. Fig. 3 represents a map of such a configurational change. As can be noted in the maps, there is a significant change in the mass flow versus pressure ratio characteristics. Also a significant decrease in peak efficiency is attained within the map as the smaller turbine casing A/R is used with the wheel. The performance depicted by Fig. 2 represents nearly the optimum developed by this wheel configuration because it matches the wheel's pressure ratio versus mass flow characteristic so as to minimize wheel exit losses. These configurations will be referred to later as standards of comparisons for the new design approach when it is used to develop a fixed and variable inlet area turbine casing.

When experimentally mapping the performance of such turbine casings, some discrepancies were noted with regard to the desired wheel inlet states. By measuring the distribution of static pressures around the turbine wheel as it was tested with various casings, the experiments indicated that significant variations in the static pressure existed about the wheel. Thus the gas state presented to the turbine wheel was nonuniform in all such turbine casings. This variation in entrance state was accompanied by a concurrent variation in exit state around the periphery of the turbine exducer. The size of these variations for the range of turbine casings sizes which had been designed by this means increased as turbine casing size varied either side of the optimum configuration as depicted in Fig. 2.

Since the approaches described above produce turbine casings which are three-dimensional in nature with converging sidewalls, the analyses of the fluid mechanics within these systems become a three-dimensional problem. When this fact is considered along with the desire to accommodate an analysis of the friction losses in some appropriate manner, the problem becomes a difficult mix of three-dimensional viscous gas dynamics. Additional analysis indicated that it might be possible to focus on a one-dimensional analytical approach and obtain a reasonable approximation to an ideal solution. This basic one-dimensional approach was used to provide the heart of a new turbine casing design technique which has successfully been applied to a wide variety of configurations.

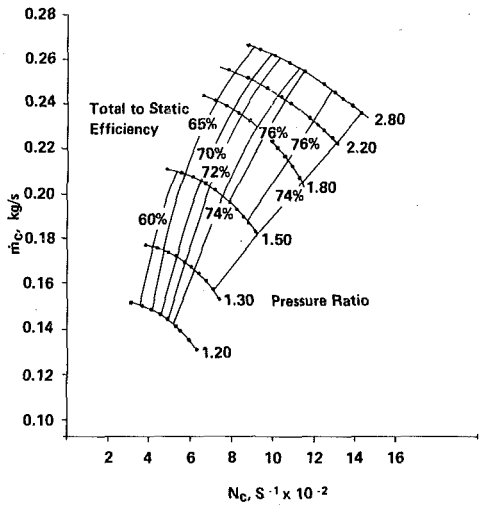

Fig. 2 Turbine performance map of a 26.7 mm A/R turbine casing

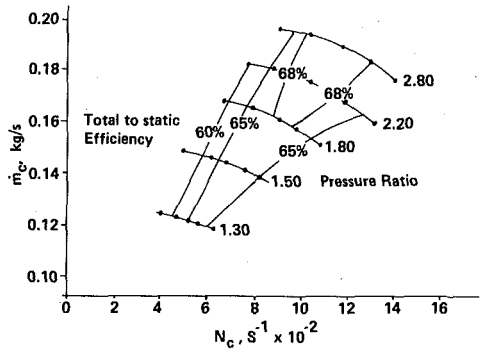

Fig. 3 Turbine performance map of a 18.5 mm turbine casing

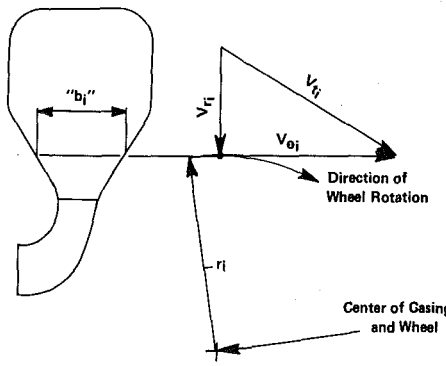

Fig. 4 Sketch showing the gas velocity triangle and the location of b_i and r_i

New Casing Design Approach

In appraising the design of boarding states for a radial turbine, it became apparent that the wheel should ideally be surrounded by a

Nomenclature

A/R = volute cross-sectional area divided by centroidal radius, mm
b_i = local casing axial width, m
H_d = hydraulic diameter, m
$\dot{m}_c$ = corrected mass flow rate $\dot{m}_0 (\sqrt{T_0/922\text{K}})/(P_0/99.6 \times 10^3\text{Pa})$
$\dot{m}_0$ = mass flow rate, kg/s
N_c = corrected rotor speed $N_0/\sqrt{T_0/922\text{K}}$
N_0 = observed rotor speed, s^{-1}
P_0 = casing inlet stagnation pressure, Pa
P_S = static pressure, Pa
P_T = total pressure, Pa
R_a = gas constant, J/Kg-K
r_i = radius from center of casing, m
r_0 = wheel inlet radius, m
T_0 = casing inlet stagnation temperature, K
T_S = static temperature, K
V_r = radial component of velocity, m/s
V_t = total velocity, m/s
V_θ = tangential component of velocity, m/s
V_{θ_i} = tangential component of velocity at radius r_i, m/s
V_{θ_0} = tangential component of velocity at wheel inlet radius, m/s
γ = ratio of specific heats

flow which as it boards the wheel has the characteristics of an irrotational free vortex centered about the wheel center line. This conclusion has also been expressed by several other authors [4, 5]. Since this desired configuration subjects itself easily to a one-dimensional analysis, it was chosen as a basis for the turbine casing design calculation.

Initial analyses of the configuration desired were done neglecting the effects of friction. The equations presented below which relate dimensionally to Fig. 4 represent a description of the assumptions and analysis used to describe the desired free vortex about the turbine wheel:

$$V_t = \sqrt{\left(\left(\frac{P_t}{P_s}\right)^{\left(\frac{\gamma-1}{\gamma}\right)} - 1\right)\left(\frac{2\gamma R_a T_s}{\gamma - 1}\right)} \tag{1}$$

$$V_r = \frac{\dot{m} R_a T_s}{2\pi r_i b_i P_s} \tag{2}$$

$$V_\theta = \sqrt{V_t{}^2 - V_r{}^2} \tag{3}$$

$$V_{\theta_i} = V_{\theta_0} \times \frac{r_0}{r_i} \tag{4}$$

Equation (1) is simply a statement that relates the locally existing total velocity to the total-to-static pressure ratio between the local conditions and inlet stagnation and as such it represents a statement of conservation of energy within the system. Equation (2) depicts the radial velocity as a function of local densities in the areas of interest and represents a statement of mass flow continuity. Equation (3) represents a simple required geometric interrelationship between the existing tangential and radial velocities. Equation (4) presents the relationship that must exist between the tangential velocity at any radius within the free vortex to the tangential velocity existing at the wheel boarding radius and represents a statement of the conservation of angular momentum within the free vortex about the wheel. In order to start the calculation, it is necessary to determine the desired gas state at the wheel periphery. The design calculations can be started with assumption of the total temperature, total pressure, and the desired tangential velocity, all of the wheel outer radius. When these assumptions are considered along with knowledge of the desired mass flow rate and width of the casing at the wheel outer radius, the desired wheel boarding state is defined. With this information and an arbitrarily specified schedule of casing width versus casing radius, a series of calculations can be completed to determine the tangential and radial gas velocity components required at any given casing radius. One of the requirements for this analysis to be appropriate is that the casing sidewall be axisymmetric; that is, the sidewalls of the casing should be such that they could be lathe cut by rotation around the axis of rotation of the turbine. Thus, except for the effects of friction, there would be no resolved wall pressure components which interact with the fluid tangential velocity as the gas moves inward to smaller radii.

The calculation determines the appropriate velocity components at a series of radii moving away from the turbine wheel. It is obvious that from this series of calculations a particle path within this vortex flow field can be determined. By appropriate manipulation of the casing width dimension b, this particle path can be made to travel in a variety of spiral paths with the individual spiral shape being a direct result of the existing schedule in casing width as radius is increased. By experimenting with a variety of casing width schedules versus radius, it is possible to develop a spiral path which, within any prechosen outer radius, will make a full revolution about the turbine wheel. In order to construct a turbine casing which contains flow paths that are very similar to these desired free vortex paths, one need only insert a casing outer wall which joins the casing sidewalls and travels spirally along a path determined by the desired particle path within the vortex.

Since in this analysis the schedule of casing width versus radius can be chosen arbitrarily, a wide variety of casing shapes can be evolved with whatever overall envelope or configurational constraints might exist for a given design. In order to test these design premises, a fabricated turbine casing was constructed by clamping together two machined sidewalls in which a groove for the desired spiral path had been machined. The outer wall was formed by a sheet metal strip inserted into the spiral groove. Fig. 5 shows the mechanical configurations that were evolved. A map of this turbine casing provided us with the best performance attained to date with this turbine wheel configuration and matched the desired mass flow versus pressure ratio characteristics within 5 percent. Fig. 6 depicts the performance obtained in the first map applying this design approach, and these results can be compared to the standard map shown as Fig. 2. The efficiency levels have been improved although the original mass flow versus pressure ratio target has not quite been matched.

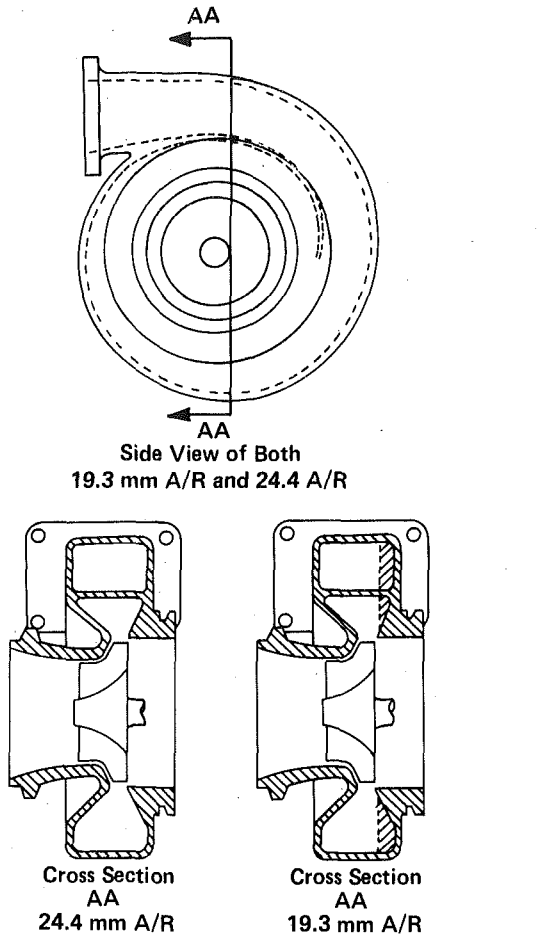

Fig. 5 Views of the fixed geometry turbine casings designed using the new approach

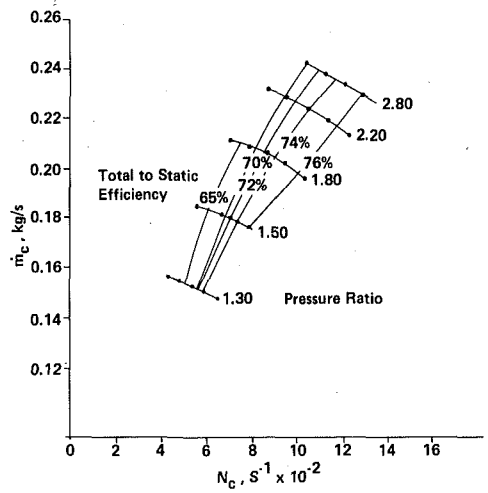

Fig. 6 Turbine performance map of the 24.4 mm *A/R* turbine casing designed using the new approach

After analyzing these data, it became obvious that one potential source of error in matching the mass flow versus pressure ratio characteristics was the exclusion of any friction analysis within the casing from our calculations. Since the original calculation represented one of a constant stagnation state, the calculation could be carried out at any radius given the starting conditions and the assumed inlet state. When changing over to a calculation that included available energy degradations because of friction losses, an approach which retained the one-dimensional nature of the calculations was used.

Starting at the wheel entrance with a given total velocity and the frictional characteristics of the surfaces involved, an elemental friction loss analysis was made for each incremental step outward in radius. The following formulation of the hydraulic diameter was chosen to carry out the necessary calculation:

$$H_D = 4 \times \text{volume/wetted surface area} \quad (5)$$

As can be noted, the hydraulic diameter is described as four times the volume of the element over the wetted area of interest for that element. This formulation reduces to the appropriate value for normal configurations such as that in standard pipe flow, and it also allows breaking out the frictional impact of individual surfaces acting upon any given element that we choose. Thus, the impact of individual surfaces which come in contact with the radial shell element being appraised in each increment can be split out and identified. The impact of the casing sidewalls and the top and bottom of the casing tongue and the outside wall can be treated independently and appraised individually in terms of their contribution to the overall state degradation. Typically, methods seen in literature use a fixed friction coefficient and the average gas velocity at the centroidal radius of the passage in question to compute state degradation [4, 6].

With this process, knowing the desired stagnation state, velocity, and static pressure conditions for wheel broading, the calculation steps incrementally outward in radius and in each step determines the required increase in stagnation pressure necessary to provide the ending gas state. This yields a schedule of the total pressure losses that would have to be accommodated with the wall friction as a function of radius. This determines the required total pressure state at any radius. In addition to the increase in stagnation state as radius increased, an adjustment was also made to the required elemental input angular momentum. The increase in angular momentum required was scaled up in direct proportion to the changes in velocity required to accommodate the state changes. Although this may not be a totally correct representation of the impact of casing frictional effects on the change of angular momentum as the fluid moves through this casing, it served the purpose in terms of improving mass flow versus pressure ratio projections. It provided a means to project mass flow versus pressure ratio characteristics of the turbine casings within 2 percent.

The relative loss distribution among the stream tubes flowing within the turbine casing is not represented by the particular friction analysis presented here. It is expected that the actual available energy losses in the stream tubes adjacent to the walls would be very large compared with those of the stream tubes travelling in the center of the channel. It was found that the overall performance of the casing, in terms of its capability to produce a uniform peripheral state for wheel entry and to match the mass flow versus pressure ratio characteristics desired, was predicted to the accuracy required. Several problems are unaddressed by this approach and some of the most difficult relate to the desires for the change in state relative to angular momentum as one enters the casing. Since the velocities are uniform or axisymmetric about the inlet pipe, there is variation in angular momentum among the various stream tubes that enter the system. The desired state for wheel boarding is one of uniform angular momentum distribution among all stream tubes. The question that arises is how to make the appropriate transition from the original state to the desired state. It was felt that the major determinent is the length and the shape of the bend that occurs in the casing before the gas is released to continue the proposed free vortex path. Experiments to date have shown that a bend of between 85 and 120 deg about the wheel axis has provided the optimum turbine efficiencies. Bends of shorter length apparently reduce the turbine efficiency measured because of state variations around the wheel periphery caused by the inlet effect. Casings in which the bend was made longer had a degradation in efficiency that was apparently associated with the frictional impact of the added wall surface within the casing.

Experimental Results

The maps in Figs. 6 and 7 depict the overall performance for two different sized turbine casings created with the design approach presented above. On the basis of mass flow versus pressure ratio relationships, the casings are comparable to Figs. 2 and 3 respectively. The efficiencies in the map depicted in Fig. 7 can be compared directly to those depicted in Fig. 3. It is evident from this comparison that a significant increase in efficiency level has been attained with the peak efficiency improvements increasing as the casing sizes move farther away from the original optimum as depicted in Fig. 2. A series of tests was run to obtain a complete map of the static pressure field in the turbine casing. These investigations indicated that the distribution of static pressure within the casing had been very well predicted by the analytical model and that the desired uniformity in wheel boarding state had been achieved. The difference in static pressures around the wheel periphery are now of the order of a few mm of water where previously, especially in casings with small A/R, these values have varied as much as 200 to 250 mm of mercury. Figure 8 shows the predicted and measured static pressure versus radius that was attained in these original fabricated casings. This design approach has been used to design a wide variety of turbine casing shapes and has proven accurate in predicting a casing's mass flow versus pressure ratio characteristics and also supplied the wheel with a uniform entrance state.

One of the nonfluid dynamic improvements that is associated with the use of such an approach is a reduction in the turbine wheel vibrational excitation. It has long been understood that the variation in peripheral state existing within turbine casings, especially as the wheel passed the end of the casing volute section, was the main source of these vibrational excitations [7]. Since the degree of variation in peripheral state has been reduced by these casings, the level of the input forces that excite this wheel vibration has been reduced.

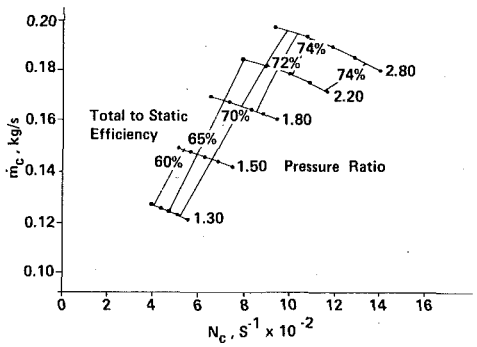

Fig. 7 Turbine performance map of the 19.3 mm A/R turbine casing designed using the new approach

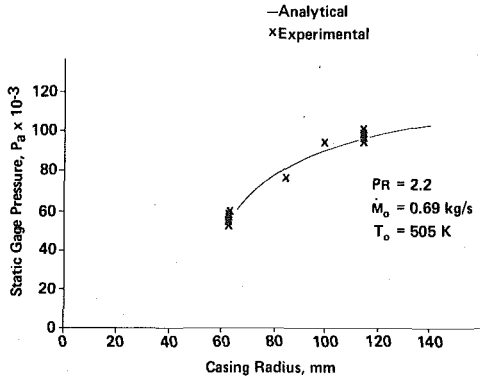

Fig. 8 Computed and observed static pressure as a function of casing radius in a 24.4 mm A/R turbine casing designed using the new approach

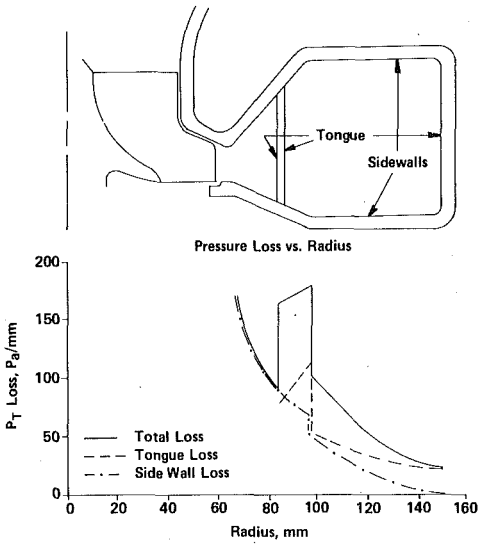

Fig. 9 Computed total pressure loss as a function of radius in a 24.4 mm *A/R* turbine casing design using the new approach

In order to appraise the overall accuracy of the friction analysis that has been used on the turbine casing, a series of steady state flow tests was conducted with measurements taken of inlet and exit total states. These analyses indicated that the size of the frictional losses that have been predicted by the turbulent flow pipe friction model are very nearly equal to those measured on actual casing friction flow tests. Figure 9 depicts the relative distribution of losses as a function of radius as determined by analysis with the friction model. Since the losses are plotted as a ΔP_0 per unit change in radius, the area underneath the curve represents the total loss encountered in travelling through the system. The height of each curve then represents the rate of local available energy degradation within the casing due to each of the contributing elements. As can be seen in the figure, the major portion of the losses are encountered very near the wheel where surface rubbing velocities are very high. Also of note is that as the wheel is approached and the velocities increase, the importance of the rubbing losses on the top and bottom of the dividing wall becomes significant. The step in the graph depicts that location where, for this particular casing, two sides of the tongue were exposed to the gas. It indicates that radius at which the outer wall of the casing had progressed inward such that the backside of it now forms the inner wall of the casing.

Variable Geometry

In doing the analysis, it became evident that the schedule of casing width versus radius is an arbitrary constraint that can be manipulated depending upon desires for the design. The capability to manipulate this variable plus the understanding that each element of axial width within the casing was assumed to carry an equivalent mass flow indicated that a simple means of creating a variable area nozzleless turbine casing would be available using similar design techniques. Figures 10 and 11 depict two different forms of prototype variable area nozzleless turbine casings that were investigated analytically and experimentally during this study.

In both cases, the design of the casing's outer configuration is identical. The schedule for outer wall placement versus angle about the casing was determined for the maximum desired mass flow by the means described in the preceding paragraphs. The insertion of a movable wall in the outer regions of the casing provides the means for varying the turbine casing size.

The desire in designing the movable wall configuration was to create a fluid passage that would develop the same energy and momentum conversions for a variety of mass flow rates at the design pressure ratio and wheel speed. After this is accomplished, these flows are delivered to the axisymmetric vaneless space about the wheel. In this vaneless space, the established free vortex flow pattern continues to accelerate

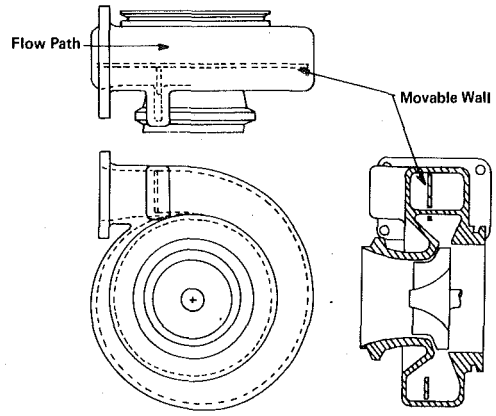

Fig. 10 View of the open wall variable geometry turbine casing

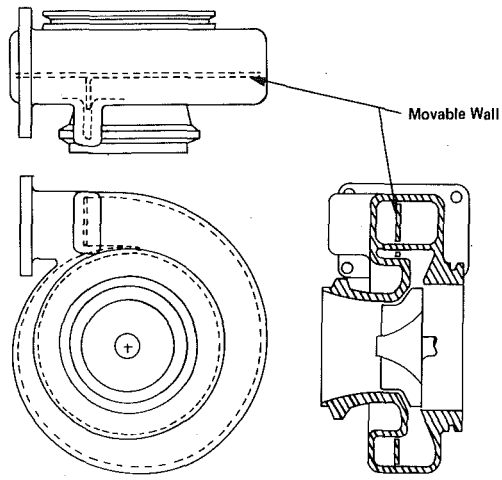

Fig. 11 View of the closed wall variable geometry turbine casing

the fluid to the desired wheel boarding state. To provide the appropriate wall forces, it is necessary to supply a movable wall which ends at a smaller radius than the turbine casing inlet tongue (outer wall extension). The movable wall has an inner radius which is positioned axisymmetrically about the turbine wheel. The casing axial width is constant for radii larger than the movable wall inner radius. This allows a constant percentage variation in casing width at all radii greater than the tongue inner radius so as to create an appropriate velocity distribution at all desired mass flows.

The accuracy of producing the desired wheel boarding states is a function of the size of the radial velocity components that exist within the casing. In the vaneless space about the wheel, the required static pressure for a given tangential velocity and prescribed total inlet gas state rises as the mass flow decreases because of the attendant reduction in radial velocity. If the radial velocity components are large, the variation in static pressure will obviously affect the condition around the end of the inlet scroll. In the casing presented here, the radial velocity component was nine percent of the tangential component and therefore it had only a minor impact on the state balance about the wheel.

The two casing configurations shown in Figs. 10 and 11 represent two approaches to handling the transition that must take place between the outer casing and the vaneless space about the wheel. The casing in Fig. 10 presents a movable wall which is free standing at its inner radius. This configuration allows the flow to possibly swirl in behind the wall after leaving the control of the scroll shaped entrance passage. In addition, the radial velocity must also decrease in the rather abrupt transition from a narrow to wide axial width when the casing is set for low mass flow.

The other casing represented in Fig. 11 presents the opposite philosophy for handling this transition. In this case, the vaneless space

is sized so as to match with the minimum width desired at the lowest mass flow and the transition in the radial direction is gradual as the gas passes into the vaneless space. At high mass flow settings, an increase in the radial velocity component is required as the gas enters the vaneless space. In this configuration, only leakage flow would enter the space behind the outer casing movable divider wall. The clearances between the movable parts and the stationary parts were set to be between .75 and 1.5 mm. These clearances were felt to typify what might be attained in a production situation.

Fig. 12 presents an abbreviated look at the relative performance capabilities of these types of configurations. The data presented in Fig. 12 represent the efficiency variations as mass flows were varied at constant turbine wheel corrected speed (1083 rps) and constant (2.2) overall pressure ratio. The same turbine wheel was used in all tests to eliminate this variable. To obtain such a plot, a series of maps was run with various wall settings for each configuration. From each map, the efficiency and mass flow obtained at the chosen pressure ratio and speed were determined and transferred to the cross plot in Fig. 12. This speed and pressure ratio was chosen because this condition was near the maximum efficiency point for optimum wheel performance shown in Fig. 2. This point also represented a point near the maximum attained efficiency for all the maps in this series. Along with the data for the two variable geometry configurations is a line that represents the results from a series of casings previously designed by the A/R distribution methods. Also plotted is the point for the casing represented in Fig. 7.

Several trends are worth noting. The overall efficiencies attained are similar in level to those attained on the range of fixed geometry casings tested. The performance of the casing shown in Fig. 10 is slightly below the envelope of the fixed casing performances throughout the range tested. This change is felt by the authors to be associated with the leakages around the movable wall inner radius and the existence of the open space behind the wall. The performance obtained with the configuration shown in Fig. 11 is improved in comparison with the fixed geometry casings at the low mass flow settings and poorer at the high mass flow settings. This comparison was felt to be tied to the fact that the casing design had been set up to favor this low mass flow setting at the expense of the high flow rate settings. The transition to the vaneless space was smooth at the low setting. At the higher mass flow setting, the wall area per unit mass flow was considerably larger and was felt to be the cause of degraded performance.

While mapping these casings, the peripheral static pressure distributions were checked as the apparent casing areas were changed. Static pressures were found to remain nearly uniform over the entire range of air flows thus substantiating the capability to form a nearly concentric vortex about the wheel even in instances where the outer areas of the casings are restricted to provide smaller apparent nozzle areas for the machine.

Turbine Wheel Design Concerns

In working through the set of experiments described, a series of concerns developed about the constraints on turbine designs when a turbine wheel has an expected use over a wide range of mass flows. Sugimoto, Khalil, and Watanabe [8, 9, 10] consider the impact of variations in angle of attack on the flow patterns within radial turbine wheels. In reviewing these projections, it became obvious that variations in angle of attack to the wheel can precipitate the formation of separation zones within the blading. Variations are by necessity encountered with the decreases in mass flow that accompany a turn down in the turbine casing area. This then yields a situation where it may be difficult to maintain attached flows all the way through the turbine wheel. In fact, it is contended that some of the losses assigned to inlet incidence variations may be indeed associated with the creation of separation zones which precipitate separated flows all the way through the machine and thereby increase exit losses [11]. Fig. 13 depicts another problem relating to the design of turbocharger turbines that becomes important when one uses a turbocharger on an engine system with small volume exhaust manifolds. The line with the positive slope in the central area of the map represents the sequence of equilibrium steady state match points of a particular compressor and turbine combination. It follows reasonably well the existing efficiency contours within this turbine map. The line which is oriented essentially perpendicular to this line represents the excursion of entering gas states as an engine operates through an individual cycle with one of its cylinders. There is a very wide range of entrance states presented in the turbine wheel, and this range represents a significant variation in instantaneous angle of attack. For the turbine wheel to successfully handle varying entrance states, whether they be created by in-cycle variations on a given engine or by a variable geometry system, it must be designed to accommodate these incidence variations efficiently. It is obvious that the aggregation of concerns that exist for a steady flow gas turbine system using a radial turbine must be significantly expanded when one considers the application of such a radial turbine to an engine turbocharger.

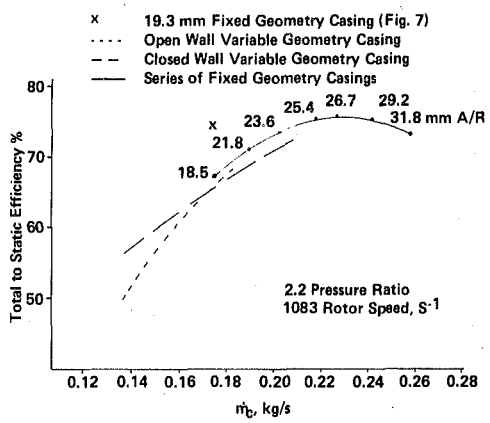

Fig. 12 Efficiency versus corrected mass flow rate for various turbine casing configurations. The same turbine wheel was used for all data.

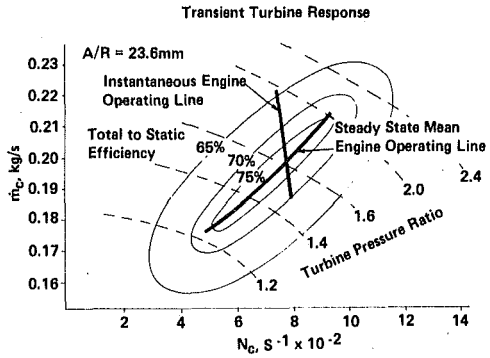

Fig. 13 Turbocharger turbine performance map with diesel engine operating lines

Another concern that arises when one considers the design of radial turbines to be used over a wide range of mass flows for a given pressure ratio and speed is the difficulty of maintaining inherent balance within the flow field through the blading. To illustrate these concerns, one might look at a radial turbine as the combination of an infinite number of turbines whose characteristics are determined by the inlet to outlet radius ratio combined with the amount of turning or area change that takes place locally within the channel. Looking across the exducer face of the radial turbine, it is obvious that near the hub of the machine the inlet to outlet radius ratios are very large and the amount of turning within the blading, therefore the area change, is relatively small. At the exducer tip of the turbine wheel, quite the contrary is true. There the differences in radius between inlet and outlet is significantly smaller but the amount of turning caused by the blades is very large. Thus the concurrent area change is significant across the wheel. Theoretically, it is only possible to balance these variations at one particular mass flow for any rotational speed. As one encounters situations where mass flow rates are forced to vary at constant rotational speed, either via instantaneous variation of inlet conditions or

via the manipulation of variable geometry hardware, it becomes obvious that the balance among the stream sheets deteriorates.

These two problems represent significant considerations to turbocharger turbine designers for the future. Presently, activities within the engine industry are creating circumstances so as to accentuate the variations in turbine inlet states that must be accommodated by the turbine wheel. Therefore, it becomes obvious then that instead of two-dimensional design point analysis, a very broad range of operating points must be considered in designing radial turbines. The performance of the machine with the variation in inlet and exit states that must be accommodated as mass flows and pressure ratios change from the design point can be even more important to a turbocharged engine's performance than the actual capability at the design point itself. It will become increasingly important that off-design performance of such turbine wheels receive as much attention as has been typically devoted to the on-design performance analysis.

Conclusions

Pre-existing methods of determining turbine casing shapes provide an inadequate control of the uniformity of gas state around the turbine wheel. These methods can also precipitate blade vibration problems which under some circumstances may lead to turbine wheel mechanical failures. The drawbacks in these methods are overcome through the development of an efficient design procedure for nozzleless turbine casings. The concept as depicted allows one to distribute the turbine casing areas in such a way as to meet varying design constraints such as overall size, while still maintaining a basically uniform turbine inlet state. This improved uniformity in turbine inlet state results in significantly improved turbine efficiencies and also provides reduced blade vibrations where the cause of the blade vibrations is aerodynamic excitation imposed upon the wheel by the casing. This concept also has application in the design of variable geometry turbine casings in which a single casing sidewall is moved to obtain a change in apparent size. The design program is of sufficient accuracy to predict on an a-priori basis the mass flow versus pressure ratio characteristics to within two percent of prespecified values. Possibly the most significant factor with regard to this procedure is that it provides the optimum turbine casing geometry for a given set of design constraints. This capability can be contrasted to other analysis programs which can only compare the aerodynamic results of pre-specified geometries and as such many geometries must be compared before any approach to an optimum can be considered to exist [12].

References

1 Hawthorne, W. R., ed, *Aerodynamics of Turbines and Compressors,* Vol. 10, Princeton University Press, N. J. 1964, pp. 533–538.

2 Wislicenus, G. F., *Fluid Mechanics of Turbomachinery,* 2nd Ed., Vol. 1, Dover Publication, New York, 1965, pp. 155–156.

3 Wislicenus, G. F., *Fluid Mechanics of Turbomachinery,* 2nd Ed., Vol. 2, Dover Publication, New York, 1965, pp. 561–564.

4 Brown, W. B. and Bradshaw, G. R., "Design and Performance of Family of Diffusing Scrolls with Mixed-Flow Impeller and Vaneless Diffuser," NACA 936, 1947.

5 Rizika, J. W., et al., "The Design and Performance Analysis of Radial In Flow Turbines," No. 1067-1, 1964, Northern Research and Engineering Corporation, Cambridge, Mass., pp. 110–111.

6 Rizika, J. W., et al., "The Design and Performance Analysis of Radial In Flow Turbines," No. 1067-2, 1964, Northern Research and Engineering Corporation, Cambridge, Mass., pp. 330–354.

7 Ellison, L. F. and Partridge, J. M., "Vane Vibration in Radial Flow Turbochargers," I *Mech E* Paper No. C76/78, 1978.

8 Sugimoto, A., Nakamura, K., and Matsumoto, K., "An Experimental Investigation of Flow in Blade Passage of Radial In Flow Turbine," *JSME Bulletin,* Vol. 18, No. 126, 1975.

9 Khalil, I., Tabakoff, W. and Hamed, A., "Viscous Flow Analysis in Mixed Flow Rotors," ASME Paper No. 78-WA/GT-3, 1978.

10 Watanabe, I., Ariga, I., and Fujie, K., "A Study on the Flow Patterns in an Impellar Channel of a Radial Turbine," ASME JOURNAL OF ENGINEERING FOR POWER, Oct. 1967, p. 467.

11 Kofskey, M., and Nusbaum, W., "Effects of Specific Speed on Experimental Performance of a Radial In Flow Turbine," NACA TN-D-6605, 1972.

12 Hamed, A., Abdallah, S., and Tabakoff, W., "Flow Study in the Cross Sectional Planes of a Turbine Scroll," AIAA Paper No. 77-714, 1977.

W. Tabakoff
Professor.
Mem. ASME

A. Hamed
Associate Professor.
Mem. ASME

J. Ramachandran
Graduate Research Assistant.

Department of Aerospace Engineering,
University of Cincinnati,
Cincinnati, OH 45221

Study of Metals Erosion in High Temperature Coal Gas Streams

In order to provide the basis for alloy selection in future turbines using pulverized coal, an investigation is undertaken to obtain a basic understanding of the mechanisms of erosion at high temperatures. The test equipment has been designed to simulate the aerodynamic and thermodynamic conditions in the turbine. This facility has the capability of providing between ambient and a 1093°C (2000°F) environment temperature for erosion testing of various materials. The effects of high temperature on the erosion rate was determined and the test results from 304 stainless steel alloy are presented.

Introduction

The use of pulverized coal as fuel in many power plants and industrial establishments is inevitable both in the present and in the future. The products of combustion will contain solid particles, whose presence cause erosion of the engine components and in a very short time possible deterioration of the power output. Filtration cannot accomplish a 100 percent removal of the particles and results in performance reduction. In coal gasification both the coal and the catalyst contribute to the resulting particulate flow. While larger particles can be removed by cyclones, a quantity of particles ranging in size between 5 and 25 μm dia still pass through the cyclones and enter the turbine resulting in a very limited life of this component.

The design and development of high performance turbomachinery operating in an ambient with coal particles or coal ash therefore requires a thorough knowledge of the fundamental erosion phenomena. The future of advanced turbomachinery for use in the coal industry, gasification, mining, pipelines' gas transport, powder coal burning, coal-oil gas refinery, and many others is dependent upon this understanding. If erosion could be incorporated as an engine design parameter, perhaps an erosion tolerant engine could be produced.

Two problems are involved in erosion prediction. First the velocity, direction, and number of particles striking the surface must be determined. These are naturally affected by the general and local flow conditions. The second part involves the calculation of the surface material removed using the information obtained from the first part. The problem of predicting erosion in rotating machinery is particularly complexed by tracing trajectories through the flow field after multiple impacts [1].

Present State of the Art

The theoretical studies concerning erosion are predominantly empirical. They involve basic assumptions as to the process governing material removal. Finnie [2] and Smeltzer, et al. [3] have conducted theoretical analyses of the erosion of ductile materials. In more recent investigations [1, 4, 5], further insight into the actual mechanism of erosion has been obtained by examining the target surface at high magnification using metallographic techniques and electron microscopy. The work reported in [2–5] has been conducted using the sand-blasting erosion test facility described in [5] or modifications of it. This facility utilizes a small jet of particle-laden air impacting on a stationary specimen, and therefore does not simulate the aerodynamic effect of the flow field over the erosion specimen. This effect can be a very important factor in turbomachine erosion, where the flow is constantly turned by rotating and stationary cascades. Two cold gas particle erosion test facilities have been built at the University of Cincinnati's Propulsion Laboratory. The first was designed to obtain basic erosion data, particle impact, and rebound characteristics for particulate flow over a stationary specimen. Another test facility was then designed to simulate and measure the erosion of stationary and rotating turbomachine blades. A detailed description of these test facilities can be found in [1] and [6].

In many turbomachinery applications, however, erosion takes place at elevated temperatures near the strength limiting temperatures of the materials used. For example, even in the case of turbojet engine compressors, titanium used in the early stages and the INCO 718 used in the aft stages are operated at metal temperatures in excess of 316°C and 593°C (600°F and 1100°F), respectively. In both cases, these temperatures are very close to the maximum operating temperatures used for these materials. The erosion characteristics can significantly change under elevated temperatures as evidenced in the data presented by Tabakoff and Hamed [6]. These data were obtained in the facility used by [1], with the sample heated to temperatures up to 204°C (400°F). Although this temperature falls far short of those experienced in turbine engines, it still indicates the significant effect of temperature on erosion and probably on the rebound characteristics.

High Temperature Erosion Rig

An erosion test facility was designed to provide erosion and rebound data in the range of operating temperatures experienced in compressors and turbines. For that purpose, this facility has been designated to operate at a test section temperature in the range of ambient to 1093°C (2000°F). In addition to high temperatures, the facility

Contributed by the Gas Turbine Division and presented at the Gas Turbine Conference and Exhibit and Solar Energy Conference, San Diego, California, March 12–15, 1979 of THE AMERICAN SOCIETY OF MECHANICAL ENGINEERS. Manuscript received as ASME Headquarters December 18, 1978. Paper No. 79-GT-88.

properly simulates all erosion parameters which were found to be important from previous testing at ambient temperatures. These parameters include particle velocity, angle of impact, particle size, particle concentration and sample size.

As with the cold flow erosion test facility, close attention was given to aerodynamic effects to insure that important parameters such as angle of attack are not masked or altered. To insure the correlation of data from the high and low temperature erosion tunnels, flowpath and acceleration tunnel length were kept almost identical with those of the facility described in [6]. The cross section was increased, however, from 76.2 mm × 25.5 mm to 88.9 mm × 25.4 mm (3 in. × 1 in. to 3½ 1n. × 1 in.) in order to reduce the tunnel blockage by the test sample.

General Description of the Erosion Rig. The schematic of the test apparatus is shown in Fig. 1. It consists of the following components: particle feeder (A), main air supply pipe (B), combustor (C), particle preheater (D), particle injector (E), acceleration tunnel (F), test section (G), and exhaust tank (H).

The equipment functions as follows: a measured amount of abrasive grit of a given constituency is placed into the particle feeder. The particles are fed into a secondary air source and blown up to the particle preheater, and then to the injector, where it mixes with the main air supply (B), which is heated by the combustor. The particles are accelerated by the high velocity air in a constant area duct, which is steam cooled, before impacting the specimen in the test section. Past the test section, the particulate flow is mixed with the coolant, and dumped in the exhaust tank. The expected range of testing parameters are listed in Table 1, but they are not necessarily restricted to the tabulated values.

The individual components of the high temperature erosion facility are described below. Each component was designed with cost, maintainability, availability and functionality as prime considerations.

Particle Feeder Assembly (A). The particles from the feeder are blown up to the particle injector area. The feeder (Fig. 2) is designed as a pressure vessel to operate at high air pressures. However, this pressure is equalized above and below the plunger by a by-pass line. This allows the system to be calibrated under gravity feed conditions. Further, an electric eye records the plunger rpm such that the operating conditions are maintained. The metering orifice is designed to be replaceable for greater versatility through using variable size orifices, along with corresponding rod diameter.

Main Air Supply (B). This air is drawn from air tank storages to allow continuous testing.

Combustor (C). High temperature combustion products are supplied by a modified General Electric J93 can combustor. The J93 can is encased in a 228.6 mm (9 in.). ID stainless steel pipe with provisions for the fuel nozzle and igniter. A system consisting primarily of a propane fired torch containing a spark plug was used for the fuel ignition. Due to heat loss in the acceleration tunnel, a combustor exit temperature of 1204.4°C (2200°F) is required in order to maintain the maximum test section temperature at 1093°C (2000°F). The J93 can combustor was modified to obtain this exit temperature. The modifications include using a large fuel nozzle and blanking off most of the downstream dilution air ports. A smaller fuel nozzle is used for tests involving low combustion temperatures in the range of 93°C (200°F) through 260°C (500°F).

Particle Preheater (D) and Injector (E). The preheater consists of a coil contained in a 203.2 mm (8 in.) ID pipe section with a distributor/injector to provide a well distributed preheated particle supply. The particles are blown up to the accelerating section of the tunnel by secondary air which flows from the particle feeder and passes through the preheater coils. As the particulate air mixture passes through the coils, it is heated by the combustion products to a temperature of 538°C (1000°F) before being injected into the tunnel. The particles are distributed in the main air stream through their impingements on a specially contoured ball. The particle gas mixture is accelerating through an elliptical nozzle to the acceleration section.

Acceleration Section (F). The acceleration tunnel has a rectangular cross section of 89 mm × 25.4 mm (3½ in. × 1 in.) which is

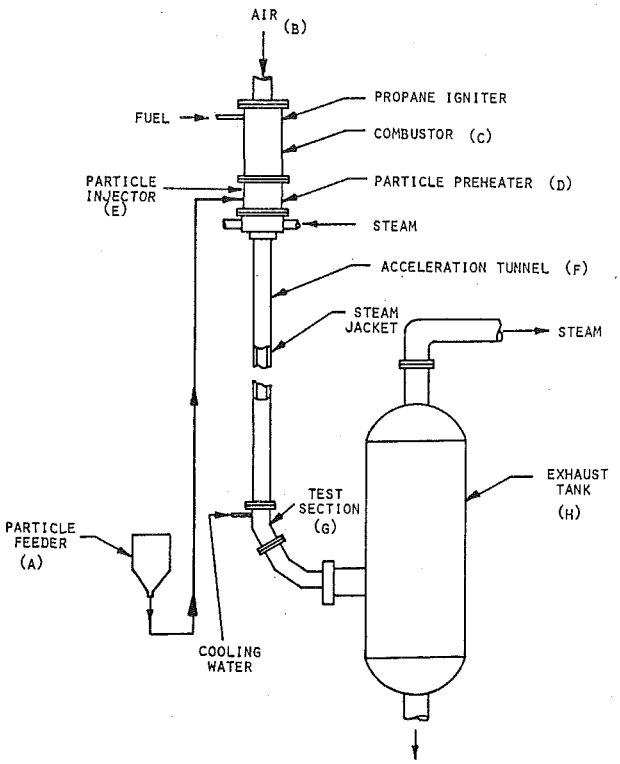

Fig. 1 Schematic of erosion test facility

Table 1 Erosion parameters

Parameters	
Temperature	10–1093°C (50–2000°F)
Particle Angle of Attack	0–90°
Particle Velocity	60–450 m/s (200–1500 ft/s)
Particle Concentration	0–5 percent
Particle Size	1μ–2000μ
Particle Type and Material	Silica Sand, Alumina, Ash and Others
Sample Size	6.35 mm–25.4 mm (¼ in.–1 in.)
Sample Material	Various Engine Materials

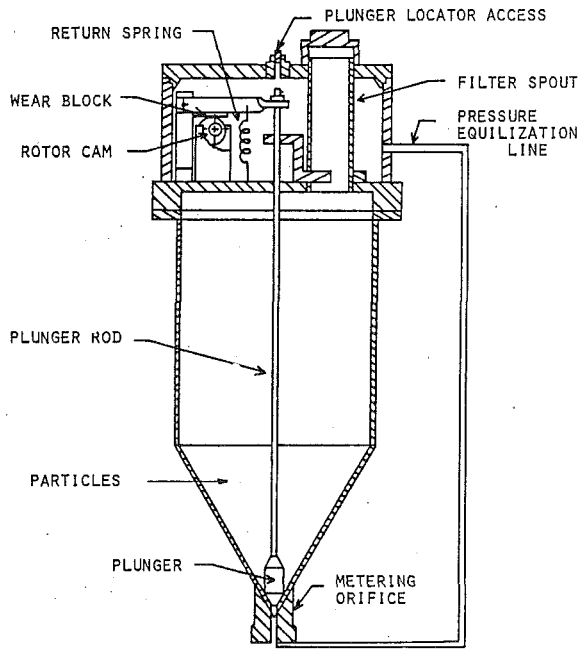

Fig. 2 Particle feeder assembly

3.66 m (12 ft) long. This section is steam cooled to minimize the heat losses. With this type of cooling, the 316 stainless steel liner operates at a maximum of 760°C (1400°F). This results in a drop in the gas stream temperature of about 93°C (200°F). The use of water as a coolant would have resulted in at least three times the heat loss and an unacceptable gas stream temperature drop in this section.

The particle velocities attained in this acceleration section were predicted analytically and verified by experimental methods. Pressure measurements at the inlet, mid-section, and exhaust were used to account for the tunnel friction when calculating the fluid velocity variation in this section. These velocities were used in calculating the particle velocities due to their acceleration by the gas stream. The calculated particle velocities are shown in Fig. 3 in the case of low fluid velocity of 122 m/s (400 ft/s) at 1093°C (2000°F) and at ambient temperature. From this figure it can be seen that the particle velocity is an exponential function of tunnel length. The law of diminishing returns would dictate that a tunnel length of 0.6 m to 0.92 m (2 to 3 ft) would be sufficient for both relatively large and small particles (200 μ and 20 μ). A tunnel length of 3.66 m (12 ft) was chosen however for several theoretical and practical reasons.

Test Section (G). The test section is designed such that the particle laden air is channeled over the specimen and the aerodynamics of the fluid surrounding the test sample are preserved. The test specimen can be oriented at different angles to the gas stream by rotating the specimen holder. The test section flowpath turns 30 deg at the plane of the test section to help turn the flow when the test specimen is oriented at an angle. The test section is water cooled, but this does not result in significant reduction in the primary gas stream temperature because of its relatively small size. The coolant water is discharged into the particulate gas stream at the downstream end of the test section.

Several interchangeable inserts can be used in this section such that the fluid profile can be determined using conventional instrumentation, and the particle impact and rebound characteristics can be recorded. A special test section with a glass window is constructed for the purpose of using photographic and L.D.V. means to measure the speeds and the angles of the impinging and rebounding particles.

Exhaust System (H). The flow leaving the test section, mixed with the cooling water, is exhausted into a settling tank. In this tank,

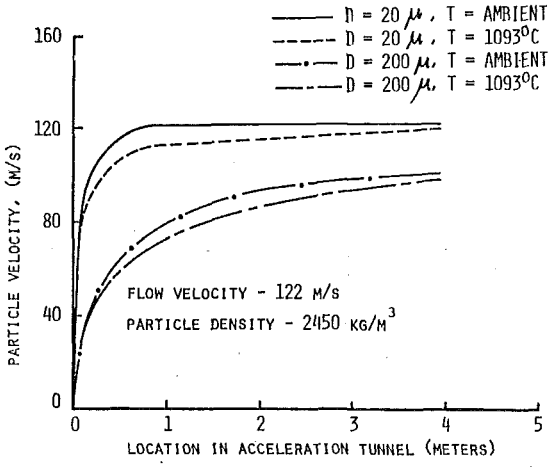

Fig. 3 Particle dynamics in a constant area acceleration tube

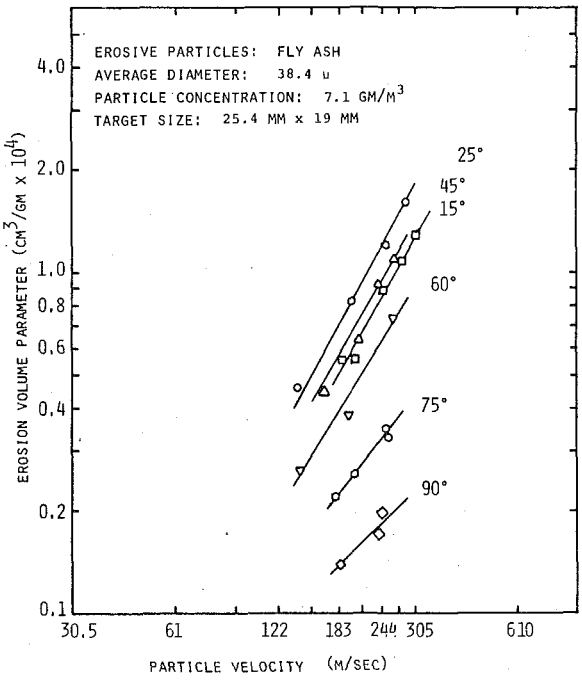

Fig. 4 Effect of velocity on erosion of 304 stainless steel at 316°C

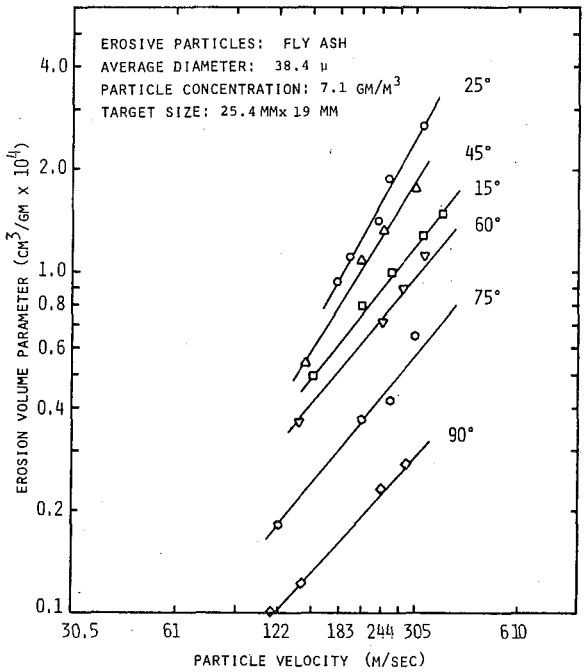

Fig. 5 Effect of velocity on erosion of 304 stainless steel at 482°C

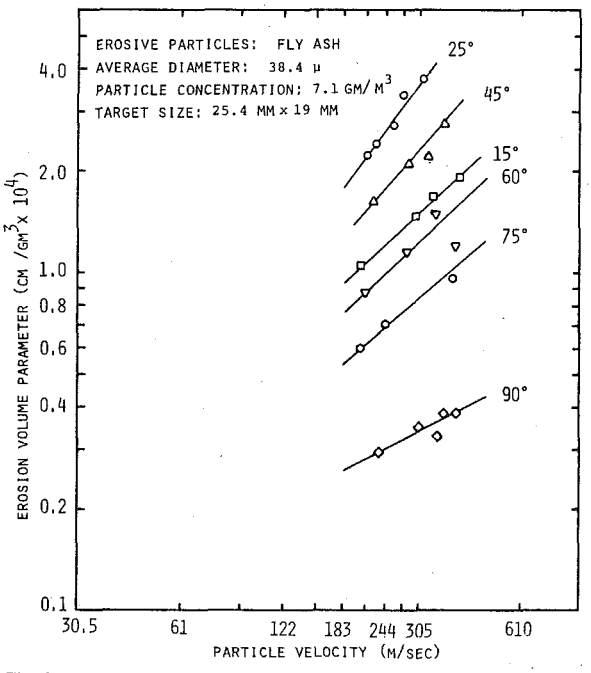

Fig. 6 Effect of velocity on erosion of 304 stainless steel at 649°C

the water is removed from the air, taking with it most of the erosion particles. The particle laden water is drained from the bottom of the tank through a 101.6 mm (4 in.) line, while the air leaves the top of the tank through a 152.4 mm (6 in.) line which discharges the air outside the building. The steam used for cooling the acceleration tunnel is also discharged through the same exit line (152.4 mm). A more detailed description of these test facilities may be found in [7].

Experimental Results and Discussion

The previously described erosion test facility was used to obtain basic erosion data for 304 stainless steel. The material erosion was determined from the weight of the 19.0 × 25.4 mm specimen before and after the testing. The abrasive particles used, consisted of fly ash supplied by the Cincinnati Gas and Electric Company with mean particle diameter of 38.4 μm. The experimental measurements were obtained for coal particle velocities varying from 120 to 350 m/s and target temperatures varying from ambient to 649°C (1200°F).

Figs. 4, 5 and 6 show plots of erosion rate versus particle velocity for various incidence angles. These figures represent the erosion data obtained for the 304 stainless steel specimen at target temperatures of 316, 482 and 649°C (600, 900 and 1200°F). An examination of these plots indicates that the maximum erosion takes place at the 25 deg incidence angle, while the minimum erosion occurs at 90 deg. The erosion rate is also shown for the intermediate incidence angles of 45, 60 and 75 deg, between these two extremes as well as at 15 deg incidence. In all the cases, the erosion rate was always found to increase with increased incidence velocities under the varying temperatures and particle incidence angles. The dependence of the erosion rate on incidence velocities is greater, at the impingement angles associated with the larger erosion rates as can be seen from these figures.

The dependence of the erosion rate on the incidence angles and velocities of the impinging particles can be seen more clearly in Figs. 7, 8 and 9. The experimental data presented in these figures are for three particle velocities, namely 305, 244 and 183 m/s (1000, 800 and 600 ft/s). From the inspection of these figures it may be seen that as the angle of attack increases beyond 25 deg, the erosion rate decreases up to a residual value at 90 deg. The effect of the angle of attack on the erosion rate is shown to persist, independent of the magnitude of the particle velocities. The definition of the point of maximum erosion becomes much more explicit, however, with increasing velocity. A comparison of the curves in Figs. 7, 8 and 9 shows that the rate of erosion increases with increased test material temperatures for all angles of attack. This can be seen more clearly in Figs. 10, 11 and 12. The maximum increase in erosion rate with increased specimen target temperatures can be observed around the 25 deg incidence which corresponds to the highest erosion rate.

Fig. 13 illustrates the effect of the temperature on erosion. In this figure the variation of the erosion rate with temperature is shown for two different velocities at the critical impingement angle of 25 deg. Two length scales are given on the horizontal axis of the same figure, one giving the ratio of the target temperature to the melting temperature, and the other, the ratio of the target temperature to the annealing temperature. For the 304 stainless steel, the melting temperature is between 1400–1455°C (2550–2650°F) and the annealing temperature between 1000–1120°C (1850–2025°F). From the two curves of Fig. 13, it can be seen that for both velocities the erosion rate decreases very slightly for increased temperatures between ambient and about 150°C (300°F). The predominant influence of the temperature on erosion is observed however at temperatures above 150°C (300°F). With increased temperature, the erosion rate is found to increase initially at a lower rate up to about 316°C (600°F) and then increases at an even higher rate.

Presently we are investigating other alloys which will be used in future gas turbine operating with coal. After the experimental work is completed, the data obtained will be used in developing empirical equations for predicting the erosion rates of ductile alloys at different temperatures. The empirical equations which were developed by Tabakoff, et al. [8] are applicable only at ambient temperatures. These relations will be used as a base for modifications to include the measured effects of higher temperatures on erosion. These modifications will incorporate the dependency of the erosion rate on the target

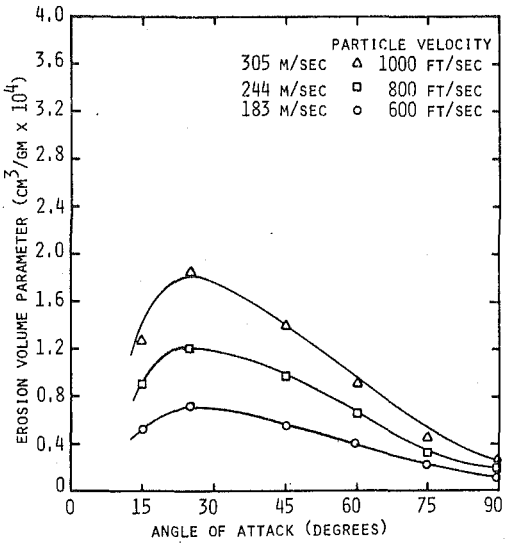

Fig. 7 Effect of angle of attack on erosion of 304 stainless steel at 316°C

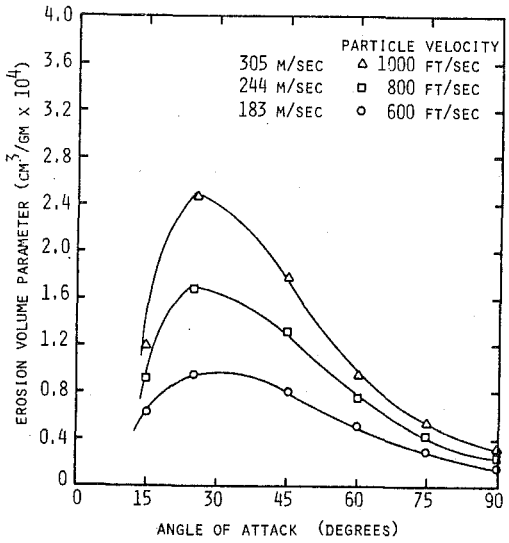

Fig. 8 Effect of angle of attack on erosion of 304 stainless steel at 482°C

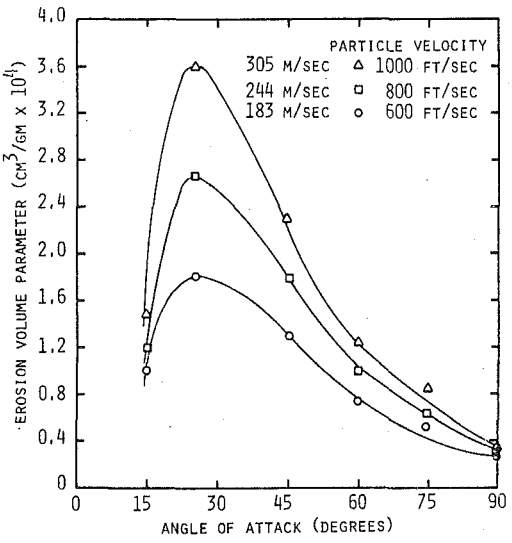

Fig. 9 Effect of angle of attack on erosion of 304 stainless steel at 649°C

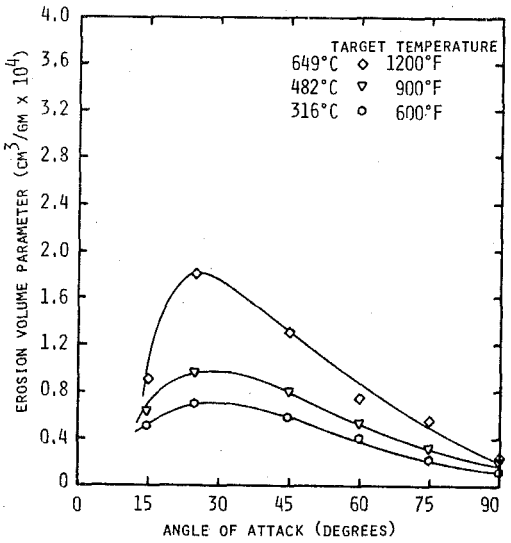

Fig. 10 Effect of angle of attack on erosion of 304 stainless steel at particle velocity of 183 m/s

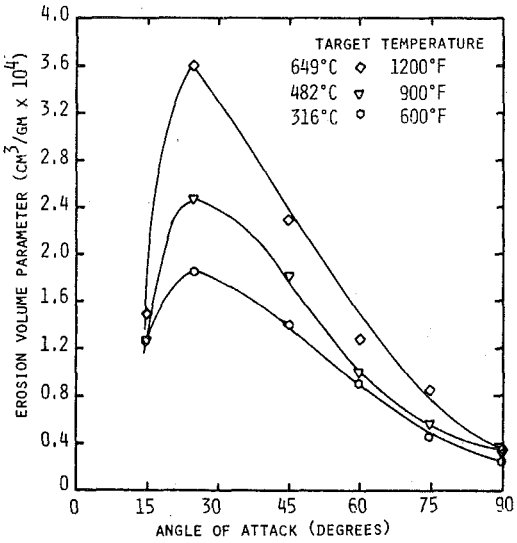

Fig. 12. Effect of angle of attack on erosion of 304 stainless steel at particle velocity of 305 m/s

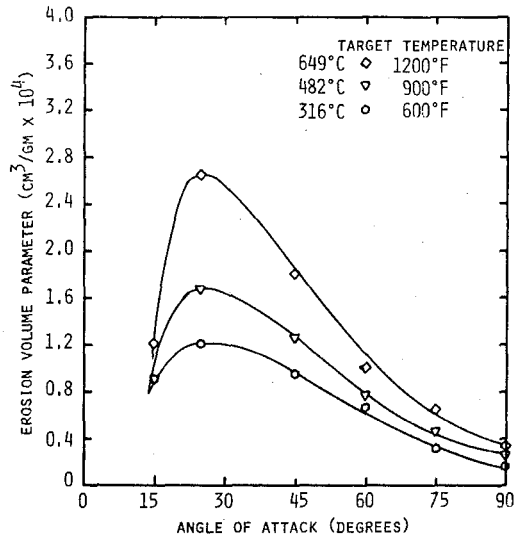

Fig. 11 Effect of angle of attack on erosion of 304 stainless steel at particle velocity of 244 m/s

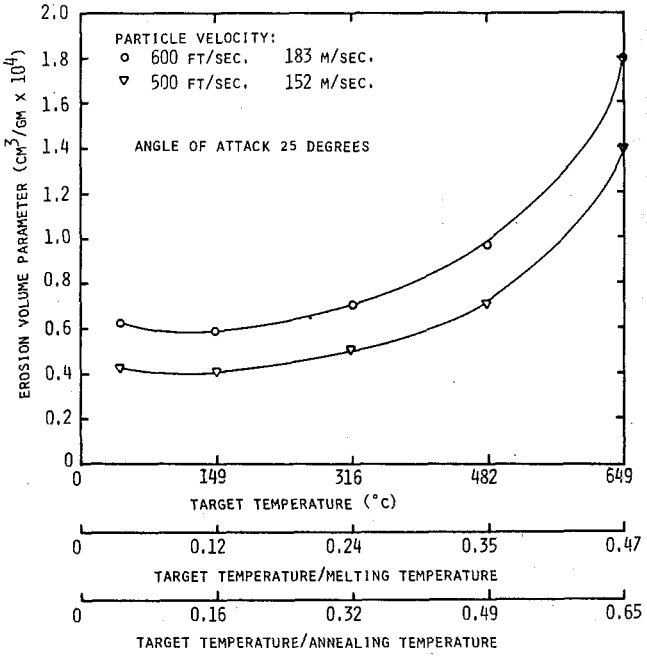

Fig. 13 Effect of temperature on erosion of 304 stainless steel

temperature, as well as, on the properties of the target material itself.

Acknowledgment

This research work was sponsored by ERDA Contract No. E(49-18)-2465.

References

1 Grant, G. and Tabakoff, W., "Erosion Prediction in Turbomachinery Resulting From Environmental Solid Particles," *Journal of Aircraft*, Vol. 12, No. 5, May 1975, pp. 471–478.

2 Finnie, I., Wolak, J., and Kabil, Y., "Erosion of Metals by Solid Particles," *Journal of Materials*, Vol. 2, No. 3, Sept. 1967, pp. 682–700.

3 Smeltzer, C. E., et al., "Mechanisms of Sand and Dust Erosion in Gas Turbine Engines," USAAVLABS Technical Report, Aug. 1970.

4 Fraas, A. P., "Survey of Turbine Bucket Erosion, Deposits, and Corrosion," ASME Paper No. 75-GT-123, presented at the Gas Turbine Conference, Houston, Texas, March 2–6, 1975.

5 Finnie, I., "An Experimental Study on Erosion," *Proceedings of the Society for Experimental Stress Analysis*, Vol. 17, No. 2, pp. 65–70.

6 Tabakoff, W. and Hamed, A., "Aerodynamic Effects on Erosion in Turbomachinery," JSME and ASME Paper No. 70, 1977 Joint Gas Turbine Congress, Tokyo, Japan, May 22–27, 1977.

7 Tabakoff, W. and Wakeman, T., "Test Facility for Material Erosion at High Temperatures," ASTM Publication, *Erosion: Prevention and Useful Applications*, STP 664, 1978.

8 Tabakoff, W., Kotwal, R. and Hamed, A., "Erosion Study in Turbomachinery Affected by Coal Ash Particles," ASME Paper No. 78-GT-136, 23rd International Gas Turbine Conference, April 9–13, 1978, London.

Z. P. Tilliette
Mem. ASME

B. Pierre

Département des Etudes Mécaniques et Thermiques
Commissariat à l'Energie Atomique
Centre d'Etudes Nucléaires de SACLAY-FRANCE

Application of Recuperative Gas Cycles with a Bypass Heat Generator to Solar Energy Power Plants

Gas cycles are being studied for solar energy power plants on account of the attractive prospects they offer for an efficient heat source utilization. By using a particular arrangement applicable to open or closed recuperative gas cycles, consisting of a heat generator partly bypassing the low pressure side of the recuperator, further improvements can be effected in gas turbine systems. They result in favorable conditions for power and high temperature heat cogeneration, for combined gas and steam cycles, and for flexible plant operation. Specific aspects of solar energy are investigated. They mainly concern variations in operating conditions, energy storage, energy conversion efficiency and combined cycles. Applications are made to open and closed cycle power plants. As the combination of a solar receiver with a fossil-fired auxiliary heat source is considered, fossil-fired power plants with an auxiliary solar heating are examined.

1 Introduction

Solar energy conversion into power is now a widely discussed matter; but it is not an easy study to carry out. The rational ways of utilizing the sun's radiation in the future have still to be thoroughly investigated. This is the case with thermodynamical conversion, which is nevertheless worth studying in all its aspects.

It is surely possible to generate steam from a solar receiver, either directly as is proposed by the 1 MW*e* project of the European Economic Community (Sicily), or through an intermediate molten salt (HITEC) circuit according to the design of the French 2 MW*e* THEMIS power plant, and to use this steam to drive a conventional turbogenerator. This method of conversion is probably the simplest one; that is the reason it has been adopted for soon to be built stations. However, related thermal and net efficiencies are passably low, namely between 25 and 28 percent nominal, and hardly open to improvement. Perhaps, a cycle top temperature limited to about 450°C will not square particularly well, in the future, with the nature of the solar energy capable, owing to appropriate collection and concentration, of providing higher temperatures.

Gas cycle systems offer the possibility of taking advantage of these attainable higher temperatures. This, nevertheless, is not the only point to be considered. Gas cycle plants can be designed according to several arrangements, certain of which—in relation to operational and congeneration conditions—could prove quite profitable to solar energy stations. Given the very high investment costs of the latter, every possible improvement in efficiency and operational conditions must be examined.

As a matter of fact, a particular gas cycle arrangement, which could lead to satisfactory solutions of some specific problems, is presented in this paper. It is applicable to gas systems provided with a recuperative heat exchanger and it offers interesting concepts as much for combined gas and steam cycles, for energy storage at intermediate temperatures, as for mixed solar-fossil-fired stations of various kinds.

2 General Principles of the Bypass Arrangement

Not entirely new in principle [1], the proposed arrangement has not been mentioned for many years although it is worthy of further investigation and applications. A new approach and applications to nuclear gas turbine—high temperature gas cooled reactors (GT-HTGR) for combined power and heat generation were presented in [2]. A refined statement of this gas cycle development, an extended assessment for power generation by combined gas-steam cycles as well as for power-heat cogeneration, and a diversified application to open or closed cycles for fossil, nuclear and solar energies can be found in [3].

The bypass or parallel arrangement basically consists of a heat generator, either a steam generator or a heat exchanger, partly bypassing the low pressure side of the recuperator, as shown in Fig. 1. By summarizing developments made in [2] and [3], it can be said that, as far as a working gas derivation corresponding to a thermal power P_1 is considered, the heat source has to supply an additional thermal power equal to P_2, which is significantly smaller than P_1. There is a

Contributed by the Gas Turbine Division and presented at the Gas Turbine Conference and Exhibit and Solar Energy Conference, San Diego, California, March 12–15, 1979 of THE AMERICAN SOCIETY OF MECHANICAL ENGINEERS. Manuscript received at ASME Headquarters December 18, 1978. Paper No. 79-GT-89.

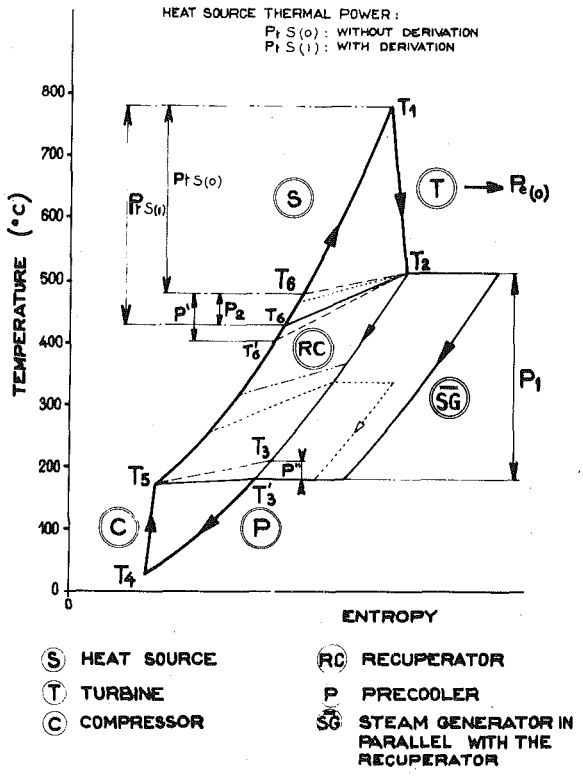

Fig. 1 Principle of the gas cycle bypass arrangement

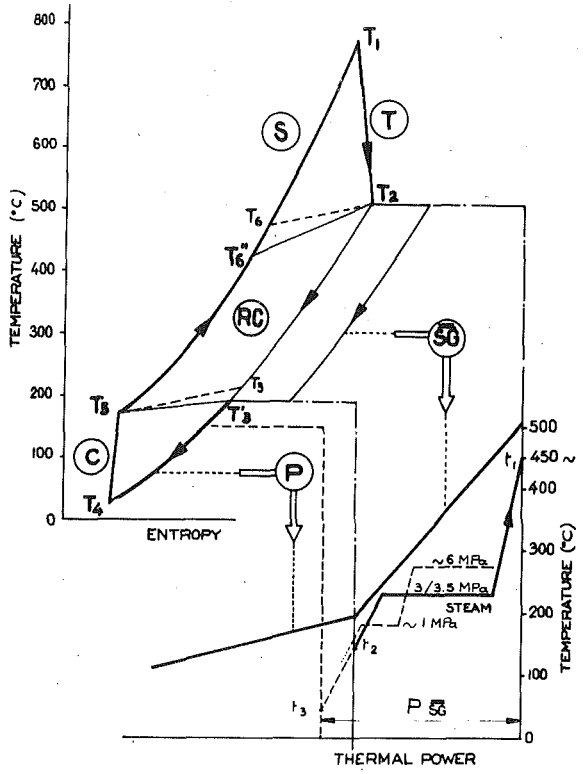

Fig. 2 Steam generation parallel to the recuperator

corresponding decrease of the outlet temperature of the recuperator low pressure flow. Thus a part of the low temperature heat transferred in the precooler is valorized, and recovered for the benefit of the high quality heat P_1. This recovered part amounts to about 35–45 percent of P_1 with which it varies inversely.

To these conditions, propitious to the overall efficiency of the system, a complementary factor has to be added (Fig. 2) in which a Brayton cycle is associated with the temperature diagram of the primary (low pressure gas flow) and secondary (steam) fluids. The feed water preheating from the temperature t_3 up to the temperature t_2 (about 150°C or more), equivalent to at least 15 percent of the total thermal rating of the parallel steam generator, is naturally achieved from the precooler in a totally free manner, without any increase in the heat source thermal power. Thereby, the overall efficiency of the plant is furthermore improved.

Fig. 2 shows another basic feature of the arrangement: high quality process heat is easily produced, for instance single pressure steam at 3.5–4 MPa/450°C or dual pressure steam at 6 MPa/450°C and roughly 1 MPa/220°C. Temperature, pressure, flow and other technological conditions are proven quite convenient to this heat generation.

In addition to these efficiency considerations, another important property of the arrangement should be pointed out. It refers to the actual flexibility of the system for operation and power/heat generation. This flexibility results from the parallel arrangement of the additional heat generator. It is expressed by the fact that neither turbine and compressor inlet and outlet temperatures, pressure ratios, nor mass flows are practically modified as the amount of the heat generated through the derivation varies from zero up to its nominal value. Only the recuperator high pressure outlet temperature, i.e., the heat source inlet temperature, changes, but in a acceptable way, owing to the concerned moderate temperature level and generally slow changes in thermal conditions.

3 Application to Solar Power Plants

3.1 General Considerations. Gas/Steam Cycles Coupling. Energy Storage. Solar power and heat generating plants offer the possibility of taking advantage of the properties of the parallel arrangement mentioned in Chapter 2. Some possible applications are dealt with in Sections 3.2, 3.3, 3.4, 3.5 and 3.6 in more detail but it seems useful to introduce these statements by general considerations.

The parallel arrangement makes it possible to reach a high thermal efficiency for the following reasons:

- the use of a recuperative heat exchanger,
- propitious operational conditions to combine a steam cycle with the main cycle,
- the improvement of the temperature conditions and the greater freedom in fixing the power rating of the combined steam cycle.

Now, it must not be forgotten that every improvement in the efficiency of a solar power plant is quite valuable owing to the very high investment costs of such plants.

The parallel arrangement offers a particularly flexible means of coupling the gas and steam cycles as well as of varying the relative power output of each cycle. This is undoubtedly appreciable, given the essentially variable nature of the solar heat source.

Thanks to the by-pass configuration, a significant amount of heat can be derived from the primary gas circuit into a secondary circuit at an intermediate temperature level. Consequently a new mean of energy storage at relatively well known technological conditions is made possible. Energy storage is indeed a basic notion in solar power stations.

Finally it is more and more spoken of an auxiliary fossil-fired heat source associated with the main solar receiver circuit in order to improve the distribution of the plant power output all day long and to

Nomenclature

T, t = temperature
P = power, pressure
LP, MP, HP = low, medium, high pressure
SG = steam generator
MWe, t = megawatt electrical, thermal
°C = degree centigrade
MPa = megapascal
Kg/s = Kilogram per second

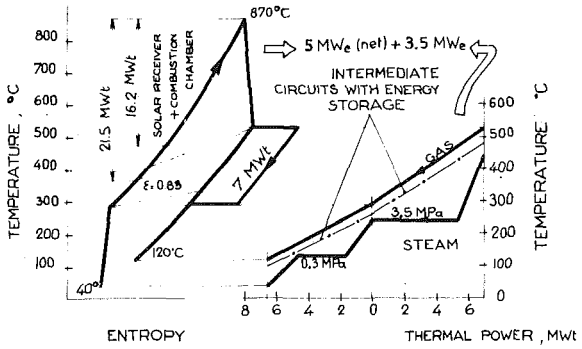

Fig. 3 Solar main power circuit. Air open cycle. Thermodynamic, temperature, power conditions

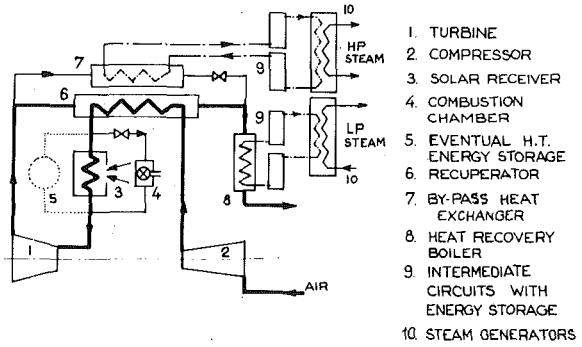

Fig. 4 Solar main power circuit. Air open cycle. Plant diagram

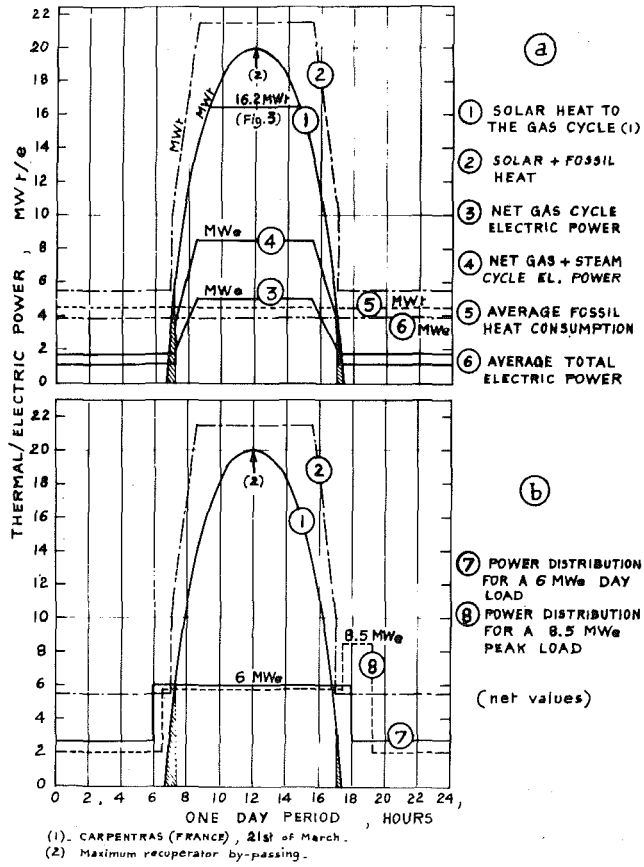

Fig. 5(*a, b*) Solar main power circuit. Air open cycle. Heat input and power distribution

reduce the variations in operational conditions at least for a noticeable part of the circuit. It will be shown that the by-pass arrangement can extend the possibilities in this field, including fossil-fired gas turbine power plants with an auxiliary solar heating.

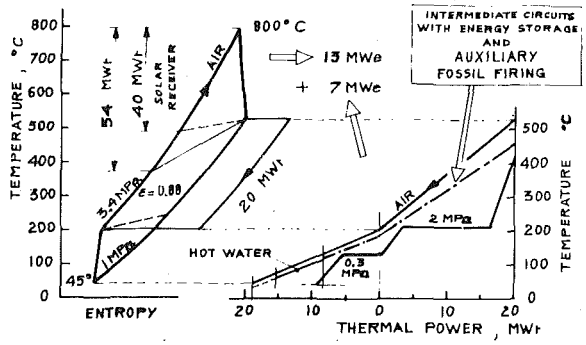

Fig. 6 Solar main power circuit. Closed air cycle. Thermodynamic, temperature, power conditions

Table 1 Solar main power circuit. Air open cycle. Main parameters and performance values

Working fluid (gas turbine)			AIR
Turbine inlet temperature		°C	870
Compressor inlet temperature		°C	40
Recuperator effectiveness			0.83
Net total electric power		MW*e*	8.5
Net gas cycle electric power		MW*e*	5
Net steam cycle electric power		MW*e*	3.5
Average combined electric power	(1)	MW*e*	3.9
Average fossil heat consumption	(1)	MW*t*	4.5
Maximum solar heat input	(2)	MW*t*	20
Maximum solar + fossil heat input	(3)	MW*t*	21.5
Recuperator by-pass thermal power		MW*t*	7

(1) According to power distribution of Fig. 5(*a, b*) (over 24 hr)
(2) Into the gas cycle
(3) Maximum recuperator by-passing

The principal related applications are illustrated in Figs. 3 to 17.

3.2 Solar Main Power Circuit. Air Open Cycle. Fossil-Fired Auxiliary High Temperature Heat Source. This concept is one of the first to be investigated because it consists of a relatively conventional primary power system and an auxiliary fossil firing, namely a combustion chamber. It could, however, be convenient to moderate power ratings only, given, for instance, possible heat transfer limitations inside the solar receiver.

The main temperature and power conditions of the thermodynamic cycle are given in Fig. 3. Air enters the turbine and the compressor at 870 and 40°C, respectively. The net nominal electric power of the gas turbine is 5 MW*e*. Parallel to the low pressure flow of the recuperator, a by-pass heat generation of 7 MW*t* is considered, which involves an increase in the amount of heat transferred to the air circuit from 16.2 MW*t* to 21.5 MW*t* (solar plus fossil-fired heat sources). An additional heat recovery boiler is arranged downstream of the recuperator on the low pressure flow and, according to fuel considerations, the exhaust temperature to the atmosphere is not lower than 120°C.

The corresponding temperature-thermal power diagram of the secondary steam cycle is also given in Fig. 3. A dual pressure steam cycle is adopted as in conventional combined cycle power plants. For the considered deviation of 7 MW*t*, the net power output of the steam cycle reaches 3.5 MW*e*. It follows that the total power output of the station is equal to 8.5 MW*e*, which results, concerning the power conversion system, in a net total electrical efficiency of about 39.5 percent, a satisfactory value for such a plant.

Main parameters and performance values are given in Table 1.

The considered combined cycle is analogous to the one presented in [3]. What is peculiar to this application is also shown in Fig. 3. It shows the energy storage achieved in this case by an intermediate circuit of appropriate fluid, for instance a molten salt mixture (HITEC) between 250 and 450°C and an organic liquid (gilotherm) for the low temperature part. This intermediate circuit receives the heat from the air circuit and transfers it to the steam system. Its other feature consists of storage facilities, essentially hot and cold tanks of intermediate fluids.

The aforementioned arrangements are shown schematically by the plant diagram in Fig. 4.

As far as solar energy is concerned, it is useful to give information about the distribution of the plant power output during a one day period on account of the essentially variable nature of the solar heat source. It is the purpose of Fig. 5(*a*) which shows, for a 24-hr period:

- the variation of the solar thermal power transferred to the gas circuit through the receiver (it corresponds to an actual solar heat distribution measured at Carpentras, in the south of France, on the 21st of March),
- the distribution of the additional amount of heat supplied by the auxiliary fossil-fired heat source in the case of a permanent auxiliary firing (other assumptions can be made for this distribution),
- the distribution of the net electric power supplied by the gas turbine only and by the combined gas and steam cycles without making use of the medium temperature storage facilities,
- the average net overall electric power and fossil heat consumption respectively equal to 3.9 MW*e* and 4.5 MW*t*, two not very different values as a matter of fact.

Similarly, Fig. 5(*b*) shows the distribution of net electric power either with or without a peak output equal to the nominal load of the plant and by assuming a night load of 20 to 25 percent of the nominal load.

It appears that both the auxiliary limited fossil firing and the energy storage at intermediate temperature for the steam cycle only, conventional technological solutions indeed, could offer satisfactory operational conditions in a fairly large number of cases.

In this concept, only the temperature conditions of the solar receiver are not permanent.

3.3 Solar Main Power Circuit. Closed Air Cycle. Fossil-Fired Auxiliary Steam Boiler. It is surely essential to investigate closed gas cycle systems as far as solar energy is concerned on account of gas circuit, heat exchangers, particularly, and solar receiver considerations for relatively high power ratings. In the present application, air under moderate pressure is proposed as a working gas but pure helium or mixtures of helium with another gas could also be chosen.

Main circuit, arrangement and operational conditions are presented in this section in the same manner as in 3.2.

As is shown in Fig. 6, inlet turbine and compressor temperatures are 800°C and 45°C, respectively. The net nominal power output of the gas turbine is 13 MW*e*. For the considered 20 MW*t* recuperator derivation, the amount of heat the solar receiver transfers to the gas circuit increases from 40 MW*t* to 54 MW*t*. Owing to the combined cycle concept of the plant, there is no intercooling and the upper temperature part of the precooler is used for the feedwater preheating and low pressure steam generation. From the lower temperature part of this precooler, waste heat can be recovered for district heating or industrial preheating.

Steam cycle conditions are also given in Fig. 6. The nominal net electric output of the steam plant is equal to 7 MW*e*, so that the total electric power and the overall net electrical efficiency of the station reach 20 MW*e* and 37 percent, respectively.

Main parameters and performance values are given in Table 2.

Like for the first application in Section 3.2, energy storage capacities are provided with on the medium temperature intermediate circuits between the low pressure gas flow and the steam cycle. The difference

Table 2 Solar main power circuit. Closed air cycle. Main parameters and performance values.

Working fluid (gas turbine)			AIR (helium)
Turbine inlet temperature		°C	800
Compressor inlet temperature		°C	45
Recuperator effectiveness			0.88
Net total electric power		MW*e*	20
Net gas cycle electric power		MW*e*	13
Net steam cycle electric power		MW*e*	7
Average combined electric power	(1)	MW*e*	10.5
Average fossil heat consumption	(1)	MW*t*	19.9
Maximum solar heat input	(2) (3)	MW*t*	54
Maximum fossil heat power	(4)	MW*t*	29
Recuperator by-pass thermal power		MW*t*	20
Hot water production (120–60°C)		MW*t*	6

(1) According to power distribution of Fig. 8(*a, b*) (over 24 hr)
(2) Into the gas cycle
(3) Maximum recuperator by-passing
(4) Including stack losses

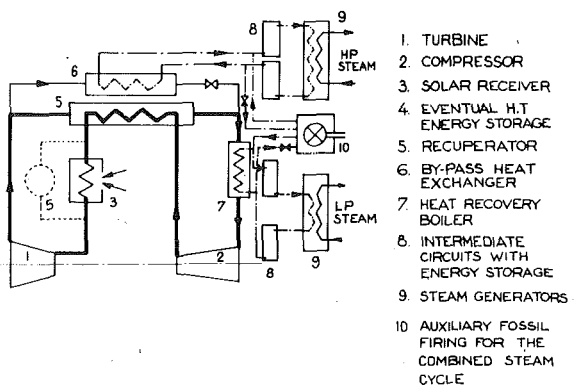

Fig. 7 Solar main power circuit. Closed air cycle. Plant diagram

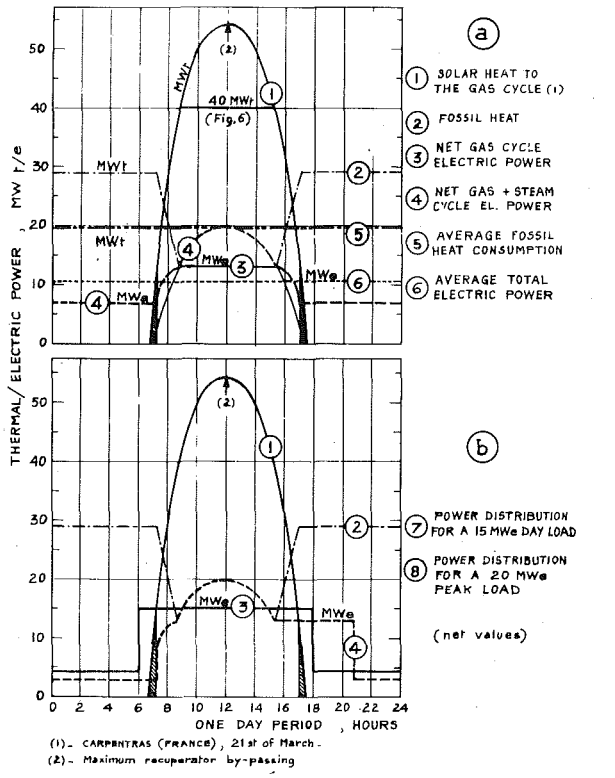

Fig. 8(*a, b*) Solar main power circuit. Closed air cycle. Heat input and power distribution

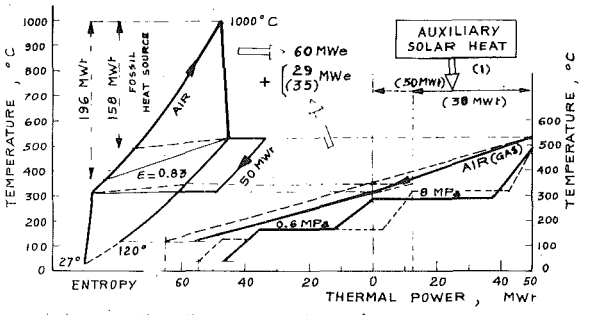

Fig. 9 Fossil-fired gas turbine main power circuit. Air open cycle. Thermodynamic, temperature, power conditions

to be pointed out is related to the auxiliary fossil-firing which only concerns the steam cycle and the heat storage intermediate circuits. As a matter of fact, a fossil-fired high temperature gas heater could be economically questionable.

The corresponding plant diagram is given in Fig. 7.

Table 3 Fossil-fired gas turbine main power circuit. Air open cycle. Main parameters and performance values

Working fluid (gas turbine)			AIR
Turbine inlet temperature		°C	1000
Compressor inlet temperature		°C	27
Recuperator effectiveness			0.83
Net total electric power		MW*e*	89(95)
Net gas cycle electric power		MW*e*	60
Net steam cycle electric power		MW*e*	29(35)
Average combined electric power	(1)	MW*e*	76
Average fossil heat consumption	(1)	MW*t*	157
Maximum solar heat input	(2) (3)	MW*t*	38(50)
Maximum fossil heat input		MW*t*	196
Recuperator by-pass thermal power		MW*t*	50
Power output over fossil fuel consumption (maximum)		percent	60

(1) According to power distribution of Fig. 11 (over 24 hr)
(2) Into the steam cycle
(3) Minimum (null) recuperator by-passing

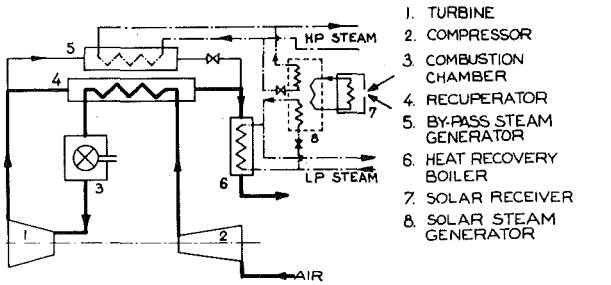

Fig. 10 Fossil-fired gas turbine main power circuit. Air open cycle. Plant diagram

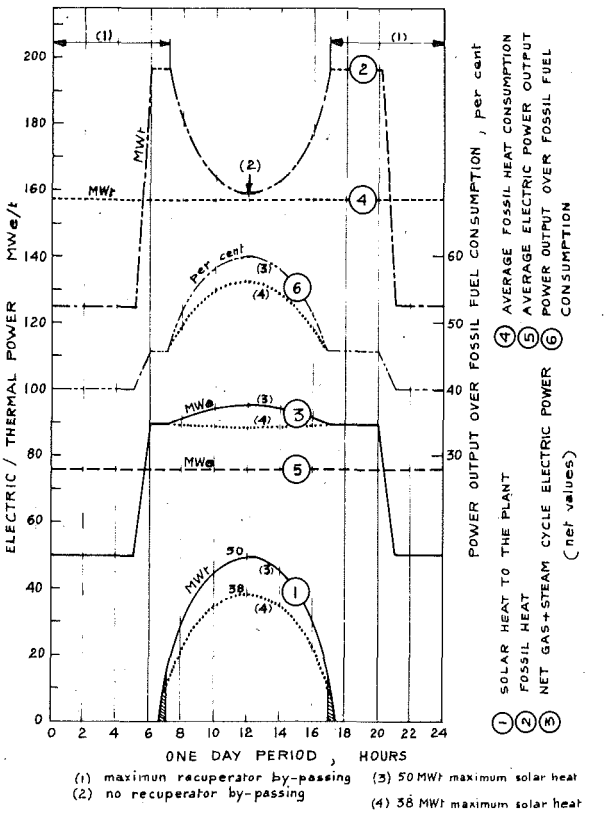

Fig. 11 Fossil fired gas turbine main power circuit. Air open cycle. Heat input and power distribution

Fig. 8(*a*,*b*) illustrates the plant power distribution over a 24-hr period and is, in this manner, comparable to Fig. 5 (*a*,*b*). The solar heat transferred to the air circuit is uprated to the new conditions, reaches the maximum value of 54 MW*t*, but is distributed similarly to the curves of Fig. 5(*a*,*b*). The distribution of the additional heat supplied by the fossil-fired auxiliary boiler does not have to meet exactly the same requirements. In the present concept, the gas cycle is not permanently operated, unlike the steam cycle. The fossil auxiliary boiler may or may not be fired permanently. The hot water supply has to be added to the electricity production.

By assuming a full auxiliary fossil firing all night along, the average electric power output of the plant is as high as 10.5 MW*e*, to be compared to an average fossil heat consumption of 19.9 MW*t* (Fig. 8(*a*)). In Fig. 8(*b*), two examples of power distribution for a 15 MW*e* day load and a 20 MW*e* peak load are given. Corresponding night power outputs are 4.3 MW*e* and 3 MW*e*, respectively.

3.4 Fossil-Fired Gas Turbine Main Power Circuit. Air Open Cycle. Solar Auxiliary Medium Temperature Heat Source. Sections 3.4, 3.5 and 3.6 concern a different approach to solar power plants. Solar energy is no longer considered to be the main heat source of the main gas circuit of the station. It becomes an auxiliary heat source which contributes to the decrease in fossil fuel consumption of the plant when the sun shines.

In Sections 3.4 and 3.5, solar energy is only used at a medium temperature for the associated steam cycle. It is the first version to be studied and thus a direct reference can be made to already well studied projects [4, 5].

As far as the air open cycle solution is concerned, the selection of the top cycle parameters is different from the one made in Section 3.2. A conventional turbine inlet temperature (1000°C) and an industrial power rating (60 MW*e*) are quite acceptable for a turbomachine arranged on the ground level and a practically standard compressor inlet temperature. Other parameters are given in Fig. 9.

A significant parallel heat generation (50 MW*t*) is considered and, when no solar energy is available, it supplies heat, together with the downstream waste heat recovery boiler, to the secondary dual pressure steam cycle. There is no intermediate circuit, no heat storage between the gas and steam circuits for such a plant when operated only with fossil energy.

Fig. 9 also shows the share of solar energy in plant power generation.

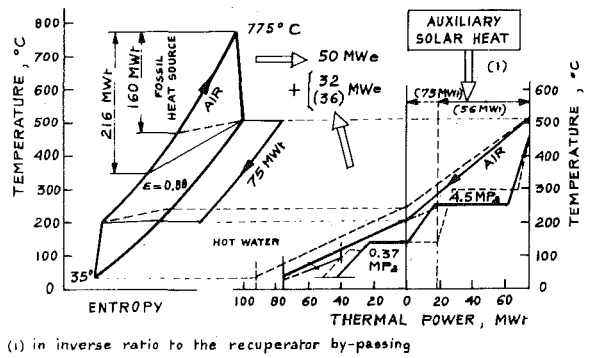

Fig. 12 Fossil-fired gas turbine main power circuit. Closed air cycle. Thermodynamic, temperature, power conditions

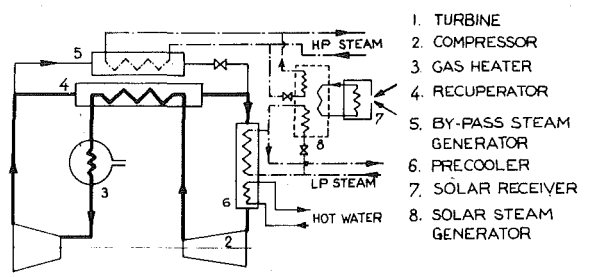

Fig. 13 Fossil-fired gas turbine main power circuit. Closed air cycle. Plant diagram

The heat from the solar receiver is transferred to the high pressure part of the steam cycle through an intermediate circuit without an energy storage capacity in principle. Appropriate circuits at this medium temperature level are already well studied. It can be mentioned that the temperature conditions concerned are quite satisfactory thanks to the parallel arrangement. For the nominal electric power of the plant, the amount of heat the solar receiver has to supply to the steam cycle (38 MWt) can be smaller than the nominal thermal power of the recuperator derivation (50 MWt) because of the temperature readjustment of the latter. In order to maintain the plant power output constant, the recuperator bypass flow increases in proportion as the sun radiation decreases. A solar heat input of 50 MWt is also possible.

Key parameters and performance results can be found in Table 3. The plant diagram is shown bv Fig. 10.

Concerning the plant power distribution over a one day period, it is interesting to compare Fig. 11 to the previous analogous ones, Fig. 5(a, b) and Fig. 8(a, b). The role of the solar heat is indeed no more preponderant in the plant energy balance but it is sufficiently noteworthy in order to raise the net plant efficiency, with regard to the fossil fuel consumption, from 45.5 percent to 60 percent. This result is satisfactory, given the relative simplicity of the combined solar plant in equipment as well as in operation.

As an example, a 56 percent night load (50 MWe) is assumed in Fig. 11 for the combined gas and steam cycles.

The feature to be pointed out is the coupling of the solar heat to the plant by using the recuperator by-pass. This solar energy input is effected in inverse ratio to the recuperator bypassing.

Table 4 Fossil-fired gas turbine main power circuit. Closed air cycle. Main parameters and performances values

Working fluid (gas turbine)			AIR (helium)
Turbine inlet temperature		°C	775
Compressor inlet temperature		°C	35
Recuperator effectiveness			0.88
Net total electric power		MWe	82(86)
Net gas cycle electric power		MWe	50
Net steam cycle electric power		MWe	32(36)
Average combined electric power	(1)	MWe	64
Average fossil heat consumption	(1)	MWt	151
Maximum solar heat input	(2) (3)	MWt	56(75)
Maximum fossil heat input	(4)	MWt	216
Recuperator by-pass thermal power		MWt	75
Hot water production (120–60°C)		MWt	15
Power output over fossil fuel consumption (maximum)		percent	54

(1) According to power distribution of Fig. 14 (over 24 hr)

Table 5 Gas turbine main power circuit with fossil-firing and auxiliary solar heating. Closed air cycle. Main parameters and performance values

Working fluid (gas turbine)			AIR (helium)
Turbine inlet temperature		°C	775
Compressor inlet temperature		°C	35
Recuperator effectiveness			0.88
Net total electric power		MWe	25
Net gas cycle electric power		MWe	15
Net steam cycle electric power		MWe	10
Average combined electric power	(1)	MWe	18.6
Average fossil heat consumption	(1)	MWt	42.2
Maximum solar heat input	(2) (3)	MWt	25
Maximum fossil heat input	(4)	MWt	67.5
Recuperator by-pass thermal power		MWt	25
Hot water production (120–60°C)		MWt	5.5
Power output over fossil fuel consumption (maximum)		percent	58.5

(1) According to power distribution of Fig. 17 (over 24 hr)
(2) Into the gas cycle
(3) Maximum recuperator by-passing
(4) Including stack losses

3.5 Fossil-Fired Gas Turbine Main Power Circuit. Closed Air Cycle. Solar Auxiliary Medium Temperature Heat Source. In this application, basically similar to the previous one from the point of view of solar energy utilization, the closed cycle concept offers, in addition to its well-known features (working fluid control in order to minimize corrosion problems, more satisfactory heat exchanger dimensioning, flexibility in the fuel selection), attractive prospects for new ways of coal utilization. Air is proposed as a working fluid but it could be helium for the selected 50 MWe rating of the gas turbine, that is to say the same value as that of the EV Oberhausen 2 plant in operation in Germany [6].

Fig. 12 gives the main parameters and fluid conditions for the two combined gas and steam cycles. The simplified plant diagram is shown in Fig. 13. The solar energy induction into the system is achieved in the same manner as in Section 3.4. Hot water is produced from the lower temperature waste heat.

Key performance values are given in Table 4. These results are not directly comparable with those obtained in Section 3.4, because plant concepts and particularly cycle top temperatures are quite different.

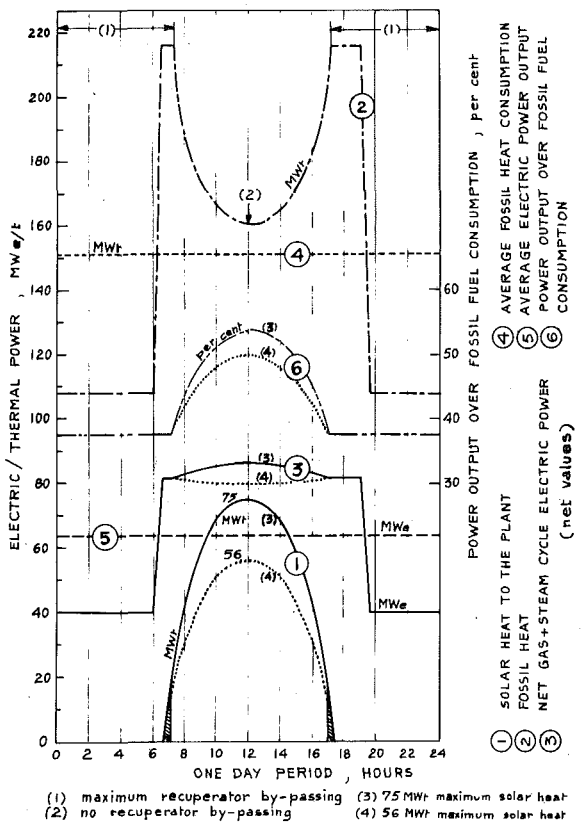

Fig. 14 Fossil-fired gas turbine main power circuit. Closed air circuit. Heat input and power distribution

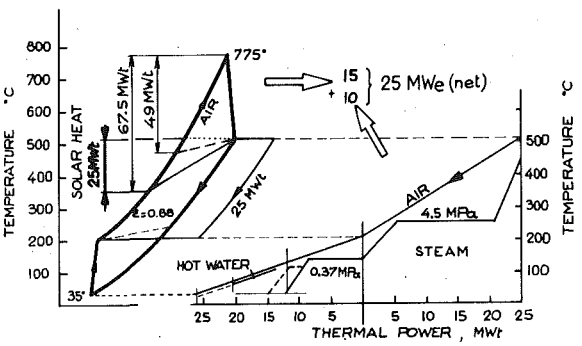

Fig. 15 Gas turbine main power circuit with fossil-firing and auxiliary solar heating. Closed air cycle. Thermodynamic, temperature, power conditions

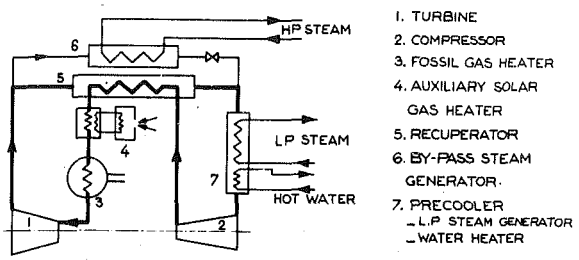

Fig. 16 Gas turbine main power circuit with fossil-firing and auxiliary solar heating. Closed air cycle. Plant diagram

Again the plant power distribution over a 24-hr period can be estimated by looking at Fig. 14. The effect of differences in recuperator effectiveness and intermediate circuit temperature conditions on the share of the solar energy in the total power generation can also be appreciated comparatively with the open cycle concept.

The maximum amount of heat supplied by the solar receiver to the steam cycle can be either limited to 56 MW*t* or as high as 75 MW*t*, the latter value resulting in a somewhat larger peak load, 86 MW*e* instead of 82 MW*e*.

By assuming a 49 percent (40 MW*e*) night load in Fig. 14, the average output of the plant is 63 MW*e*, to be compared with an average fossil heat consumption of 151 MW*t*.

The closed cycle concept makes it possible a larger solar heat utilization in comparison with an open cycle power plant. Its part load thermal efficiency can also be kept near its nominal value.

3.6 Gas Turbine Main Power Circuit with Fossil-Firing and Auxiliary Solar Heating—Closed Air Cycle. A closed air (possibly helium) cycle is also considered in this last application. As shown in Table 5 and Fig. 15, the net gas cycle and steam cycle electric outputs are 15 MW*e* and 10 MW*e*, respectively; i.e., the total electric output of the plant is 25 MW*e*.

The corresponding thermal rating of the bypass steam generator is relatively large—25 MW*t*. Without taking account of an auxiliary solar heating, it results in an increase in the thermal rating of the fossil heat source from 49 MW*t* to 67.5 MW*t*, including stack losses.

As is the case with other closed cycle systems, an additional production of hot water (60–120°C) is available up to 5.5 MWt.

What has to be pointed out in this case is the way of introducing the auxiliary solar heating into the system. The solar energy input takes place on the high pressure side of the gas cycle, at a medium temperature level, between the outlet of the partly bypassed recuperator and the fossil heat source inlet. The maximum solar heat rating is 25 MW*t*, which exceeds the compensation of the recuperator bypassing. The latter can be maintained at its maximum value all the time. Further studies would be necessary indeed in order to compare this application and its advantages to the other ones. Related thermodynamic conditions and plant diagram are shown in Figs. 15 and 16, respectively.

As before, an example of power distribution over a 24-hr period is given in Fig. 17. A 25 MW*e* load is assumed from 6 a.m. to 7 p.m. and a 10 MW*e* load is maintained during the night. The auxiliary solar heating results in a significant decrease of the day-time fossil fuel consumption. For the considered power distribution conditions, the average combined cycle electric output reached 18.6 MW*e* and the average fossil heat consumption is 42.2 MW*t*. At full load, the net plant efficiency for power generation is 37 percent without solar heating; comparatively, the ratio of the power output over the fossil fuel consumption reaches 58.5 percent for the maximal solar energy input into the system.

Similar to the two previous plant concepts, the relatively easy technological conditions of utilizing the solar energy are worth being considered in this case.

4 Conclusions

It is not possible to present more details about the investigated applications within the scope of this paper. It would certainly have been profitable to give further details. In particular, a comparative study relating to more conventional designs remains to be made. Probably other plant concepts can also be developed by making use of the parallel arrangement proposed for recuperative cycles.

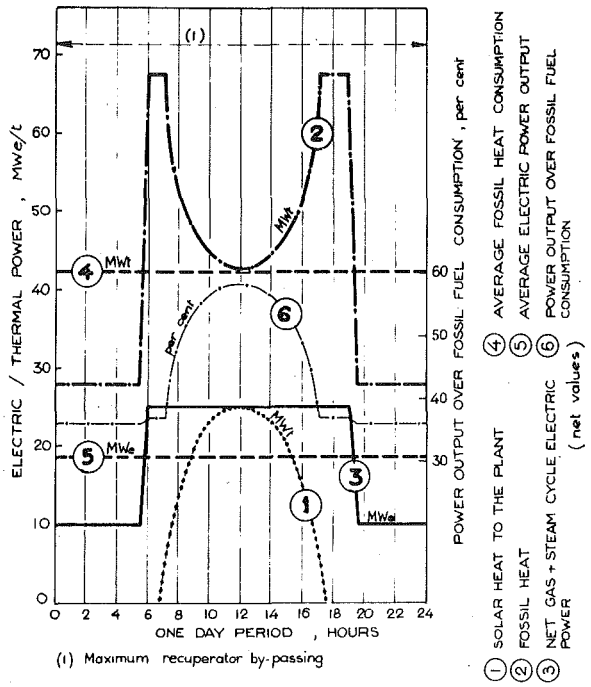

Fig. 17 Gas turbine main power circuit with fossil-firing and auxiliary solar heating. Closed air cycle. Heat input and power distribution

Solar energy should certainly be a field propitious to the described bypass configuration on account of:

- potential high plant efficiency,
- a variety of kinds of energy supplied by the plant in order to improve the heat source utilization,
- a high operation and production flexibility in order to favor the combined power and heat generation and, a very important point, to facilitate the operation of a plant, the main or auxiliary heat source of which is essentially variable and not adjustable to a given load.

In all cases the bypass arrangement induces minimal effects on the operation conditions of the main gas turbomachine in comparison to conventional combined cycle systems. It lends itself to varied solutions able to meet different requirements. It can help toward the combined use of the solar energy and fossil fuels, in particular within a coal, or even refuse, utilization program.

References

1 Bammert, K., Bünde, R., "Industrie—Kernkraftwerke mit Gasturbinen—Industrial Nuclear Gas Turbine Power Plants," *Atomkernenergie* (ATKE), 13 Jg, 1968, H.5, pp. 381–383.

2 Tilliette, Z. P., Pierre, B., "An Efficient, Flexible Arrangement to Generate High Quality Process or Domestic Heat in Recuperative Gas Cycle Power Plants—Application to Helium Direct Cycle Nuclear Power Plants," ASME Paper No. 78-GT-55.

3 Tilliette, Z. P., Pierre, B., "Improvement in Recuperative Gas Cycles by means of a Heat Generator Partly By-Passing the Recuperator—Application to Open and Closed Cycles and to Various Kinds of Energy," ASME Paper, 1979, ASME G.T. Conference, San Diego, USA.

4 Hofman, J., Gretz, J., "The Concept of the 1 MWel Solar Thermal Power Plant of the European Economic Community," *Proceedings of the 2nd International Solar Forum*, Hamburg, Germany, July 1978, Vol. 1, pp. 185–193.

5 EDF, CNRS, France, "La Centrale Solaire Expérimentale Themis," Publication *Electricité de France* et *Centre National de la Recherche Scientifique.*

6 Bammert, K., Deuster, G., "Lay-Out and Present Status of the Closed Cycle Helium Turbine Plant Oberhausen," ASME Paper No. 74-GT-132.

A. Kovats
Consultant.
13 Baker Rd.
Livingston, N.J. 07039
Mem. ASME

A Simple Solar Gas Turbine Plant

The Solar powered gas turbine plant has a storage system which is also capable of supplying instant heat at short interruptions of sunshine by clouds. The storage tank is not under pressure and is built of inexpensive material.

Introduction

Power generation by solar energy on a large scale is not economical at the present state of the art. Annual capital carrying charge of solar collectors alone is 15 to 20 times as high as that of fossil fueled plants, and the total cost of energy production, based on the life expectancy of solar collectors, is at least ten times higher.

Yet the situation may change in the future, if:

1 The cost of solar collecting equipment actually estimated to be 10,000 to 15,000 dollars per KW[1] can be reduced to 2000 to 3000 dollars;

2 the cost of fossil fuels (oil and coal) would increase considerably in the future.

However, even under actual conditions there are some situations in which solar power can be economical and some instances where it's the only solution. Such cases are:

3 Industrial plants far from power supply facilities which operate only in the daytime,

4 supply electricity to towns in remote areas where transporting fuel is expensive or is liable to interruption, and sunshine is abundant.

We can assume that in these cases the power requirement is mostly between 5 to 20 MW.

As power generating units, closed cycle GT seem to be the most advantageous, except for less than 5 MW power, for which plants open cycle GT can be considered. Not only because the gas turbine plant's cost is lower than costs for steam plants, but because regions of ample sunshine usually are in arid land where water is scarce and cooling water for steam plants would not be available or would increase the costs enormously.

The GT unit would differ from conventional units only insofar as the combustor or furnace would be substituted by a furnace heated with solar radiation reflected by the collectors.

The problems are temporary backup power for periods of time when sunshine is interrupted by clouds and storage of power during nights and possibly for sunless days.

The first requirement: backup power during interruption of sunshine must be instantaneously available. It could be a connection to a power grid; but if such possibility exists, it would make the solar plant practically unnecessary since the power reserve should be available all the time to be a "spinning reserve."

For instant backup power and storage independent of an outside source, two methods are possible: electric power storage (accumulator battery or hydro-storage) and an auxiliary heat-source or heat storage.

Electric power storage would not be instantaneously available when needed, it has only a 60 to 70 percent efficiency and would be very expensive because the whole power plant, including the GT unit, has to have the capacity of supplying the normal load and the energy to be stored.

An auxiliary heat source for instant backup power would be adequate only if oil or gas could be used. Yet for this purpose heat energy produced by the collectors could be used which is in excess when the load is lower than the full capacity of the plant, if the storage system is such that it permits instant heat extraction. Then for sunless days an auxiliary heat source of coal or refuse fired furnace would be more economical.

Description of the Plant

A simple solar powered GT plant is proposed in which heat is stored in a relatively cheap material, such as crushed rock, iron ore or chamotte, etc. Air is circulated through the storage material and the solar heated furnace.

The gas from the compressor passes through the heatexchanger and a pipeline where it picks up the heat from the hot air during sunshine and from the storage material in the absence of insolation (Fig. 1).

Due to the ample heat-transfer surface, a very small temperature difference, about 10 to 20° can be assured between the gas and the air.

Using air at atmospheric pressure to transfer heat from the furnace to the storage tank has the advantage that the pipe and the storage tank are not exposed to pressure.

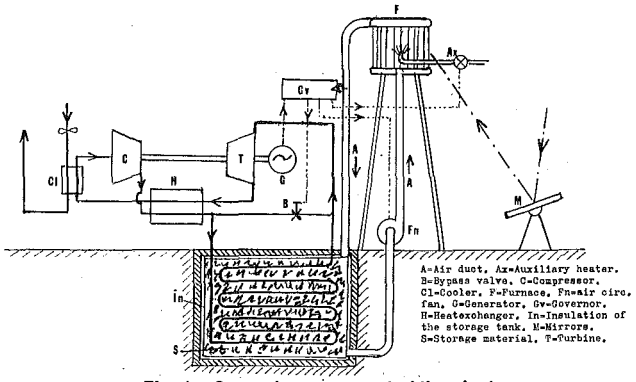

Fig. 1 General arrangement of the plant

[1] Concluded from: S. Baron, "Energy Cycles," *Mechanical Engineering*, June 1976.

Contributed by the Gas Turbine Division and presented at the Gas Turbine Conference and Exhibit and Solar Energy Conference, San Diego, California, March 12–15, 1979 of THE AMERICAN SOCIETY OF MECHANICAL ENGINEERS. Manuscript received at ASME Headquarters December 18, 1978. Paper No. 79-GT-90.

Instant heat is available from the storage. To reduce power a bypass valve, activated by the governor, is provided. An auxiliary burner can be built in the furnace, if oil or gas is to be used for fuel for longer sunless periods; yet, as mentioned before, coal or refuse burning would be more economical. In this case another furnace is needed, connected in series with the heating pipeline.

The temperature chosen for the turbine inlet temperature, t_{Ti}, depends on the cost of the different types of collectors.

In Fig. 2, the amount of the circulated gas (G kg/s) for the same power is shown in function of the turbine inlet temperature (t_{T1}). It is nearly twice as much for 800 K as for 1140 K inlet temperature. The dimensions and the cost of the turbine unit are about proportional to the amount of the circulated gas. The heat input, Q, is about in the ratio of 1.2 to 1.0. Since 80 percent to 90 percent of the invested capital is the cost of the solar collectors and of the storage facility, the total cost ratio is about 1.4 to 1.0. Higher temperatures can be achieved only with tracking mirrors, while lower temperatures are produced by fixed collectors.

Actually cost estimates of collectors vary between very wide limits. It can be said only that if the cost of mirrors with tracking mechanism is more than 1.4 times the cost of fixed collectors (in the tables we assume a limit of 800 K), the lower turbine inlet temperature is preferable.

For the heatexchanger we assumed 85 percent to 90 percent effectiveness, because the higher cost of a larger heatexchanger is less than the costs of collectors which would be necessary to compensate for higher heat loss.

Table 1 gives the main characteristics of the plant.

In Figs. 3 and 4 two typical load and power production curves are superimposed. The capacity of the solar collectors and the GT should be equal to the maximum load anticipated on sunny days.

1 **Industrial Plants.** In the case of power plants supplying only the needs of an industrial plant which operates only by daytime, a very small storage capacity is required since the excess energy at periods of lower than the maximum capacity is sufficient for covering short periods of interruption of sunshine. It may even be possible to have sufficient storage for one or two sunless days by increasing only the storage facility. Industrial plants usually do not operate on weekends and during these days the collectors designed for daytime use could supply the heat for cloudy days.

2 **Electricity Supply of Towns.** The situation is different in the case of power stations providing electricity for residential towns. In this application, night power requirements, at the very least, should be covered by storage. The collector capacity should be equal to the maximum daytime load plus night load minus excess capacity at daytime. The storage capacity evidently must cover the maximum night load.

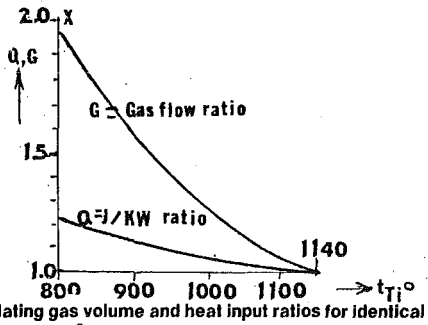

Fig. 2 Circulating gas volume and heat input ratios for identical power production in function of $t°$

Table 1

Gas:		air	
Compression ratio:	1.8		2.0
Compression inlet pressure bar:		20	
Turbine inlet temp., K:	800		1140
Heatexchanger eff. percent:		90	
Pressure loss in pipeline, Pa:		5000	
Leakage & Mech. losses, percent:		5	
Turbine power KW/kg gas:	64		122
Solar heat input, MJ/kg gas:	0.18		0.28
Solar heat input, MJ/KWh:	10.0		8.5
Storage material kg/KWh:	580		450
Storage material m^3/KWh:	0.30		0.28
cm = J/t/kg:	830 to		1000
Δt (deg.):	20		

In the load curve we have included airconditioning, which can be anticipated in regions where there is enough sunshine to justify building solar plants. In average it can be assumed that the load from sunset to sunrise is about 0.7 × Q, where Q = max. KW of the GT × 8 hr.

The heat extracted by the cooler could be used for heating or airconditioning the plant.

Evidently all these estimates may vary depending on local conditions.

To cover sunless days also, for each day, the solar collectors and storage capacity equal to a full day and night's consumption should be added. But the cost would be more than the proportion of the increased capacity, because the cost of the additional equipment must be amortized in fewer hours of operation than the daily utilization (Fig. 5.).

Storage for one or more sunless days is so costly that it could be considered only in some exceptional cases. Auxiliary heating is more economical.

Conclusion

It will be a long time, if ever, before solar power generation on a large scale could be economically possible. Only a breakthrough in production methods of solar collectors, storage systems or solar cells can decrease the costs so much that solar energy can compete with fossil fuel or nuclear energy.

The system described is feasible in the actual state of the arts and where solar power is justfiable, it could be applied with lower costs than most other systems.

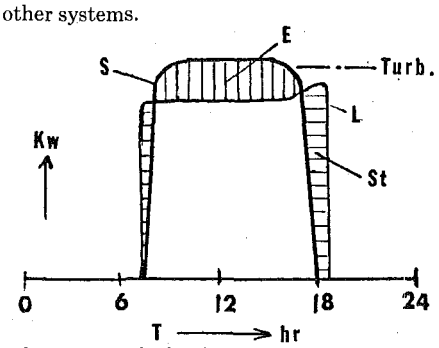

Fig. 3 Typical solar input and load of an industrial plant

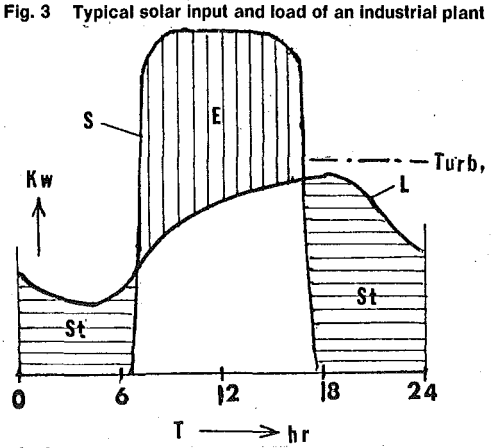

Fig. 4 Typical solar input energy requirement of residential power supply. E = excess solar energy, L = load curve, S = solar energy, St = stored energy, T = time

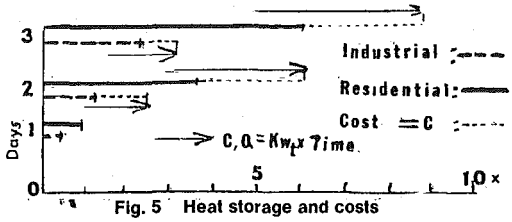

Fig. 5 Heat storage and costs

R. S. Mazzawy
Senior Research Engineer,
Pratt & Whitney Aircraft Group,
East Hartford, Conn.
Assoc. Mem. ASME

Surge-Induced Structural Loads in Gas Turbines

The axial flow compression system of a modern gas turbine engine normally delivers a large quantity of airflow at relatively high velocity. The sudden stoppage (and reversal) of this flow when an engine surges can result in structural loads in excess of steady state levels. These loads can be quite complex due to inherent asymmetry in the surge event. The increasing requirements for lighter weight engine structures, coupled with the higher pressure ratio cycles required for minimizing fuel consumption, make the accurate prediction of these loads an important part of the engine design process. This paper is aimed toward explaining the fluid mechanics of the surge phenomenon and its impact on engine structures. It offers relatively simple models for estimating surge-induced loads on various engine components. The basis for these models is an empirical correlation of surge-induced inlet overpressure based on engine pressure ratio and bypass ratio. An approximate estimate of the post-surge axial pressure distribution can be derived from this correlation by assuming that surge initiation occurs in the rear of the compression system.

Introduction

The axial compression system of a modern gas turbine engine delivers large quantities of airflow at pressure ratios typically ranging from 20 to 30. Future engine designs are being considered which have pressure ratios approaching 40. Needless to say, the structural requirements posed by these pressure levels are quite formidable during steady state operation. Often, however, the limiting load condition is not imposed during steady operation, but rather during the sudden instability known as surge.

Surge is an event characterized by the stoppage and reversal of engine flow in a matter of milliseconds. This large flow transient is accomplished through an internally generated shock wave of high strength. The force of this shock wave is sometimes sufficient to deflect compressor airfoils and rotor shafts, and damage compressor cases and inlets. The flow stoppage also leads to a rapid depressurization of the engine core which can further stress internal engine structures. The purpose of this paper is to provide insight into the surge phenomenon in order to assist the structural designer faced with the task of estimating surge-induced loads. With this insight, it is presumed, more sophisticated analyses can then be developed for predicting structural response to surge loading.

Characteristics of Surge

At the onset of this discussion it is appropriate to emphasize the extremely short duration of an engine surge. Typically, the entire event: Shock wave, flow reversal, depressurization and re-establishment of normal flow takes less than $1/10$ s. The shock wave formation and the flow reversal are the most rapid events, requiring only several milliseconds. This paper will concern itself primarily with those first few milliseconds during which the most rapid load changes take place.

Even though an engine surge is so rapid, modern high response pressure transducers have enabled the quantitative measurement and differentiation of the major portions of the event. Let us now review them in chronological order. It is to be noted that the time intervals discussed here are typical of large transport size engines. Information will be provided, however, which will allow the reader to determine these intervals for any engine size. The surge begins with a large flow separation from the airfoils within the compression system. This separation is induced by the adverse pressure gradient from the compressor inlet to the combustor. While this gradient is typically quite high (pressure ratios of 20 to 30 are common), it can be sustained by the compressor until an upsetting transient such as inlet distortion or an accel-decel causes a momentary increase above the compressor's limit. When this happens, the flow separation initially blocks several blade passages as shown in Fig. 1.

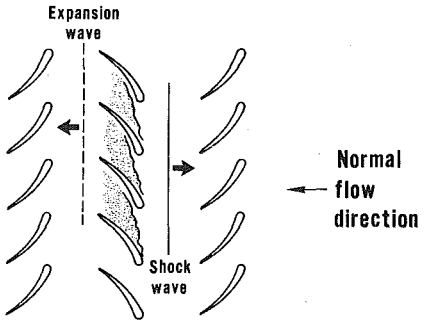

Fig. 1 Initiation of surge shock wave

Contributed by the Gas Turbine Division and presented at the Gas Turbine Conference and Exhibit and Solar Energy Conference, San Diego, California, March 12–15, 1979 of THE AMERICAN SOCIETY OF MECHANICAL ENGINEERS. Manuscript received at ASME Headquarters December 18, 1978. Paper No. 79-GT-91.

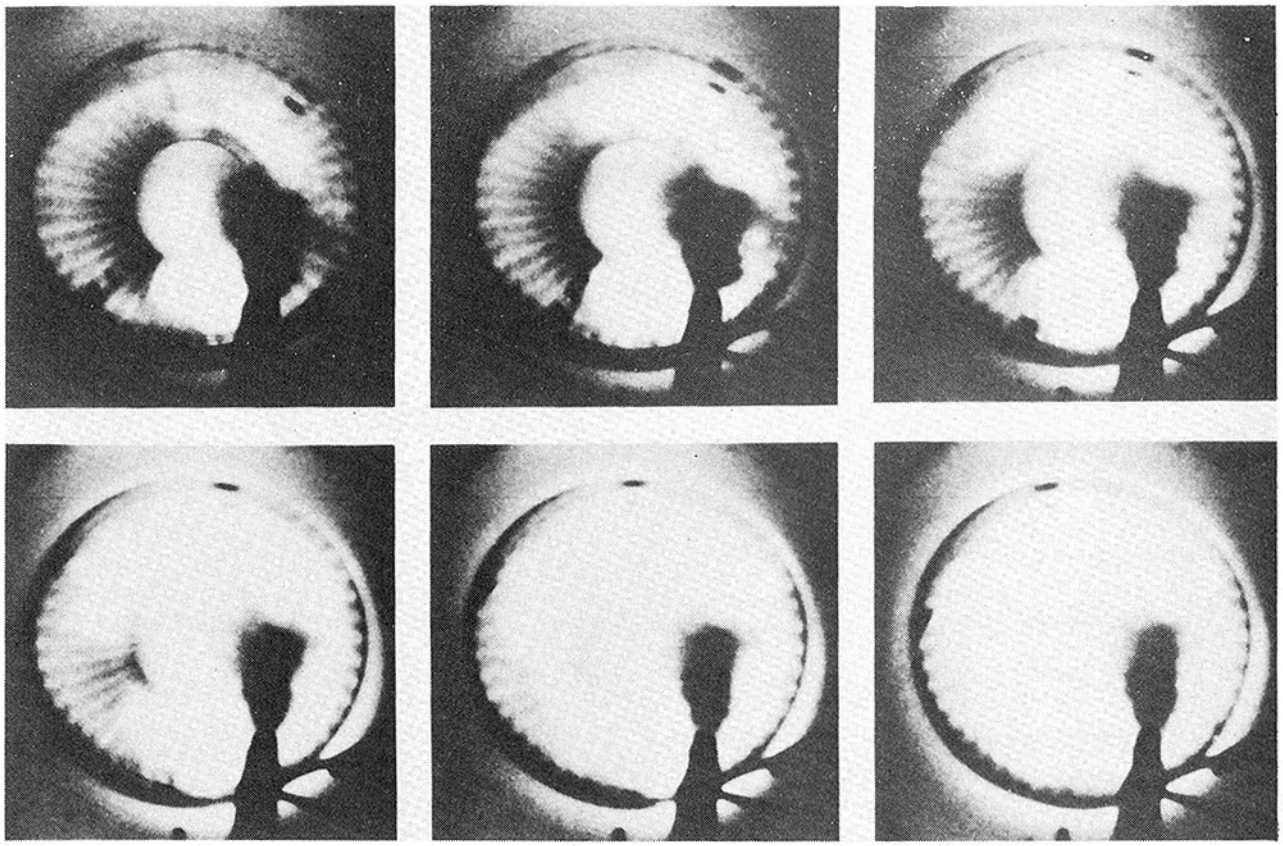

Fig. 2 Illustration of surge asymmetry

Two events now proceed as the surge develops. First of all, the blocked region progresses around the annulus and increases in extent at a rate which is proportional to rotor speed until it encompasses the entire circumference of the machine. This typically requires a time period of approximately one or two rotor revolutions. For large machines, a single revolution requires about 5 ms. The flow blockage also results in the formation of a shock wave which moves upstream to the engine inlet. (There is also an expansion wave which moves downstream into the combustor, but it is of little structural consequence.) This shock wave is of sufficient strength to exceed local sonic velocity. Hence, it can typically reach the inlet within 1 to 3 ms after the initial flow blockage. The picture which evolves is thus one of a very asymmetric flow field with some portion of the annulus flowing normally while another portion has experienced the shock wave and complete flow reversal from inlet to exit. A vivid illustration of this fact is provided by the series of photographs in Fig. 2. The figure shows the spewing of flame at the engine inlet caused by the flow reversal following the shock. Initially, this flame is visible over only a small circumferential sector and grows to full annulus in a time period corresponding to approximately one revolution of the high pressure compressor of this engine. During this period, severe axial, radial and twisting loads are imposed on the engine.

After a period of approximately 10 ms, (two rotor revolutions) the machine exhibits a more or less axisymmetric flow reversal and events proceed as shown in Fig. 3. The flow reversal is sustained because the instantaneous pressure ratio is not much less than the pre-surge pressure ratio and far exceeds the compressor's output capability after

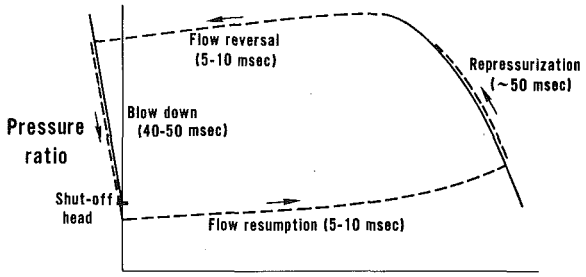

Fig. 3 Sequence of surge events

the flow breakdown. In fact, the compressor output is reduced to its zero flow or "shutoff head" level. [1] This level of pressure is typically less than 15 percent of that at the pre-surge condition for multi-stage compressors. It represents the compressor pressure ratio which would be achieved if the machine were brought to the pre-surge speed with the exit area completely blocked off. During this period, the engine depressurizes or "blows down" as air continues to escape via the normal turbine route as well as the flow reversal through the compressor. As the blowdown progresses, the internal pressure levels drop until the pressure ratio across the compressor falls below the shut-off head. In the time scale of surge events, blowdown is a relatively long event, lasting approximately 40–50 ms depending upon the size of the combustor section volume. Once the shut-off head is reached, the compressor resumes pumping and repressurizes the system, typically

Nomenclature

A = area
ARR_{EFF} = effective expansion area ratio at fan splitter
C = sonic velocity
C_p = specific heat
F = force
G = gravitational constant
γ = ratio of specific heats
J = Joules constant
K = orifice area contraction coefficient
M = Mach number
$\dot{m}$ = mass flow rate
N = number of compressor stages
P = pressure
ρ = density
T = temperature
V = flow velocity

Subscripts

ex = exit plane
in = inlet plane

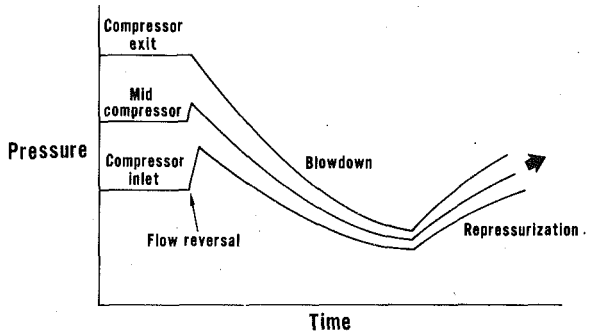

Fig. 4 Pressure-time history of surge

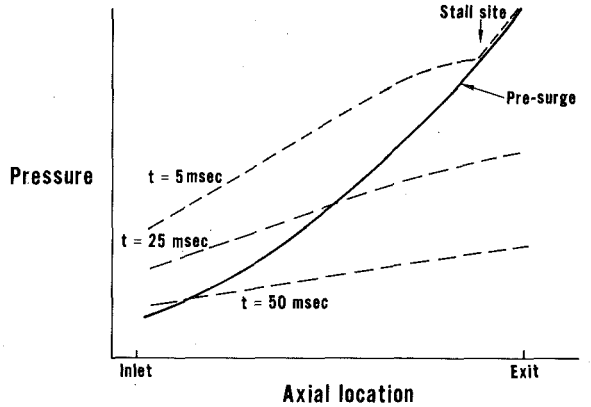

Fig. 5 Axial pressure distribution before and after surge

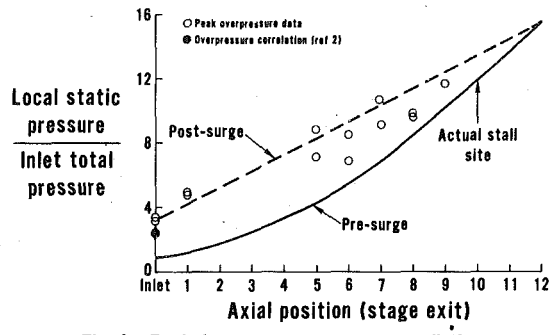

Fig. 6 Basis for surge overpressure prediction

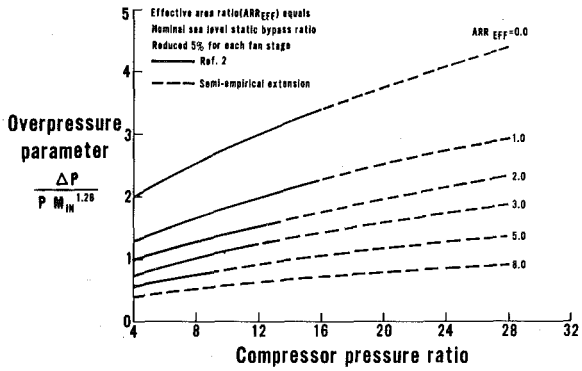

Fig. 7 Surge inlet overpressure correlation

requiring another 50 ms or so to approach pre-surge pressure levels. A repeat of the initial surge event then again becomes possible unless the condition which caused the initial engine surge has been alleviated.

The sequence of events just described is also shown for illustration in Figs. 4 and 5. In Fig. 4, the pressure levels at the inlet, exit and middle of a compressor are shown as a function of time. In this illustration, the initiation of the surge shock wave was located between the middle and the exit. Therefore, post-surge pressures at the inlet and middle location exceed the pre-surge levels, with the inlet showing the greater percentage increase. As noted earlier, the shock wave event is of short duration compared with the blowdown and repressurization periods. Fig. 5 further illustrates the axial distribution of pressure through the end of blowdown. The extremely rapid change from the pre-surge to the post-surge pressure distribution induced by the shock wave will now be considered in some detail in order to evaluate its impact on engine structures.

Shock Wave Strength

It is of considerable interest, considering its structural importance, to more fully investigate the surge shock event and to have some means of estimating its strength. Referring to Fig. 6, it can be seen that the axial distribution of peak post-surge pressure data from a twelve stage compressor test rig is fairly linear from the inlet to the initial surge location. These data were derived from measurements made with miniature high response pressure transducers (Kulite) mounted on the OD of the compressor gaspath. This instrumentation had a maximum frequency response of 1000 Hz with relative timing synchronization of different probes accurate to within one percent. Accuracy of pressure measurements were on the order of one to three percent (RMS). The data presented represent the peak pressure measured immediately following the surge event. Variations in peak pressure at axial stations having redundant instrumentation are due to the previously mentioned asymmetry of the surge event.

A conservative estimate of the post-surge pressure distribution can be obtained if one assumes linearity to the compressor exit, rather than the actual surge location. This approximation is also illustrated in Fig. 6. The approximation is only valid if the surge initiates in the rear stages of a compressor as it did in our example case. The rear stage surge location is most likely to occur at the highest rotational speeds of a compressor. This fact is derived from the high incidence experienced by these stages as increased density reduces axial flow velocity in the rear section of a machine at the maximum rotational speeds. Since the greatest pressures, and, consequently the limiting structural loads also occur at high rotational speed, the approximation using exit location is justified.

The large black circle shown at the inlet location in Fig. 6 represents a prediction of the post-surge *inlet* pressure level. The prediction is derived from a correlation [2] based on pre-surge compressor pressure ratio and engine bypass ratio. This correlation has been reproduced in Fig. 7 and provides an estimate for turbojets ($ARR_{EFF} = 0.0$) as well as turbofan engines ($ARR_{EFF} > 0.0$). The relationship between shock strength and bypass ratio (ARR_{EFF}) accounts for the sudden expansion experienced by the surge shock at the engine bypass splitter plane. This correlation underestimates the data shown in Fig. 6, but does provide an approximate means for predicting inlet surge overpressure for a wide range of engine designs. On the basis of this prediction and the assumption of a rear stage stall, reasonable estimates can be made of the post-surge internal pressure distribution. Note that the original correlation has been extended to higher levels of pressure ratio and bypass ratio. This was done through the use of additional data of two types. First of all, inlet overpressure measurements of a single bypass ratio (approximately 1.0) allowed extension of that line to the maximum pressure ratio. Secondly, the reduction in shock strength after a sudden expansion was derived from the correlation at lower values of pressure ratio and a separate data source [3]. Overpressure levels at the high pressure ratios could then be estimated for effective area ratios ranging from 0.0 to 8.0.

The most general case for illustration of the use of this correlation can be developed using a representative turbofan engine cycle. In this situation, the turbojet correlation must be used to estimate post-surge overpressure at the fan splitter location, and the appropriate turbofan correlation must be used at the inlet. An example, consider the following case:

Turbofan Cycle

Fan Pressure Ratio	2.0
Compressor Pressure Ratio	12.0
Overall Pressure Ratio	24.0

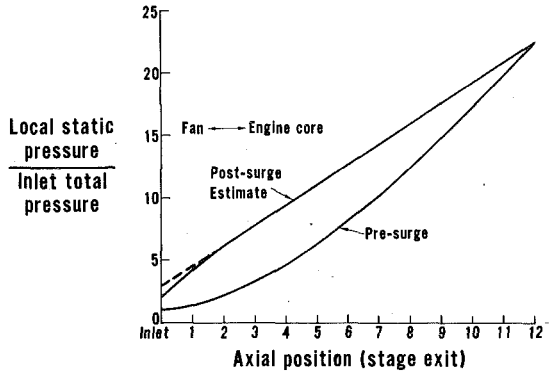

Fig. 8 Example overpressure calculation for turbofan

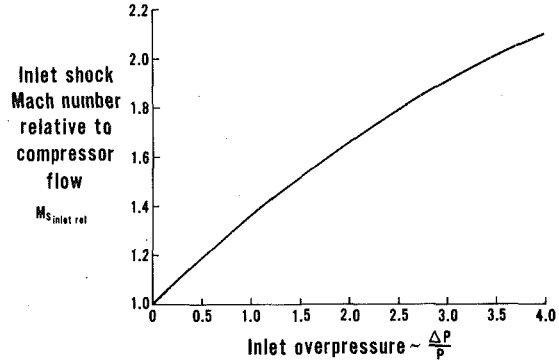

Fig. 9 Inlet shock propagation Mach number

Bypass Ratio	2.0
Number of Fan Stages	2
Number of Compressor Stages	10
Fan Inlet Mach Number	.55

First, the pre-surge static pressure distribution is established using standard procedures and a knowledge of the design details of the compression system. The correlation in Fig. 7 is then used to estimate *inlet* overpressure conditions for a pressure ratio of 24. Two estimates are made: one for $ARR_{EFF} = 0.0$, and one for $ARR_{EFF} = (2.0 \times .90) = 1.8$. The factor of 0.9 is in accordance with reducing the bypass ratio by five percent for each fan stage to determine the proper ARR_{EFF} for use in the overpressure correlation. The two resultant levels of inlet $\Delta P/P$ are 1.9 and 1.1, respectively. The first of these overpressure levels can be used to establish the axial distribution of post-surge pressure from the compressor exit to the fan splitter, as shown in Fig. 8. This is done because the splitter expansion does not alter the pressures within the engine core. The second overpressure level sets conditions from the splitter to the fan inlet. The expansion of the shock wave at the fan splitter diminishes the level of overpressure through the fan, resulting in the break in the linearity of the post-surge pressures. It now remains to propose and illustrate some physical models for various loads imposed by the surge shock wave.

Case Loads

The increased internal pressure level resulting from the shock wave can significantly raise compressor stress levels. Since the shock wave is asymmetric, a relatively complex load is placed on the compressor case (and the rotor) during a surge. The exact amount of asymmetry is difficult to predict since it depends upon such things as the variation in fits and tolerances, the relative amount of airfoil erosion, and the level of engine inlet distortion. In general, it can only be stated that this asymmetry remains for a period of one to two rotor revolutions which typically (for transport size engines) exceeds the time required for propagation of the shock from the initial stall site to the engine inlet. For purposes of this discussion, the asymmetry will be ignored in order to provide a conservative estimate of the case loads. This is done by applying the post-surge pressure distribution, such as shown in Fig. 8, over the case inner surface area. It is important, of course, to recognize that the incremental increase in pressure load above the pre-surge level is applied progressively and impulsively over a very short time interval. Hence, the stress realized as a result of this load may be increased significantly. The precise increase is a function of geometry and the suddenness with which the load is applied to the structure. The elapsed time interval over which the incremental surge load is applied depends upon the shock wave propagation velocity and the axial length of the compressor. The distance which the shock wave travels is in excess of the axial length by about 20–30 percent for typical compressor due to the non-axial stagger of the rotor blades and vanes. This effect is partially compensated for by using the entire length of the compression system since stall normally initiates a few stages forward of the exit. In general, it is estimated that the use of axial length provides about a ten percent error in the calculation of the total impulsive load application time. It now remains to determine

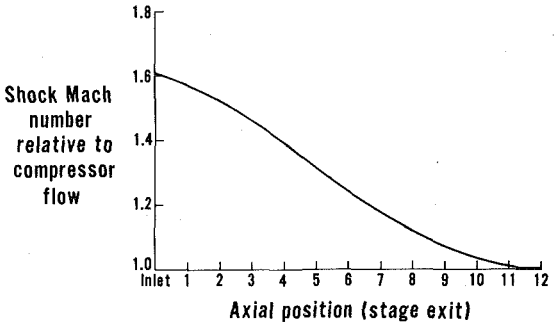

Fig. 10 Axial variation of shock Mach number

the shock propagation velocity. Relative to the air flowing through the compressor, the shock Mach number is a known function of shock strength as measured by the local overpressure. (For convenience, a simple curve relating surge overpressure and shock Mach number is provided in Fig. 9.) Consequently, this relative Mach number is 1.0 at the exit and increases to a maximum at the inlet. As an example, the relative shock propagation Mach number distribution was calculated using the overpressures from Fig. 6, and this result is shown in Fig. 10. It can be seen from this Figure that the shock propagation Mach number so derived changes in a continuous manner over the compressor length. At any axial location the shock propagation *velocity* relative to a *fixed* reference frame can be calculated from the following relation:

$$V_{SHOCK} = (M_{SHOCK_{REL}} - M_{FLOW}) \cdot C_{LOCAL} \quad (1)$$

It turns out, conveniently, that the shock propagation velocity calculated at the compressor inlet provides a good estimate at other axial locations. This fortuitous result comes from the fact that the shock Mach number is decreasing at about the same rate at which the sonic velocity is increasing due to the normal air temperature rise through the compressor. Consequently, the total impulsive load application time can be estimated as follows:

$$\Delta T_{load} = \frac{\text{Axial Length of Compressor}}{V_{\text{shock inlet}}} \quad (2)$$

The progressive load application time at any particular axial location can be calculated by linearly scaling the result from equation (2) with the length increment of interest for calculating local hoop stress. It is recommended that the overpressure correlation for $ARR_{EFF} = 0.0$ be used together with Fig. 9 to make estimates of the engine core section inlet shock Mach number. The propagation velocity through the fan can be determined from the correlation based on the engine bypass ratio (ARR_{EFF}). The estimate for the fan is a bit low since the shock wave requires some finite length [4] to completely expand from the engine core into the fan section. In fact, typical fan lengths are short enough to assume a continuous expansion to the fan inlet. Consequently, an average of the fan and the engine core propagation velocities calculated from equation (1) should yield the best estimate of fan case load application time.

Blade Deflection

This particular problem involves the interaction of the shock wave and reverse flow with the airfoils of a compressor. As illustrated in Fig. 11, the surge shock wave is partially reflected and partially transmitted through the cascade of airfoils. The exact details of the shock/airfoil interaction are quite complex and beyond the intended scope of this paper. Some features of the problem, however, will be discussed here to at least qualitatively describe a solution. In order to do this, we will consider the row of airfoils in the sense of an actuator disk of infinitesimal axial length. From this point of view, the major feature is the blockage which the cascade offers to the shock and to reverse flow. Consequently, the problem can be likened to the interaction of a shock wave with a discontinuous flow area constriction such as an orifice. It is strongly emphasized that this is an oversimplified one dimensional view of the problem, but it will be useful for determining which parameters are most important for calculating loads. It also serves the purpose here of aiding in the interpretation of the internal surge overpressure measurements.

First of all, consider the case of a shock interacting with a stationary cascade. This problem is best described by the time-distance plot shown in Fig. 12. In this figure it is assumed that flow normally proceeds axially from right to left. The incident surge shock therefore moves from left to right, approaching the cascade (area contraction). This shock is partially reflected and partially transmitted. The imposed load on the airfoils will be related to the difference in pressure behind the reflected shock (Region 4) and pressure of the undisturbed flow ahead of the cascade (Region 1). Conditions in Region 3 are set by the incident shock strength and can be considered a known variable. Similarly, conditions in Region 6 can be calculated for a range of assumed transmitted shock strengths. Between Regions 5 and 6 there can be no static pressure or velocity differential in the strict sense of such an interface [7]. The solution requires the calculation of the reflected shock strength and conditions in Region 4 and 5. In order to do this, an estimate must be made of the reverse flow characteristic of the row of airfoils. This will depend on the incidence angle on the trailing edge as well as on the pertinent airfoil cascade geometry: principally the stagger angle, solidity and, probably, to some extent, aspect ratio. Typical values of reverse flow for a compressor are quite low. This was demonstrated by a low speed, single stage compressor experiment [8] were measured reverse flows were less than 15 percent of the forward flow rates at the same rotational speed. High response flow measurements made in high speed, multistage compressors have shown similar levels. For purposes of this illustration, the posed problem will be solved for a range of reverse flow coefficients. It will be assumed that we can describe the reversed flow in terms of an equivalent quasi-steady orifice flow characteristic. Use of quasi-steady flow characteristics under such nonsteady flow conditions is quite adequate and has been verified experimentally [4, 5, 6].

Based on this model and its assumptions, the following equations can be derived.

$$\left(\frac{P_6/P_1}{P_4/P_3}\right) = \left[\frac{1+\frac{\gamma-1}{2}M_4^2}{1+\frac{\gamma-1}{2}M_C^2}\right]^{\gamma/\gamma-1} \tag{3}$$

$$\left(\frac{T_C}{T_2}\right) = \left(\frac{P_6/P_1}{P_4/P_3}\right)^{\gamma-1/\gamma} \tag{4}$$

$$M_c^2 = \frac{M_4^2}{K^2}\left[\frac{P_6/P_1}{P_4/P_3}\right]^{-(\gamma+1)/\gamma} \tag{5}$$

$$\left(\frac{T_5}{T_C}\right) = \frac{1}{K^2}\left(\frac{M_4}{M_C}\right)^2 = \frac{\left(1+\frac{\gamma-1}{2}M_C^2\right)}{\left(1+\frac{\gamma-1}{2}M_4^2\right)} \tag{6}$$

where: M_C = Mach number at contraction for reverse flow after reflected shock, K = Reverse flow coefficient = A_c/A_4.

The problem can be solved for a given incident shock strength and reverse flow coefficient by determining the transmitted and reflected shock wave strengths which satisfy the interface requirement ($P_5 = P_6$, $V_5 = V_6$). This was done for a pre-surge flow Mach number of 0.5 (typical compressor value) over a range of incident shock strengths and is documented in Fig. 13. In this figure, the ratio of P_4 to P_2 is plotted versus the ratio of P_3 to P_2. The size of the ordinate (P_4/P_2) relative to the abscissa (P_3/P_2) is a measure of the amplification of the surge overpressure due to shock reflection. For infinite flow resistance ($K = 0$) such as the surface of an airfoil, the overpressure load is amplified more than when the resistance is finite ($K > 0$). This latter solution (in particular, $K < 0.2$) is more indicative of the overpressure sensed by instrumentation positioned on the annulus wall in a compressor. Such instrumentation would measure some sort of "mixed out" merger of airfoil-reflected shocks into regions between airfoils with little or no reflections. The limiting case ($K = 1.0$) represents no shock reflection.

The primary interest from a blade deflection point of view concerns the infinite resistance ($K = 0$) curve. The results shown in Fig. 13,

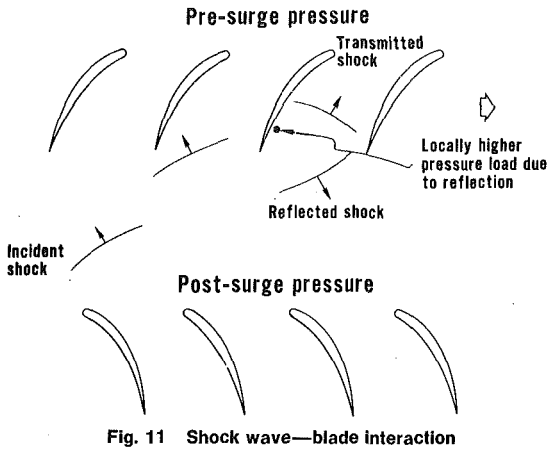

Fig. 11 Shock wave—blade interaction

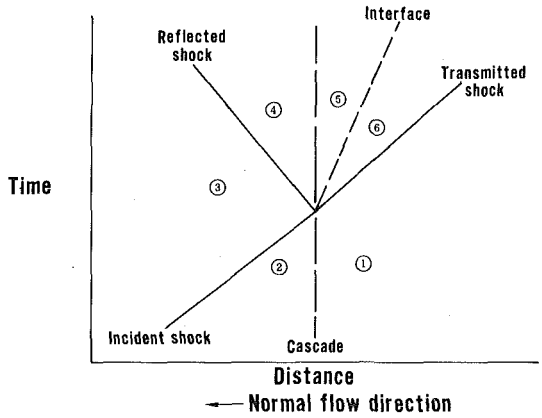

Fig. 12 Simple shock reflection model

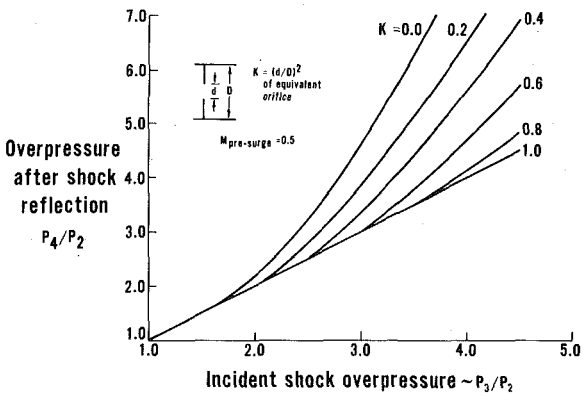

Fig. 13 Results of simple shock reflection model

however, apply only to a stationary cascade. When rotation effects are introduced, the reflection shock strength will increase by a factor which may be more dependent on wheel speed, cascade geometry and local reverse flow velocity triangles than on the incident shock strength. This is because even for a weak incident shock and small absolute reverse flow velocity there is a large *relative* velocity component behind the incident shock which is normal to the airfoil. This component must be abruptly reduced to zero by the airfoil during the shock reflection. The complexity of this shock/reverse flow/blade interaction prevents a precise solution. However, since wheel speeds typically approach sonic velocity at the front of a compressor, amplification factors as high as 2.5 – 3.0 seem feasible.

Rotational effects will also influence the results for finite flow resistance ($K > 0$), but to a lesser degree. Furthermore, in an actual compressor, there are interactions of multiple reflections from adjacent blade rows which were not considered here. All results presented must, therefore, be regarded as qualitative, at best. However, it is useful to note that for low values of reverse flow coefficient ($K < .2$) internal overpressure levels may be under predicted at high engine pressure ratios using the correlation given earlier in Fig. 7. This is because the correlation is based upon inlet data which presumably had no reflection component. There was relatively good agreement for the data shown in Fig. 6, but in that case the incident shock strength level (P_3/P_2) was approximately 2.5 where only small reflection effects are predicted by this simple model. The reader is therefore cautioned to use the correlation judiciously at high engine pressure ratios, perhaps guided by the results shown in Fig. 13.

Axial Thrust Loads

Two types of problems exist in this general category. One pertains to the axial thrust load (and moment because of asymmetry) on an engine mounting system. The second involves the rotor shaft thrust bearing loads during a surge transient.

The engine mount load is most easily calculated by considering momentum conservation arguments. To do this, a control volume is drawn around the perimeter of the engine such as in Fig. 14. It is sufficient to consider the problem over the time period from the initiation of surge to just before the emergence of the shock wave at the inlet, since the peak thrust load change will occur within this interval. If this is done, the external pressures and the momentum transfer across the inlet and exit plane are balanced by the steady (pre-surge) thrust. Consequently, the additional thrust force due to the surge can be equated to the non-steady momentum change within the control volume.

$$P_{in}A_{in} - P_{ex}A_{ex} + F_T - F_{surge} = \int_{C.V.} \frac{\partial(\rho V)}{\partial t} d\nu + \dot{m}_{ex}V_{ex} - \dot{m}_{in}V_{in} \tag{7}$$

But, $F_T = \dot{m}_{ex}V_{ex} - \dot{m}_{in}V_{in} + P_{ex}A_{ex} - P_{in}A_{in}$

$$\therefore F_{\text{surge}} = -\int_{\text{C.V.}} \frac{\partial(\rho V)}{\partial t} d\nu \tag{8}$$

We consider the momentum change with the control volume to be controlled by the movement of the shock from the surge site to the inlet location. Therefore, it reduces to the product of the mass flux change across the shock and the average shock propagation velocity relative to a fixed reference frame.

$$F_{\text{surge}} = -(\dot{m}_{\text{post-surge}} - \dot{m}_{\text{pre-surge}}) \cdot C$$

$$= \dot{m}_{\text{pre-surge}} \cdot C \left(1 - \frac{\dot{m}_{\text{post-surge}}}{\dot{m}_{\text{pre-surge}}}\right) \tag{9}$$

The direction of the surge-induced thrust load on the *engine* is in the rearward direction (opposite to the direction of force on the fluid as shown in Fig. 14).

In order to calculate this thrust load for a particular case, it is necessary to know the average shock propagation velocity as well as the average mass flux ratio. As the shock wave moves forward through a compressor, it gains in strength (overpressure) and velocity. The change in overpressure is relatively linear and consequently, the change in mass flux ratio is nearly linear. The shock propagation velocity was established earlier to be relatively constant. Consequently, a simple, slightly conservative solution can be obtained by using *one-half* of the surge overpressure from the turbojet ($ARR_{EFF} = 0.0$) correlation (Fig. 7) based upon overall engine pre-surge pressure ratio. Fan splitter expansion effects can be ignored because the shock, although weakened, influences a greater portion of the total engine airflow consistent with momentum conservation requirements. This solution is presented in Fig. 15, as a function of the surge overpressure parameter. Note that this solution is applicable to turbofans and turbojets alike, but only the engine core mass flow must be used to obtain the required thrust force. One final note concerning this load is that the asymmetry of the surge wave induces a twisting moment on the engine mount system. A conservative approach assumes that the shock propagation is completed over one-half the circumference before it starts for the remaining half. This imparts a moment equal to half the force from the previous solution acting at the centroid of the engine core flowpath.

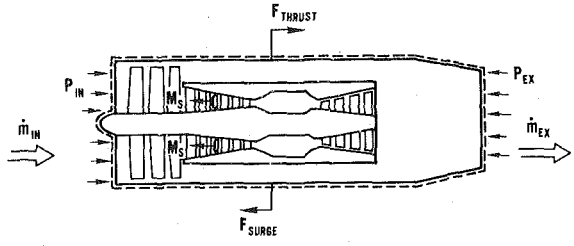

Forces shown in direction acting on fluid

Fig. 14 Engine post-surge control volume

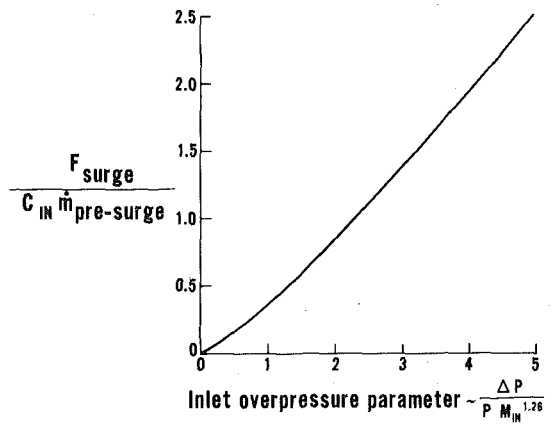

Fig. 15 Axial thrust load due to surge flow reversal

The final problem in axial loading concerns the rotor thrust bearings. These are normally loaded forward or rearward depending on the relative levels of pressure loading on compressor and turbine airfoils and disks. When a surge occurs, there is a rapid change in the compressor airfoil loading. Turbine airfoil loading is not initially altered since the combustion chamber volume serves as a damper and prevents rapid changes in turbine flow. Similarly, the compressor and turbine disk loading remain effectively constant for the time period of shock wave propagation since very little depressurization of disk cavities can occur during such a short interval. All the loads then decrease as the system blows down. It is possible for an excessive *net* load to be generated during the blowdown period if a significant flow restriction exists between the main gaspath and one or more disk cavities. While this may be a problem in compressor rig testing, it is not typical of gas turbine engines, and the discussion here will be limited to effects of the initial surge shock wave.

The load in question is derived from the solution in the preceding section. As stated earlier, the net load associated with the flow reversal is toward the rear. This load is applied to the rotor and stator airfoils and, because of gaspath convergence, the inner and outer walls. The distribution of the load among these three surfaces at any axial location can be estimated on the basis of the axial projected area of each

surface. In general, the rotor and stator projected areas are approximately the same, with the totals being about equal to the average of the inlet and exit annulus areas time the number of compressor stages. The total wall area, on the other hand, equals the difference between the inlet and exit annulus area.

$$F_{surge} = F_{rotor} + F_{stator} + F_{wall} \tag{10}$$

$$F_{surge} = k \cdot \left[\frac{N(A_{in} + A_{ex})}{2} + \frac{N(A_{in} + A_{ex})}{2} + (A_{in} - A_{ex})\right] \tag{11}$$

$$F_{rotor} = F_{surge} \Big/ \left[2 + \frac{2(A_{in} - A_{ex})}{N(A_{in} + A_{ex})}\right] \tag{12}$$

The exit area for a multi-stage machine is generally much smaller than the inlet area so that the impulsive load to the rotor (rearward) will be about one-half of the total axial thrust load resulting from surge. Note that this average rearward load over the entire rotor contrasts with the very localized forward load due to the shock reflection from a single row of airfoils. A final point to this discussion concerns turbofan engines. Use of engine core inlet area (at the fan splitter) in equation (12) avoids ambiguity and should provide no compromise in conservatism of the solution.

Summary

Surge has been shown to be a rapid transient during which extreme flow and pressure excursions occur within an engine. These excursions are associated with a shock wave of high strength emanating from an airfoil separation and stall site within the compression system. Moreover, this shock wave and the subsequent flow reversal result in significant structural loads in a gas turbine engine. Due to inherent asymmetries in the stall process, the shock wave and resultant structural loads are also asymmetric.

Despite the complexities of the surge event, rather detailed descriptions of its major features have been made possible through the use of high response pressure instrumentation. On the basis of these descriptions, several relatively simple models for surge-induced loads have been proposed for the following:

1 Compressor Case Loads
2 Airfoil Deflection
3 Thrust Mount and Thrust Bearing Loads

These models rely primarily on an empirical correlation of inlet surge overpressure and known pre-surge operating conditions. While simplistic in nature, they provide information which can be used to develop more complete analyses of the various engine structures and their response to the surge load.

Acknowledgment

The author wishes to thank Pratt & Whitney Aircraft Group, Division of United Technologies, for permission to publish this paper. He also acknowledges the helpful suggestions and criticism received from Professor Edward M. Greitzer and Mr. Pentti Nikkanen and the informative discussions with Mr. Michael D. Rudy.

References

1 Day, I. J., Greitzer, E. M., and Cumpsty, N. A., "Prediction of Compressor Performance in Rotating Stall," ASME JOURNAL OF ENGINEERING FOR POWER, Vol. 100, No. 1, Jan. 1978.

2 Marshall, F. L., "Prediction of Inlet Duct Overpressures Resulting from Engine Surge," *Journal of Aircraft,* Vol. 10, May, 1974, pp. 274–278.

3 Dini, D., DiGiorgio, A. and Cardia, S., "Gas Turbine Operating Conditions Due to an External Blast Wave Impulse," AGARD-CP-177 *Unsteady Phenomena in Turbomachinery,* April, 1976.

4 Benson, R. S. and Elshafie, H. M. F., "Nonsteady Flow Through a Square—Edged Orifice in a Pipe," *Journal Mech. Engineering Science,* Vol. 7, No. 4 1965.

5 Dadone, A. and Pandolfi, M., "Interaction of Travelling Shock Waves with Orifices Inside Ducts," *Int. J. Mech. Sci.,* Vol. 13, 1971 pp. 1–16.

6 Abdel—Ghany, S. M. and Horlock J. H., "Some Experiments on Steady and Unsteady Flow of Air Through Wire Gauzes," *Int. Journal Mech. Science,* Vol. 8, 1966, pp. 491–507.

7 Rudinger, G., *Nonsteady Duct Flow: Wave-Diagram Analysis,* Dover Publications, N.Y., 1969.

8 Turner, R. C. and Sparkes, D. W., "Complete Characteristics for a Single-Stage Fan," Paper 29, Thermodynamic and Fluid Mechanics Convention, April 1964, Institution of Mechanical Enginers, London.

H. E. Gallus
Prof. Dr.-Ing.
Mem. ASME

J. Lambertz
Dipl.-Ing.

Th. Wallmann
Dipl.-Ing.

Institute for Jet Propulsion and Turbomachines,
Technical University Aachen,
West Germany

Blade-Row Interaction in an Axial-Flow Subsonic Compressor Stage

This paper contains the results of the measurements of fluctuating pressures on the midspan profile surfaces of both rotor and stator blades for several points of operation. By the aid of rotating probes behind the rotor, the shapes of the rotor wakes were measured, too. All the measurements have been performed twice, at first with guide vanes in front of the rotor, and afterwards without the latter. The results of the measurements are evaluated with respect to the parameters involved, like Strouhal-number, reduced frequency, and circumferential Mach number. The flow analysis is done for various wake-fields behind the rotor correspondent to different operation points. Emphasis is given to the establishment of correlations for the blade-row interaction and to the comparison of the measured pressure distributions with computed results according to well-known theoretical approaches.

Introduction

The bladings of axial-flow compressors and turbines are excited to vibrations by pressure fluctuations unavoidably generated by the relative movements of the blade rows. In the case of resonances, a fracture of the blading causes much trouble as is well-known. The tendency to higher unit powers as well as the development of bladings for transonic flow led to the use of long and flat blades with a higher sensitivity to vibrational excitation.

Hence, there is an urgent need to overcome these difficulties by a more detailed and more reliable prediction of the real exciting forces of blade vibration. In spite of the enormous endeavours of industrial engineering and research institutions it is difficult to find a satisfying solution to the problem, as there are many important influences which have nonlinear interactions. As viscosity and its consequences are involved, a superposition of the individual potential-theoretic approaches made by several authors [1–6] does not meet the requirements of reality. A comprehensive and satisfactory theoretical prediction of the whole process of blade-row interaction will only be available, when viscous and mixing effects can be taken into account numerically. At present, the most effective procedure seems to be the separate development of idealized computation methods for each of the most important aspects of interaction. From the comparison with measurements, correlations will result which reveal the interdependency of the blade-row interaction and the most important construction parameters of neighboring blade rows downstream and upstream, taking into consideration the profile and blade-row geometry, the relative axial clearances, reduced frequency, and relative blade numbers as main parameters. The validity range of all the preliminary prediction methods for the fluctuation of static pressure distribution on the blade surfaces must be examined. Such investigations will provide a better or, at least, practicable approach to the urgent problem of predicting the excitation forces for the blade vibration on the one hand and the behavior of boundary layers and stall on the other.

A comprehensive survey of all the research activities in the field of unsteady flow in turbomachines was published very recently by M. Platzer [7]. Previous contributions of the authors to this topic were made in [8–13].

Experimental Investigations

Construction and Data of the Test Compressor Stage. The investigations have been made in a one-stage axial-flow compressor whose main data are listed in Table 1. The details of construction can be gathered from Fig. 1. The inlet guide vanes (IGV) can be removed in order to check their dynamic interaction with rotor and stator. Pneumatically measured static pressure distributions were taken from the blade profiles of the inlet guide vanes, M, of the stator, D, and of midspan of two adjacent rotor blades, F, G. One of the blades can be seen in Fig. 2. In addition, the flow vectors in the absolute system were measured by shifting five-hole probes in the axial clearances 0, 1, 2, and 3. The midspan vectors of the relative flow behind the rotor were determined by a three-hole probe rotating with the rotor and traversed circumferentially during rotation with the help of a planetary gear (L in Fig. 1). The distance between the outer holes of this probe is 1.98 mm (3.36 percent of the midspan rotor pitch). Therefore an error of the spatial attachment of the measured values is arising. Thus, the influence of the probe geometry is taken into account by an in-

Table 1

outer diameter	0.4218 m		
inner diameter	0: 0.160 m	3: 01922 m	
number of blades	$z_{IGV} = 14$	$z_R = 16$	$z_S = 14$
profile systematics	NACA-65-series		
design rotor speed	9500 rpm		

Contributed by the Gas Turbine Division and presented at the Gas Turbine Conference and Exhibit and Solar Energy Conference, San Diego, California, March 12–15, 1979 of THE AMERICAN SOCIETY OF MECHANICAL ENGINEERS. Manuscript received at ASME Headquarters December 18, 1978. Paper No. 79-GT-92.

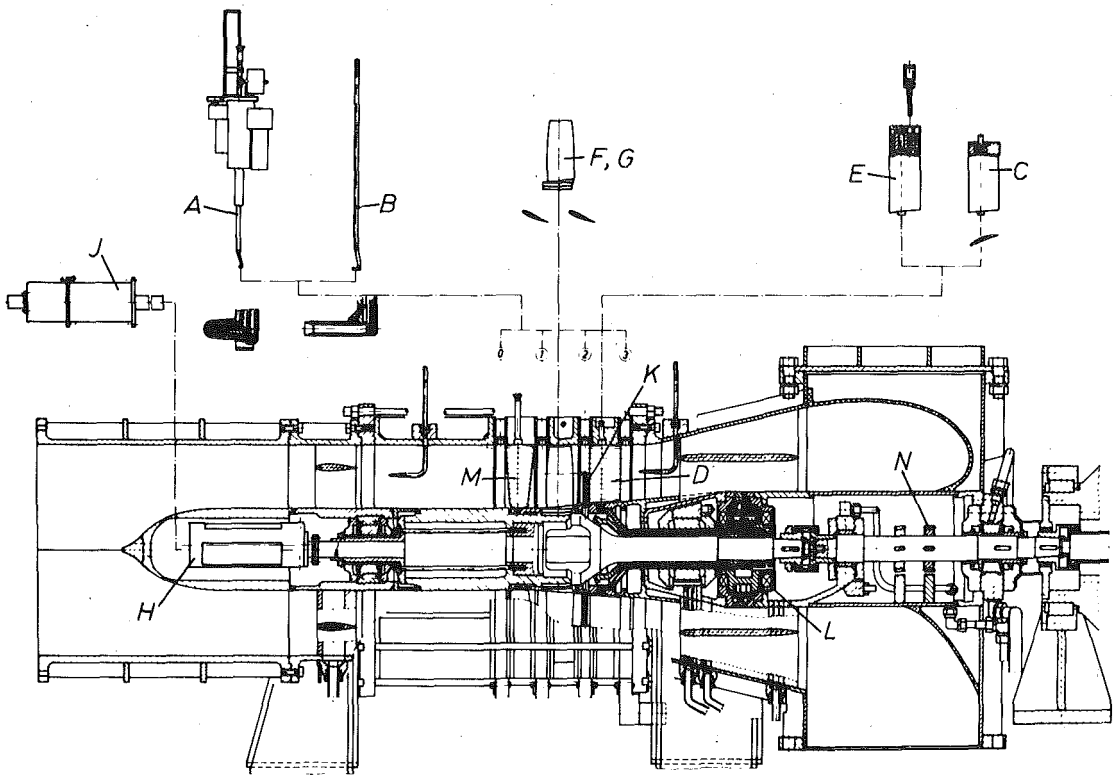

Fig. 1 Meridional section of the axial flow compressor stage

terpolation of the measured values at each probe hole in order to find the pressure in the local position of the central hole. This is a first step of controlling the results measured by probes that are large compared with the width of the wake. In a second step, further measuring techniques will be used to prove the results achieved by pneumatic probe measurements. The pressure transfer out of the rotor was done by a rotating transmitter (J in Fig. 1).

The *fluctuating pressure distributions* of the unsteady flow were measured in the midspan section on the surface of a stator blade and on the surface of two adjacent rotor blades. The fluctuating total pressures in the axial clearances between the blade-rows were measured by a semi-conductor total pressure probe.

All the fluctuating pressures were detected by "Kulite"-type semiconductor transducers which are small in size and of high natural frequency. Fig. 3 gives a view of these transducers mounted on the midspan surface of a stator blade. Five transducers are distributed both on the pressure surface and on the suction surface of the measuring blade. For the measurements in the rotor, only three transducers were mounted on the pressure side and four (Fig. 4) on the suction side of the adjacent blades both forming the measuring channel. The transducer positions along the midspan surface of rotor and stator blades are listed in Table 2. These positions can also be seen from Fig. 5, where the transducers of the rotor blades are represented in *one* rotor blade (for better correspondence with Fig. 12). Because of the small thickness of the blade profiles, the transducers could be mounted only in a certain distance from both the leading and the trailing edges. Fig. 5 additionally contains the measuring positions of the probes. Fig. 6 shows the measuring devices of the rotor in the mounting phase.

The electrical output of the pressure transducers is transferred out

Nomenclature

A = amplitude
b = width of the wake
b_p = width of the profile
c = chord length
c_L = lift coefficient
c_D = drag coefficient
f = frequency of oscillation, Hz
F_x = unsteady axial force
F_y = unsteady tangential force
h = velocity difference in the wake = $(w_0 - w_{min})/w_0$
l = wave length
L = lift
M = unsteady aerodynamic moment of forces
Ma = Mach number
n - number of revolutions
p = pressure
p_t = total pressure
r = radius
s = spacing
St = Strouhal number
t = time
T = period of $p(t)$
u = blade speed
v = absolute flow velocity
w = relative flow velocity
x = axial coordinate
x' = coordinates parallel to chord
y = circumferential coordinate
y' = coordinates normal to chord
α = angle of absolute flow
Δx = axial clearance between the blade rows
$\Delta\alpha$ = change of α
β = angle of relative flow
ν = frequency of oscillation
ξ = dimensionless coordinate of the profile contour
ρ = fluid density
φ = flow coefficient (= v_x/u)
ω^* = reduced frequency
ϕ = phase angle

Subscripts

0 = upstream of the IGV
1 = upstream of the rotor
2 = downstream of the rotor
3 = downstream of the stator
d = design point
D = deformation of wake
e = effective
IGV = inlet guide vanes
k = harmonic components
min = minimum
max = maximum
rel = in the relative system
R = rotor
S = stator
u = circumferential component

Superscripts

$\bar{}$ = time-averaged
$\sim$ = unsteady
$\|$ = absolute value

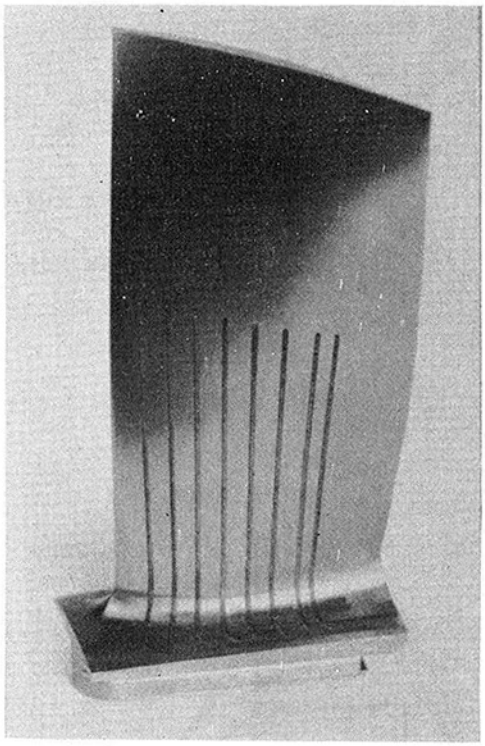

Fig. 2 Rotor blade provided with pneumatic midspan pressure taps

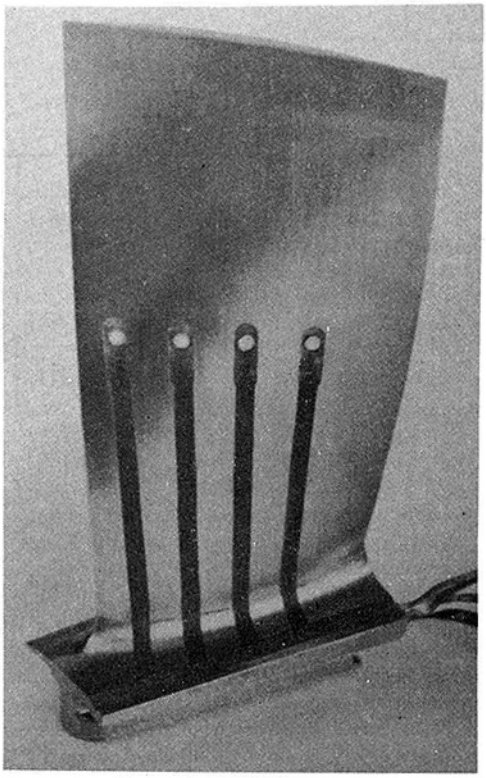

Fig. 4 Rotor blade with semiconductor transducers

of the rotor by a slipring transmitter (H in Fig. 1). The considerable temperature drift of the semiconductor transducers cannot be compensated completely. Therefore only the fluctuating portions of the pressures were measured in this way, whereas the measurement of the absolute values would have been less exact. In order to determine the latter, the local fluctuating pressure parts, were superposed on the local pneumatic pressure values measured at the same positions. According to Weyer [14], these local pneumatically measured pressures can be taken for the time-averaged local mean values, as long as the local pressure fluctuations are sufficiently small. This is ap-

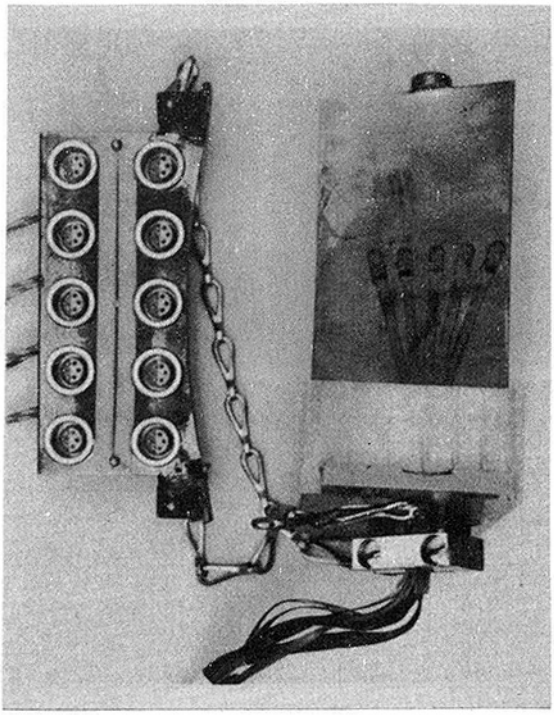

Fig. 3 Stator blade with semiconductor transducers

Table 2

	midspan section: r = 150 mm	
x/b_p	suction side	pressure side
rotor blades	0.089	0.140
b_{pR} = 51.5 mm	0.270	0.413
	0.464	0.681
	0.668	
stator blade	0.121	0.060
b_{pS} = 61.9 mm	0.266	0.210
	0.427	0.363
	0.589	0.528
	0.762	0.677

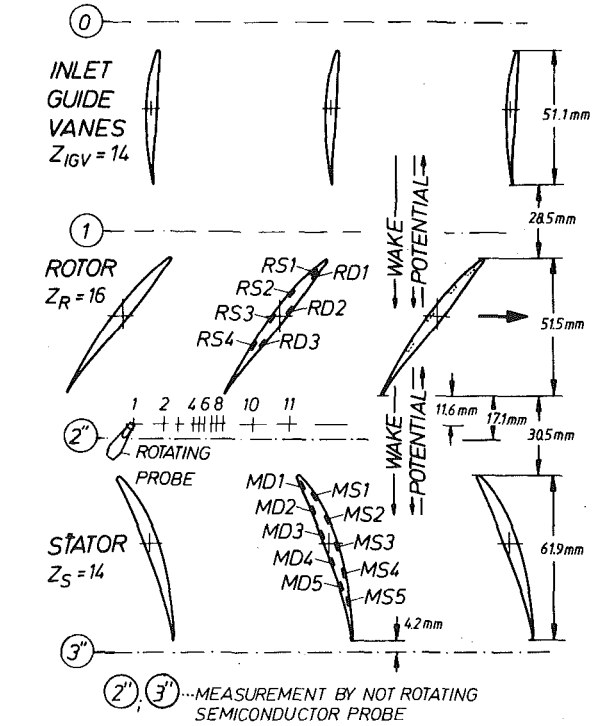

Fig. 5 Measuring positions in the midspan section of the compressor. The figure also indicates the rotor-stator configuration at the instant t = 0, corresponding to Figs. 11–13

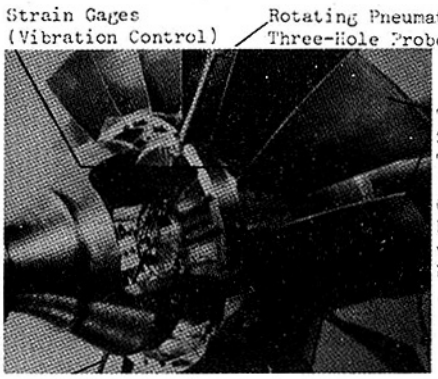

Fig. 6 View of measuring devices of the rotor in the mounting state

Table 3

with IGV		Stator		Rotor	
n rpm	φ_0	Sr[1)]	ω^*[2)]	Sr	ω^*
5000	0.80	1.22	3.02	0.79	2.10
6500	0.80	1.22	3.00	0.79	2.10
6500	0.70	1.32	3.22	0.82	2.05
6500	0.60	1.45	3.56	0.85	2.00
8000	0.80	1.22	3.01	0.79	2.10
without IGV		**Stator**			
n rpm	φ_0	Sr	ω^*		
3500	0.83	1.12	3.24		
5000	0.83	1.13	3.25		
6500	0.83	1.12	3.21		
6500	0.73	1.22	3.36		
6500	0.63	1.28	3.48		
8000	0.83	1.13	3.25		

1) $\mathrm{Sr} = \dfrac{n \cdot z \cdot c}{w}$

2) $\omega^* = \dfrac{\pi \cdot c}{l}$

plicable to the present case.

The measured signals are transferred either to a multi-channel tape recorder or directly to a frequency analyzer. For a time-lag recording of the periodical signals, some kind of sampling technique [8] was employed. By the latter, the averaged and retarded signals can be either plotted on a x-y-writer or given to the computer via an analog-digital-converter.

Program of Experiments. The experiments under consideration in this paper are aimed at the measurement of the blade-row interaction in the above described axial-flow compressor stage with and without inlet guide vanes. The interactions of the blade rows were measured in the midspan section.

At first, the inlet-flow conditions were determined for different speeds and flow coefficients by means of systems measuring pneumatically. Special attention was paid to the measurement of the shape of wakes originating from the trailing edges of the rotor blades. As mentioned before, that was done by the aid of a rotating three-hole probe continuously shifted along one spacing behind the rotor.

The unsteady total pressures were measured by the semiconductor probe situated in the axial clearances between the blade rows as shown in Fig. 5. The measuring positions of the unsteady pressures along the profile surfaces can be seen from Fig. 5, too. The test series were performed at different speeds and flow coefficients. In Table 3 the corresponding characteristic data of various points of operation are listed.

It should be mentioned that noticeable changes of the Strouhal-number or the reduced frequency with turbomachines of fixed geometry can be achieved merely by a change of the flow coefficient.

Experimental Results

The flow vectors measured by pneumatical five-hole probes in the axial clearances are represented in the midspan velocity triangles of

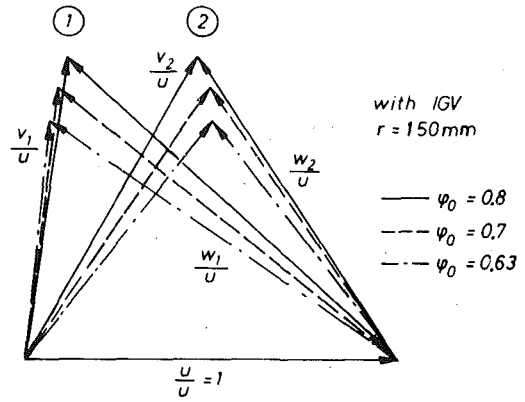

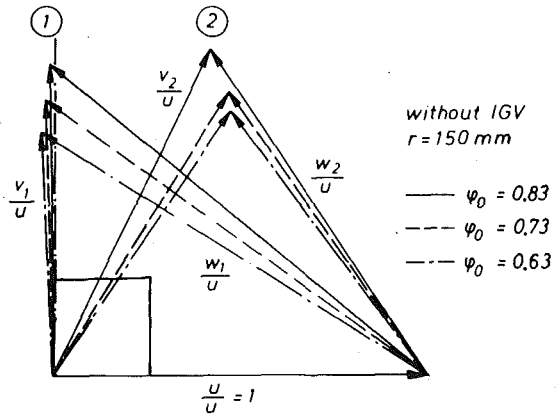

Fig. 7 Velocity vector diagram with and without IGV

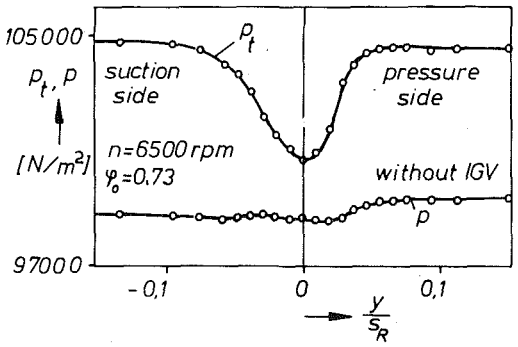

Fig. 8 Static and total pressure variation in rotor wake

Fig. 7, the upper demonstration being valid in case of the presence of the inlet guide vanes (IGV), the lower in case of inlet guide vanes being absent. It is obvious that the measured flow vector in front of the rotor with removed inlet guide vanes shows a very slight circumferential component opposite to the circumferential speed, whereas axial flow is expected. This might be caused by a beginning streamline curvature in the measuring plane near the leading edges of the rotor blading on the one hand and by a slight influence due to still existing wakes from the upstream airfoil struts on the other hand. A frequency analysis of the signals of pressure fluctuation at some measuring positions on the rotor blade surface could prove this, since the wakes from the struts upstream are still noticeable in the rotor.

In the following some results are presented which have been achieved by wake measurements with the aid of the rotating three hole probe in the relative flow system behind the rotor. From the characteristics of the three probe holes gained by the calibration measurements the total pressure, static pressure, and flow angle along the circumferential direction can be determined. As is shown in Fig. 8 the static pressure changes along the pitch.

Fig. 9 shows the distribution of Mach number and its circumfer-

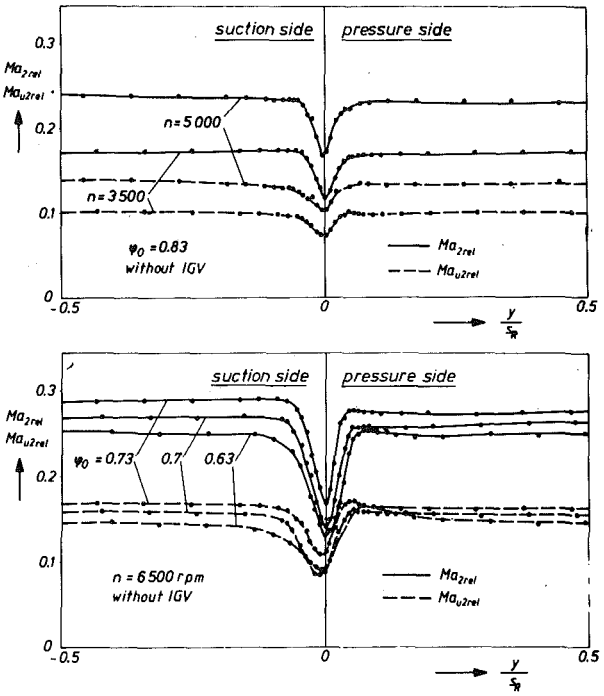

Fig. 9 Measured wakes in the relative flow behind the rotor

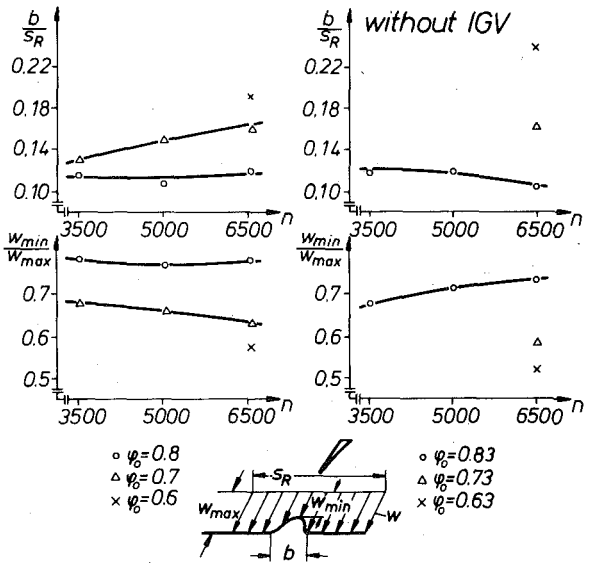

Fig. 10 Results of wake measurements behind the rotor

ential component along one rotor-blade spacing for different points of operation without guide vanes in front of the rotor. Point "0" of the abscissa was always settled in the velocity minimum. In all cases an asymmetry of the wake shape can be remarked. The slope of the velocity decrease within the wake is steeper on the pressure side of the profile than on the suction side. This tendency grows with decreasing flow coefficient. Fig. 10 summarizes the results of the wake measurements. It becomes obvious that for increasing throttling, i.e., decreasing flow coefficients φ_0, both the depth and the width of the wake grow considerably, while the influence of the rotor speed n is not as strong. The measurements without inlet guide vanes resulted in deeper wakes due to the increasing incidence angles for lower flow coefficients. It should be indicated that the above values in Figs. 9 and 10 were measured comparatively close behind the rotor, as can be seen in Fig. 5 which is to scale. On their way downstream into the stator, the measured shape of the wake is deformed to lower depth and increasing width. This kind of wake deformation behind cascades was investigated and reported in [15].

Fig. 11 shows results of measurements by total pressure probes of

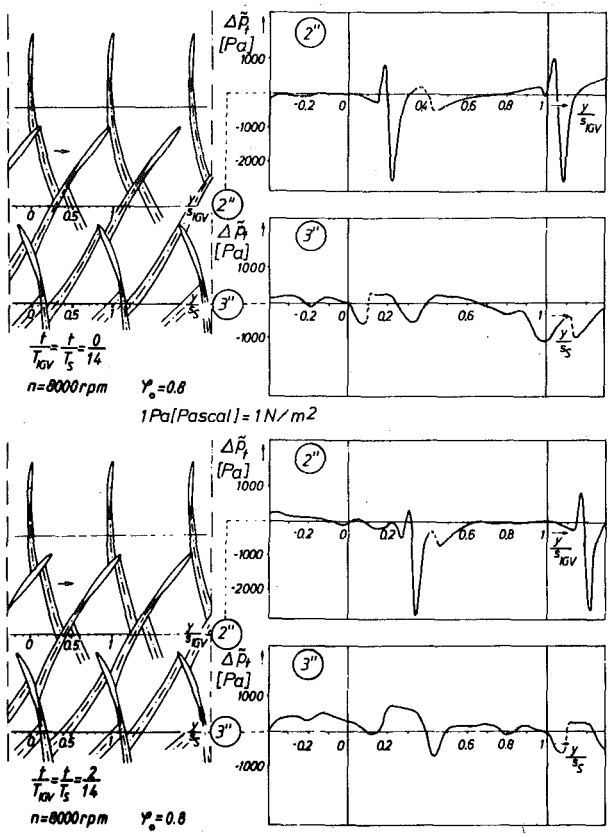

Fig. 11 Dynamic part of the total pressure at the rotor and stator exit at two instants in correlation to the cascade-wake-configuration

semiconductor type in the axial clearance behind the rotor and behind the stator. The fluctuating parts of the time-dependent periodic total pressures ($\Delta\tilde{p}_t = \tilde{p}_t - \overline{p}_t$) at two different instants of a rotor blade passing period (t/T_s = 0/14; t/T_s = 2/14) are plotted. Additionally the corresponding rotor-stator configurations are illustrated. The wake positions in the measuring sections 2 and 3 in. resulted from total pressure measurements. The propagation of the wakes within the cascades was derived from the course of assumed potential flow streamlines along the rims of the wakes. This includes the simplification that the rim streamlines are not disturbed by the wake material between them.

By the total pressure distributions measured in the plane 2 in. behind the rotor and represented in Fig. 11 one can recognize very distinctly the position of the rotor wakes at different instants. The wakes generated by the inlet guide vanes always cross the plane 2 in. within the region y/s_{IGV} = 0.4 . . . 0.6, and are nearly stationary. Generally, they are not registered by the system measuring only fluctuating pressures. Just at the moment when the wake generated by the inlet guide vane is interacting with the rotor wake in its pressure side region close to the measuring plane, the fluctuating part of the total pressure shows a relative minimum at about y/s_{IGV} = 0.45 (upper presentation of Fig. 11). Discussing the fluctuating component of the total pressure measured in plane 3 in. one can observe a relative minimum, wherever the chopped portions of a wake cross the measuring plane. These regions are passing with the circumferential velocity of the rotor. As was already published in [16], the wakes of blade rows can be observed in a reduced and deformed shape still behind some blade rows downstream.

Fig. 12 shows results of dynamic pressure measurements in the midspan section of the stator blade surface. The fluctuating component $\Delta\tilde{c}_L = \tilde{c}_L - \bar{c}_L$ of the time-dependent lift coefficient was calculated from the measured fluctuating pressures on the midspan blade surface. The relative rotor-stator position at t/T_S = 0 had been defined in Fig. 5. Pressures between the positions of the pressure transducers had to be interpolated; and at the leading and trailing edges it was assumed that the difference of the fluctuating pressures

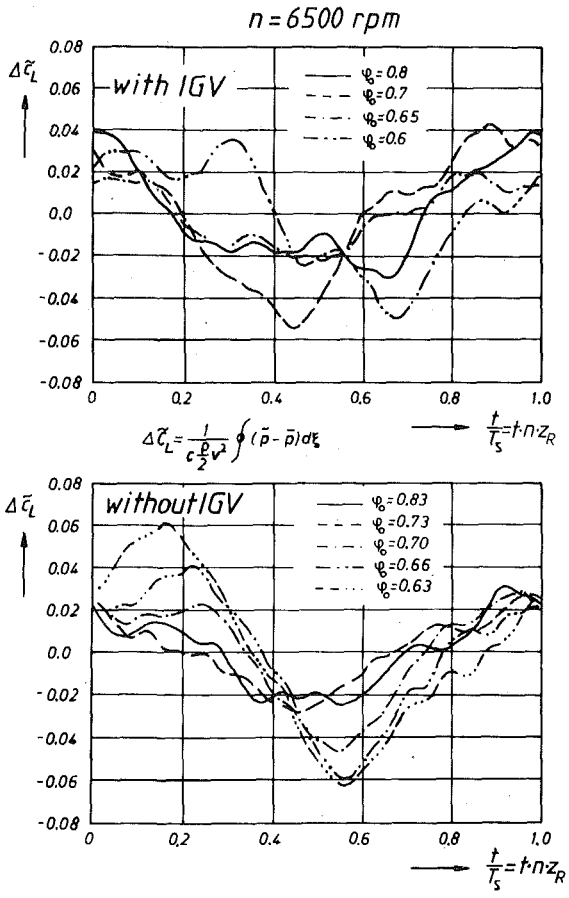

Fig. 12 Measured periodic fluctuations of the stator lift coefficient

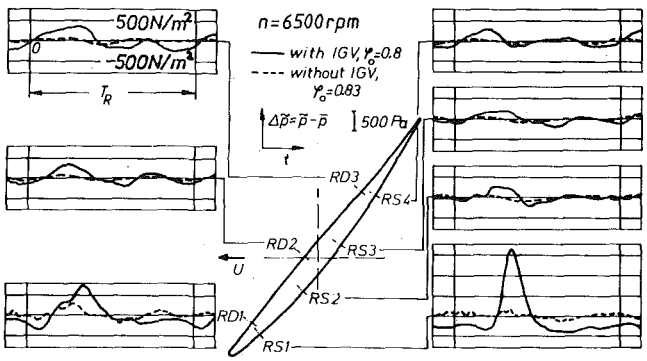

Fig. 13 Comparison of the measured periodic pressure fluctuations on the rotor blade surface with and without IGV

at the suction side and the pressure side of the profile becomes zero. The curves in the upper part of Fig. 12 are valid for the stage *with* inlet guide vanes and for constant rotational speed $n = 6500$ rpm, but for various flow coefficients $\varphi_0 = 0.8$; 0.7; 0.65; 0.6. There are remarkable changes of the tendency of the curves due to the fact that besides the varying angle of attack additional fluctuation is caused by the chopped wakes generated by the inlet guide vanes.

The curves in the lower part of Fig. 12 correspond to the stage *without* inlet guide vanes. We find a clear tendency to increase fluctuations with increased throttling. It becomes obvious that the fluctuating lift coefficient rises progressively with decreasing flow coefficients. This can be explained by the increase of the wake size on the one hand and by the increase of the mean level of the angle of attack on the other hand.

Fig. 13 contains results of the midspan measurements of the fluctuating static pressures on the rotor blade surface. The measuring positions were already presented in Fig. 5 together with the relative

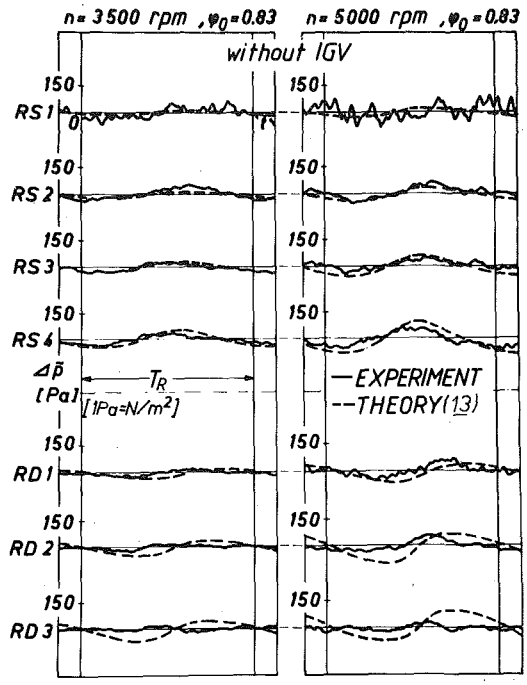

Fig. 14 Computed and experimental results of unsteady pressure distributions

blade-row configuration defining the instant $t = 0$. As Fig. 13 demonstrates for comparable data ($n = 6500$ rpm and $\varphi_0 = 0.8$ (with IGV) and $\varphi_0 = 0.83$ (without IGV)) the fluctuations are considerably smaller in case of removed inlet guide vanes. Here the measured unsteady effects are induced by the potential flow interaction between the rotor and the downstream stator.

The measured pressure fluctuation in the stage with inlet guide vanes in front of it shows a remarkable peak at the position of the first semiconductor transducer RS1 on the suction side. This phenomenon occurred in the unthrottled stage ($\varphi_0 = 0.8$) at all speeds and disappeared with throttling. The fluctuations in the downstream measuring positions were considerably smaller. Along the pressure side of the profile, the measurement shows a maximum at RD1, when the wake meets the leading edge. The amplitude is diminishing at RD2 and RD3. Because of the smaller number of semiconductor transducers mounted on the rotor blades, the computation of the fluctuating lift coefficients seemed to become too inaccurate and therefore was dispensed with. Instead, the results of the measurements are used for a comparision with the values calculated according to various theoretical approaches to predict the time-dependent pressure distribution on the profile surface.

Comparison of the Experimental Results with Well-Known Theoretical Approaches

The computation of the complete problem of blade-row interaction becomes very difficult due to the simultaneous appearance and the mutual interference of various influences of the fluctuating flow in turbomachines. Therefore it seems advantageous to restrict the first attempts of calculations to single parameters of main influence as follows:

1 potential flow interaction
2 interaction due to downstream wakes
3 influence of separating vortices

The extent of the various influences on the fluctuation of blade forces determined by single theoretical approaches is compared with measured results containing all the influences in their true physical superposition.

Fig. 5 indicates the most important blade-row interactions in the midspan section of the axial-flow compressor stage under consideration. Besides the potential flow and the wake interaction already pointed out, the vortices separating from the trailing edges of the blades must be mentioned.

Potential Flow Interaction. The first comparison of experiment and theoretical approach deals with a method for calculating quasi-steady, two-dimensional and incompressible potential flow proposed by Ispas and Lücking [13], members of the team of the authors. For the purpose of introducing the periodicity condition along the boundaries of the flow field, the calculation was extended to seven flow channels of the stator and eight flow channels of the rotor. It should be mentioned here that the blade number of the rotor is 16 and that of the stator is 14. The comparison was performed for the stage without inlet guide vanes. In this case, the fluctuations in the rotor are mainly caused by the potential flow retroaction of the downstream stator. The results of the computations for the rotational speeds n = 3500 rpm and n = 5000 rpm are plotted in Fig. 14 and compared with the experimental values obtained from measurements in the rotor. Due to the low speeds there is a certain conformity both of phase and amplitude. With increasing speed larger deviations occurred due to compressibility effects that are not taken into account by this theory.

In order to check the influence of a main parameter of unsteady flow, i.e., the axial clearance between the adjacent blade rows, the exciting blade forces were calculated for different axial gaps. Fig. 15 illustrates the results, and shows a progressive diminution of the force and moment of force amplitudes with increasing axial distances between the blade rows. The flow angles determined by measurement for n = 6500 rpm and $\varphi_0 = 0.83$ were kept constant for the computation. The decreasing excitation can be generally described by an exponential function

$$\left(\frac{F}{\bar{F}}\right)_k = K_1 \cdot e^{-K_2 \cdot (\Delta x/b_p)} \tag{1}$$

The constants K_1 and K_2 represent the flow conditions and the geometry of the stage. The following values of K_1 and K_2 were found for the first harmonic of the exciting force, for the rotor: $K_1 = 0.331$; $K_2 = 4.838$. For the stator: $K_1 = 0.287$; $K_2 = 6.391$.

The method of Lotz [5] was used for another comparison. Here the exciting forces are computed for two-dimensional incompressible potential flow, too. The procedure traces back to the fundamental approaches by Kemp and Sears [1], but considers the unsteady retroaction of the rest of the cascade including the trailing vortices. Because of the linearized theory, incidence angle, camber, and

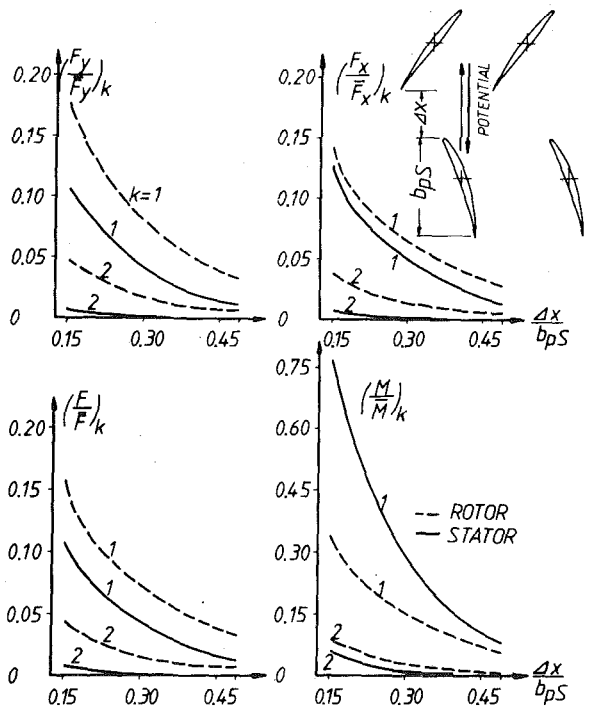

Fig. 15 Computed unsteady force and moment of forces due to potential-theoretic interaction as a function of the axial distance between the trailing edge of the rotor blade and the leading edge of the stator blade

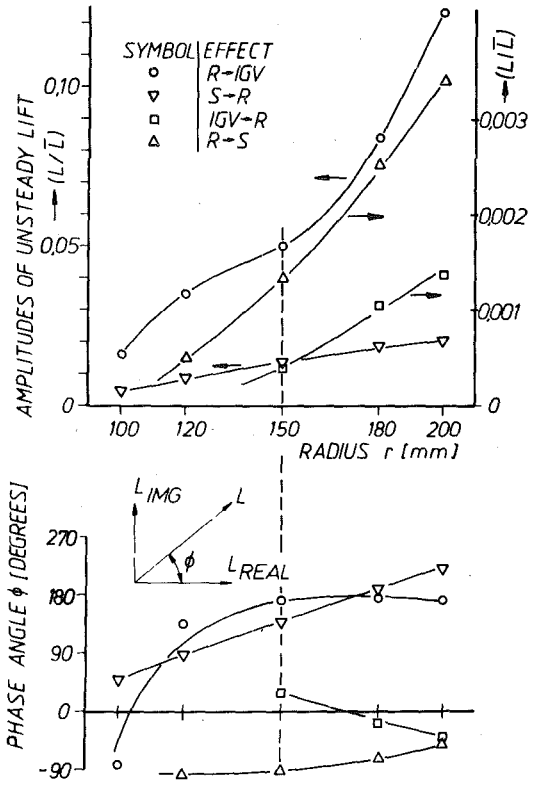

Fig. 16 Unsteady force and phase angle of the first harmonic of the potential-theoretic interaction as a function of the radius

thickness of the blades are assumed to be small. Fig. 16 shows the interacting lift forces computed according to this method. The results are demonstrated along the radius. It becomes obvious that the first harmonic of the potential flow interaction increases progressively with the radius. This is due to the strongly twisted rotor blade. The high amplitudes near the casing wall may cause blade vibrations.

The large amplitudes of the unsteady lift caused by the rotor in the inlet guide vanes are most remarkable. Generally, it can be stated that the downstream cascade acts more intensively upon the upstream cascade than vice versa. This can be explained by the vortex distribution on the blade. Considering, e. g., the lift distribution along a flat plate with incidence in the steady flow theory, the neutral point, for which the moment M is zero, lies at $x = c/4$, as is well-known. Moreover, it is a well-known fact that a stronger vortex intensity is needed for the compensation of the upwash induced by the adjacent blade near the trailing edge than for an upwash near the leading edge. Both afore-mentioned methods show good agreement with respect to stronger upstream interactions.

Wake Interactions. The axial-flow compressor stage under consideration has relatively large axial clearances between the blade-rows as shown in Fig. 5 which is according to scale. In this case, the wake interactions are dominating over the potential flow interactions. For large axial clearances between the blade rows, the first harmonics of the wake distribution, which are decisive for the excitation to vibrations, achieve relatively higher values. Fig. 17 shows the intensity spectrum of an idealized wake. The higher part of the first Fourier components of the total distribution is, however, compensated by the decreasing wake depth due to velocity equalization. For a qualitative demonstration we consider a wake of a single airfoil without camber. The process of equalization may be described by the following empiric equations [17]:

$$b = 0.68 \cdot c \sqrt{4 c_D \left(\frac{x'}{c} - 0.35\right)} \tag{2}$$

and

$$h = \frac{w - w_{\min}}{w} = 1.21 \cdot \frac{\sqrt{c_D}}{\frac{x'}{c} - 0.2} \tag{3}$$

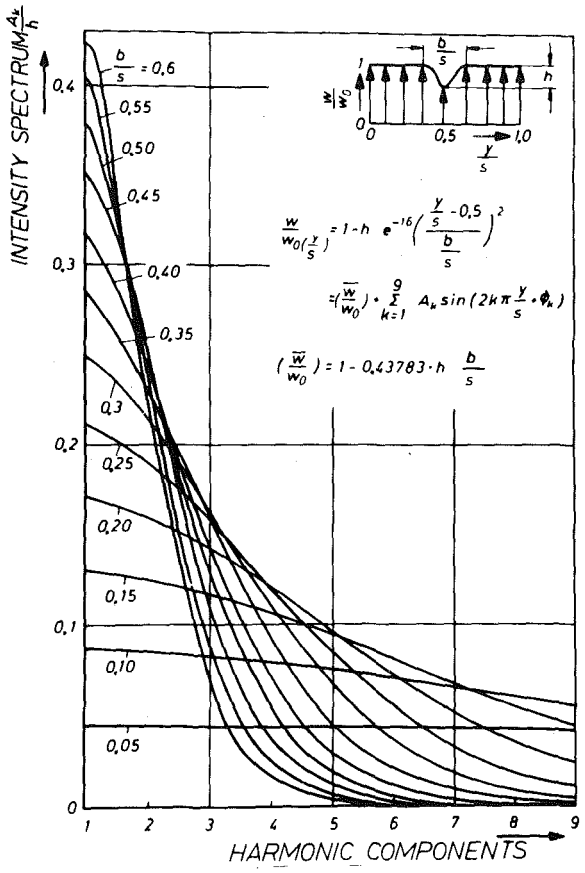

Fig. 17 Harmonic analysis of a wake given by an idealized function of the two parameters h and b/s

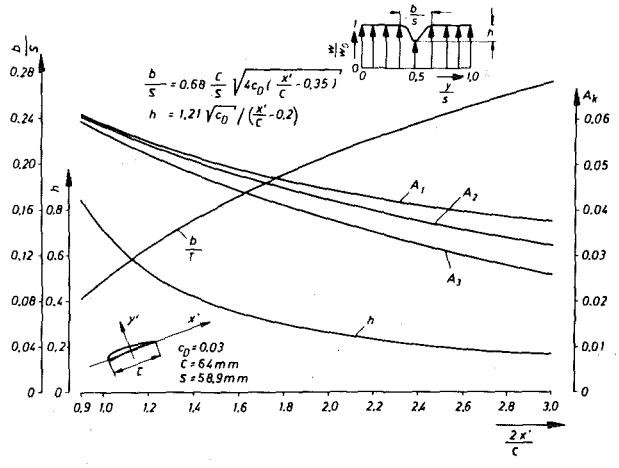

Fig. 18 Downstream change of the wake parameters

Using these formulas for the equalization of the velocity distribution in the wake, and assuming the velocity distribution in Fig. 17, Fig. 18 shows the calculated curves of the first three harmonics of the wake distribution downstream. In spite of the fast velocity equalization in the wake, the first order harmonics only diminish slowly. From this tendency the well-known experience can be derived that there is a wake interaction still far downstream.

The above approximations are valid for the flow behind stators. Rotor wakes seem to be equalized more quickly [15].

For a further comparison with the experimental results the authors followed well-known theoretical approaches by other authors, e. g., Naumann and Yeh [3], and Henderson [4], aiming at the computation of the wake interaction on the basis of the classic publications of Kemp and Sears [1]. Some characteristic assumptions of these approaches are:

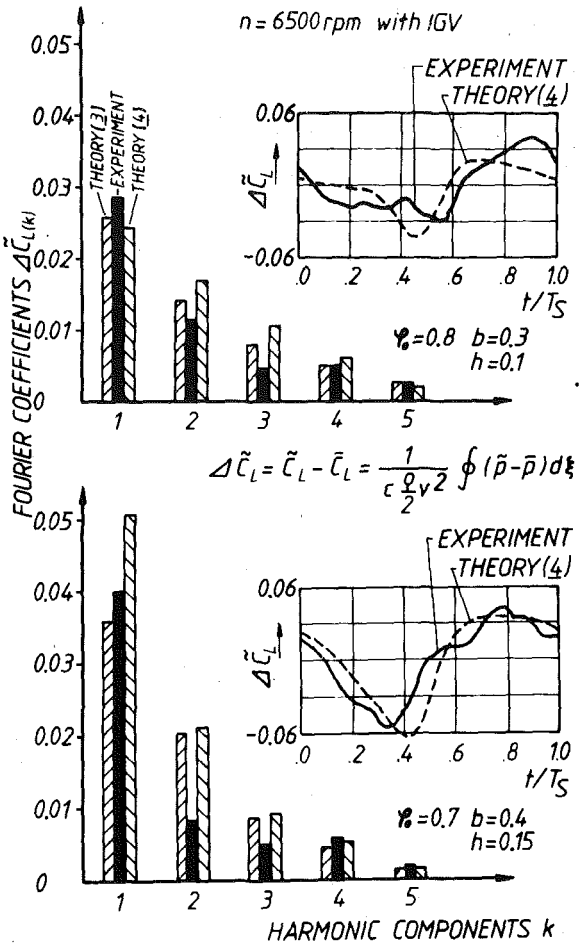

Fig. 19 Comparison of measured and predicted unsteady lift coefficient

- incompressible flow: one of the undoubtedly severest restrictions for a generally valid theory, but useful in the present case, as the Mach-numbers did not exceed 0.3 for the purpose of comparison,
- two-dimensional flow,
- thin profiles with only slight curvature: this condition is also nearly met in the investigated compressor,
- the blades are represented by their chords;
- single airfoil (Naumann and Yeh).

The periodic upstream flow of the blade is simulated by oscillations of perturbative velocities parallel and perpendicular to the chord. By the aid of the harmonic analysis any periodic perturbation can be decomposed into components. Then, the shares of the latter in the lift fluctuation can be determined as well. Because of the linearisation involved, the perturbations are supposed to be small, compared with the main flow.

In order to compute the components of lift fluctuation, the shape of the wake meeting the blade has to be analyzed. By experiments, the shape of the wake was measured in the axial clearance between rotor and stator. Between the planes of wake measurement and wake arrival at the leading edge of the following blade a further deformation of the measured wake occurs.

In order to overcome these difficulties, results of the investigations reported in [15] were used. At a speed of 6500 rpm and a flow coefficient of $\varphi_0 = 0.8$, the probe measurement yielded the dimensionless wake shape factors $b/s_R = 0.12$ and $w_{min}/w_{max} = 0.77$ (see Fig. 10). The consideration of the further deformation according to [15] leads to the values $(b/s_R) = 0.3$ and $(w_{min}/w_{max})_D = 0.9$. The results of this way of procedure are shown in Fig. 19. Additionally, the results for $\varphi_0 = 0.7$ are plotted there.

Certain differences between experimental and theoretical results crop up with respect to the first three harmonic components of the unsteady lift fluctuation, especially for decreasing flow coefficients.

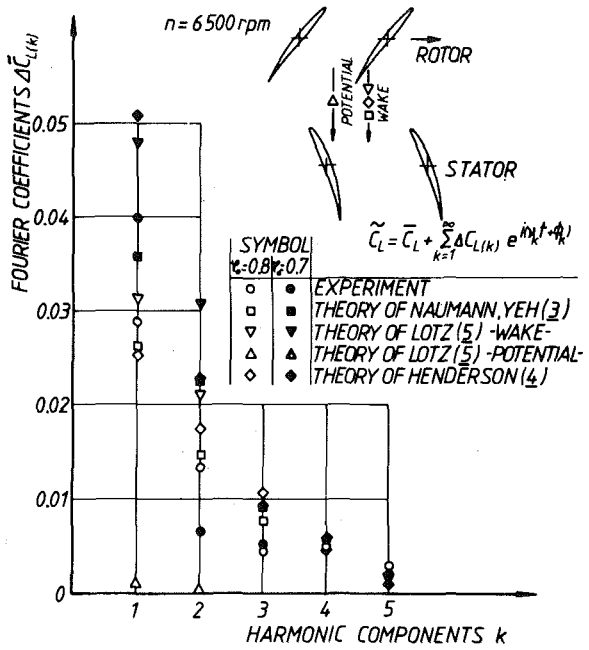

Fig. 20 Comparison of interaction effects, measured and computed according to methods of several authors

That is due to the fact that the wake becomes broader and deeper with decreasing φ_0 (see Fig. 10). With a broadening wake, the first harmonics are increasing, whereas the higher harmonics are decreasing (see Fig. 17). The influence of the relative width of wake b/s on the intensity lessens for increasing harmonics. This tendency can also be concluded from the experimental results plotted in Fig. 19. The comparison of measured and calculated values shows better agreement for the higher harmonics which obviously agree more closely with the theoretical assumption of small perturbative velocities. Considering the accuracy of the experimental results plotted in Fig. 19 (Fig. 12) it should be pointed out that the fluctuating lift coefficient was determined by integration of the pressure distribution along the profile contour on the basis of only ten semiconductor transducers.

Comparison of Various Results. Fig. 20 contains the Fourier coefficients of the fluctuating lift coefficient for the interactions of rotor and stator at a rotational speed n = 6500 rpm in conformity with various theoretical approaches made by several authors. The comparison shows for the stage under consideration that in this case (large axial clearance of 48 percent of rotor chord length) the potential flow interaction has only a small share in the lift fluctuation (see also Fig. 15). Moreover, it became obvious that the harmonics caused by wake interaction decrease more slowly. This results from the wake zones, which are small compared with the spacing. For a smaller axial distance of the blade rows the higher harmonics would have higher values. Then, the temporal sequence of wake zones seen from the blades of the downstream cascade, approaches a periodic sequence of small impulses whose harmonics do not vanish at all.

Conclusions

On the basis of the above-mentioned methods the fluctuation forces were computed for various points of operation. The conclusions from these results are the following:

1 The well-known fact of decreasing fluctuation forces with increasing axial clearances was proved quantitatively by the computation for potential flow interaction (see Fig. 15). The higher harmonics of the potential flow interaction are decreasing very fast. In most cases the amplitude of the second harmonic amounts to only 20 to 40 percent of that of the first one. The influence of higher harmonics on blade vibration is small, since, because of the high rotor and stator blade numbers in thermal axial-flow turbomachines, resonances of the higher exciting harmonics with the eigenfrequencies of the blades will appear only for very small rotational speeds.

2 The downstream cascade induces stronger potential flow interaction in the upstream cascade, since a velocity perturbation induces higher lift fluctuations near the trailing edge than near the entrance edge.

3 Stronger throttling leads to increasing wake sizes and consequently to stronger fluctuation forces.

4 For the stage under consideration in this paper, having a large axial clearance, the wake interaction proves to be the main source of fluctuation forces, as is convincingly demonstrated in Fig. 20. In this stage, the results of computation methods considering only the influence of the wakes meet the experimental results, at least to some extent, astonishingly well. On the one hand this is due to the fact that for compressor blades with a small camber as in the investigated stage the conditions for a comparison of measured results with results of linearized theoretical approaches correspond better than for turbine profiles with a large camber. On the other hand the comparison was performed for incompressible flow conditions. Moreover, the large axial clearance led to a negligible small potential flow influence compared with that of the wakes. At present, measurements and computations without linearization are performed in order to compare the above-mentioned influences of blade-row interaction for compressible flow in compressor and turbine stages.

References

1 Kemp, N. M., and Sears, W. R., "The Unsteady Forces due to Viscous Wakes in Turbomachines," *Journal of the Aeronautical Sciences*, Vol. 22, No. 7, 1955, pp. 478–483.

2 Horlock, J. H., "Fluctuating Lift Forces on Airfoils Moving through Traverse and Chordwise Gusts," *ASME Journal of Basic Engineering*, 1968, pp. 494–500.

3 Naumann, H., and Yeh, H., "Lift and Pressure Fluctuations of a Cambered Airfoil under Periodic Gusts and Applications in Turbomachinery," ASME JOURNAL OF ENGINEERING FOR POWER, 1973, pp. 1–10.

4 Henderson, R. E., "The Unsteady Response of an Axial Flow Turbomachine to an Upstream Disturbance," Ph.D. Diss., Engineering Department, University of Cambridge, 1972.

5 Lotz, M., and Raabe, J., "Blade Oscillations in One Stage Axial Turbomachinery," ASME *Journal of Basic Engineering*, Dec. 1968, p. 485.

6 Lienhart, W., "Berechnung der instationären Strömung durch gegeneinander bewegte Schaufelgitter und der instationären Schaufelkräfte," VDI-Tagung Braunschweig 1973, VDI-Berichte, Nr. 193.

7 Platzer, M. F., "Unsteady Flows in Turbomachines—A Review of Current Developments," *AGARD Conference Proceedings* No. 227, Ottawa, Canada, 1977.

8 Gallus, H. E., "Results of Measurements of the Unsteady Flow in Axial Subsonic and Supersonic Compressor Stages," *AGARD Conference Proceedings* No. 177, Monterey: Calif. (USA), 1975.

9 Gallus, H. E., Kümmel, W., and Wallmann, Th., "Messungen zur Wechselwirkung von Laufrad- und Leitrad-Beschaufelungen in einer Axialverdichterstufe," VDI-Berichte, Nr. 164, 1976, S. 103–112.

10 Gallus, H. E., Kümmel, W., Lambertz, J. and Wallmann, Th., "Measurement of the Rotor-Stator-Interaction in a Subsonic Axial-Flow Compressor Stage," R. F. M., Symposium I. U. T. A. M., sur l'Aeroelasticité dans les Turbomachines, Paris, Oct. 1976.

11 Gallus, H. E., Lambertz, J., und Wallmann, Th., "Experimentalle Untersuchung der Relativströmung im Laufrad einer Axialverdichterstufe," *Forschungsbericht des Landes* NRW Nr. 2711, 1978, Westdeutscher Verlag, G.m.b.H., Leverkusen-Opladen.

12 Gallus, H. E., Lambertz, J., und Wallmann, Th., "Untersuchungen der instationären Vorgänge in einer subsonischen Axialverdichterstufe infolge Laufrad-Leitrad-Interferenz," Mitteilung Nr. 78-01 des Instituts für Strahlantriebe und Turboarbeitsmaschinen der RWTH Aachen, Juli 1978.

13 Ispas, I., und Lücking, P., "Berechnung der inkompressiblen Potentialströmung in einer axialen Gitterstufe mit Hilfe eines Differenzvenverfahrens," Mitteilung Nr. 77-08 des Instituts für Strahlantriebe und Turboarbeitsmaschinen der RWTH Aachen, Okt. 1977.

14 Weyer, H., "Bestimmung der zeitlichen Druckmittelwerte in stark fluktuierender Strömung, insbesondere in Turbomaschinen," Diss. TH Aachen, 1973.

15 Reynolds, B., Lakshminarayana, B., and Ravindranath, A., "Characteristics of the Near Wake of a Compressor or Fan Rotor Blade," AIAA Paper No. 14, 1978.

16 Wagner, J. H., Okiishi, T. H., and Holbrook, G. J., "Periodically Unsteady Flow in an Imbedded Stage of a Multistage, Axial-Flow Turbomachine," ASME Paper No. 78-GT-6.

17 Silverstein, A., Katzoff, S., and Bullivant, W. K., "Downwash and Wake behind Plain and Flapped Airfoils," NACA Rep. 651.

A. M. Yocum
Research Assistant.
Mem. ASME

R. E. Henderson
Assoc. Professor of
Mechanical Engineering.
Mem. ASME

Applied Research Laboratory,
The Pennsylvania State University,
Post Office Box 30,
State College, PA 16801

The Effects of Some Design Parameters of an Isolated Rotor on Inlet Flow Distortions

A study of the effects of rotor-blade geometry, steady loading, and distortion wavelength on the distortion flow field upstream and downstream of an unstalled isolated rotor shows that the attenuation of the distortion as it passes through the rotor is a function of the blade stagger angle and the distortion-reduced frequency or the ratio of rotor blade spacing to the distortion wavelength s/ℓ. Maximum attenuation occurs when $s/\ell = 0.5$ and increases with increasing stagger angle. Little influence of rotor incidence angle or steady loading was observed.

Introduction

The term distorted inlet flow is generally used to describe the flow entering a turbomachine in which there are radial and/or circumferential variations in the time-mean total pressure, static pressure, and velocity and/or temperature. Although both radial and circumferential distortions are present in compressors and fans, the circumferential distortion poses an additional complication, since the flow relative to a moving blade row is time-dependent or unsteady. The causes of distorted inlet flows are numerous and are especially prevalent in jet aircraft engines, since the engines must operate under many different conditions. For example: a vortex can be created in the inlet of an engine if the engine is drawing air from a boundary layer; flow separation may occur in an engine inlet during a maneuver of the aircraft; or wakes may be caused by protuberances in the inlet. Regardless of the cause, distorted inlet flows are detrimental to the performance of an engine, since they cause noise and vibration and a reduction in the efficiency and in the stability or stall limits of the engine.

Designers of axial-flow fans and compressors should know if distorted flow is either attenuated or amplified through each blade row and if the performance and the stability limit are affected. While theoretical predictions can be valuable in understanding the distortion phenomenon and in making some design decisions, present theories have several shortcomings when used in the design process. For example, when trying to predict distortion attenuation, performance loss, or stability limits, methods such as the parallel compressor theory [1, 2] and acutator disk theory [1] require that the steady performance of the blade row or compressor be known. This means that the designer must obtain this information from a similar existing engine with fixed design parameters—blade stagger angle, solidity, camber, and incidence angle. In addition, these theoretical methods are usually based on a quasisteady analysis. When the unsteady response of the blades is included [1, 3], an isolated-airfoil or actuator-disk analysis is used that neglects the unsteady cascade effects.

Contributed by the Gas Turbine Division and presented at the Gas Turbine Conference and Exhibit and Solar Energy Conference, San Diego, California, March 12–15, 1979 of THE AMERICAN SOCIETY OF MECHANICAL ENGINEERS. Manuscript received at ASME Headquarters December 18, 1978. Paper No. 79-GT-93.

The purpose of the present study was to provide some fundamental experimental data to describe the response of an unstalled isolated rotor as a function of the blade stagger angle, steady loading, and the type of distortion, i.e., square-wave or sinusoidal of varying wavelength. Detailed circumferential surveys were made of the time-mean flow upstream and downstream of an isolated rotor with various operating and geometrical parameters and operated in various inlet flow distortions. These surveys were conducted only at the rotor mean radius representing, therefore, a high hub/tip ratio rotor. These data were then analyzed to determine the values of these parameters that result in attenuation of the distortion as it passes through the rotor.

Since an isolated rotor was employed, the distortion characteristics of an isolated rotor should be contrasted to those of a single stage and a multi-stage machine; i.e., what is the importance of this study? Ehrich [4] points out that by neglecting blade-row interference effects, it is possible to study the quasisteady influence of the rotor on the distortion characteristics of a stage by considering the characteristics of an isolated rotor. For design purposes, it is important to know the effect of these rotor parameters on the distortion; i.e., which parameters are most significant in producing an attenuation of the distortion.

In applying isolated rotor data to a multi-stage machine, the important parameter is the axial gap between blade rows. If the axial gap is small, there is no opportunity for flow redistribution to occur. In this case, the distortion response is governed by the overall compressor characteristic rather than the characteristic of each stage even if each stage has a different characteristic [5]. However, even if the axial gaps are small, flow redistribution is possible within a multi-stage machine due to crossflows in cavities such as the roots of shrouded stators or bleed plenums. These crossflows can be significant as pointed out by Mazzaway [2].

This study experimentally investigates the influence of the operational and geometrical parameters of an isolated rotor. The major emphasis is placed on the unsteady response of the rotor to the spatially varying distortions and the changes in the unsteady response with distortion wavelength, i.e., reduced frequency or intrablade frequency, which were not considered by Ehrich [4]. The values of intrablade frequency at which the major influence of the unsteady effects were observed in this study are greater than those which are

usually of a practical interest for compressor stability considerations. Therefore, this study is of most significance in aeroelastic and noise related problems.

Experimental Apparatus

Axial-Flow Research Fan. The experiments were conducted in a facility referred to as the Axial Flow Research Fan (AFRF). This facility was designed specifically for studying unsteady flow phenomena in turbomachinery and, thus, the test rotor and the facility are large enough to permit the blades to be instrumented and flow surveys to be made. Fig. 1 shows the key components and dimensions of the facility; a detailed description is contained in [6].

The AFRF is a subsonic, incompressible, open-circuit wind tunnel with an annular cross section whose inlet was carefully designed to provide, in the absence of the disturbance-producing screen, a steady, uniform flow to the annulus. For studies involving distorted inlet flows, screens are placed in the inlet to produce sinusoidal or square-wave circumferential variations of total pressure. The design and the performance evaluation of these screens are described in [7]. Immediately downstream of the screens, a section of the annulus serves as a settling section where small velocity fluctuations and the static pressure gradient mix out. The section between the screen and test rotor also isolates the rotor from the screen, which is very important, since it is well known that a rotor will strongly alter the upstream flow when the inlet flow is nonuniform.

The test rotor employed in this study was designed to produce a zero circumferential-mean total-pressure rise at its design operating condition in an ideal uniform flow. This design criterion enables accurate comparisons with unsteady cascade theories, which are usually restricted to zero or lightly loaded blades. The blades have no camber and are simply twisted as a function of radius to yield a zero incidence with a 45 deg stagger angle at the mean radius of 7.75 in. (19.69 cm). The blades have a 6.0 in. (15.24 cm) chord, a symmetrical Cl thickness distribution with a ten percent maximum thickness, and a 0.442 hub-to-tip ratio.

For the tests conducted in this study, the rotor was assembled with 12 blades, which results in a space-to-chord ratio of 0.68 at the mean radius. All of the measurements presented in this paper were made at the mean radius of the rotor with the rotor rotation in the direction of increasing values of circumferential position θ. Blade stagger angle was varied by rotating the blades in the hub. In addition to the 45 deg stagger angle, stagger angles of 35 deg and 55 deg were also evaluated. In these configurations, the blade angles at radii other than the mean radius are at an off-design condition that results in three-dimensional flows; however, the deviation of the blade angle from a design based on that particular stagger angle is not large. Therefore, the three-dimensional effects are small, and it is justifiable to consider the flow as two-dimensional at the mean radius. All of the data measured in this study were obtained with the rotor operating in the linear portion of its operating characteristic.

Downstream of the test rotor, another section of annulus isolates the test rotor from influences of the auxiliary fan and throttle. The mean flow velocity in the facility is controlled by the speed of the auxiliary fan. Since the mean flow velocity and the speed of the test rotor are independently controlled, the flow incidence angle to the test rotor blades can be varied. The test rotor can thus be operated with a nonzero incidence angle, which results in a steady load on the blades. This enables the facility to be used to investigate the effects of steady loading on the unsteady response of the blade row.

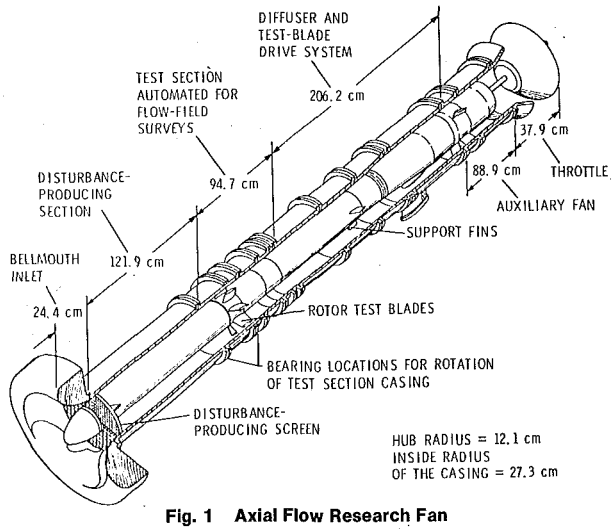

Fig. 1 Axial Flow Research Fan

The casing surrounding the test rotor can be rotated which permits circumferential surveys of the flow to be made by attaching instrumentation to the casing and indexing it in preselected increments. The indexing of the casing is done electrically and is automatically controlled by the data acquisition system.

Instrumentation. As previously mentioned, the approach taken to measure the response of the rotor was to conduct time-mean measurements of the circumferential variation of the flow upstream and downstream of the rotor with two five-hole probes. The probes were located at the two Stations 1-D and 15, which are axially located 0.137 chord lengths upstream of the rotor and 0.82 chord lengths downstream of the rotor, respectively, at the mean radius. For all measurements, the probes were radially positioned with the center hole of the probe at the mean radius of the annulus.

Five-hole probes were employed since they enable the total pressure, static pressure, and the three components of velocity to be determined. These probes were commercially available United Sensor prism probes.

The five-hole probes were used in the non-nulling mode, which means the probes had a fixed orientation with respect to the casing during the tests. The two flow angles and the true total and static pressure are then calculated from the five pressure measurements, through the use of a detailed calibration conducted in an uniform flow. This calibration technique is described in [8]. From these data, four pressure coefficients, a yaw coefficient, a pitch coefficient, a total-pressure coefficient, and a static pressure coefficient are determined. These coefficients, which are a function of the yaw and pitch angle, completely describe the response of the probes to the known flow.

With the probe response known, the yaw and pitch angles of an unknown flow can now be determined through the use of the calibration data. After the two angles are known, the total and static

Nomenclature

A = distortion amplitude defined by equation (2)
A_n = Fourier amplitude of n^{th} harmonic
c = chord length, ft, m
i = angle of incidence, deg
ℓ = distortion wavelength in circumferential direction, ft, m
ℓ_c = distortion wavelength along the blade chord, ft, m
P_{atm} = atmospheric pressure, psf, pascals
P_s = static pressure, psf, pascals
P_T = total pressure, psf, pascals
$P_{T_{15}} - P_{T_{1D}}/\frac{1}{2}\rho V^2_{x_{\text{avg}}}$ = pressure rise coefficient
r_m = mean radius, ft, m
s = blade spacing, ft, m
U = blade speed at mean radius, fps, mps
V_x = axial velocity, fps, mps
$V_{x_{\text{avg}}}$ = circumferential averaged axial velocity, fps, mps
$V_{x_{\text{avg}}}/U$ = flow coefficient
V_θ = tangential or circumferential velocity, fps, mps
W_m = mean relative velocity, fps, mps
x = axial position, ft, m
θ = circumferential position, deg
ν = distortion frequency, $= 2\pi U/\ell$
ξ = stagger angle, deg
ρ = mass density, slugs/ft^3, kg/m^3
ϕ = Fourier phase angle, deg

Superscripts

$'$ = perturbation quantity, $p_T = \bar{p}_T + p'_T$
$\bar{\ }$ = time or circumferential mean

Subscript

$-\infty$ = without the rotor installed

pressure coefficients are interpolated from the calibration data, and the two pressures calculated. The resultant velocity is calculated from the Bernoulli's equation and then broken into its components using the known angles. This procedure is described in [8].

One disadvantage of a five-hole probe is that the calibration curves are usually weakly dependent on velocity or Reynolds number; however, calibrations over a range of Reynolds numbers revealed that, for the range tested, only the static pressure coefficient was affected—and that by approximately two percent. These data were used for calculating correction curves based on the average static-pressure coefficient for the range of Reynolds numbers experienced by the probes.

The repeatability of the measurements made with the five-hole probes and the pressure-sensing system was determined during the calibration of the probes. Compared to a known pressure source, the pressure-sensing system demonstrated a repeatability of 0.2 percent. Subsequent calibration of the five-hole probes in a known flow field showed their repeatability to be 2.0 percent of the reference dynamic pressure.

Experimental Studies

The experimental program consisted of three phases. The first phase involved the measurement of the steady performance of the rotor with uniform inlet flow. This information was necessary to determine the performance degradation caused by the flow distortions and to predict the distortion variation with an actuator-disk model. To determine the rotor performance, flow measurements were made at the mean radius of the rotor both upstream and downstream of the rotor over a range of flow coefficients.

The second phase of the experiments consisted of measuring the distortion produced by the screens when the rotor was removed. Circumferential flow surveys were conducted at the same axial locations as those when the rotor was present, thus providing a direct reference with which to determine the changes caused by the rotor. The determination of the flow-field characteristics without the rotor installed is very important, since the rotor will alter both the inlet and exit flows. A true measure of the velocity-distortion attenuation requires a knowledge of the flow in the absence of the rotor. The auxiliary fan of the AFRF provided the through-flow for conducting this phase of the program.

Six different screens were used to produce 1-, 2-, 4- and 6-cycle sinusoidal distortions and 90 and 180 deg square-wave distortions. The amplitudes of all the velocity distortions were approximately 20 percent of the circumferential-mean velocity. The sinusoidal distortions were selected to investigate the affects of distortion wavelength or reduced frequency. The two square-wave distortions were investigated because they are more likely to be encountered in practice and have been investigated in many previous studies.

The third phase of the program consisted of conducting circumferential flow surveys both upstream and downstream of the rotor while it was operated in a distorted inflow. A parametric study was conducted employing each of the six distortion screens; the three rotor configurations with blade stagger angles of 35, 45 and 55 deg; and four values of mean loading or incidence angle. Two of the incidence angles were selected near the condition of zero loading; a zero incidence angle and a value corresponding to the condition of zero total-pressure rise. A zero total-pressure rise requires a small positive incidence to overcome the total pressure loss due to the viscous and induced effects. In addition to these loading conditions, two higher values of incidence angle were investigated to evaluate the influence of steady loading on the rotor's response.

Typical Experimental Results. Typical results showing the circumferential variation of axial velocity ratio ($V_x/V_{x_{avg}}$) without the rotor installed are shown in Fig. 2 for the four-cycle sinusoidal distortion at the two axial measurement stations. The axial velocities at the two locations agree within three percent. Similarly the circumferential variation of the total-pressure coefficient is nearly constant, since the static pressure was circumferentially uniform at both axial stations. For these reasons, it can be concluded that any flow redistribution caused by the screen occurs upstream of the

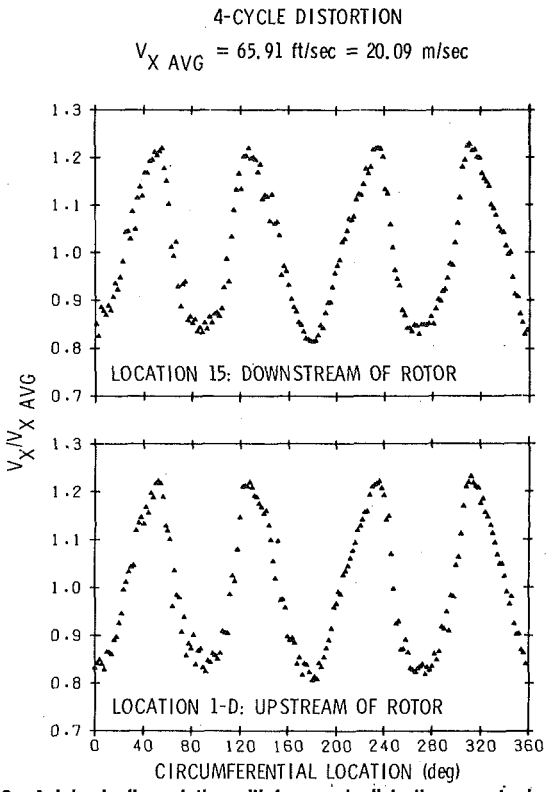

Fig. 2 Axial velocity variation with four-cycle distortion, no rotor installed

measurement locations, and the viscous effects of the flow are not important over the short distance between the measurement locations. Therefore, any change observed when the rotor is installed will be due to the rotor alone. The fact that the velocity and total-pressure profiles at the two locations are nearly identical also indicates the precision of the probe calibrations and instrumentation.

Typical results from the third phase of the experiments (for a four-cycle distortion), are presented in Figs. 3(*a*)–3(*d*), where the axial velocity, circumferential velocity, total-pressure and static-pressure coefficients are plotted, respectively. A comparison of the axial velocity in Figs. 2 and 3(*a*) for Location 1-D shows that the axial-velocity distortion was attenuated upstream of the rotor. Accompanying the axial-velocity distortion attenuation upstream, Figs. 3(*b*) and 3(*d*) reveal that a variation in the circumferential component of velocity is created, and a static pressure gradient arises. These two changes are necessary to maintain the same total-pressure distortion upstream of the rotor. Downstream of the rotor (Location 15), the axial-velocity distortion is observed to have undergone a further reduction in amplitude, the circumferential velocity is almost uniform, and the static pressure is constant.

A comparison of Fig. 3(*c*) with similar data obtained without the rotor installed shows that the total-pressure distortion upstream of the rotor is unchanged, as would be expected, since no work has been done on the flow. The total-pressure data for Location 15, however, does show that the amplitude of the distortion is significantly reduced by the rotor. Plots similar to those presented in Figs. 3(*a*)–3(*d*) were produced for each of the other tests. The basic phenomena discussed above were also observed for these tests. A complete description of these tests and the presentation of all of the data are contained in [9] and [10], respectively.

It has been demonstrated by Mokelke [11] that the actuator disk model provides a good representation of a square-wave distortion as it passes through a stage. To further verify the validity of the present experiments, the data measured for the 90 deg square-wave distortion were compared with that predicted by the actuator disk model. The results of this comparison, shown as perturbations to the circumferential-mean quantities in Fig. 4, indicate excellent agreement in the circumferential variation of total and static pressure and of the axial and circumferential velocity both upstream and downstream of the

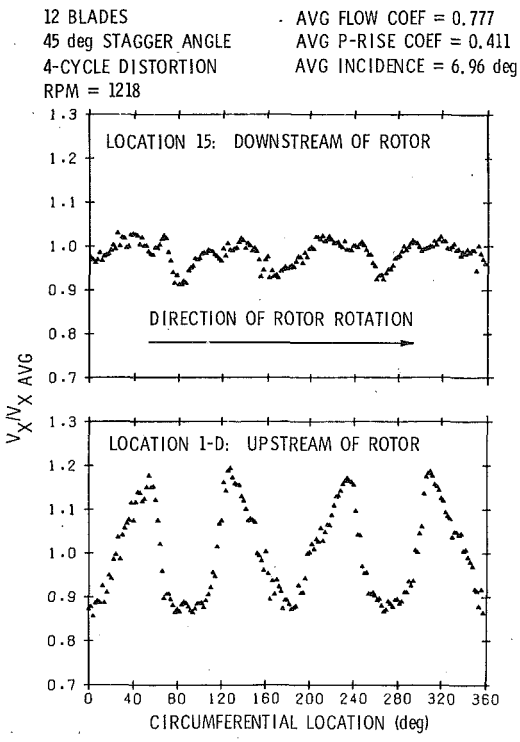

Fig. 3(*a*) Axial velocity variation upstream and downstream of rotor with four-cycle distortion

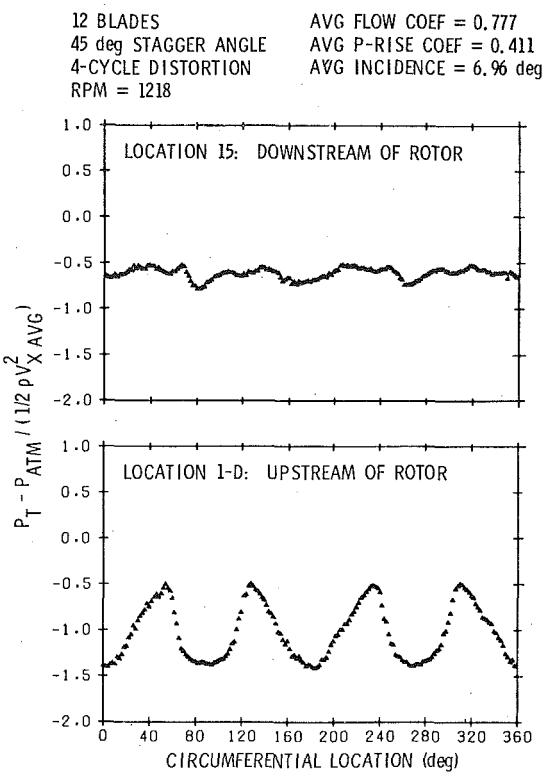

Fig. 3(*c*) Total pressure variation upstream and downstream of rotor with four-cycle distortion

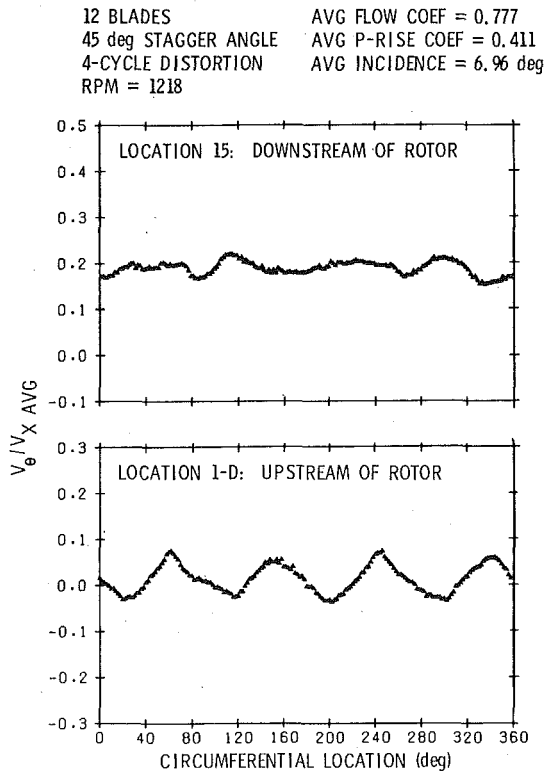

Fig. 3(*b*) Circumferential velocity variation upstream and downstream of rotor with four-cycle distortion

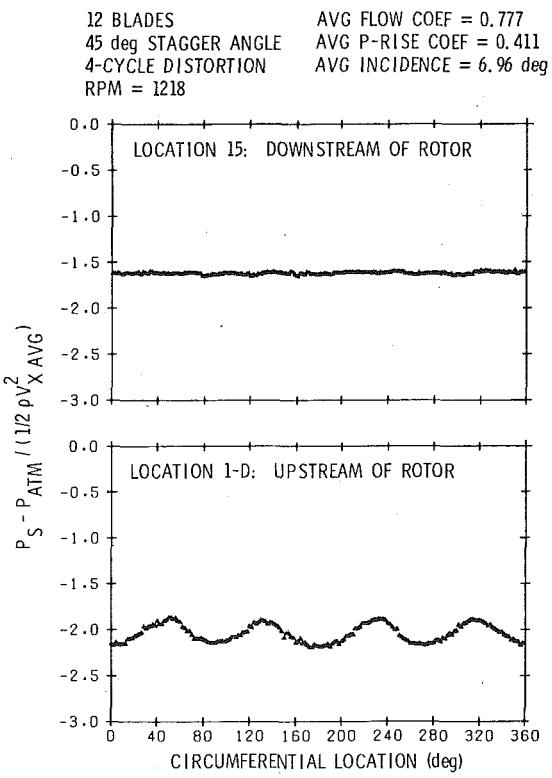

Fig. 3(*a*) Static pressure variation upstream and downstream of rotor with four-cycle distortion

rotor. Also shown in Fig. 4 is the predicted variation of each of these quantities at various axial locations upstream and downstream of the rotor. These comparisons clearly show the redistribution of the flow and the corresponding induced variation in static pressure (P_s) and circumferential velocity (V_θ) upstream of the rotor.

Discussion of Results

Description of Distortion Attenuation. Information concerning the attenuation of an inlet distortion through a blade row is important when designing a turbomachine, since downstream blade rows are subjected to the exit flow of the preceding blade row. The fact that

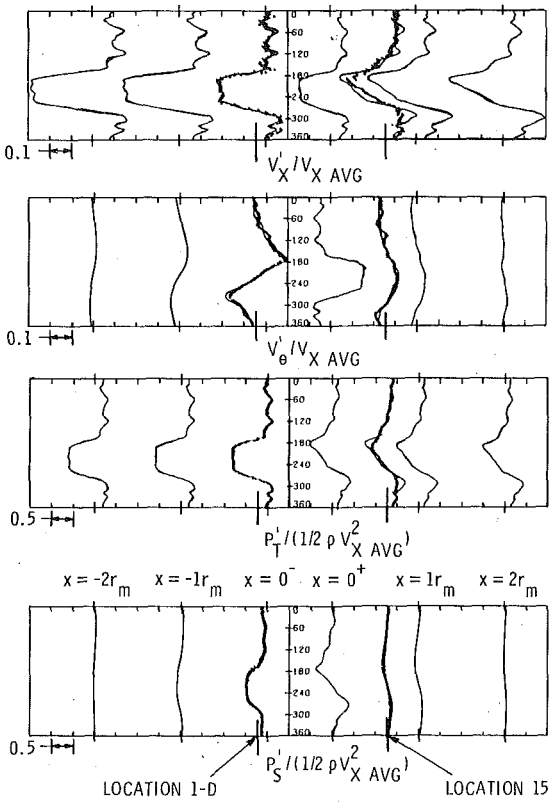

Fig. 4 Comparison of experimental data and actuator disk theory predictions for a 90 deg distortion (12 blades, 45 deg stagger, $V_{x\ avg}/U = .883$

a total-pressure distortion will be attenuated by a rotor is easily understood if the flow is considered to be quasisteady. Higher incidence angles in the low-velocity region will result in a larger total-pressure rise across the rotor (unless separation occurs) than in the remaining regions and, thus will make up some of the total-pressure defect. This characteristic is demonstrated by the predictions by Plourde and Stenning [12] showing an increased distortion attenuation with increasing slope of the rotor, or compressor, characteristic. However, the influence of reduced frequency is not addressed in [12].

To quantify the attenuation of the distortions measured in these studies, a means of representing the distortion amplitude is necessary. One such method is to represent the circumferential variation of the distortion data as a Fourier series, so that the amplitudes of the various harmonics can be examined and compared. For this reason, the dimensionless axial velocity and total-pressure data obtained in this study were represented as:

$$\frac{P_T - P_{\text{atm}}}{\frac{1}{2}\rho V^2_{x\,\text{avg}}} \quad \text{or} \quad \frac{V_x}{V_{x\,\text{avg}}} = \frac{A_0}{2} + \sum_{n=1}^{\infty} A_n \sin(n\theta - \phi_n), \qquad (1)$$

where $A_0/2$ is the circumferential mean value and A_n the amplitude of the n^{th} harmonic. Equation (1) is especially convenient for describing the sinusoidal distortions, where one harmonic will be dominant (Fig. 5), and it can be used to represent the distortion amplitude. In addition, a single parameter representing the amplitude of the square-wave distortions was calculated by taking the difference between the maximum and minimum values of the axial velocity and total pressure. Thus, the amplitude of the total pressure distortion for the square-wave inlet distortion was defined as:

$$A = \frac{P_{T_{\max}} - P_{T_{\min}}}{\frac{1}{2}\rho V^2_{x\,\text{avg}}}, \qquad (2)$$

and a similar definition was used for describing the axial velocity. This definition is demonstrated in Fig. 6 for a typical variation of total pressure observed with the 90 deg square-wave distortion.

For a sinusoidal distortion of n cycles, a distortion amplitude ratio is defined as a ratio of the n^{th} harmonic of the distortion amplitude with the rotor operating (A_n) to the n^{th} harmonic of the distortion

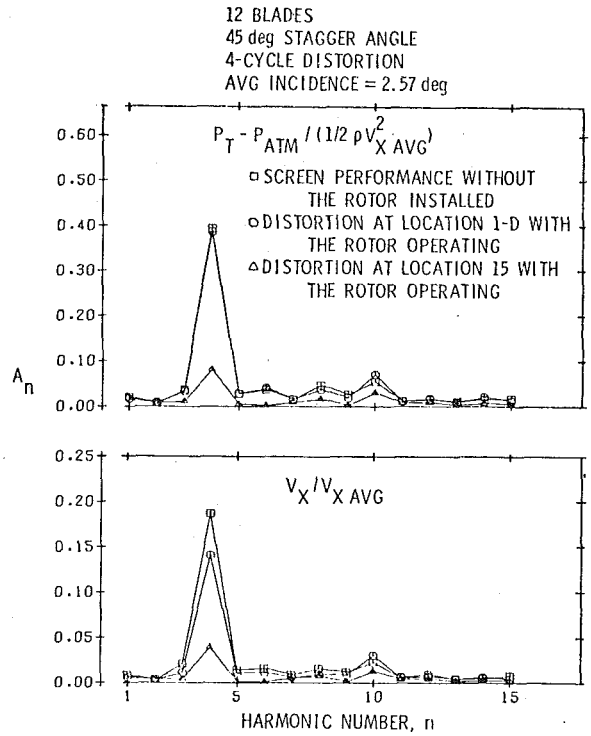

Fig. 5 Magnitudes of Fourier coefficients, four-cycle distortion

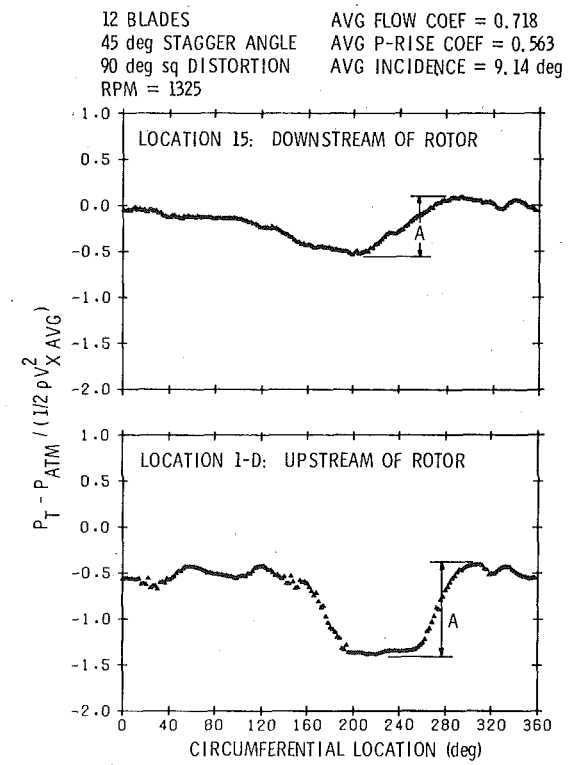

Fig. 6 Definition of distortion amplitude for square wave distortion

amplitude without the rotor installed ($A_{n-\infty}$). A similar ratio was formed for the square-wave distortions using the amplitude definition of equation (2). With the data represented in this manner, a value of the amplitude ratio of zero indicates the distortion was completely eliminated and a uniform flow exits, while a value of 1 indicates no effect due to the rotor. Values less than 1 indicate an attenuation, and values greater than 1 indicate an amplification of the distortion due to the presence of the rotor.

Influence of Incidence Angle on Distortion Amplitude. Fig. 7 presents the amplitude ratio measured with the four-cycle distortion

versus the circumferential averaged angle of incidence. Similar results were obtained for the one, two and six-cycle sinusoidal distortions. Both the axial velocity and total-pressure amplitude ratios are presented for the measurement stations upstream and downstream of the rotor; the three curves for each axial measurement station indicate various blade stagger angles. It is seen that neither the total pressure nor the axial velocity are strongly influenced by a change in incidence angle, or mean blade loading over the range investigated. This behavior is probably due to the fact that the performance characteristic of the rotor, i.e., total-pressure rise versus flow coefficient, is nearly linear.

The most important characteristic of the data in Fig. 7, is that the blade stagger angle has an important influence on the amount of attenuation realized downstream of the rotor. The rotor configurations with the higher blade stagger angles produce a larger attenuation of both the total-pressure and axial-velocity distortions. Several quasi-steady actuator disk studies [4, 13, 14] predict that the maximum distortion attenuation across an isolated rotor is achieved for a rotor stagger angle of 45 deg. However, this result assumes the special case of an unloaded rotor with no inlet or exit fluid swirl. The increase in attenuation of the total-pressure distortion with increased stagger angle observed in these experiments is partially explained by

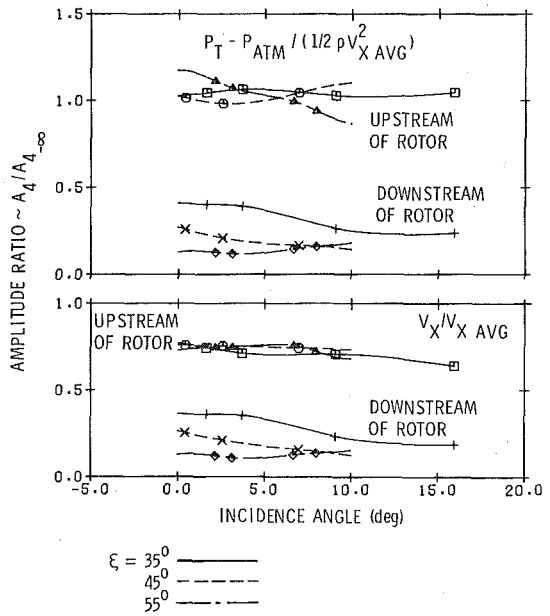

Fig. 7 Distortion attenuation versus incidence angle, four-cycle distortion

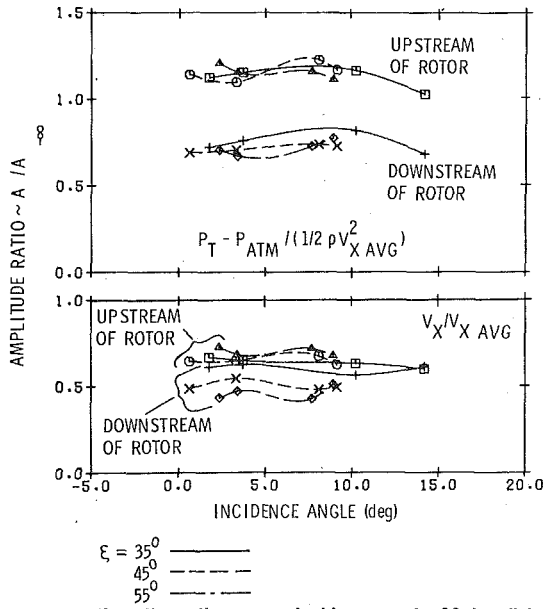

Fig. 8 Distortion attenuation versus incidence angle, 90 deg distortion

the more negative slope of the total-pressure rise versus flow coefficient, or incidence angle curve, for the higher stagger angles. However, the results presented in Fig. 7 show a greater attenuation with increased stagger angle than that predicted by a quasisteady actuator disk theory [9], indicating an unsteady effect.

Fig. 7 and subsequent figures also show that the total-pressure amplitude ratio upstream of the rotor is not exactly 1.0, as would be expected. Since a mixing process would decrease the measured amplitude of the distortion, the increase in amplitude must be caused by a radial total-pressure gradient produced by the screen and a radial shift in the streamlines caused by the flow redistribution near the rotor inlet. This change in the amplitude of the total-pressure distortion is not significant in the conclusions drawn regarding the amplitude ratio downstream of the rotor, since this ratio is defined using the downstream measurements and those at the inlet without the rotor installed, i.e., the far upstream conditions.

The variation of the amplitude ratio of the total-pressure and axial-velocity distortions, defined by equation (2), as a function of incidence angle are presented for the 90 and 180 deg square-wave distortions in Figs. 8 and 9, respectively. These data are presented for constant values of stagger angle, as in Fig. 7. As for the case of the sinusoidal distortions, the effects of incidence angle on the attenuation are very small for the square-wave distortions and the magnitudes are similar for the two square-wave distortions at equal values of incidence. The variation of attenuation with blade stagger angle is less with these distortions than with the 4-cycle distortion of Fig. 7. This indicates an increased influence of stagger angle as the reduced frequency is increased.

Influence of Unsteady Rotor Response on Distortion Amplitude. Four different sinusoidal distortions were investigated to determine the effect of the unsteady response of the rotor on the distortion flow field. The principal parameter used to describe the unsteady aerodynamic response of a surface is the reduced frequency. The reduced frequency ω used in this study is defined as:

$$\omega = \frac{2\pi}{\ell_c}\left(\frac{c}{2}\right), \tag{3}$$

which is the same as that employed in unsteady isolated airfoil theory for a convected gust [15]. Physically, this definition represents the ratio of the chord length of the rotor, c, to the distortion wavelength along the rotor chord, ℓ_c. The wavelength, ℓ_c is related to the measured wavelength of the distortion in the circumferential direction ℓ as:

$$\ell_c = \ell/\sin\xi,$$

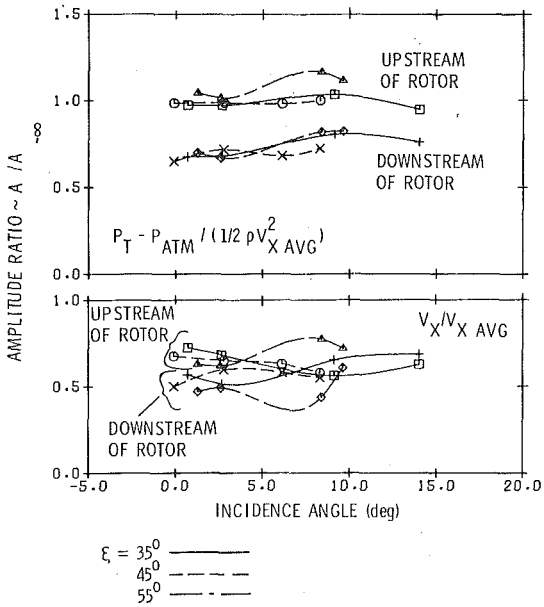

Fig. 9 Distortion attenuation versus incidence angle, 180 deg distortion

where ξ is the stagger angle of the blade at the blade radius being studied. Thus,

$$\omega = \frac{\pi}{\ell} c \sin \xi. \tag{4}$$

In addition to ω, an additional frequency parameter is associated with the unsteady response of a cascade or blade row. This frequency parameter, τ, is termed the intrablade frequency and relates the unsteady response of a blade in the cascade to that of its neighboring blades. For a rigid, nonvibrating blade row or cascade as assumed in this study,

$$\tau = -2\pi \frac{s}{\ell}, \tag{5}$$

where s is the blade spacing [16]. Thus, τ and ω are related as:

$$\tau = -2\omega \frac{s}{c} \csc \xi. \tag{6}$$

Therefore, either the reduced frequency or the intrablade frequency can be used to represent the unsteady characteristics of the cascade. In this study ω and τ were varied by changing the number of cycles of the distortion around the circumference of the AFRF.

Fig. 10 presents the amplitude ratio of the total pressure and axial velocity distortions as a function of ω for a zero incidence angle, thus minimizing the influence of three-dimensional flow, although the angle of incidence has been shown to have little influence on the distortion amplitude ratio (Fig. 7). This ratio was determined using the amplitude of the predominate harmonic for each sinusoidal distortion as determined by Fourier analysis of the data. As in the previous figures, data for the two axial measurement locations and the three stagger angles are presented. Fig. 10 shows that as the frequency is increased the attenuation of the total-pressure and axial-velocity distortion observed downstream of the rotor increases.

It is obvious from Fig. 10 that the unsteady response of the rotor is a major contributor to the attenuation of the distortion as it passes through the rotor. In fact, these data seem to indicate the possible existence of a condition at the higher values of ω which results in a maximum attenuation. To examine this possibility, the amplitude ratios for both the total-pressure and velocity distortions were examined as a function of the ratio s/ℓ or intrablade frequency, since $s/\ell = -\tau/2\pi$. The data measured downstream of the 12 bladed rotor are presented in Fig. 11 to a value of $s/\ell = 0.5$. This representation shows two major factors contributing to the attenuation of the distortion amplitude; the stagger angle ξ and the unsteady response, in this case indicated by s/ℓ.

Data have also been measured by Barr [17] using the same rotor discussed above but operated with 6 rather than 12 blades. These data were obtained using the same five-hole probes and data reduction techniques, but with only the four and six-cycle sinusoidal distortion screens. These experiments by Barr provide data at values of s/ℓ greater than 0.5, Fig. 11. At values of $s/\ell > 0.5$, these data indicate a reduction in the amount of attenuation of the distortion, or an increase in the amplitude ratio, as the value of s/ℓ increases. Thus, an optimum value of s/ℓ exists in the range $0 < s/\ell < 1.0$ which produces a maximum attenuation of the distortion as it passes through the rotor. These data indicate this value to be $s/\ell = 0.5$.

The mechanism by which this maximum attenuation occurs is related to the differences in unsteady response of the blade row as the value of s/ℓ, or intrablade frequency τ, is changed. Since the blades are nonvibrating, this is equivalent to a change in reduced frequency. Physically, a value of $s/\ell = 1.0$ means that the circumferential wavelength of the distortion ℓ, equals the circumferential, or pitchwise, spacing of the blades, s. At this condition, each blade of the cascade operating in a sinusoidal distortion experiences the identical distortion velocity, in magnitude and direction, at a given instant of time. Thus, the instantaneous angle of incidence and, hence, blade loading, are equal and in phase on each blade of the cascade. In this situation, the blades of the cascade act to reinforce each other, i.e., adjacent blade channels act to increase the time-mean total pressure by equal amounts. In an inviscid quasisteady flow, the distortion

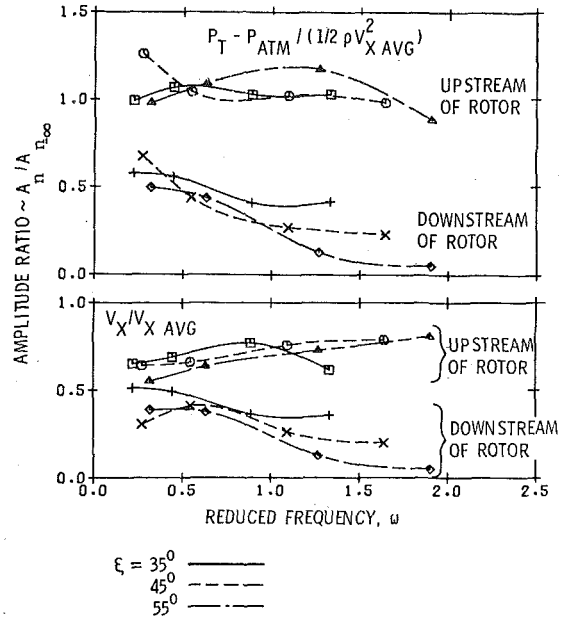

Fig. 10 Distortion attenuation versus reduced frequency, $i = 0$ deg

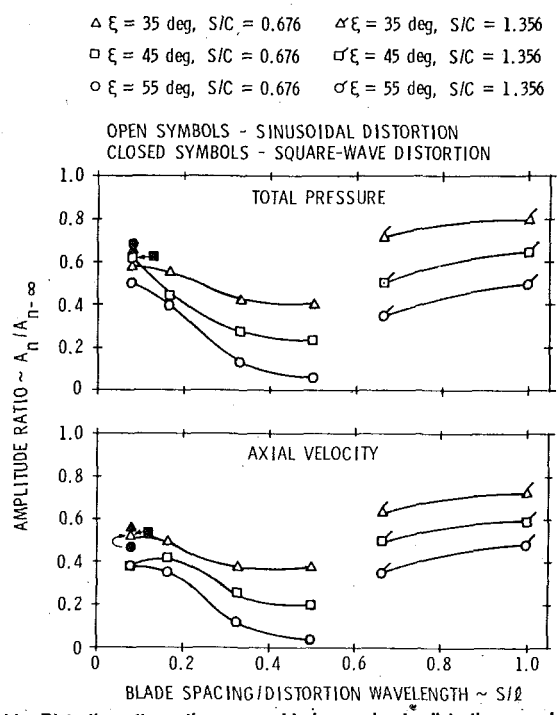

Fig. 11 Distortion attenuation versus blade spacing-to-distortion wavelength ratio downstream of the rotor, $i = 0$ deg

would pass through each blade channel with no attenuation and would experience only an increase in the level of circumferential-mean total pressure. A similar situation exists in a quasisteady flow where $\omega = 0$ and $s/\ell = 0$.

Conversely, when the value of $s/\ell = 0.5$, the distortion velocity experienced by adjacent blades of the cascade in a sinusoidal distortion are equal in magnitude but opposite in direction at a given instant in time. Thus, the instantaneous angle of incidence and blade loadings are nearly equal in magnitude (assuming no camber or mean angle of incidence) but 180 deg out of phase. The net effect is a partial cancellation of the unsteady response of a particular blade by the unsteady response of its neighbor. This situation would also result in a maximum amount of mixing since the flow through adjacent blade channels would alternately appear as positive and negative jets of fluid superimposed upon the circumferential-mean flow. This additional mixing would result in further attenuation of the distortion.

For values of $0 < s/\ell < 0.5$ and $0.5 < s/\ell < 1.0$, varying amounts of unsteady response and mixing occur as the blade-to-blade flows are neither completely in or out of phase. It is anticipated that this effect will continue for values of $s/\ell > 1.0$. However, the amount of change in attenuation of the amplitude ratio would presumably decrease in a manner similar to the unsteady lift experienced by a cascade, which decreases with increasing reduced frequency [18].

At this time, care should be taken regarding the magnitude of the measured levels of amplitude ratio between the 12-bladed rotor and the 6-bladed rotor. While the trends of the attenuation of this amplitude ratio with s/ℓ are valid, the amount of attenuation may be influenced by the space-to-chord ratio, s/c, or solidity. This would not be surprising, since the unsteady lift response of a cascade is primarily dependent on ω, ξ and s/c [18]. At present, no systematic data are available that quantify the effect of s/c, at constant values of s/ℓ (or ω) and ξ, on the magnitude of the amplitude ratio. However, the two values of s/c presented do present a trend similar to that predicted by unsteady cascade lift theories [18].

Also shown in Fig. 11 are the measured amplitude ratios for the 180 deg square-wave distortion. These data do not show as strong a dependence on stagger angle as the sinusoidal data, but they are at the same approximate level of amplitude ratio. The magnitude of the amplitude ratio for 90 deg square-wave distortion data agree with the 180 deg data at $i = 0$ (Figs. 8 and 9). Since a Fourier analysis of the 90 deg distortion data shows it to be primarily composed of the first and second harmonics [9] with $A_3 \cong 0.1A_1$, it would appear at values of $s/\ell < 0.166$ on Fig. 11.

Because of the predominance of the first and second harmonics in the 180 and 90 deg distortion data, the corresponding values of s/ℓ are small, and the unsteady interaction—and subsequent attenuation of the distortion amplitude as the flow passes through rotor—is minimal. This explains why the parallel-compressor and actuator-disc theoretical models, which neglect the unsteady cascade effects, give such good agreement with experimental data for these types of square-wave distortions (Fig. 4 for example). A comparison of the actuator-disk-model predictions and the experimental data for $s/\ell = 0.33$ are shown in Fig. 12. This comparison shows poor agreement between the predicted and measured distortion amplitude downstream of the rotor, since the unsteady effects are significant at this value of s/ℓ, as indicated in Fig. 11.

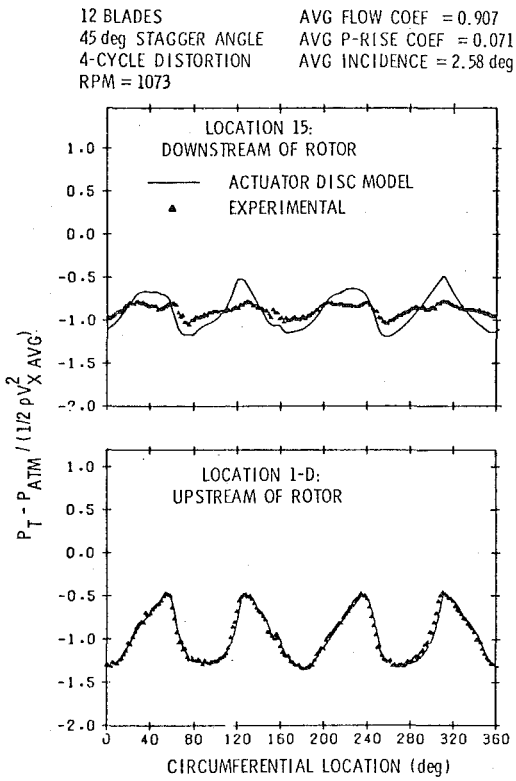

Fig. 12 Comparison of experimental data and actuator-disk theory four-cycle distortion, $s/\ell = 0.33$

Summary and Conclusions

The purpose of this experimental investigation was to obtain a systematic set of data, using an isolated rotor, that describes the influence of various geometrical and operational parameters (stagger and incidence angle) and distortion characteristics (number of distortion cycles and, hence, reduced frequency) on an inlet distortion flow field. These data, assumed to be two-dimensional, were examined to determine if there were optimum values of these parameters that would result in a maximum attenuation of the distortion as it passed through the rotor.

A distortion amplitude ratio has been defined as the amplitude of the distortion at a particular axial location with the rotor operating to the amplitude of the same distortion without the rotor installed. Examination of this distortion amplitude ratio results in the following conclusions regarding the passage of the distortion through the rotor.

1 The distortion is not significantly changed as the incidence angle of the blades, or steady blade loading, is increased.

2 The distortion amplitude is significantly attenuated as the stagger angle of the blades is increased. The observed increase in attenuation is greater than that predicted by a quasisteady analysis.

3 The unsteady response of the blades acts to attenuate the distortion. This attenuation is a function of the intrablade frequency τ, or the ratio of the blade spacing to distortion wavelength in the circumferential direction s/ℓ. The inclusion of the unsteady blade response in a distortion-prediction model must be based on an unsteady cascade rather than isolated airfoil analysis to account for the blade-to-blade interaction.

4 When the value of $s/\ell = 0.5$, the attenuation of the distortion is a maximum. The amount of the attenuation decreases as the value of s/ℓ approaches 0 and 1. While data is not presented to confirm it, it is presumed that a similar variation in the amount of attenuation will occur between higher integer values of s/ℓ.

5 The attenuation of the distortion due to the unsteady response of the rotor to a circumferentially nonuniform distortion is not significant for values of $0 < s/\ell < 0.2$. As a result, the attenuation of the 180 and 90 deg square-waved distortions investigated can be accurately predicted using a quasisteady actuator-disk theory. However, if the performance characteristic of the rotor were not linear as it was in this study, an unsteady influence would exist because the boundary layer can not respond instantaneously to changes in incidence. This type of unsteady response is most prevalent near a compressor's stall point as pointed out by [2], but can be accounted for using an empirical time constant when modeling the loss and deviation data.

6 Unsteady cascade theories show that the unsteady lift is a function of stagger angle ξ, reduced frequency ω, and space-to-chord ratio s/c. It is shown that the distortion attenuation is a function of ξ and ω (or $\tau = -2\pi s/\ell$) and also appears to be a function of s/c. While only two values of s/c are presented, these data exhibit the same trend as predicted by unsteady cascade lift theories; i.e., increased unsteady response or attenuation with decreasing values of s/c.

With these observations, the turbomachinery designer can select the rotor-blade geometry, ξ and s, to maximize the attenuation if the characteristic wavelength, ℓ of the distortion is known.

Acknowledgments

This study was conducted at The Applied Research Laboratory, The Pennsylvania State University, under the sponsorship of NASA Grant NSG 3031. The authors wish to thank Mr. L. C. Barr for permitting us to use a portion of his data.

References

1 Mokelke, H., "Prediction Techniques," *Distortion Induced Engine Instabilities*, AGARD Lecture Series, AGARD-LS-72, 1974.

2 Mazzaway, R. S., "Multiple Segment Parallel Compressor Model for Circumferential Flow Distortion," *Unsteady Phenomena in Turbomachinery*, AGARD-CP-177, 1976.

3 Seidel, B., "Asymmetric Inlet Flow in Axial Turbomachines," *ASME Transactions, Journal of Engineering for Power,* Vol. 86, No. 1, 1964, pp. 18–28.

4 Ehrich, F., "Circumferential Inlet Distortions in Axial-Flow Compressors," *Journal of Aeronautical Sciences,* Vol. 24, No. 6, 1957, pp. 413–417.

5 Dunham, J., "Non-Axisymmetric Flows in Axial Compressors," Mechanical Engineering Science Monograph No. 3, Institution of Mechanical Engineers, 1965.

6 Bruce, E. P., "The Axial Flow Research Fan—A New Facility for Investigation of Time-Dependent Turbomachinery," ASME Paper 74-FE-27, May 1974.

7 Bruce, E. P., "Design and Evaluations of Screens to Produce Multi-Cycle ± 20% Amplitude Sinusoidal Velocity Profiles, AIAA Paper 74-623, July 1974.

8 Treaster, A. L. and Yocum, A. M., "The Calibration and Application of Five-Hole Probes," *Proceedings of the 24th International Instrumentation Symposium,* Instrument Society of America, May 1978.

9 Yocum, A. M., "The Effects of Design and Operating Variables on the Response of an Axial Flow Fan to Inlet Flow Distortions," M.S. Thesis, Department of Mechanical Engineering, The Pennsylvania State University, August 1978.

10 Yocum, A. M., "Measurements of Flow Distortions in an Axial Flow Fan," Applied Research Laboratory, The Pennsylvania State University, TM 78-193, July 1978.

11 Mokelke, H., "Circumferential Inlet Flow Distortions in Multi-Stage Axial Compressors," Ph.D. Thesis, Engineering Department, The University of Cambridge, England, 1974.

12 Plourde, G. and Stenning, A., "Attenuation of Circumferential Inlet Distortion in Multistage Axial Compressors," *Journal of Aircraft,* Vol. 5, No. 3, 1968, pp. 236–242.

13 Mokelke, H., "Dynamic Stall Detection and Design Aids for Distortion Tolerant Compressors Using Quasi-Steady Actuator Disc Analysis," *Proceedings of Workshop on Unsteady Flows in Jet Engines,* Project SQUID Report UARL-3-PU, July 1974.

14 Savell, C. and Wells, W., "Rotor Design to Attenuate Flow Distortions, Part I and Part II," ASME, JOURNAL OF ENGINEERING FOR POWER, Vol. 97, No. 1, 1975, pp. 11–20 and 37–46.

15 Fung, Y. C., *An Introduction to the Theory of Aeroelasticity,* Dover Publications, Inc., New York, 1969.

16 Henderson, R. E., "The Unsteady Response of an Axial Flow Turbomachine to an Upstream Disturbance," Ph.D. Thesis, Engineering Department, University of Cambridge, England, October 1972.

17 Barr, L. C., "The Unsteady Response of an Axial Flow Turbomachinery Rotor to Inlet Flow Distortions," M.S. Thesis, Department of Aerospace Engineering, The Pennsylvania State University, March 1979.

18 Henderson, R. E., "The Unsteady Design of Axial-Flow Turbomachines," *Proceedings of Joint ASCE/IAHR/ASME Symposium on Fluid Machinery,* Vol. II, Fort Collins, Colorado, June 1978.

Ho-Tien Shu
System Engineer.

S. C. Kuo
Program Director.
Mem. ASME

T. L. O. Horton
System Engineer.
Mem. ASME

E. R. Fisher
System Engineer

United Technologies Research Center,
East Hartford, Conn.

Conceptual Design of an 80,000-shp Fossil-Fired Closed-Cycle Helium Turbine Propulsion System for Naval Ship Applications

A conceptual design was made of an 80,000-shp fossil-fired closed-cycle helium turbine system for naval propulsion applications. Various oil-fired heater and power conversion system configurations were investigated, and a reference system was selected based on a trade-off between the system performance and the component size and weight characteristics which would yield the maximum payload capability for the ship type considered. The conceptual design of major components was made based on the parametric design results identified from a comprehensive computer program incorporating extensive past design experiences. The conceptual design drawing for the propulsion engine is presented, and a preliminary propulsion system layout applicable to a conceptual high-speed destroyer is shown. The analysis indicates that no severe integration problem is anticipated for this type propulsion engine for lightweight ship propulsion applications.

Introduction

The mission capabilities and cost effectiveness of a particular ship type often depend greatly on the specific weight and cost characteristics of the propulsion system utilized. For Navy ships, implementation of lightweight propulsion systems can be beneficial in many ways which include: improved strategic and tactical operational capabilities resulting from increased speed and/or endurance time, increased payload, or reduced ship size and cost. Under the Office of Naval Research (ONR) sponsorship, the Lightweight Ship Propulsion System (LWSPS) research group at the United Technologies Research Center (UTRC) has conducted an extensive parametric system analysis to characterize the performance, size, weight, and cost of selected open- and closed-cycle gas turbine systems capable of providing adequate power levels for naval ship applications [1]. The results indicate that a fossil-fired, closed-cycle helium turbine (CCHT) with a rating of 80,000-shp appears to be a most desirable and promising propulsion system (see the schematic diagram in Fig. 1). Further study of this system was proceeded.

The fossil-fired closed-cycle gas turbine (CCGT) concept is not new, and many CCGT plants operating with either air or helium as the working fluid have been built and operated, mostly in Germany and a few in Japan, during the past three decades [2], and many more conceptual designs utilizing various heat sources [3–4] have also been reported. There have even been a few conceptual designs reported for marine applications [5–7]. In these marine applications, however, the selections of power level and heater types have been addressed to a specific naval application. For example, the conceptual designs reported in [5] and [6] are fossil-fired CCHT propulsion engines for cargo marine applications where the power levels selected are 9000 and 40,000 shp. The 40,000-shp engine requires two 20,000-shp heater modules. These engines would not be applicable to such ship types as high-speed destroyers, high-performance ships, cruisers, or aircraft carriers which require installed power levels greater than 120,000-shp, since the number of heater units needed would impose significant installation problems. [7] describes a conceptual design of a compact 70,000-shp closed-cycle Brayton system suitable for integration with a very high temperature reactor in a Surface Effect Ship (SES) application. In order to reduce the weight of radiation shielding, the turbomachinery and heat exchangers were assumed to be installed

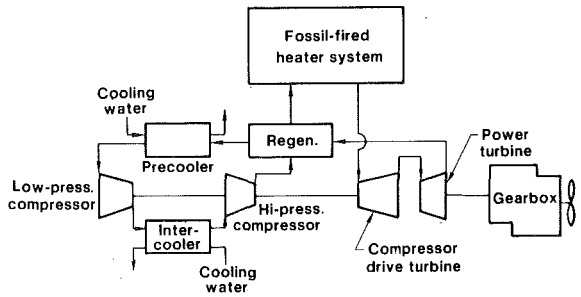

Fig. 1 Schematic diagram of fossil-fired closed-cycle helium turbine propulsion system

Contributed by the Gas Turbine Division and presented at the Gas Turbine Conference and Exhibit and Solar Energy Conference, San Diego, California, March 12–15, 1979 of THE AMERICAN SOCIETY OF MECHANICAL ENGINEERS. Manuscript received at ASME Headquarters December 18, 1978. Paper No. 79-GT-94.

in a 2.3 m by 5.4 m steel vessel. This may be attractive from a system compactness viewpoint, but it would be almost impossible to repair a damaged component or to perform the regular on-board maintenance, a common naval practice.

The assessment of the closed-cycle gas turbine technologies [1] indicates that the turbine inlet temperature of a CCGT engine is dictated by the gas (air or helium) heater design and that the design of a heater system for naval applications is quite stringent. Requirements placed on the helium heater include the necessity: to burn marine diesel fuel to heat the helium gas to temperatures of 1500°F or higher, to operate at pressure of 600 psia or higher, to provide rapid thermal response compatible with the load variation requirements, and to be compact, lightweight and low in cost with high reliability and good maintainability. Presently there is no heater system which can totally satisfy these requirements. Various design models have been proposed and investigated, including the Rocketdyne dual-concentric-tube "Variflux" helium heater [8], the Garrett AiResearch multipass crossflow tube/shell helium heater [9], the General Electric composite tube crossflow air heater (coal-fired) [10], and the Sulzer EVO helium heater [11]. Except the EVO heater which has been operating since 1974, all these heaters are still in different stages of development. In the sections which follow, the results of heater system study, propulsion engine conceptual design, propulsion system performance characteristics, and propulsion system layout are presented.

Heater System Study

The critical problems encountered in helium heater design include the material selection, homogeneous temperature design, high-temperature heater fabrication, and means to cope with tubes and headers thermal expansion problems. The material selection depends on the size and weight constraints, lifetime requirements, and cost characteristics. In this respect, one of the most important factors which should be considered in any system with an indirect-fired heater is the temperature and/or material limitations imposed by the vanadium, sodium, and other harmful ash elements in the fuel. These limitations are, in many respects, similar to those imposed on present-day steam boiler systems used in central power stations and in marine propulsion applications. In residual-oil-fired marine applications, the upper temperature limit for the steam is presently about 510 to 540°C, while in the coal-fired central power station the maximum steam temperature is restricted to a level near 565 to 595°C. Field and laboratory tests have indicated that the corrosion from the ash in both fuels increases rapidly at metal temperatures above 595°C. In oil-fired boilers, magnesium-based additives can be added to the fuel prior to or during combustion to suppress excessive ash corrosion at temperatures as high as 705°C. Shields have also been used successfully in some instances where liquid-ash corrosion has occurred in operational boilers. However, an appreciable reduction in heat transfer coefficient (25 to 30 percent) may limit the use of such shields for compact heater designs.

For metal temperatures above 700°C, the use of additives and/or more corrosion resistant materials such as nickel-base alloys would be required. The materials commonly specified for the high-temperature section of a heater system are Inconel 800, Inconel 617, Hastalloy X, and Nb-1Zr. Prices for these materials vary from 1.70 dollars to 28.00 dollars per ft for a typical 19 mm OD type tube. Another important cost factor is that for header fabrication which could conceivably be as high as 60 dollars per tube if Nb-1Zr were considered. The GE composite tube used in demonstration tests consists of an Inconel metal liner inside a silicon carbide sheath. At high combustion-gas temperatures (above 1090°C), the silicon carbide sheath is strong enough to contain the pressurized gases while the Inconel acts as a seal to prevent leakage. The ceramic outer sheath also provides a corrosion-resistant barrier to the coal ash (and presumably would also be suitable for oil ash) and hence permits use of turbine inlet temperatures as high as 930°C. Another study [12] conducted by the Navy also indicates that the use of an indirect-fired gas turbine power-plant using compact heat exchanger surfaces in the heater offers a possible solution to the sulfidation problem.

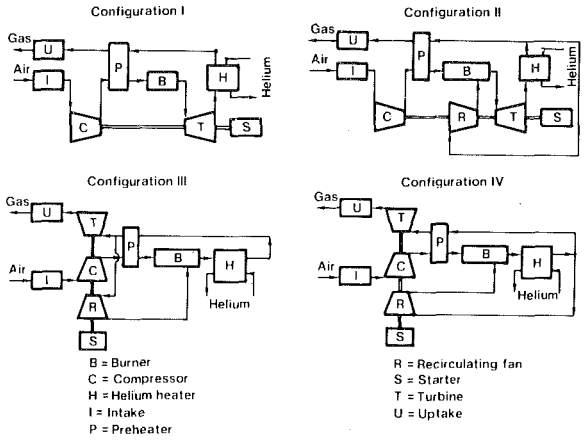

Fig. 2 Schematic diagrams of alternative fossil-fired heater systems

Parametric Performance Analyses. A heater system which can satisfy all the propulsion requirements obviously would require a significant departure in design approach aimed at achieving lower specific weight and shock-resistance when compared with conventional practices relating to steam boilers and gas heaters in the chemical-process or stationary-power industries. Based on the results of a literature survey, four candidate configurations were selected for parametric analyses. These are depicted in Fig. 2.

In general, the fossil-fired heater required in a closed-cycle gas turbine ship propulsion system consists of seven major subsystems: an air intake, an air compressor or blower with mechanical drive, a fuel combustor, a turbine to drive the compressor, a gas heater, an air preheater (often optional), and a gas uptake. The required air filtration and exhaust gas soundproofing equipment are included as part of the intake and uptake subsystems. A compressor or blower is used not only to supply the combustion air but also to enhance the combustion efficiency in the combustor in order to reduce the size, weight, and capital cost of the overall heater system.

Before parametric heater performance analyses were undertaken, it was necessary to establish two basic ground rules: (1) the integration requirements as they related to the power conversion systems (i.e., thermal capacity and helium inlet and outlet conditions and mass flow rate) had to be identified; and (2) the parameters (and their applicable ranges) which might significantly affect the heater performance had to be selected.

The integration parameters were obtained from earlier studies where the helium flow rate of the power conversion system was 76.25 kg/s, where the temperature of the helium was raised from 453.3 to 815.6°C, and where the pressure levels of the helium flow into and out of the heater were 46.16 and 44.83 bars, respectively. The major parameters considered and their applicable ranges which could significantly affect the heater system performance include: the compression ratio (3:1 to 5:1), the cycle pressure loss (8 to 20 percent), the air preheater effectiveness (0 to 90 percent), the hot-gas inlet and helium-exit temperature difference (55.5 to 277.7°C), and the hot-gas exit and helium-inlet temperature difference (27.8 to 138.9°C). This selection was based on the author's past experience in system analysis and component conceptual design and based on the physical constraints imposed by the ships considered (i.e., component size, weight, life time and maximum metal temperature limitation).

The UTRC State-of-the-Art Performance Programs (SOAPP) were used during this part of the study, and typical results produced by this model are presented graphically in Figs. 3 and 4. Fig. 3 presents comparisons of heater system efficiencies as a function of the helium inlet-gas exit temperature difference and the combustion gas temperature (which has been converted into fuel air ratio) for a selected heater inlet temperature and cycle pressure loss. The results indicate that Configurations III and IV (Fig. 2) are superior to the other two configurations. The effect of cycle pressure drop and air-preheater effectiveness on the heater performance for Configurations III and

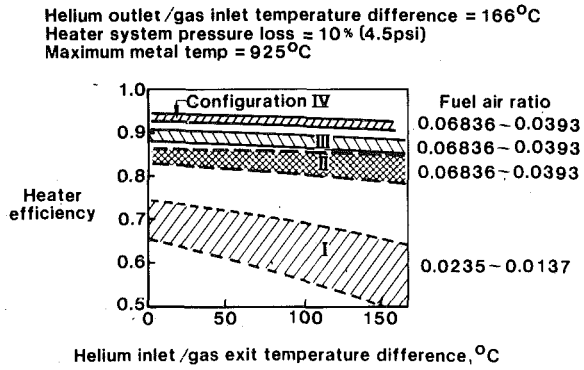

Fig. 3 Comparison of fossil heater thermal efficiency for various configurations and operating conditions

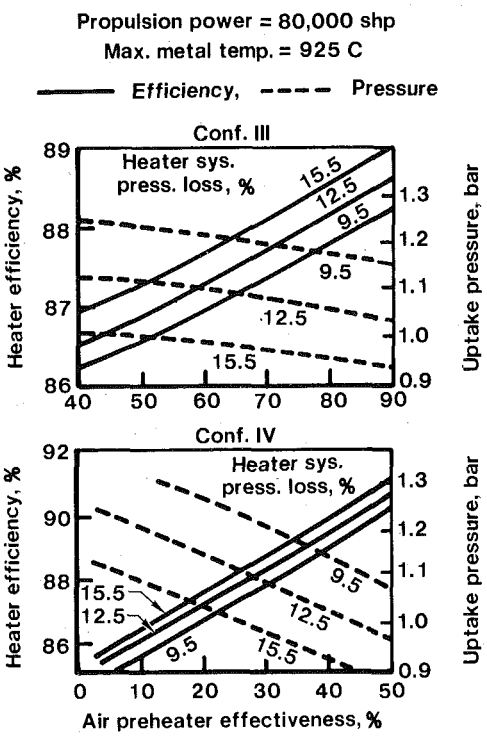

Fig. 4 Effect of pressure loss and air preheater effectiveness on fossil heater performance

IV are presented in Fig. 4. These results indicate that within certain limits, a higher system pressure drop would provide improved heater efficiency. However, the requirement that the uptake discharge pressure must exceed one atmosphere limits the maximum attainable pressure drop level. For example, a system having the overall pressure drop greater than 15.5 percent would be unable to discharge combustion gases through its uptake, and therefore, such a system would be unfeasible. On the other hand, for a system pressure drop less than or equal to nine percent, system efficiency is not the only factor that would suffer. Such a system would also become very bulky and heavy and therefore, it would not be attractive. As a result of these analyses, it became obvious that the applicable overall cycle pressure drop for the LWSP fossil heater system should fall between 10 to 15 percent.

Parametric Size and Weight Estimates. The heater system cycle definition and component design point specifications (inlet and exit temperature, pressure, and mass flow rate) identified from performance analyses were used as input data for the component parametric design programs to estimate the heater system size and weight characteristics. Material selections for each component were also needed at this point to provide the necessary bases for stress analyses. It should be mentioned that whereas the material selection depends on the component operating conditions, it also dictates the component

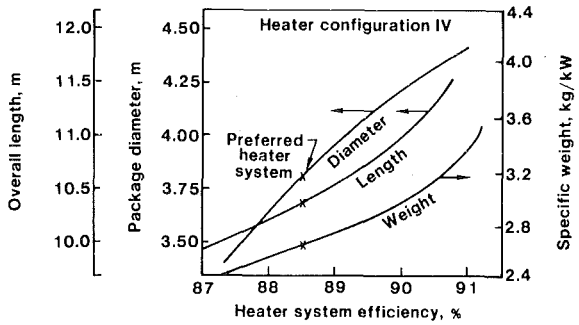

Fig. 5 Size and weight characteristics for 80,000-shp fossil-fired heater system

Table 1 80,000-shp fossil-fired CCHT propulsion system component design conditions

	MASS FLOW RATE KG PER SEC	TEMPERATURE, C IN/OUT	PRESSURE, BAR IN/OUT
I HEATER SYSTEM			
COMPRESSOR	69.582	26.7/191.1	1.0/4.01
PREHEATER (T)	69.582	191.1/292.8	4.01/3.94
(S)	73.392	481.1/391.7	3.70/3.63
COMBUSTOR	73.392	292.8/1926.7	3.94/3.92
HEATER (T)	76.250	453.3/815.6	46.16/44.83
(S)	194.685	1093.3/481.1	3.92/3.70
TURBINE	73.392	391.7/220.6	3.63/1.06
RECIRCULATION FAN	121.338	481.1/495.0	3.70/3.92
II POWER CONVERSION SYSTEM			
LOW COMPRESSOR	76.25	37.8/126.7	15.48/27.30
HIGH COMPRESSOR	↓	37.8/123.9	26.82/46.46
HIGH TURBINE		815.6/640.0	44.83/27.48
POWER TURBINE		640.0/490.0	27.48/16.70
REGENERATOR (T)		123.9/453.3	46.39/46.16
(S)		490.0/160.6	16.66/16.08
PRECOOLER (S)		160.6/37.8	16.01/15.53
INTERCOOLER (S)	76.25	126.7/37.8	27.26/26.85

size and cost. However, detailed material selection would be reviewed during the conceptual design phase. For this parametric analysis, tentative selections were: for the low-temperature sections, such as intake and uptake components, low carbon steel was used; and for high temperature sections (such as combustor, mixer, helium heater tubing and shell), INCO 718 and/or Hastalloy X were used. AISI 410 was selected for compressor airfoils and disks, and Udimet 700 and AMS 5718 for turbine airfoils and disks, respectively. For air preheater tubing and shell, AISI 347 and the low alloy steel, AISI 4340, were used.

Comparisons of the results of this analysis were based on the size, weight, and efficiency of the heater. It was found that Configuration IV appears to be the best heater system among the four configurations investigated; the results for this configuration are shown in Fig. 5. Data presented in Fig. 5 show that for an attractive range of heater efficiencies the overall heater length varies from 9.75 to 11.5 m, the diameter from 3.3 to 4.2 m, and the weight from 2.4 to 3.4 kg/kW. These dimensions could conceivably be reduced through appropriate rearrangement of each component within the package if conceptual design of the heater system were undertaken. However, this was beyond the scope of the present program.

Propulsion Engine Conceptual Design

Prior to the conceptual design of the 80,000-shp CCHT propulsion system, the results of parametric analyses, the cycle definition, component specification, life and duty cycles, and installation requirements published previously [13] were reviewed and some of the more important component design conditions are summarized in Table 1.

Turbomachinery Conceptual Design. The turbomachinery conceptual design [14], including material selections, component designs, engineering drawing, and weight estimates were performed by the engine design group of Pratt & Whitney Aircraft Group (P&WA), a subsidiary of United Technologies Corporation. The LWSP research group from United Technologies Research Center (UTRC) provided the general design guidelines such as the turbomachinery configuration, the component performance requirements, the operational characteristics, and the installation constraints.

The turbomachinery configuration selected for the 80,000-shp CCHT propulsion engine consists of two compressors and two turbines (see Fig. 1). The low and high compressors on the same spool would be driven by the high pressure turbine while the low pressure free power turbine would deliver the propulsion power through a gearbox to the thrustor. The rotational speed of the free power turbine was selected to be 4800 rev/min. The turbine inlet temperature (TIT) of 815.6°C (1500°F) was selected based on a survey of existing closed-cycle gas turbine power systems and a projected heater technology in the 1990's. The component operating conditions were selected based on the results of a system optimization study [13]. Based on these operating conditions, the flow rate and the inlet and outlet temperature and pressure for each component were calculated and listed in Table 1. The life expectancy of the engine was assumed to be 30 years or longer, with time between removal of 15,000 hr, and time between minor overhauls of 5000 hr. The turbomachinery and attached hardware (oil pumps, bleed lines, linkages, etc.) are expected to fit inside a cylindrical envelope of 2.1 m dia and 9.1 m length.

The preliminary design drawing shown in Fig. 6 consists of a low and a high compressor of 12 stages each, driven by a three-stage turbine operating at 8200 rpm. Propulsion power is provided by a five-stage free turbine operating at 4800 rpm. The estimated turbomachinery component efficiencies are 89.5 percent and 87.5 percent, respectively, for the low and high compressor and 90.4 percent and 90.6 percent for the compressor drive turbine and free power turbine respectively. The overall turbomachinery dimensions were estimated to be 6.70 m in length and 1.52 m in diameter.

Since the gas working fluid selected is helium, internal corrosion problems are not expected to be severe. For the most part, external surfaces are expected to be sufficiently cool that the only necessary protection from the salt air environment would be the use of a high temperature paint. Also, a thermal blanket surrounding the external cases aft of the thrust mount would be desirable to prevent excessive heat radiation in the engine room and accidental burning of personnel. Materials selected for the conceptual turbomachinery design are based on the life and duty cycle requirements specified as well as the requirements for low weight and low cost, plus ease of weld repair and reoperation without stress relief. Materials selected for the high pressure turbine blades, nozzles, and disks are INCO 100, INCO 713, and Astroloy respectively, with the exception of the first stage nozzles which would be made of INCO 100. For the power turbine, the materials selected for the blades, nozzle, and disks are AMS 5382, INCO 713, and Waspaloy respectively. Materials selected for compressor blades, stators, and disks are Greek Ascoloy, 17-4 PH, and AISI 410 respectively. The hot section inlet or exit scrolls are manufactured from Haynes 188 and for low temperature sections, from INCO 718. With these materials selected, the estimated total system weight for the unit shown in Fig. 6 is about 9550 kg (0.16 kg/kW).

Heat Exchanger Conceptual Design. Preliminary conceptual designs of the regenerator, the precooler, and the intercooler for the 80,000-shp CCHT propulsion engine were also made based on the component design requirements presented in Table 1. These specifications and the dimensions of the conceptual-design turbomachinery discussed above were utilized in a series of computer-aided parametric designs for each of the three heat exchangers in order to identify the optimum geometry which would minimize the length of the ducts as well as the number of bends and thereby reducing the pressure loss throughout the piping system. The parameters considered included the tube and shell materials selections, the pressure loss split between the tube and shell sides, the cooling water velocity, and the ratio of tube pitch to tube diameter. The maximum effective tube length was estimated to be approximately 5.5 m (18 ft) for the regenerator, and 1.4 m (4.6 ft) for both precooler and intercooler. This tube length specification provides the most desirable integration of the three heat exchangers and the turbomachinery for a minimum of duct work.

For the mechanical arrangement selected and the use of the unconventionally small tubing (0.25 in. OD) and close tube spacing (less than 2 mm) in all three exchanger designs, an unconventional module assembly concept was required (see Fig. 7). The close tube spacing was maintained by a wire-wrap spacer (1.70 mm dia for the regenerator and 1.91 mm dia for the precooler and intercooler) at a wrapping axial pitch of about 30 cm. There are 300 active tubes and one no-flow (idle) tube per module; this no-flow tube is placed on the centerline of the tube bundle to provide the required flow velocity in the shell at the design condition. As shown in the (lower) module assembly drawing of Fig. 7, all 300 active tubes are brazed to a 108 mm OD module header tube; however, the no-flow tube is not joined to the header tube because of the stress level limitation. The cone-shaped module header provides a stronger joint between the exchanger tubes and the module header tube because the ligament in the tube sheet is thicker. When compared with a hemispherical or a flat-plate header at the same header thickness, the cone-shaped header has a safety factor approximately 1.5 times greater than the other two types. As a result, the cone-shaped header concept was selected for the conceptual design.

Each heat exchanger tube bundle would be wrapped with a module sleeve which not only guides the flow direction on the shell side but also provides better modular rigidity for structural support. The modules are evenly supported by several module support plates, and the maximum tube length between adjacent support plates does not exceed 914.4 mm (36 in.).

Each module header tube would be belled and welded to a double packed floating tube sheet one inch in thickness. The floating tube sheet design was used to eliminate some of the thermal expansion problems which could be encountered during the normal duty cycle

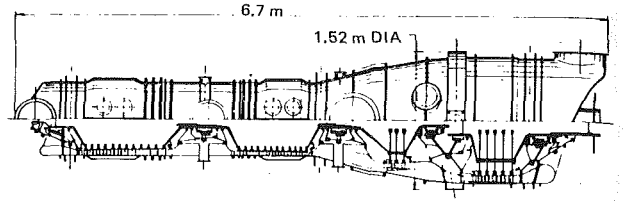

Fig. 6 80,000-shp closed cycle ship propulsion turbomachinery

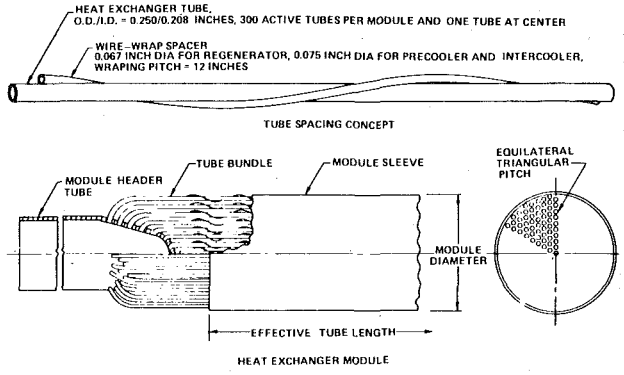

Fig. 7 Heat exchanger module concept

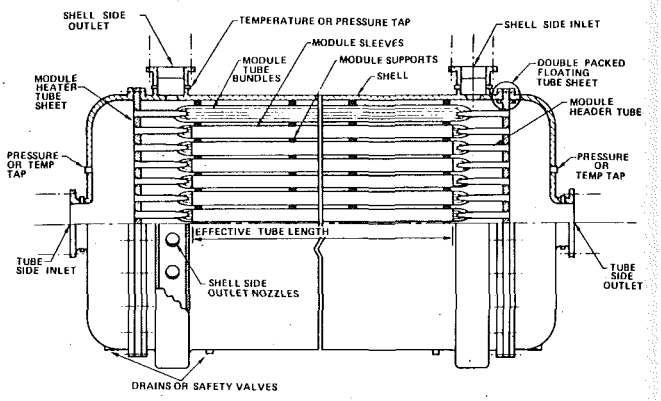

Fig. 8 Preliminary heat exchanger design for 80,000-shp lightweight ship propulsion system

or during emergency ship operation. A representative conceptual design drawing for the floating tube sheet is shown in Fig. 8.

Propulsion System Characteristics

With the propulsion engine conceptual designs and the results of the fossil-fired heater system parametric studies in hand, the characteristics of a candidate lightweight ship propulsion system can be identified. Their major component sizes and weights are summarized in Table 2, and the specific fuel consumption characteristics are shown in Fig. 9. It was estimated that the specific weights for the propulsion engine and the heater system were approximately 1.82 kg/kW (3.0 lb/shp) and 2.65 kg/kW (4.35 lb/shp), respectively.

Fig. 9 shows the effect of various heater and propulsion engine efficiencies on the specific fuel consumption. For the candidate system with a turbine inlet temperature of 816°C and a regenerator effectiveness of 90 percent, the computed propulsion engine efficiency is approximately 41.5 percent. Combining this propulsion engine with the candidate heater system having a heater efficiency of 88.5 percent, the design-point specific fuel consumption of the lightweight propulsion system was calculated to be approximately .228 kg/kW-hr (.375 lb/shp hr). Whereas the SFC of the regenerative open-cycle gas turbine (OCGT) is comparable to this value, the superior part-load performance of the lightweight CCGT engine, when compared with that of OCGT engines, would provide a significant fuel savings when total fuel consumption is calculated for a given duty cycle mission and a particular ship type.

Propulsion System Layout

A preliminary selection of a reference ship type and its performance requirements was made in order to provide a basis for installation and layout studies of the selected lightweight CCHT propulsion system. A high-speed destroyer (HSD) of 3500 to 4000 metric tons displacement, capable of 25.7 m/s (50 knots) maximum speed and 10.3 m/s (20 knots) cruise was selected from a "Benefit-Matrix" screening process [15].

In order to prepare the propulsion system layout, the maximum dimensions available for the machinery platform first had to be identified. Based on the results of a ship analysis [16], the hull dimensions which would meet the operational requirements of the high-speed destroyer and also would meet its necessary stability requirements were estimated to be approximately 120 to 150 m in length and 13 to 14 m in width (beam). The usable width inside the engine room can be obtained by subtracting approximately 2 ft from the hull width dimension, while the maximum length of the space available for the machinery is derived from the floodable length believed to be about 15 percent of the overall hull length. For all possible arrangements, the available engine room dimensions were approximately 13 m in width and 14 to 16 m in length. This information provided a guideline for the propulsion system layout plan.

After the engine room sizes were identified, the preliminary propulsion system layout was made based on the sizes of the major components of the propulsion system. These results are presented in Fig. 10. Based on this layout, the propulsion system, including the power conversion system, the inventory control system, the heater system, and the transmission gearbox were estimated to occupy a space of about 11.4 m (37.5 ft) in width, 12.8 m (42 ft) in length, and 5.3 m (17.5 ft) in height. Relating these dimensions to those available in the proposed engine room indicates that the installation of the candidate CCHT lightweight propulsion system into the selected high-speed destroyer ship should not encounter any major installation problem.

Conclusions

The results of performance analyses carried out for both the fossil-fired helium heater system and the propulsion engine system indicated that, at the design point operation, the specific fuel consumption of an 80,000-shp lightweight CCHT propulsion system is much better than that of conventional steam or diesel engine systems and comparable to that of the regenerative open-cycle gas turbine engines of the same overall rating. If comparisons were made based on the normal naval ship duty cycle operation, a significant fuel savings relative to all three types of competing systems could be expected when the lightweight CCHT propulsion system was installed. This is attributed to the superior part-load performance of the CCHT system. The preliminary engine conceptual design and system layout indicate that no major integration problem would be encountered when this system is installed on the conceptual high-speed destroyer considered.

Table 2 High speed destroyer lightweight propulsion system component dimensions and weights

	COMPONENTS	LENGTH (m)	DIAMETER (m)	WEIGHT (kg)
A.	POWER CONVERSION SYSTEM			
	TURBOMACHINERY	6.70	1.52	9,550
	REGENERATOR	7.62	2.36	44,040
	PRECOOLER	3.16	1.60	6,020
	INTERCOOLER	3.16	1.43	5,430
	INVENTORY VESSELS (6 UNITS)	6.60	0.67	6,300
	DUCTING	9.45	0.3~0.4	730
	SUPPORTING STRUCTURE			36,700
	TOTAL			108,770
B.	HEATER SYSTEMS			
	HELIUM HEATER	6.55x5.33	2.74	40,130
	TURBOMACHINERY	1.22	1.22	3,000
	AIR RECUPERATOR	1.98	1.37	2,600
	COMBUSTOR AND MIXER	1.98x1.52	0.76	680
	DUCTING	6.10	3.66	440
	INTAKE	12.20	3.66	18,730
	UPTAKE	12.20	3.05	48,640
	SUPPORTING STRUCTURE			43,900
	TOTAL			158,120

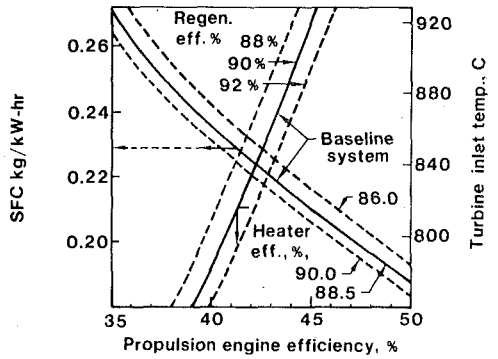

Fig. 9 Fossil-fired CCGT propulsion system cycle thermal efficiency and specific fuel consumption characteristics

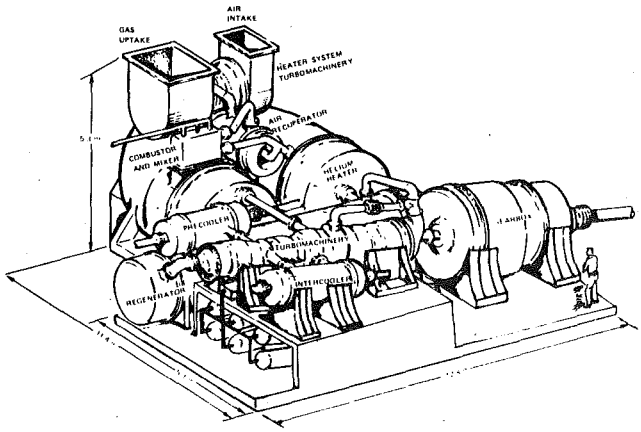

Fig. 10 Preliminary high speed destroyer propulsion system perspective

Acknowledgment

The work reported in this paper was performed by the United Technologies Research Center as part of the research program

sponsored by the Office of Naval Research under Contract N00014-77-C-0735.

References

1 Kuo, S. C., et al., "The Prospects for Lightweight Ship Propulsion Systems," ASME Paper, 78-GT-179, April 1978.

2 Keller, C. and H. Frutschi, "Closed-Cycle Plants Conventional and Nuclear-Design, Application, Operation," Chapter 20, Vol. II, *Sawyer's Gas Turbine Engineer Handbook,* 2nd Ed., 1976.

3 McDonald, C. F., et al., "Primary System Design Studies for Advanced Direct Cycle Nuclear Gas Turbine Plant," ASME paper 77-GT-75, March 1977.

4 Kuo, S. C., "Solar Farms Utilizing Low-Pressure Closed-Cycle Gas Turbines." *Proceedings of the 9th IECEC,* San Francisco, CA, Aug. 26–30, 1974.

5 Gritelli, F., et al., "Closed Gas Turbine Engines for Future Marine Propulsion," *Marine Technology,* Vol. 13, No. 3, July 1976.

6 Dobler, F. X. and R. A. Rackley, "Closed Gas Turbine Marine Power Systems," *Proceedings of the 10th IECEC,* 1975.

7 Thompson, R. E., "Lightweight Nuclear Powerplant Applications of a Very High Temperature Reactor," *Proceedings of the 10th IECEC,* 1975.

8 Larson, V. R., and S. V. Gunn, "Helium Heater Design for the Helium Direct Cycle Component Test Facility." AIAA Paper No. 75-1262, presented in Anaheim, CA, Sept. 1975.

9 Rackley, R. A., "Marine Closed Gas Turbine and LNG Refrigeration System Study, Part 1—Closed Gas Turbine Marine Power Systems," Rep. No. MA-RD-920-75003, AiResearch Mfg. Co., June 1974.

10 LaHaye, P. G., "High Temp Heat Exchanger for Closed-Cycle Coal-Fired Gas Turbine," *Gas Turbine,* March–April 1967.

11 Innocente, G. and H. Wydler, "Helium Heater for the Helium Turbine Installation at Oberhausen," *Sulzer Technical Review,* Feb. 1977.

12 Garrett, J. H., "An Indirectly Heated Gas Turbine Cycle for Minimizing Sulfidation Corrosion," US Navy MEL Technical Memorandum, Oct. 1966.

13 Kuo, S. C. and H. T. Shu, "Alternate Closed-Cycle Gas Turbine System Design Considerations for Ship Propulsion Applications," ASME paper, 78-GT-18, April 1978.

14 Coyle, J. K. et al., "Conceptual Design of a Closed-Cycle Gas Turbine for Marine Propulsion," P&WA Report FR-9701 to UTRC, April 1978.

15 Kuo, S. C., H. T. Shu, and T. L. O. Horton, "Closed-Cycle Gas Turbine Heater Analysis and Conceptual Design of an 80,000-shp Turbo-machinery," UTRC Report R78-952979-2, March 1978.

16 Bullock, H. O., Jr., "Consultation on Light-weight Propulsion System Layout and Integration," J. J. Henry Report No. 6654 to UTRC, July 1978.

I. Khalil[2]
Graduate Research Assistant.

W. Tabakoff
Professor.
Mem. ASME

A. Hamed
Associate Professor.
Mem. ASME

Department of Aerospace Engineering
and Applied Mechanics,
University of Cincinnati,
Cincinnati, OH 45221

Viscous Flow Analysis in Mixed Flow Rotors[1]

A method for analyzing the viscous flow through turbomachine rotors is presented. The field analysis is based on the solution of the full Navier-Stokes equations over the rotor blade-to-blade stream channels. An Alternating-Direction-Implicit method is employed to carry out the necessary numerical integration of the elliptic governing equations. The flow analysis may be applied to various types of turbomachine rotors. Preliminarily, only the case of laminar flows are considered in this paper. The flow characteristics within the rotors of a radial inflow turbine and a radial bladed compressor are investigated over a wide range of operating conditions. Excellent results are obtained when compared with existing experimental data. The method of this analysis is quite general and can deal with wide range of applications. Possible modification of the present study to deal with turbulent flow cases are also identified.

Introduction

A unified theoretical approach to the flow through turbomachinery presents a formidable problem. It involves the solution of the equations of motion of the three-dimensional unsteady nonadiabatic viscous flow through the complex of rotating and stationary cascades of blades comprising the machine. The complexity of the entire problem requires more or less serious simplifications of the flow processes. These idealizations must cover the essential physical process with sufficient quantitative accuracy and still permit a clear and rational calculation of the flow processes. Most recent efforts, in this respect, have been concentrated on the solution of the nonviscous version of the flow governing equations [1, 2, 3]. These solutions have been marked by increased versatility in the ability to deal with subsonic [4], transonic [5], as well as supersonic flow regimes [6]. In order to give a more accurate representation of the actual flow processes, approaches [7 and 8] have been devised to account for viscous effects. Most of these approaches are based on the assumption that a two layer model is representative, i.e., an inviscid flow solution which interacts with an end wall boundary layer solution. Important contributions to viscous flow analyses in turbomachinery have been made more recently by [9, 10, 11]. The important features of these are the attempts to solve the parabolized version of the complete three-dimensional viscous flow equations with special techniques.

Although the inviscid analysis is useful for providing a considerable insight into the character of the flow, the neglect of viscous effects is a serious shortcoming if detailed quantitative information is desired to calculate viscous losses or heat transfer. The approach used to account for viscous losses effects by using the boundary layer concept in conjunction with an inviscid flow analysis proves to have a number of drawbacks. First, the correct means for matching boundary layer and inviscid solution has not been established if the inviscid flow is rotational, such as in the case of a curved or a rotating passage. Second, most of the existing interacting boundary layer techniques are not capable of handling strong interaction mechanisms of the types present in turbomachine rotors. The parabolic flow approximation neglects completely the downstream influences. Consequently important effects such as surface curvature, downstream blockage and reversed flow regions are totally ignored. On the other hand, the full Navier-Stokes equations have defied accurate numerical solutions due to the limitations imposed on core size and speed of present computers. Moreover, the lack of powerful numerical schemes capable of achieving a rapid convergence for three-dimensional elliptic equation renders the solution to be costly.

The present study attempts to demonstrate the feasibility of obtaining viscous flow details within turbomachine passages by appropriately combining several blade-to-blade viscous flow solutions. Each of these solutions is obtained through the numerical integration of the full Navier-Stokes equations over predetermined computational surfaces that extends between the blades. The set of stream surfaces required for the analysis are themselves generated from the solution of the nonviscous version of the Navier-Stokes equations as suggested by Wu [1]. Because of the constraints implied by the use of these surfaces the resulting viscous flow details are regarded as a quasi-three-dimensional description of the flow field.

Flow Analysis

The partial differential equations that govern the flow behavior within the turbomachine rotor passages are presented. A transformation of the three-dimensional flow equations to several particular two-dimensional forms, on predetermined computational surfaces, is then outlined. The details of the mathematical formulation used

[1] This research was sponsored by U. S. Army Air Mobility Research and Development Laboratory, under Contract No. NAS2-7850.

[2] Currently Senior Engineer, Turbomachinery Research, Corning Engine Co.

Contributed by the Gas Turbine Division of The American Society of Mechanical Engineers and presented at the Winter Annual Meeting, San Francisco, Calif., December 10–15, 1978. Manuscript received at ASME Headquarters August 4, 1978.

to perform the transformation is reported in [12] with the final results given below as equations (6–8) and (16). These flow equations are further expressed in the conservative law form using the vorticity-stream function formulation. Finally, the boundary conditions necessary to obtain a unique solution to the problem are discussed.

Fundamental Aerothermodynamic Relations. The three-dimensional viscous, compressible flow within turbomachine rotor is governed by the following set of laws.

Conservation of Mass:

$$\frac{\partial \rho}{\partial t} + \nabla \cdot (\rho \overline{W}) = 0 \tag{1}$$

Conservation of Momentum:

For a blade row rotating at a constant angular velocity ($\overline{\Omega}$) about its axis, Newton's second law of motion when combined with Stokes hypothesis can be written as

$$\rho\left(\frac{\partial \overline{W}}{\partial t} + \overline{W} \cdot \nabla \overline{W} + 2\overline{\Omega} \times \overline{W} - \Omega^2 \overline{R}\right) = -\nabla p - \nabla \times [\mu(\overline{\nabla} \times \overline{W})] + \frac{4}{3}\nabla(\mu \nabla \cdot \overline{W}) \tag{2}$$

Conservation of Energy:

In the absence of heat sources or sinks, the first law of thermodynamics for a heat conducting fluid with a thermal conductivity (K) can be written as:

$$\rho\left(\frac{\partial h}{\partial t} + \overline{W} \cdot \nabla h\right) = \frac{\partial p}{\partial t} + (\overline{W} \cdot \nabla)p + D + \nabla \cdot (\mathrm{K} \nabla T) \tag{3}$$

In the above equations p, ρ, T, h denote the static pressure, density, temperature and enthalpy, respectively. While, μ represents the kinematic viscosity coefficient and D is the viscous dissipation function. $\overline{W}$ is the relative velocity vector at any point, whose location is defined by the relative position vector $\overline{R}$, in the rotating frame of reference. The relations among the flow state variables are those of the ideal gas

$$p = \rho R T \tag{4}$$

and

$$dh = C_p dT \tag{5}$$

The mass-averaged variables principle is utilized in the above equations in order to describe the behavior of a turbulent flow. According to this principle, the components of the velocity vector $\overline{W}$, and the temperature T, are expressed on a mass-averaged basis, while the pressure p and the density ρ are expressed by their mean values only. For any flow variable $Q(x_1, x_2, x_3, t)$, its mass-averaged value, q, is given by:

$$q(x_1, x_2, x_3) = \overline{Q(x_1, x_2, x_3, t)\rho^*(x_1, x_2, x_3, t)}/\rho$$

where $\rho^*(x_1, x_2, x_3, t)$ is the instantaneous value of the density at any point whose location is defined by the coordinate (x_1, x_2, x_3). The over bar in the above equation represents the conventional time average, thus $\overline{\rho}^* \equiv \rho$. An effective viscosity μ_e is also used instead of the kine-

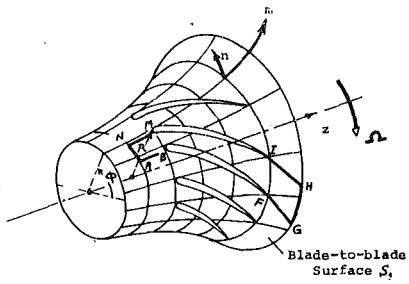

Fig. 1(*a*) Blade row intersection with a stream surface

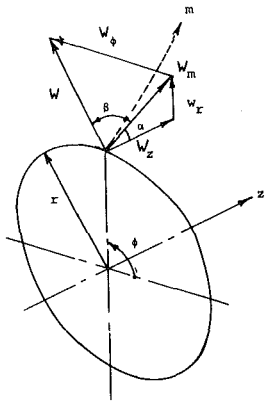

Fig. 1(*b*) Coordinate system and velocity components

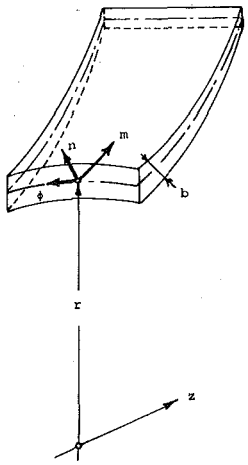

Fig. 1(*c*) Details of stream surface coordinate system with finite thickness sheet

Fig. 1 Blade-to-blade stream surface S_1

Nomenclature

b = normal stream annulus thickness, mt
C_1, C_2, C_3 = constants in the turbulence model
C_p = specific heat, J/(Kg) (K), or pressure coefficient
D = dissipation function, equation (3)
E = kinetic energy of turbulence, J/Kg
G_1, G_2, G_3 = denoting source terms in the flow governing equations
h = static enthalpy, J/Kg
H = total enthalpy, J/Kg, see equation (15)
m = meridional distance, mt
$\dot{M}$ = mass flow per blade flow through stream annulus, Kg/s
p = static pressure, N/mt^2
Pr = effective turbulent Prandtl number
r = radius from axis of rotation, mt
Re = Reynolds number
S_{CE} = Schmidt number for kinetic energy of turbulence
$S_{C\epsilon}$ = Schmidt number for dissipation of kinetic energy of turbulence
$\overline{V}$ = absolute velocity vector, mt
V = magnitude of $\overline{V}$, mt/s
$\overline{W}$ = relative velocity vector, mt/s
W = magnitude of $\overline{W}$, mt/s
W_m = meridional component of the relative velocity vector
W_ϕ = tangential component of the relative velocity vector
z = axial coordinate, mt
Z = number of blades
α = angle between meridional and axis, rad, see Fig. 1
ϵ = dissipation of kinetic energy of turbulence
Ω = rotational speed, rad/s
ϕ = relative angular coordinate, rad, see Fig. 1
ψ = stream function
ω = vorticity, 1/s

matic viscosity μ. This effective viscosity is assumed to describe the effects of Reynolds stress. The value of μ_e may be determined from a two equation turbulence model such as that given in [13].

Stream Surface Equations. An approach will be taken to reduce the spatial dimensions of the problem from the general three-dimensional form to several particular two-dimensional forms. The objective is to obtain a solution to the flow governed by the equations (1–5) through an appropriate combination of two-dimensional flow solutions. The reduction in spatial dimension is achieved through the consideration of the blade-to-blade stream surface concept [1]. The blade-to-blade stream surface, S_1, may be described by the annulus that would extend from the pressure surface of a blade to the suction surface of the next blade, as shown in Fig. 1. This annulus is characterized by the variation of its filament thickness, b, and the radius, r. For the purpose of the present discussion, the stream surface S_1 will be considered to represent the mean geometric properties of the annulus. It is possible to trace out the shapes and the filament thicknesses for a finite number of these blade-to-blade stream surfaces (annuli) in any turbomachine passage, using a meridional flow analysis as that indicated in [4]. On these surfaces the flow equations (1, 2) and (3) are transformed to several two-dimensional mathematical expressions. This is possible since each surface provides relations among the coordinates, such that the variation of flow properties over each surface may be described in terms of two space variables only. If a solution to the resulting two dimensional equations is obtained for each surface, then the flow properties throughout the three dimensional field may be readily evaluated.

Considering the flow annulus shown in Fig. 1, the curvilinear distance along the intersection of the mid-surface of the annulus with a meridional plane is denoted by m. The distance normal to the mid-surface is represented by n. The circumferential coordinate ϕ is considered positive in the counterclockwise direction when viewed down the positive z axis. The thickness of the annulus, b, is assumed to be small compared to the radius, r. Hence, the n component of the velocity vector and all variations in the n direction are neglected. The transformation of the flow governing equations (1) and (2) to the stream surface annulus coordinate system (m-ϕ-n) is outlined in [12] with the following results.

Continuity:

$$br\frac{\partial \rho}{\partial t} + \frac{\partial}{\partial m}(br\rho W_m) + \frac{\partial}{\partial \phi}(b\rho W_\phi) = 0 \tag{6}$$

Meridional Momentum:

$$\rho\frac{\partial W_m}{\partial t} + \rho\left(W_m\frac{\partial W_m}{\partial m} + \frac{W_\phi}{r}\frac{\partial W_m}{\partial \phi} - \frac{W^2\phi}{r} \times \sin\alpha - \Omega^2 r\sin\alpha - 2\Omega W_\phi \sin\alpha\right)$$
$$= -\frac{\partial p}{\partial m} - \frac{2}{3}\frac{\partial}{\partial m}\left[\mu_e\left(\frac{\partial W_m}{\partial m} + \frac{W_m}{r}\sin\alpha + \frac{1}{r}\frac{\partial W_\phi}{\partial \phi}\right)\right]$$
$$+ \frac{1}{r}\left\{\frac{\partial}{\partial m}\left(2\mu_e r\frac{\partial W_m}{\partial m}\right) + \frac{\partial}{\partial \phi}\left[\mu_e\left(\frac{\partial W_\phi}{\partial m} - \frac{W_\phi}{r}\sin\alpha + \frac{1}{r}\frac{\partial W_m}{\partial \phi}\right)\right]\right.$$
$$\left. - 2\frac{\mu_e}{r}\left[\frac{1}{r}\frac{\partial W_\phi}{\partial \phi} + \frac{W_m}{r}\sin\alpha\right]\sin\alpha\right\} \tag{7}$$

Tangential Momentum:

$$\rho r\frac{\partial W_\phi}{\partial t} + \rho\left(rW_m\frac{\partial W_\phi}{\partial m} + W_\phi\frac{\partial W_\phi}{\partial \phi} + W_m W_\phi\sin\alpha + 2\Omega r W_m\sin\alpha\right)$$
$$= -\frac{\partial p}{\partial \phi} - \frac{2}{3}\frac{\partial}{\partial \phi}\left[\mu_e\left(\frac{\partial W_m}{\partial m} + \frac{W_m}{r}\sin\alpha + \frac{1}{r}\frac{\partial W_\phi}{\partial \phi}\right)\right]$$
$$+ \frac{\partial}{\partial m}\left[\mu_e\left(r\frac{\partial W_\phi}{\partial m} - W_\phi\sin\alpha + \frac{\partial W_m}{\partial \phi}\right)\right]$$
$$+ \frac{\partial}{\partial \phi}\left[2\mu_e\left(\frac{1}{r}\frac{\partial W_\phi}{\partial \phi} + \frac{W_m}{r}\sin\alpha\right)\right]$$
$$+ \mu_e\sin\alpha\left[\frac{\partial W_\phi}{\partial m} - \frac{W_\phi}{r}\sin\alpha + \frac{1}{r}\frac{\partial}{\partial \phi}W_m\right] \tag{8}$$

where W_m, W_ϕ are the components of the mean relative velocity vector $\overline{W}$ in the meridional and tangential directions, respectively, and α is the angle between the mid-line of the annulus, m and the axis of rotation, z.

The system of the differential equations (6, 7) and (8), can be written alternatively in terms of a stream function ψ and a vorticity ω. In the present study, the stream function-vorticity formulation is considered for the purpose of reducing the difficulties of the coupling and nonlinearities associated with the presence of pressure in the flow equations (7) and (8). In addition, this formation offers the possibility to express the governing equation in their conservative law form. Consequently, no excessive accumulation of errors in the fluxes of the conserved quantities will result in the finite difference approximation of the governing equations. Roaches [14] illustrates that by showing how the Gauss divergence theorem is satisfied for the finite difference equations.

For steady-state flow, the continuity equation (6) is satisfied by introducing a stream function ψ, which is related to the flow velocity components by:

$$W_m = \frac{\dot{M}}{b}\frac{1}{\rho r}\frac{\partial \psi}{\partial \phi}$$

and

$$W_\phi = -\frac{\dot{M}}{b}\frac{1}{\rho}\frac{\partial \psi}{\partial m} \tag{9}$$

where $\dot{M}$ is the mass flow rate passing through the annulus, S_1, of Fig. 1. If the pressure terms are eliminated from equations (7) and (8) by cross differentiation and the mean vorticity variable ω is introduced, one obtains the *vorticity transport equation:*

$$\frac{\partial}{\partial m}\left(\frac{\dot{M}}{b}\frac{\partial \psi}{\partial \phi}\omega\right) - \frac{\partial}{\partial \phi}\left(\frac{\dot{M}}{b}\frac{\partial \psi}{\partial m}\omega\right) - \frac{\partial}{\partial m}\left[r\frac{\partial}{\partial m}(\mu_e\omega)\right]$$
$$+ \frac{\partial}{\partial \phi}\left[\frac{1}{r}\frac{\partial}{\partial \phi}(\mu_e\omega)\right] + G_1 = 0 \tag{10}$$

where

$$G_1 = 2\Omega\left[\frac{\partial}{\partial m}\left(\frac{\dot{M}}{b}\sin\alpha\frac{\partial \psi}{\partial \phi}\right) - \frac{\partial}{\partial \phi}\left(\frac{\dot{M}}{b}\sin\alpha\frac{\partial \psi}{\partial m}\right)\right]$$
$$+ \frac{\partial \rho}{\partial m}\frac{\partial W^2/2}{\partial \phi} - \frac{\partial \rho}{\partial \phi}\frac{\partial W^2/2}{\partial m} + \Omega^2 r\sin\alpha\frac{\partial \rho}{\partial \phi} \tag{11}$$

$$W^2 = W_m{}^2 + W_\phi{}^2 \tag{12}$$

and ω is defined by:

$$\omega = \frac{1}{r}\left[\frac{\partial}{\partial m}(rW_\phi) - \frac{\partial}{\partial \phi}(W_m)\right] \tag{13}$$

When the velocities W_m and W_ϕ in equation (13) are expressed in terms of the stream function variable, as defined in equation (9), equation (13) would reduce to the stream function equation:

$$\omega = -\frac{1}{r}\left[\frac{\partial}{\partial m}\left(\frac{\dot{M}r}{b\rho}\frac{\partial \psi}{\partial m}\right) + \frac{\partial}{\partial \phi}\left(\frac{\dot{M}}{b\rho r}\frac{\partial \psi}{\partial \phi}\right)\right] \tag{14}$$

Energy Equation. For a turbomachine rotor it is convenient to express the energy equation in terms of the total enthalpy, H, of the gas, besides its velocity components. The total enthalpy for turbulent flow is expressed as follows:

$$H = h + \frac{W^2}{2} + \Omega W_\phi r + \frac{\Omega^2 r^2}{2} + E \tag{15}$$

where E is the kinetic energy of turbulence.

Therefore, the energy equation (3), when transformed to the two-

dimensional stream surface coordinate system, results in [12]:

$$\frac{\partial}{\partial m}\left(\frac{\dot{M}}{b}H\frac{\partial\psi}{\partial\phi}\right)-\frac{\partial}{\partial\phi}\left(\frac{\dot{M}}{b}H\frac{\partial\psi}{\partial m}\right)-\frac{\partial}{\partial m}\left(\frac{\mu_e}{Pr}r\frac{\partial H}{\partial m}\right)-\frac{1}{r}\frac{\partial}{\partial\phi}\left(\frac{\mu_e}{\mathrm{Pr}}\frac{\partial H}{\partial\phi}\right)$$
$$+\frac{\partial}{\partial m}\left\{\mu_e r\left[\frac{1}{\mathrm{Pr}}\frac{\partial W^2/2}{\partial m}-\left(\frac{1}{S_{CE}}-\frac{1}{\mathrm{Pr}}\right)\frac{\partial E}{\partial m}\right]\right\}$$
$$+\frac{\partial}{\partial\phi}\left\{\frac{\mu_e}{r}\left[\frac{1}{\mathrm{Pr}}\frac{\partial W^2/2}{\partial\phi}-\left(\frac{1}{S_{CE}}-\frac{1}{\mathrm{Pr}}\right)\frac{\partial E}{\partial\phi}\right]\right\}-W_\phi\frac{\partial}{\partial m}(\mu_e\omega)$$
$$+\frac{W_m}{r}\frac{\partial}{\partial\phi}(\mu_e\omega)-Dr+G_2=0 \quad (16)$$

where Pr is the turbulent Prandtl number and S_{CE} is the turbulent Schmidt number for the kinetic energy of turbulence, E. The source term G_2 in the above equation represents the generation or decay in energy, due to the effect of rotation. It is given by:

$$G_2=-\Omega\frac{\dot{M}}{b}\left\{\frac{\partial}{\partial m}\left[(W_\phi r+r^2\Omega)\frac{\partial\psi}{\partial\phi}\right]-\frac{\partial}{\partial\phi}\left[(W_\phi r+r^2\Omega)\frac{\partial\psi}{\partial m}\right]\right\}$$
$$+\Omega\left\{\frac{\partial}{\partial m}\left[\frac{\mu_e}{\mathrm{Pr}}r\frac{\partial}{\partial m}\left(W_\phi r+\frac{r^2}{2}\right)\right]\right.$$
$$\left.+\frac{1}{r}\frac{\partial}{\partial\phi}\left[\frac{\mu_e}{\mathrm{Pr}}\frac{\partial}{\partial\phi}\left(W_\phi r+\frac{\Omega r^2}{2}\right)\right]\right\} \quad (17a)$$

The dissipation function, D, can be written as

$$D=2\mu_e\left\{\left(\frac{\partial W_m}{\partial m}\right)^2+\left(\frac{1}{r}\frac{\partial W_\phi}{\partial\phi}+\frac{W_m}{r}\sin\alpha\right)^2\right\}$$
$$+\mu_e\left\{\frac{\partial W_\phi}{\partial m}+\frac{1}{r}\frac{\partial W_m}{\partial\phi}-\frac{W_\phi}{r}\sin\alpha\right\}^2 \quad (17b)$$

The properties of flow passing through the stream annulus S_1, are completely defined by equations (4, 9, 10, 14) and (16) together with the known variations of μ_e, Pr, and the given boundary conditions. The effective viscosity, μ_e, is calculated from a two equation model, one expressing the development of the turbulent kinetic energy, E, and the other its dissipation rate, ϵ. These equations may be expressed, in terms of the stream annulus system of coordinate (m, ϕ, n) as follows.

Turbulent Kinetic Energy Equation:

$$\frac{\partial}{\partial m}\left(\frac{\dot{M}}{b}E\frac{\partial\psi}{\partial\phi}\right)-\frac{\partial}{\partial\phi}\left(\frac{\dot{M}}{b}E\frac{\partial\psi}{\partial m}\right)-\frac{\partial}{\partial m}\left(\frac{\mu_e}{S_{CE}}r\frac{\partial E}{\partial m}\right)$$
$$+\frac{\partial}{\partial\phi}\left(\frac{\mu_e}{S_{CE}}\frac{\partial E}{r\partial\phi}\right)-rD+\rho\epsilon r=0 \quad (18)$$

Dissipation Rate Equation:

$$\frac{\partial}{\partial m}\left(\frac{\dot{M}}{b}\epsilon\frac{\partial\psi}{\partial\phi}\right)-\frac{\partial}{\partial\phi}\left(\frac{\dot{M}}{b}\epsilon\frac{\partial\psi}{\partial m}\right)-\frac{\partial}{\partial m}\left(\frac{\mu_e}{S_{C\epsilon}}r\frac{\partial\epsilon}{\partial m}\right)$$
$$+\frac{\partial}{\partial\phi}\left(\frac{\mu_e}{S_{C\epsilon}}\frac{1}{r}\frac{\partial\epsilon}{\partial\phi}\right)-C_1\frac{\epsilon}{E}rD+C_2\frac{\epsilon^2}{E}\rho r=0 \quad (19)$$

The relation among E, ϵ and μ_e is given by [13]:

$$\mu_e=C_D\rho E^2/\epsilon \quad (20)$$

where C_1, C_2, C_D, C_{CE} and $S_{C\epsilon}$ are constants to be determined from available data (see for example [13]).

In general, equations (4–20) are valid for any turbomachine geometry or any number of stream annuli except for the two stream annuli $S_{1/0}$ and $S_{1/N}$ shown in Fig. 2, which contain the hub and shroud contours. This exception may be attributed to the existence of a large variation in flow properties along the normal, $\bar{n}$, to these two annuli resulting from the presence of the solid boundaries. The determination of the flow properties within these stream annuli constitute a study by itself and is not intended for inclusion in the present work.

The solution of the above system of equations within the turbomachine passages is carried out numerically. One can observe that equations (10, 14, 16, 18) and (19), constitute a system of coupled elliptic partial differential equations, involving second order derivatives of ψ, ω, H, E, and ϵ which are the dependent variables. From the nature of the problem, none of the terms are negligible in the governing equations. The convective terms introduce nonlinearity and also instability if the proper differences are not taken into account. Once a solution for these variables has been obtained, the velocity distribution can be determined from equation (9). The pressure distribution can then be evaluated from either equations (7) or (8). In order to solve the elliptic equations by the usual numerical methods, it is necessary to define a selected region in the physical domain with boundary conditions specified for all the dependent variables.

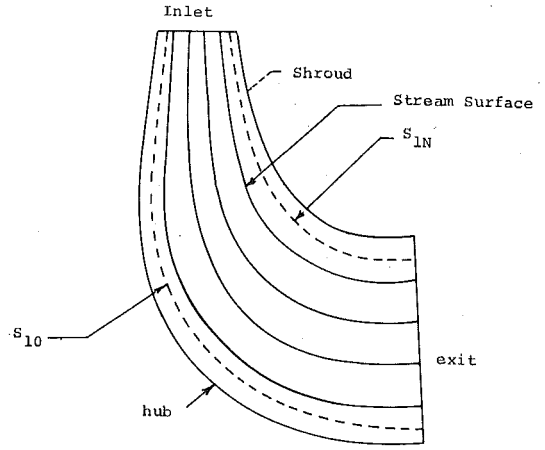

Fig. 2 Stream surface contours, obtained from a meridional flow analysis for a radial inflow turbine

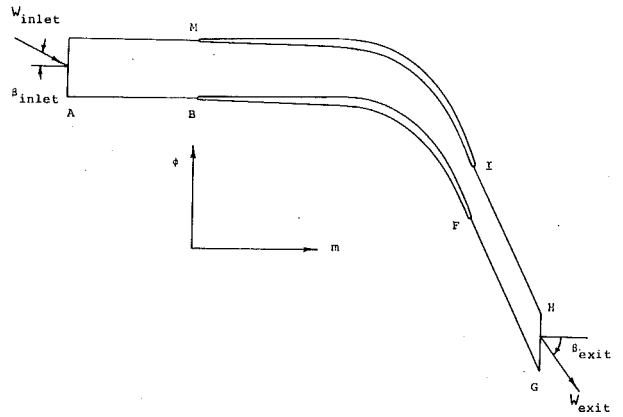

Fig. 3 Computational domain in the physical space

Description of the Computational Domain. The flow region of interest, as shown in Fig. 3, contains the blade row and segments of the stream surface, S_1, extending upstream and downstream of the row. Due to the circumferential periodicity in turbomachine passages, the selected domain needs to encompass only that fraction of the flow annulus containing a single blade to blade passage. The shape and location of the periodic boundaries (*AB, NM, IH* and *FG*) may be defined arbitrarily as long as their spacing corresponds to the blade pitch $2\pi/Z$. The upstream and downstream boundaries (*AN, GH*) are located sufficiently far from the blade so that tangential variation along them are ignored. The flow properties are consequently considered to be uniform along the boundaries *AN* and *GH*.

Boundary Conditions. In specifying the boundary conditions, two flow situations were investigated [12]. Preliminarily, only the case of the laminar flow is considered in this paper. The turbulent flow case will be reported in future work. Accordingly, in the following specification of boundary conditions, no assignment for the boundary values of E and ϵ in equations (18) and (19) is needed. Moreover, the flow properties within the turbomachine channels is completely defined through the simultaneous solution of only equations (10, 14) and (16).

Upstream Flow Boundary AN. It is a common practice in turbomachine flow calculations that the magnitude and the direction

of the flow velocities, the total temperature and the total pressure or density are defined at the turbomachine inlet. Therefore, along the boundary AN the values of ψ, ω, H or their derivatives can be evaluated using the defined flow properties. The known magnitude of the inlet relative velocity and its direction, as shown in Fig. 3, specify the values of $\partial\psi/\partial m$ and $\partial\psi/\partial\phi$ according to the relations

$$\frac{\partial\psi}{\partial m} = -\frac{b\rho}{\dot{M}} W_\phi, \quad \frac{\partial\psi}{\partial\phi} = \frac{b\rho r}{\dot{M}} W_m \tag{21}$$

Since the inlet stream of the gas is considered to be uniform, the absolute value of vorticity ω has to be zero along the boundary AN. In a rotating frame of reference, as it is in the present case, the relative value of ω is given by the following expression

$$\omega = -[2\Omega \sin\alpha]_{\text{inlet}} \tag{22}$$

The value for the total enthalpy, H, can be defined using the specified flow properties.

The Periodic Flow Boundaries AB, NM and FG, IH. The periodicity condition requires that the magnitude and direction of the flow velocity as well as other fluid properties be equal at every two corresponding points along AB and MN. Similarly, the same condition should apply at every two corresponding points along FG and IH. The periodicity condition in terms of the dependent variables is satisfied through the following conditions. First, equating ω, $\partial\omega/\partial\phi$, $\partial\psi/\partial\phi$, H, and $\partial H/\partial\phi$ values on each corresponding points. Second, ensuring that the ψ values are differed by unity between the corresponding points.

The Blades Surfaces Boundary MI and BF. For the laminar flow case, two boundary conditions over the blades surfaces are usually specified. These are the nonslip condition and the impermeability of the surface in the case of blades with no injection. The non-slip condition requires that

$$\frac{\partial\psi}{\partial\eta} = 0 \tag{23}$$

where η is the normal to the blade surface. On the other hand, the impermeability condition requires that no component of velocity exist in the direction normal to the blade surface. Therefore, the blade surfaces are treated as streamlines with the ψ values specified as zero on the (MI) surface and unity on the (BF) surface. On either MI or BF surfaces, one has therefore, two boundary conditions for ψ but none for ω. It is a well accepted fact in computational fluids mechanics to rely on a modified evaluation of equation (14) to determine the boundary condition for ω [14]. The modification is introduced in an attempt to insure that equation (23) holds, that is, to satisfy the no slip condition. This approach is utilized in the current study to determine the value of the vorticity, ω, over the blade surfaces.

In regard to the thermal boundary conditions either the blade surface temperature is known or the normal derivative $\partial T/\partial\eta$ is specified to zero for the adiabatic wall conditions. In either case, equation (15) is used to determine the value of H or its derivative that is used as boundary condition for equation (16).

The Downstream Boundary GH. Two basic problems arise in the specification of the boundary functions for the dependent variables along GH. The first concerns the behavior of the dependent variables H and ω. The nature of the problem is that, physically, these are known only if the boundary is located at an arbitrarily large distance from the blade surface. In this case the values of H and ω are that of the corresponding surroundings. The placement of GH at exceedingly large distances from the blade boundary is quite obviously not possible for numerical considerations. Therefore, one has to employ some auxiliary condition, usually obtained by experience, to define H and ω implicitly. The conditions of zero gradient in the meridional direction, i.e.,

$$\frac{\partial H}{\partial m} = 0 \tag{24a}$$

seems to be appropriate and therefore is employed. For the vorticity ω, the absolute value is taken to be zero, hence

$$\omega = -[2\Omega \sin\alpha]_{\text{exit}} \tag{24b}$$

More important than the specification of the remote boundary functions of ω and H along GH is the determination of the ψ values at the same boundary. The downstream flow velocities, which may be used to determine ψ derivatives along GH, and that guarantee a unique solution to the problem are not known in general apriori. Therefore, one has to introduce a supplementary condition, generally resulting from physical intuition, to define the ψ derivatives. Generally, two approaches have been utilized by investigators working in the inviscid flow area to deal with this problem. Both of them are based on an iteration procedure, through which the Kutta condition for tangency of the flow at the blade trailing edge is satisfied [15]. This is equivalent to specify the unique solution to the problem. Unfortunately, the Kutta condition cannot be applied in a realistic manner to solve the present flow problem due to its viscous nature. The conservation of angular momentum principle is employed as an alternative supplementary condition that results in the required unique solution. The procedure is as follows.

Estimated exit flow angles, β_{exit}, along GH are used to specify the values of ψ derivatives in m direction through the following relation:

$$\frac{\partial\psi}{\partial m} = \frac{1}{2\pi/Z} \frac{\tan\beta_{\text{exit}}}{r_{\text{exit}}} \tag{25}$$

The flow field equations are then solved for the boundary function of ψ given by equation (25) to obtain the velocity and the pressure distribution throughout the turbomachine channel. An evaluation of the torque developed by the channel is obtained through the integration of the difference in pressure and shear forces acting on the blade surfaces. The change in the angular momentum between the known inlet and the estimated exit flow conditions is calculated. If the value of the predicted torque was not equal to the rate of change of the angular momentum then the direction of the exit flow velocity is altered. The whole procedure is repeated until a satisfactory result is obtained.

Numerical Solution

In the present phase of the study, where the case of laminar flow is considered, the governing equations (10, 14) and (16) are solved numerically using an Alternating Direction Implicit (ADI) method [12]. In using this method of solution one has to include a fictitious time-derivative term in the right hand side of each of the governing equations. The resulting set of, parabolic in time, partial differential equations are then solved by relaxing them in a two half step procedure towards their asymptotic steady-state solution, During the first half step, the equations are solved implicitly along the ϕ direction. While, during the second half-step, the equations are solved implicitly along the m direction. The time levels for the various terms in the equations are assigned so as to maintain the ADI method to be second-order accurate. This consists of writing the time-derivative terms as backward differences at both half-steps. Moreover, all the spatial derivatives are represented by central differences except in those situations dictated by stability, an upwind differencing technique is used for the convective terms. With this procedure, the governing equations are reduced to a tridiagonal system of algebraic equations during each half-step. These can be solved using the Thomas Algorithm [16]. Some important aspects of the numerical procedures as well as the details of the solution techniques are given in [12].

A computer program is developed for the numerical solution of the resulting system of algebraic equations subjected to the prescribed boundary conditions. The program is arranged to handle general flow situations within turbomachinery. These may be axial, radial or mixed flow types. In general, the program requires as an input the shape and the configuration of the stream surface S_1, the blades geometry, the inlet flow conditions, and the rotational speed of the machine. The configuration of the stream surface S_1, is generated from the meridional flow analysis given in [4]. The output consists of the distribution of the stream function, the vorticity and the static pressures within the blade passages. The variation of meridional and tangential velocity components from blade-to-blade and from the inlet of the machine to its exit is also generated. In cases where blade cooling is considered the program has the capability to generate the temperature distribution and the local heat transfer coefficients along the blade surfaces. In order to keep the computer time always within reasonable limits

Table 1 Parameter for the numerical solutions

Case No.	Designation	$\dot{M}\sqrt{T_0}/P_0$	$N/\sqrt{T_0}$	U_{tip} m/s	β at upstream boundary AN	β at downstream boundary HG	Reynolds No. $\left(\frac{W_{min}\dagger \cdot r_{tip}}{\nu}\right)_{inlet}$	T_0 K	P_0 kg/m²	Remarks* Computation Time (s)
1	Inward	0.0011	87.9	39.3	72.27 deg	33.7 deg	1.175×10^5	288	10540	117
2	Inward	0.0012	87.3	39.3	74.25 deg	37.7 deg	1.208×10^5	288	10600	121
3	Inward	0.0012	116.6	52.0	79.77 deg	10.5 deg	1.219×10^5	288	10670	106
4	Inward	0.0012	145.6	65.4	81.28 deg	6.3 deg	1.275×10^5	288	10750	119
5	Outward	0.00343	589.25	261.8	44.50 deg	81.2 deg	1.370×10^5	288	10330	130

* In all cases studied, the upstream boundary AN of Fig. 3 is located at radius ratio r/r_{tip} of 1.35, while the downstream boundary HG is located at radius ratio r/r_{tip} of 0.254.
† W_{min} ≡ Meridional velocity at inlet

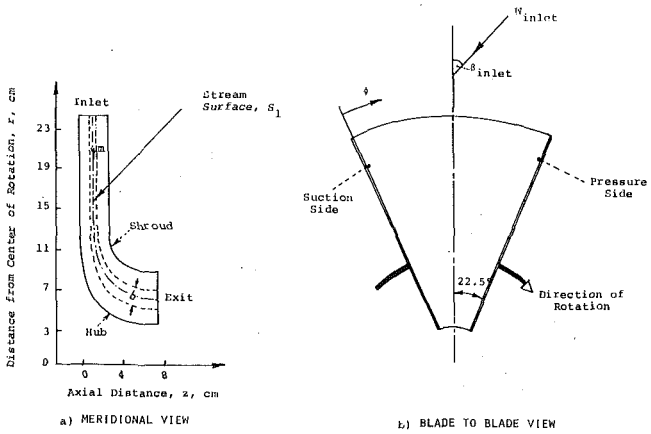

Fig. 4 Hub-shroud profile with the stream surface S_1, used for blade-to-blade analysis

(see Table 1), the flow domain has been divided for all calculations into 30 × 40 nodes with the greater number of nodes distributed in the meridional direction. These grid nodes were found to be sufficiently fine to suppress grid-size influence.

Results and Discussion

Five flow cases are investigated using the developed program. The main purpose was to check the accuracy of the present method of analysis in predicting the actual flow behavior within turbomachine channels. The accuracy of the method was confirmed by a comparison with available experimental data. Four of those investigated cases were concerned with inward flow situation, while the fifth one dealt with an outward flow case. In all cases investigated, the flow was considered to be incompressible and having a constant effective viscosity μ_e. The blade surfaces are assumed to be adiabatic with no heat sources or sinks. Other solutions dealing with cases where different thermal boundary conditions are considered, can be found in [12].

Inward Flow Cases. These flow cases are those of a radial inflow turbine whose rotor consists of eight radial straight blades. A full description of the rotor geometry is given in Fig. 4. The flow patterns are investigated on a blade-to-blade stream surface, S_1, located midway the passage depth of the rotor as shown in Fig. 4. The results are presented over a wide range of operating conditions, which are summarized in Fig. 4. The results are presented as stream function contour plots, velocity profiles across the rotor passages together with some information concerning the pressure distribution within these passages.

The streamline contours for the four inward solution cases are shown in Figs. 5(*a*) and 5(*b*). The streamlines are plotted for the region between a pair of blades, represented by the heavy thick lines. The streamlines are designated by a stream function ratio ψ/ψ_{total} such that the value on a streamline indicates the ratio of flow through the passage between the streamline and the pressure surface of the blade. Thus, for the given channel configuration, the streamline spacing is indicative of the velocity relative to the rotor, with close spacing indicating high velocities and wide spacing indicating low velocities. For the operating conditions corresponding to case 1, as shown in Fig. 5(*a*), it is observed that a recirculating eddy began to form near the pressure

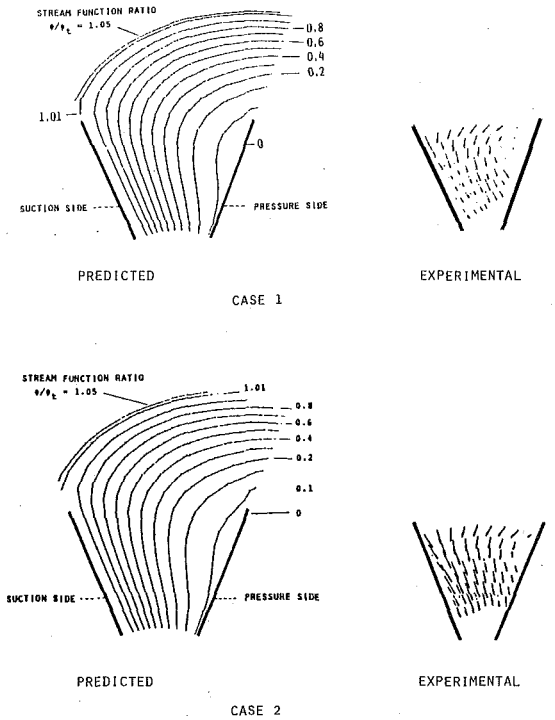

Fig. 5(*a*) Relative streamlines for flow through radial inflow turbine

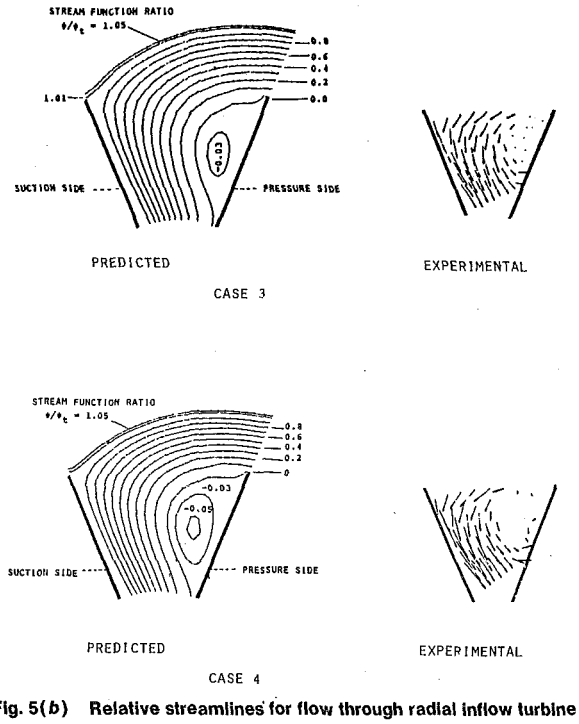

Fig. 5(*b*) Relative streamlines for flow through radial inflow turbine

surface of the blades. As the rotating speed increases, the recirculating zone grows much larger, as shown for case 3 in Fig. 5(*b*). The relative velocity near the suction side of the blades increases in the later case. This may be attributed to the fact that the effective sectional area of the rotor decreases with the growth of the recirculating zone. In actual practice, large recirculatory zones are expected to cause higher losses in total pressure. Hence, it is desirable to avoid them through an efficient design of the rotor and by selecting a proper operating condition. From inspection of Figs. 5(*a*) and 5(*b*), it is clear that the size of the recirculating eddy depends upon the relative magnitude of the flow rate ($\dot{M}\sqrt{T}/p$) and the rotor tip speed U_{tip}. In general, these zones can be reduced by increasing the mass flow rate or decreasing the rotor tip speed.

The most remarkable feature of the present results is the good agreement obtained between the predicted flow behavior and the experimental evidence taken from [17]. In all cases studied, the size and the extent to which the recirculating zone grows compares favorably well with the experimental data, as indicated in Figs. 5(*a*) and 5(*b*).

Figs. 6(*a*) and 6(*b*) show the predicted meridional velocity distribution across the blade passages at three different radial locations. These locations are selected to correspond to a radius of 23.2, 15 and 6.8 cms, respectively. The dotted line shown on each figure represents the velocity distribution for the inviscid case. From the profile distributions in the previous figures, it is evident that near the turbine inlet the boundary layers formed over the blade pressure surfaces are thicker compared to those formed on the blade suction surfaces. One of the unique features of the viscous flow in rotating channels is the large variation in the meridional velocity profiles as the flow travels downstream in the channel. The profile distribution, at stations located away from the turbine inlet, shows that regions of high meridional velocities are shifted towards the blades suction surface, as shown in Figs. 6(*a*) and 6(*b*). While, regions of high relative meridional velocities are observed to exist near the blades pressure surface at

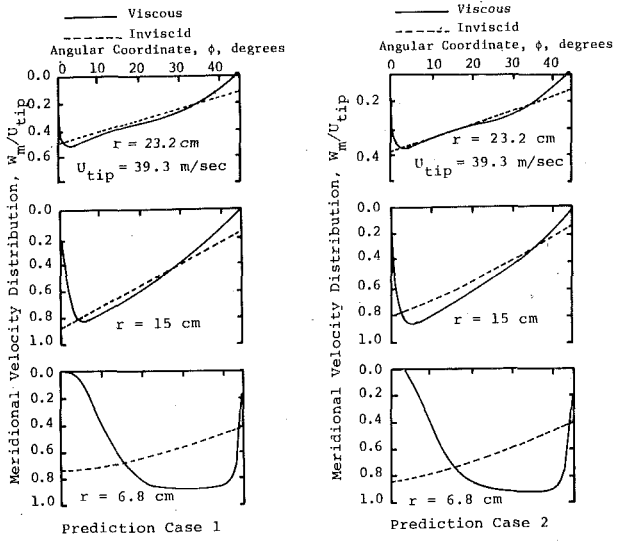

Fig. 6(*a*) Nondimensional velocity distribution at different radial locations

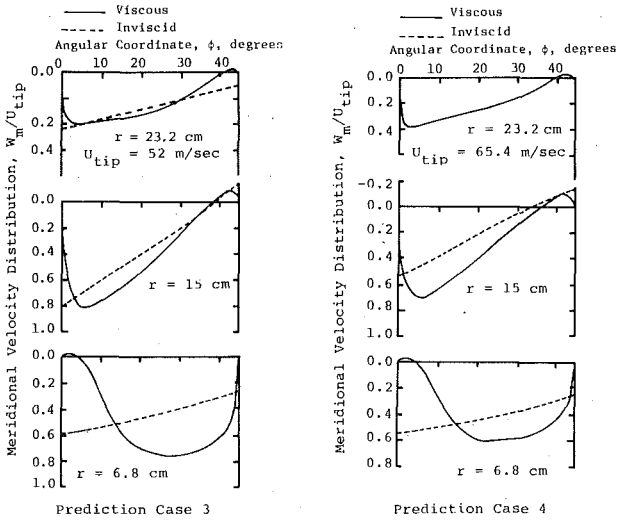

Fig. 6(*b*) Nondimensional velocity distribution at different radial locations

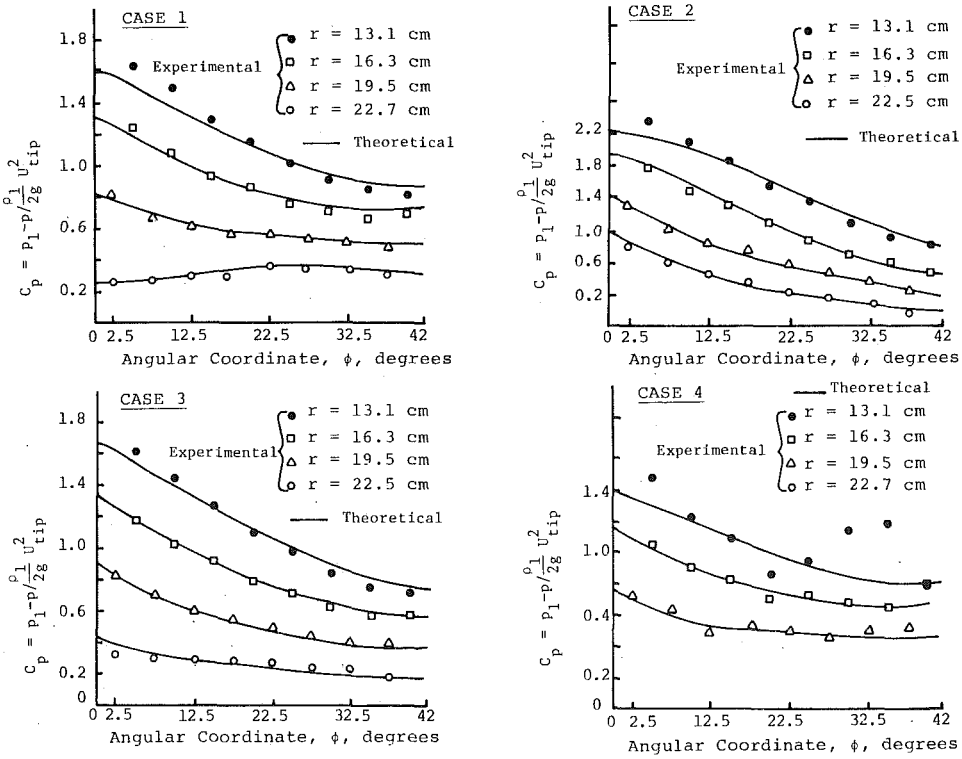

Fig. 7 Comparison of predicted static pressure distribution with experimental data of [12]

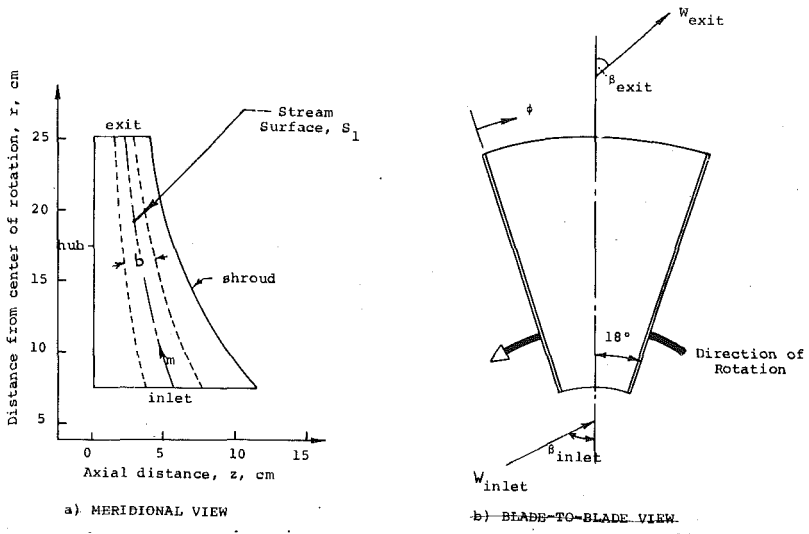

Fig. 8 Hub-shroud profile with the stream surface, S_1, used for blade-to-blade analysis (compressor case)

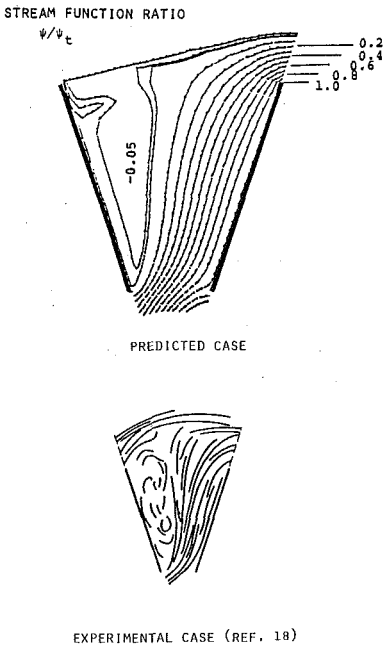

Fig. 9 Relative streamlines for flow through radial compressor

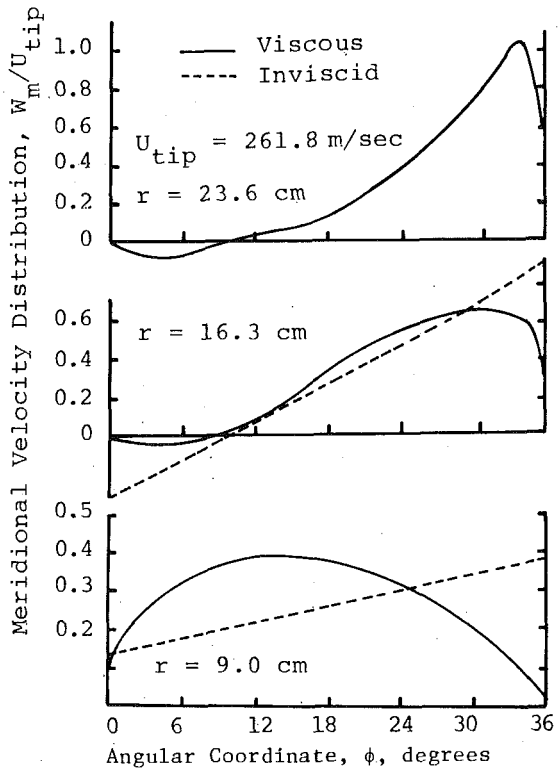

Fig. 10 Velocity profiles across the compressor passages at different radial locations (case 5 in Table 1)

subsequent downstream stations. The inviscid flow solution gives a completely different flow behavior, in this respect, when compared with the viscous calculations. Moreover, in some flow situations where severe changes take place near the rotor tip as in case 4 in Fig. 6(b), the inviscid flow solution fails completely even in predicting the flow characteristics. All these factors, in addition to the appearance of the reversed flow regions made it clear why the inviscid solutions always fail to produce a realistic prediction of boundary layer characteristic parameters in rotating machines when used in conjunction with standard boundary layer interacting techniques.

Fig. 7 shows the pressure variation between blades at different radial locations. These radial locations correspond to radius, r = 13.1, 16.3, 19.5 and 22.7 cms. The static pressure, p, is plotted in these figures using the nondimensional quantity, $C_p = p_1 - p/\rho_1/gU_{tip}^2$, where p_1, ρ_1 are the mean static pressure and density at rotor inlet respectively. As with the stream function and velocity results, the present method of analysis provides an excellent prediction of the pressure distribution over a wide range of operating conditions. Correlation with experimental data of [17] as shown in the previous figures verify this statement. On the whole, the value of C_p is observed to be larger on the suction side of the blades and decreases near the pressure surface. The rate of decrease of C_p values is smaller when the rotational speed is increased. Also, in the region lying between the center of the passage and the pressure surface, the C_p values become smaller as the rotational speed decreases. All these observations imply that the static pressure drop from the rotor inlet increases with high rotational speed. Near the suction surface, the pressure drop increases with the decrease of rotational speed. Such a tendency is remarkable, particularly near the rotor inlet.

Some comments might also be made concerning the discrepancies observed between the predicted and experimental values of pressure distribution near the rotor exit (i.e., at r = 13.7) in case 4. As reported in the experimental work of [17], the operating conditions for this case cause the flow to be heavily separated from the rotor hub surface. The existance of large separation zone within the rotor is believed to modify the channel shape in such a way as if the zone acts as a pseudo blade. This in turn affects the pressure distribution in the manner shown in Fig. 6(b). Therefore, it appears that in order to deal with flow

cases where heavy separation is encountered within the rotor channel, one has to incorporate a Zonal model for such separation in the present method of analysis. Such development in the method of solution is essential for further use of this method of analysis in performance prediction in turbines.

Outward Flow Case. The capability of the method of analysis to deal with flow in diffusion cascades is demonstrated by studying the flow behavior within the rotor of a radial bladed compressor. The compressor rotor under consideration has 12 straight radial blades. Other data pertaining to the rotor geometry is shown in Fig. 8. The input data for this case is presented also in Table 1. A typical distribution of the flow properties on the stream surface located midway (between the shroud and the hub) as shown in Fig. 8 are calculated and the corresponding results are presented in Figs. 9 and 10. As with the inward flow cases, the stream function profile of Fig. 9 reflects the appearance of the recirculatory eddy. The inviscid flow solution, although shows the existance of the negative flow regions as illustrated in Fig. 10, it overestimates the size of the recirculating eddy. This overestimation is supported by the existance of large negative meridional velocities near the blades suction surface. In an actual case, boundary layer phenomena are expected to reduce the effective flow area of the passage, thus increasing the volume flow rate per unit area through the effective area and thereby reducing the size of the eddy. This is exactly the same result obtained using the present viscous flow solution.

In conclusion, it may be stated that the present method of analysis gives a better representation of the actual flow situation within the passage of turbomachine rotors. The preservation of the ellipticity of the flow problem is believed to be the major reason that results in this better representation. The ellipticity is preserved through the consideration of all the diffusion terms of the governing equations during the solution procedures. The method proves also to be accurate and provides invaluable information on the rotor flow characteristics. This is evidenced by the good agreement obtained between the predicted results and the available experimental data. The results obtained for the radial bladed passages of turbine and compressor has provided a great insight into the flow phenomena and this should encourage the efforts undertaken currently to deal with more complicated blade shapes. Such development in addition to the inclusion of the turbulence model in the method of solution are undoubtably essential for further aerodynamic improvement and performance prediction of turbomachines.

Acknowledgments

This research work was sponsored by NASA Contract No. NAS2-7850, U. S. Army Air Mobility Research and Development Laboratory, Ames Research Center, Moffett Field, CA.

References

1 Wu, Chung-Hua, "A General Theory of Three-Dimensional Flow in Subsonic and Supersonic Turbomachines of Axial, Radial and Mixed-Flow Types," National Advisory Committee for Aeronautics, TN 2604, 1952.

2 March, H., "A Digital Computer Program for the Through-Flow Fluid Mechanics in an Arbitrary Turbomachine, Using a Matrix Method," A.R.C. R&M No. 3509, 1968.

3 Novak, R. A., "Streamline Curvature Computing Procedures," ASME JOURNAL OF ENGINEERING FOR POWER, Vol. 89, No. 4, Oct. 1967, pp. 478–490.

4 Katsanis, T., "Use of Arbitrary Quasi-Orthogonals for Calculating Flow Distribution on a Blade-to-Blade Surface in a Turbomachine," NASA TN D-2546, Dec. 1964.

5 Katsanis, T., "Fortran Program for Calculating Transonic Velocities on a Blade-to-Blade Stream Surface of a Turbomachine," NASA TN D-5427, 1969.

6 Wennerstrom, A. J. and Frost, G. R., "Design of a Rotor Incorporating Splitter Vanes for a High Pressure Ratio Supersonic Axial Compressor Stage," Wright-Patterson AFB, Ohio, ARL TR 74-0110, AD 786025, August 1974.

7 Dring, R. P., "A Momentum Integral Analysis of the Three-Dimensional Turbine End-Wall Boundary Layer," ASME Paper No. 71-GT-6, 1971.

8 Kenny, D. P., "A Method for Calculating Cascade/Channel End Wall Boundary Layer Cross Flow," ASME Paper No. 76-GT-77, 1976.

9 Briley, W. R., "Numerical Method for Predicting Three-Dimensional Steady Viscous Flow in Ducts," *Journal of Computational Physics,* 14, 1974, pp. 8–28.

10 Pratap, V. S., Majumda, "Numerical Computation of Flow in Rotating Ducts," ASME Paper No. 76-FE-25, 1976.

11 Dodge, P. R., "A Numerical Method for 2-D and 3-D Viscous Flow," AIAA Paper No. 76-425, 1976.

12 Khalil, I. M., "A Study of the Viscous Nonadiabatic Flow in Turbomachines," Ph.D. Thesis, University of Cincinnati, 1978.

13 Gosman, A. D., Spalding, D. B., "Transfer of Heat in Rotating Systems," ASME Paper No. 76-GT-25, 1976.

14 Roache, P. J., *Computational Fluid Dynamics,* Hermosa Publishers, Albuquerque, New Mexico, 1972.

15 Stanitz, J. D., "A Rapid Approximation Method for Determining Velocity Distribution on Impeller Blades of Centrifugal Compressors," N.A.C.A TN 2421, 1951.

16 Carnahan, B., and Lutter, H. A., *Applied Numerical Methods,* John Wiley & Sons, Inc.

17 Watanabe, I., Ariga, I. and Fujie, K., "A Study of the Flow Patterns in an Impeller Channel of a Radial Turbine," JOURNAL OF ENGINEERING FOR POWER, Oct. 1967, p. 467.

18 Benson, R. S., and Cartwright, "Analytical and Experimental Studies of Two-Dimensional Flow in a Radial Blade Impeller," ASME Paper No. 71-GT-20, 1971.

A. Ray[1]
D. A. Berkowitz[2]
V. H. Sumaria
The MITRE Corporation,
Bedford, Mass.

Nonlinear Dynamic Model of a Fluidized-Bed Steam Generation System

A dynamic model of an atmospheric pressure fluidized-bed steam generation system is presented which allows digital simulation and analytical controller design. The nonlinear, time-invariant, deterministic, continuous-time model is derived in state-space form from conservation relations, empirical correlations and system design data. The model has been verified for steady-state and transient performance with measured data from experimental test runs. Transient responses of several process variables, following independent step disturbances in coal feed rate and air flow, are illustrated.

Introduction

Fluidized-bed combustion (FBC) is an alternative technique being considered for application to commercial scale electric power generation. Fluidized-bed technology is well known in chemical engineering and fuel processing industries [1]. For coal combustion, the fluidized bed furnace offers an alternative to scrubbers for capturing flue gas SO_2.

Several fluidized-bed combustion facilities with equivalent capacities in the range 1–10 MWe are in operation at present, or in various stages of design and construction [2]. A 30 MWe multicell unit installed at Monongahela Power Company's Rivesville Station in West Virginia is now being tested. 200 MWe plants suitable for commercial use by utility companies are being considered. This technology is being developed much more rapidly than has been the case with conventional fossil power plants. Mathematical modeling and simulation are useful tools for analyzing performance and control problems in complex, interactive systems such as power plants [3, 4]; their application to FBC systems is very timely.

This paper presents a nonlinear dynamic model of an atmospheric pressure FBC steam generation system, which allows digital simulation and analytical controller design. The model provides the basis for: (1) understanding complex and interactive process dynamics, (2) design verification and predicting effects of subsystem changes on the entire process, (3) interactive multivariable controller design, and (4) overall system (process and controller) performance evaluation. The model was verified with experimental measurements for both steady-state and transient performance. Although related to a particular system, the modeling and simulation techniques presented in this paper have general applicability and can be readily adapted to other fluidized-bed power generation systems.

Model equations are solved numerically using CSMP-III [5]. A FORTRAN version of the CSMP-III code is incorporated as a subroutine in general purpose analytical programs to obtain steady-state solutions, for model linearization, and for other purposes such as eigenvalue and transfer function determination [6].

Contributed by the Power Division of THE AMERICAN SOCIETY OF MECHANICAL ENGINEERING for publication in the JOURNAL OF ENGINEERING FOR POWER. Manuscript received at ASME Headquarters October 18, 1978.

[1] Currently Assistant Professor of Mechanical Engineering, Carnegie-Mellon University, Pittsburgh, PA 15213.

[2] Currently with JAYCOR, Bedford, MA 01730.

System Description

In fluidized-bed combustion, coal particles of about 1 cm top size are introduced pneumatically into a course bed of calcined limestone. The major bed particle dimension is about 3 mm. At any instant, coal fraction in the bed is about 2 percent; once coal has ignited, combustion is self-sustaining. Coal separates into a volatile component and a solid component of char and ash. A portion of the char and ash are blown out of the bed, or elutriated, with the flue gas.

Calcined limestone, CaO, acts as SO_2 sorbent. It reacts with O_2 and SO_2 in the bed to form $CaSO_4$. As the amount of available limestone decreases, it is necessary to add fresh limestone with the coal. With continual addition of fresh bed material, spent bed material must be removed to maintain constant bed mass or bed height. In addition, continual bed recirculation and screening removes nonreactive bed material.

To optimize sorbent effectiveness, and to avoid ash sticking and agglomerating, fluidized-bed temperature is controlled to approximately 840°C (1550°F) Thermal energy is continually removed from the bed by water or steam cooled heat transfer surface. Use of immersed heat transfer assemblies gives the fluidized-bed boiler its major distinctive feature, creating at the same time several advantages and several new problems.

Above the minimum fluidization condition, pressure drop across the bed varies very little with further increases in superficial air velocity, and remains equal to weight per unit area of the bed. The air distributor plate and bed geometry are designed to minimize occurrence of channeling and unstable flow which alter the fluidization characteristic.

Combustion occurs primarily within the bed (overbed combustion accounts for a small portion of the energy release), and bed heat transfer is a combination of conduction, convection and radiation. Heat transfer rate to immersed surfaces is high, but only weakly dependent on fluidizing air velocity in the normal operating range [1].

The atmospheric pressure fluidized-bed Process Development Unit (PDU) at Alexandria, Virginia, has a single cell 1.83 m × 0.46 m (6 ft × 1.5 ft) with steam generating capacity of 0.63 kg/s (5000 lbm/hr) at 1.724×10^6 N/m^2 (250 psia) and 204°C (400°F), equivalent to approximately 0.5 MWe. The schematic in Fig. 1 includes major components that were modeled. The immersed cooling water bundle was removed during the particular experiments reported here, and was removed from the model, as well. Waterwalls were the only immersed heat transfer surfaces in the bed.

Modeling Approach

The physical process consists of distributed parameter dynamic elements, most generally represented by nonlinear partial differential equations with space and time as independent variables. To obtain numerical solutions, the partial differential equations are approximated by a finite set of ordinary differential equations with time as the independent variable. This approach has proven to be adequate in the simulation of other power generation systems [7–9].

A model solution diagram for the fluidized-bed plant is shown in Fig. 2. Each block represents a physical component or group of components. Lines interconnecting blocks indicate direction of information flow or "model causality." This diagram shows how individual component models mathematically interface with each other, and ensures consistent causality for the complete set of equations defining the physical process.

Following the arrangement in Fig. 2, plant modeling is accomplished in two steps: (1) modeling of individual components or groups of components and (2) formulation of an overall plant model by appropriate interconnection of the individual component models.

Step 1 includes determination of steady-state solutions and eigenvalues (of linearized models) at several operating points. Steady-state solutions are verified with design data and eigenvalues are examined for frequency range. Step 2 incorporates sequential interconnection of component models according to the solution diagram. Steady-state solutions and eigenvalues of the augmented model are examined at each phase of interconnection.

Development of Model Equations

Model structure is formulated from: conservation relations for mass, momentum, and energy, semi-empirical relationships for fluid flow and heat transfer, and state relations for thermodynamic properties of working fluids. Model parameters are evaluated from design and experimental data.

Major assumptions in addition to the lumped parameter approximation are: (1) uniform fluid flow over pipe, duct or furnace cross-section, (2) perfect thermal insulation between plant components and

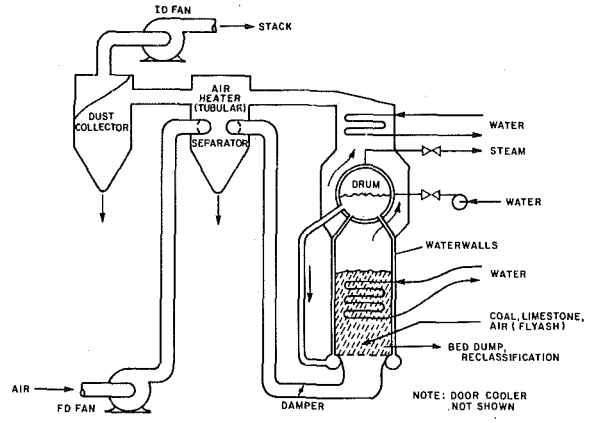

Fig. 1 Atmospheric Pressure fluidized-bed Process Development Unit (PDU), Alexandria, Va

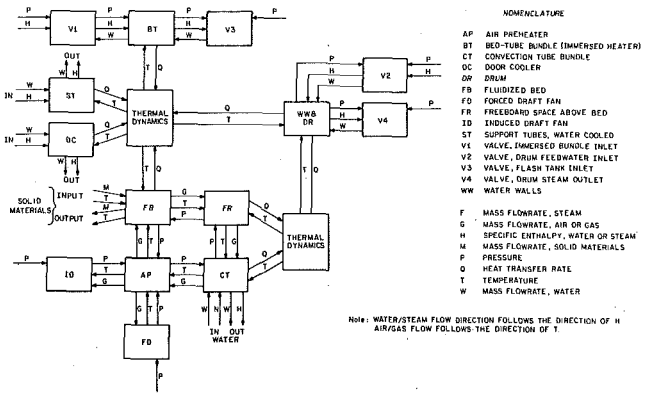

Fig. 2 Model solution diagram

the environment, (3) negligible pressure drop due to velocity and gravitational heads in gas and steam paths, (4) uniform fluidized-bed temperature, (5) coal division into solid and gas fractions independent of superficial air velocity, (7) constant average value of coal particle residence time in the fluidized bed, (8) elutriation rate proportional to total air flow, and (9) overbed combustion rate proportional to air flow and in-bed combustion rate. Assumptions 1, 2 and 3 have been used in modeling conventional steam generators [7–10]. Assumptions (4–9), which will be discussed more fully in this section, are unique to the fluidized-bed system and reflect areas of current research into heat transfer coefficients, flue gas residence time, bed depth, etc. In the model reported here, simple relations or constant input values

Nomenclature

A = area
C = specific heat
F = fluid flow rate
H = fuel heating value, effective
h = specific enthalpy
K = constant
k = thermal conductivity of tube material
ℓ = length
M = flow rate of solid materials
m = mass
p = fluid pressure
Q = heat transfer rate
r = tube radius
T = temperature
t = time
u = specific internal energy
V = volume
α = part of Q_b* due to conduction and convection
β = part of M_f consumed in bed
η = exponent for convection heat transfer coefficient
Θ = conversion factor to absolute temperature
ρ = density
τ = time-constant related to fuel residence time

Superscript

* = design condition

Subscripts

a = average
b, bg, bz = bed, gaseous products in bed, solid materials in bed
$b\ell$ = boiling
c = convection tube water
d = air damper
e = elutriated material
f, fx = fuel, fraction consumed in bed
fd = forced draft fan
fg = flue gas
fw = feedwater
h = freeboard
i = inlet, inner
id = induced draft fan
j = door coolant
ℓ = limestone
m, mi, mo = tube material, inner surface, outer surface
o = outlet, outer
ob = overbed combustion
pa, pg = air at constant pressure, gas at constant pressure
q = carrier air
s = saturated steam
sv = steam valve
t = fluidized air
u = dumped materials from bed
vg = gas at constant volume
w = saturated water

have been assumed for certain variables and parameters. The model structure permits them to be readily changed or replaced when more appropriate information is available.

In utilizing the model, it is assumed that for the particular coal and limestone being utilized, and for their respective particle size distributions, coal residence time and elutriation rate, for example, will be calculated initially and used as model input parameters. The purpose of the model is not to determine such parameters which pertain primarily to processes occurring within the bed itself, but rather to study their effect on the overall steam generator system.

Model equations are developed in the following subsections and rationale for selection of state variables is discussed. Input and state variables are listed in the Appendix.

Fluidized-Bed. The control volume selected for modeling fluidized-bed dynamics is shown in Fig. 3. Its top surface determines bed depth which is a function of time-dependent process variables such as superficial velocity, mass of solid materials, etc. No explicit functional relations for bed depth appear to be available in the literature. Since bed depth is customarily held constant during individual experiments, heat transfer areas, bed mass, etc., are computed assuming constant bed depth for each experimental condition. Thus, fixed control volume is assumed. A time-varying control volume [10] can be incorporated in the model when a suitable analytical relation for bed depth is available.

Mass conservation in the control volume yields

$$\frac{d}{dt}(m_{bg} + m_{bz}) = M_f + M_\ell + F_t + F_q - F_{bg} - M_e - M_u \quad (1)$$

Air and flue gas dynamics inside the cell were found to be very fast, with time constants less than a few milliseconds. Control systems and measuring instruments are low pass filters with respect to such transients, which will have little bearing on overall process dynamics and controller design. Thus, dm_{bg}/dt is set to zero and flue gas flow is computed algebraically by direct mass balance with air flow and instantaneous rate of coal combustion. This is equivalent to setting one eigenvalue of the linearized system to negative infinity.

$$F_{bg} = F_t + F_q + M_{fx} \quad (2)$$

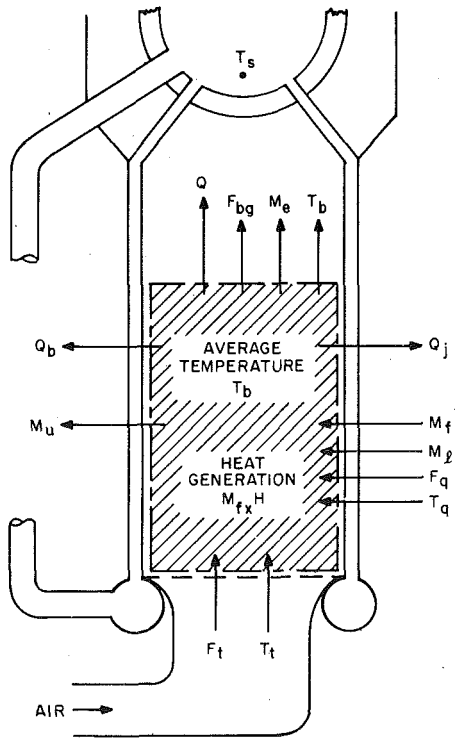

Fig. 3 Fluidized-bed control volume

The sulfur fraction in coal adds to bed mass by the sulfation reaction. CO_2 evolution by calcination of freshly added limestone reduces bed mass. For a Ca:S mol ratio of two, the gain and loss in bed mass approximately balance, and these effects are ignored in the model.

Mass flow of elutriated solids is assumed proportional to total air flow. The proportionality constant is characteristic of the coal and bed material being used.

$$M_u = K_u(F_t + F_q) \quad (3)$$

Coal combustion dynamics inside the bed are approximated by a first order lag.

$$M_{fx} = \frac{m_f}{\tau}; \quad \frac{dM_{fx}}{dt} = \frac{1}{\tau}\frac{dm_f}{dt} = \frac{1}{\tau}(\beta M_f - M_{fx}) \quad (4)$$

Coal introduced into the burning bed has a volatile component which burns in a few seconds, and a solid char component which burns slowly [11]; mass fractions for each component are often comparable. In equation (4), τ is related to an average residence time assumed to be characteristic of the coal being burned, including its char reaction rate and fractional partition into volatile and solid components. Although an Arrhenius temperature dependence of char reaction rate could be included in τ, the simplifying assumption of temperature independence has been made for the following reasons: (1) rapid combustion of the volatile component diminishes the effect of char combustion rate temperature dependence; (2) in normal operation, during which stable combustion is assumed, the range of bed temperature variation will be kept small (perhaps ± 60°C); and (3) in terms of overall steam generator performance, thermal relaxation time of stored energy in the bed (a very slow process) has a much greater effect on system response than changes in char combustion rate.

In this paper, a constant value of $\tau = 10$ s has been assumed. A more detailed functional relationship can be incorporated in the model when available. Similarly, β, the coal fraction consumed in the bed, is assumed to be a constant characteristic of the coal type and bed material; it can also be replaced by some other functional relationship if necessary. System senstivity to τ and β can be readily investigated with the model.

Substituting equation (2) in (1) and setting $dm_{bg}/dt = 0$,

$$\frac{dm_{bz}}{dt} = M_f + M_\ell - M_{fx} - M_e - M_u \quad (5)$$

Equation (5) represents solid mass dynamics in the bed, which behave as a free integrator in the absence of a bed level controller. An ideal bed level controller was assumed which brings bed mass to steady-state value instantaneously, and

$$\frac{dm_{bz}}{dt} = 0; \quad M_u = M_f + M_\ell - M_{fx} - M_e \quad (6)$$

The effect of an ideal controller is to eliminate one eigenvalue of the linearized system. (This is analogous to drum water level control which is discussed in a later section). Without an ideal controller, it is necessary to postulate or simulate a real controller whose characteristics could influence mass storage dynamics in the fluidized-bed.

Average bed temperature, selected as a state variable, provides dynamic information about fluidized-bed thermal conditions. The governing equation is obtained from dynamic energy balance for gases and solids in the control volume (see Fig. 3). Assuming $dm_{bg}/dt = 0$ as discussed previously, and ideal bed level control $dm_{bz}/dt = 0$,

$$\frac{dT_b}{dt} = [(M_f C_f + M_\ell C_\ell)T_q - (M_e + M_u)C_{bz}T_b + (F_t T_t + F_q T_q)C_{pa} - F_{bg}T_b C_{pg} + M_{fx}H - \Sigma Q_b]/(m_{bz}C_{bz} + m_{bg}C_{vg}) \quad (7)$$

ΣQ_b is total heat transfer rate from bed, and thermal energy generated in the bed is $M_{fx}H$ which is the product of effective coal heating value and instantaneous combustion rate.

Mass of gas in the bed is obtained as

$$m_{bg} = (V_b - m_{bz}/\rho_{bz})\rho_{bg} \tag{8}$$

where ρ_{bg} is the average gas density. Since $m_{bg} \ll m_{bz}$ and m_{bg} occurs only in equation (7) in conjunction with m_{bz}, approximating ρ_{bg} by a constant average value improves computational efficiency. However, ρ_{bg} can be evaluated assuming isobaric conditions ($\rho_{bg}(T_b + \Theta)$ = constant), which is justified because variations in absolute bed pressure are small.

Main Air Flow. Main air flow is damper-regulated, and is computed from pressure drop across ducts, damper and distributor plate. Typically, fluid flow F is expressed in terms of inlet and exit pressures, and average density [12].

$$F \propto \sqrt{(p_i - p_o)\rho_a} \tag{9}$$

Assuming constant spatial temperature distribution, average density is approximately proportional to average pressure $\rho_a = (p_i + p_o)/2$. Therefore,

$$F \propto \sqrt{(p_i^2 - p_o^2)} \tag{10}$$

This approximation yields a simple algebraic expression for main air flow in terms of forced draft fan pressure, bed pressure (above the distributor plate) and damper area; flow resistances due to ducts, damper and distributor plate are lumped together.

$$F_t = \frac{K_d A_d K_{fd}}{\sqrt{(K_d A_d)^2 + K_{fd}^2}} \sqrt{(p_{fd}^2 - p_b^2)} \tag{11}$$

K_d and K_{fd} are calculated from design data.

Similarly, total flue gas flow is obtained in terms of bed pressure and induced draft fan inlet pressure.

$$F_{fg} = K_{fg} \sqrt{(p_b^2 - p_{id}^2)} \tag{12}$$

Total flue gas flow includes gas leaving the bed plus the rate of overbed combustion in the freeboard.

$$F_{fg} = F_{bg} + M_{ob} \tag{13}$$

Overbed combustion rate is assumed proportional to elutriation rate and to coal combustion rate in the bed.

$$M_{ob} = K_{ob}(F_t + F_q)M_{fx} \tag{14}$$

K_{ob} is estimated from system design data.

Equations (2) and (11–14) are combined into a quadratic for F_{fg}, eliminating F_{bg} and p_b.

Heat Transfer. The heat transfer coefficient for immersed waterwall tubes is assumed independent of superficial air velocity, but dependent on bed temperature. Thus, heat transfer rate has a linear part due to conduction and convection, and a nonlinear part due to radiation.

$$Q_b = K_b \ell \left[\alpha + (1 - \alpha) \left(\frac{T_b + T_{mo} + 2\Theta}{T_b^* + T_{mo}^* + 2\Theta} \right) \times \left(\frac{(T_b + \Theta)^2 + (T_{mo} + \Theta)^2}{(T_b^* + \Theta)^2 + (T_{mo}^* + \Theta)^2} \right) \right] (T_b - T_{mo}) \tag{15}$$

α is the fraction of total heat transfer due to conduction and convection at the design load condition, only, for which $T_b = T_b^*$ and $T_{mo} = T_{mo}^*$. K_b and α were evaluated from steady-state experimental data at two different operating conditions.

Boiling heat transfer from waterwall inner surface to water/steam mixture is obtained using the empirical correlation of Thom, et al. [14].

$$Q_{b\ell} = K_b A_i \ell \, exp\,(p_s)(T_{mi} - T_s)^2 \tag{16}$$

Conductive heat transfer through the waterwalls is assumed radial.

$$Q_{b\ell} = \frac{A_i \ell k}{r_i \ln(r_0/r_i)} (T_{mo} - T_{mi}) \tag{17}$$

Equations (16) and (17) are solved simultaneously for $Q_{b\ell}$ eliminating T_{mi}.

Convective heat transfer rates in the freeboard, convection tube bank, air preheater, etc., are computed using established formulae [13, 14]. Heat transfer coefficients are assumed flow-dependent, only.

$$Q \propto AF^{\eta}\Delta T \tag{18}$$

The proportionality constant is determined from fluid properties at mean thermodynamic conditions.

Door Coolant. A small part of the energy generated in the bed is absorbed by the water-cooled access door.

$$Q_j = F_j(T_{jo} - T_{ji}) \tag{19}$$

(Specific heat of cooling water is taken to be unity). Because of constant flow, bed to cooling water heat transfer is approximately

$$Q_j = K_j(T_b - T_{ja}) \tag{20}$$

K_j includes heat transfer area and coefficient. Mean water temperature is obtained as a weighted average of inlet and outlet water temperatures.

$$T_{ja} = T_{ji} + (1 - \xi)T_{jo}, \qquad 0 < \xi < 1 \tag{21}$$

Equations (19–21) are solved for Q_j and T_{jo} in terms of input variables F_j and T_{ji}.

Freeboard. The steam drum is located in the freeboard directly above the fluidized bed. Transients associated with freeboard stored energy are very high frequency, and energy balance for freeboard gases and solids is considered in steady-state form.

$$Q_h = M_{ob}H + (F_{fg}C_{pg} + M_eC_{bz})(T_b - T_{ho}) - M_{ob}(C_{pg}T_b - C_{bz}T_{ho}) \tag{22}$$

Using equation (18) for convective heat transfer from freeboard to waterwalls, and treating mean freeboard temperature as a weighted average of T_b and T_{ho} (as in equation 21), the resulting equations are solved simultaneously for Q_h and T_{ho}.

Radiative heat transfer above the bed, expressed in the form

$$Q \propto [T_b + \Theta)^4 - (T_{mo} + \Theta)^4] \tag{23}$$

is applied separately to freeboard waterwalls and drum surface. The proportionality constants include emissivity, effective surface area, and the Stefan-Boltzmann constant.

Convection Tube Bank. After flowing past the drum, flue gas is cooled by convection tubes where a substantial amount of energy is absorbed. Flue gas temperature entering this section is obtained by direct heat balance. Temperature drop across thin tube walls is neglected. Heat transfer Q_c from flue gas to convection tube water is obtained by combining heat transfer coefficients from flue gas to tube wall and from tube wall to water.

Treating water as incompressible, conservation of energy in the tube water control volume yields

$$\frac{d}{dt} T_{ca} = [F_c(T_{ci} - T_{co}) + Q_c]/m_c \tag{24}$$

Outlet water temperature T_{co} is extrapolated from inlet and average temperatures, T_{ci} and T_{ca}, as in equation (21).

Drum and Waterwall Tubes. The drum model is formulated using established techniques [8], assuming saturated conditions and uniform pressure. Mass and energy conservation in the drum control volume yield

$$\frac{d}{dt}(\rho_s V_s + \rho_w V_w) = F_{fw} - F_s \tag{25}$$

$$\frac{d}{dt}(\rho_s V_s u_s + \rho_w V_w u_w) = F_{fw}h_{fw} - F_s h_s + \Sigma Q_{b\ell} \tag{26}$$

$\Sigma Q_{b\ell}$ is total heat transfer rate to water/steam. ρ_s and V_w are selected as state variables, and thermodynamic properties of water and steam at saturated conditions are expressed as functions of ρ_s. Using partial derivatives of thermodynamic variables with respect to ρ_s, equations (25) and (26) become

$$\left(V_s + V_w \frac{\partial \rho_w}{\partial \rho_s}\right) \frac{d\rho_s}{dt} + (\rho_w - \rho_s) \frac{dV_w}{dt} = F_{fw} - F_s \quad (27)$$

$$\left[V_s \left(u_s + \frac{\partial u_s}{\partial \rho_s} \rho_s\right) + V_w \left(u_w \frac{\partial \rho_w}{\partial \rho_s} + \rho_w \frac{\partial u_w}{\partial \rho_s}\right)\right] \frac{d\rho_s}{dt}$$

$$+ (\rho_w u_w - \rho_s u_s) \frac{dV_w}{dt} = F_{fw} h_{fw} - F_s h_s + \Sigma Q_{b\ell} \quad (28)$$

which are solved algebraically for $d\rho_s/dt$ and dV_w/dt.

Saturated steam flow vented to the atmosphere is determined from drum pressure assuming choked flow in the steam flow control valve [12].

$$F_s = K_{sv} A_{sv} \sqrt{p_s \rho_s} \quad (29)$$

Feedwater flow F_{fw}, determined by pressure drop across the flow control valve, is regulated by a controller whose response is fast with respect to drum level transients. During experimental runs, drum level hardly changes. Consequently, an ideal drum level controller is assumed, with feedwater and steam flow rates balanced at every instant. dV_w/dt is set to zero, and drum level is constant.

Thermal energy stored in waterwall tube metal, as well as in the water/steam mixture inside the tubes, and heat transfer from tube metal to the water/steam mixture are considered separately for the bed and the freeboard regions because of different thermal dynamics using the form of equations (16) and (17). Heat transfer areas and thermal capacitances of these regions are directly proportional to their respective lengths, and average outer tube wall surface temperatures are selected as state variables. Since waterwall steam quality varies with firing rate, lumped average thermal capacitance changes with load. However, fixed average values were assumed for bed and freeboard regions because thermal capacitance of tube material is significantly larger than that of water.

Gas Emission Characteristics. In a fluidized-bed steam generator, limestone feed rate is controlled on the basis of SO_2 concentration; air flow and coal feed rate are influenced by O_2 concentration. Thus, O_2 and SO_2 concentrations must be available as output variables when the model is applied to analytical controller design. An understanding of fluidized-bed chemical kinetics, a subject of current research, is required to formulate model equations for O_2 and SO_2 concentration, and is not included in this paper.

Experimental Program and Model Validation

A flexible data acquisition system ideally suited to recording data during transient response tests, as well as steady-state operation, has been installed at the Alexandria Process Development Unit. Signals from up to 128 channels can be sampled, amplified, digitized, and stored on magnetic tape. Scanning of all 128 channels can be repeated as often as five times per second. Normally, the period between scans is 1–4 s.

For the measurements reported here, the scan list consists of 18 flow rate, 14 pressure, one level, 35 temperature, and eight gas analysis signals, plus a variety of test and calibration signals. Characteristics of the data acquisition system have been described elsewhere [15]. Copies of magnetic tapes are available for studying the process in more detail.

Major input variables manipulated for open loop transient response tests are: (1) rotary coal feeder speed to change firing rate, (2) inlet air damper position to change fluidizing air flow, and (3) drum steam valve position to change steam pressure and steam flow rate. Feedwater valve operation is normally on automatic control to insure stable drum water level; it was not available for changing feedwater flow.

Initial tests were conducted to obtain steady-state data at several operating conditions corresponding to different firing rates and bed depths. Observed steady-state values were compared with predicted values of process variables for validating the model as an acceptable steady-state process description.

The area of greatest model uncertainty concerns the heat transfer coefficient for immersed surface. Parameters and equation structure in that portion of the model were adjusted to obtain close agreement between model predictions and measured performance at several operating points. This adjustment provided deeper insight into process characteristics, requiring detailed examination of modeling assumptions and equation structures and adoption of the temperature dependence expressed in equation (15).

Transient response tests involved independent step changes in rotary coal feeder speed and inlet air damper position. To achieve agreement between model transient response predictions and observed data depicted in the figures which follow, it was necessary to increase thermal capacity of the fluidized-bed approximately 20 percent. This reflects the fact that the limestone bed partially converts to calcium sulfate with a higher density and specific heat, which was not considered in the initial estimate of bed thermal capacity.

Model Results

Comparisons of steady-state model predictions and test results at two different load levels are given in Table 1. These two operating conditions were starting points for transient response tests. Figs. 4–6 compare transient response predictions with measured values of bed temperature, drum steam pressure, and steam flow, respectively, for an 8.22 percent step decrease in coal feed rate. Equivalent static bed depth for this test was 0.508 m (20 in.). Model results for bed temperature transients (Fig. 4) agree closely with experimental data. For drum steam pressure (Fig. 5), model predictions appear somewhat faster than test data. This may be due to inaccuracy in drum water level, i.e., drum water thermal capacitance. Steam flow data (Fig. 6) is noisy, due to instrumentation, but the average profile appears to agree with model results.

Table 2 shows system eigenvalues of the linearized model at steady-state conditions before and after the 8.22 percent decrease in coal feed rate. The eigenvalues decrease at lower firing rate, indicating that the process slows down. The smallest eigenvalue is strongly associated with fluidized-bed thermal relaxation and corresponds to a time-constant of approximately 220 s before the change and 235 s after, which illustrates the effect of process nonlinearity. The −0.100 eigenvalue corresponds to coal residence time constant in the bed during combustion, which is assumed to have a constant value of 10 s.

Figs. 7–9 compare model transient response with measured values of bed temperature, drum steam pressure, and steam flow for a 6.75 percent increase in main air flow. Equivalent static bed depth for this test was 0.305 m (12 in.). For bed temperature (Fig. 7), model results and test data are in close agreement until about ten minutes after the disturbance, when test results show an upward drift. This was caused by a small inadvertent increase in coal feed rate which was identified by a decrease in observed flue gas O_2 content. This drift is also obvious in drum steam pressure response (Fig. 8) but cannot be identified in the noisy steam flow response (Fig. 9).

Following the air flow disturbance, both model results and test data show an initial overshoot in steam pressure (Fig. 8) which then relaxes to a lower value. Overshoot occurs in response to increasing flue gas flow and convective heat transfer in the freeboard. Then, as bed temperature decreases, flue gas temperature drops reducing freeboard heat transfer below the initial level. Test data show a larger overshoot than model results attributed to inaccuracy in formulating model equations for overbed combustion, which for the model reported here, probably underestimated the portion of total heat transfer to drum and waterwalls in the freeboard region.

Conclusions

A dynamic model of an atmospheric pressure fluidized-bed combustion steam generation system has been developed, and model results verified with experimental data for both steady-state and transient performance. The state-space model structure allows digital simulation and analytical controller design. Furthermore, the model can be used for design verification and predicting effects of subsystem changes on the entire process.

Simple correlations for fluidized-bed heat transfer coefficient and fuel residence time were assumed due to lack of more reliable data. However, the model structure allows replacement and addition of appropriate functional relationships without difficulty. Even in the present form, the model closely represents the actual process and has

Table 1 Comparison of steady-state model results with test data

Process Variables	Bed depth 0.508 m (20 in.)	
	Model Results	*Test Data*
Bed Temperature	884.4°C (1624°F)	882.2°C (1620°F)
Drum steam pressure	0.7633 × 10^6 N/m^2 (110.7 psia)	0.7653 × 10^6 N/m^2 (111 psia)
Main steam flow	0.3404 kg/s (0.7504 lbm/s)	0.3402 kg/s (0.75 lbm/s)
Coal feed rate*	0.0857 kg/s (0.189 lbm/s)	0.0857 kg/s (0.189 lbm/s)
Limestone feed rate*	0.0367 kg/s (0.0809 lbm/s)	0.0367 kg/s (0.0809 lbm/s)
FD Fan air flow	0.5770 kg/s (1.272 lbm/s)	0.5783 kg/s (1.275 lbm/s)
Carrier air flow*	0.0506 kg/s (0.1114 lbm/s)	0.0506 kg/s (0.1114 lbm/s)
Process Variables	Bed depth 0.304 m (12 in.)	
	Model Results	*Test Data*
Bed Temperature	920.56°C (1689°F)	918.33°C (1685°F)
Drum steam pressure	0.7543 × 10^6 N/m^2 (109.4 psia)	0.7584 N/m^2 (110 psia)
Main steam flow	0.3329 kg/s (0.7339 lbm/s)	0.3311 kg/s (0.73 lbm/s)
Coal feed rate*	0.0844 kg/s (0.186 lb/s)	0.0844 kg/s (0.186 lbm/s)
Limestone feed rate*	0.0367 kg/s (0.0809 lbm/s)	0.0367 kg/s (0.0809 lbm/s)
FD Fan air Flow	0.516 kg/s (1.238 lbm/s)	0.5171 kg/s (1.240 lbm/s)
Carrier air flow*	0.0506 kg/s (0.1114 lbm/s)	0.0506 kg/s (0.1114 lbm/s)

* Given as input to the model

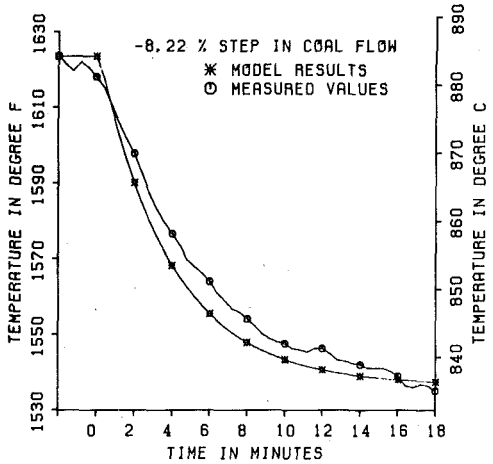

Fig. 4 Bed temperature transient due to 8.22 percent step decrease in coal feed rate

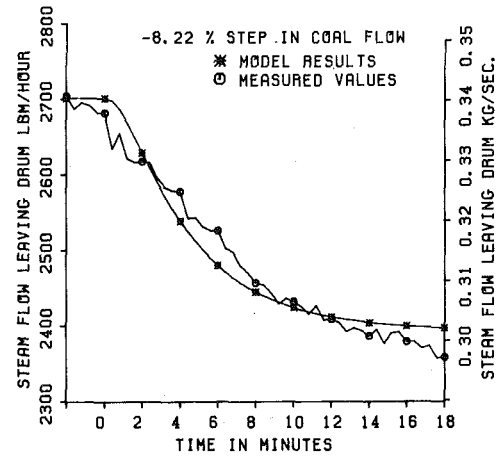

Fig. 6 Steam flow transient due to 8.22 percent step decrease in coal feed rate

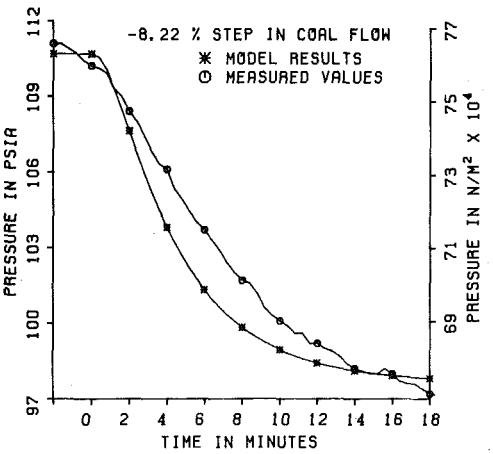

Fig. 5 Drum steam pressure transient due to 8.22 percent step decrease in coal feed rate

Table 2 Eigenvalues of linearized model before and after −8.22 percent change in coal feed rate

Before	*After*
−.00451 s^{-1}	−.00425 s^{-1}
−.00642	−.00641
−.0103	−.0103
−.0168	−.0162
−.100	−.100
−.535	−.524
−.780	−.764

become a useful tool in studying the less well-understood parts of it.

Although the model is related to a particular fluidized-bed plant, the method of analysis has general applicability and can be readily adapted to study other fluidized-bed steam power generation systems.

Acknowledgment

This work was supported by the Coal Conversion and Utilization Division of ERDA/Fossil Energy under Contract Number EX-76-C01-2453. The experimental facility at Alexandria, Va., is operated for ERDA by Pope, Evans and Robbins. The authors are thankful to Mr. Mark D. Wilson for assistance in formulating the model.

References

1 Kunii, D. and Levenspiel, O., *Fluidization Engineering,* Wiley, New York, 1969.

2 Berkowitz, D. A., Ray, A., Sumaria V. and Wilson, M. D., "Dynamic Modeling Testing and Control of Fluidized Bed Systems," *Proceedings of 5th International Conference on Fluidized Bed Combustion,* Dec. 12–14, 1977, Washington, DC.

3 Lin, Y., Nielsen, R. S., and Ray, A., "Fuel Controller Design in a Once-through Subcritical Steam Generator System," ASME JOURNAL OF ENGINEERING FOR POWER, Vol. 100, No. 1, Jan. 1978, pp. 189–196.

4 Berkowitz, D. A., ed., *Proceedings of the Seminar on Boiler Modeling,* The MITRE Corporation, Bedford, MA., Oct. 1975.

5 *IBM Continuous System Modeling Program (CSMP-III),* Program Reference Manual Ser. No. SH19-7001-2, Sept. 1972.

6 Springer, T. E. and Farmer, O. A., "TAF—A Steady State, Frequency Response Simulation Program," *Proceedings-Fall Joint Computer Conference,* 1968.

7 Adams, J., Clark, D. R., Louis, J. R., and Spanbauer, J. P., "Mathematical Modeling of Once-through Boiler Dynamics," *IEEE Trans.,* PAS-84, Feb. 1965,

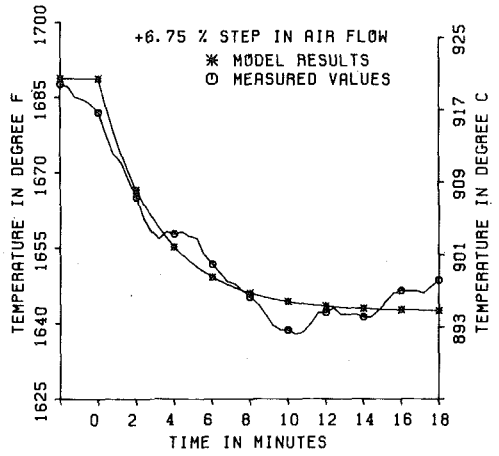

Fig. 7 Bed temperature transient due to 6.75 percent step increase in air flow

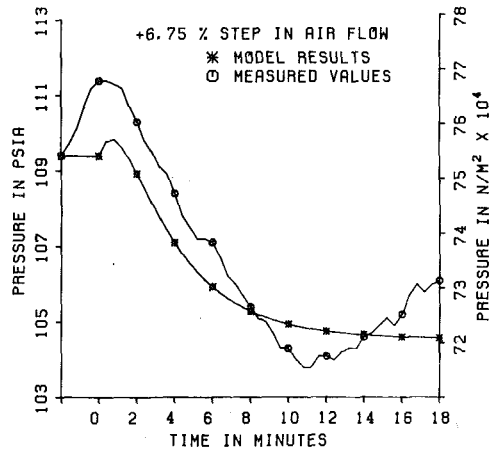

Fig. 8 Drum steam pressure transient due to 6.75 percent step increase in air flow

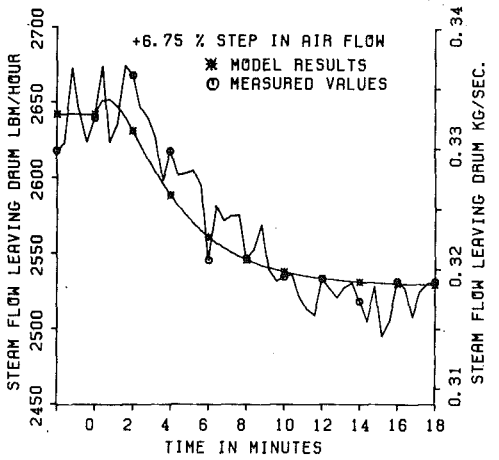

Fig. 9 Steam flow transient due to 6.75 percent step increase in air flow

pp. 146–156.

8 Kwatny, H. G., McDonald, J. P., and Spare, J. H., "A Nonlinear Model for Reheat Boiler-Turbine-Generator Systems: Part II-Development," *Proceedings of Joint Automatic Control Conference,* 1971, pp. 227–236.

9 McNamara, R. W., Ringham, M. R., Bramblett, C. C. and Southworth, L. C. "Practical Simulation of an Industrial Fluid System with Controls—The Circulator Auxiliaries for the Fort St. Vrain Nuclear Generating Station," *Proceedings of Joint Automatic Control Conference,* 1977, pp. 332–339.

10 Ray, A. and Bowman, H. F., "A Nonlinear Dynamic Model of a Once-through Steam Generator," ASME *Journal of Dynamic Systems, Measurement and Control,* Vol. 98, No. 3, Sept. 1976.

11 Beer, J. M., Baron, R. E., Borghi, G., Hodges, J. L. and Sarofim, A. F., "A Model of Coal Combustion in Fluidized Bed Combustors," *Proceedings of 5th International Conference on Fluidized Bed Combustion,* Dec. 12–14 1977, Washington, DC.

12 Blackburn, J. F., Reethof, G., and Shearer, L., eds., *Fluid Power Control,* M.I.T., Cambridge, 1960.

13 Rohsenow, W. M., and Hartnelt, J. P., eds., *Handbook of Heat Transfer,* McGraw-Hill, New York, 1973.

14 Holman, J. P., *Heat Transfer,* McGraw-Hill, 1976

15 Berkowitz, D. A., Ray, A., and Sumaria, V., "Dynamic Modeling of Fluidized-Bed Boilers for Control System Design," *Proceedings of 12th International Energy Conversion Engineering Conference,* Aug. 28–Sept 2, 1977, Washington, D. C.

APPENDIX

List of Model Input Variables and State Variables

The model input variables and state variables, together with steady-state values at a typical operating condition, are listed below:

Input Variables

u_1 coal feed rate 0.0837 kg/s (0.1846 lbm/s)

u_2 main air flow damper area (normalized) 0.85

u_3 drum steam flow valve area (normalized) 0.8

u_4 limestone feed rate 0.03674 kg/s (0.081 lbm/s)

State Variables

x_1 average bed temperature 884.22°C (1623.6°F)

x_2 instantaneous coal combustion rate in the bed 0.0728 kg/s (0.1605 lbm/s)

x_3 average waterwall outer surface temperature in the immersed region 194.22°C (381.6°F)

x_4 average waterwall outer surface temperature in the freeboard region 178.44°C (353.2°F)

x_5 average cooling water temperature in the convection tube bank 50.54°C (122.98°F)

x_6 average tube wall temperature at the mean radius in air preheater 309.39°C (588.9°F)

x_7 saturated steam density in the boiler drum 3.992 kg/m^3 (0.2492 lbm/ft^3)

x_8 drum water volume 0.30667 m^3 (10.83 ft^3)

x_9 mass of solid materials in the bed 725.75 kg (1600 lbm)

The state variables x_8 and x_9 are held fixed at constant values, and $\dot{x}_8$ and $\dot{x}_9$ are constrained to zero.

K. M. Kundu
Scientist.
Central Mechanical Engineering Research Institute,
Durgapur 713209, India

D. Banerjee
Director of Technical Education,
Government of West Bengal,
Calcutta 700001, India

D. Bhaduri
Assistant Director.
Central Mechanical Engineering Research Institute,
Durgapur 713209, India

On Flame Stabilization by Bluff-Bodies

Flame stabilization by bluff-bodies has been investigated to highlight the role of recirculation zone on the phenomenon. It has been observed that close correlations exist between heat exchange from recirculation zone and flame stability as controlled by recirculation strength.

Introduction

Recirculation zone plays an important role in the process of flame stabilization by bluff-bodies in high velocity combustible streams. Among the earlier investigations [1, 2, 3, 4] which were mostly experimental, a few have thrown some light on recirculation zone. Several physical models have been proposed; but the detailed role of recirculation zone on the mechanism of flame stabilization has not yet been revealed. It seems plausible that flame stabilization is achieved by heat and mass exchange between the recirculation zone and the mainstream as supported by the results of simplified theoretical analysis on the phenomenon [5] satisfying the conditions of flame development and flame stability. It is shown that the stability of a generated flame is maintained if heat exchange from the recirculation zone to combustible stream is balanced by the heat gained by the recirculation zone from the flame. The process of heat exchange in such flame stabilization is controlled by the complex fluid mechanics of recirculating flow; hence it should be related to the parameters of recirculation zone. In this study attempts have been made to understand the behavior of recirculation zone behind two-dimensional bluff-bodies in order to assess its role on flame stabilization.

Analysis

Recirculation Zone. Recirculation zone formed in two-dimensional flow past bluff-body flame stabilizer is shown schematically in Fig. 1. For mainstream velocities of practical interest the whole wake is turbulent. The time-mean streamline from the separation point encloses the recirculation zone. Exchange of mass and energy between the recirculation zone and the mainstream takes place by turbulent fluctuations normal to the recirculation zone boundary. The time-average of mass flow crossing the boundary is zero implying that the same mass is transported in both the directions. The longitudinal velocity within the recirculation zone is negative near the axis and becomes positive near the boundary of recirculation zone such that at some transverse position ($y = y_c$), $u = 0$. The reverse mass flow rate at an axial position is,

$$\dot{m}_r\Big]_x = \int_0^{y_c} \rho u(y)dy\Big]_x \tag{1}$$

If velocity distribution is known, equation (1) computes $\dot{m}_r$ at different positions along the axis of recirculation zone and its maximum value $\dot{M}_r$ is the total reverse mass flow rate which may be termed as recirculation strength and made non-dimensional as $\dot{M}_r/\dot{M}_0$.
Volume of recirculation zone (for unit depth) may be expressed as,

$$V_r = F_{RV} \cdot L \cdot d \tag{2}$$

where F_{RV} is the nondimensional shape factor which can be calculated from the configuration of recirculation zone.
From the definition of mean residence time within the recirculation zone (i.e., $\bar{t}_r = \bar{\rho}_r V_r/\dot{m}_e$) and nondimensional residence time $K(= \bar{t}_r U_0/d)$ the average mass exchange between the recirculation zone and the mainstream across the boundary per unit length of recirculation zone is,

$$\dot{m}_e/L = \frac{\bar{\rho}_r F_{RV} U_0}{K} \tag{3}$$

For two-dimensional bluff-bodies nondimensional residence time, K, in combustion may be taken as 104 from the observations of Bovina [6] and Winterfield [7].

Flame Stabilization. The region between the outer edge of recirculation zone and the combustible stream (Fig. 1) represents a turbulent mixing zone where the flame generates at a short distance from the initial contact point. Flame stabilization is achieved by satisfying the conditions of (1) flame development and (2) heat balance within the recirculation zone i.e., heat supplied by the recirculating flow to fresh combustibles (across OR) be balanced by heat flow into the recirculation zone from hot flame zone (across RF). With simplified estimates of heat exchange associated with mass exchange (equation (3)) and flame development distance (Williams [8]) the following results as obtained [5] are written:

$$\dot{q}_{r0} = \bar{\rho}_r x_i \frac{F_{RV}}{K} U_0(c_{pr}T_r - c_{p0}T_0) \tag{4}$$

Contributed by the Fuels Division of THE AMERICAN SOCIETY OF MECHANICAL ENGINEERS for publication in The JOURNAL OF ENGINEERING FOR POWER. Manuscript received at ASME Headquarters October 31, 1978.

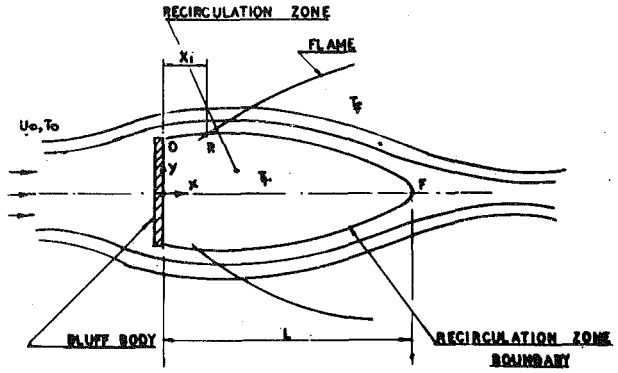

Fig. 1 Recirculation zone and model of flame stabilization

$$\dot{q}_{fr} = \bar{\rho}_r (L - x_i) \frac{F_{RV}}{K} U_0 (c_{pf} T_f - c_{pr} Tr) \tag{5}$$

Condition for heat balance for steady state (i.e., $\dot{q}_{r0} = \dot{q}_{fr}$),

$$\frac{x_i}{L} = \frac{c_{pf} T_f - c_{pr} T_r}{c_{pf} T_f - c_{po} T_0} \tag{6}$$

Condition for flame development,

$$\frac{x_i}{L} = \frac{U_0 k_0 \exp(E/R^0 (T_r)}{2 L \rho_0 c_{p0} S_L{}^2 \exp(E/R^0 T_f)} \tag{7}$$

For flame stability nondimensional flame development distance (x_i/L) from equations (6) and (7) are to be equal while at the critical condition of equilibrium at blow-off the slope $d(x_i/L)/d(T_r/T_f)$ from both the equations also should be equal which yield the critical value of recirculation zone temperature as,

$$T_r{}^* = \frac{1}{2}\left\{ -\frac{E}{R^0} + \sqrt{\left(\frac{E}{R^0}\right)^2 + 4 \frac{E}{R^0} \frac{c_{pf} T_f}{c_{pr}{}^*}} \right\} \tag{8}$$

Equating (x_i/L) from equations (6) and (7) at the condition of blow-off,

$$\tau = \frac{L}{U_{b0}} = \frac{\dfrac{k_0}{2 \rho_0 c_{p0} S_L{}^2} \exp\left[\dfrac{E}{R^0 T_f}\left(\dfrac{T_f}{T_r{}^*} - 1\right)\right]}{\left(\dfrac{c_{pf} T_f - c_{pr}{}^* T_r{}^*}{c_{pf} T_f - c_{p0} T_0}\right)} \tag{9}$$

Further, by equations (6) and (7),

$$\frac{x_i}{x_i{}^*} = \frac{U_0 \exp\left(\dfrac{E}{R^0 T_r}\right)}{U_{b0} \exp\left(\dfrac{E}{R^0 T_r{}^*}\right)} = \frac{c_{pf} T_f - c_{pr} T_r}{c_{pf} T_f - c_{pr}{}^* T_r{}^*} \tag{10}$$

which gives values of T_r at different nondimensional mainstream velocities (U_0/U_{b0}).

Total amount of heat of exchanged mass of recirculation zone is,

$$\dot{Q}_r = \bar{\rho}_r \frac{F_{RV}}{K} L \, U_0 c_{pr} T_r \tag{11}$$

Heat required for continuous ignition of combustible stream (Williams, et al. [3]) is,

$$\dot{q}_i = \left(\frac{k_0}{\rho_0 c_{p0} S_L}\right) \cdot c_{p0} U_0 \rho_0 (T_i - T_0) = \frac{k_0 U_0}{S_L} (T_i - T_0) \tag{12}$$

$\dot{Q}_r$ and $\dot{q}_i$ have been used in $(\dot{q}_{r0}/\dot{Q}_r)$ and $(\dot{q}_{r0}/\dot{q}_i)$ for correlation.

Experiments

Air was supplied through a calming chamber insuring almost a flat velocity profile into a rectangular test section (50mm × 50mm) in which a bluff-body (plate, wedge, cylinder) could be fitted transverse to the flow direction. Provision of upper sliding wall (with cross slides) of the test section along with a three-dimensional traversing arrangement permitted a calibrated single hole cylindrical probe (about 0.8mm OD) held parallel to the axis of bluff-body to scan the flow-field in isothermal flow.

In combustion premixed (gaseous) fuel-air flame was studied. The fuel contained mostly propane. The combustion chamber, fitted with two quartz glass windows for visual observations, was provided with longitudinal and vertical traversing facility through the upper wall. A platinum wire coated with Na-salt was used for measuring the recirculation zone boundary by Na-color indication. Temperature distribution was obtained with a Platinum-Platinum-Rhodium (13 per cent) thermocouple (silica coated) incorporating radiation correction. Blow-off velocity was also measured.

Results and Discussions

It has been observed [9] that in isothermal flow non-dimensional velocity $(u/U_0, v/U_0)$ distributions for a bluff-body remain unchanged for all mainstream velocities i.e., flow similarity is maintained within the recirculation zone as was mentioned by Winterfield [17]. Reverse mass flow rate $(\dot{M}_r/\dot{M}_0)$ within the recirculation zone is independent

Nomenclature

B = maximum width of recirculation zone
C_p = specific heat
d = dimension of bluff-body $(2R)$
D = diameter of test section as in [10, 16]
E = activation energy
k = thermal conductivity of fluid
L = length of recirculation zone
$\dot{m}_r$ = reverse mass flow rate at an axial position of recirculation zone
$\dot{M}_r$ = maximum reverse mass flow rate
$\dot{m}_e$ = mass exchange rate between recirculation zone and mainstream
$\dot{M}_0$ = mass flow rate through the test section
$\dot{q}_{r0}$ = heat exchange rate to combustible stream from recirculation zone
$\dot{q}_{fr}$ = heat exchange rate to recirculation zone from flame zone
$\dot{q}_i$ = heat required per unit time for continuous ignition of combustible stream as in [3]
$\dot{Q}_r$ = heat content of exchanged mass of recirculation zone
R^0 = universal gas constant
S_L = laminar burning velocity
t_r = mean residence time
$T_r{}^*$ = temperature of recirculation zone at the critical condition of blow-off
T_r = temperature of recirculation zone
T_0 = temperature of combustible stream approaching the bluff-body
T_i = ignition temperature of combustibles
T_f = adiabatic flame temperature
$\tau = L/U_{b0}$ = characteristic ignition time as in [4]
u, v = longitudinal and transverse (average) velocity components respectively
U_0 = mainstream velocity of fluid stream upstream of bluff-body
U_{b0} = blow-off velocity
W = reaction rate, i.e., rate at which the combustible is being converted due to chemical reaction (mass per unit volume per second)
x, y = longitudinal and transverse co-ordinates respectively
x_i = distance (from the initial contact point) at which the flame develops
$x_i{}^*$ = distance at which the flame develops at the critical condition of blow-off
ρ = density of fluid
ϕ = equivalence ratio

Subscripts

0 = condition upstream of bluff-body
$b0$, $*$ = condition at blow-off
r = condition in recirculation zone
L = for laminar case
T = for turbulent case
$-$ = average value.

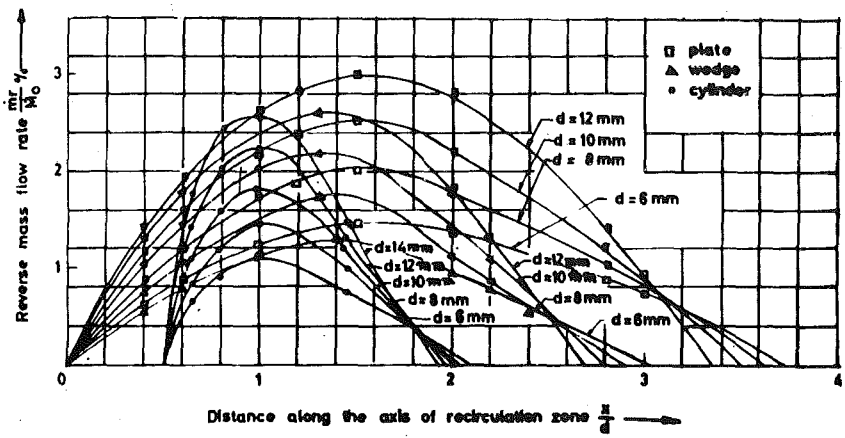

Fig. 2 Variation of reverse mass flow rate $\dot{m}_r/\dot{M}_0$ along the axis of recirculation zone (isothermal flow, experiment)

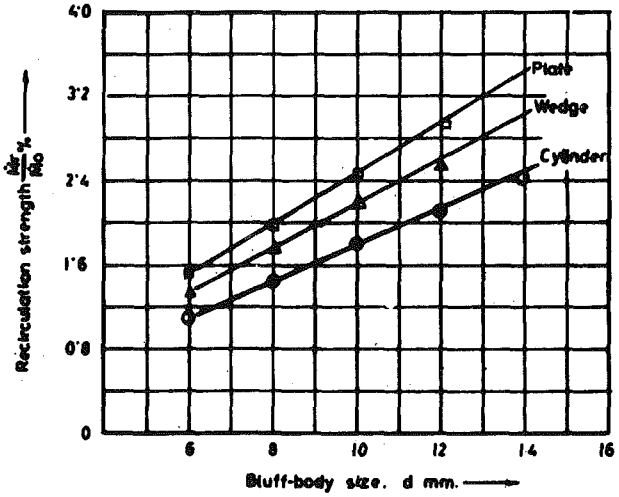

Fig. 3 Variation of recirculation strength with shape and size of bluff-body (isothermal flow, exponent)

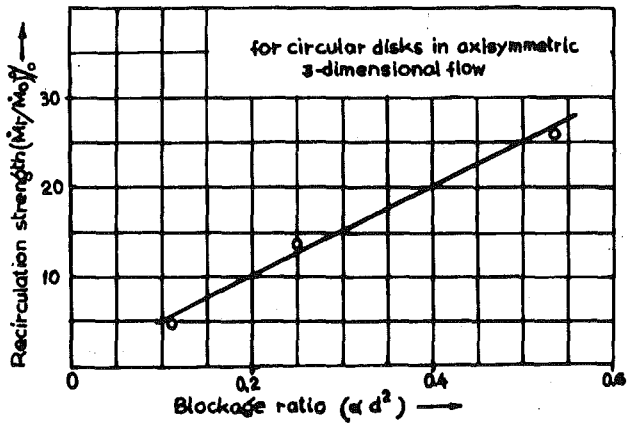

Fig. 4 Variation of recirculation strength with blockage ratio from experimental results of Davis and Beér [10]

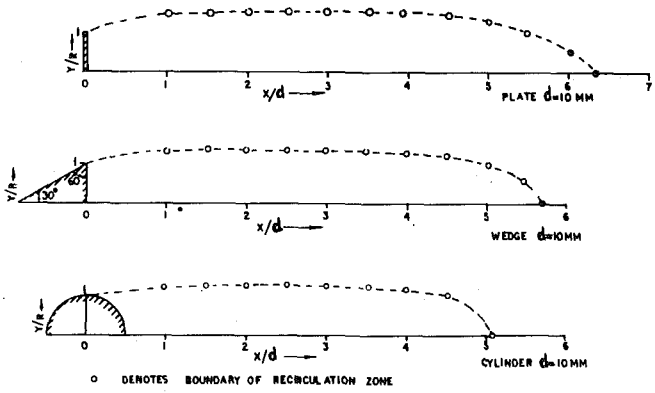

Fig. 5 Recirculation zone boundary in combustion

of mainstream velocity. Distribution of reverse mass flow rate along the axis of recirculation zone is shown in Fig. 2. The behavior is of similar to that reported by Davis and Beér [10]. Maximum value of reverse mass flow rate $\dot{M}_r$ is the total reverse mass flow rate within the recirculation zone which is a measure of strength of recirculation. This parameter denoted by $(\dot{M}_r/\dot{M}_0)$ may be called nondimensional recirculation strength which is independent of mainstream velocity but increases almost linearly (Fig. 3) with the size of (two-dimensional) bluff-body. The slope of variation, however, changes with geometry. A careful observation of the results of Davis and Beér [10] indicates that for circular disks in axisymmetric three-dimensional flow the maximum nondimensional reverse mass flow rates are 5 per cent, 14.4 per cent and 26.4 per cent for blockage ratios (d^2/D^2) of 0.11, 0.25 and 0.54 respectively and interestingly, the variation of $(\dot{M}_r/\dot{M}_0)$ with blockage ratio follows a linear relationship (Fig. 4). Linear relation with square of bluff-body size (d^2) in their case is justified as the flow is axisymmetric three-dimensional.

Recirculation zone boundary as measured in combustion is shown in Fig. 5 which was observed to be almost the same for a bluff-body over a wide range of mainstream velocities and equivalence ratios. Maximum width of recirculation zone (B/d) was about 1.25, 1.35 and 1.50 for cylinder, wedge and plate respectively. Measurements from photograph of Zukoski and Marble [4] indicates a value of about 1.28 for cylinder which compares closely with the present results. Gradual increase of temperature along the axis towards the end of recirculation zone was also observed by Matton and Fouré [11] and gives a fair indication of its length (Fig. 6).

For premixed propane-air flame (initial temperature 300 K) the activation energy E is 24000 Kcal/kg.mol. [12]. Calculations for the analysis have been carried out with parameters S_L, T_f, k, T_i and C_P chosen from or computed as in [13, 14, 15, 16]. Results of the analysis on the mechanism of flame stabilization have been published in details elsewhere [5]. In order to highlight the role of recirculation zone a few important results [5] are presented here which are followed by the new information relating to recirculation strength. It is established (Fig. 7) from predictions and experiments that variation of recirculation zone temperature (T_r/T_f) with mainstream velocity (U_0/U_{b0}) can be represented by a generalized curve irrespective of bluff-body configurations and equivalence ratios. Such a trend was shown by Zukoski and Marble [4] from their experimental results for a particular equivalence ratio whereas this study establishes the validity of a generalized variation for all equivalence ratios. Recirculation zone temperature gradually decreases with increase in mainstream velocity

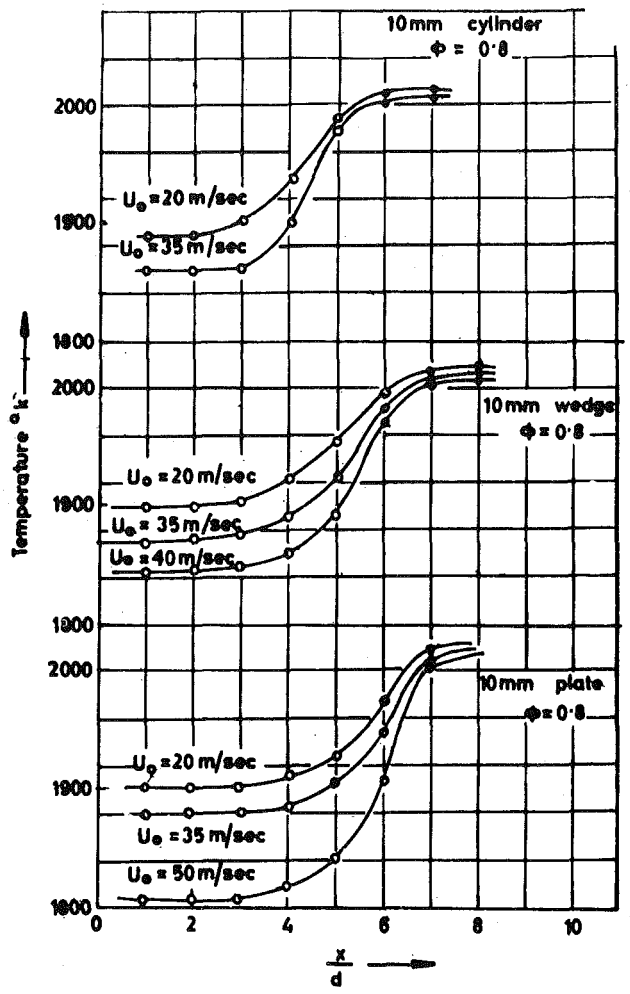

Fig. 6 Temperature distribution along the axis of the wake (experiment)

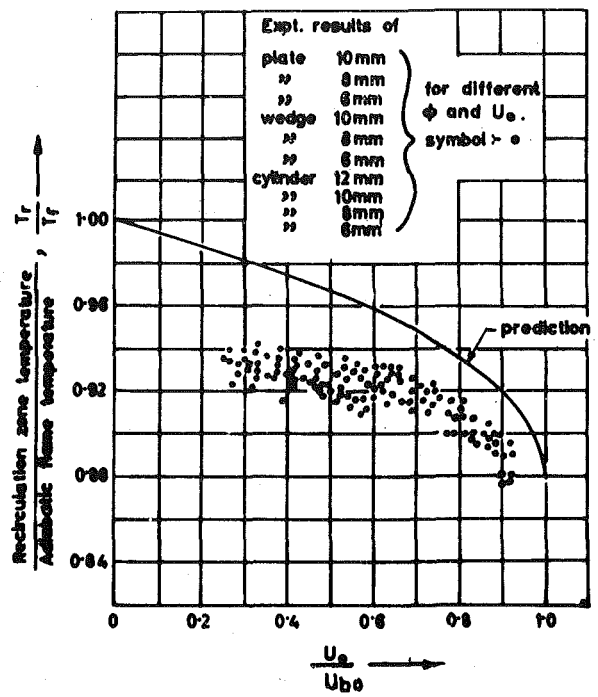

Fig. 7 Generalized behavior of recirculation zone temperature with mainstream velocity for all equivalence ratios

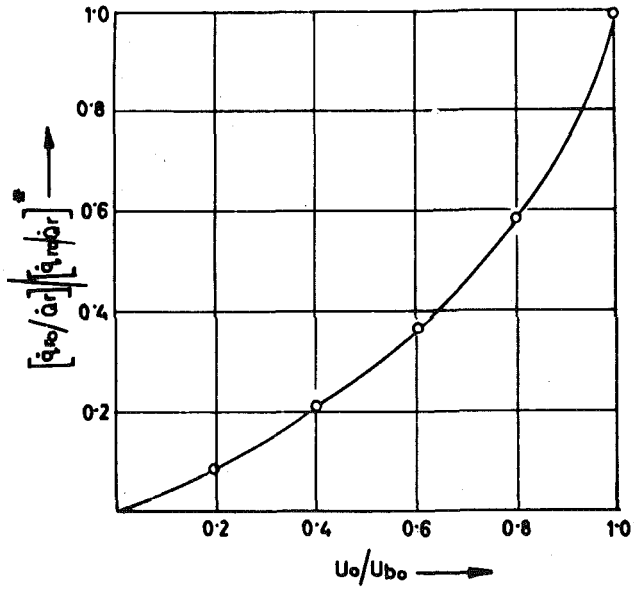

Fig. 8 Variation of heat transfer to combustible steam from recirculation zone at different mainstream velocities and equivalence ratios

till it reaches a critical value T_r^* (equation (8)) just at blow-off which, although contrary to the conclusion of Zukoski and Marble [4], agrees with the trend of their experimental results. It is further shown (Fig. 8) that the variation of nondimensional heat exchange expressed as a fraction of its value at blow-off can be represented by a single curve for all bluff-bodies and equivalence ratios. Thus the behavior of recirculation zone in respect of temperature and heat exchange is generalized with dependence on the property of the combustibles only and are such that at any normal operating condition they maintain definite relationships to the respective values at blow-off. Experimental results on characteristic ignition time τ ($=L/U_{b0}$) and predictions (equation (9)) as shown in Fig. 9 illustrate that τ is a function of equivalence ratio only irrespective of bluff-body configurations. The apparent constancy of τ as observed by Zukoski and Marble [4] from experimental results is justified from the considerations of the proposed model on flame stabilization. Equation (9) is an approximate correlation on blow-off velocity and implies that the recirculation zone length is an important parameter in flame stabilization.

It has been highlighted by the proposed model and the results that flame stabilization is achieved by the heat exchange between the recirculation zone and the mainstream as guided by the complex fluid mechanics of recirculating flow. As such heat exchange should be related to the entrainment capacity of recirculation zone i.e., to the reverse mass flow rate or recirculation strength. In the present investigation it was not possible to assess the behavior of recirculation strength in combustion. Beér and Chigier [17] inferred for a particular equivalence ratio that reverse mass flow in combustion remained almost the same as in cold flow considering increase of volume and temperature of recirculation zone due to combustion. On the premise that in the absence of such data on combustion the behavior of recirculation strength may be considered qualitatively the same as in cold flow, attempts have made to understand its effect on flame stabilization. Heat exchange from recirculation zone to combustible stream at blow-off made nondimensional as ($\dot{q}_{r0}/\dot{q}_i$) could be represented (Fig. 10) on the basis of recirculation strength irrespective of bluff-body configuration for a wide range of equivalence ratios. Satisfactory correlations are also observed (Fig. 11) between blow-off velocity and recirculation strength. In Fig. 12 both blow-off velocity and heat exchange are plotted on the basis of recirculation strength on the same graph illustrating the interrelations between them. Without claiming any undue credit for the quantitative exactness of the correlations it may be inferred that the trends indicated by the correlations are no less encouraging to reveal the role of recirculation strength on flame stabilization. The basic function of the recirculation zone is that it should convey the necessary heat to the combustible stream from the hot flame zone for flame stabilization. Capacity of this heat exchange is determined by the recirculation strength. Thus

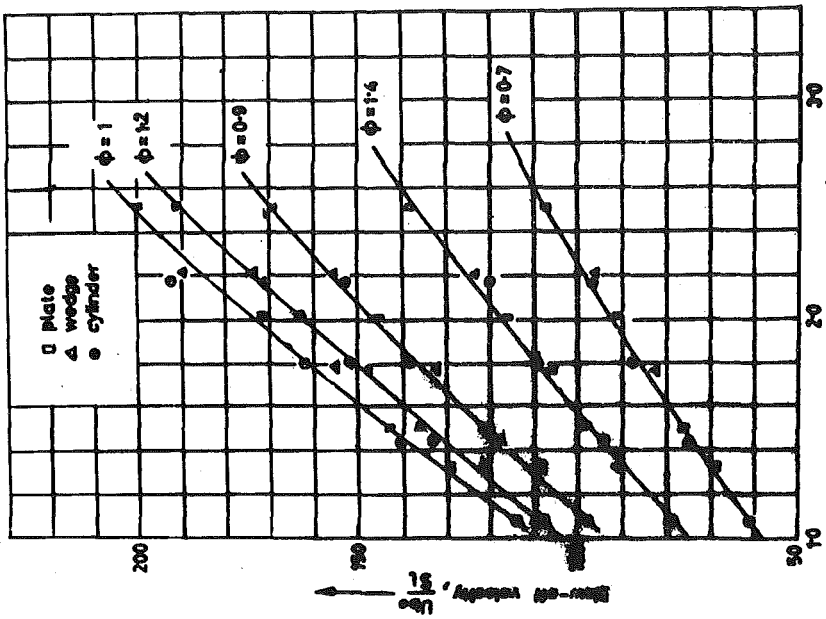

Fig. 11 Correlation between blow-off velocity and recirculation strength

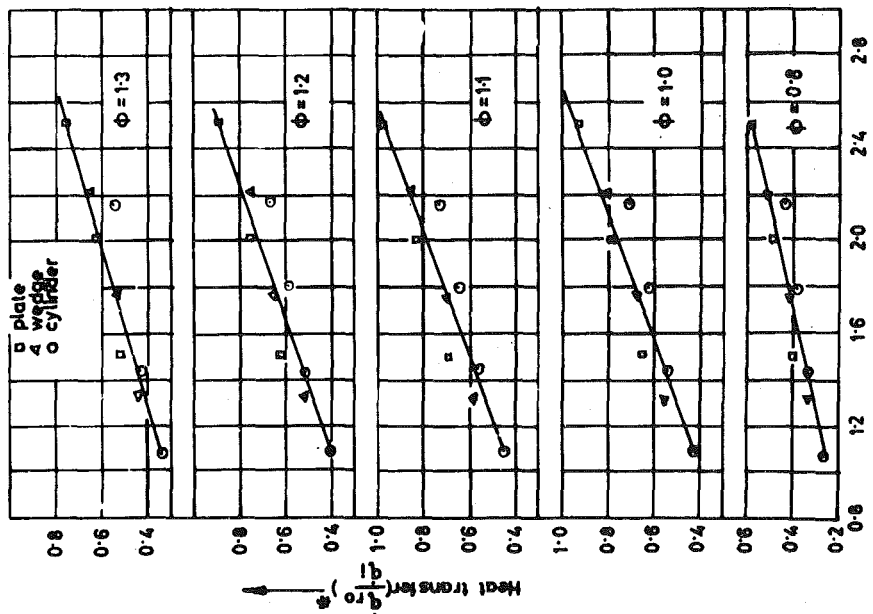

Fig. 10 Correlation between recirculation strength and heat transfer to combustible stream

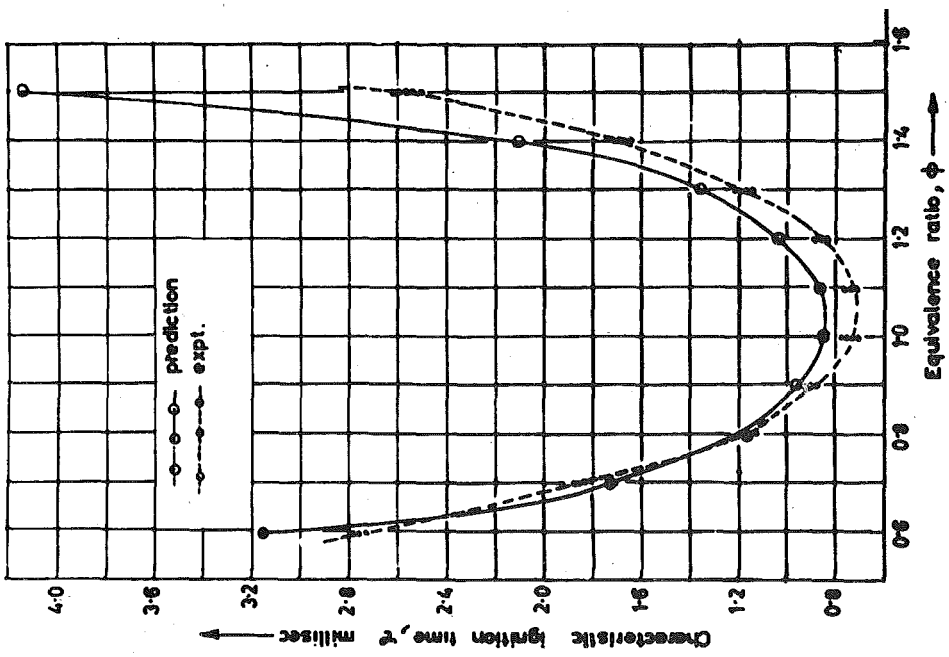

Fig. 9 Characteristic ignition time (comparison between prediction and experiment)

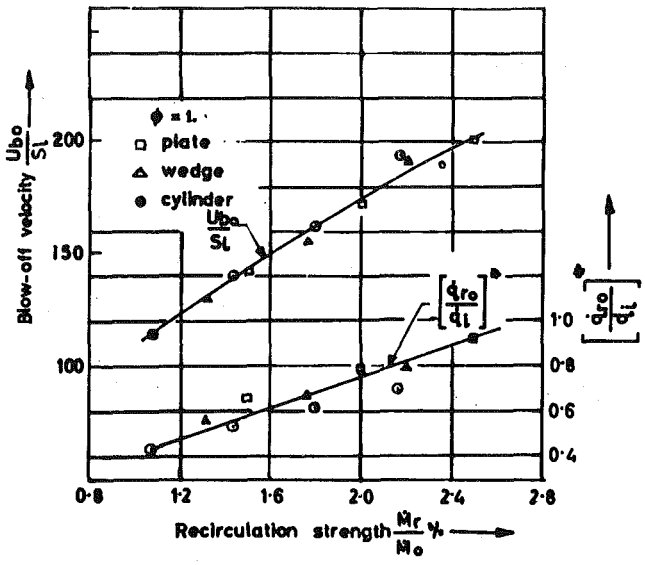

Fig. 12 Correlation of blow-off velocity with recirculation strength and heat transfer to combustible stream

recirculation strength appears to play an important role in the process of flame stabilization. However, this aspect may be further investigated with hot flow results using facilities of sophisticated technique like Laser Doppler Anemometry.

Conclusion

The role of recirculation zone in the process of flame stabilization by bluff-body is highlighted. It has been established that the generalized behavior of recirculation zone temperature and heat exchange holds good irrespective of bluff-body configurations and equivalence ratios. In the absence of hot flow data on recirculation strength, correlations have been attempted on the basis of cold flow results and the trends noticed indicate that close correlations exist between blow-off velocity, heat exchange and recirculation strength. The recirculation zone conveys to the combustible stream the necessary heat for flame generation; the strength of recirculation determines its heat exchange capacity and thus controls the flame stability.

Acknowledgment

The authors wish to thank the Director, CMERI, for his kind permission to publish the paper.

References

1 Penner, S. S. and Williams, F., "Recent Studies on Flame Stabilization of Premixed Flames," *Appl. Mech. Reviews,* Vol. 10, No. 6, 1957.

2 Williams, G. C., "Flame Stabilization of Premixed Turbulent Gases," *Appl. Mech. Survey,* 1966, p. 1157.

3 Williams, G. C., Hottel, H. C. and Scurlock, A. C., *Third Symposium on Combustion, Flame and Explosion,* Baltimore, The Williams and Wilkins Co., 1949, p. 21.

4 Zukoski, E. E. and Marble, F. E., "Experiments Concerning the Mechanism of Flame Blow-Off from Bluff-Bodies," *Proc. of the Gas-Dyanmics Symp. on Thermochemistry,* North Western University, Evanston, Ill., 1956, p. 205.

5 Kundu, K. M., Banerjee, D. and Bhaduri, D., "Theoreical Analysis on Flame Stabilization by a Bluff-body," *Combustion Science and Technology,* Vol. 17, Nos. 3 and 4, 1977, p. 153.

6 Bovina, T. A., *Seventh Symposium (International) on Combustion,* Butterworths Sct. Pub., Lond, 1959, p. 692.

7 Winterfield, G., *Tenth Symposium (International) on Combustion,* The Combustion Institute, Pittsburg, 1965, pp. 1265.

8 Williams, F. A., *Combustion Theory,* Addison Wesley, London, 1965, pp. 319–323.

9 Kundu, K. M., Banerjee, D. and Bhaduri, D., "Mathematical Modelling of Flows in Bluff-Body Flame Stabilizers" *Applied Mathematical Modelling,* Vol. 1, June 1977, p. 276.

10 Davis, T. W. and Beér, J. M., *Thirteenth Symp. (International) on Combustion,* The Combustion Institute, Pittsburg, 1971, p. 617.

11 Matton, G. and Fouré, C., *Sixth Symp. (International) on Combustion,* Reinholdt, New York, 1957, p. 757.

12 Fristrom, R. M. and Westenberg, A. A., *Flame Structure,* McGraw Hill, 1965, p. 330.

13 Lewis, B. and Von-Elbe, G., *Combustion, Flames and Explosion of Gases,* Academic Press, London, 1961, pp. 339, 389, 436–446.

14 Keenan, J. H. andKaye, J., *Gas Tables,* 12th ed., John Wiley and Sons Inc., New York, London, Sydney, 1966.

15 Spiers, H. M., *Technical Data on Fuel,* 6th ed., The British National Committee on World Power Conference, London, 1962.

16 Khitrin, L. N., *The Physics of Combustion and Explosion,* 2nd ed., Israel Prog. for Sct. Translation, Jerusalem, 1965., pp. 83, 142.

17 Beér, J. M. and Chigier, N. A., *Combustion Aerodynamics,* Applied Science Publishers Ltd., London, 1972 p. 79.

D. D. Rosard

Power Dynamics,
Havertown, PA 19083

Generalized Parameters for Selection of Turbines and Working Fluids for OTEC Power Systems

The choice of working fluid has a significant impact on the size and design characteristics of turbines for closed cycle OTEC (Ocean Thermal Energy Conversion) power systems. This paper examines turbine sizes and speeds for various candidate working fluids. The turbine performance and design limits are strongly influenced by blade stress criteria which have been ignored by previous investigators. Illustrative design parameters are given for a turbine using ammonia and scaling parameters are listed to compare the power outputs of turbines using other fluids. The design of a turbine for open-cycle OTEC power systems is largely dictated by the very high specific volume of the exhaust steam at a pressure of about 0.14 psia. In order to minimize the cost of turbines and generators through economy of scale, it is desirable to maximize the power output of a single turbine, and this leads to very large diameters and blade lengths. This paper explores the considerations which influence the choice of turbine size, blade length, speed, power output and efficiency.

Introduction

In the search for energy sources to replace the diminishing reserves of oil and natural gas, exploitation of the thermal gradient between ocean surface temperature which near the tropics can range from 80 to 85°F and the deep ocean water which can be 40 or 45°F, depending on depth, appears to be an effective use of solar energy. The ocean surface acts as a collector of immense surface, the volume of water between the surface and the thermoclyne 100 ft below surface acts as a thermal storage reservoir which provides a continuous source of power through night and day.

Several types of thermodynamic cycles have been conceived to translate this temperature gradient into useful electrical power. One is an open cycle, Fig. 1(*a*) in which warm ocean water is flashed into steam which flows through a turbine and is then condensed. Another is a closed cycle, Fig. 1(*b*), in which the warm sea water is used to vaporize a working fluid, such as ammonia, propane, freon, etc. in a heat exchanger. This vapor then flows through a turbine and is condensed in another heat exchanger through which cold water flows after an upward journey of 2000 to 4000 ft through a pipe. The total temperature difference between warm water and cold water varies as a function of site, depth from which the cold water is drawn, and season. Typical values range from 35 to 40°F (19.5° to 22.2°C).

In a number of studies of ocean thermal power [1–6], it has been found that the allocation of the total ΔT available between evaporator, turbine and condenser follows approximately the pattern shown in Table 1, (the exact allocation for minimum total plant cost can be established by a detailed system cost optimization).

The turbine design has a strong influence on the overall system. The first influence is related to the maximum power which can be gener-

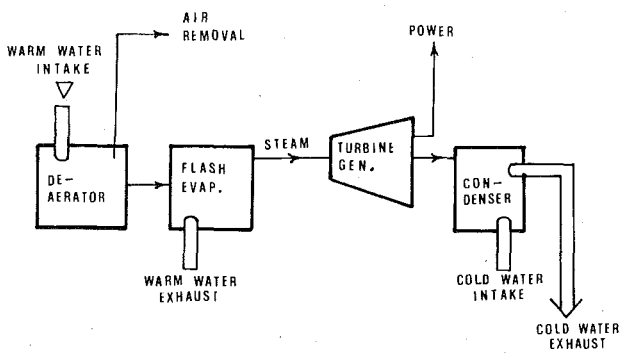

Fig. 1(*a*) Open cycle

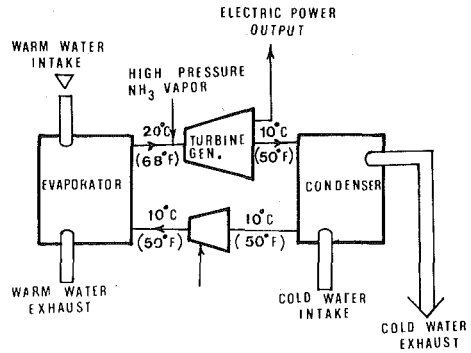

Fig. 1(*b*) Closed cycle

Fig. 1 Schematic diagrams

Contributed by the Power Division for Publication in THE JOURNAL OF ENGINEERING FOR POWER. Manuscript received at ASME Headquarters November 17, 1978.

Table 1 Allocation of ΔT

	Closed Cycle	Open Cycle
Warm water inlet °F	80	80
outlet °F	75	76
Working Fluid inlet °F	70	75
outlet °F	50	45
Cold water inlet °F	40	40
outlet °F	45	44

ated by a single turbine generator, since this determines the scale of all system components. Secondly, the turbine efficiency directly affects the net power output and therefore, the cost per unit of power. Finally, the cost of the turbine-generator itself affects the total system cost, particularly with an open cycle in which the turbine generator cost is a large fraction of total plant cost.

The pressure ratio in either open or closed cycle turbines is suited to a single stage of axial flow blading. The maximum power output is limited either by the bending stresses caused by the aerodynamic blade loading or by the centrifugal stresses in blades, blade fastenings and rotor. This paper will discuss the thermodynamic and mechanical relations which affect turbine design performance and size limitations. While the relations presented here are less general than those of Balje [7–9], they provide a more comprehensive overview of the important design parameters in the range of interest.

Thermodynamic Relations

Two key design parameters influence the turbine efficiency, as illustrated in Fig. 2. One is velocity ratio, or ratio of the linear blade velocity at the mean diameter to the fluid velocity. The other is average gauging or ratio of the total flow area at the throat of the blades to the total annulus area. The gauging is related to the stagger angle of the blades, varies from hub to tip, and is generally larger in the rotating blade than in the stationary blade which precedes it. The relationship between stationary and rotating blade gauging depends on the "degree of reaction" and on the objective to avoid tangential velocity or swirl at the exit of the rotating row since this would increase the exhaust loss. In this paper, all curves are drawn for stages with 50 percent reaction and axial exhaust velocity.

A study of Fig. 2 leads to the following observations:

1 The optimum velocity ratio varies only slightly with gauging.
2 The higher values of gauging lead to lower efficiency, as a result of the higher axial exit velocity, thus higher leaving loss. If an exhaust diffuser is used to reduce the turbine exit pressure, thus recovering some of the exit kinetic energy, the leaving loss is effectively reduced as shown and the penalty for using higher values of gauging is reduced. As will be discussed later, the advantages of higher gauging are substantial reductions in blade length and width.

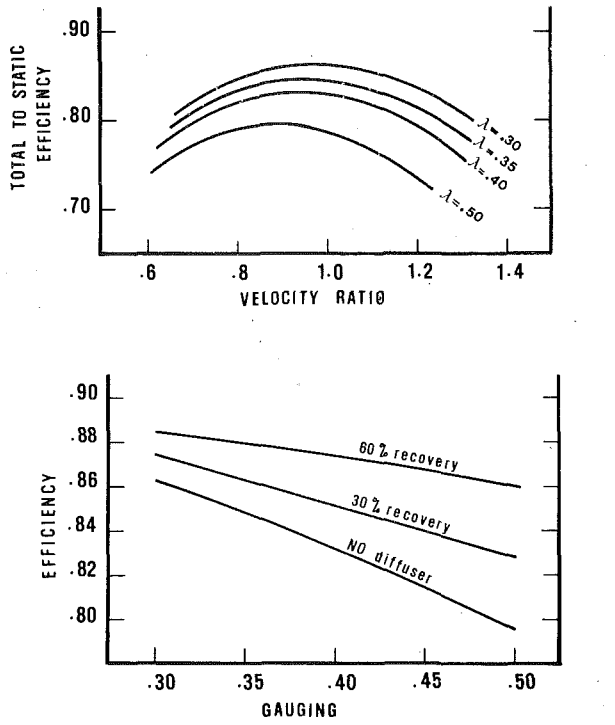

Fig. 2 Efficiency versus velocity ratio, gauging and exhaust diffuser recovery

Solidity—Ratio of Blade Chord to Pitch

A good discussion of the aerodynamic factors which affect solidity selection can be found in Chapter 4 of [10].

For 50 percent reaction blading, the optimum solidity is generally between 1.5 and 2 at the mean diameter. At the blade tip, the chord is smaller and the spacing larger; therefore, the solidity will be smaller. At the hub, the chord is larger and the spacing smaller; therefore, the solidity is larger. For long blades, a solidity at the hub which is higher than the optimum value is usually dictated by mechanical blade design considerations. Beyond a solidity of 4, however, significant increases in losses can be expected.

Ratio of Hub Diameter to Tip Diameter

For a mean diameter selected to provide a favorable velocity ratio, the flow area can be increased by selecting longer blades. One of the limitations to the blade length stems from the need to maintain a positive pressure drop across the rotating blades along their whole length, including the hub. Radial equilibrium of the flow is maintained

Nomenclature

A = annulus area = $DM\ell$
C = constant (= 1 if ΔP across rotor blade is constant from hub to tip)
D_m = mean diameter
G = mass flow
J = unit conversion factor = 778 ft-lb/btu = 4.187 W.S./cal.
K = ℓ/D
ℓ = blade length, in.
N = RPM
n = no. of rotor blades
P = power output, KW
Q = volumetric flow
R = unit conversion factor = 737.6 ft-lb/kw s = 1000 N.m./kw.s.
s = permissible centrifugal stress in turbine blades
S = solidity = chord/pitch
u = wheel speed at the mean diameter, ft/s
v = specific volume at turbine exit
V_a = axial exit velocity
W_m = blade chord at mean diameter
X = total plant cost
X_1 = turbine cost
X_2 = balance of plant cost
Z_{min} = minimum blade section modules at hub
Z_{max} = maximum blade section modules at hub
N_s, D_s = specific speed, specific diameter
α = angle between total moment vector and blade Imin axis
η = turbine efficiency
ρ = vapor density at turbine exit
ΔP = pressure drop across rotating blade row
Δh = enthalpy drop from turbine inlet to exit
λ = gauging $\cong$ sin (exit flow angle)
σ_{cf} = centrifugal stress at base of rotor blade
σ_b = gas bending stress at base of rotor blade

Subscripts

m = at mean diameter
i = isentropic
a = axial
t = tangential

by a variation of pressures and velocities from hub to tip. At the hub, the pressure drop across the rotating row is smaller than at the mean diameter and in long blades the hub section approaches that of an impulse blade. Some reaction (or pressure drop) must be maintained, however, to avoid recirculation and other flow anomalies in the hub regions. How much reaction is required at the hub for best overall performance is the subject of detailed flow field investigations, but for this general study a reaction of at least 5 percent will be used. For the pressure ratios, and velocities associated with the OTEC cycle, this places a lower limit on the ratio of hub diameter to tip diameter of approximately 0.48 corresponding to an upper blade length limit of 35 percent of the mean diameter.

Mechanical Relations

Maximum Blade Length. The centrifugal stress at the base of a rotor blade can be expressed as:

$$\sigma_{CF} = 4\ell D_m N^2 K_1 K_2 \times 10^{-6}$$

where K_1 is a density factor, K_2 is a taper factor, ℓ and D are in inches, σ is in psi.

If the permissible centrifugal stress, as established to provide the required safety margin and the capability to withstand overspeed contingencies is specified as s, the maximum blade length is

$$\ell_{\max} = \frac{10^6\, s}{4\, D_M N^2 K_1 K_2}$$

$$\frac{\ell_{\max}}{D_m} = \frac{685\, s}{u^2 K_1 K_2}$$

Power Output and Flow

The power generated can be expressed as

$$P = 1.05\, \eta G \Delta h_i = 1.05\, \eta \Delta h_i \frac{Q}{v}$$

The exit volumetric flow is

$$Q = 0.95 \frac{Pv}{\eta \Delta h_i}$$

It can also be expressed as

$$Q = Av_a$$

where $v_a = \lambda(2gJ\Delta h)^{1/2}$

A = annulus area, $= \pi D_m \ell$

Blade Bending Stress

The tangential moment at the base of each blade is equal to:

$$M_t = \frac{30\, R}{\pi^2} \frac{P\ell W_m}{N D_m{}^2 S_m}$$

An axial moment is also produced by the pressure drop across the rotating row of blades.

$$M_a = \frac{\ell^2 W_m}{2S_m} \Delta P_m C$$

where C reflects the radial variation of ΔP.

The total bending moment, M, is the vector sum of M_t and M_a. The maximum bending stress is then

$$\sigma_b = \frac{M \cos \alpha}{Z_{\min}} + \frac{M \sin \alpha}{Z_{\max}}$$

where α is the angle between the total moment vector and the $I_{\min}$ axis.

Fluid Properties

The significant properties of candidate working fluids which influence the turbine design are listed in Table 2.

Turbine Design Parameters

Values of specific mean diameter D_s, blade length ℓ_s and blade width W_s are given in Fig. 3 as a function of specific speed N_s. The plots reflect the following relations.

$$D_s N_s = 108.3\, [(1 - \lambda^2)\eta]^{0.5}$$

$$D_s \ell_s = \frac{1}{\pi (g\eta)^{0.5} \lambda} = \frac{0.0575}{\lambda}$$

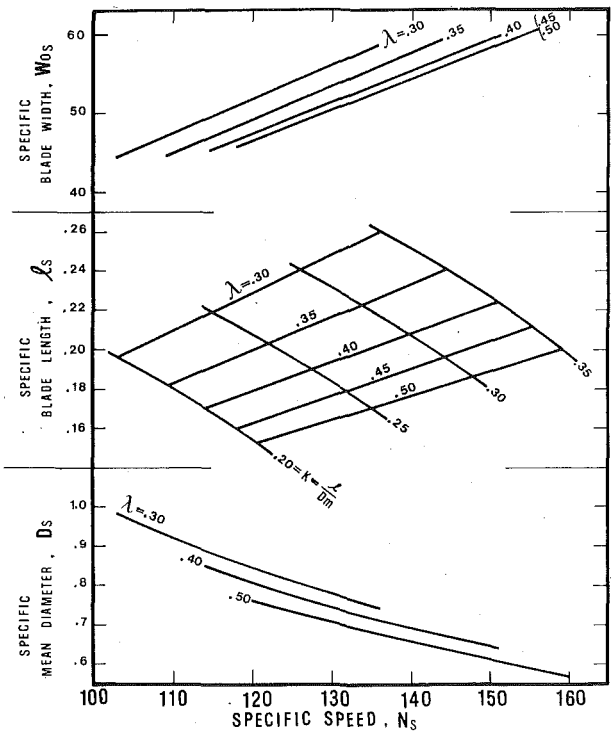

Fig. 3 Specific dimensions versus specific speed and gauging

Table 2 Fluid properties and scaling parameters

	Δhi Btu/lb	v ft3/lb	For P = 37 MW D/Ds ft	W/Ws in	N/Ns RPM	For Fixed Size P/Po	N/No
CO_2	2.73	0.120	6.28	0.366	7.33	1.40	0.37
Ammonia	19.85	3.294	7.43	0.223	16.7	1.0	1.0
Propane	5.92	1.15	10.88	0.302	6.23	0.46	0.55
F-22	3.23	0.556	11.91	0.351	4.20	0.39	0.40
F-502	2.37	0.379	12.41	0.379	3.46	0.36	0.35
F-500	2.91	0.669	14.13	0.360	3.36	0.28	0.38
R-12/21	2.87	0.77	15.38	0.362	3.08	0.23	0.38
F-12	2.41	0.655	16.1	0.378	2.69	0.21	0.35
F-114	2.22	1.645	27.15	0.386	1.53	0.075	0.33
F-11	3.02	4.41	35.3	0.357	1.37	0.044	0.39
F-113	2.62	8.43	54.3	0.370	0.83	0.019	0.36

* for a gas bending stress of 6000 psi

As shown, the blade length and blade width both increase if the gauging is reduced to increase turbine efficiency (see Fig. 2). The blade width is also influenced by the permissible level of gas bending stress, which is related to the possibility of blade vibration caused by the lack of perfect uniformity of flow around the circumference. Since the damping in turbine blades is small, large amplifications of loading variations are possible if one of the blade modes of vibration happens to be in resonance with a multiple of the running speed. Stress limits are influenced by the natural frequencies of the blades, the fatigue strength of the blade material, stress concentrations, centrifugal stress, effect of the working fluid on corrosion fatigue and on the degree of nonuniformity in the inlet and exit flows.

Illustrative Design—Closed Cycle Turbines

A double-flow turbine design for closed cycle applications is illustrated in Fig. 4.

Using ammonia as the working fluid, and a turbine output of 37 MW[1] for each stage, the range of speeds, diameters and blade dimensions is shown in Fig. 5. For other working fluids, the speeds can be derived from the relation:

$$\frac{N}{N_s} = \frac{H^{0.75}}{Q^{0.5}} \quad \text{where} \quad H = 778\,\Delta h_i$$

$$Q = 0.95\,\frac{P_U}{\Delta h_i \cdot \eta_T}$$

The dimensions can be derived from:

$$\frac{D}{D_s} = \frac{\ell}{\ell_s} = \frac{Q^{0.5}}{H^{0.25}} \qquad \frac{W}{W_s} = \frac{P^{0.5}}{H^{0.25}\sigma^{0.5}}$$

Values of D/D_s and N/N_s for 37 MW are listed in Table 2. If the power output of an ammonia turbine of given dimensions is P_0 and its speed is N_0, the comparative values of power output and speed with other fluids can also be derived from Table 2.

Illustrative Design—Open Cycle Turbine

An interesting design option utilizes the largest disk which can be forged using currently available facilities (about 17 ft in diameter). This is also a size which can be shipped by rail. The tip diameter is limited by thermodynamic relations to maintain a positive pressure gradient at the blade hub.

Illustrative turbine design parameters, using a blade gauging of 0.40, are listed in Table 3.

If the blade gauging is reduced, thus reducing the flow through the turbine, the turbine efficiency can be increased, but its power output will be reduced, thus increasing the unit cost of the turbine while reducing the cost of the balance of plant. The optimum selection of gauging to minimize total plant cost is discussed in Appendix C.

The combination of speed, diameter and blade length are well within the limits of acceptable centrifugal stresses for a variety of blade materials including steel, titanium, aluminum or Fiberglas.

Conclusions

The generalized curves, tables, and formulas provided in this paper can be used to optimize the selection of turbine speed, diameter, blade length and blade width for any working fluid, enthalpy drop and desired power output.

Of the various working fluids examined, carbon dioxide leads to the smallest turbine size, but the high operating pressure makes it unattractive. Ammonia is a good choice for a closed cycle OTEC turbine, since it provides more than twice as much power for the same turbine size as its nearest competitor, propane.

An open cycle turbine is much larger, but obviates the need for expensive heat exchangers.

Selection of the best cycle, fluid, unit size and turbine parameters requires a system study which reflects cost, performance and reliability of all the elements of a complete power plant. The turbine selection curves can aid in such studies.

[1] Corresponding, approximately, to 25 MW net power output per stage.

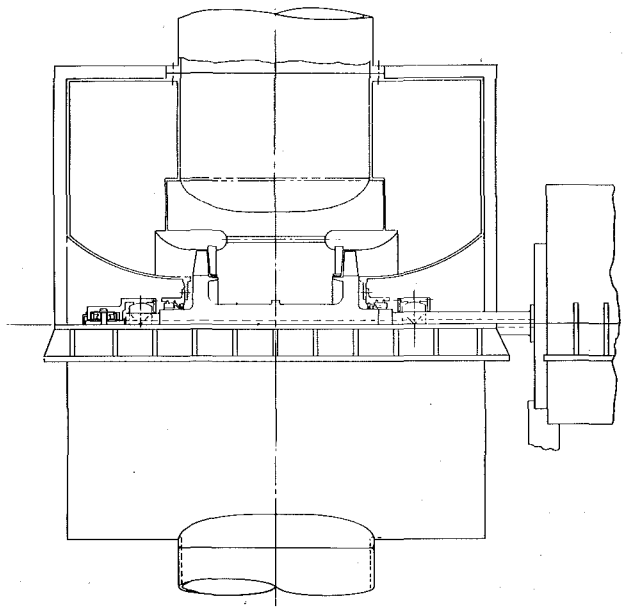

Fig. 4 Double flow turbine

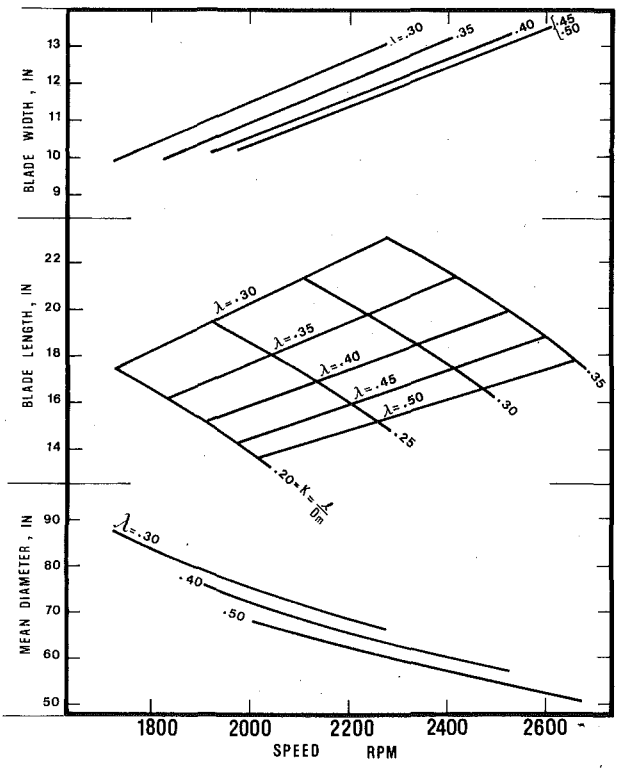

Fig. 5 Turbine diameter blade length and blade width versus speed and gauging for a 37 MW ammonia turbine stage with gas bending stress of 6000 psi.

References

1 TRW Systems Group "Ocean Thermal Energy Conversion Research on an Engineering Evaluation and Test Program," PB-246182, June 1975.

2 Nelson M. I., "Ocean Thermal Energy Conversion (OTEC) Plant Working Fluid Study," Proceedings Miami International Conference on Alternative Energy Sources, Dec. 1977.

3 Watt, A. D., Mathews, F. S. and Hathaway, R. E., "Potential of Open Cycle OTEC, A General Survey," Proceedings Fourth Ocean Thermal Energy Conversion (OTEC) Conference, University of New Orleans, New Orleans, La., March 1977.

4 Watt, A. D., Mathews, F. S. and Hathaway, R. E., "Open Cycle Ocean Thermal Energy Conversion, A Preliminary Engineering Evaluation," Fifth OTEC Conference, University of Miami, Coral Gables, Fla., Feb. 1978.

Table 3 Sample turbine design parameters—open cycle

Base dia = 17 ft
Mean dia = 27.5 ft
Tip dia = 38 ft
Blade length = 10.5 ft

Speed = 720 RPM
u, at mean dia = 1037 ft/s
Annulus area = 907 ft^2
Blade gauging = 0.40
Power output = 12.6 Kw/ft^2
= 11.5 MW

Blade material	Steel			Titanium		Fiberglas	
No. of Blades	250			200		100	
	Hub	Mean	Tip	Hub	Tip	Hub	Tip
Pitch, in.	2.6	4.2	5.8	3.2	7.2	6.4	14.4
Solidity	3.4	1.5	1.1	3.4	1.1	3.4	1.1
Chord, in.	8.8	6.4	6.2	11	7.8	22	15.6
Avg. thickness, in.	0.4	0.2	0.12	0.5	0.15	1.0	0.5
Area, in.^{2}	3.5	1.3	.75	5.5	1.2	22	7.8
Density, lb/in.^{3}		0.281		0.162		0.020	
Area ratio, hub/tip		4.7		4.7		3.3	
K_1		1		0.57		0.07	
K_2		0.39		0.39		0.46	
C.F. Stress, Ksi		33.6		19.2		3.1	
Steam bend. stress, Ksi		3.1		2.0			
Wt. per blade, lbs.		79		70		12	
Wt. per row, lbs		19,700	14000	1200			
C.F. per row, 10^6 lbs		30		21.1		7.6	
Rim weight, lbs		7500					
Rim C.F., 10^6 lbs		11					
Disk weight, lbs.		41000					
Disk avg. stress, Ksi		27					

5 Sciubba, C. "New Concepts Enhance Position of Open and Hybrid OTEC Power Cycles," Fifth OTEC Conference, Feb. 1978.

6 Barsness, E. J., Rosard, D. D., Miller, R. T., and Cunninghis, S. "Conceptual Design of an OTEC Power System Using Modular Heat Exchangers," Fifth OTEC Conference, Feb. 1978.

7 O. E. Balje, "A Study on Design Criteria and Matching of Turbomachines: Part A—Similarity Relations and Design Criteria of Turbines," ASME JOURNAL OF ENGINEERING FOR POWER, Vol. 84, No. 1 Jan., 1962, pp. 83–102.

8 O. E. Balje and R. L. Binsley, "Axial Turbine Performance Evaluation. Part A Loss-Geometry Relationships," ASME JOURNAL OF ENGINEERING FOR POWER, Vol. 90, No. 4 Oct. 1968, pp. 341–348.

9 O. E. Balje and R. L. Binsley, "Axial Turbine Performance Evaluation. Part B—Optimization With and Without Constraints," ASME JOURNAL OF ENGINEERING FOR POWER, Vol. 90, Oct. 1968, pp. 349–360.

10 Glassman, A. J., ed "Turbine Design and Application," Vol. 2 1973 NASA SP-290.

APPENDIX A

Derivation of Formulas for Specific Speeds and Specific Dimensions

Mean Diameter

$$\text{let} \quad \ell = KD$$

$$A = \pi D\ell = \frac{Q}{V_a} = \frac{Q}{\lambda(\eta g H)^{0.5}}$$

$$\pi D^2 K = \frac{Q}{\lambda(\eta g H)^{0.5}}$$

$$D = \frac{Q^{0.5}}{(\pi K\lambda)^{0.5}(\eta g H)^{0.25}}$$

$$D_s = D\frac{H^{0.25}}{Q^{0.5}} = \frac{1}{(\pi K\lambda)^{0.5}(\eta g)^{0.25}}$$

Blade Length

$$\ell_s = \ell\frac{H^{0.25}}{Q^{0.5}} = KD_s = \frac{K^{0.5}}{(\pi\lambda)^{0.5}(\eta g)^{0.25}}$$

Speed

$$u = \frac{\pi DN}{60} = (\eta g H)^{0.5}(1-\lambda^2)^{0.5}$$

$$N = \frac{60}{\pi}\frac{(\eta g\mathrm{H})^{0.5}(1-\lambda^2)^{0.5}(\pi Kg)^{0.5}(\eta g H)^{0.25}}{Q^{0.5}}$$

$$= \frac{60}{\pi}(\eta g)^{0.75}(1-\lambda^2)^{0.5}(\pi Kg)^{0.5}\frac{H}{Q^{0.5}}$$

$$N_s = N\frac{Q^{0.5}}{H^{0.75}} = \frac{60}{\pi^{0.5}}(\eta g)^{0.75}K^{0.5}[\lambda(1-\lambda^2)]^{0.5}$$

Blade Width

$$\text{Number of blades} \quad n = \frac{\pi DS}{W_m}$$

Tangential force per blade

$$F_t = \frac{60}{\pi}\frac{RP}{NDn}\frac{60R}{\pi^2}\frac{P}{ND^2S}W_m$$

where R = unit conversion factor

= 737.6 ft-lb/s/KW

= 1000 N.m/s/KW

$$M_t = F_t\frac{\ell}{2} = \frac{30R}{\pi^2}\frac{\ell W_m P}{ND^2S}$$

Bending Stress

$$\sigma_t = \frac{Mt}{Z}$$

$$\text{let} \quad Z = a\,W_0{}^3$$

$$W_m = b\,W_0$$

$$W_0{}^3 = \frac{M_t}{a\sigma}$$

$$W_0{}^2 = \frac{M_{t\,b}}{a\sigma W_m} = \frac{30R}{\pi^2}\frac{b\ell P}{ND^2S\,a\sigma}$$

$$\text{since} \quad ND = \frac{60}{\pi}[\eta g(1-\lambda^2)]^{0.5}H^{0.5}$$

$$\text{and} \quad \frac{\ell}{D} = K$$

$$W_0 = \left(\frac{R}{2\pi}\right)^{0.5}\frac{(bK)^{0.5}}{(Sa)^{0.5}(\eta g)^{0.25}(1-\lambda^2)^{0.25}}\frac{P^{0.5}}{\sigma^{0.5}H^{0.25}}$$

$$W_{0s} = W_0\frac{H^{0.25}\sigma^{0.5}}{P^{0.5}} = \left(\frac{R}{2\pi}\right)^{0.5}\frac{b^{0.5}}{(Sa)^{0.5}(\eta g)^{0.25}}\frac{\mathrm{K}^{0.5}}{(1-\lambda^2)^{0.25}}$$

Summary

$$a = Z/W_0{}^3$$

$$b = W_m/W_0$$

$$K = \ell/D$$

$$D_s = \frac{0.564}{(\eta g)^{0.25}} \frac{1}{(K\lambda)^{0.5}}$$

$$\ell_s = \frac{0.564}{(\eta g)^{0.25}} \left(\frac{K}{\lambda}\right)^{0.5}$$

$$N_s = 33.85\ (\eta g)^{0.75}\ [K\lambda(1-\lambda^2)]^{0.5}$$

$$W_{0s} = \frac{1}{(\eta g)^{0.25}} \left(\frac{R}{2\pi}\right)^{0.5} \left(\frac{b}{Sa}\right)^{0.5} \frac{K^{0.5}}{(1-\lambda^2)^{0.25}}$$

$$\frac{D}{D_s} = \frac{Q^{0.25}}{H^{0.25}}$$

$$\frac{\ell}{\ell_s} = \frac{Q^{0.5}}{H^{0.25}}$$

$$\frac{N}{N_s} = \frac{H^{0.75}}{Q^{0.5}}$$

$$\frac{W}{W_s} = \frac{P^{0.5}}{H^{0.25}\sigma^{0.5}}$$

J = 778 ft-lb/Btu = 4.187 W.s/cal.

R = 738 ft-lb/KW.s = 1000 N.m/Kw.s

$$H = J\,\Delta hi$$

$$Q = \frac{RPv}{\eta_T H}$$

Table 1(*A*) Specific speeds and dimensions

g = 32.2 ft/s^2, η = 0.95, S = 1.8, b = 0.8, a = 0.01

	$K/\lambda \rightarrow$	0.3	0.35	0.4	0.45	0.5
$N_s = 440$	0.2	103	109	114	118	120
$[K\lambda(1-\lambda^2)\sigma^{0.5}$	0.25	115	122	127	132	135
	0.3	126	133	140	144	148
	0.35	136	144	151	156	159
$D_s = \frac{0.24}{(K\lambda)^{0.5}}$	0.2	0.98	0.91	0.85	0.80	0.76
	0.25	0.81	0.76	0.72	0.72	0.68
	0.3	0.80	0.74	0.69	0.65	0.62
	0.35	0.74	0.69	0.64	0.61	0.57
$\ell s = 0.24\left(\frac{K}{\lambda}\right)^{0.5}$	0.2	0.196	0.181	0.170	0.16	0.152
	0.25	0.219	0.203	0.190	0.279	0.170
	0.3	0.24	0.222	0.207	0.196	0.186
	0.35	0.26	0.24	0.224	0.21	0.20
$W_{0s} = 97.13$	0.2	44.5	44.87	45.4	45.9	46.7
$\frac{K^{0.5}}{(1-\lambda^2)^{0.25}}$	0.25	49.7	50.15	50.7	51.47	52.26
	0.3	54.5	54.9	55.56	56.2	57.3
	0.35	58.86	59.4	59.9	60.7	61.8

APPENDIX B

Stress and Weight of "Uniform Stress" Blade

In a blade of uniform cross section areas from hub to tip the maximum centrifugal stress is at the hub and is equal to:

$$\sigma_P = \frac{\rho\omega^2}{2}(R_t^2 - R_b^2)$$

This stress can be reduced by tapering the blade from hub to tip. The optimum taper is one which allows the largest tip area while maintaining the stresses below the allowable value for the selected material. This is achieved by profiling the area from tip to hub as shown on Fig. 1(*B*).

The area is constant from the tip to an intermediate radius R, where the stress reaches the allowable value. From R, to the hub, the area varies to produce a uniform stress.

Stress at R_1

$$\sigma = \rho\omega^2 \int_{R_1}^{R_t} RdR = \frac{\rho\omega^2}{2}(R_t^2 - R_1^2)$$

$$R_t^2 - R_1^2 = \frac{2\sigma}{\rho\omega^2}$$

Let $\frac{2\sigma}{\rho\omega^2} = B^2$

$$R_1^2 = R_t^2 - B^2$$

For constant stress from R_1 to R_b

$$\sigma dA = \rho AR\omega^2 dR$$

$$\frac{dA}{A} = \frac{\rho\omega^2}{\sigma} RdR$$

$$= \frac{2}{B^2} RdR$$

$$1n\frac{A_b}{A_1} = \frac{1}{B^2}(R_1^2 - R_b^2) = \frac{1}{B^2}(R_t^2 - B^2 - R_b^2)$$

$$1n\frac{A_b}{A_1} = \frac{1}{B^2}(R_t^2 - R_b^2) - 1$$

$$\sigma = \frac{B^2}{2}\rho\omega^2 = \frac{1}{1n\frac{A_b}{A_1} + 1}(R_t^2 - R_b^2)\frac{\rho\omega^2}{2}$$

Stress Taper Factor $K_2 = \frac{\sigma}{\sigma_p} = \frac{1}{1n\frac{A_b}{A_1} + 1} = \frac{1}{1n\frac{A_b}{A_t} + 1}$

Blade Weight. The weight of an ideally tapered blade is equal to:

$$W = A_b \frac{g\sigma}{\omega^2} \frac{1}{R_b} + \frac{A_t}{A_b}\left(\frac{2}{R_t + R_1} - \frac{1}{R_1}\right)$$

The weight of a parallel blade is

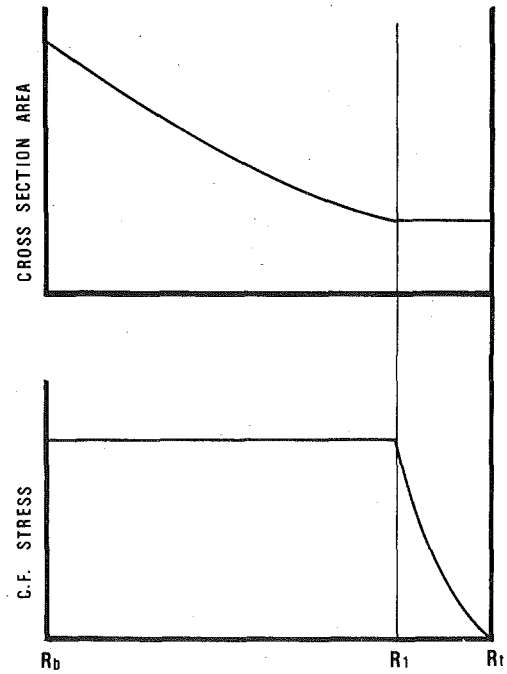

Fig. 1(*B*) Optimum blade taper

$$W_p = A_b\, \rho g \ell$$

The taper factor $K_4 = W/W_p$ is equal to:

$$K_4 = \frac{1 + \frac{A_t}{A_b}\frac{R_b}{R_t + R_1}\left(1 - \frac{R_t}{R_1}\right)}{1 + \ln\frac{A_b}{A_t}} \frac{R_t + R_b}{2R_b}$$

where $R_1 = (R_t{}^2 - B^2)^{1/2}$

$$B^2 = \frac{2\sigma}{\rho\omega^2}$$

If $R \cong R$ and $\frac{A_t}{A_b}$ is small,

$$K_4 \cong \frac{R_m}{R_b}\frac{1}{1 + \ln\frac{A_b}{A_t}} = \frac{R_m}{R_b} K_2$$

In summary, the blade stress is

$$\sigma = \frac{\rho\omega^2}{2}(R_t{}^2 - R_b{}^2)\, K_1 K_2$$

$$= 4 \times 10^{-6}\, \ell\, D_m N^2\, K_1 K_2$$

where K_1 = density factor = 1 for steel

$$K_2 = \text{taper factor} = \frac{1}{1 + \ln\frac{A_b}{A_t}}$$

the blade weight is

$$w = 0.28\, A_b\, \ell K_1 K_4$$

K_4 = taper factor

$$= \frac{R_m}{R_b}\frac{1 + \frac{A_t}{A_b}\frac{R_b}{R_b + R_1}\left(1 - \frac{R_t}{R_1}\right)}{1 + 1n\frac{A_b}{A_t}}$$

APPENDIX C

Disk Stresses

For preliminary design purposes, it is prudent to assume that the disc rim to which the blades are attached by means of pins, serrated roots, etc., does not carry any tangential loads and acts as dead weight supported by the remainder of the disk.

The centrifugal load of the disk rim and blade roots is:

$$F = 16.67 \times 10^{-6}\, bN^2(R_2{}^3 - R_1{}^3)K_1$$

Where N = rotating speed, RPM, b = rim width, R_2 = blade hub radius, and R_1 = inner rim radius.

The centrifugal stresses in a flat rotating disk without rim load are:

$$\text{Max. stress (at center)} = \frac{3 + \upsilon}{8}\frac{\gamma\omega^2 R^2}{g}$$

$$\text{Average tangential stress} = \frac{1}{3}\frac{\gamma\omega^2 R^2}{g} = 2.65 \times 10^{-6} N^2 R^2 K_1$$

where υ = Poisson's ratio, γ = density of disk material, R = disk outer radius, and K_1 = density factor = 1 for steel ($\gamma = 0.28$ lb/in.^{3})

The bursting speed of disks made of ductile material is closely related to the average tangential stress. The average tangential stress in a rotating profiled disk with rim loads due to the blades and rim is:

$$\sigma_{AT} = F_1\, \sigma_R + F_2 \sigma_0$$

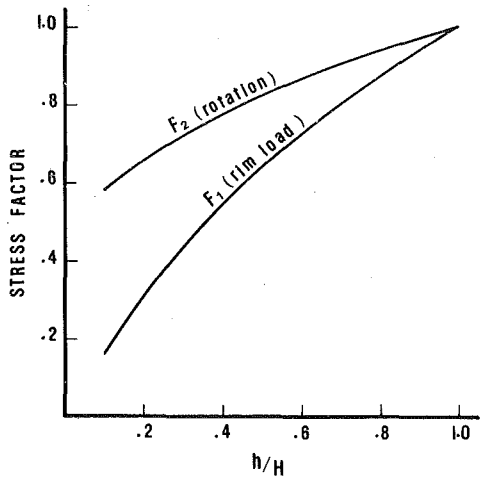

Fig. 1(C) Stress factors for profiled disk

where σ_R = radial stress at the junction with the rim

$$= \frac{\text{C.F. (blades)} + \text{C.F. (rim)}}{2\pi Rh}$$

σ_0 = average tangential stress of a flat disk without rim load

$$= 2.65 \times 10^{-6} N^2 R^2 K_1$$

The stress factors F_1 and F_2 are plotted in Fig. 1(C) as a function of the taper h/H.

APPENDIX D

Selection of Gauging

As illustrated in Fig. 2, the turbine efficiency decreases with increasing gauging. The power output for a selected turbine size, however, increases almost linearly with gauging as illustrated in Fig. 3 which presents the power output per unit of annulus area. The total cost of turbines to generate a specified output is thus significantly reduced, but since more flow is required to generate this output as a result of the lower efficiency, the cost of the balance of plant must increase.

The choice of gauging to minimize the total plant cost is influenced by the ratio of turbine cost to total plant cost, x_1/x

Since the power output of each turbine is

$$P = \left[\frac{1.05\,\Delta hi}{\upsilon} \mathrm{A}(2gJ\Delta h)^{1/2}\right]\eta\lambda$$

we can write that the cost of turbines is inversely proportional to the output of each turbine

$$\text{turbine cost} \quad X_1 = \frac{C_1}{\eta\lambda}$$

Since the vapor flow is inversely proportional to turbine efficiency the cost of the balance of plant can be expressed as

$$X_2 = C_2/\eta$$

To find the optimum value of λ, set $dX_1 + dX_2 = 0$

$$\frac{dX_1}{X_1} = -\frac{d\eta}{\eta} - \frac{d\lambda}{\lambda}$$

$$\frac{dx_2}{x_2} = -\frac{d\eta}{\eta}$$

$$\frac{dx_1 + dx_2}{x} = -\frac{d\eta}{\eta} - \frac{x_1}{x}\cdot\frac{d\lambda}{\lambda}$$

$$\frac{d\eta}{\eta} = \frac{x_1}{x}\frac{d\lambda}{\lambda}$$

Table 1(*D*) Optimum values of λ

X_1/X =	0.05	0.1	0.2	0.3	0.4
a = 0.42 (no diffuser)	0.23	0.32	0.44	0.53	0.60
a = 0.29 (30 percent recovery)	0.275	0.38	0.53	0.64	—
a = 0.16 (60 percent recovery)	0.37	0.52	—	—	—

Table 2(*D*) Fractional plant cost variations compared to $\lambda_0 = 0.4$ for various values of X_1/X (turbine cost/total plant cost) and λ (gauging)

X_1/X =	0.05	0.1	0.2	0.3	0.4
1) a = .42					
λ = 0.3	−0.018	−0.002	0.030	0.062	0.095
0.35	−0.011	−0.005	0.009	0.023	0.037
0.4	0	0	0	0	0
0.45	0.016	0.010	−0.001	−0.012	−0.023
0.5	0.037	0.027	0.006	−0.015	−0.036
0.55				−0.010	−0.040
0.6					−0.036
2) a = 0.29					
0.3	−0.007	0.009	0.042	0.074	0.107
0.35	−0.006	0.001	0.016	0.030	0.044
0.4	0	0	0	0	0.0
0.45	0.009	0.003	−0.008	−0.019	−0.030
0.5	0.021	0.011	−0.010	−0.030	−0.051
0.55			−0.006	−0.035	−0.064
0.6				−0.034	−0.070
0.65					−0.071
3) a = 0.16					
0.3	0.004	0.020	0.053	0.086	0.119
0.35	0.0003	0.007	0.022	0.036	0.050
0.4	0	0	0	0	0
0.45	0.002	−0.003	−0.015	−0.26	−0.037
0.5	0.007	−0.0036	−0.024	−0.4	−0.065
0.55		−0.001	−0.029	−0.057	−0.085
0.60			−0.031	−0.066	−0.100

$$\eta = 0.9 - a\lambda^2$$

$$d\eta = -2a\lambda d\lambda$$

$$(0.9 - a\lambda^2)x_1/x = 2a\lambda^2$$

$$\lambda = \left[\frac{0.9\, x_1/x}{a(x_1/x + 2)}\right]^{1/2}$$

It is of interest to establish the sensitivity of plant cost to nonoptimum gauging selections. To obtain a measure of this sensitivity, let us determine the fractional increase or decrease in plant cost as a function of gauging when compared to a nominal plant with an arbitrary gauging selection

$$X_1 = \text{turbine cost} = c_1/\eta\lambda$$

$$X_2 = \text{balance of plant cost} = c_2/\eta$$

$$X = \text{total plant cost} = X_1 + X_2$$

$$\frac{\Delta X_1}{X_1} = \frac{\eta_0\lambda_0}{\eta\lambda} - 1$$

$$\frac{\Delta X_2}{X_2} = \frac{\eta_0}{\eta} - 1$$

$$\frac{\Delta X_1 + \Delta X_2}{X} = \left(\frac{\eta_0\lambda_0}{\eta\lambda} - 1\right)\frac{X_1}{X} + \left(\frac{\eta_0}{\eta} - 1\right)\left(1 - \frac{X_1}{X}\right)$$

where $\eta = 0.9 - a\lambda^2$

$\eta_0 = 0.9 - a\lambda_0^2$

Table 2(D) illustrates the plant cost variations compared to an arbitrary selection of $\lambda_0 = 0.40$ with: 1) no exhaust diffuser (a = 0.42), 2) with 30 percent recovery in the exhaust diffuser (a = .28) and 3) with 60 percent recovery in the exhaust diffuser (a = .16).

It may be noted that for the smaller values of X_1/X, the cost increment is negative for small values of gauging, verifying that a gauging smaller than 0.40 would be optimum; for the larger values of X_1/X, on the other hand the cost increments are negative for values of gauging above 0.40.

With the more effective exhaust diffusers, the optimum gauging is higher, since the high exit velocities are less detrimental to the efficiency.

Journal of Engineering for Power

Technical Briefs

Some Dynamic and Time-Averaged Flow Measurements in a Turbine Rig

L. N. Krause[1] and G. C. Fralick[1]

Four types of sensors were used to make both dynamic and time-averaged flow measurements in a cold turbine rig to determine the magnitude of errors in time- averaged total-pressure measurement at a station 5 1/2 blade cords downstream from the rotor. The errors turned out to be negligible. The sensors and their intended use are discussed.

Introduction

There has been an increased interest in precision measurements of aircraft engine component efficiencies due to energy considerations. A desirable goal is to determine efficiency to within a fractional part of one percent. One of the common methods of determining component efficiency involves the use of total-pressure survey probes.

During the testing of the aircraft-type turbine described in [1], the accuracy of determining exit total pressure by use of conventional total-pressure probes downstream of the exit guide vanes was questioned (the station location (4.5) is shown in Fig. 1). One concern was that the time-varying total-pressure fluctuation associated with the rotating turbine wheel might be severe enough to influence the accuracy of the probes, resulting in error in efficiency determination.

An experiment was designed to determine the magnitude of existing fluctuations and associated errors. The experiment consisted of the use of four special purpose sensors (built into three probes) designed to measure both dynamic and time-averaged flow conditions at the station in question. The following will describe the probes and their intended use, and the results obtained. It is the intent of this short paper to focus the reader's attention more on the experimental technique rather than the results obtained, in case he has occasion in the future to make such measurements.

Probes and Intended Use

Several factors involving total-pressure probe geometry and pulsating flow conditions influence the time-averaged pressure indicated by total-pressure probes. These factors are discussed in [2] along with criteria to follow in order to obtain accurate time-averaged total pressures. Flow conditions which are important in influencing the accuracy of time-averaged total-pressure measurement and therefore important in knowing are the wave shape and magnitude of the total-pressure pulsations, and also the magnitude of the dynamic flow-direction variation (total-pressure measurement errors occur when excessive flow angle variations are encountered). So two dynamic probes were used, one to measure total-pressure pulsations, and one to measure dynamic flow direction variation. Fig. 2 shows the sensing tips of the probes.

The sensing portion of the dynamic total-pressure probe was a flush-mounted solid state pressure transducer 1.5 mm in diameter. A screen was located just in front of the silicon pressure sensing diaphragm to protect the diaphragm from air laden particles. This probe had a natural frequency greater than 50 kHz. The dynamic flow-direction probe consisted of a miniature strain-gaged cantilevered beam, 0.25 mm thick, 1.5 mm wide, and 2.5 mm long with an integral solid-state strain gage bridge at the base [3]. The bridge output was approximately proportional to the beam's angle-of-attack and this signal was used to measure the dynamic flow direction. This probe had a natural frequency of about 40 kHz.

Two other sensors were used in the experiment. Both were designed to measure the true time-averaged total pressure. One was a conventional total-pressure sensor which followed all of the criteria outlined in [2]. The outside tip diameter of this probe was 1.0 mm. The other probe was the so called double orifice or pneumatic probe. Two sonic orifices in series were used, and, by measuring steady-state

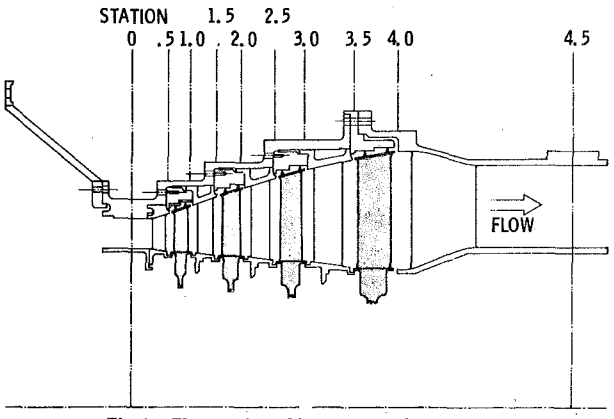

Fig 1 Flow path and instrumentation stations

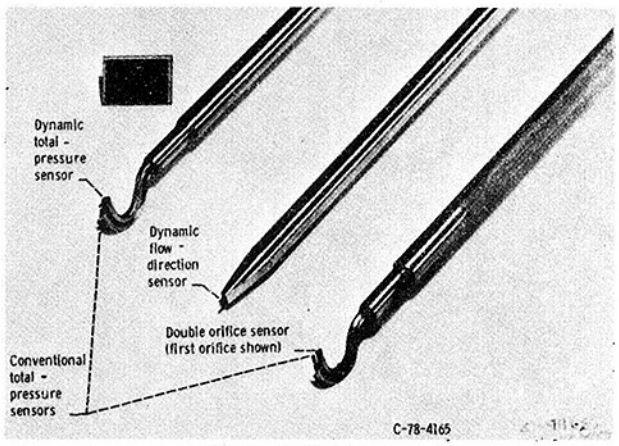

Fig. 2 Probe tips

[1] NASA-Lewis Research Center, 21000 Brookpark Rd., Cleveland, OH 44135.

Contributed by the Gas Turbine Division for publication in the JOURNAL OF ENGINEERING FOR POWER. Manuscript received at ASME Headquarters June 12, 1979.

conditions existing at the second orifice, the true time-averaged total pressure in front of the first orifice can be calculated. The outside tip diameter was 1.5 mm. This type of probe is discussed further in [4]. Oil filled averaging probes [5] and the double orifice probes (which are more elaborate and time consuming to use than conventional total-pressure probes) are considered the most accurate instruments for measuring time-averaged pressures in turbomachinery.

Test Conditions

The tests were conducted 5 1/2 blade cord widths downstream of the last rotor stage of the multi-stage turbine described in [1]. Total pressure at the test station was 1/2 atmosphere, and total temperature was 300 K. Turbine speed was 3700 rpm, and, with 50 blades, blade passing frequency was about 3100 blades per second. Measurements were made at a fixed circumferential position and two radial positions (mid and 3/4 span).

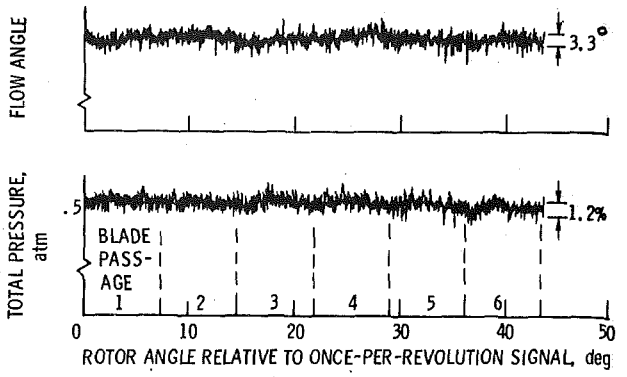

Fig. 3 Typical dynamic flow angle and total-pressure measurements 5 1/2 blade chord widths behind rotor

Results, Discussion, and Concluding Remarks

Typical results of the dynamic total-pressure probe and the dynamic flow-direction probe are shown on Fig. 3. Both dynamic flow angle and dynamic total pressure are plotted against rotor angle relative to a once per revolution signal. Six blade passages are shown and they are typical of all blade passages. The traces shown represent many revolutions of the rotor and were recorded using a sampling attachment on an oscilloscope feeding into a X-Y plotter.

The results shown on Fig. 3 indicate that, at station 4.5, fluctuations in both total pressure and flow direction are small enough to have negligible effect on the ability of a conventional total-pressure probe to indicate the correct time-averaged pressure. Peak-to-peak flow angle variations were only 3 deg, and peak-to-peak total pressure variations were only a little over 1 percent.

The double orifice probe agreed with the total-pressure probe (which was designed to give the correct average). These two measurements differed at most by 0.6 percent. This 0.6 percent difference in total pressure at station 4.5 corresponds to only 0.2 percent difference in turbine efficiency.

These experiments involving both dynamic and time-averaging probes indicate that there is no problem in time averaging using conventional total-pressure probes 5 1/2 blade chords behind the rotor reported in [1]. No measurements of the type discussed above were made closer to the rotor because of priority of other turbine tests. However, closer to the rotor the time-averaging problem can become serious, and measurements like those described herein are useful in determining the magnitude of such problems.

References

1 Whitney, W. J., Behning, F. P., Moffitt, T. P. and Hotz, G. M., "Cold-Air Investigation of 4 1/2 Stage Turbine with Stage Loading Factor of 4.66 and High Specific Work Output. I: Overall Performance," NASA TM X-3498, 1977.

2 Grant, H. P., "Measuring Time-Averaged Stagnation Pressure in Pulsating Air Flow," *Instrumentation in the Aerospace Industry*, Vol. 23, B. W. Washburn, ed., Instrument Society of America, 1977, pp. 425–438.

3 Krause, L. N. and Fralick, G. C., "Minature Drag-Force Anemometer," *Instrumentation in the Aerospace Industry*, Vol. 23, B. W. Washburn, ed., Instrument Society of America, 1977, pp. 461–467.

4 Krause, L. N., "Total-Pressure-Tube Averaging in Pulsating Flows," *Instrument Society of America Transactions*, Vol. 13, No. 2, 1974, pp 142–148.

5 Weyer, H. and Schodl, R., "Development and Testing of Techniques for Oscillatory Pressure Measurements Especially Suitable for Experimental Work in Turbomachinery," ASME Paper No. 71-FE-28, May 1971.